# Progress in Understanding Structure and Reactivity of Transition Metal Oxide Surfaces

Habilitationsschrift
zur Erlangung der Lehrbefähigung
für das Fach Physikalische und Theoretische Chemie

vorgelegt dem Rat der Mathematisch-Naturwissenschaftlichen Fakultät
der Humboldt-Universität zu Berlin
von
Dr. Joachim Paier

Prof. Dr.-Ing. Dr. Sabine Kunst
Präsidentin der Humboldt-Universität zu Berlin

Prof. Dr. Elmar Kulke
Dekan der Mathematisch-Naturwissenschaftlichen Fakultät

Berlin, den 16. Januar 2019

Gutachterinnen und Gutachter:

1. Prof. Dr. Joachim Sauer
2. Prof. Dr. Karsten Reuter
3. Prof. Dr. Thomas Heine

Vortrag vor dem Fakultätsrat: 21.01.2020

# Preface

The present thesis summarizes my research on elucidating atomic and electronic structure details of complex metal oxide surfaces. The work started in 2010, and it was embedded in two fruitful initiatives funded by the Deutsche Forschungsgemeinschaft (DFG), namely the Collaborative Research Center (CRC) 546 "*Structure, Dynamics and Reactivity of Aggregates of Transition Metal Oxides*" and the CRC 1109 "*Understanding of Oxide/Water Systems at the Molecular Scale: Structural Evolution, Interfaces and Dissolution*" with Professor Joachim Sauer and Professor Christian Limberg taking the lead as respective spokesmen. CRC 546, which was funded from 1999 to 2011, aimed at understanding structure-property or -functionality relationships based on atomic-level details of various aggregations of metal oxides. The CRC 1109 was funded from 2014 to 2018. It focused on the interaction of water with metal oxides of various length scales ranging from individual molecules, clusters, and oxide nanoparticles up to extended oxide surfaces of crystalline and amorphous bulk materials. Both CRCs involved tight collaboration between experimentally and theoretically working research groups offering me the great opportunity to contribute as a project leader.

# Contents

# 1 List of Publications

The star next to the publications' short-cuts **P1** to **P15** means corresponding authorship. The list follows an *order by oxide*. Publications **P1** and **P2** discuss $V_2O_3$ and hybrid functionals, **P3** to **P8** discuss $CeO_2$ as a support for $VO_x$, as well as the dehydrogenation of methanol, Au adatoms on ceria are examined in publications **P9** and **P10**, results on an Fe-based metal-organic framework, as well as on CO and $H_2O$ adsorption on $Fe_3O_4$ are reported in publications **P11** to **P15**.

**P1*** *The Surface Structure of $V_2O_3$ revisited*
F. E. Feiten, J. Seifert, J. Paier,* H. Kuhlenbeck,* H. Winter, J. Sauer, H.-J. Freund, *Phys. Rev. Lett.* **2015**, *114*, 216101.

**P2*** *Hybrid Density Functionals Applied to Complex Solid Catalysts: Successes, Limitations, and Prospects*
J. Paier,* *Catal. Lett.* **2016**, *146*, 861.

**P3*** *Oligomeric Vanadium Oxide Species Supported on the $CeO_2$(111) Surface: Structure and Reactivity Studied by Density Functional Theory*
C. Penschke, J. Paier,* and J. Sauer, *J. Phys. Chem. C* **2013**, *117*, 5274.

**P4*** *Stability and Migration Barriers of Small Vanadium Oxide Clusters on the $CeO_2$(111) Surface Studied by Density Functional Theory*
J. Paier,* T. Kropp, C. Penschke, and J. Sauer, *Faraday Discuss.* **2013**, *162*, 233.

**P5** *Support Effect in Oxide Catalysis: Methanol Oxidation on Vanadia/Ceria*
T. Kropp, J. Paier, and J. Sauer,* *J. Am. Chem. Soc.* **2014**, *136*, 14616.

**P6*** *Reactions of Methanol with Pristine and Defective Ceria (111) Surfaces: A Comparison of Density Functionals*
T. Kropp and J. Paier,* *J. Phys. Chem. C* **2014**, *118*, 23690.

**P7*** *Activity versus Selectivity of the Methanol Oxidation at Ceria Surfaces: A Comparative First-Principles Study*
T. Kropp and J. Paier,* *J. Phys. Chem. C* **2015**, *119*, 23021.

**P8** *Oxygen Defects and Surface Chemistry of Ceria: Quantum Chemical Studies Compared to Experiment*
J. Paier, C. Penschke, and J. Sauer,* *Chem. Rev.* **2013**, *113*, 3949.

**P9*** *Titration of $Ce^{3+}$ Ions in the $CeO_2$(111) Surface by Au Adatoms*
Y. Pan, N. Nilius,* H.-J. Freund, J. Paier,* C. Penschke, and J. Sauer,
*Phys. Rev. Lett.* **2013**, *111*, 206101; Erratum: *ibid.* **2015**, *115*, 9901.

**P10*** *Reduction and oxidation of Au adatoms on the $CeO_2$(111) surface – DFT+U versus hybrid functionals*
C. Penschke and J. Paier,* *Phys. Chem. Chem. Phys.* **2017**, *19*, 12546.

**P11*** *Structural and Electronic Effects on the Properties of $Fe_2$(dobdc) upon Oxidation with $N_2O$*
J. Borycz, J. Paier,* P. Verma, L.E. Darago, D.J. Xiao, D.G. Truhlar,* J.R. Long,* L. Gagliardi,* *Inorg. Chem.* **2016**, *55*, 4924.

**P12*** *Adsorption of Water on the $Fe_3O_4$(111) Surface: Structures, Stabilities, and Vibrational Properties Studied by Density Functional Theory*
X. Li and J. Paier,* *J. Phys. Chem. C* **2016**, *120*, 1056.

**P13*** *Surface Termination of $Fe_3O_4$(111) Films Studied by CO Adsorption Revisited*
X. Li, J. Paier,* J. Sauer, F. Mirabella, E. Zaki, F. Ivars-Barceló, S. Shaikhutdinov,* and H.-J. Freund, *J. Phys. Chem. B* **2018**, *122*, 527.

**P14*** *Cooperative Formation of Long-Range Ordering in Water Ad-layers on $Fe_3O_4$(111) Surfaces*
F. Mirabella, E. Zaki, F. Ivars-Barceló, X. Li, J. Paier,* J. Sauer, S. Shaikhutdinov,* H.-J. Freund, *Angew. Chem. Int. Ed.* **2018**, *57*, 1409; *Angew. Chem.* **2018**, *130*, 1423.

**P15*** *Water Adsorption on the $Fe_3O_4$(111) Surface: Dissociation and Network Formation*
E. Zaki, F. Mirabella, F. Ivars-Barceló, J. Seifert, S. Carey, S. Shaikhutdinov,* H.-J. Freund, X. Li, J. Paier,* J. Sauer, *Phys. Chem. Chem. Phys.* **2018**, *20*, 15764.

# 2 Introduction

## 2.1 Significance of Metal Oxide Surfaces and Their Characterization

Many chemical reactions of industrial relevance are catalyzed by solid metal oxides (see [1-5] and references therein). The products of these reactions are of tremendous economic importance (for instance dehydration and dehydrogenation of alcohols to either alkenes or ethers and carboxylates [6]). Heterogeneous catalysis science is relevant in energy conversion and storage as well as $CO_2$ capture [7-8]. The latter is a major component of pollutants emitted into the atmosphere and responsible for the so-called greenhouse effect. Also, developing sustainable alternative (green) energy techniques represents one of the most urging problems of society, which needs to be solved soon. Metal oxides are going to play an important role in this line of research, for instance, as electrolytes, catalysts, or porous gas storage materials.

Metal oxides are industrially applied as polycrystalline powders and reaction conditions are most often "harsh", meaning that applied temperatures are high enough to induce dynamic phase changes upon reaction and employed pressures are usually large, which in turn may also induce changes, for instance, in the structure of a catalyst. Therefrom originating problems are: i) the active centers or sites on surfaces are usually unknown (missing structure information), ii) their distribution on the surface is usually unknown, and iii) their spectroscopic characterization is most often incomplete or is not available at all (for the example of supported vanadia catalysts see, e.g., [9-10]).

This opens a large gap to be bridged by so-called knowledge-based catalysis research [7]. In a synergistic effort of both experiment and theory, computational chemistry applied to model systems, which can be prepared and characterized experimentally by surface science techniques, contributes significantly to fill this gap as recently discussed by Sauer and Freund [4]. Herein presented results were obtained for three important reducible and thus complex oxide surfaces: $V_2O_3(0001)$, $CeO_2(111)$, and $Fe_3O_4(111)$. Relevant aspects related to computational modeling of reducible oxides are outlined in the next section.

# 3 Computational Modelling of Extended Systems

## 3.1 Cluster Models *versus* Periodic Boundary Conditions

Structure models of crystalline (solid) surfaces can be generated by two distinct approaches: (i) by cutouts from the infinite solid as extensively discussed by Sauer [11-12] or (ii) by applying unit cells of a certain depth corresponding to a certain number of atomic layers. The latter is also known as the slab model of a surface. Ideally, the slab model has an infinite depth. In practice, convergence tests using slabs of a stepwise increased number of layers—possibly preserving a zero-dipole moment—must be made. These tests ensure that layer relaxation effects are sufficiently taken care of. Similar convergence tests need to be accomplished for the size of the unit cell along periodic directions to enable potential reconstruction effects. Calculations are performed subject to periodic (Born-von Kármán) boundary conditions [13].

With regard to the first approach, one may discriminate cluster models for metals, e.g. [14] and ionic solids, e.g. [15], and molecular models for solids with directional bonding, as it is the case in zeolites [11-12]. This is inspired by a chemical viewpoint on reactions as a local phenomenon, e.g., reactions at the active site like a point defect. The second approach originates from a physical viewpoint to describe the wavevector dependence of crystal orbitals properly. This is commonly called the band structure of a solid. Dealing with molecular or cluster models enables one to apply molecular quantum chemical methods or ab initio methods but calls for strategies to describe effects beyond "the local picture" correctly. These long-range effects may be electrostatic interactions, i.e., the interactions stemming from the Madelung potential of an ionic crystalline solid. Slab models subject to periodic boundary conditions usually employ DFT together with pseudo or effective core potentials and plane waves as a basis set. The Hartree-Fock (HF) self-consistent field (SCF) procedure as well as the calculation of the correlation energy contribution is very demanding for bulk systems and with respect to the calculation of the correlation energy prohibitively demanding for solid surfaces. For this purpose, cluster models are clearly advantageous in terms of computational efficiency and scalability [16].

## 3.2 Wavefunction-based Techniques

The (AO) basis set for expanding the molecular (or crystal) orbitals is crucial to ensure results of high quality, i.e., results converged with respect to the size of the basis set (number of basis functions). Gaussian-type orbitals (GTO) are commonly used as an AO basis in quantum chemical methods. This is because evaluation of the four-center two-electron integrals is very efficient using GTOs [17].

Ab initio methods are understood as "HF plus correlation energy" methods [11], however the basis set demands to calculate the correlation energy are high. Convergence with respect to the cardinal number is relatively slow and usually so-called two-point extrapolation formulas are used (see [18] for extrapolation of SCF energies and [19] for correlation energies).

Explicitly correlated two-electron basis functions, depending on the interelectron distances $r_{ij}$ substantially improve the convergence behavior of results with respect to basis set size (see, e.g., [20]). In this realm, Klopper and coworkers have made explicitly correlated second order Møller-Plesset perturbation theory and coupled-cluster-based methods to a general quantum chemistry audience available via efficient implementation into the Turbomole package [21-22].

Recent developments exploiting the fact that the electron correlation between a pair of electrons decays rapidly as $1/(r_{ij})^6$, a combination of the pair natural orbital approach and the concept of orbital domains appear to be promising [23]. Neese and coworkers have implemented this approach in the framework of the coupled cluster method within the quantum chemistry package ORCA [24].

## 3.3 Density Functional Theory Applied to Complex Oxides

Density functional theory (DFT) after Kohn and Sham (KS) [25-27] based on the local density (LDA) or generalized-gradient approximation (GGA) to electron exchange and correlation (xc) is important in materials science and catalysis, because it provides atomic as well electronic structure information of extended systems at a low computational cost. LDA was and very often is the favorite choice in the condensed matter community (e.g., [28]). The advent of GGA functionals and—few years later—the introduction of orbital-dependent hybrid functionals convinced also the chemistry community to value DFT, as recently discussed by Thiel [29]. Regarding molecular chemistry, LDA cannot be used, because of unacceptably large errors in binding or atomization energies [30-31]. Conversely, errors in several solid-state properties

obtained using LDA and GGA are comparable in magnitude. The sign of these errors may be opposite though [32].

GGA functionals provide fairly accurate molecular structures and structures of metal clusters [33-34]. They offer sensible insights into basic material properties such as band structures and lattice parameters of simple metals, semiconductors, and insulators [35-37]. Total energy calculations employing GGA functionals are fast, and atomic forces can be evaluated at little extra computational cost. The numerical workload using GGA scales moderately with system size [38-39], and convergence of the total energy with respect to the size of the employed basis set is easier to achieve compared to wavefunction-based methods (see, e.g., [18, 40]).

Supposed that all technical parameters employed in calculations have been converged, remaining errors are exclusively due to the approximate description of xc effects. In addition to the errors incurred by DFT (*vide infra*), the technical quality of selected structural models for extended systems may also affect the accuracy of results. For instance, single crystal surfaces or thin crystalline films may be modelled using clusters or slabs [11, 41-42]. Cluster models offer the possibility to employ more accurate wavefunction-based approaches [43-45]. This allows to calculate local properties like adsorption energies with high accuracy. Slab models exploiting periodic boundary conditions may be more efficient in computing other properties like surface energies or band-structures. Finite size effects in both cluster and slab models prevent the system under study to relax or reconstruct appropriately, significantly affecting stability and reactivity.

LDA and GGA functionals suffer from so-called self-interaction errors (SIEs) [46-47], which manifest themselves in overly delocalized orbitals and notoriously underestimated band gaps (see [48] and references therein). SIEs may drastically affect the accuracy of computational results, as discussed in many recent review articles focusing on reducible or semiconducting metal oxides [49-52]. GGAs underestimate activation barriers [53]. This is related to the fact, that a GGA functional does not correctly describe the "stretched bond" situation encountered in a transition state [54]. Related to a different type of error, GGAs fall short of correctly describing dispersion-type van der Waals interactions [55]. The latter may substantially affect calculated adsorption energies, i.e. the stability of the adsorption complex [12]. Extensive methodologically motivated discussions on these shortcomings can be found in [56-57] and [58].

Surfaces of reducible metal oxides are interesting model systems for oxidation reactions in catalysis [4, 59]. However, the accurate description of their physical and chemical properties by DFT represents a formidable task. The various 3d transition metal oxide phases of, e.g., vanadium, chromium, and iron as well as oxides of rare-earth metals like cerium featuring 4f

orbitals represent particularly challenging systems from a computational point of view. As mentioned in [49, 51], cerium oxides (ceria) require methods that are capable to describe 4f orbitals involved in bonding as well as in the spatially localized (reduced) $Ce^{III}$. Oxides like $Fe_2O_3$, also known as Mott-Hubbard systems, have partially occupied d orbitals being subject to strong intra-atomic Coulomb correlation effects. A correct description of the latter is largely elusive to the GGA approximation [58, 60].

In catalysis, surface oxygen defects play a central role in the Mars-van Krevelen oxidation mechanism [61]. Oxygen defect formation energies are important descriptors to assess the activity of an oxide catalyst [62]. Formation of O defects in insulating or semiconducting reducible oxides incurs occupation of energetically low-lying empty d or f orbitals, which implies formation of defect-induced electronic states below the conduction band minimum. Since GGA functionals substantially underestimate band gaps, electron occupation of the conduction band is energetically too facile. Instead of the formation of a defect state within the gap, the reduced system may spuriously metallize. The spatially localized nature of the defect state is lost, as shown for an O defect in the $CeO_2$(111) surface (see Fig. 3.1a). Similar problems occur, if positively charged holes in the O 2p valence band are formed upon introduction of undervalent substitutional or interstitial cationic point defects (*p*-type doping) [63-65]. This shortcoming affects defect formation energies. As discussed in **P8**, hybrid functionals like the HSE [66] range-separated hybrid as well as the more ad hoc DFT+U approach represent viable routes to rectify the delocalization or SIE induced by the GGA approximation (Figure 3b). Figure 3c shows that the Tao, Perdew, Staroverov, and Scuseria (TPSS) [67-68] functional, a meta-GGA (see next section), also remedies to a certain degree over-delocalization of defect electrons. This is can be understood, because introduction of a dependence on the kinetic energy density eliminates the so-called one-electron self-interaction, however many-electron self-interaction errors are still present. Hence, alleviating the band gap problem as well as orbital-overdelocalization may improve the accuracy in thermodynamic properties. However, we underline that a correct gap is not a sufficient condition for accurate thermodynamic predictions based on DFT (publication **P8**).

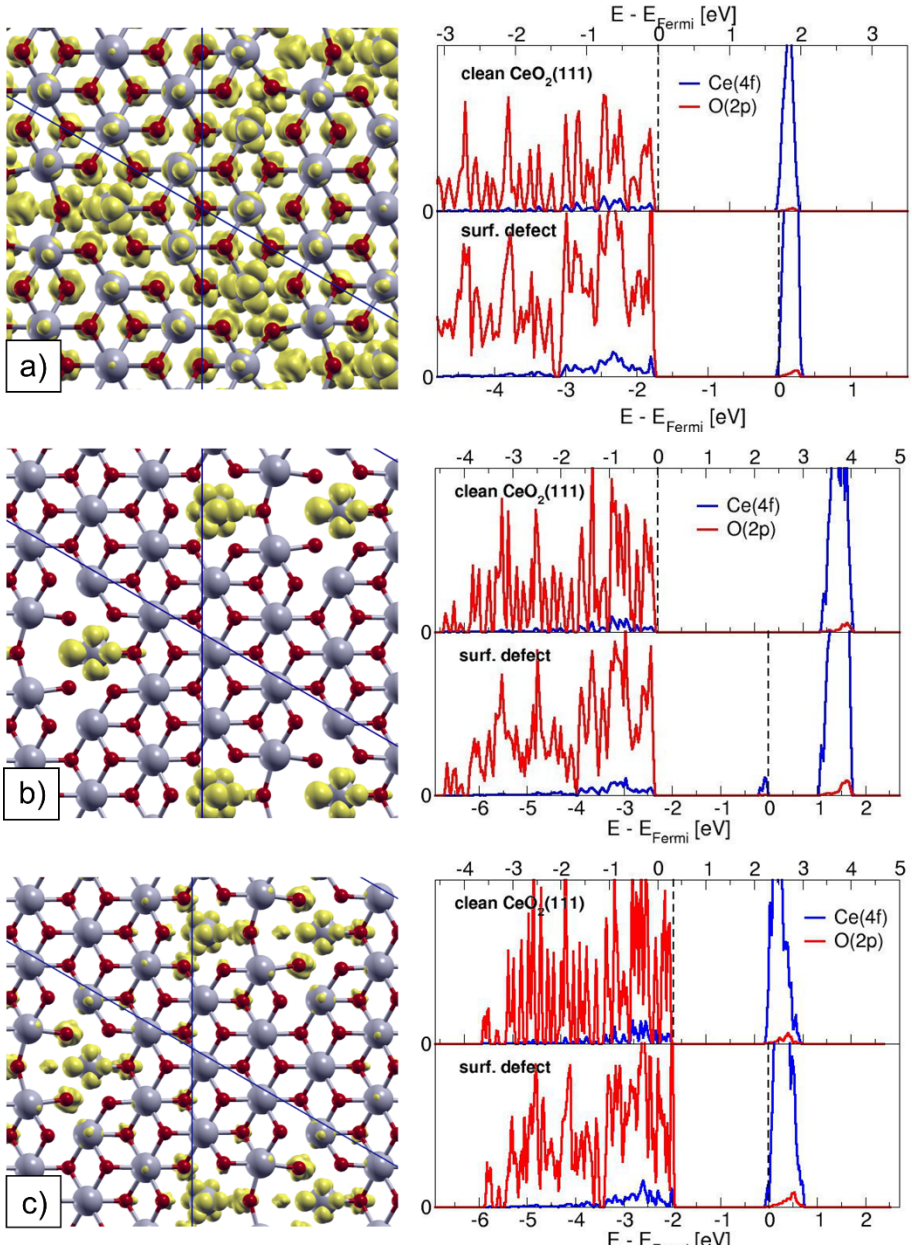


**Figure 3.1.** (a) Spin-densities (yellow) for a surface O defect in $CeO_2$(111) obtained using PBE. Corresponding PDOS for the clean surface (top panel) and O defect (bottom panel) on lhs. Blue lines indicate the Ce 4f states, and red lines indicate O 2p states. (b) Analogous graphs showing spin-densities as well as PDOS obtained using the hybrid functional HSE (see below). (c) Analogous results obtained using the TPSS meta-GGA. For results on the $CeO_2$(110) and (100) surfaces, see [69] and publication **P7**. Reprinted and adapted with permission from publication **P8**. Copyright (2013) American Chemical Society.

## 3.4 Jacob's Ladder of Density Functional Approximations

It is frequently stated that DFT does not offer possibilities to systematically improve the accuracy of results in the way, e.g., wavefunction-based techniques do [70-79]. "Jacob's ladder of density functional approximations" [80-81] is an attempt to introduce, at least to a certain extent, the aforementioned systematics. Currently the ladder comprises five rungs or classes of approximations. The underlying idea is that functionals accommodating several physical or exact constraints, e.g., meeting the uniform electron gas (UEG) limit for vanishing density gradients, are expected to be rather universally applicable and transferable. This means that the accuracy of results does neither critically depend on the material nor on the calculated property. The number of satisfied constraints or degree of complexity increases for higher rungs, but the amount of empiricism used for their construction should be minimal to avoid "overfitting" [82]. This way, the functionals' accuracies are expected to improve using higher rungs on the ladder.

LDA and GGA are known as the first and second rung on the ladder. The third rung refers to the meta-GGA approximation [83], which is on the point of becoming widely recognized in the catalysis community [84-88]. LDA, GGA, and meta-GGA are pooled by the term *semilocal* functionals, because of their dependence on the local electron density $\rho(\mathbf{r})$ as well as on derivatives of $\rho(\mathbf{r})$. While LDA only depends on $\rho$ (including spin-polarization [89]), GGA also incorporates information on the reduced density gradient, which is proportional to $\frac{|\nabla\rho|}{\rho^{4/3}}$. [90-94] A meta-GGA, in addition to its dependence on density and density gradient, includes information that originate from the kinetic energy density [68]. The information contained in the latter was shown to be almost equivalent to the one carried by the second derivative or the Laplacian of the density [67].

The fourth rung functionals contain also non-local information due to the explicit dependence on the occupied orbitals. In theory, this requires developing a generalization of KS-DFT [95]. In practice, this means that a fraction of non-local Fock exchange (FX) replaces the corresponding amount of semilocal exchange. The 'mixing ratio' is material-specific and therefore a semi-empirical parameter [96-98]. Several hybrid functionals use 20 to 25% of FX, which is a useful choice for many materials or systems of interest. This choice was supported by non-empirical arguments [99], but they turned out to be imprecise [81].
The present work does not discuss hybrid functionals relying on many parameters [100-101]. Regarding local hybrid functionals employing position dependent admixture of FX, we refer the interested reader to the literature (see, e.g., [102-104]).

The generalized random-phase approximation (RPA) is the fifth rung on Jacob's ladder (see, e.g., [40, 105-107]). This rung adds non-locality also in the correlation energy via

dependence on occupied as well as virtual orbitals (and orbital energies). Thus, RPA is a fully non-local functional. RPA can be applied to small-gap and metallic systems, in contrast to double-hybrid functionals, which add a fraction of correlation energy based on second order Møller-Plesset perturbation theory [108-110]. Any 'order-by-order' perturbation theory breaks down when applied to systems with zero gap [111]. RPA describes dispersion-type van der Waals interactions correctly (e.g. [112-113]). Up-to-date applications of RPA mostly use semilocal orbitals and orbital energies as input (e.g., [40, 114-119]. This also applies to the FX energy expression, which is then called exact exchange (EXX) energy. However, advantages by using the FX energy (i.e. using HF orbitals in the EXX energy expression) were reported by Ren and coworkers [120-121]. Throughout this work, we will not discriminate between EXX and FX. Self-consistent RPA calculations have not yet been applied to extended systems, although the number of recent publications indicate intense research activities [122-128].

## 3.5 Historic and Technical Remarks on Hybrid Functionals

Becke introduced hybrid functionals in 1993 [129]. He used arguments based on the so-called adiabatic connection formula [130-131] to theoretically motivate the employed mixing-ratio, i.e. 50% of FX and 50% of Slater-Dirac (LDA) exchange [132-133]. This hybrid, known as the "Becke-Half-and-Half" (HH) functional substantially outperformed both HF and LDA with respect to errors in molecular atomization energies. Moreover, the work reports improvements by employing two independent mixing parameters obtained from fitting against experimental data. The modified functional uses a smaller amount of FX (33%) and sacrifices a constraint, namely the uniform electron gas (UEG) limit [129]. Despite its excellent performance in molecular atomization energies, this parametrization spoiled the accuracy in other properties such as proton affinities.

The three-parameter functional B3PW91 [134] was also introduced by Becke (eq. 3.1).

$$E_{xc}^{B3PW91} = E_{xc}^{LDA} + a_0 \cdot (E_x^{FX} - E_x^{LDA}) + a_x \cdot \Delta E_x^{B88} + a_c \cdot \Delta E_c^{PW91} \qquad (3.1)$$

It outperformes HH in terms of molecular atomization energies and preserves the UEG limit. The three parameters in eq. 3.1 refer to the admixing factors for FX ($a_0$ = 0.2), the Becke-88 (B88) [135] gradient-correction to the LDA exchange ($a_x$ = 0.72), and the Perdew-Wang-91 (PW91) [91, 136] gradient-correction to the LDA correlation energy ($a_c$ = 0.81), respectively. These parameters were fitted to minimize errors in calculated molecular properties such as atomization energies, ionization potentials etc. Note that the popular B3LYP hybrid functional

finds its origin in B3PW91 replacing the LDA correlation and the PW91 gradient corrections by the Lee-Yang-Parr (LYP) correlation functional [137]. LYP consists of density dependent (local) terms as well as gradient-dependent (semilocal) contributions [138]. B3LYP was employed and published by Frisch und coworkers for the first time in 1994 [139].

LYP is based on the Colle-Salvetti (CS) functional and does not fulfill the UEG limit. For vanishing density gradients, it lacks some of the correlation energy compared to LDA [140-141]. As discussed in [142], electron correlation at the short range, i.e. small inter-electron distance, is less affected. However, at the long range, the effect of the aforementioned failure becomes noticeable. It is less problematic for calculations on atoms and molecules, but for solids errors may be significant. This shortcoming of LYP is also displayed in Fig. 5 of [140].

Figure 3.2 shows atomization energies for several archetypal metals, semiconductors, and insulators obtained with the Perdew, Burke, and Ernzerhof (PBE) GGA [92] and the Heyd, Scuseria, Ernzerhof (HSE, *vide infra*), the B3PW91, as well as the B3LYP hybrid functionals [143]. The large negative relative errors illustrate the failure in LYP when applied to free electron-gas-like systems, such as metals. The systematic underestimation of atomization energies can be readily understood. Supposed that the calculations for the atoms are reasonably accurate, the stability of the bulk material is underestimated by B3LYP, very likely due to the underestimation of correlation for the UEG described above. As indicated by the pronounced error bar for Si, problems also arise for small gap semiconductors, featuring delocalized orbitals or a density matrix decaying slowly with distance [144]. For B3PW91, which fulfills the UEG limit, errors in metallic systems are substantially smaller compared to B3LYP [143]. Except for Na and Mg, B3PW91 and HSE perform similarly.

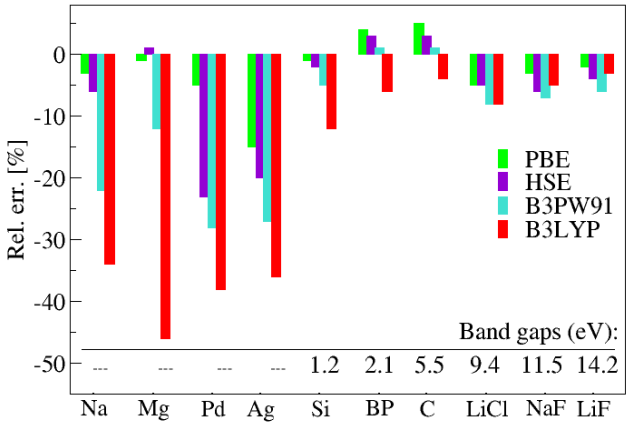


**Figure 3.2.** Relative errors in atomization energies (theory minus experiment) obtained using PBE (green), HSE (violet), B3PW91 (light blue), and B3LYP (red) [143]. Adapted with permission from publication **P2**.

To avoid errors incurred by LYP and to single out the effect of admixed FX, it is advisable to compare the performance of PBE solely with B3PW91 and HSE. Both hybrids fulfill the UEG constraint. As shown in Fig. 3.2, admixture of FX yields suboptimal results for metallic systems. This finding is along the lines of, e.g., [87].

The UEG is the prototype model for metallic systems and applying HF to the UEG causes that the electronic density of states vanishes logarithmically at the Fermi level [145-146]. This artifact is a consequence of the long-range nature of the Coulomb $1/|\mathbf{r}_1-\mathbf{r}_2| = 1/r_{12}$ interaction among electrons [144]. Two electrons at large distance do not feel the full $1/r_{12}$ potential, but a "screened" version due to the presence of, e.g., the other electrons as an intervening medium. So-called polarization or rearrangement effects of the electron gas cancel out the long-range part of the potential. Therefore, higher-order correlation effects, e.g., within the (non-local) RPA approximation, compensate this singular behavior of the potential [147]. Semilocal approximations to correlation employed in a hybrid functional insufficiently compensate the aforementioned singularity. A body of work in the literature points out the underperformance of hybrid functionals when applied to extended metallic systems [87, 97, 143, 148-150].

Summarizing the discussion on B3LYP, Fig. 3.2 shows a relation between B3LYP errors in atomization energies and the size of the band gap. Larger band gaps relate to smaller errors. Supposed that all these functionals are comparably accurate for atoms, this finding is sensible, because the density matrix of wide-gap systems decays rapidly with the distance [39, 151]. It implies a high degree of localization in orbitals [152]. Apparently, the case involving a more localized scenario is unproblematic for the LYP functional. Recalling that B3LYP is plagued by two important shortcomings: a) the long-range part of FX, which is problematic in metallic systems; b) LYP does not describe long-range contributions of correlation effects in delocalized (metallic) states accurately. Using B3LYP, both shortcomings add up and lead to conspicuously large error bars for metallic systems as well as for small-gap semiconductors like Si.

In 1996, Becke introduced a simplified one-parameter hybrid functional shown in eq. 3.2.

$$E_{xc}^{hybrid} = E_{xc}^{DFT} + a_0 \cdot (E_x^{FX} - E_x^{DFT}) \tag{3.2}$$

The admixing factor for FX, $a_0$, is usually small and varies between 0.16 and 0.28 depending on the GGA exchange functional used (i.e. $E_x^{DFT}$ in eq. 3.2) [153]. The popular PBE0 or PBEh hybrid functional is based on the PBE GGA functional and uses 25% of the FX energy ($E_x^{FX}$). It was introduced into the literature and independently assessed by Adamo and Barone [154] as

well as Ernzerhof and Scuseria [155]. Both groups reported high accuracy for a broad variety of molecules and their properties.

As mentioned before, the long-range asymptote of the Coulomb interaction (see Figure 3.3 on the lhs, black line) renders the application of hybrid functionals to metallic and semiconducting solids with a small band gap numerically difficult. As demonstrated in [97], the slow decay of $1/r_{12}$ with distance requires dense *k*-point grids (or equivalently large supercells) to converge the FX energy.

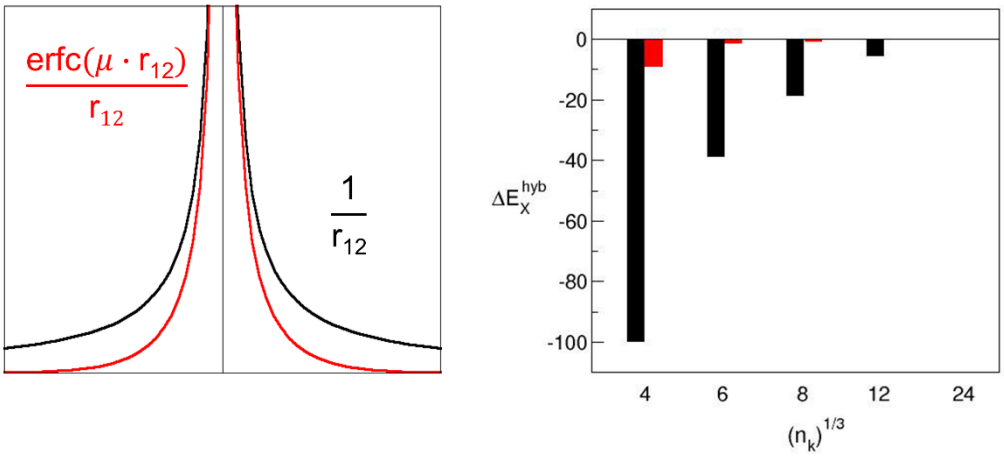


**Figure 3.3.** Decay of a screened (red) and unscreened (black) Coulomb kernels (left). Error in the exchange energy $\Delta E_X$ of fcc Al with (HSE, red) and without (PBE0, black) screening as a function of *k* points (right). See also [97]. Adapted with permission from publication **P2**.

To remedy this problem, one may resort to screening or a range-separation of the interelectron Coulomb interaction. In molecular quantum chemistry, this technique was successfully applied to describe short-range correlation using DFT and long-range correlation effects using wavefunction-based methods [156]. In Figure 3.3 the screened Coulomb interaction using the complementary error function is shown on the lhs (eq. 3.3).

$$\frac{1}{r_{12}} = \underbrace{\frac{\mathrm{erfc}(\mu \cdot r_{12})}{r_{12}}}_{\mathrm{SR}} + \underbrace{\frac{\mathrm{erf}(\mu \cdot r_{12})}{r_{12}}}_{\mathrm{LR}} \tag{3.3}$$

In principle, any functions summing up to 1/r are suitable for range separation. A screening based on the error function like in eq. 3.3 is advantageous using GTOs or plane waves as a basis set [66, 97]. Historically, the first application of the error function dealt with efficient lattice summations of the long-range electrostatic interactions in crystalline solids. It is

commonly known as the Ewald technique [157]. The HSE or equivalently HSE06 hybrid functional, defined in eq. 3.4, uses range separation in the exchange energy contribution according to eq. 3.3 [66].

$$E_{HSE\text{-}X}=E_{PBE\text{-}X}+a_0\left(E_{FX}^{SR}(\mu)-E_{PBE\text{-}X}^{SR}(\mu)\right) \tag{3.4}$$

In eq. 3.4, the superscript "SR" refers to "short-range" and $a_0$—similar to PBE0—amounts to 25%. This means that the FX energy (as well as the FX potential) is evaluated using the short-range kernel of the Coulomb interaction (see Fig. 3.3, red lines). The empirically set parameter $\mu$ is 0.207 $Å^{-1}$ and determines the length scale of SR and LR interactions [158]. This offers substantial computational savings for metallic systems as shown on the rhs in Fig. 3.3 [97]. The figure shows respective errors in the FX energy for the fcc bulk phase of Al with (red bars) and without range separation (black bars) as a function of the number of *k* points. In other words, the figure compares the convergence in HSE and PBE0 exchange energies. Apparently, range-separation drastically enhances technical convergence. HSE is very useful for treating metals and insulators on the same footing [48, 97, 159]. The high accuracy in band gaps obtained with HSE is amply discussed in recent review articles [48, 52, 160].

Hybrid functionals have been commonly used in the field of molecular quantum chemistry almost instantaneously after their introduction by Becke. At the same time, they were offered to the computational solid state community by virtue of the CRYSTAL code [161] using GTOs to expand the crystal orbitals [162-163]. GTOs are also used in the GAUSSIAN suite of programs [66, 164-165]. Local (atom-centered) basis functions offer the possibility to treat all electrons, i.e. core as well as valence orbitals in the self-consistent field optimization. However, incompleteness or superposition errors [166-167] have to be tackled by techniques like, e.g., the Boys-Bernardi counterpoise correction [168].

Hybrid functionals are implemented in many solid-state electronic structure codes. The required FX energy can be computed employing various basis sets such as all-electron numeric (localized) orbitals as used in FHI-aims [169-170] and full-potential linearized augmented plane waves as used in WIEN2K [171-172], exciting [173] , or Fleur [174-175]. Moreover, projector-augmented pseudopotentials and plane waves are used in VASP [97, 176] or GPAW [177-178], and mixed basis sets are employed in CP2K [179] or pseudopotentials and plane waves as used in Quantum ESPRESSO [180-181] or CASTEP [182-184]. Consequently, hybrid functionals are now accessible to a large manifold of computational communities.

## 3.6 Hybrid Functionals and the DFT+U Approach

Both, hybrid functionals as well as the DFT+U approach [185-188] assist in treating localized d or f electrons within a (generalized) DFT framework. The fraction of FX used in a hybrid functional partially alleviates one-electron SIEs in semilocal functionals, thus enhances localization.

Within DFT+U, the orbitals are subdivided into two groups, namely rather delocalized orbitals that form bands and spatially localized, atomic-like orbitals. These groups of orbitals are treated differently. This is justified by the assumption that semilocal functionals describe the band formation within s and p orbitals well, but corrections are required for the other case (d and f orbitals). The Mott-Hubbard theory [189-192] serves as the conceptual basis for DFT+U, relying on the idea of a hindered transfer of electrons among neighboring sites. The electron interaction is described by the Hubbard Hamiltonian involving effective Coulomb (U) and exchange (J) interactions. The meaning of U was extensively discussed by Herring [193]. For instance, in a 3d electron system with n electrons per atom, U is defined as the energy cost involving electron detachment at one site and attachment at a neighboring site, i.e. the 'redox' reaction energy.

Following [194], bypassing above mentioned deficiencies in LDA or GGA requires the introduction of a U-dependent correction to the total energy. The one-electron SIE-free HF theory is used as a reference. The correction to the DFT energy reads

$$\Delta E_{corr}[\{n_i\}]=E^{HF}[\{n_i\}]-E_{dd}^{DFT}[n_d], \tag{3.5}$$

with $E_{dd}^{DFT}[n_d]$ as the energy contribution stemming from the erroneous DFT description of interacting d electrons. eq. 3.5 uses $n_i$ as the occupation number of orbital $i$ and $n_d$ refers to the total number of $d$ electrons, i.e. $n_d = \Sigma_i n_i$. The HF energy expression, with $E^{HF}[\{n_i\}]$ as a functional depending on the set of d orbitals, reads

$$E^{HF}[\{n_i\}]=\frac{e^2}{2}\sum_{i\neq j}(U_{ij}-J_{ij})\, n_i n_j, \tag{3.6}$$

with $U_{ij}$ and $J_{ij}$ as orbital-dependent Coulomb and exchange integrals. To illustrate the working principle, the electron exchange term J in eq. 3.6 can be neglected [194], which leads to a simplified expression for the correction

$$\Delta E_{corr}[x]=-\frac{1}{2}U\, x(x-1),\quad 0\leq x\leq 1, \tag{3.7}$$

with *x* as the variation of the total number of *d* electrons [194]. This expression involves a $E_{dd}^{DFT}[n_d]$ of similar structure (see [194]). In consequence, the corresponding correction to the one-electron potential is equal to

$$\Delta V_{corr}[x] = \frac{d\Delta E_{corr}}{dx} = U\left(\frac{1}{2} - x\right). \tag{3.8}$$

Equations 3.7 and 3.8 convey the essential physics underlying the DFT+U approach. Supposing a half-filled d orbital, the correction to the total energy will result in a maximal increase in energy, whereas the correction to the Kohn-Sham eigenvalue vanishes. Conversely, integer occupation will be (variationally) preferred by the orbital-dependent DFT+U functional, which in turn leads to the opening of the band gap (eq. 3.8). Unoccupied orbitals (x = 0) will be shifted by $+^1/_2\,U$ and occupied orbitals (x = 1) will be lowered by $-^1/_2\,U$ (see Fig. 3.4). Localization of d or f electrons is therefore inherent to DFT+U, which incorporates orbital-dependence in a somewhat less rigorous manner compared to HF theory. Using a hybrid functional, all occupied orbitals are subject to the same generalized Kohn-Sham Hamiltonian [95], whereas in DFT+U only a subspace of orbitals is corrected in the aforementioned *ad hoc* manner. In practical applications, the size of U matters. It is usually chosen in a way to trade off the accuracy in describing the band gap against the accuracy reached for other system properties such as lattice parameters or reaction energies. (e.g., [195-197]). Applying U together with semilocal functionals leads to increased lattice parameters. This is beneficial for LDA, because it underestimates lattice constants, but unfavorable for GGA functionals like PBE, which overestimate them [32]. For further discussions on DFT+U, we refer the interested reader to the literature [51, 198-199].

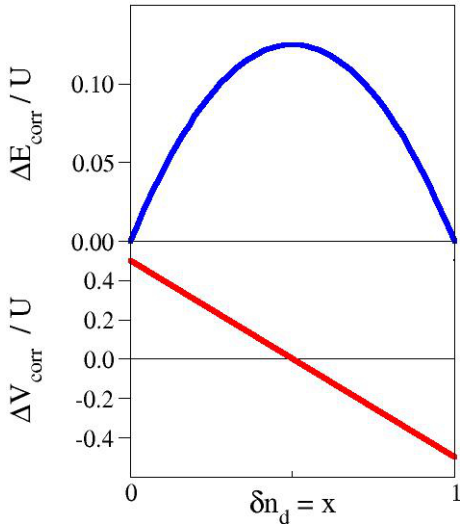


**Figure 3.4.** Correction to the total energy ($\Delta E_{corr}$, blue line) and the potential ($\Delta V_{corr}$, red line) within DFT+U as a function of the variation of *d* orbital occupation x. See also [194]. Adapted with permission from publication **P2**.

# 4 Case studies

## 4.1 The Structure of the $V_2O_3$(0001) Surface

**P1*** *The Surface Structure of $V_2O_3$ revisited*
F. E. Feiten, J. Seifert, J. Paier,* H. Kuhlenbeck,* H. Winter, J. Sauer, H.-J. Freund, *Phys. Rev. Lett.* **2015**, *114*, 216101.

**P2*** *Hybrid Density Functionals Applied to Complex Solid Catalysts: Successes, Limitations, and Prospects*
J. Paier,* *Catal. Lett.* **2016**, *146*, 861.

The $V_2O_3$(0001) surface termination stable under ultrahigh vacuum (UHV) conditions was debated until its resolution by a recent study combining experiments and theoretical calculations published in **P1**. The surface structure of its outermost layers was unclear because previously published density functional theory (DFT) results were inconsistent to several experimental results [200-201]. Ion scattering combined with DFT calculations within the generalized gradient approximation (GGA) supported the reconstructed so-called $O_3$ termination of the $V_2O_3$(0001) surface as the predominant surface structure for preparations under UHV conditions [201-203]. These results had to be reinterpreted based on infrared reflection-absorption spectroscopy (IRAS) [204-205], I/V low-energy electron diffraction (LEED), scanning tunneling microscopy (STM), fast atom diffraction, as well as DFT calculations on surface free energies employing a hybrid functional (publication **P1**). There is clear experimental evidence for the vanadyl, V=O, termination. Since DFT was invoked to support the reconstructed $O_3$ termination, we have shown that care must be taken because results may depend on the employed functional. These novel hybrid functional results on the stabilities of various surface phases suggest a substantially broader stability range for the V=O termination in contrast to results based on the GGA approximation [200, 206]. These hybrid functional results are also expected to be more accurate because errors in computed heats of formations for various vanadium bulk oxide phases are smaller when compared to observed values as shown in the present section. This extensive work characterizing the $V_2O_3$(0001) surface eventually resolved its atomic structure.

Stabilities of various $V_2O_3$(0001) surface terminations (publication **P1**) calculated using hybrid functionals as a function of the amount of employed FX is essential content of the above-mentioned publications. When the xc functional does not include FX, it usually implies that it is a mere GGA functional like the Perdew, Burke, and Ernzerhof (PBE, [92]) GGA. The

latter is frequently used in studies on structures and stabilities of surfaces [49] due to lower computational demands compared to hybrids. However, as discussed in publication **P2** and outlined in chapter 3, GGA functionals suffer from shortcomings. Hence, it is justified to raise the question, whether stabilities of surface terminations predicted by DFT are robust with respect to the employed xc functional, especially when DFT is used as decisive means to conclude on the atomic structure of surfaces under specific conditions.

Vanadium oxides represent major components of active phases of several important solid oxidation catalysts [207-208]. Hence, knowing the precise positions of the atoms in the surface is crucial to understand its reactivity, when it comes to the elaboration of a mechanism. The $V_2O_3$(0001) surface is one important and representative vanadium oxide surface. $V_2O_3$ crystallizes in the corundum structure and we outline in the following the problem, which has been solved within a combined approach using I/V LEED, STM, fast atom scattering, and DFT employing the Heyd, Scuseria, Ernzerhof (HSE, [66, 158]) hybrid functional.

For approximately a decade, this surface prepared under ultrahigh vacuum conditions was considered to be vanadyl (V=O) terminated. Experimental evidence originating from a characteristic and intense IR vibrational band [204-205], STM, XPS, and near edge X-ray absorption fine structure data are in support of this conclusion [204-205, 209]. The (0001) surface can be cut in three different ways. One may cut at the first of two inequivalent metal atoms resulting in a $\cdots O_3\text{-}V_2\text{-}O_3\text{-}V$ (single metal, SM) termination, at the second metal atom resulting in a $\cdots O_3\text{-}V_2\text{-}O_3\text{-}V_2$ (double metal, DM) termination, or at the $O_3$ oxygen layer, $\cdots O_3\text{-}V_2\text{-}O_3\text{-}V_2\text{-}O_3$, corresponding to the ideal (bulk-like) $O_3$ termination. However, DFT results (obtained using the PW91-GGA [210]) indicate that several reconstructed surface terminations exist, which are thermodynamically more favorable compared with ideal bulk terminations [200, 206]. These reconstructed terminations are shown in Fig. 4.1.

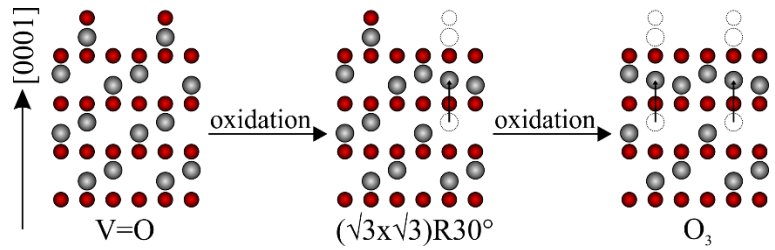


**Figure 4.1.** Structure models showing possible reconstructed terminations of the $V_2O_3$(0001) surface. V is gray, O is red. Reprinted with permission from publication **P1**. Copyright (2015) American Physical Society.

At relatively low chemical potentials of oxygen (corresponding to a temperature of about 800 K and UHV pressure conditions), DFT predicts the vanadyl (V=O) terminated surface to be the most stable phase. At higher (more positive) potentials, the (hypothetical) phase equilibrium is pushed towards ordered superstructures at $^{2}/_{3}$ or $^{1}/_{3}$ of a monolayer (ML) V=O coverage. At even higher chemical potentials of oxygen, DFT within the PW91-GGA approximation predicts a reconstructed $O_3$ termination to be the prevalent stable phase [200]. In the reconstructed $O_3$ termination every other V atom from the subsurface cationic layer is supposed to move up into the cationic surface layer (Fig. 4.1). Recent studies [201-202] employing ion scattering and DFT (PW91-GGA) concluded on the reconstructed $O_3$ termination, which however contrasts with the previously observed intense V=O stretching vibrations as well as other observed results (*vide supra*).

The $V_2O_3$(0001) surface has recently been thoroughly revisited using a large spectrum of surface sensitive techniques [see publication **P1**, but also [211] and [212]). Therefore, about 100 Å thick films grown on an Au(111) substrate were prepared. The conditions like oxygen partial pressure and temperature were systematically varied and the resulting surface phases analyzed by virtue of LEED. These results are summarized in Fig. 4.2. Within a pressure range of $1\times10^{-7}$ to $1\times10^{-6}$ mbar only structures showing a (1×1) LEED pattern were prepared. A (√3×√3)*R*30° superstructure appears only at higher pressures of oxygen. Importantly, at even higher oxygen pressures the films disappeared and dewetting was observed, probably because sublimation of $V_2O_5$ set in. The (√3×√3)*R*30° structure can be readily identified using LEED. However, both V=O as well as the reconstructed $O_3$ termination would show the same (1×1) pattern. Thus, I/V LEED using a total of 14 different structures with varying interlayer distances were used for the structure refinement procedure. The comparison between the V=O and $O_3$ terminations are not shown here (see Fig. 3 in publication **P1**), but the calculated I/V LEED curves for the V=O terminated surface agree much better with observed results.

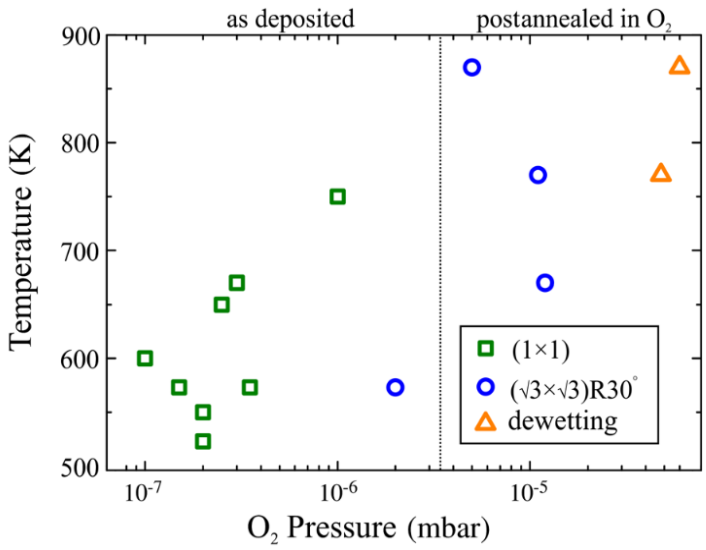


**Figure 4.2.** Observed surface phases as a function of preparation conditions. Reprinted with permission from publication **P1**. Copyright (2015) American Physical Society.

Before discussing computational aspects of the calculated stability diagrams using a hybrid functional, another experimental evidence supporting the V=O termination is shown, namely a comparison between observed and calculated STM micrographs (see Fig. 4.3). The observed STM images are consistent with Tersoff-Hamann [213-214] positive bias simulations for a fully vanadyl-covered surface of hexagonal symmetry. The triangular features typical of reconstructed and ideal $O_3$ terminations (see also Fig. 14 in [201]) were not observed.

Given the shortcomings of GGA xc functionals and the fact that the PW91-GGA functional has been employed to support the reconstructed $O_3$ termination, it seems worthwhile to check surface energies or stabilities with a different, supposedly more accurate functional. As discussed in sections 3.3 to 3.5 and publication **P2**, the amount of FX used within a hybrid functional is a material-specific quantity and may affect results (for functional-dependent electron-localization and its effect on IR spectra of anionic vanadium oxide clusters see work by Sauer and Asmis, and coworkers [96]). Hence, the question arises, whether surface stabilities of $V_2O_3$(0001) terminations critically depend on the amount of FX used.

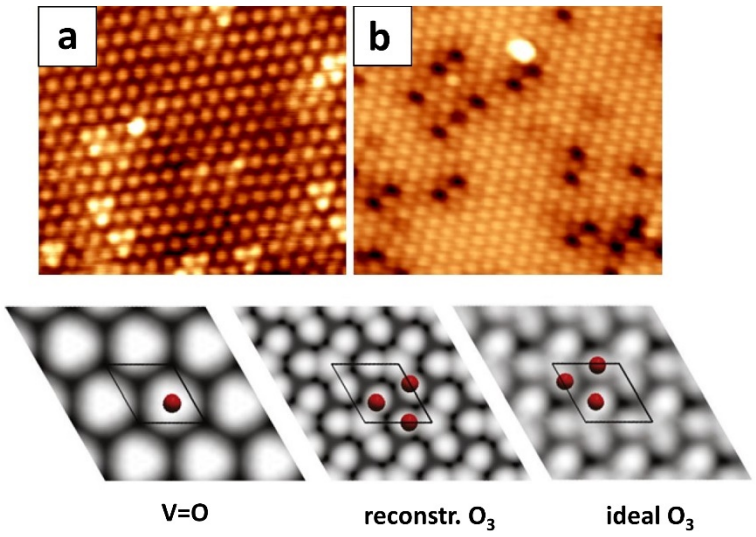


**Figure 4.3.** Upper panel: Atomically resolved STM images of the $V_2O_3$(0001) surface. (a) Slightly reduced; (b) slightly overoxidized. Reprinted with permission from publication **P1**. Copyright (2015) American Physical Society. Lower panel: Simulated STM images for terminations as indicated below. Reprinted figure with permission from [201]. Copyright 2012 by Elsevier B.V.

To assess calculated phase or stability diagrams of important $V_2O_3$(0001)-(1×1) terminations, we compare heats of formations of relevant bulk phases obtained using the HSE hybrid with observed values. In addition, we calculate the reduction ($\Delta H^r_1$, eq. 4.1) and oxidation enthalpies ($\Delta H^r_2$, eq. 4.2), as well as the reaction enthalpy for the disproportionation of $V_2O_4$ ($\Delta H^r_3$, eq. 4.3). These results are shown in Tab. 4.1. Note that zero-point vibrational energy (ZPVE) corrections as well as inclusion of T-dependent terms (for a derivation see [215]) are smaller than 2 kJ/mol and are therefore neglected. For the $V_2O_4$ bulk structure we used the monoclinic (M1) phase, since the rutile structure becomes stable at temperatures larger than 340 K [216]. Work published in the literature suggests using a smaller amount of FX for a more accurate description of $VO_2$ bulk phases [217-218]. However, in this work spin non-polarized calculations were employed except for the VO phase (antiferromagnetic-II order, see [219]), because $V_2O_3$ is a nonmagnetic metallic system at ambient temperature.

$$V_2O_3 \rightleftarrows 2\ VO + {}^1/_2\ O_2 \qquad (4.1)$$

$$V_2O_3 + {}^1/_2\ O_2 \rightleftarrows V_2O_4 \qquad (4.2)$$

$$V_2O_4 \rightleftarrows {}^1/_2\ V_2O_3 + {}^1/_2\ V_2O_5 \qquad (4.3)$$

Among the three functionals used, errors in heats of formation obtained using HSE (25% FX) for $V_2O_3$, $V_2O_4$, and $V_2O_5$ relative to observed values are smallest. The tendency of the PBE-GGA to underestimate heats of formations for these vanadium oxide phases is substantially

alleviated using HSE. Also, the oxidation of the $V_2O_3$ phase (eq. 4.2) is more accurately described. The disproportionation of $V_2O_4$ (eq. 4.3) is accurately described using PBE, but this appears to be a fortuitous cancellation of errors comparing the involved heats of formations with observed values. They are significantly underestimated using the PBE-GGA functional.

**Table 4.1.** Heats of formation[a] and reaction energies (solid phase) for $VO_x$ phases. Energies given in eV/formula unit.

| | PBE | HSE (10% FX) | HSE (25% FX) | Obsd. |
|---|---|---|---|---|
| $\Delta H^f_{VO}$ | -3.24 | -3.86 | -4.94 | -4.47[b] |
| $\Delta H^f_{V2O3}$ | -10.89 | -10.86 | -11.58 | -12.64[b] |
| $\Delta H^f_{V2O4}$ | -13.58 | -13.75 | -14.15 | -14.66[c] |
| $\Delta H^f_{V2O5}$ | -15.43 | -15.51 | -15.67 | -16.07[b] |
| $\Delta H^r_1$ | +5.34 | +3.14 | +1.70 | +3.70 |
| $\Delta H^r_2$ | -2.69 | -2.89 | -2.57 | -2.15 |
| $\Delta H^r_3$ | +0.42 | +0.56 | +0.52 | +0.43 |

[a] Corrections involving zero-point vibrational energies (ZPVE), as well as temperature-dependent terms for T = 298 K for metallic vanadium and $O_2$ (the latter includes translational and rotational degrees of freedom) are ca. 0.01 eV/f.u. (≈ 1 kJ/mol) and are therefore neglected.
[b] Ref. [220]; [c] Ref. [221].

We use the fact that the HSE heats of formation for $VO_x$ bulk phases agree better with observed values as a strong argument in favor of application of this functional. Thus, we studied the important terminations of $V_2O_3$(0001)-(1×1), i.e., the SM V, the vanadyl V=O, and the reconstructed $O_3$ termination using HSE with the "as defined" [158] amount of 25% FX. These results are summarized in the stability diagram shown in Fig. 4.4. It displays surface energies of respective terminations as a function of the chemical potential of oxygen.

The black arrows at the bottom of the diagram refer to the stability ranges of $VO_x$ bulk phases. Relevant preparation conditions, i.e., ca. 500-800 K and ca. $1 \times 10^{-7}$ mbar, correspond to a chemical potential of ca. -1.3 to -1.2 eV. The V=O termination is predicted to be the most stable phase for this range. Compared to the phase diagrams obtained using PW91-GGA [200-201], this means that the reconstructed $O_3$ termination is drastically destabilized. Hence, the equilibrium with noticeable amount $O_3$ terminated surface area locates at much more positive values for the chemical potential of oxygen, in turn corresponding to higher partial pressures. This conclusion even holds under assumption of DFT errors in the binding energy of the $O_2$ molecule, which may be as large as several hundred

meV (ca. several tens of kJ/mol; see also Tab. 1 in [62]). Importantly, it was also observed that applying higher oxygen pressures led to dewetting of the films. The oxidation of the $V_2O_3$ films to $V_2O_5$ and its sublimation are plausible explanations for the dewetting. This is consistent with the phase diagram shown in Fig. 4.4, because it predicts $V_2O_5$ as the stable bulk phase under oxygen-rich conditions. According to the diagram, $V_2O_3$ is never the stable bulk phase under relevant conditions (in fact it is out of reach experimentally, due to a too negative chemical potential). This gives a hint on kinetic stabilization of the V=O terminated films. Put another way, the formation of higher oxide films is probably prevented by too large activation barriers.

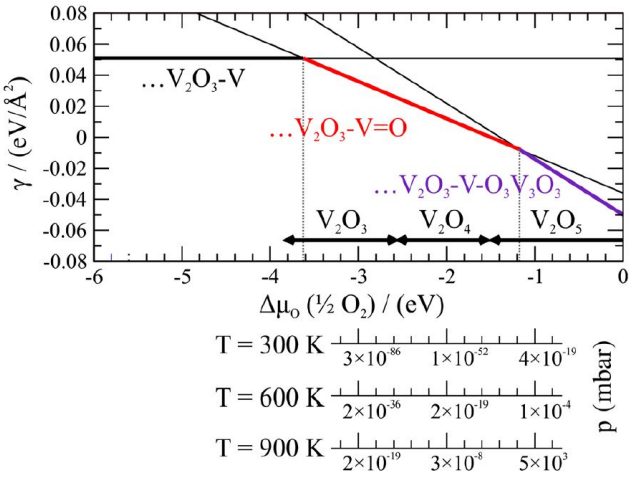


**Figure 4.4.** Surface energy (eV/Å$^2$) as a function of the chemical potential of oxygen for relevant surface terminations. Results obtained using the HSE (25% FX) hybrid functional. Reprinted with permission from publication **P1**. Copyright (2015) American Physical Society.

## 4.2 Oxidative Dehydrogenation of Methanol at Vanadia/Ceria

**P3*** *Oligomeric Vanadium Oxide Species Supported on the $CeO_2$(111) Surface: Structure and Reactivity Studied by Density Functional Theory*
C. Penschke, J. Paier,* and J. Sauer, *J. Phys. Chem. C* **2013**, *117*, 5274.

**P4*** *Stability and Migration Barriers of Small Vanadium Oxide Clusters on the $CeO_2$(111) Surface Studied by Density Functional Theory*
J. Paier,* T. Kropp, C. Penschke, and J. Sauer, *Faraday Discuss.* **2013**, *162*, 233.

**P5** *Support Effect in Oxide Catalysis: Methanol Oxidation on Vanadia/Ceria*
T. Kropp, J. Paier, and J. Sauer,* *J. Am. Chem. Soc.* **2014**, *136*, 14616.

**P6*** *Reactions of Methanol with Pristine and Defective Ceria (111) Surfaces: A Comparison of Density Functionals*
T. Kropp and J. Paier,* *J. Phys. Chem. C* **2014**, *118*, 23690.

**P7*** *Activity versus Selectivity of the Methanol Oxidation at Ceria Surfaces: A Comparative First-Principles Study*
T. Kropp and J. Paier,* *J. Phys. Chem. C* **2015**, *119*, 23021.

**P8** *Oxygen Defects and Surface Chemistry of Ceria: Quantum Chemical Studies Compared to Experiment*
J. Paier, C. Penschke, and J. Sauer,* *Chem. Rev.* **2013**, *113*, 3949.

Regarding the $CeO_2$(111) surface, temperature programmed desorption (TPD) experiments revealed a drastically enhanced oxidative dehydrogenation (ODH) activity in terms of a low-temperature desorption or $\alpha$ peak of formaldehyde upon deposition of small amounts of $VO_x$ [222]. Importantly, the desorption peak was only observed in context of mononuclear vanadia species as shown by atomically resolved STM obtained in the group of Freund [222-223]. Remarkably, the vanadia induced an activity higher than that of individual components, i.e. pure ceria on one hand and vanadia ($V_2O_5$) on the other. The latter conclusion is based on a comparison of TPD spectra of adsorbed methanol on $CeO_2$(111) without, with low, and with high loadings of $VO_x$, where in the latter case the support is de facto fully covered by two-dimensionally grown vanadia [222]. The mechanistic reasons (involving atomic structure

details) for this high activity were unknown for a long time. Based on DFT calculations summarized in the present section as well as in publications **P3**-**P8** and [224], we understand the aforementioned exceptionally high ODH activity.

The work on the $CeO_2(111)$ surface had essentially two aims: prediction of structures and stabilities of deposited $VO_x$ oligomers on the $CeO_2(111)$ surface and the elucidation of possible elementary steps in the ODH of methanol adsorbed at—as shown by TPD [222]—very active monomeric $VO_x$ clusters. The high activity of $VO_x$ can be explained by the cooperativity between the vanadia species and the ceria support in the rate-determining H-transfer step (see also [222]): $VO_x$ accepts the proton and the two electrons are stabilized in Ce 4f orbitals creating two additional $Ce^{3+}$ ions in the surface. It was shown that $VO_2$ clusters agglomerate strongly exothermically on the surface (publication **P3**). Specifically, a very stable $(VO_2)_3$ trimer is formed, which is V=O terminated and built from V-O-V-bridging units commensurate to the hexagonal $CeO_2(111)$ surface structure. The activity of $VO_2$ monomers, dimers, and trimers was studied using the oxygen defect formation and the hydrogenation energies as activity descriptors. Both descriptors have been shown before to be efficient means to assess the ODH activity of metal oxide surfaces [62, 225]. In agreement with TPD results, the $VO_2$ monomer, stabilized on the $CeO_2(111)$ surface by large activation barriers for migration (publication **P4**), is predicted to perform most actively in the ODH of methanol. The high activity of $VO_2$ monomers was confirmed by detailed mechanistic studies calculating surface adsorption complexes of methanol, transition structures involving the H- or more precisely the proton-coupled-electron transfer, and adjacent reaction intermediates. Calculated harmonic wavenumbers enabled to compute activation barriers and pre-exponential factors in the Polanyi-Wigner equation (of first order). Based on these results for several pathways, the simulated TPD spectrum using activation barriers obtained with more accurate hybrid functionals (see, e.g., [62]) agrees very well with observed results (publications **P5** and **P6**). These mechanistic studies lead to the understanding of the observed $\alpha$ desorption peak of formaldehyde. It involves binding of methoxide into a "$VO_2$-induced" pseudo-oxygen-vacancy and subsequent transfer of a methyl-hydrogen atom to the V-O-Ce interphase bond.

While section 4.1 discusses stabilities of surface reconstructions, herein summarized publications **P3** to **P8** discuss more complex problems, namely thermodynamic as well as kinetic properties of vanadia aggregations on a ceria support and their catalytic activity with respect to the ODH of methanol to formaldehyde. Ceria as a very special support is reviewed in publication **P8**. Main motivation for the extensive collaborative study of the Sauer and Freund groups within CRC 546 (see, e.g., [226] and references therein), is the importance of vanadia as an oxidation catalyst on the one hand [227], and the lack of atomic-level understanding in the functioning of metal oxides as support on the other hand. The supporting

oxide may drastically affect reactivity (see also refs. [208, 228]). Turnover frequencies for methanol oxidation on vanadia may vary within three to four orders of magnitude depending on the reducibility of the supporting oxide [208, 228-230]. However, size and distribution of active (as well as less or inactive) vanadia species on different supports have been unknown and spectroscopic characterization, for instance by IRAS, was not available until recently [9-10, 231].

Experiments accomplished in the group of Freund revealed a strong cooperativity between vanadia species of low nuclearity and a ceria support [222]. This cooperative effect was monitored by TPD experiments using $CeO_2$(111) thin film model catalysts. These films were pre-saturated with methanol and the mass signal typical of formaldehyde was detected upon heating. It was found that formaldehyde desorbs at significantly lower temperatures when mononuclear vanadia species (examined by atomically resolved STM [9]) are present on the ceria surface compared with the pristine $CeO_2$(111) on one hand and the ceria film de facto fully covered with two-dimensionally grown vanadia. The reasons for this cooperative effect were unclear and called for a detailed mechanistic study using for instance DFT. The present section describes how this problem was solved in a step-by-step manner.

A well-ordered $CeO_2$(111) film was grown on a Ru(0001) substrate [9]. Vanadium was deposited on the fully oxidized film by physical vapor deposition in an oxygen atmosphere employing a partial pressure of $10^{-6}$ mbar $O_2$. The aforementioned collaborative efforts in Berlin generated crucial insights into the atomic structure of the submonolayer vanadia catalyst deposited on a $CeO_2$(111) surface [232]. These systems were investigated by applying several surface science techniques, such as atomically resolved STM, IRAS, XPS, TPD, as well as DFT. These studies concluded on the following main points: (i) $VO_x$ wets the support in a two-dimensional manner (Fig. 4.5) according to the constant apparent height of the occupied state STM images as well as DFT calculations (see publications **P3** and [231]). (ii) $VO_x$ clusters are terminated by V=O, i.e., vanadyl bonds as evidenced by IR and DFT. (iii) Larger $VO_x$ agglomerations like, e.g., trimers (Fig. 4.5b) are created upon annealing at 700 K of larger deposited amounts of vanadia. (iv) The IR-active V=O stretching mode, featuring a large perpendicular component of its dynamic dipole moment with respect to the surface plane (according to selection rule), is blue-shifted for larger vanadia oligomers. This is explained by the coupling of V=O dipole moments and is reproduced by DFT calculations (see [9] and publication **P3**). This structure-IR relationship was corroborated by computational results: the larger the $VO_x$ clusters, the larger the blue-shift in IR wavenumbers. (v) XPS indicates occupied Ce 4f orbitals in agreement with DFT. $VO_x$ clusters on the $CeO_2$(111) surface contain a tetrahedrally coordinated V atom in its highest oxidation state (+5). Ce atoms accommodate

the 3d electrons of V in one of the 4f orbitals, hence upon V deposition and oxidation, a fraction of $Ce^{4+}$ ($4f^0$) ions is reduced to $Ce^{3+}$ ($4f^1$) ions.

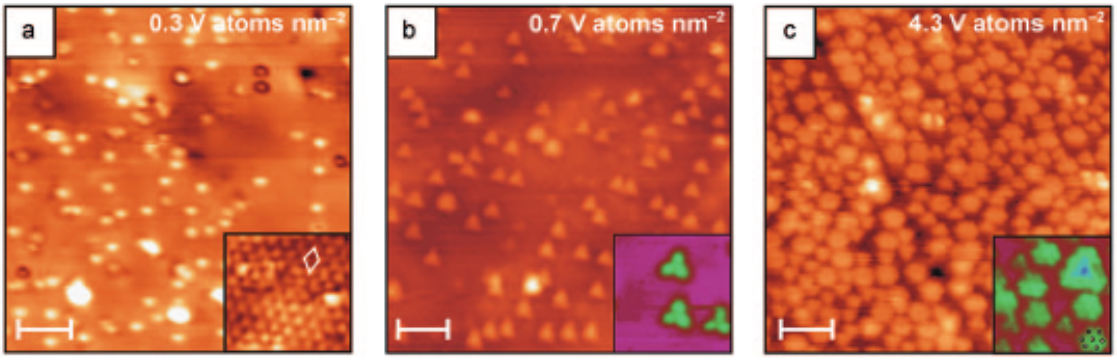


**Figure 4.5.** STM images of $VO_x$ species at the $CeO_2$(111) surface showing monomers (a), trimers (b), and larger oligomers (c) for loadings corresponding to 0.3, 0.7, and 4.3 V atoms/nm$^2$, respectively. Adapted with permission from [9]. Copyright (2009) John Wiley and Sons.

Thus, the composition of $VO_x$ clusters on the $CeO_2$(111) surface is inaccessible experimentally. This question could be successfully answered by DFT+U calculations combined with statistical thermodynamics [233]. These calculations use the PBE-GGA xc functional and an effective U parameter of 4.5 eV applied to the Ce 4f orbitals. The U value for Ce 4f was calculated self-consistently by Fabris et al. [234]. It was found that under relevant, slightly reducing conditions, VO or $VO_2$ originating from the gas phase represent prevalent surface species [235]. This finding was confirmed in publication **P4** for lower coverage using a larger surface unit cell than the one applied in [235].

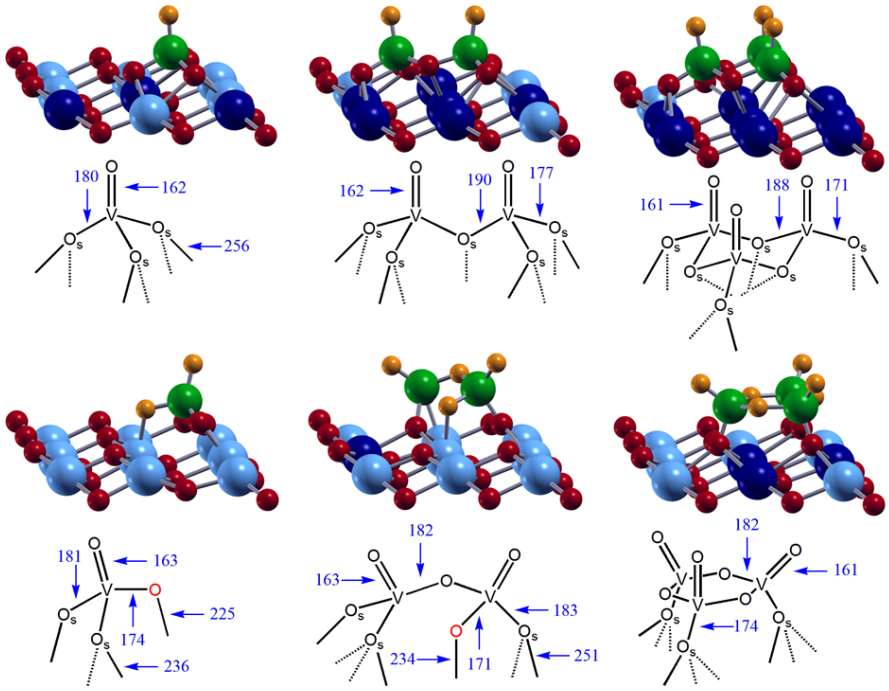


**Figure 4.6.** Energy minimum structures of VO (top) and $VO_2$ species (bottom) represented as ball and stick models. For clarity reasons a (3x3) cutout of the first O-Ce-O trilayer is shown ($Ce^{4+}$ light blue, $Ce^{3+}$ dark blue, $V^{5+}$ green, $O^{2-}$ in the surface red, $O^{2-}$ from the gas phase orange). Corresponding schemes are given below with bond distances in pm. The "special" O atom in $VO_2$ and $V_2O_4$ is highlighted in red and "$O_s$" refers to a surface O. Adapted from publication **P4**.

Thermodynamic stabilities of various $VO_x$ oligomers and their respective reactivities were extensively studied in publication **P3**. The calculated structures of the monomer, the dimer, and the trimer of VO deposited at the $CeO_2(111)$ surface as well as respective oligomers of $VO_2$ units on that surface are shown in Fig. 4.6. It also shows how the $VO_x/CeO_2(111)$ catalyst is modelled for computational studies: uncharged VO with V featuring a $3d^3$ occupation (in an ionic picture), and $VO_2$ with V ($3d^1$) are put on the clean $CeO_2(111)$ surface. Figure 4.6 shows the optimized structures. The V 3d electrons are spontaneously transferred into Ce 4f orbitals during optimizations. Consequently, one VO unit leads to three surface $Ce^{3+}$ ions (dark blue), and one adsorbed $VO_2$ unit features one $Ce^{3+}$ in the surface.

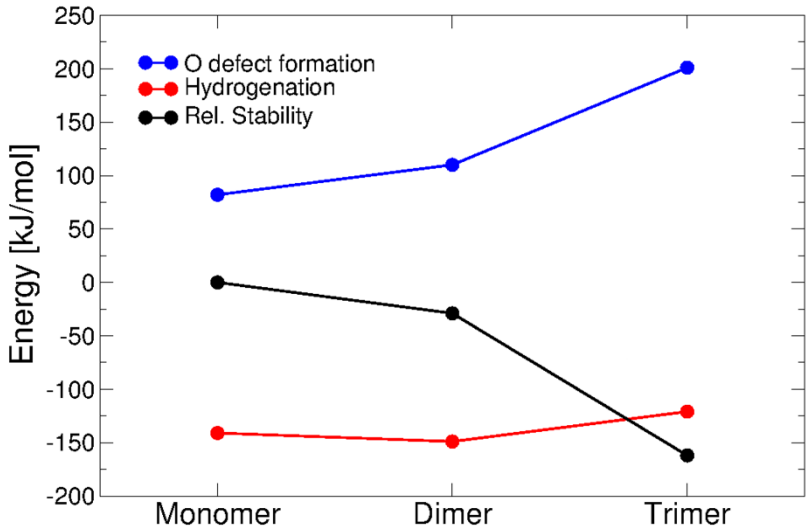


**Figure 4.7.** Relative stability, O-defect formation energy (with respect to $^1/_2\ O_2$), and hydrogenation energy (with respect to $^1/_2\ H_2$) of $VO_2$ aggregates supported on $CeO_2(111)$. Reprinted and adapted with permission from publication **P8**. Copyright (2013) American Chemical Society.

A decisive property of $VO_x$ clusters on the $CeO_2(111)$ surface, which was calculated using PBE+U, is the agglomeration energy. Trimerization of VO monomers at the surface requires 333 kJ/mol. Thus, agglomeration of VO into $(VO)_3$ trimers is thermodynamically highly unfavorable. In contrast, deposited $VO_2$ monomers trimerize pronouncedly exothermically releasing 162 kJ/mol upon trimerization. The strong thermodynamic driving force of $VO_2$ clusters to trimerize is shown in terms of relative stability (black line) in Fig. 4.7. This computational result is consistent with observation, because at moderate V loadings trimers become an abundant surface species after slight annealing [9]. Calculated vibrational properties of $(VO_2)_3$ also agree with experiment. Particularly, the calculated value of 25 $cm^{-1}$ based on harmonic wavenumbers agrees well with the observed blue shift of 27 $cm^{-1}$ for the V=O stretching mode.

Mechanistically, to form oligomers, $VO_2$ monomers need to migrate on the $CeO_2(111)$ surface. Early on, it was suggested that the monomers are stabilized by large migration barriers [9]. For a mechanistic study, two pathways have been examined using the nudged elastic band [236] as well as the so-called improved dimer method [237] to locate transition structures on the (multi-dimensional) potential energy surface spanned by the degrees of freedom of the cluster and the surface atoms. The associated energy profiles are shown in Fig. 4.8a. The pathway shown using black lines involves a moderate first activation barrier of 0.77 eV (74 kJ/mol) corresponding to a lift of the special oxygen (shown in red in the $VO_2$-scheme of Fig. 4.6) and a rotation of the $VO_4$-tetrahedron except for one surface oxygen ion,

which detaches upon rotation. The second quite pronounced barrier of 1.95 eV (188 kJ/mol) corresponds to the detachment of this anchoring oxygen ion, which relaxes back into the surface, and the V ion passing through the plane spanned by the remaining three oxygens, reminiscent to an umbrella motion. Another surface oxygen moves up and binds to the undercoordinated V ion to restore the energetically favorable four-fold coordination. Interestingly, the undercoordinated V ion is reduced as shown by its 3d spin density (Fig. 4.8b). On passing through the transition structure, the V 3d orbitals become partially occupied and the Ce 4f orbital occupancy corresponding to the (unique) $Ce^{3+}$ ion is depleted. Thus, it appears that atomic degrees of freedom are coupled to electronic degrees of freedom. Both undercoordination and reduction of the V ion come with a substantial increase in energy, i.e., a destabilization explaining the high migration barriers.

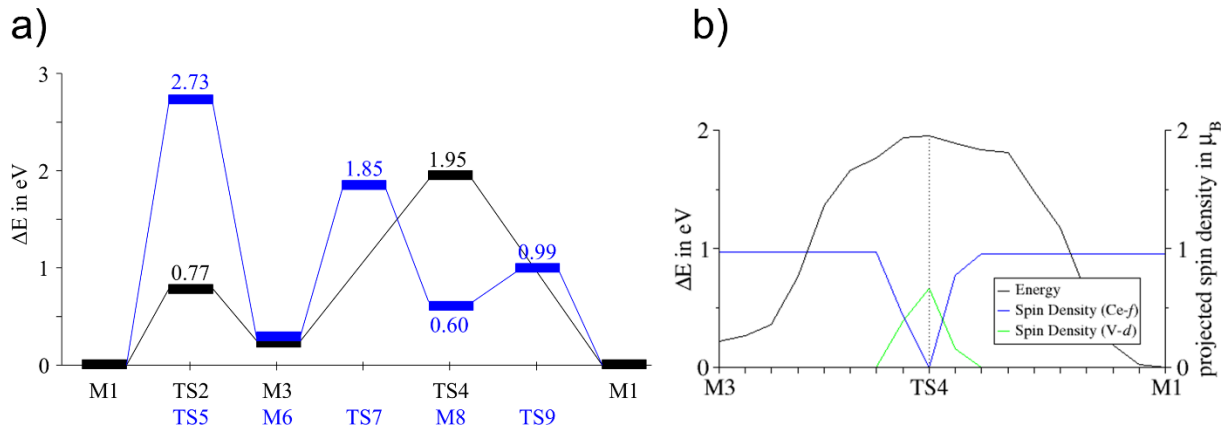


**Figure 4.8.** (a) Proposed energy profile for two different migration pathways of $VO_2/CeO_2(111)$. Activation barriers are given in eV. Local minima on the PES are indicated with "M", whereas transition structures are indicated with "TS". (b) Projected Ce 4f and V 3d spin densities shown in blue and green, respectively, for several NEB images to determine transition structure TS4. Courtesy of Dr. Thomas Kropp.

Regarding oxidation states, the V $3d^1$ electron of the $VO_2$ cluster is always transferred into a Ce 4f orbital upon adsorption on the surface. It is energetically more favorable as discussed in the previous paragraph. Therefore, a single $Ce^{3+}$ cation is created per $VO_2$ unit and V adopts its highest oxidation state +5. An energy-minimum structure featuring (partially) reduced V was not found (see [9, 235] and publications **P3** and **P4**).

With respect to the oxidation states, similar findings were obtained for mixed V/Ce-oxide clusters in the gas phase [238]. Thus, also in gas phase clusters $V^{5+}(3d^0)/Ce^{3+}(4f^1)$ is thermodynamically more favorable as shown by Sauer and Asmis using IR spectroscopy and DFT. Concerning surface structures of $VO_2$ monomers, dimers, and trimers, the V atom is always fourfold coordinated by oxygen atoms resulting in a slightly distorted tetrahedron on

the $CeO_2$(111) surface. However, as shown recently, in structures involving higher coverage, especially in so-called monolayers of $VO_2$ and $V_2O_5$ composition, also five-fold and six-fold coordinated V atoms occur [231]. However, these structures do not feature terminal V=O groups anymore.

The marked thermodynamic driving force of $VO_2$ deposited on $CeO_2$(111) for four-fold coordination involves a surface oxygen ion relaxing strongly outward from the surface to enable bonding to the V atom. This oxygen atom is so strongly lifted out of its lattice position such that a cavity is opened. This cavity, in analogy to an oxygen vacancy, was described as a pseudo-oxygen-vacancy (publications **P4** and **P5** as well as refs. [224] and [231]). This modified local lattice structure, which is not only characteristic of $VO_2$ monomers, but also of chain-type dimers and chain-isomers of higher nuclearity (see [231]), has drastic consequences on reactivity in the ODH of methanol. This was shown for the $VO_2$ monomer (publication **P5**).

Before examining important mechanistic details about the ODH of methanol at the $VO_2/CeO_2$(111) catalyst, we discuss efficient means to assess reactivity of metal oxides towards ODH of alcohols or alkanes, namely descriptors such as the oxygen defect formation energy and the hydrogenation energy. As shown by Sauer and Döbler [62], the oxygen defect formation energy relates to the overall activity of a catalyst with respect to a reaction, which proceeds according to the Mars-van Krevelen mechanism [61]. The hydrogenation energy relating to the rate-determining step, i.e., hydrogen transfer onto the catalyst, represents a measure for relative activation barriers. These considerations are in the spirit of the Brønsted-[239] or Bell-Evans-Polanyi [240-241] principle. As shown in Fig. 4.7, the oxygen defect formation energy increases with increasing stability (as well as nuclearity) of the $VO_2$ oligomers. This suggests that the overall activity in the ODH behaves inversely proportional to stability. Hence, it decreases, the larger the vanadia agglomerates on the surface. Similarly, calculated hydrogenation energies reflect, that the corresponding activation barrier for the H-transfer is expected to be higher for trimers compared to monomers and dimers (publication **P3**). This qualitative result is in line with observation shown within a series of TPD experiments done for methanol adsorbed on a clean (oxidized) $CeO_2$(111) film (topmost panel in Fig 4.9), and the film with low and higher amounts of $VO_x$ (middle and bottommost panel).

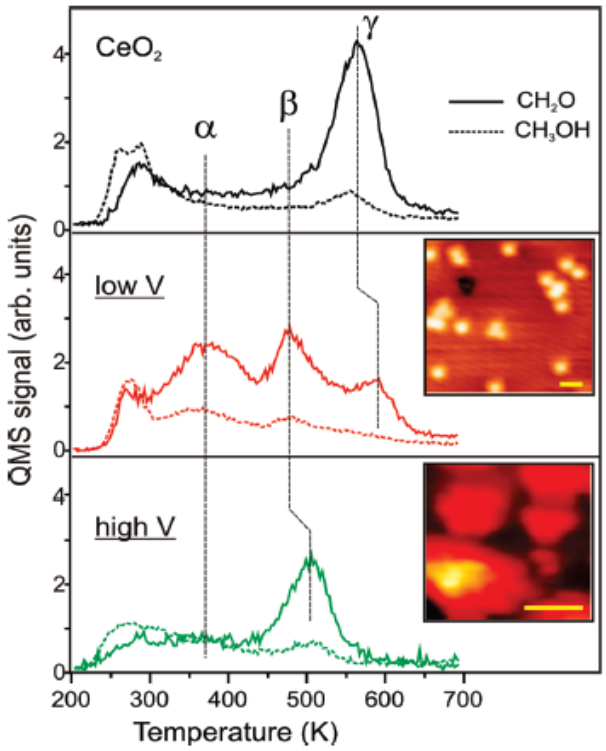


**Figure 4.9.** TPD spectra for ~5 L of $CH_3OH$ adsorbed at 300 K on $CeO_2$(111) and $VO_x/CeO_2$ (111) surfaces at low (<2 V at/nm$^2$) and higher (~4 V at/nm$^2$) vanadia loadings. Solid lines indicate the raw signal for $CH_3OH$ (31 amu), whereas dashed lines indicate $CH_2O$ (29 amu, corrected for the methanol cracking pattern). Signal intensity below 300 K is assigned to the tail of $CH_3OH$ monolayer desorption. The insets show typical STM images of vanadia species at respective coverage. The scale bar corresponds to 1 nm. Reprinted with permission from ref. [222]. Copyright (2010) American Chemical Society.

For low $VO_x$ loadings, the TPD spectrum of $VO_x/CeO_2$(111) markedly differs from the one of the clean surface. A so-called α peak of desorbing formaldehyde centers at about 370 K. This desorption temperature ($T_{des}$) is much lower than $T_{des}$ of the γ peak, characteristic of the clean $CeO_2$(111) surface ($T_{des}$ ~570 K). Employing the approximate Redhead formula [242] based on a heating rate of 3 K·s$^{-1}$ and a pre-exponential factor of $10^{13}$ s$^{-1}$, corresponding desorption barriers for α and γ have been estimated and are 100 kJ/mol and 150-160 kJ/mol, respectively [222]. Thus, deposition of mononuclear vanadia clusters on $CeO_2$(111) drastically enhances the dehydrogenation activity of the ceria support.

To understand this observation, individual elementary steps, i.e., possible energy minimum pathways for the dehydrogenation of methanol adsorbed on the clean $CeO_2$(111) surface (fully oxidized and reduced model, see publication **P6**) and on the $VO_2/CeO_2$(111) model system (publication **P5**) were studied using PBE+U and the HSE hybrid functional including the Grimme D2-type dispersion correction [243-244], which is henceforth indicated by a "+D". For the $VO_2/CeO_2$(111) surface additional calculations using the B3LYP hybrid

functional were accomplished. This was carried out having the well-defined surfaces under UHV conditions in mind. Importantly, prior to the TPD experiments, the surfaces were pre-saturated with methoxide species by dosing methanol ("high-pressure limit" of the Langmuir adsorption isotherm). DFT calculations suggest that for low methanol coverage under experimentally relevant conditions, dissociative adsorption occurs ([245-247] and publication **P6**). This is valid for the clean and defective $CeO_2$(111) surface (involving an oxygen vacancy), as well as the $VO_x/CeO_2$(111) systems (publication **P5** and [224]). Hence, observed desorption temperatures for formaldehyde correspond to intrinsic barriers involved in the partial oxidation of the adsorbed methoxide.

Regarding PBE+U results corrected for dispersion effects (+D) for methanol adsorbed on the pristine $CeO_2$(111) surface (publication **P6**), the adsorption energy including zero-point-vibrational-energy (ZPVE) correction is -88 kJ/mol. This value is smaller than the activation barrier of 104 kJ/mol for the H-transfer toward the surface (Tab. 4.2). Surface O-defects in $CeO_2$(111) are very reactive sites for the methanol oxidation. The methoxy binds in the vacant site with -230 kJ/mol obtained using PBE+U+D. This value appears to be slightly overestimated compared with the supposedly more accurate adsorption energy of -206 kJ/mol obtained using HSE+D. The PBE+U+D reaction barrier (methoxide in the O-defect) is 119 kJ/mol, which is 15 kJ/mol higher than the corresponding barrier for the pristine surface. Using HSE+D, the barrier for the ODH in the O-defect increases by 20 kJ/mol compared with the PBE+U+D result.

In addition to the (111) surface, also the oxidation of methanol adsorbed on the (100) surface has been studied in publication **P7**. This may be the relevant surface facet for different preparation conditions, for instance involving nanoparticles of cubic shape [248]. Although the precise surface structure is still under debate because of its intrinsic polarity and polarity compensating mechanisms [249], calculations have been carried out for the stable and established "missing row structure", with every other oxygen row on (100) surface placed on the bottom of the slab model .The ZPVE-corrected PBE+U+D barrier for the oxidation of the adsorbed methoxide to formaldehyde is 91 kJ/mol and is thus even lower than the activation barrier for the pristine surface. The lower barrier corresponds to lower formaldehyde desorption temperatures as observed in the TPD experiments of Albrecht and Mullins [250]. The higher activity is in accordance with predicted lower oxygen defect formation energy in the (100) surface (publication **P7**). Thus, defect formation energies are valid reactivity descriptors for oxidation reactions following a Mars-van Krevelen mechanism as discussed by Sauer and Döbler [62].

Experimentally it is known that the integral of the relevant TPD peak increases with an increasing number of O defects in the surface [6, 251]. This is consistent with the results discussed above. It appears plausible that more vacancies in the surface may convert more methoxide to formaldehyde giving rise to higher intensities in TPD desorption peaks. Neglecting temperature effects, the above mentioned ZPVE-corrected HSE+D barrier of 139 kJ/mol is similar to the estimate obtained by TPD and Redhead analysis (~145-155 kJ/mol) [222].

**Table 4.2** ZPVE-corrected intrinsic activation barriers (kJ/mol) corresponding to transition structures TS1 and TS2 (see Fig. 4.10) for the oxidation step of methoxide at vanadia/ceria and vanadia/silica, respectively.

| | | | TS1 | | TS2 |
|---|---|---|---|---|---|
| | **$CeO_2$** | **$CeO_{2-x}$** | **$VO_x/SiO_2$** | **$VO_x/CeO_2$** | **$VO_x/CeO_2$** |
| PBE+U | 104[a] | 119 | | 169[a] | 120[a] |
| HSE | | 139 | | 177[a] | 150[a] |
| B3LYP | | | 191[b] | 198[a] | 149[a] |
| B3LYP+ΔCCSD(T) | | | 175[b] | | |

[a] Table 5 in publication **P5**.
[b] Ref. [252]

For the $VO_2/CeO_2(111)$ model system, many distinct adsorption structures and pathways for the H-transfer in the oxidation step were studied (publication **P5**). One of them involves the methoxy species bound to vanadium, i.e., methoxide inserted into an "anchoring" V-O-Ce bond. This adsorption complex may be dehydrogenated passing through transition structures **TS1** or **TS2** (see Fig. 4.10). The H atom from the methyl group may be transferred to a surface oxygen, which leads to **TS2**. In this pathway, one electron localizes in a Ce 4f orbital close to the vanadia moiety. In contrast to **TS1**, **TS2** shows a spin-density contour indicating a rather localized electronic structure. As outlined in section 3.5 (see publication **P2**), B3LYP is expected to perform well for situations involving localized electron densities. In support of this conjecture, the barrier is largely independent of the hybrid functional used. B3LYP and HSE results are de facto identical for the "TS2 barrier" (B3LYP 149 and HSE 150 kJ/mol, Tab. 4.2). PBE+U is expected to suffer from SIE in the more localized situation. The PBE+U barrier of 120 kJ/mol is substantially smaller compared with results obtained using HSE or B3LYP.

The low temperature desorption or α peak of the TPD spectrum shown in Fig. 4.9 (middle panel) can be explained mechanistically based on the DFT calculations presented in publication **P5**. A pathway involving a low barrier of approximately 100 kJ/mol is reported. It represents the lowest intrinsic barrier among all studied pathways. The pronounced local relaxation of

the oxygen lattice induced by $VO_2$ plays an important role. The methanol adsorbs at the so-called pseudo-oxygen-vacancy thermodynamically de facto as favorably as the insertion of the methoxy group into the V-O-Ce "interphase" bridge. Subsequently, the H atom from the methyl group is transferred to the oxygen atom in the V-O-Ce unit and the electron is accommodated in a (surface) Ce 4f orbital, creating a $Ce^{3+}$ ion. The hybrid functional calculation on the corresponding transition structure was not done, but an estimate for the difference in calculated PBE+U and (anticipated) HSE barriers was computed based on the "TS2 pathway". The correction for the supposedly underestimated PBE+U barrier is estimated to be 30 kJ/mol. Adding this correction to the PBE+U activation barrier yields a value of ca. 100 kJ/mol. This result agrees with the estimated barrier derived from the observed TPD.

It is remarkable that the sites involved in the H-atom or coupled proton and electron transfer are spatially well separated. However, a case involving an even larger distance between these sites has been published by Goddard and coworkers [253-254]. This is work about oxidation of butane to maleic anhydride on a vanadyl pyrophosphate catalyst. In this case, the proton is transferred to P=O bonds, whereas the electron occupies vanadium d states.

Previously, Sauer and coworkers studied the partial methanol oxidation at vanadia supported on silica [252]. To model the surface, silsesquioxane clusters were employed. The transition structure involves the H-atom transfer from the methoxy group to the nearby oxygen atom in the V=O bond forming a five-membered ring. This transition structure is very similar to the analogue transition structure for vanadia on ceria (**TS1**, Fig. 4.10). Ref. [252] concludes on an overestimated reaction barrier obtained using B3LYP within the broken-symmetry approach [255] required for biradicaloid systems. This was shown by comparing results obtained with CCSD(T) [256-257] and B3LYP single-point calculations for the $O=V(OCH_3)_3$ molecule. The CCSD(T) correction to the B3LYP dehydrogenation barrier (191 kJ/mol, see Table 4.2) is 16 kJ/mol. Hence, the B3LYP barrier corrected by the $\Delta$CCSD(T) decrement is 174 kJ/mol. These results for the non-reducible silica support are instructive, because silica remains "electronically innocent" during the rate-determining step.

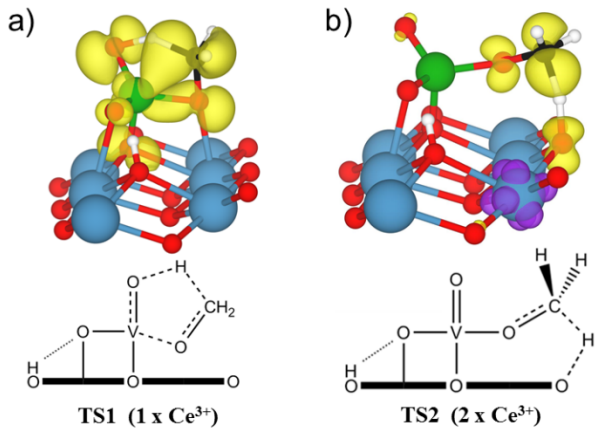


**Figure 4.10.** Electron and spin density (positive: yellow; negative: purple) contour plots at 0.01 $Å^{-3}$ showing the frontier orbitals involved in the formation of transition state **TS1** (a) and **TS2** (b). Total number of $Ce^{3+}$ ions in the $CeO_2$(111) surface is given in the schemes below. Reprinted and adapted with permission from publication **P5**. Copyright (2014) American Chemical Society.

The same pathway, i.e. H-atom transfer from the methyl group to the vanadyl O-atom, was studied for $VO_2/CeO_2$(111) in publication **P5**. Like in the transition state calculated for the silica support, no electrons were transferred to the surface, thus no additional $Ce^{3+}$ cations were formed upon H-abstraction. The electrons remained delocalized over the constituent atoms of the five-membered ring (**TS1** in Fig. 4.10a). The barrier for the oxidation step found employing B3LYP subject to periodic-boundary conditions is 198 kJ/mol (Table 4.2) and is very close to the dehydrogenation barrier for the silica supported vanadia using the silsequioxane cluster model. Subtracting the ΔCCSD(T) correction of 16 kJ/mol yields a barrier of 182 kJ/mol. This value agrees well with the HSE barrier of 177 kJ/mol. Thus, we believe that HSE performs accurately for this system, as stated in publication **P5**. The PBE+U barrier (169 kJ/mol) involving **TS1** is only 8 kJ/mol smaller compared with the HSE result. Thus, one may conclude that PBE+U performs well in case of rather nonpolar transition states involving a delocalized electron density but suffers from SIEs in states involving more localized electrons.

## 4.3 Metal-Support Interactions: The Case of Au/Ceria

**P9*** *Titration of $Ce^{3+}$ Ions in the $CeO_2(111)$ Surface by Au Adatoms*
Y. Pan, N. Nilius,* H.-J. Freund, J. Paier,* C. Penschke, and J. Sauer,
*Phys. Rev. Lett.* **2013**, *111*, 206101; Erratum: *ibid.* **2015**, *115*, 9901.

**P10*** *Reduction and oxidation of Au adatoms on the $CeO_2(111)$ surface – DFT+U versus hybrid functionals*
C. Penschke and J. Paier,* *Phys. Chem. Chem. Phys.* **2017**, *19*, 12546.

Another way to enhance catalytic activities of metal oxide surfaces is the deposition of noble metals (see chapter 6 in publication **P8**). Oxide supported gold in nanoparticulate form enjoys an outstanding appeal in the community, because it was shown to be an active low-temperature CO oxidation catalyst (see, e.g., [258]). However, even for the—at first glance—simplest case of depositing Au atoms, the situation is very complex when surface oxygen defects are involved due to potential electron transfer. In other words, reduction-oxidation processes occur changing the charge or oxidation state of the adatom (publications **P9** and **P10**). The determination of the oxidation state of Au atoms on reducible oxide surfaces is a nontrivial task but has been achieved due to collaborative efforts between experimentalists and theoreticians (see publication **P9**). In defective surfaces, the number of potential adsorption sites is usually large, and individual sites may feature drastically different redox activities. Thus, studying these sites like $Ce^{3+}$ cations in the reduced surface is important. For example, $Ce^{3+}$ ions are involved in the reverse oxygen spillover from the ceria support to Pt nanoparticles as shown by Libuda and coworkers [259]. Examining $Ce^{3+}$ ions in the reduced $CeO_2(111)$ surface as potential adsorption sites for Au atoms within a combined STM and DFT study was done for the first time in publication **P9**.

Specifically, atomically resolved STM on Au atoms deposited on the reduced $CeO_2(111)$ surface containing O-vacancies in subsurface positions obtained in the group of Freund indicated the formation of characteristic pairs of Au atoms in a distance equivalent to twice the length of the surface unit cell vector. Exploring the potential energy surface of individual Au atoms adsorbed on a $CeO_2(111)$-(2x2) slab model containing a subsurface O-vacancy and two $Ce^{3+}$ ions (one in the Ce-surface, the second one in the subsurface layer [260]) using hybrid functionals revealed that adsorption of Au atoms in atop position of $Ce^{3+}$ cations leads to a stable adsorption structure. The bonding interaction between gold and cerium can be explained by concomitant electron transfer from the $Ce^{3+}$ ($4f^1$) orbital into the Au ($6s^1$) orbital,

thereby creating $Ce^{4+}$ ($4f^0$) and $Au^-$ ($6s^2$) ions. Due to the larger ionic radius of $Ce^{3+}$ compared to $Ce^{4+}$, stabilizing relaxation effects decreasing surface strain and reinforcing the Au-Ce bond set in once $Ce^{3+}$ is reoxidized. Thus, Au atoms titrate $Ce^{3+}$ ions in reduced $CeO_2$(111) surfaces. The formation of distinct Au pairs is explained by the favorable 2x2-ordering of $Ce^{3+}$ ions relative to an O-vacancy in subsurface position. This means that two $Ce^{3+}$ ions located in nearest-neighbor positions relative to the vacancy is thermodynamically unfavorable, while the second coordination shell with respect to the O-vacancy corresponds to very stable sites.

In analogy to section 4.2. discussing vanadium oxide clusters on a ceria surface, ceria is also a non-innocent support material for noble metals because of its high reducibility. Regarding Pt clusters deposited on the $CeO_2$(111) surface, observed high catalytic activities were explained by Libuda and coworkers by two cooperative factors: (i) electron or charge transfer from the metal to the ceria support, and (ii) oxygen spillover from the support to the metal, i.e., oxidation of the metal [259]. Due to the propensity of ceria to form O defects [49], vacancies will play a role, particularly with respect to binding, e.g., single Au adatoms or Au atoms located on the rim of nanoparticles. Every (electroneutral) O defect in the surface is associated with two $Ce^{3+}$ ions. Thus, $Ce^{3+}$ is a mediator in electron transfer processes involved in metal-ceria support interactions. Consequently, polaron hopping may also be involved in the electron-transfer mechanism (see [261] and references therein).

The interaction between Au atoms and the surface O vacancy in the $CeO_2$(111) surface was profoundly studied by DFT+U [262-264] and amply reviewed by Zhang et al. [265]. It was found that the electron from neighboring $Ce^{3+}$ ions is spontaneously transferred into the Au 6s orbital. Hence, $Ce^{3+}$ is reoxidized and the $Au^0$ is reduced, thereby creating $Ce^{4+}$ and $Au^-$. The latter binds in the vacancy with a large binding or adsorption energy of ca. -2.6 eV, because of attractive electrostatic interactions ($Au^-$ mimics the missing $O^{2-}$, see publication **P8**).

Publication **P9** focuses on $Ce^{3+}$ ions as potential adsorption sites for Au atoms. This was achieved by preparation of a reduced $CeO_2$(111) surface containing O vacancies in subsurface position within the terminating O-Ce-O trilayer. Annealing conditions, particularly the oxygen partial pressure, determine whether surface or subsurface O vacancies are created. After annealing to 1000 K, the density of subsurface defects was ~$5 \times 10^{12}$ $cm^{-2}$. Subsequent dosing of low amounts of Au by physical vapor deposition induced the formation of pairs with Au-Au distances commensurate to the lattice of the $CeO_2$(111) surface. 40% of the pairs had a distance equal to twice the lattice parameter of the $CeO_2$(111) surface unit cell (~7.6 Å, see Fig. 4.11a). The smallest observed Au-Au distance (~4.8 Å) is substantially larger than the distance typical of the $Au_2$ bond (~2.5 Å [266]). These Au pairs were metastable species, because a 3.0 V pulse via the STM tip rearranged them into upright standing $Au_2$ dimers. In

some cases, the subsurface O vacancy near Au was identified by its characteristic STM image (see Fig. 1 in publication **P9**). Thus, it was conjectured that formation of the Au pairs is causally related to the $Ce^{3+}$ ions associated with subsurface O vacancies. Paired Au atoms as well as some of the isolated monomers, showed a halo-like contrast in STM images recorded at low bias. This contrast is typical of *charged* metal atoms when adsorbed on metal oxides such as alumina [267] or magnesia [268].

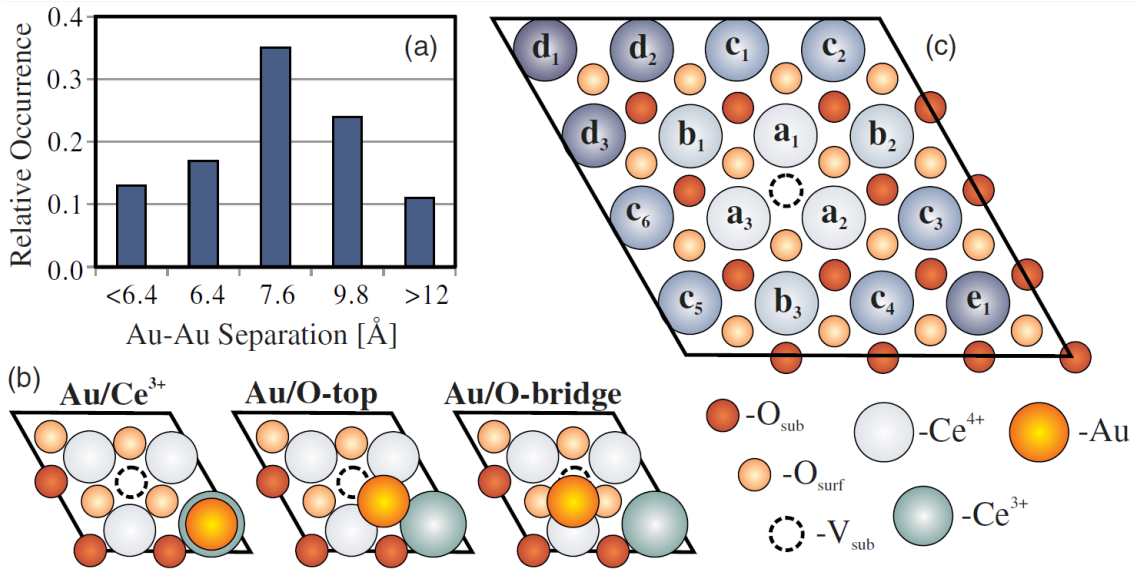


**Figure 4.11.** (a) Distance histogram determined for ca. 150 Au pairs on the ceria surface. (b) Configurations of a single Au adatom on reduced $CeO_2$(111) containing a subsurface O vacancy in a *p*(2×2) unit cell. (c) Labels indicating the Ce coordination shells in a *p*(4×4) unit cell relative to the vacant site (see Table 3.3). Reprinted with permission from publication **P8**. Copyright (2013) American Physical Society.

Various adsorption configurations for an Au atom in the O-defective *p*(2×2) surface unit cell were studied using the HSE and B3LYP hybrid functionals (Fig. 4.11b). The surface contained a single O vacancy in subsurface position, which corresponds to a defect concentration of ca. 200 × $10^{12}$ $cm^{-2}$. Four adsorption structures were found. It was shown that electron transfer from a $Ce^{3+}$ $4f^1$ into $Au^0$ $6s^1$ orbital leads to more stable structures relative to Au in atop O or O-O bridge positions. The latter sites do not yield $Au^-$ but preserves the $Au^0$ charge state (see Fig. 4.12). The thermodynamic preference of $Au^-$ relative to $Au^0$ is ca. 0.09 eV, when the $Ce^{3+}$ in subsurface position is oxidized. This means that the final adsorption state is an $Au^-$ ion adsorbed on top of a $Ce^{3+}$ ion.

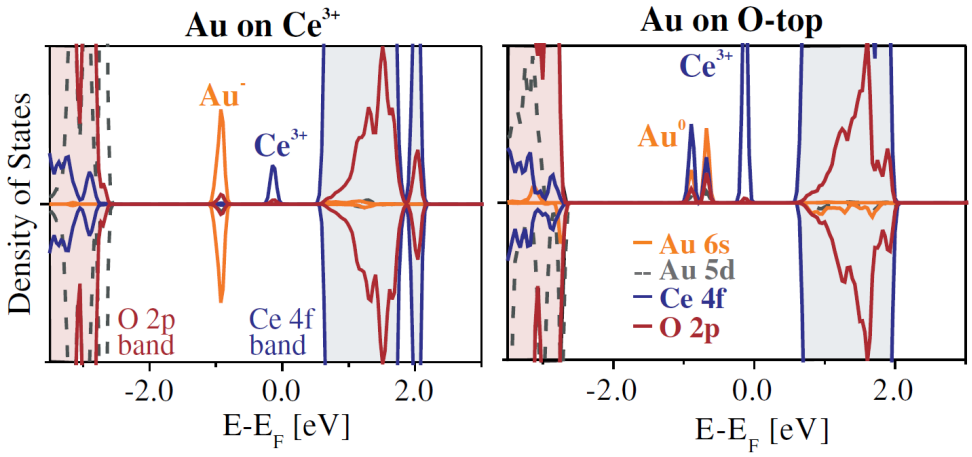


**Figure 4.12.** Respective projected local densities of states obtained with HSE for an $Au^-$ ion bound to a surface $Ce^{3+}$ (left) and to a $O^{2-}$ in atop position (right) in a $p(2\times2)$ cell of $CeO_2(111)$. Reprinted with permission from publication **P9**. Copyright (2013) American Physical Society.

The stability of structures involving an $Au^-$ ion is caused by large relaxation effects upon electron transfer or oxidation of the $Ce^{3+}$. As discussed in publication **P8**, $Ce^{3+}$ has a larger ionic radius than the $Ce^{4+}$ cation and electron transfer from $Ce^{3+}$ to $Au^0$ relieves some of the surface strain induced upon O defect formation. Oxidation of $Ce^{3+}$ to $Ce^{4+}$ involves pronounced stabilizing relaxation in the surface. $Au^-$ ions formed upon oxidation of $Ce^{3+}$ located in the surface or subsurface layer of the reduced $CeO_2(111)$ surface were recently confirmed [269] to be stable species. The latter work also uses a $p(2\times2)$ cell and reports a fifth, distinct adsorption structure with Au located at the hollow site atop a subsurface O. Also, for this configuration electron transfer from the $Ce^{3+}$ in subsurface position to $Au^0$ occurs and the $Au^-$ resides as a nearest neighbor to the surface $Ce^{3+}$. This structure is almost 0.5 eV more stable relative to the O-atop position [269]. However, as shown in publication **P10**, this structure turned out to be unstable at lower O-defect concentration using a $p(4\times4)$ surface unit cell.

**Table 4.3** Structure and vacancy formation energy ($E_{def}$) with respect to $^1/_2O_2$ for different subsurface O vacancy/$Ce^{3+}$ configurations obtained with HSE.

| $Ce^{3+}$ configuration | $Ce^{3+}$-$Ce^{3+}$ distance | $Ce^{3+}$-$V_O^{sub}$ distance | $E_{def}$ ($^1/_2O_2$) [eV] | |
|---|---|---|---|---|
| | | | High spin | Low spin |
| ***b₁–b₃*** | 7.67 | 4.41; 4.42 | **2.32** | 2.27 |
| ***a₁–b₃*** | 6.77 | 2.33; 4.44 | 2.43 | 2.41 |
| ***b₃–c₆*** | 6.65 | 4.41; 5.84 | 2.41 | |
| ***a₃–b₃*** | 3.89 | 2.34; 4.43 | 2.50 | 2.54 |
| ***b₃–d₃*** | 10.11 | 4.40; 7.94 | 2.47 | |
| ***c₅–c₆*** | 3.88 | 5.84; 5.85 | 2.69 | |
| ***c₁–c₆*** | 7.66 | 5.85; 5.84 | 2.66 | |
| ***a₁–d₃*** | 7.63 | 2.35; 7.93 | 2.62 | |
| ***a₃–c₅*** | 3.77 | 2.32; 5.86 | 2.63 | |
| ***a₁–a₃*** | 4.08 | 2.37; 2.37 | 2.71 | 2.71 |

In a next step, a number of $Ce^{3+}$ pair configurations in the larger $p(4\times4)$ surface unit cell of the $CeO_2(111)$ surface containing a single subsurface O vacancy were generated (see Fig. 4.11c). These structures were optimized using the HSE hybrid functional and corresponding defect formation energies are presented in Tab. 4.3. These results show that the stability of the O defect strongly depends on the $Ce^{3+}$-pair configuration. The nearest-neighbor sites of the vacancy, i.e., **$a_1$-$a_3$** (Fig. 4.11c), are thermodynamically unfavorable [260, 270]. In contrast, the **$b_1$-$b_3$** configuration of two $Ce^{3+}$ ions, i.e., the second cationic shell with respect to the vacancy) is ca. 0.40 eV more stable than the **$a_1$-$a_3$** configuration. The distance between $Ce^{3+}$ ions in structure **$b_1$-$b_3$** is equal to two lattice parameters of the $CeO_2(111)$ surface unit cell. The low spin (antiferromagnetic) state is 0.05 eV more stable than the high spin (ferromagnetic) ordered state of structure **$b_1$-$b_3$**. Effects induced by the magnetic order are therefore considered as negligibly small. Thus, the favorable stability of $Au^-$ created upon electron transfer from surface or near-surface $Ce^{3+}$ together with the preferred $(2\times2)$ arrangement of $Ce^{3+}$ around the vacancy explains the Au pair formation.

However, we point out that the problem is complicated by several reasons. One complication arises because of the calculated, admittedly small energy differences. Illas and coworkers examined various theoretical models, including the HSE hybrid, to predict the oxidation state of Au adsorbed on the clean $CeO_2(111)$ surface as well as stabilities of the respective adspecies [271]. They concluded that the prediction of the oxidation state is difficult using current GGA-based approaches, since solutions for the energy minimum structures for $Au^0$ or $Au^+$ are nearly degenerate in energy. In contrast, HSE predicts $Au^0/CeO_2(111)$ to be 0.15 eV more stable than the positively charged Au, which causes a $Ce^{3+}$ ion in the surface.

This finding is consistent with a recent STM study concluding on close-to-neutral charge states for Au atoms adsorbed on defect-poor ceria surfaces [272].

For a ceria surface containing O defects, the complexity in the adsorption of Au atoms on the surface increases drastically and requires addressing the influence of the defect concentration. Clearly, many defects in the surface build up considerable amounts of strain due to the high $Ce^{3+}$ concentration. Thus, the thermodynamic driving force to reoxidize some of them to $Ce^{4+}$ is large when Au adatoms offer half-filled 6s orbitals as "acceptor states". Therefore, the Au will titrate the $Ce^{3+}$. The effect of the defect concentration is supported by observation, because the STM revealed that the Au pairs did not homogeneously cover the surface, but large variations in the abundance of pairs were observed. This suggests that the local degree of reduction affects the pairs as explained in publication **P9**.

## 4.4 Cluster versus Periodic Models of an Fe-O-based MOF

**P11*** *Structural and Electronic Effects on the Properties of $Fe_2$(dobdc) upon Oxidation with $N_2O$*
J. Borycz, J. Paier,* P. Verma, L.E. Darago, D.J. Xiao, D.G. Truhlar,* J.R. Long,* L. Gagliardi,* *Inorg. Chem.* **2016**, *55*, 4924.

Sections 4.4 and 4.5 discuss the characterization of periodic multivalent Fe-O compounds like the Fe-based metal-organic framework ($Fe_2$(dobdc) or Fe-MOF-74; see publication **P11**) and the (111) surface of the inverse spinel $Fe_3O_4$ (publications **P12**-**P15**). Both studies represent collaborative efforts between experimentalists and theoreticians to establish clear-cut structure-property or structure-activity relationships. Apparently, both materials have the iron in common and are challenging due to open-shell 3d electrons involving the oxidation states $Fe^{+2}$ and $Fe^{+3}$ with distinct magnetic properties. These properties have been measured in case of the Fe-MOF-74 and compared with computational results. The modelling of the MOF's atomic structure used both cluster as well as periodic models. As described later in this thesis, cluster models allow to use wavefunction-based electronic structure methods [273] with the advantage of systematically improvable methodological accuracy. An extensive characterization of a complex Fe-based MOF via electronic, vibrational, and magnetic properties as done in **P11** is scarce, if not unique in the literature.

MOFs are an intensively studied class of porous and multifunctional so-called hybrid materials with potentially versatile technical applications, such as adsorption and separation of fluids, and as catalysts (see, e.g., [274] and [275], and references therein). Especially,

they appear to be active catalysts in oxidation reactions, when redox active metal centers like Fe [276] or Co are used [277-278].

Publication **P11** studies vibrational, electronic, and magnetic properties of an Fe-MOF known as $Fe_2$(dobdc), with $dobdc^{4-}$ = 2,5-dioxido-1,4-benzenedicarboxylate. It is also commonly referred to as Fe-MOF-74 [279]. Like in metal oxides, oxygen ions involved in so-called linker molecules bind coordinatively to a metal center. The Fe ions have magnetic properties due to their open-shell 3d electrons. Regarding $Fe_2$(dobdc) different iron-oxo-compounds, like $Fe_2(O)_2$(dobdc) and $Fe_2(OH)_2$(dobdc) are expected to occur as suggested for the mechanism of the oxidation of ethane to ethanol using $N_2O$ [276]. The parent framework, $Fe_2$(dobdc), contains $Fe^{+2}$ centers with a quintet ground state, while $Fe_2(OH)_2$(dobdc) contains $Fe^{+3}$ centers with a sextet ground state, and $Fe_2(O)_2$(dobdc) contains highly active (and thus short-lived) $Fe^{+4}$ centers with a quintet ground state [276, 280]. These different high-spin states involving magnetic couplings relate to the electronic ground states of these Fe-O compounds and were previously calculated by Gagliardi and coworkers [273] using cluster models and accurate wavefunction-based techniques like complete-active-space SFC (CASSCF, see e.g. [281]) combined with multi-reference perturbation theory [282]. Direct measurements of these properties are very difficult and thus tight collaboration between experimentalists and theoreticians is needed to study the electronic and magnetic structure properties, which might in turn serve to detect individual reaction intermediates to rationalize observed activities.

**Table 4.4** Isotropic magnetic coupling constants of the Fe centers for each studied MOF. Cluster calculations (cl) are compared with periodic results (per).

| | $J_{NN}$ ($cm^{-1}$) | | | | | |
|---|---|---|---|---|---|---|
| | **$Fe^{+2}$ - $Fe_2$(dobdc)** | | **$Fe^{+3}$ - $Fe_2(OH)_2$(dobdc)** | | **$Fe^{+4}$ - $Fe_2(O)_2$(dobdc)** | |
| method | cl | per | cl | per | cl | per |
| PBE//PBE | 64.6 | 113.9 | -18.2 | -23.1 | -9.9 | -12.4 |
| PBE//PBE+U | 14.3 | | -18.7 | | -9.0 | |
| PBE+U// | | 0.5 (0.3) | | -10.2 (-1.1) | | -1.2 (-0.9) |
| HSE//PBE+U | 2.4 (0.4) | 2.7 | -3.2 (-0.1) | -5.6 | 0.3 (-0.2) | -0.5 |
| PBE0//PBE+U | 2.5 | | -3.1 | | -0.1 | |
| obsd. | 4.1[c] | | | | | |

[a] X//Y indicates a cluster calculation with method X employing a fragment of a MOF optimized by periodic calculations with method Y. Only nearest- and next-nearest-neighbor intrachain coupling values ($J_{NN}$ and $J_{NNN}$) were computed.
[b] Values shown in parentheses represent the $J_{NNN}$ value (in $cm^{-1}$).
[c] Data taken from [279].

Table 4.4 summarizes magnetic coupling constants obtained using DFT and DFT+U for nearest- and next-nearest Fe ions in the above-mentioned MOFs containing $Fe^{+2}$, $Fe^{+3}$, and $Fe^{+4}$ centers. The comparison between periodic and cluster results suggests that differences in nearest-neighbor couplings are small, thus they can be computed quite accurately using cluster models. This implies that they can be used conveniently with a wider array of computational methods at a lower cost compared to periodic calculations. Regarding the electronic structure methods, hybrid functionals and PBE+U outperform the PBE-GGA functional based on the comparison with the observed result for $Fe_2$(dobdc). From the results presented in publication **P11** it is not clear whether next-nearest neighbor couplings suffer from using clusters, although it is advised to be careful in this case.

## 4.5 Adsorption of Water on the $Fe_3O_4$(111) Surface

**P12*** *Adsorption of Water on the $Fe_3O_4$(111) Surface: Structures, Stabilities, and Vibrational Properties Studied by Density Functional Theory*
X. Li and J. Paier,* *J. Phys. Chem. C* **2016**, *120*, 1056.

**P13*** *Surface Termination of $Fe_3O_4$(111) Films Studied by CO Adsorption Revisited*
X. Li, J. Paier,* J. Sauer, F. Mirabella, E. Zaki, F. Ivars-Barceló, S. Shaikhutdinov,* and H.-J. Freund, *J. Phys. Chem. B* **2018**, *122*, 527.

**P14*** *Cooperative Formation of Long-Range Ordering in Water Ad-layers on $Fe_3O_4$(111) Surfaces*
F. Mirabella, E. Zaki, F. Ivars-Barceló, X. Li, J. Paier,* J. Sauer, S. Shaikhutdinov,* H.-J. Freund, *Angew. Chem. Int. Ed.* **2018**, *57*, 1409; *Angew. Chem.* **2018**, *130*, 1423.

**P15*** *Water Adsorption on the $Fe_3O_4$(111) Surface: Dissociation and Network Formation*
E. Zaki, F. Mirabella, F. Ivars-Barceló, J. Seifert, S. Carey, S. Shaikhutdinov,* H.-J. Freund, X. Li, J. Paier,* J. Sauer, *Phys. Chem. Chem. Phys.* **2018**, *20*, 15764.

The work on the $Fe_3O_4$(111) surface represents the first step towards a comprehensive description of the oxide-water interface for an important mineral. It examines the adsorption and desorption of water on the surface by characterization of adsorption complexes using IRAS (including isotope labeling techniques), LEED, TPD, microcalorimetry, and DFT focusing on the monolayer coverage regime (and below). In a first step of the project, the controversy on the surface termination was solved based on computed wavenumbers of the CO stretching mode in various adsorption structures. This study included models of stable line defects or steps. Modelling steps in the surface is complex yet justified because growth of $Fe_3O_4$ islands was observed by STM. The double metal also known as $Fe_{oct2}$ termination as the prevalent surface structure could be ruled out. Based on a comparison of calculated and observed IR active modes of CO, it was shown that the single $Fe_{tet1}$ ion represents the regular surface termination (publication **P13**). I/V LEED [283] and phase diagrams obtained using DFT [284] support this conclusion.

Once the surface structure of $Fe_3O_4$(111) was resolved, the study of its interfacial structure to water, as one of the most important solvents and reagents in nature, was envisaged. The formation of a long-range ordered water adlayer was shown. Hydrogen-bonding between molecularly adsorbed water molecules and dissociatively adsorbed monomers leads to the formation of a two-dimensional (2D) network structure connecting adjacent surface unit cells, which translates into a (2x2) overlayer as observed by LEED (publication **P14**). It could be shown that these 2D structures require a minimal amount of water of ca. 6 $H_2O$ molecules per (2x2) unit cell or a (formal) coverage of 1.5 monolayer. Once this coverage is exceeded, intermolecular H-bonding leads to slightly more stable 2D structures as compared to agglomerated or clustered structures (publication **P15**).

Iron oxides are technically versatile materials as recently reviewed by Parkinson [285]. Hematite ($\alpha$-$Fe_2O_3$) is a common solid catalyst in the so-called water splitting reaction, and magnetite ($Fe_3O_4$) is an active component in the Fischer-Tropsch process, because it is a known catalyst for the water-gas shift reaction [286-287]. The surface chemistry of iron oxide thin films supported on metal substrates show novel catalytic properties, the oxides are abundant and stable as discussed by Freund, Pacchioni, and coworkers recently [288-289]. Due to the abundance of iron oxides in the Earth's crust, they are almost inevitably in contact with water (under ambient conditions). The high interest of geochemists in the interaction between water and iron oxides with respect to soil formation (e.g., via weathering) is therefore obvious [290].

Publications **P14** and **P15** examine the early stages of water adsorption on the $Fe_3O_4$(111) surface at relatively low temperature using LEED, TPD, IRAS, and DFT, while publication **P13** studies via IRAS, TPD, and DFT the atomic structure of the outermost layers of the (111) surface of $Fe_3O_4$ to prove its most stable atomic structure when applying UHV conditions. Thus, the work presented in publication **P13** determines the atomic structure of the outermost layers of the $Fe_3O_4$(111) surface prior to adsorption by application of several surface science techniques. In addition to the adsorption studies on the natural growth facet of magnetite, also systematic comparison of water adsorption on $Fe_2O_3$, as a reducible oxide, and $Al_2O_3$ (0001) surfaces featuring both the corundum structure were accomplished by Sauer and coworkers [291].

Studying the adsorption of water or any other adsorbate on surfaces requires precise knowledge of their atomic structure prior to adsorption. Surfaces of the (inverse) spinel magnetite in [111] orientation can be cut in six different ways according to the stacking sequence of Fe and O layers (see Fig. 4.13, left). The termination of the $Fe_3O_4$(111) surface has been controversially discussed [292-293]. This is because previous DFT calculations predicted, based on stability diagrams, that the $Fe_3O_4$(111) surface is terminated by a single

Fe ion (see $Fe_{tet1}$ termination shown in Fig. 4.13, light blue ball). This Fe ion is four-fold (tetrahedrally) coordinated in the bulk phase [284, 294]. The commonly chosen acronym for this termination is $Fe_{tet1}$, although the Fe ion loses one coordination partner upon cutting the surface in [111] orientation. In agreement with this prediction, recent I/V LEED studies determined a very small Pendry-R (reliability) factor of ~ 0.1 for the $Fe_{tet1}$-terminated surface model [283], which indicates that the structure is de facto solved.

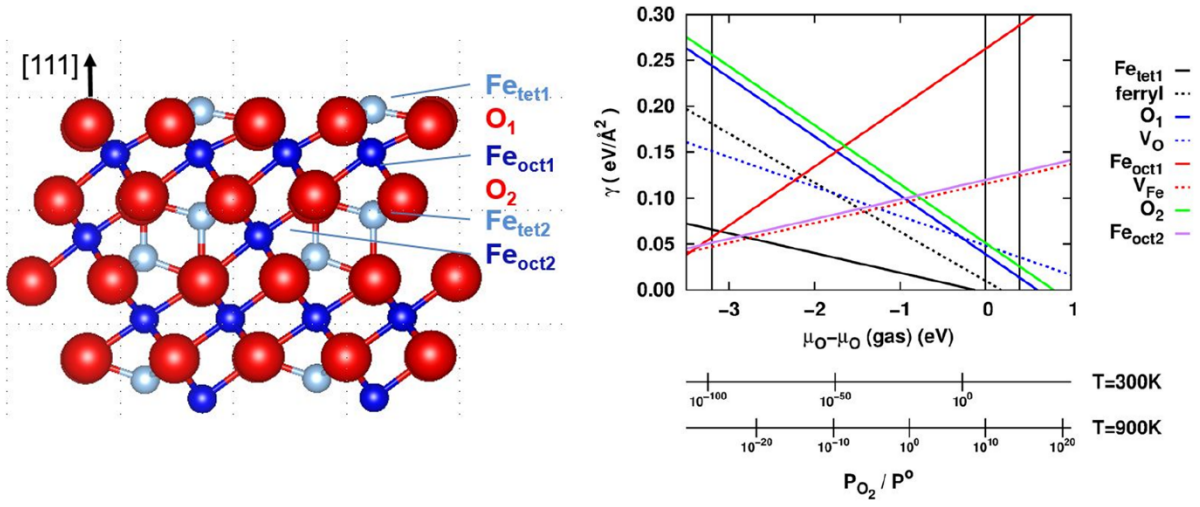


**Figure 4.13.** Stacking sequence of atomic layers in $Fe_3O_4$ in the [111] crystallographic direction (left); Stability diagram of various terminations; $p^o$ = 1 bar (right). Adapted from [294] and reprinted with permission. Copyright (2013) American Physical Society.

In contrast, two independent adsorption studies using CO [292] and $H_2O$ [293] as probe molecules found that the obtained results can only be rationalized if two metal ions, a tetrahedrally and an octahedrally coordinated one, terminate the surface. It is common practice to refer to tetrahedrally and octahedrally coordinated surface iron ions (see, e.g., [285]), although these ions lost—compared with the bulk phase—one and three coordination partners, respectively. The commonly used acronym for this "double metal" terminated surface is $Fe_{oct2}$ (Fig. 4.13, left). This apparent controversy had to be addressed to resolve the $Fe_3O_4$(111) surface structure.

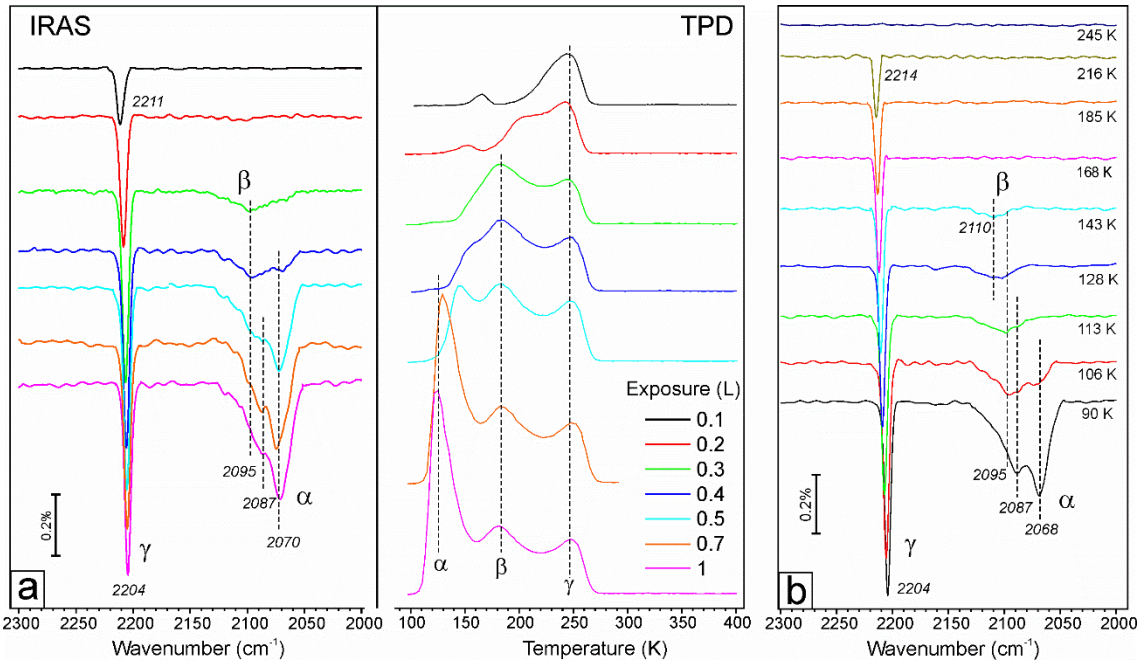


**Figure 4.14.** Series of CO-IRAS and TPD spectra (CO adsorbed at 90 K) as a function of exposure on $Fe_3O_4$(111) (a). IRAS spectra of 1 L CO at 90 K and after thermal flash to the temperatures as indicated. (b). Reprinted with permission from publication **P10**. Copyright (2017) American Chemical Society.

Figures 4.14a and 4.14b show observed CO-TPD and IRAS spectra recorded for a thin $Fe_3O_4$(111) film grown on Pt(111). Both techniques were applied to CO adsorbed at 90 K for a series of exposures given in the legend. The TPD shows that three states are populated. At lowest exposure, the so-called $\gamma$ state is predominantly populated. Upon increasing the CO exposure, the $\beta$ and eventually at higher exposure of >0.4 L the $\alpha$ state is populated. A similar experiment combined with IR reflection-absorption spectroscopy was applied. At low exposures up to 0.3 L only the $\gamma$ and the $\beta$ bands are observed. The band attributed to $\alpha$ is visible for exposures >0.4 L. Importantly, the $\gamma$ band is a sharp peak with a relatively low integral, whereas the $\beta$ band is relatively broad, developing a shoulder at 2095 $cm^{-1}$ for >0.4 L. Results of the present study are de facto identical to those discussed in [292], but structure-IR relationships can be drawn for the first time by virtue of—within the present work—computed (harmonic) wavenumbers of CO adsorption structures (publication **P13**). Based on these results, CO stretching vibrations and adsorption enthalpies for various structures on the $Fe_3O_4$(111) surface terminations of interest, namely $Fe_{tet1}$ as well as $Fe_{oct2}$ can be compared with experiment.

**Table 4.5** Unscaled and scaled harmonic CO stretching frequencies ($cm^{-1}$) and CO adsorption enthalpies at 0 K including *RT* for 90 K[c] (kJ/mol).

| Structure | Termination | Adsorption site[a] | ν(CO), $cm^{-1}$ | | $E_{ads}$ | $E^0_{ads}$[c] |
|---|---|---|---|---|---|---|
| | | | unscaled | scaled [b] | | |
| free CO | - | - | 2123 | 2143 | - | |
| **A** | Tet1 | $Fe_{tet}^{3+}$(3) | 2085 | 2105 | −44.0 | −39.8 |
| **B** | Oct2 | $Fe_{tet}^{3+}$(3) | 2015 | 2034 | −26.1 | −21.4 |
| **C** | Oct2 | $Fe_{oct}^{2+}$(3) | 2030 | 2049 | −102.6 | −97.0 |
| **D** | Oct2 | $Fe_{oct}^{2+}$(5) | 2180 | 2200 | −40.4 | −35.9 |

[a] Coordination number of Fe ions in the pristine surface given in parenthesis.
[b] Scaling factor 1.0094 is obtained for free CO to fit the experimental value (2143 $cm^{-1}$ [295]).
[c] At 90 K, *RT* corresponds to 0.75 kJ/mol.

Table 4.5 shows calculated unscaled as well as scaled harmonic wavenumbers of the CO stretching mode, $\nu_s$(CO), for structures **A**, **B**, **C**, and **D** displayed on the right-hand side in Fig. 4.15. Structure **A** is an energy minimum structure with the CO molecule adsorbed carbon-down in atop position of the terminating $Fe_{tet1}$ ion (light blue) in the single metal $Fe_{tet1}$ terminated $Fe_3O_4$(111) surface. As discussed in previous sections, DFT suffers from shortcomings and to (partially) take care of DFT errors and the errors incurred by the harmonic approximation when calculating force constants of vibrational modes, a scaling with respect to the observed fundamental of the free CO molecule was applied. This factor is 1.0094. The calculated $\nu_s$(CO) in structure **A** is 2105 $cm^{-1}$ and agrees well with the upper boundary of the observed β band at 2095 $cm^{-1}$, although slightly overestimated by 10 $cm^{-1}$. With respect to the free CO molecule, the calculated wavenumber is red-shifted by 38 $cm^{-1}$. The red-shift can be explained by a d-π* electron back donation from the surface Fe ion to the antibonding CO-π* orbital comparable to the bonding mechanism in metal carbonyls [296-298].

Comparing several calculated structural candidates using $\nu_s$(CO), only structure **D** corresponding to the facet of a step in the $Fe_3O_4$(111) surface agrees with the observed $\nu_s$(CO) associated with the γ peak shown in Fig. 4.14. The model for the step features an oxygen adlayer on top of the $Fe_{oct2}$-terminated surface and refers to a so-called A-type step discussed in [292] and [299]. Based on principles like minimal loss of coordination partners as well as preservation of charge neutrality, A- and B-type steps are supposed to be the most stable line defects on the $Fe_3O_4$(111) surface [299]. The calculated wavenumber of the CO stretching mode is 2200 $cm^{-1}$ and underestimates the observed value by 7 $cm^{-1}$. Compared with $\nu_s$(CO) of the free molecule, this value is blue-shifted by 57 $cm^{-1}$. Strong blue shifts of CO wavenumbers can be explained by the wall effect or—closely related—Pauli repulsion [300]. It relates to the repulsive interaction between the lone pair of CO localized at the carbon atom

and the valence electrons of the $O^{2-}$ ions. The induced steep potential wall translates into a narrowing of the potential causing the larger wavenumber.

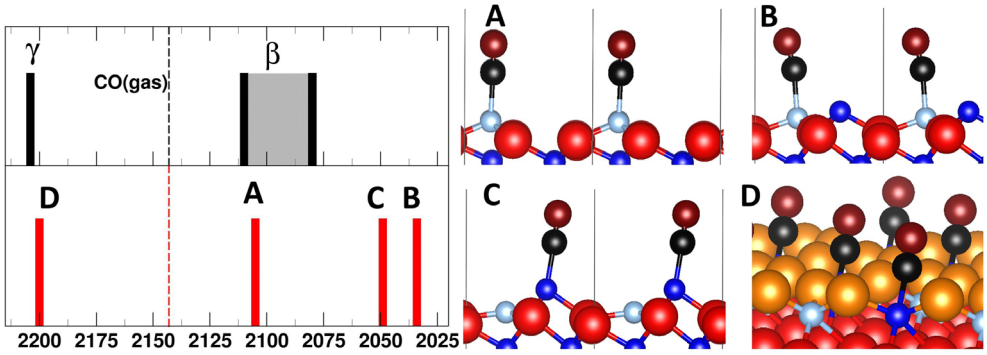


**Figure 4.15.** Comparison of experimentally observed (upper panel, black) and calculated (lower panel, red) $\nu_s$(CO) bands for corresponding structures (**A**-**D**) shown on the rhs. The $Fe_{oct2}$ ions and $Fe_{tet1}$ ions are shown in dark and light blue, respectively. Lattice oxygen is red; oxygen in O-adlayer (structure **D**) to model the step facet is orange; carbon is black; oxygen in CO is dark red.

Structures **B** and **C** represent a single CO molecule adsorbed on either the $Fe_{tet}$ (structure **B**) or the $Fe_{oct}$ (structure **C**) ion of the double metal $Fe_{oct2}$ terminated $Fe_3O_4$(111) surface. The CO stretching wavenumber is 2034 and 2049 $cm^{-1}$, respectively. These wavenumbers are red-shifted with respect to the free molecule by 109 and 94 $cm^{-1}$, respectively. Although the above-mentioned observed IR band corresponding to the β state in the TPD is (compared to the γ peak) relatively broad and spans a range between 2110 and 2080 $cm^{-1}$, such low wavenumbers as these calculated for structures **B** and **C** have never been observed. Additionally, calculated adsorption enthalpies for structure **B** and **C** are –21.4 and –97.0 kJ/mol, respectively. The latter adsorption enthalpy corresponds to a CO desorption temperature of ca. 400 K (using the approximate Redhead analysis with a pre-factor of $10^{13}$ $s^{-1}$ for first-order desorption. This was not observed in the TPD spectra (see Fig. 4.14a). Regarding a comparison of TPD desorption enthalpies with calculated values, we refer to [301] and [302] by Sauer and coworkers. These works outline, that experimental values are Arrhenius activation energies of desorption and differ from the enthalpy of desorption by *RT*. The strongly exothermic adsorption of CO on the $Fe_{oct2}$ terminated surface is in principle consistent with its lower stability under relevant conditions ($\mu_O \sim -1.4$ eV; see Fig. 4.13 right) based on bond-order conservation or the rule of electrostatic valence [303-304]. Recall that the terminating $Fe_{oct2}$ ion loses three coordinating oxygen ions and the terminating $Fe_{tet1}$ ion

loses one upon cutting the (111) surface. In contrast, the adsorption enthalpy for CO on the $Fe_{tet1}$-terminated surface is −39.8 kJ/mol. Employing eq. 4.4,

$$E_{des} \approx R \cdot T_{peak} \left( \ln \frac{\nu \cdot T_{peak}}{\beta} - 3.64 \right), \tag{4.4}$$

with a pre-exponential factor $\nu = 10^{13}\ s^{-1}$ and a heating rate $\beta = 3\ K\ s^{-1}$, this adsorption enthalpy corresponds to ca. 180 K, which agrees with observation. This estimate approximates the desorption barrier $E_{des}$ by the adsorption enthalpy $E_{ads}^{0}$ of −39.8 kJ/mol. However, we consider this approximation as reasonable due to expected small structural changes in the transition state.

Thus, we attribute the observed IR band at 2207 $cm^{-1}$ to CO adsorbed on line defects or equivalently step edges such as the one displayed in structure **D**. The occurrence of steps is supported by the observed growth of islands shown in STM images (Fig. 5 in publication **P13**). For structure **A**, i.e., CO adsorbed on the $Fe_{tet1}$ terminated $Fe_3O_4(111)$ surface, the calculated wavenumber of the CO stretching mode falls into the range observed for the β state, and the CO adsorption enthalpy is consistent with the TPD spectrum shown in Fig. 4.14a. Thus, we conclude that the outermost surface layer consists of a single $Fe_{tet}$ coordinated iron ion. This conclusion is in line with previous DFT calculations on stabilities of the various surface terminations as well as with the most recent I/V LEED analysis [283]. Therefrom drawn conclusions for the adsorption of water will be discussed in the following section.

Once, the question about the surface structure was answered, we could go ahead to study the adsorption of water on the $Fe_3O_4(111)$ surface focusing on relatively low coverages. From a computational point of view, this required utilization of larger surface unit cells, specifically the p(2x2) unit cell. Note that the computational approach, particularly results for the water adsorption on the $Fe_3O_4(111)$-(1x1) cell using 12 atomic layers, was assessed in publication **P12**. Both, PBE+U and the HSE hybrid functional was applied to calculate a stability or phase diagram for the adsorption of water. Utilization of (2x2) supercell imposes a particularly high computational work load and is challenging with respect to obtaining the magnetic ground state.

Figure 4.16 shows some of the relevant adsorption structures. In addition, so-called incremental adsorption energies according to

$$Fe_3O_4(111) \cdot n\ H_2O + H_2O \rightleftharpoons Fe_3O_4(111) \cdot (n+1)\ H_2O \tag{4.5}$$

$$\Delta E(n) = E_{n+1} - (E_n + E_{H2O}) \tag{4.6}$$

are shown in kJ/mol. This is central content of publication **P14**. In this article we describe a 2D network structure formed by the water adlayer. This structure has a (2x2) translational

symmetry with respect to the $Fe_3O_4$(111) primitive unit cell. This network structure has been experimentally studied using LEED and TPD (see Fig. 1 in publication **P14**).

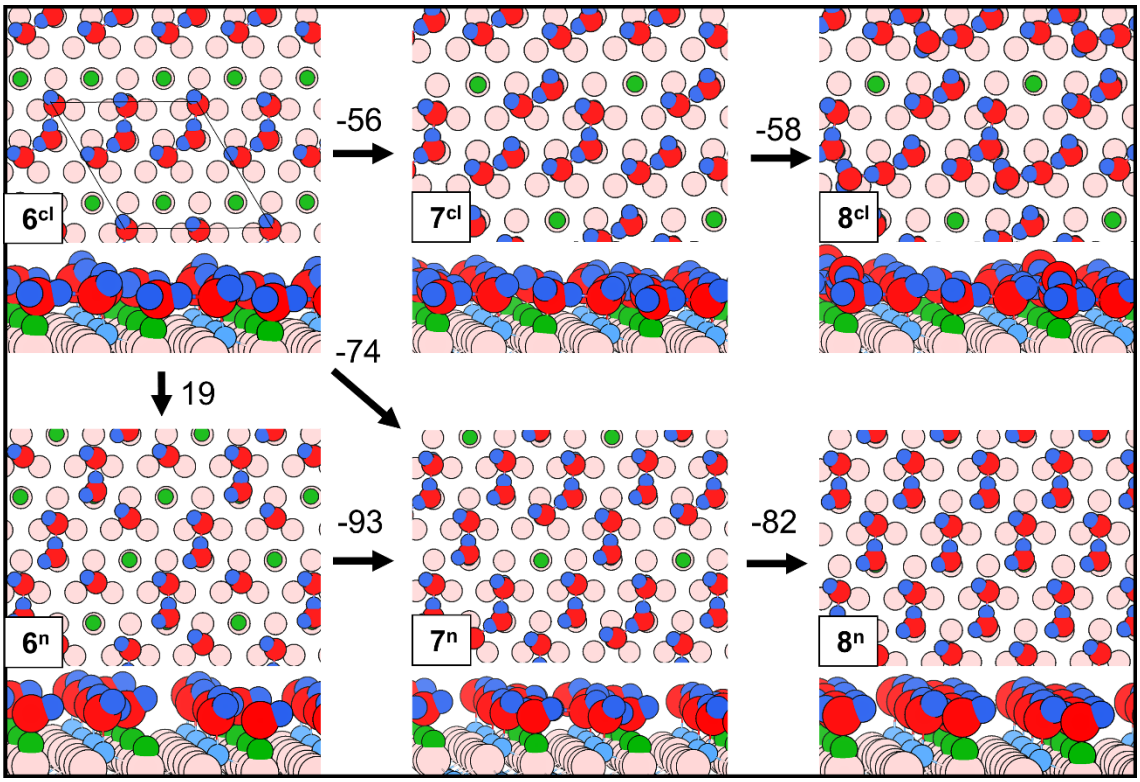


**Figure 4.16.** Top views and perspective views of several computed structures containing 6, 7, and 8 water molecules in a (2x2) supercell of $Fe_3O_4$(111) surface. The top panel displays the formation of cluster-like water oligomers (structures **$6^{cl}$**, **$7^{cl}$**, and **$8^{cl}$**). The bottom panel shows development of the H-bonded 2D network (structures **$6^{n}$**, **$7^{n}$**, and **$8^{n}$**). Incremental reaction energies are given in kJ/mol. Fe, O and H on the surface are purple, pink and green, respectively. Water-related O and H atoms are red and blue, respectively.

According to the strongly exothermic adsorption energy of -123 kJ/mol for a single water molecule, water starts to preferentially dissociatively adsorb. Upon dissociative adsorption two hydroxyl groups are formed: One terminal $O_WH$ (water-related OH) as well as an $O_SH$ hydroxyl group (protonated surface oxygen ion) will be created (see scheme on the lhs shown in Fig.4.17). The $O_WH$ group coordinates to the terminating Fe ion. Increasing the coverage, will lead to formation of typical water dimers as shown on the rhs in Fig. 4.17. We followed two pathways going systematically through the structural manifold. Figure 4.16 shows structures with more clustered or dimer-type motifs with the superscript **cl** on the one hand (upper panel) and more pronounced 2D network character triggered by H- bonding between dimers with superscript **n** on the other hand (lower panel). As shown, beyond a critical coverage (ca. 6

$H_2O$ molecules per (2x2) unit cell or equivalently 1.5 monolayer coverage), 2D-network structures are more stable than clustered structures.

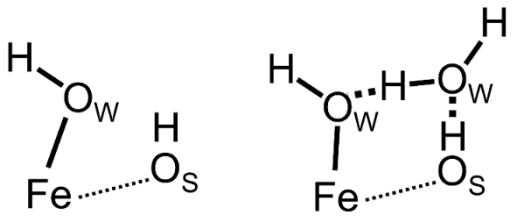


**Figure 4.17.** Schemes for the dissociatively adsorbed water monomer (left) and water dimer (right). The water-related OH groups are displayed as $O_WH$ and surface hydroxyl groups are shown as $O_SH$. The thin dotted line indicates the surface plane and does not indicate a bond.

As one of the essential results, the structure **7$^n$** is more stable than **7$^{cl}$** and shows (2x2) symmetry as observed by LEED. The required ZPVE-correction to calculate the adsorption enthalpies (at 0 K) for each structure shown in Fig. 4.16 is a constant value of ca. 16.0 kJ/mol. Hence, differences in stabilities calculated using enthalpies are negligible compared with the values given in Fig. 4.16 (i.e. PBE+U energy differences).

To get a detailed structure-IR relationship a combined IRAS-DFT study published in publication **P15** was accomplished. To understand the observed IR properties as well as the apparent evolution of structures during the adsorption of water on the $Fe_3O_4$(111) surface, IR wavenumbers of structures involving a wide range of coverage were calculated. To introduce the elementary "building blocks" of (dissociative) water adsorption on the surface, one and two $H_2O$ molecule were adsorbed and optimized using DFT. The obtained energy minimum structures are shown in Fig. 4.18.

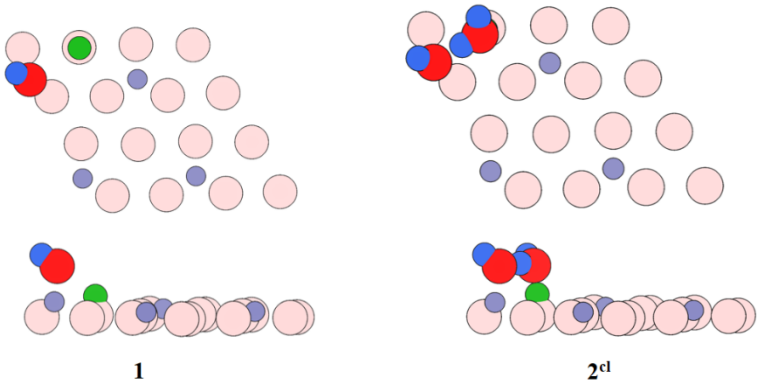


**Figure 4.18.** Top view (above) and side view (below) of structure **1** (left) and **2$^{cl}$** (right) on the $Fe_3O_4$(111)-(2×2) supercell. Color code as in Fig. 4.16.

Two distinct OH groups result from a dissociative adsorption of a single water molecule, i.e. monomer formation. A terminal $O_wH$ group coordinating to the Fe ion is formed and in addition—due to proton transfer—also a surface hydroxyl group, $O_sH$, is created. We underline the difference between water-related $O_wH$ groups as well as undissociated water with oxygen

and hydrogen atoms shown in red and blue, respectively, while oxygen and hydrogen atoms involved in surface hydroxyl groups are shown in pink and green, respectively. Due to these two distinct functional groups, two IR bands are expected. With respect to dimer structure **2$^{cl}$** (Fig. 4.18), the additional molecularly adsorbed water molecule bridges the $O_wH$ and $O_sH$ groups resulting from monomer formation (see also Fig. 4.17). The inserted water molecule in the dimer features one further terminal $O_wH$ group pointing off the surface but is tilted by ca. 50° with respect to the surface normal. The second proton of the additional water molecule is involved in an H-bond connecting to the terminal $O_wH$ of the monomer. The H-bond vibrational mode involves coupling to the $O_sH$ proton of the monomer.

The formation of a dimer leads to four distinct OH modes, i.e. the stretching vibrations of two terminal $O_wH$ groups and symmetric and antisymmetric H-bond vibrations involved in the undissociated water. Based on the surface selection rules [305-308], the second $O_wH$ group will feature little intensity due to tilting. Once enough hydrogen bonds are formed to yield an IR signal with sufficient intensity, the wavenumbers fall into an area of relatively low energy and associated observed spectra are broad [309]. Hence, structural assignments are difficult. Consequently, H-bonding interactions will be considered to yield non-relevant contributions to the spectra and will therefore not be discussed in the following section. To partially correct for the error of neglected anharmonicities [310] in OH vibrations, a scaling factor 0.9935 is used (see ref. [293] and supplemental information of it). The scaling factor is calculated as $\frac{\frac{1}{2}(\nu_s+\nu_{as})}{\frac{1}{2}(w_s+w_{as})}$, i.e. the ratio of the means of observed fundamentals and calculated harmonic wavenumbers of symmetric (s) and antisymmetric (as) stretching modes in the free water molecule, as suggested in [12]. The scaling applied throughout this work refers to scaled terminal OD stretching wavenumbers induced upon dosage of $D_2O$.

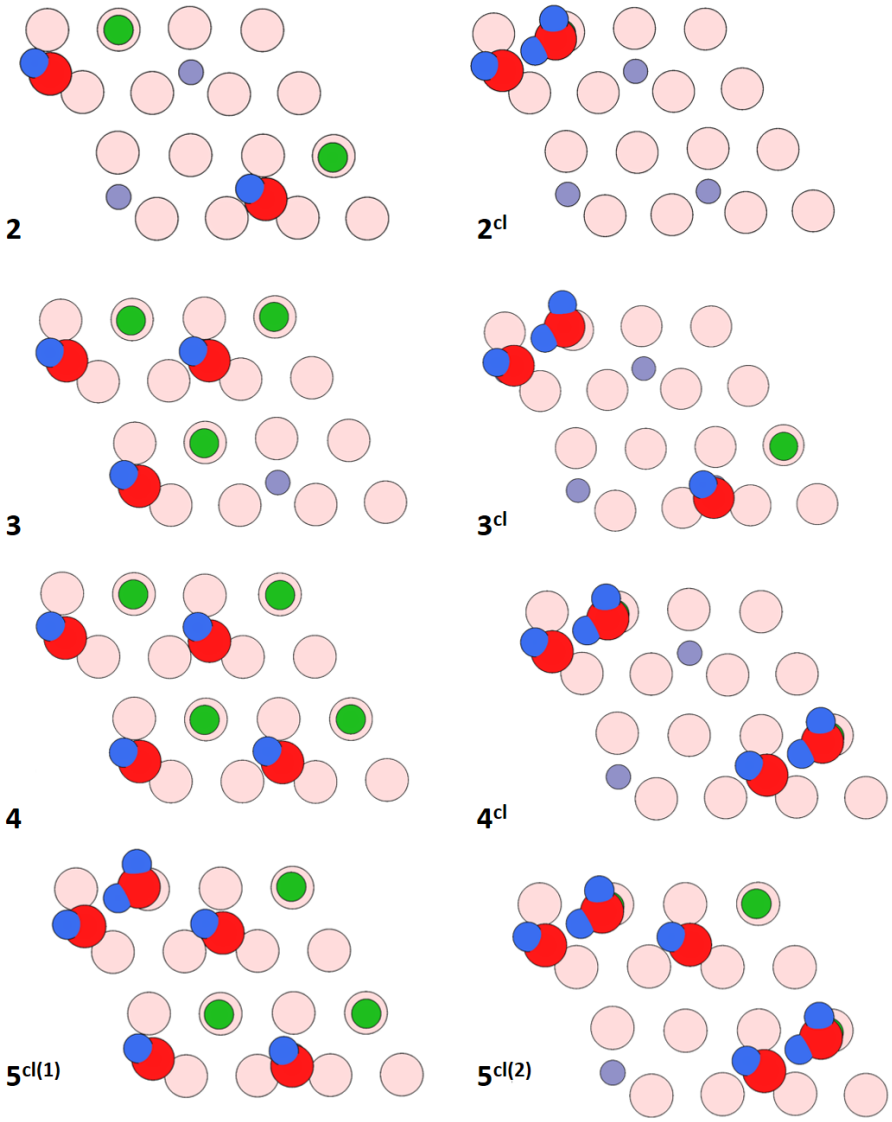


**Figure 4.19.** Top views of energy minimum structures involving two, three four and five water molecules on the $Fe_3O_4$(111)-(2×2) cell. Color code as in Fig. 4.16.

**Table 4.6** Scaled harmonic wavenumbers (in $cm^{-1}$) of terminal OD stretching vibrations for structures shown in Figures 4.18 and 4.19 (publication **P15**).

| | θ (ML) | ν(Fe-$O_w$D) | ν(OD) in non-diss. water | ν($O_s$D) |
|---|---|---|---|---|
| **1** | 0.25 | 2736 | | 2699 |
| **2** | 0.5 | 2730, 2729 | | 2698, 2697 |
| **$2^{cl}$** | 0.5 | 2735 | 2732 | |
| **3** | 0.75 | 2740,2737,2728 | | 2704, 2698, 2694 |
| **$3^{cl}$** | 0.75 | 2731, 2730 | $2431^{(p)*}$ | 2710 |
| **4** | 1 | 2737,2735,2732,2731 | | 2704,2703,2700, 2693 |
| **$4^{cl}$** | 1 | 2718, 2717 | 2713,2712 | |
| **$5^{cl(1)}$** | 1.25 | 2738, 2736, 2734, 2711 | | 2714, 2700, 2699 |
| **$5^{cl(2)}$** | 1.25 | 2723, 2718, 2715 | 2711, 2708 | 2709 |
| **$6^{n}$** | 1.5 | 2722, 2718, 2714, 2698 | 2713, 2678 | 2703, 2702 |
| **$6^{cl}$** | 1.5 | 2741, 2732, 2709, 2698 | $2426^{(p)*}$ | 2715 |
| **$7^{n}$** | 1.75 | 2720, 2719, 2707, 2690 | 2714, 2693 | 2717 |
| **$7^{cl}$** | 1.75 | 2724, 2708, 2699, 2690 | 2715, 2702 | 2717 |
| **$8^{n}$** | 2 | 2709, 2698, 2697 2685 | 2709, 2704, 2692, 2684 | |
| **$8^{cl}$** | 2 | 2723, 2709, 2689 | 2710, 2708, 2699 | 2712 |

*p indicates vibrations parallel to the surface

As shown in Tables 4.6, in the initial stages of water adsorption modeled by a single water molecule adsorbed on a $Fe_3O_4$(111)-(2×2) supercell, the most stable configuration is reached via a dissociative pathway leading to an $O_wH$ and an $O_sH$ group featuring stretching wavenumbers of 2736 and 2699 $cm^{-1}$, respectively. These stretching wavenumbers define a difference $\Delta\nu$ of 37 $cm^{-1}$, which agrees well with the observed difference of 32 $cm^{-1}$ corresponding to the bands at 2720 and 2688 $cm^{-1}$ (see Fig. 4 in publication **P15**). Regarding adsorption of two water molecules on the (2×2) supercell, two possible structures must be considered. The first one corresponds to a complete dissociative adsorption on two surface Fe ions (structure **2**) and the second structure is a half-dissociated "dimer" complex (structure **$2^{cl}$**). Calculated adsorption enthalpies [301-302] are shown in Tab. 4.7 and are -77.9 and -87.1 kJ $mol^{-1}$ for structure **2** and **$2^{cl}$**, respectively. These results suggest comparable stabilities based on mere differences of DFT enthalpies. Regarding vibrational wavenumbers,

structure **2** and **2$^{cl}$** feature a small red shift of ca. 5 cm$^{-1}$ for $O_wH$ compared with one dissociated $H_2O$. In contrast, the $O_sH$ stretching wavenumber is de facto identical. Upon increasing the coverage to 1 ML (i.e., 4 $H_2O$ on the (2×2) cell), structures **3** and **4** show a blue shift in $\nu(O_sH)$ of around 5 cm$^{-1}$. The corresponding wavenumbers of the $O_wH$ stretch still locates at ca. 2732 cm$^{-1}$, which is slightly red-shifted compared to the initial structure, the single $O_wH$. Structure **4$^{cl}$** has a more pronounced red shift of 19 cm$^{-1}$. Experimentally (at 200 K shown in Fig. 4 of publication **P15**), a shoulder at 2707 cm$^{-1}$ appears with increasing the coverage, which may be assigned to the $O_wH$ vibration of structure **4$^{cl}$**. Moreover, the bands caused by $O_sH$ stretches are always observed, proving that water dissociates on the surface, hence forming monomeric species. However, water clustering may represent a competing pathway. For a coverage greater than 1 ML, the obtained energy minimum structures always involve the half dissociated dimer (see structures **5$^{cl(1)}$** and **5$^{cl(2)}$** in Fig. 4.19).

**Table 4.7** Adsorption energies, ZPVE, and heat of adsorption including RT for T = 200 K [301-302]. Results are given per $H_2O$ molecule. The ZPVE for the $H_2O$ molecule is 54.8 kJ mol$^{-1}$ (as published in publication **P15**).

| | $\Delta E^{ads}$ | ZPVE | $\Delta H^{ads}$ | $\Delta H^{ads}+RT$ |
|---|---|---|---|---|
| **1** | -123.6 | 19.6 | -104.0 | -102.3 |
| **2** | -100.0 | 20.3 | -79.7 | -77.9 |
| **2$^{cl}$** | -103.7 | 15.0 | -88.7 | -87.1 |
| **3** | -82.1 | 19.4 | -62.7 | -61.1 |
| **3$^{cl}$** | -100.0 | 16.8 | -83.2 | -81.6 |
| **4** | -78.0 | 19.6 | -58.4 | -56.7 |
| **4$^{cl}$** | -92.2 | 15.7 | -76.5 | -74.9 |
| **5$^{cl(1)}$** | -83.5 | 18.0 | -65.5 | -63.8 |
| **5$^{cl(2)}$** | -83.9 | 16.5 | -67.4 | -65.8 |
| **6$^{n}$** | -85.1 | 17.3 | -67.8 | -66.2 |
| **6$^{cl}$** | -88.3 | 16.9 | -71.4 | -69.7 |
| **7$^{n}$** | -86.3 | 15.8 | -70.5 | -68.8 |
| **7$^{cl}$** | -83.7 | 16.3 | -67.4 | -65.8 |
| **8$^{n}$** | -85.8 | 15.9 | -69.9 | -68.3 |
| **8$^{cl}$** | -80.5 | 15.7 | -64.9 | -63.2 |

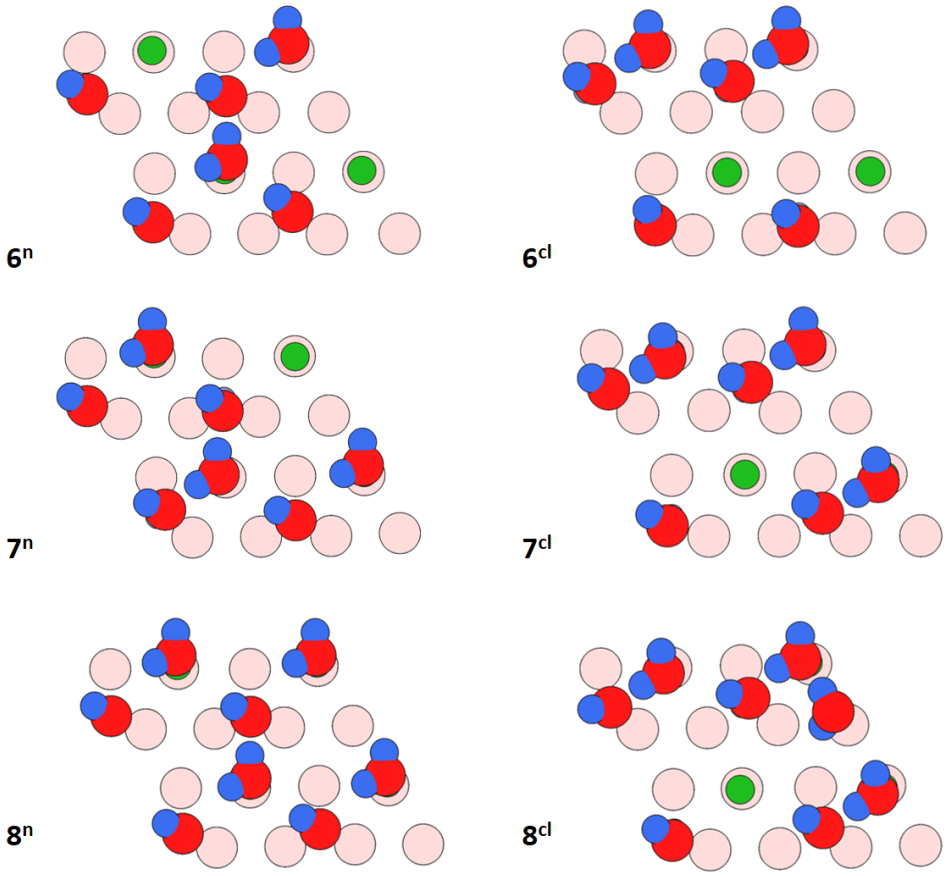


**Figure 4.20.** Top views of energy minimum structures involving six, seven, and eight water molecules on the $Fe_3O_4(111)$-(2×2) cell. Color code as in Fig. 4.16.

For even higher coverages involving 6, 7 and 8 water molecules discussed above, 2D network formation caused by H-bonding interaction occurs and is labelled with the superscript n. Regarding the corresponding $O_wH$ stretching wavenumbers, all studied structures yield wavenumbers ranging from 2698 to 2722 $cm^{-1}$. The $O_sH$ stretch shifts from 2702 $cm^{-1}$ (structure **6$^n$**) to ca. 2717 $cm^{-1}$ (structures **7$^n$** and **7$^{cl}$**). Thus, these results indicate that the characteristic wavenumber ranges for $O_wH$ and $O_sH$ stretching modes overlap (at higher coverage). Figure 4.21 shows stick representations of calculated wavenumbers for the relevant structures compared with observed results.

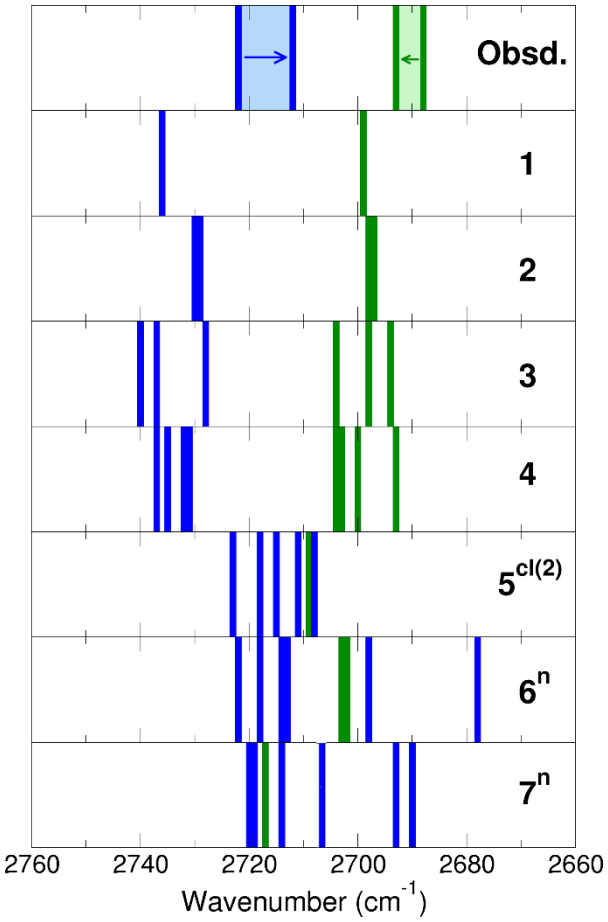


**Figure 4.21.** Stick representations of calculated, scaled wavenumbers (in $cm^{-1}$) of $\nu_S(O_wD)$ (blue) and $\nu_S(O_sD)$ (green) for structures shown in Figs. 4.19 and 4.20. Identifying structure labels are given on the rhs.

At lowest dosage (and at higher temperatures) the band at 2722 $cm^{-1}$ characteristic of $O_wH$ appears first. Repeatedly dosing water using a molecular beam pulse five times, induces a small red-shift of 3 $cm^{-1}$. Each dosage increases the coverage by $0.6\times10^{14}$ $cm^{-2}$, which is equal to 0.1875 ML. With respect to the $Fe_3O_4(111)$-(2×2) supercell, this corresponds to 0.75 additional water molecules per pulse. Hence, after five pulses, the surface coverage increases to around 4 $H_2O$ on the supercell. Figure 4.21 shows that the calculated $O_wH$ stretching wavenumbers of structures **1** to **4** undergo a small red shift of 3-5 $cm^{-1}$. Regarding surface hydroxyl groups $O_sH$, the computed wavenumbers shift to higher energies by ca. 5 $cm^{-1}$. These values agree well with observation.

Experimentally, an isosbestic point is observed when going from the 5$^{th}$ to the 9$^{th}$ pulse. The corresponding coverage increases from 4 to 6.75 $H_2O$ molecules per (2×2) supercell. The $O_wH$ stretching wavenumber is further red-shifted by 8 $cm^{-1}$ (in total it shifts by 10 $cm^{-1}$ with respect to the initial wavenumber for the monomer). Computationally, for structure **4** and

structure **5$^{cl(2)}$**, an obvious red-shift of 17 $cm^{-1}$ is obtained by comparing the centers for both groups of wavenumbers. The formation of a 2D network via an H-bonding interaction occurs in structure **6$^{n}$** and structure **7$^{n}$** and is consistent with LEED and IRAS results. As observed in these experiments, the initially (at low coverage) separated $O_wH$ and $O_sH$ bands start to overlap at higher dosage. Again, computational results are consistent with observation, because calculated ranges for $O_sH$ and $O_wH$ stretching wavenumbers also overlap with increasing coverage. With respect to adsorption energies or enthalpies, the relevant structures have similar stabilities. Adsorption energies as well as enthalpies suggest that structures corresponding to higher coverage (>5 $H_2O$ per (2×2) supercell) are similarly stable with ca. -65 kJ/mol (see Tab. 4.7).

# 5 Acknowledgements

This work was only possible due to the contributions of many colleagues. I thank first and foremost Professor Joachim Sauer (Humboldt University of Berlin) for his continuous support and many fruitful discussions. I am indebted to past and present members of his group, who have contributed to the herein presented research by stimulating discussions. I sincerely thank Professor Hans-Joachim Freund (Fritz-Haber-Institute-of-the-Max-Planck-Society, FHI, Berlin) for many collaborations, thus many opportunities to be exposed to challenging questions on experimental surface science. I thank all my colleagues doing experiments for their great work on ambitious projects. My sincere thanks therefore go to Dr. Shamil Shaikhutdinov, Dr. Helmut Kuhlenbeck, Professor Niklas Nilius, and all the excellent scientists working at the FHI in Berlin.

I had the great pleasure to co-supervise Dr. Christopher Penschke, who did a large share of the calculations on $VO_x$/ceria and Au/ceria, Dr. Thomas Kropp, who did the mechanistic studies on the ODH of methanol at $VO_x$/ceria, and Xiaoke Li, who performed the calculations on the water/magnetite system. Without their extraordinarily high motivation, thoroughness, and patience, the important computational results would not have been achieved.

Several generous grants for computing time at the HLRN (North-German Supercomputing Alliance in Berlin and Hannover) and JUROPA (Forschungszentrum Jülich) are thankfully acknowledged. I owe tremendous thanks to Dr. Jens Döbler, Dr. Christian Tuma, and Dr. Stefan Wollny, representatives of the HLRN, for their continuous efforts. I thank Dipl.-Chem. Thomas Dargel for his excellent job on administering our local computer cluster at the Institute of Chemistry, Humboldt University. Financial support from the Deutsche Forschungsgemeinschaft within CRC (SFB) 1109, titled "Understanding of Oxide/Water Systems at the Molecular Scale: Structural Evolution, Interfaces and Dissolution", as well as COST action CM1104, "Reducible Oxide Chemistry, Structure and Functions" are gratefully acknowledged. Furthermore, I also thank for financial support by the Fonds der Chemischen Industrie, FCI, and the Stiftung Industrieforschung, Humboldt-Universität zu Berlin.

# 6 Bibliography


[1] Sauer, J., Probing Catalysts with Water. *Science* **1996**, *271*, 774-775.

[2] Sauer, J., C-H Bond Activation by Transition Metal Oxides. In *Computational Modeling for Homogeneous and Enzymatic Catalysis*, K. Morokuma; Musaev, D. G., Eds. Wiley-VCH: Weinheim, 2008; pp 231-244.

[3] Büchner, C.; Lichtenstein, L.; Yu, X.; Boscoboinik, J. A.; Yang, B.; Kaden, W. E.; Heyde, M.; Shaikhutdinov, S. K.; Włodarczyk, R.; Sierka, M.; Sauer, J.; Freund, H.-J., Ultrathin Silica Films: The Atomic Structure of Two-Dimensional Crystals and Glasses. *Chem. Eur. J.* **2014**, *20*, 9176-9183.

[4] Sauer, J.; Freund, H.-J., Models in Catalysis. *Catal. Lett.* **2015**, *145*, 109-125.

[5] Freund, H. J., Model Studies in Heterogeneous Catalysis. *Chem. Eur. J.* **2010**, *16*, 9384-9397.

[6] Vohs, J. M., Site Requirements for the Adsorption and Reaction of Oxygenates on Metal Oxide Surfaces. *Chem. Rev.* **2013**, *113*, 4136-4163.

[7] Schlögl, R., Heterogeneous Catalysis. *Angew. Chem. Int. Ed.* **2015**, *54*, 3465-3520.

[8] Yu, K. M. K.; Curcic, I.; Gabriel, J.; Tsang, S. C. E., Recent Advances in $CO_2$ Capture and Utilization. *ChemSusChem* **2008**, *1*, 893-899.

[9] Baron, M.; Abbott, H.; Bondarchuk, O.; Stacchiola, D.; Uhl, A.; Shaikhutdinov, S.; Freund, H.-J.; Popa, C.; Ganduglia-Pirovano, M. V.; Sauer, J., Resolving the Atomic Structure of Vanadia Monolayer Catalysts: Monomers, Trimers, and Oligomers on Ceria. *Angew. Chem. Int. Ed.* **2009**, *48*, 8006-8009.

[10] Döbler, J.; Pritzsche, M.; Sauer, J., Vibrations of Silica Supported Vanadia: Variation with Particle Size and Local Surface Structure. *J. Phys. Chem. C* **2009**, *113*, 12454-12464.

[11] Sauer, J., Molecular Models in Ab Initio Studies of Solids and Surfaces: From Ionic Crystals and Semiconductors to Catalysts. *Chem. Rev.* **1989**, *89*, 199-255.

[12] Sauer, J.; Ugliengo, P.; Garrone, E.; Saunders, V. R., Theoretical Study of van der Waals Complexes at Surface Sites in Comparison with the Experiment. *Chem. Rev.* **1994**, *94*, 2095-2160.

[13] Kittel, C., *Introduction to Solid State Physics*, 8$^{th}$ ed.; Wiley: USA, 2005.

[14] Cremaschi, P.; Whitten, J. L., Chemisorption Theory: Dissociation of $H_2$ on Ti (0001). *Phys. Rev. Lett.* **1981**, *46*, 1242-1244.

[15] Kwapien, K.; Paier, J.; Sauer, J.; Geske, M.; Zavyalova, U.; Horn, R.; Schwach, P.; Trunschke, A.; Schlögl, R., Sites for Methane Activation on Lithium-Doped Magnesium Oxide Surfaces. *Angew. Chem. Int. Ed.* **2014**, *53*, 8774-8778.

[16] Piccini, G.; Alessio, M.; Sauer, J.; Zhi, Y.; Liu, Y.; Kolvenbach, R.; Jentys, A.; Lercher, J. A., Accurate Adsorption Thermodynamics of Small Alkanes in Zeolites. Ab Initio Theory and Experiment for H-Chabazite. *J. Phys. Chem. C* **2015**, *119*, 6128-6137.

[17] Jensen, F., *Introduction to Computational Chemistry*; John Wiley & Sons: Chichester, New York, Weinheim, 2001.

[18] Jensen, F., Polarization Consistent Basis Sets. II. Estimating the Kohn–Sham Basis Set Limit. *J. Chem. Phys.* **2002**, *116*, 7372-7379.

[19] Helgaker, T.; Klopper, W.; Koch, H.; Noga, J., Basis-Set Convergence of Correlated Calculations on Water. *J. Chem. Phys.* **1997**, *106*, 9639-9646.

[20] Noga, J.; Kutzelnigg, W.; Klopper, W., CC-R12, a Correlation Cusp Corrected Coupled-Cluster Method with a Pilot Application to the $Be_2$ Potential Curve. *Chem. Phys. Lett.* **1992**, *199*, 497-504.

[21] Klopper, W.; Samson, C. C. M., Explicitly Correlated Second-Order Møller-Plesset Methods With Auxiliary Basis Sets. *J. Chem. Phys.* **2002**, *116*, 6397-6410.

[22] Klopper, W.; Manby, F. R.; Ten-No, S.; Valeev, E. F., R12 Methods in Explicitly Correlated Molecular Electronic Structure Theory. *Int. Rev. Phys. Chem.* **2006**, *25*, 427-468.

[23] Saitow, M.; Becker, U.; Riplinger, C.; Valeev, E. F.; Neese, F., A New Near-Linear Scaling, Efficient and Accurate, Open-Shell Domain-Based Local Pair Natural Orbital Coupled Cluster Singles and Doubles Theory. *J. Chem. Phys.* **2017**, *146*, 164105.
[24] Neese, F., The ORCA program system. *Wires Comput. Mol. Sci.* **2012**, *2*, 73-78.
[25] Kohn, W.; Sham, L. J., Self-Consistent Equations Including Exchange and Correlation Effects. *Phys. Rev.* **1965**, *140*, 1133.
[26] Dreizler, R. M.; Gross, E. K. U., *Density Functional Theory*; Springer Verlag: Berlin, 1990.
[27] Jones, R. O.; Gunnarsson, O., The Density Functional Formalism, Its Applications and Prospects. *Rev. Mod. Phys.* **1989**, *61*, 689-746.
[28] Grabowski, B.; Wippermann, S.; Glensk, A.; Hickel, T.; Neugebauer, J., Random phase approximation up to the melting point: Impact of anharmonicity and nonlocal many-body effects on the thermodynamics of Au. *Phys. Rev. B* **2015**, *91*.
[29] Thiel, W., Computational Catalysis-Past, Present, and Future. *Angew. Chem. Int. Ed.* **2014**, *53*, 8605-8613.
[30] Curtiss, L. A.; Raghavachari, K.; Redfern, P. C.; Pople, J. A., Assessment of Gaussian-2 and density functional theories for the computation of enthalpies of formation. *J. Chem. Phys.* **1997**, *106*, 1063-1079.
[31] Zhao, Y.; Truhlar, D. G., Design of Density Functionals That Are Broadly Accurate for Thermochemistry, Thermochemical Kinetics, and Nonbonded Interactions. *J. Phys. Chem. A* **2005**, *109*, 5656-5667.
[32] Csonka, G. I.; Perdew, J. P.; Ruzsinszky, A.; Philipsen, P. H. T.; Lebegue, S.; Paier, J.; Vydrov, O. A.; Ángyán, J. G., Assessing the performance of recent density functionals for bulk solids. *Phys. Rev. B* **2009**, *79*, 155107.
[33] Rapps, T.; Ahlrichs, R.; Waldt, E.; Kappes, M. M.; Schooss, D., On the Structures of 55-Atom Transition-Metal Clusters and Their Relationship to the Crystalline Bulk. *Angew. Chem. Int. Ed.* **2013**, *52*, 6102-6105.
[34] Koch, W.; Holthausen, M. C., *A Chemist's Guide to Density Functional Theory*; Wiley-VCH Verlag GmbH: Weinheim, 2001.
[35] Ozolins, V.; Körling, M., Full-Potential Calculations Using the Generalized Gradient Approximation - Structural-Properties of Transition-Metals. *Phys. Rev. B* **1993**, *48*, 18304-18307.
[36] Peverati, R.; Truhlar, D. G., Exchange-Correlation Functional with Good Accuracy for Both Structural and Energetic Properties while Depending Only on the Density and Its Gradient. *J. Chem. Theory Comput.* **2012**, *8*, 2310-2319.
[37] Kim, Y.-S.; Marsman, M.; Kresse, G.; Tran, F.; Blaha, P., Towards efficient band structure and effective mass calculations for III-V direct band-gap semiconductors. *Phys. Rev. B* **2010**, *82*.
[38] Payne, M. C.; Teter, M. P.; Allan, D. C.; Arias, T. A.; Joannopoulos, J. D., Iterative Minimization Techniques for Ab Initio Total-Energy Calculations - Molecular-Dynamics and Conjugate Gradients. *Rev. Mod. Phys.* **1992**, *64*, 1045-1097.
[39] Goedecker, S., Linear scaling electronic structure methods. *Rev. Mod. Phys.* **1999**, *71*, 1085-1123.
[40] Furche, F., Molecular tests of the random phase approximation to the exchange-correlation energy functional. *Phys. Rev. B* **2001**, *64*, 195120.
[41] Pacchioni, G.; Lomas, J. R.; Illas, F., Electric field effects in heterogeneous catalysis. *J. Mol. Catal. A: Chem.* **1997**, *119*, 263-273.
[42] Gillan, M. J., The virtual matter laboratory. *Contemporary Physics* **1997**, *38*, 115-130.
[43] Pykavy, M.; Stämmler, V.; Seiferth, O.; Freund, H. J., Adsorption of CO on $Cr_2O_3$(0001). *Surf. Sci.* **2001**, *479*, 11-25.
[44] Schmitt, I.; Fink, K.; Stämmler, V., The method of local increments for the calculation of adsorption energies of atoms and small molecules on solid surfaces Part I. A single Cu atom on the polar surfaces of ZnO. *Phys. Chem. Chem. Phys.* **2009**, *11*, 11196-11206.

[45] Müller, C.; Hermansson, K.; Paulus, B., Electron correlation contribution to the $N_2O$/ceria(111) interaction. *Chemical Physics* **2009**, *362*, 91-96.
[46] Perdew, J. P.; Zunger, A., Self-Interaction Correction to Density-Functional Approximations for Many-Electron Systems. *Phys. Rev. B* **1981**, *23*, 5048-5079.
[47] Ruzsinszky, A.; Perdew, J. P.; Csonka, G. I.; Vydrov, O. A.; Scuseria, G. E., Density functionals that are one- and two- are not always many-electron self-interaction-free, as shown for $H_2^+$, $He_2^+$, $LiH^+$, and $Ne_2^+$. *J. Chem. Phys.* **2007**, *126*, 104102.
[48] Janesko, B. G.; Henderson, T. M.; Scuseria, G. E., Screened Hybrid Density Functionals for Solid-State Chemistry and Physics. *Phys. Chem. Chem. Phys.* **2009**, *11*, 443-454.
[49] Ganduglia-Pirovano, V.; Hofmann, A.; Sauer, J., Oxygen Vacancies in Transition Metal and Rare Earth Oxides: Current State of Understanding and Remaining Challenges. *Surf. Sci. Rep.* **2007**, *62*, 219-270.
[50] Pacchioni, G., Modeling doped and defective oxides in catalysis with density functional theory methods: Room for improvements. *J. Chem. Phys.* **2008**, *128*, 182505.
[51] Paier, J.; Penschke, C.; Sauer, J., Oxygen Defects and Surface Chemistry of Ceria: Quantum Chemical Studies Compared to Experiment. *Chem. Rev.* **2013**, *113*, 3949-3985.
[52] Freysoldt, C.; Grabowski, B.; Hickel, T.; Neugebauer, J.; Kresse, G.; Janotti, A.; Van de Walle, C. G., First-principles calculations for point defects in solids. *Rev. Mod. Phys.* **2014**, *86*, 253.
[53] Zhao, Y.; Gonzalez-Garcia, N.; Truhlar, D. G., Benchmark database of barrier heights for heavy atom transfer, nucleophilic substitution, association, and unimolecular reactions and its use to test theoretical methods. *J. Phys. Chem. A* **2005**, *109*, 2012-2018.
[54] Janesko, B. G.; Scuseria, G. E., Hartree-Fock orbitals significantly improve the reaction barrier heights predicted by semilocal density functionals. *J. Chem. Phys.* **2008**, *128*.
[55] Kohn, W.; Meir, Y.; Makarov, D. E., van der Waals energies in density functional theory. *Phys. Rev. Lett.* **1998**, *80*, 4153-4156.
[56] Kümmel, S.; Kronik, L., Orbital-Dependent Density Functionals: Theory and Applications. *Rev. Mod. Phys.* **2008**, *80*, 3-60.
[57] Cohen, A. J.; Mori-Sanchez, P.; Yang, W., Challenges for Density Functional Theory. *Chem. Rev.* **2012**, *112*, 289-320.
[58] Perdew, J. P.; Ruzsinszky, A.; Constantin, L. A.; Sun, J.; Csonka, G. I., Some Fundamental Issues in Ground-State Density Functional Theory: A Guide for the Perplexed. *J. Chem. Theory Comput.* **2009**, *5*, 902-908.
[59] Kuhlenbeck, H.; Shaikhutdinov, S.; Freund, H.-J., Well-Ordered Transition Metal Oxide Layers in Model Catalysis - A Series of Case Studies. *Chem. Rev.* **2013**, *113*, 3986-4034.
[60] Jacob, D.; Haule, K.; Kotliar, G., Combining the hybrid functional method with dynamical mean-field theory. *Europhys. Lett.* **2008**, *84*.
[61] Mars, P.; van Krevelen, D. W., Oxidations Carried Out by Means of Vanadium Oxide Catalysts. *Chem. Eng. Sci.* **1954**, *3, Supplement 1*, 41-59.
[62] Sauer, J.; Döbler, J., Structure and Reactivity of $V_2O_5$: Bulk Solid, Nanosized Clusters, Species Supported on Silica and Alumina, Cluster Cations and Anions. *Dalton Trans.* **2004**, *19*, 3116-3121.
[63] Keating, P. R. L.; Scanlon, D. O.; Morgan, B. J.; Galea, N. M.; Watson, G. W., Analysis of Intrinsic Defects in $CeO_2$ Using a Koopmans-Like GGA plus U Approach. *J. Phys. Chem. C* **2012**, *116*, 2443-2452.
[64] Pacchioni, G.; Freund, H., Electron Transfer at Oxide Surfaces. The MgO Paradigm: from Defects to Ultrathin Films. *Chem. Rev.* **2013**, *113*, 4035-4072.
[65] Solans-Monfort, X.; Branchadell, V.; Sodupe, M.; Sierka, M.; Sauer, J., Electron hole formation in acidic zeolite catalysts. *J. Chem. Phys.* **2004**, *121*, 6034-6041.
[66] Heyd, J.; Scuseria, G. E.; Ernzerhof, M., Hybrid Functionals Based on a Screened Coulomb Potential. *J. Chem. Phys.* **2003**, *118*, 8207-8215.

[67] Perdew, J. P.; Constantin, L. A., Laplacian-level density functionals for the kinetic energy density and exchange-correlation energy. *Phys. Rev. B* **2007**, *75*, 155109.
[68] Tao, J. M.; Perdew, J. P.; Staroverov, V. N.; Scuseria, G. E., Climbing the Density Functional Ladder: Nonempirical Meta-Generalized Gradient Approximation Designed for Molecules and Solids. *Phys. Rev. Lett.* **2003**, *91*, 146401.
[69] Nolan, M., Hybrid density functional theory description of oxygen vacancies in the $CeO_2$ (110) and (100) surfaces. *Chem. Phys. Lett.* **2010**, *499*, 126-130.
[70] Gillan, M. J.; Alfè, D.; De Gironcoli, S.; Manby, F. R., High-precision calculation of Hartree-Fock energy of crystals. *J. Comput. Chem.* **2008**, *29*, 2098-2106.
[71] Pisani, C.; Maschio, L.; Casassa, S.; Halo, M.; Schütz, M.; Usvyat, D., Periodic local MP2 method for the study of electronic correlation in crystals: Theory and preliminary applications. *J. Comput. Chem.* **2008**, *29*, 2113-2124.
[72] Nolan, S. J.; Gillan, M. J.; Alfè, D.; Allan, N. L.; Manby, F. R., Calculation of properties of crystalline lithium hydride using correlated wave function theory. *Phys. Rev. B* **2009**, *80*.
[73] Paier, J.; Diaconu, C. V.; Scuseria, G. E.; Guidon, M.; VandeVondele, J.; Hutter, J., Accurate Hartree-Fock energy of extended systems using large Gaussian basis sets. *Phys. Rev. B* **2009**, *80*.
[74] Binnie, S. J.; Nolan, S. J.; Drummond, N. D.; Alfè, D.; Allan, N. L.; Manby, F. R.; Gillan, M. J., Bulk and surface energetics of crystalline lithium hydride: Benchmarks from quantum Monte Carlo and quantum chemistry. *Phys. Rev. B* **2010**, *82*.
[75] Voloshina, E.; Usvyat, D.; Schütz, M.; Dedkov, Y.; Paulus, B., On the physisorption of water on graphene: a CCSD(T) study. *Phys. Chem. Chem. Phys.* **2011**, *13*, 12041-12047.
[76] Pisani, C.; Schütz, M.; Casassa, S.; Usvyat, D.; Maschio, L.; Lorenz, M.; Erba, A., CRYSCOR: a program for the post-Hartree-Fock treatment of periodic systems. *Phys. Chem. Chem. Phys.* **2012**, *14*, 7615-7628.
[77] Booth, G. H.; Grüneis, A.; Kresse, G.; Alavi, A., Towards an exact description of electronic wavefunctions in real solids. *Nature* **2013**, *493*, 365-370.
[78] Grüneis, A., A coupled cluster and Moller-Plesset perturbation theory study of the pressure induced phase transition in the LiH crystal. *J. Chem. Phys.* **2015**, *143*.
[79] Grüneis, A., Efficient Explicitly Correlated Many-Electron Perturbation Theory for Solids: Application to the Schottky Defect in MgO. *Phys. Rev. Lett.* **2015**, *115*.
[80] J. P. Perdew; Schmidt, K., In *Density-Functional Theory and Its Applications to Materials*, V. E. Van Doren; K. Van Alsenoy; Geerlings, P., Eds. American Institute of Physics: Melville, NY, 2001.
[81] Perdew, J. P., Climbing the ladder of density functional approximations. *MRS Bulletin* **2013**, *38*, 743-750.
[82] Perdew, J. P.; Staroverov, V. N.; Tao, J.; Scuseria, G. E., Density functional with full exact exchange, balanced nonlocality of correlation, and constraint satisfaction. *Phys. Rev. A* **2008**, *78*.
[83] Perdew, J. P.; Kurth, S.; Zupan, A.; Blaha, P., Accurate density functional with correct formal properties: A step beyond the generalized gradient approximation. *Phys. Rev. Lett.* **1999**, *82*, 2544-2547.
[84] De Jong, G. T.; Geerke, D. P.; Diefenbach, A.; Sola, M.; Bickelhaupt, F. M., Oxidative addition of the ethane C-C bond to Pd. An ab initio benchmark and DFT validation study. *J. Comput. Chem.* **2005**, *26*, 1006-1020.
[85] Sun, J.; Marsman, M.; Csonka, G. I.; Ruzsinszky, A.; Hao, P.; Kim, Y.-S.; Kresse, G.; Perdew, J. P., Self-consistent meta-generalized gradient approximation within the projector-augmented-wave method. *Phys. Rev. B* **2011**, *84,* 035117.
[86] Sun, J.; Marsman, M.; Ruzsinszky, A.; Kresse, G.; Perdew, J. P., Improved lattice constants, surface energies, and CO desorption energies from a semilocal density functional. *Phys. Rev. B* **2011**, *83,* 121410(R).

[87] Janthon, P.; Luo, S. J.; Kozlov, S. M.; Vines, F.; Limtrakul, J.; Truhlar, D. G.; Illas, F., Bulk Properties of Transition Metals: A Challenge for the Design of Universal Density Functionals. *J. Chem. Theory Comput.* **2014**, *10*, 3832-3839.
[88] Maier, T. M.; Boese, A. D.; Sauer, J.; Wende, T.; Fagiani, M.; Asmis, K. R., The vibrational spectrum of $FeO_2^+$ isomers-Theoretical benchmark and experiment. *J. Chem. Phys.* **2014**, *140,* 204315.
[89] Vosko, S. H.; Wilk, L.; Nusair, M., Accurate Spin-Dependent Electron Liquid Correlation Energies for Local Spin-Density Calculations - A Critical Analysis. *Can. J. Phys.* **1980**, *58*, 1200-1211.
[90] Becke, A. D., Density Functional Calculations of Molecular-Bond Energies. *J. Chem. Phys.* **1986**, *84*, 4524-4529.
[91] Perdew, J. P.; Wang, Y., Accurate and Simple Analytic Representation of the Electron-Gas Correlation-Energy. *Phys. Rev. B* **1992**, *45*, 13244-13249.
[92] Perdew, J. P.; Burke, K.; Ernzerhof, M., Generalized Gradient Approximation Made Simple. *Phys. Rev. Lett.* **1996**, ***77***, 3865-3868.
[93] Armiento, R.; Mattsson, A. E., Functional designed to include surface effects in self-consistent density functional theory. *Phys. Rev. B* **2005**, *72,* 085108.
[94] Mattsson, A. E.; Armiento, R., Implementing and testing the AM05 spin density functional. *Phys. Rev. B* **2009**, *79,* 155101.
[95] Seidl, A.; Görling, A.; Vogl, P.; Majewski, J. A.; Levy, M., Generalized Kohn-Sham Schemes and the Band-Gap Problem. *Phys. Rev. B* **1996**, *53*, 3764-3774.
[96] Asmis, K. R.; Santambrogio, G.; Brümmer, M.; Sauer, J., Polyhedral Vanadium Oxide Cages: Infrared Spectra of Cluster Anions and Size-Induced d-Electron Localization. *Angew. Chem. Int. Ed.* **2005**, *44*, 3122-3125.
[97] Paier, J.; Marsman, M.; Hummer, K.; Kresse, G.; Gerber, I. C.; Ángyán, J. G., Screened hybrid density functionals applied to solids. *J. Chem. Phys.* **2006**, *124*, 154709; *125*, 249901 (Erratum).
[98] Ramprasad, R.; Zhu, H.; Rinke, P.; Scheffler, M., New Perspective on Formation Energies and Energy Levels of Point Defects in Nonmetals. *Phys. Rev. Lett.* **2012**, *108,* 066404.
[99] Perdew, J. P.; Emzerhof, M.; Burke, K., Rationale for mixing exact exchange with density functional approximations. *J. Chem. Phys.* **1996**, *105*, 9982-9985.
[100] Zhao, Y.; Truhlar, D. G., Density functional for spectroscopy: No long-range self-interaction error, good performance for Rydberg and charge-transfer states, and better performance on average than B3LYP for ground states. *J. Phys. Chem. A* **2006**, *110*, 13126-13130.
[101] Zhao, Y.; Truhlar, D. G., The M06 suite of density functionals for main group thermochemistry, thermochemical kinetics, noncovalent interactions, excited states, and transition elements: two new functionals and systematic testing of four M06-class functionals and 12 other functionals. *Theor. Chem. Acc.* **2008**, *120*, 215-241.
[102] Jaramillo, J.; Scuseria, G. E.; Ernzerhof, M., Local hybrid functionals. *J. Chem. Phys.* **2003**, *118*, 1068-1073.
[103] Arbuznikov, A. V.; Kaupp, M., Local hybrid exchange-correlation functionals based on the dimensionless density gradient. *Chem. Phys. Lett.* **2007**, *440*, 160-168.
[104] Haunschild, R.; Janesko, B. G.; Scuseria, G. E., Local hybrids as a perturbation to global hybrid functionals. *J. Chem. Phys.* **2009**, *131,* 154112.
[105] Kurth, S.; Perdew, J. P., Density-functional correction of random-phase-approximation correlation with results for jellium surface energies. *Phys. Rev. B* **1999**, *59*, 10461-10468.
[106] Grüneis, A.; Marsman, M.; Harl, J.; Schimka, L.; Kresse, G., Making the random phase approximation to electronic correlation accurate. *J. Chem. Phys.* **2009**, *131,* 154115.
[107] Ren, X.; Rinke, P.; Joas, C.; Scheffler, M., Random-phase approximation and its applications in computational chemistry and materials science. *J Mater Sci* **2012**, *47*, 7447-7471.

[108] Zhao, Y.; Lynch, B. J.; Truhlar, D. G., Doubly hybrid meta DFT: New multi-coefficient correlation and density functional methods for thermochemistry and thermochemical kinetics. *J. Phys. Chem. A* **2004**, *108*, 4786-4791.
[109] Schwabe, T.; Grimme, S., Towards chemical accuracy for the thermodynamics of large molecules: new hybrid density functionals including non-local correlation effects. *Phys. Chem. Chem. Phys.* **2006**, *8*, 4398-4401.
[110] Karton, A.; Tarnopolsky, A.; Lamere, J.-F.; Schatz, G. C.; Martin, J. M. L., Highly Accurate First-Principles Benchmark Data Sets for the Parametrization and Validation of Density Functional and Other Approximate Methods. Derivation of a Robust, Generally Applicable, Double-Hybrid Functional for Thermochemistry and Thermochemical Kinetics. *J. Phys. Chem. A* **2008**, *112*, 12868-12886.
[111] F. E. Harris; H. J. Monkhorst; Freeman, D. L., *Algebraic and Diagrammatic Methods in Many-Fermion Theory*; Oxford University Press: New York, Oxford, 1992.
[112] Niquet, Y. M.; Fuchs, M.; Gonze, X., Exchange-correlation potentials in the adiabatic connection fluctuation-dissipation framework. *Phys. Rev. A* **2003**, *68,* 032507.
[113] Dobson, J. F.; Gould, T., Calculation of dispersion energies. *J. Phys.-Condens. Matter* **2012**, *24,* 073201.
[114] Harl, J.; Kresse, G., Cohesive energy curves for noble gas solids calculated by adiabatic connection fluctuation-dissipation theory. *Phys. Rev. B* **2008**, *77,* 045136.
[115] Ren, X.; Rinke, P.; Scheffler, M., Exploring the random phase approximation: Application to CO adsorbed on Cu(111). *Phys. Rev. B* **2009**, *80,* 045402.
[116] Ma, J.; Michaelides, A.; Alfè, D.; Schimka, L.; Kresse, G.; Wang, E., Adsorption and diffusion of water on graphene from first principles. *Phys. Rev. B* **2011**, *84,* 033402.
[117] Karlicky, F.; Lazar, P.; Dubecky, M.; Otyepka, M., Random Phase Approximation in Surface Chemistry: Water Splitting on Iron. *J. Chem. Theory Comput.* **2013**, *9*, 3670-3676.
[118] Macher, M.; Klimeš, J.; Franchini, C.; Kresse, G., The random phase approximation applied to ice. *J. Chem. Phys.* **2014**, *140,* 084502.
[119] Bao, J. L.; Yu, H. S.; Duanmu, K.; Makeev, M. A.; Xu, X.; Truhlar, D. G., Density Functional Theory of the Water Splitting Reaction on Fe(0): Comparison of Local and Non local Correlation Functionals. *ACS Catalysis* **2015**, *5*, 2070-2080.
[120] Ren, X.; Tkatchenko, A.; Rinke, P.; Scheffler, M., Beyond the Random-Phase Approximation for the Electron Correlation Energy: The Importance of Single Excitations. *Phys. Rev. Lett.* **2011**, *106,* 153003.
[121] Paier, J.; Ren, X.; Rinke, P.; Scuseria, G. E.; Grüneis, A.; Kresse, G.; Scheffler, M., Assessment of correlation energies based on the random-phase approximation. *New J. Phys.* **2012**, *14,* 043002.
[122] Hellgren, M.; Rohr, D. R.; Gross, E. K. U., Correlation potentials for molecular bond dissociation within the self-consistent random phase approximation. *J. Chem. Phys.* **2012**, *136,* 034106.
[123] Jemai, M.; Delion, D. S.; Schuck, P., Self-consistent random-phase approximation from a coupled-cluster wave function perspective. *Phys. Rev. C* **2013**, *88,* 044004.
[124] Bleiziffer, P.; Hesselmann, A.; Görling, A., Efficient self-consistent treatment of electron correlation within the random phase approximation. *J. Chem. Phys.* **2013**, *139,* 084113.
[125] Nguyen, N. L.; Colonna, N.; de Gironcoli, S., Ab initio self-consistent total-energy calculations within the EXX/RPA formalism. *Phys. Rev. B* **2014**, *90*, 045138.
[126] Moussa, J. E., Cubic-scaling algorithm and self-consistent field for the random-phase approximation with second-order screened exchange. *J. Chem. Phys.* **2014**, *140*, 014107.
[127] Hellgren, M.; Caruso, F.; Rohr, D. R.; Ren, X.; Rubio, A.; Scheffler, M.; Rinke, P., Static correlation and electron localization in molecular dimers from the self-consistent RPA and GW approximation. *Phys. Rev. B* **2015**, *91*, 165110.

[128] Bleiziffer, P.; Krug, M.; Görling, A., Self-consistent Kohn-Sham method based on the adiabatic-connection fluctuation-dissipation theorem and the exact-exchange kernel. *J. Chem. Phys.* **2015**, *142*, 244108.
[129] Becke, A. D., A New Mixing of Hartree-Fock and Local Density-Functional Theories. *J. Chem. Phys.* **1993**, *98*, 1372-1377.
[130] Harris, J.; Jones, R. O., Surface-Energy of a Bounded Electron-Gas. *J. Phys. F* **1974**, *4*, 1170-1186.
[131] Langreth, D. C.; Perdew, J. P., Exchange-Correlation Energy of a Metallic Surface - Wave-Vector Analysis. *Phys. Rev. B* **1977**, *15*, 2884-2901.
[132] Dirac, P. A. M., Quantum mechanics of many-electron systems. *Proc Royal Soc (London) A* **1929**, *123*, 714-733.
[133] Slater, J. C., A simplification of the Hartree-Fock method. *Phys. Rev.* **1951**, *81*, 385-390.
[134] Becke, A. D., Density-Functional Thermochemistry .3. The Role of Exact Exchange. *J. Chem. Phys.* **1993**, *98*, 5648-5652.
[135] Becke, A. D., Density-Functional Exchange-Energy Approximation with Correct Asymptotic-Behavior. *Phys. Rev. A* **1988**, *38*, 3098-3100.
[136] Perdew, J. P., In *Electronic Structure of Solids*, Ziesche, P.; Eschrig, H., Eds. Akademie Verlag: Berlin, 1991.
[137] Lee, C. T.; Yang, W. T.; Parr, R. G., Development of the Colle-Salvetti Correlation-Energy Formula Into a Functional of the Electron-Density. *Phys. Rev. B* **1988**, *37*, 785-789.
[138] Miehlich, B.; Savin, A.; Stoll, H.; Preuss, H., Results Obtained With the Correlation-Energy Density Functionals of Becke and Lee, Yang and Parr. *Chem. Phys. Lett.* **1989**, *157*, 200-206.
[139] Stephens, P. J.; Devlin, F. J.; Chabalowski, C. F.; Frisch, M. J., Ab-Initio Calculation of Vibrational Absorption and Circular-Dichroism Spectra Using Density-Functional Force-Fields. *J. Phys. Chem.* **1994**, *98*, 11623-11627.
[140] Kurth, S.; Perdew, J. P.; Blaha, P., Molecular and solid-state tests of density functional approximations: LSD, GGAs, and meta-GGAs. *Int. J. Quantum. Chem.* **1999**, *75*, 889-909.
[141] Tao, J. M.; Gori-Giorgi, P.; Perdew, J. P.; McWeeny, R., Uniform electron gas from the Colle-Salvetti functional: Missing long-range correlations. *Phys. Rev. A* **2001**, *63*, 032513.
[142] Caratzoulas, S.; Knowles, P. J., Critical analysis of the Colle-Salvetti model for electron correlation in closed shell systems: pair correlations. *Mol. Phys.* **2000**, *98*, 1811-1821.
[143] Paier, J.; Marsman, M.; Kresse, G., Why does the B3LYP hybrid functional fail for metals? *J. Chem. Phys.* **2007**, *127*, 024103.
[144] Pisani, C.; Apra, E.; Causa, M., Density-Matrix of Crystalline Systems .1. Long-Range Behavior and Related Computational Problems. *Int. J. Quantum. Chem.* **1990**, *38*, 395-417.
[145] Gross, E. K. U.; Runge, E., *Vielteilchentheorie*; Teubner: Stuttgart, 1986.
[146] Ashcroft, N. W.; Mermin, N. D., *Solid State Physics*; Saunders College Publishing: Orlando, 1976.
[147] Mahan, G. D., *Many-particle physics*, 2nd ed.; Plenum Press: New York, 1990.
[148] Corà, F.; Alfredsson, M.; Mallia, G.; Middlemiss, D. S.; Mackrodt, W. C.; Dovesi, R.; Orlando, R., The performance of hybrid density functionals in solid state chemistry. In *Principles and Applications of Density in Inorganic Chemistry II*, Kaltsoyannis, N.; McGrady, J. E., Eds. Springer-Verlag Berlin: Berlin, 2004; Vol. 113, pp 171-232.
[149] Heyd, J.; Scuseria, G. E., Efficient hybrid density functional calculations in solids: Assessment of the Heyd-Scuseria-Ernzerhof screened Coulomb hybrid functional. *J. Chem. Phys.* **2004**, *121*, 1187-1192.
[150] Stroppa, A.; Kresse, G., The shortcomings of semi-local and hybrid functionals: what we can learn from surface science studies. *New J. Phys.* **2008**, *10*, 063020.

[151] Kohn, W., Density-Functional Theory for Systems of Very Many Atoms. *Int. J. Quantum. Chem.* **1995**, *56*, 229-232.
[152] Resta, R., Kohn's theory of the insulating state: a quantum-chemistry viewpoint. *J. Chem. Phys.* **2006**, *124*, 104104-104104.
[153] Becke, A. D., Density-functional thermochemistry .4. A new dynamical correlation functional and implications for exact-exchange mixing. *J. Chem. Phys.* **1996**, *104*, 1040-1046.
[154] Adamo, C.; Barone, V., Toward reliable density functional methods without adjustable parameters: The PBE0 model. *J. Chem. Phys.* **1999**, *110*, 6158-6170.
[155] Ernzerhof, M.; Scuseria, G. E., Assessment of the Perdew-Burke-Ernzerhof exchange-correlation functional. *J. Chem. Phys.* **1999**, *110*, 5029-5036.
[156] Leininger, T.; Stoll, H.; Werner, H. J.; Savin, A., Combining long-range configuration interaction with short-range density functionals. *Chem. Phys. Lett.* **1997**, *275*, 151-160.
[157] Ewald, P. P., The calculation of optical and electrostatic grid potential. *Ann. Phys.* **1921**, *64*, 253-287.
[158] Krukau, A. V.; Vydrov, O. A.; Izmaylov, A. F.; Scuseria, G. E., Influence of the Exchange Screening Parameter on the Performance of Screened Hybrid Functionals. *J. Chem. Phys.* **2006**, *125*, 224106.
[159] Marsman, M.; Paier, J.; Stroppa, A.; Kresse, G., Hybrid functionals applied to extended systems. *J. Phys.-Condens. Matter* **2008**, *20*, 064201.
[160] Henderson, T. M.; Paier, J.; Scuseria, G. E., Accurate treatment of solids with the HSE screened hybrid. *Phys. Status Solidi B-Basic Solid State Phys.* **2011**, *248*, 767-774.
[161] Dovesi, R.; Civalleri, B.; Orlando, R.; Roetti, C.; Saunders, V. R., Ab initio Quantum Simulation in Solid State Chemistry. In *Reviews in Computational Chemistry*, Lipkovitz, K. B.; Thomas, R. L.; Cundari, T. R., Eds. Wiley-VCH: New York, 2005; Vol. Vol. 21, p 1.
[162] Mackrodt, W. C.; Harrison, N. M.; Saunders, V. R.; Allan, N. L.; Towler, M. D.; Apra, E.; Dovesi, R., Ab-Initio Hartree-Fock Calculations of CaO, VO, MnO and NiO. *Philos. Mag. A* **1993**, *68*, 653-666.
[163] Towler, M. D.; Allan, N. L.; Harrison, N. M.; Saunders, V. R.; Mackrodt, W. C.; Apra, E., Ab-Initio Study of MnO and NiO. *Phys. Rev. B* **1994**, *50*, 5041-5054.
[164] Kudin, K. N.; Scuseria, G. E.; Martin, R. L., Hybrid density-functional theory and the insulating gap of $UO_2$. *Phys. Rev. Lett.* **2002**, *89*, 266402.
[165] Frisch, M. J., et al. *Gaussian 09*, Gaussian, Inc.: Wallingford, CT, USA, 2009.
[166] VandeVondele, J.; Hutter, J., Gaussian basis sets for accurate calculations on molecular systems in gas and condensed phases. *J. Chem. Phys.* **2007**, *127*, 114105.
[167] Chalasinski, G.; Szczesniak, M. M., State of the art and challenges of the ab initio theory of intermolecular interactions. *Chem. Rev.* **2000**, *100*, 4227-4252.
[168] Boys, S. F.; Bernardi, F., Calculation of Small Molecular Interactions by Differences of Separate Total Energies - Some Procedures With Reduced Errors. *Mol. Phys.* **1970**, *19*, 553.
[169] Blum, V.; Gehrke, R.; Hanke, F.; Havu, P.; Havu, V.; Ren, X.; Reuter, K.; Scheffler, M., Ab initio molecular simulations with numeric atom-centered orbitals. *Comput. Phys. Commun.* **2009**, *180*, 2175-2196.
[170] Ren, X.; Rinke, P.; Blum, V.; Wieferink, J.; Tkatchenko, A.; Sanfilippo, A.; Reuter, K.; Scheffler, M., Resolution-of-identity approach to Hartree-Fock, hybrid density functionals, RPA, MP2 and GW with numeric atom-centered orbital basis functions. *New J. Phys.* **2012**, *14*, 053020.
[171] Tran, F.; Blaha, P.; Schwarz, K.; Novak, P., Hybrid exchange-correlation energy functionals for strongly correlated electrons: Applications to transition-metal monoxides. *Phys. Rev. B* **2006**, *74*, 155108.
[172] Tran, F.; Blaha, P., Implementation of screened hybrid functionals based on the Yukawa potential within the LAPW basis set. *Phys. Rev. B* **2011**, *83*, 235118.

[173] Gulans, A.; Kontur, S.; Meisenbichler, C.; Nabok, D.; Pavone, P.; Rigamonti, S.; Sagmeister, S.; Werner, U.; Draxl, C., Exciting: A Full-Potential All-Electron Package Implementing Density-Functional Theory and Many-Body Perturbation Theory. *J. Phys.: Condens. Matter.* **2014**, *26*, 363202.
[174] Betzinger, M.; Friedrich, C.; Blügel, S., Hybrid functionals within the all-electron FLAPW method: Implementation and applications of PBE0. *Phys. Rev. B* **2010**, *81*, 195117.
[175] Friedrich, C.; Schindlmayr, A.; Blügel, S., Efficient calculation of the Coulomb matrix and its expansion around k=0 within the FLAPW method. *Comput. Phys. Commun.* **2009**, *180*, 347-359.
[176] Paier, J.; Hirschl, R.; Marsman, M.; Kresse, G., The Perdew-Burke-Ernzerhof exchange-correlation functional applied to the G2-1 test set using a plane-wave basis set. *J. Chem. Phys.* **2005**, *122*, 234102.
[177] Rostgaard, C.; Jacobsen, K. W.; Thygesen, K. S., Fully self-consistent GW calculations for molecules. *Phys. Rev. B* **2010**, *81*, 085103.
[178] Yan, J.; Hummelshoj, J. S.; Norskov, J. K., Formation energies of group I and II metal oxides using random phase approximation. *Phys. Rev. B* **2013**, *87*, 075207.
[179] Guidon, M.; Hutter, J.; VandeVondele, J., Auxiliary Density Matrix Methods for Hartree-Fock Exchange Calculations. *J. Chem. Theory Comput.* **2010**, *6*, 2348-2364.
[180] Giannozzi, P., et al., QUANTUM ESPRESSO: a modular and open-source software project for quantum simulations of materials. *J. Phys.-Condens. Matter* **2009**, *21*, 395502.
[181] Alkauskas, A.; Broqvist, P.; Pasquarello, A., Defect levels through hybrid density functionals: Insights and applications. *Phys. Status Solidi B-Basic Solid State Phys.* **2011**, *248*, 775-789.
[182] Lee, H.-Y.; Clark, S. J.; Robertson, J., Calculation of point defects in rutile $TiO_2$ by the screened-exchange hybrid functional. *Phys. Rev. B* **2012**, *86*, 075209.
[183] Guo, Y.; Clark, S. J.; Robertson, J., Calculation of metallic and insulating phases of $V_2O_3$ by hybrid density functionals. *J. Chem. Phys.* **2014**, *140*, 054702.
[184] Guo, Y.; Clark, S. J.; Robertson, J., Electronic and magnetic properties of $Ti_2O_3$, $Cr_2O_3$, and $Fe_2O_3$ calculated by the screened exchange hybrid density functional. *J. Phys.-Condens. Matter* **2012**, *24*, 325504.
[185] Anisimov, V. I.; Zaanen, J.; Andersen, O. K., Band Theory and Mott Insulators - Hubbard-U instead Of Stoner-I. *Phys. Rev. B* **1991**, *44*, 943-954.
[186] Liechtenstein, A. I.; Anisimov, V. I.; Zaanen, J., Density-Functional Theory and Strong-Interactions - Orbital Ordering in Mott-Hubbard Insulators. *Phys. Rev. B* **1995**, *52*, R5467-R5470.
[187] Anisimov, V. I.; Aryasetiawan, F.; Lichtenstein, A. I., First-principles calculations of the electronic structure and spectra of strongly correlated systems: The LDA+U method. *J. Phys.-Condens. Matter* **1997**, *9*, 767-808.
[188] Dudarev, S. L.; Botton, G. A.; Savrasov, S. Y.; Humphreys, C. J.; Sutton, A. P., Electron-energy-loss spectra and the structural stability of nickel oxide: An LSDA+U study. *Phys. Rev. B* **1998**, *57*, 1505-1509.
[189] Mott, N. F., The Transition to the Metallic State. *Philos. Mag.* **1961**, *6*, 287-309.
[190] Mott, N. F., On The Transition To Metallic Conduction In Semiconductors. *Can. J. Phys.* **1956**, *34*, 1356-1368.
[191] Mott, N. F., The Basis Of The Electron Theory Of Metals, With Special Reference To The Transition Metals. *Proc. R. Soc. London, Sec. A* **1949**, *62*, 416-422.
[192] Hubbard, J., Electron correlations in narrow energy bands. *Proc. R. Soc. London, Sec. A* **1964**, *277*, 237-259.
[193] Herring, C., Magnetism, edited by Rado, G. T. and Suhl H., Academic, New York, 1966; Vol. IV.
[194] Solovyev, I. V.; Dederichs, P. H.; Anisimov, V. I., Corrected Atomic Limit in the Local-Density Approximation and the Electronic-Structure of *d*-Impurities in Rb. *Phys. Rev. B* **1994**, *50*, 16861-16871.

[195] Da Silva, J. L. F.; Ganduglia-Pirovano, M. V.; Sauer, J.; Bayer, V.; Kresse, G., Hybrid Functionals Applied to Rare-Earth Oxides: The Example of Ceria. *Phys. Rev. B* **2007**, *75*, 045121.
[196] Lutfalla, S.; Shapovalov, V.; Bell, A. T., Calibration of the DFT/GGA plus U Method for Determination of Reduction Energies for Transition and Rare Earth Metal Oxides of Ti, V, Mo, and Ce. *J. Chem. Theory Comput.* **2011**, *7*, 2218-2223.
[197] Hu, Z.; Li, B.; Sun, X.; Metiu, H., Chemistry of Doped Oxides: The Activation of Surface Oxygen and the Chemical Compensation Effect. *J. Phys. Chem. C* **2011**, *115*, 3065-3074.
[198] Fabris, S.; Vicario, G.; Balducci, G.; de Gironcoli, S.; Baroni, S., Electronic and atomistic structures of clean and reduced ceria surfaces. *J. Phys. Chem. B* **2005**, *109*, 22860-22867.
[199] Allen, J. P.; Watson, G. W., Occupation matrix control of d- and f-electron localisations using DFT plus U. *Phys. Chem. Chem. Phys.* **2014**, *16*, 21016-21031.
[200] Kresse, G.; Surnev, S.; Schoiswohl, J.; Netzer, F. P., $V_2O_3$(0001) Surface Terminations: A Density Functional Study. *Surf. Sci.* **2004**, *555*, 118-134.
[201] Window, A. J.; Hentz, A.; Sheppard, D. C.; Parkinson, G. S.; Woodruff, D. P.; Unterberger, W.; Noakes, T. C. Q.; Bailey, P.; Ganduglia-Pirovano, M. V.; Sauer, J., The Structure of Epitaxial $V_2O_3$ Films and Their Surfaces: A Medium Energy Ion Scattering Study. *Surf. Sci.* **2012**, *606*, 1716-1727.
[202] Window, A. J.; Hentz, A.; Sheppard, D. C.; Parkinson, G. S.; Niehus, H.; Ahlbehrendt, D.; Noakes, T. C. Q.; Bailey, P.; Woodruff, D. P., $V_2O_3$(0001) Surface Termination: Phase Equilibrium. *Phys. Rev. Lett.* **2011**, *107*, 016105.
[203] Seifert, J.; Meyer, E.; Winter, H.; Kuhlenbeck, H., Surface Termination of an Ultrathin $V_2O_3$-Film on Au(111) Studied via Ion Beam Triangulation. *Surf. Sci.* **2012**, *606*, L41-L44.
[204] Dupuis, A. C.; Abu Haija, M.; Richter, B.; Kuhlenbeck, H.; Freund, H. J., $V_2O_3$(0001) on Au(111) and W(110): Growth, Termination and Electronic Structure. *Surf. Sci.* **2003**, *539*, 99-112.
[205] Schoiswohl, J.; Sock, M.; Surnev, S.; Ramsey, M. G.; Netzer, F. P.; Kresse, G.; Andersen, J. N., $V_2O_3$(0001) Surface Terminations: From Oxygen- to Vanadium-Rich. *Surf. Sci.* **2004**, *555*, 101-117.
[206] Todorova, T. K.; Ganduglia-Pirovano, M. V.; Sauer, J., Vanadium Oxides on Aluminum Oxide Supports. 1. Surface Termination and Reducibility of Vanadia Films on $\alpha$-$Al_2O_3$(0001). *J. Phys. Chem. B* **2005**, *109*, 23523-23531.
[207] Göbke, D.; Romanyshyn, Y.; Guimond, S.; Sturm, J. M.; Kuhlenbeck, H.; Döbler, J.; Reinhardt, U.; Ganduglia-Pirovano, M. V.; Sauer, J.; Freund, H. J., Formaldehyde Formation on Vanadium Oxide Surfaces $V_2O_3$(0001) and $V_2O_5$(001): How Does The Stable Methoxide Intermediate Form? *Angew. Chem. Int. Ed.* **2009**, *48*, 3695-3698.
[208] Deo, G.; Wachs, I. E., Reactivity of Supported Vanadium-Oxide Catalysts - The Partial Oxidation of Methanol. *J. Catal.* **1994**, *146*, 323-334.
[209] Kolczewski, C.; Hermann, K.; Guimond, S.; Kuhlenbeck, H.; Freund, H. J., Identification of the Vanadyl Terminated $V_2O_3$(0001) Surface by NEXAFS Spectroscopy: A Combined Theoretical and Experimental Study. *Surf. Sci.* **2007**, *601*, 5394-5402.
[210] Perdew, J. P.; Chevary, J. A.; Vosko, S. H.; Jackson, K. A.; Pederson, M. R.; Singh, D. J.; Fiolhais, C., Atoms, Molecules, Solids, and Surfaces - Applications of the Generalized Gradient Approximation for Exchange and Correlation. *Phys. Rev. B* **1992**, *46*, 6671-6687.
[211] Feiten, F. E.; Kuhlenbeck, H.; Freund, H.-J., Surface Structure of $V_2O_3$(0001): A Combined I/V-LEED and STM Study. *J. Phys. Chem. C* **2015**, *119*, 22961-22969.
[212] Wu, Z.; Płucienik, A.; Feiten, F. E.; Naschitzki, M.; Wachsmann, W.; Gewinner, S.; Schöllkopf, W.; Staemmler, V.; Kuhlenbeck, H.; Freund, H.-J., Vibrational Action Spectroscopy of Solids: New Surface-Sensitive Technique. *Phys. Rev. Lett.* **2017**, *119*, 136101.

[213] Tersoff, J.; Hamann, D. R., Theory and Application for the Scanning Tunneling Microscope. *Phys. Rev. Lett.* **1983**, *50*, 1998-2001.
[214] Tersoff, J.; Hamann, D. R., Theory of the Scanning Tunneling Microscope. *Phys. Rev. B* **1985**, *31*, 805-813.
[215] Piccini, G.; Alessio, M.; Sauer, J., Ab Initio Calculation of Rate Constants for Molecule–Surface Reactions with Chemical Accuracy. *Angew. Chem. Int. Ed.* **2016**, *55*, 5235-5237; *Angew. Chem.* **2016**, *128*, 5321-5323.
[216] Eyert, V., $VO_2$: A Novel View from Band Theory. *Phys. Rev. Lett.* **2011**, *107*, 016401.
[217] Grau-Crespo, R.; Wang, H.; Schwingenschlögl, U., Why the Heyd-Scuseria-Ernzerhof Hybrid Functional Description of $VO_2$ Phases is Not Correct. *Phys. Rev. B* **2012**, *86*, 081101.
[218] Wang, H.; Mellan, T. A.; Grau-Crespo, R.; Schwingenschlögl, U., Spin Polarization, Orbital Occupation and Band Gap Opening in Vanadium Dioxide: The Effect of Screened Hartree-Fock Exchange. *Chem. Phys. Lett.* **2014**, *608*, 126-129.
[219] Schrön, A.; Rödl, C.; Bechstedt, F., Energetic Stability and Magnetic Properties of MnO in the Rocksalt, Wurtzite, and Zinc-Blende Structures: Influence of Exchange and Correlation. *Phys. Rev. B* **2010**, *82*, 165109.
[220] Chase, M. W., Jr., *NIST-JANAF Thermochemical Tables*; AIP: New York, 1998.
[221] W. Brückner; H. Oppermann; W. Reichelt; J. I. Terukow; F. A. Tschudnowski; Wolf, E., *Vanadiumoxide, Darstellung, Eigenschaften, Anwendung*; Akademie: Berlin, 1983.
[222] Ganduglia-Pirovano, M. V.; Popa, C.; Sauer, J.; Abbott, H. L.; Uhl, A.; Baron, M.; Stacchiola, D.; Bondarchuk, O.; Shaikhutdinov, S.; Freund, H.-J., Role of Ceria in Oxidative Dehydrogenation on Supported Vanadia Catalysts. *J. Am. Chem. Soc.* **2010**, *132*, 2345-2349.
[223] Abbott, H. L.; Uhl, A.; Baron, M.; Lei, Y.; Meyer, R. J.; Stacchiola, D. J.; Bondarchuk, O.; Shaikhutdinov, S.; Freund, H. J., Relating methanol oxidation to the structure of ceria-supported vanadia monolayer catalysts. *J. Catal.* **2010**, *272*, 82-91.
[224] Kropp, T.; Paier, J.; Sauer, J., Oxidative Dehydrogenation of Methanol at Ceria-Supported Vanadia Oligomers. *J. Catal.* **2017**, *352*, 382-387.
[225] Rozanska, X.; Fortrie, R.; Sauer, J., Oxidative Dehydrogenation of Propane by Monomeric Vanadium Oxide Sites on Silica Support. *J. Phys. Chem. C* **2007**, *111*, 6041-6050.
[226] Beck, B.; Harth, M.; Hamilton, N. G.; Carrero, C.; Uhlrich, J. J.; Trunschke, A.; Shaikhutdinov, S.; Schubert, H.; Freund, H.-J.; Schlögl, R.; Sauer, J.; Schomäcker, R., Partial Oxidation of Ethanol on Vanadia Catalysts on Supporting Oxides with Different Redox Properties Compared to Propane. *J. Catal.* **2012**, *296*, 120-131.
[227] Artiglia, L.; Agnoli, S.; Granozzi, G., Vanadium Oxide Nanostructures on Another Oxide: The Viewpoint from Model Catalysts Studies. *Coordin. Chem. Rev.* **2015**, *301-302*, 106-122.
[228] Wachs, I. E.; Chen, Y.; Jehng, J.-M.; Briand, L. E.; Tanaka, T., Molecular Structure and Reactivity of the Group V Metal Oxides. *Catal. Today* **2003**, *78*, 13-24.
[229] Wachs, I. E.; Deo, G.; Juskelis, M. V.; Weckhuysen, B. M., Methanol Oxidation. In *Dynamics of Surfaces and Reaction Kinetics in Heterogeneous Catalysis*, Froment, G. F.; Waugh, K. C., Eds. Elsevier: Amsterdam, 1997; pp 305-314.
[230] Wachs, I. E. In *Catalysis*, Spivey, J. J., Ed. The Royal Society of Chemistry: 1997; p. 37.
[231] Penschke, C.; Paier, J.; Sauer, J., Vanadium Oxide Oligomers and Ordered Monolayers Supported on $CeO_2$(111): Structure and Stability Studied by Density Functional Theory. *J. Phys. Chem. C* **2018**, *122*, 9101-9110.
[232] Baron, M.; Bondarchuk, O.; Stacchiola, D.; Shaikhutdinov, S.; Freund, H.-J., Interaction of Gold with Cerium Oxide Supports: $CeO_2$(111) Thin Films vs $CeO_x$ Nanoparticles. *J. Phys. Chem. C* **2009**, *113*, 6042-6049.
[233] Reuter, K.; Scheffler, M., Composition, Structure, and Stability of $RuO_2$(110) As a Function of Oxygen Pressure. *Phys. Rev. B* **2001**, *65*, 035406.

[234] Fabris, S.; de Gironcoli, S.; Baroni, S.; Vicario, G.; Balducci, G., Reply to "Comment on 'Taming Multiple Valency with Density Functionals: A Case Study of Defective Ceria'". *Phys. Rev. B* **2005**, *72*, 237102.
[235] Popa, C.; Ganduglia-Pirovano, M. V.; Sauer, J., Periodic Density Functional Theory Study of $VO_n$ Species Supported on the $CeO_2$(111) Surface. *J. Phys. Chem. C* **2011**, *115*, 7399-7410; 2012,**116**, 18572-18573(Erratum).
[236] H. Jonsson; G. Mills; Jacobsen, K. W., Nudged Elastic Band Method for Finding Minimum Energy Paths of Transitions. In *Classical and Quantum Dynamics in Condensed Phase Simulations*, J. Berne; G. Ciccotti; Coker, D. F., Eds. World Scientific: 1998.
[237] Heyden, A.; Bell, A. T.; Keil, F. J., Efficient Methods for Finding Transition States in Chemical Reactions: Comparison of Improved Dimer Method and Partitioned Rational Function Optimization Method. *J. Chem. Phys.* **2005**, *123*, 224101.
[238] Jiang, L.; Wende, T.; Claes, P.; Bhattacharyya, S.; Sierka, M.; Meijer, G.; Lievens, P.; Sauer, J.; Asmis, K. R., Electron Distribution in Partially Reduced Mixed Metal Oxide Systems: Infrared Spectroscopy of $Ce_mV_nO_o^+$ Gas-Phase Clusters. *J. Phys. Chem. A* **2011**, *115*, 11187-11192.
[239] Brönsted, J. N., Acid and Basic Catalysis. *Chem. Rev.* **1928**, *5*, 231-338.
[240] Bell, R. P., The Theory of Reactions Involving Proton Transfers. *Proc. R. Soc. London, Sec. A* **1936**, *154*, 414.
[241] Evans, M. G.; Polanyi, M., Inertia and Driving Force of Chemical Reactions. *Trans. Faraday Soc.* **1938**, *34*, 11-23.
[242] Redhead, P. A., Thermal Desorption of Gases. *Vacuum* **1962**, *12*, 203-211.
[243] Grimme, S., Semiempirical GGA-Type Density Functional Constructed With a Long-Range Dispersion Correction. *J. Comput. Chem.* **2006**, *27*, 1787-1799.
[244] Kerber, T.; Sierka, M.; Sauer, J., Application of Semiempirical Long-Range Dispersion Corrections to Periodic Systems in Density Functional Theory. *J. Comput. Chem.* **2008**, *29*, 2088-2097.
[245] Beste, A.; Mullins, D. R.; Overbury, S. H.; Harrison, R. J., Adsorption and Dissociation of Methanol on the Fully Oxidized and Partially Reduced (111) Cerium Oxide Surface: Dependence on the Configuration of the Cerium 4f Electrons. *Surf. Sci.* **2008**, *602*, 162-175.
[246] Beste, A.; Overbury, S. H., Dehydrogenation of Methanol to Formaldehyde Catalyzed by Pristine and Defective Ceria Surfaces. *Phys. Chem. Chem. Phys.* **2016**, *18*, 9990-9998.
[247] Capdevila-Cortada, M.; García-Melchor, M.; López, N., Unraveling the Structure Sensitivity in Methanol Conversion on $CeO_2$: A DFT+U Study. *J. Catal.* **2015**, *327*, 58-64.
[248] Mullins, D. R., The surface chemistry of cerium oxide. *Surf. Sci. Rep.* **2015**, *70*, 42-85.
[249] Pan, Y.; Nilius, N.; Stiehler, C.; Freund, H.-J.; Goniakowski, J.; Noguera, C., Ceria Nanocrystals Exposing Wide (100) Facets: Structure and Polarity Compensation. *Adv. Mater. Interf.* **2014**, *1*, 1400404.
[250] Albrecht, P. M.; Mullins, D. R., Adsorption and Reaction of Methanol over $CeO_X$(100) Thin Films. *Langmuir* **2013**, *29*, 4559-4567.
[251] Ferrizz, R. M.; Wong, G. S.; Egami, T.; Vohs, J. M., Structure Sensitivity of the Reaction of Methanol on Ceria. *Langmuir* **2001**, *17*, 2464-2470.
[252] Döbler, J.; Pritzsche, M.; Sauer, J., Oxidation of Methanol to Formaldehyde on Supported Vanadium Oxide Catalysts Compared to Gas Phase Molecules. *J. Am. Chem. Soc.* **2005**, *127*, 10861-10868.
[253] Cheng, M.-J.; Nielsen, R. J.; Tahir-Kheli, J.; Goddard III, W. A., The Magnetic and Electronic Structure of Vanadyl Pyrophosphate from Density Functional Theory. *Phys. Chem. Chem. Phys.* **2011**, *13*, 9831-9838.
[254] Cheng, M.-J.; Goddard, W. A., The Critical Role of Phosphate in Vanadium Phosphate Oxide for the Catalytic Activation and Functionalization of n-Butane to Maleic Anhydride. *J. Am. Chem. Soc.* **2013**, *135*, 4600-4603.

[255] Noodleman, L., Valence Bond Description of Anti-Ferromagnetic Coupling in Transition-Metal Dimers. *J. Chem. Phys.* **1981**, *74*, 5737-5743.
[256] Hampel, C.; Peterson, K. A.; Werner, H. J., A Comparison of the Efficiency and Accuracy of the Quadratic Configuration-Interaction (QCISD), Coupled Cluster (CCSD), and Brueckner Coupled Cluster (BCCD) Methods. *Chem. Phys. Lett.* **1992**, *190*, 1-12.
[257] Deegan, M. J. O.; Knowles, P. J., Perturbative Corrections to Account for Triple Excitations in Closed and Open-Shell Coupled-Cluster Theories. *Chem. Phys. Lett.* **1994**, *227*, 321-326.
[258] Haruta, M.; Tsubota, S.; Kobayashi, T.; Kageyama, H.; Genet, M. J.; Delmon, B., Low-Temperature Oxidation of CO over Gold Supported on $TiO_2$, $\alpha$-$Fe_2O_3$, and $Co_3O_4$. *J. Catal.* **1993**, *144*, 175-192.
[259] Vayssilov, G. N.; Lykhach, Y.; Migani, A.; Staudt, T.; Petrova, G. P.; Tsud, N.; Skala, T.; Bruix, A.; Illas, F.; Prince, K. C.; Matolin, V.; Neyman, K. M.; Libuda, J., Support Nanostructure Boosts Oxygen Transfer to Catalytically Active Platinum Nanoparticles. *Nat. Mater.* **2011**, *10*, 310-315.
[260] Ganduglia-Pirovano, M. V.; Da Silva, J. L. F.; Sauer, J., Density Functional Calculations of the Structure of Near-Surface Oxygen Vacancies and Electron Localization on $CeO_2$(111). *Phys. Rev. Lett.* **2009**, *102*, 026101.
[261] Plata, J. J.; Marquez, A. M.; Sanz, J. F., Transport Properties in the $CeO_{2-x}$(111) Surface: From Charge Distribution to Ion-Electron Collaborative Migration. *J. Phys. Chem. C* **2013**, *117*, 25497-25503.
[262] Hernandez, N. C.; Grau-Crespo, R.; de Leeuw, N. H.; Sanz, J. F., Electronic Charge Transfer Between Ceria Surfaces and Gold Adatoms: A GGA+U Investigation. *Phys. Chem. Chem. Phys.* **2009**, *11*, 5246-5252.
[263] Chen, Y.; Hu, P.; Lee, M. H.; Wang, H. F., Au on (111) and (110) Surfaces of $CeO_2$: A Density-Functional Theory Study. *Surf. Sci.* **2008**, *602*, 1736-1741.
[264] Camellone, M. F.; Fabris, S., Reaction Mechanisms for the CO Oxidation on Au/$CeO_2$ Catalysts: Activity of Substitutional $Au^{3+}$/$Au^{+}$ Cations and Deactivation of Supported $Au^{+}$ Adatoms. *J. Am. Chem. Soc.* **2009**, *131*, 10473-10483.
[265] Zhang, C. J.; Michaelides, A.; Jenkins, S. J., Theory of Gold on Ceria. *Phys. Chem. Chem. Phys.* **2011**, *13*, 22-33.
[266] Pyykkö, P., Theoretical Chemistry of Gold. *Angew. Chem. Int. Ed.* **2004**, *43*, 4412-4456.
[267] Nilius, N.; Ganduglia-Pirovano, M. V.; Brazdova, V.; Kulawik, M.; Sauer, J.; Freund, H. J., Counting Electrons Transferred Through a Thin Alumina Film into Au Chains. *Phys. Rev. Lett.* **2008**, *100*, 096802.
[268] Sterrer, M.; Risse, T.; Pozzoni, U. M.; Giordano, L.; Heyde, M.; Rust, H.-P.; Pacchioni, G.; Freund, H.-J., Control of the Charge State of Metal Atoms on Thin MgO Films. *Phys. Rev. Lett.* **2007**, *98*, 096107.
[269] Kośmider, K.; Brázdová, V.; Ganduglia-Pirovano, M. V.; Pérez, R., Do Au Atoms Titrate $Ce^{3+}$ Ions at the $CeO_{2-x}$(111) Surface? *J. Phys. Chem. C* **2016**, *120*, 927-933.
[270] Li, H.-Y.; Wang, H.-F.; Gong, X.-Q.; Guo, Y.-L.; Guo, Y.; Lu, G.; Hu, P., Multiple Configurations of the Two Excess 4f Electrons on Defective $CeO_2$(111): Origin and Implications. *Phys. Rev. B* **2009**, *79*, 193401.
[271] Branda, M. M.; Castellani, N. J.; Grau-Crespo, R.; de Leeuw, N. H.; Hernandez, N. C.; Sanz, J. F.; Neyman, K. M.; Illas, F., On the Difficulties of Present Theoretical Models to Predict the Oxidation State of Atomic Au Adsorbed on Regular Sites of $CeO_2$(111). *J. Chem. Phys.* **2009**, *131*, 094702.
[272] Pan, Y.; Cui, Y.; Stiehler, C.; Nilius, N.; Freund, H. J., Gold Adsorption on $CeO_2$ Thin Films Grown on Ru(0001). *J. Phys. Chem. C* **2013**, *117*, 21879-21885.
[273] Maurice, R.; Verma, P.; Zadrozny, J. M.; Luo, S.; Borycz, J.; Long, J. R.; Truhlar, D. G.; Gagliardi, L., Single-Ion Magnetic Anisotropy and Isotropic Magnetic Couplings in the Metal–Organic Framework $Fe_2$(dobdc). *Inorg. Chem.* **2013**, *52*, 9379-9389.

[274] Murray, L. J.; Dincă, M.; Long, J. R., Hydrogen Storage in Metal–Organic Frameworks. *Chem. Soc. Rev.* **2009**, *38*, 1294-1314.
[275] Czaja, A. U.; Trukhan, N.; Müller, U., Industrial Applications of Metal–Organic Frameworks. *Chem. Soc. Rev.* **2009**, *38*, 1284-1293.
[276] Xiao, D. J., et al., Oxidation of Ethane to Ethanol by $N_2O$ in a Metal–Organic Framework With Coordinatively Unsaturated Iron(II) Sites. *Nat. Chem.* **2014**, *6*, 590.
[277] Llabrés i Xamena, F. X.; Casanova, O.; Galiasso Tailleur, R.; Garcia, H.; Corma, A., Metal Organic Frameworks (MOFs) As Catalysts: A Combination of $Cu^{2+}$ and $Co^{2+}$ MOFs As an Efficient Catalyst For Tetralin Oxidation. *J. Catal.* **2008**, *255*, 220-227.
[278] Tonigold, M.; Lu, Y.; Mavrandonakis, A.; Puls, A.; Staudt, R.; Möllmer, J.; Sauer, J.; Volkmer, D., Pyrazolate-Based Cobalt(II)-Containing Metal–Organic Frameworks in Heterogeneous Catalytic Oxidation Reactions: Elucidating the Role of Entatic States for Biomimetic Oxidation Processes. *Chem. Eur. J.* **2011**, *17*, 8671-8695.
[279] Bloch, E. D.; Queen, W. L.; Krishna, R.; Zadrozny, J. M.; Brown, C. M.; Long, J. R., Hydrocarbon Separations in a Metal-Organic Framework with Open Iron(II) Coordination Sites. *Science* **2012**, *335*, 1606-1610.
[280] Verma, P.; Vogiatzis, K. D.; Planas, N.; Borycz, J.; Xiao, D. J.; Long, J. R.; Gagliardi, L.; Truhlar, D. G., Mechanism of Oxidation of Ethane to Ethanol at Iron(IV)–Oxo Sites in Magnesium-Diluted $Fe_2$(dobdc). *J. Am. Chem. Soc.* **2015**, *137*, 5770-5781.
[281] Siegbahn, P. E. M.; Almlöf, J.; Heiberg, A.; Roos, B. O., The complete active space SCF (CASSCF) method in a Newton–Raphson formulation with application to the HNO molecule. *J. Chem. Phys.* **1981**, *74*, 2384-2396.
[282] Angeli, C.; Cimiraglia, R.; Evangelisti, S.; Leininger, T.; Malrieu, J. P., Introduction of n-electron valence states for multireference perturbation theory. *J. Chem. Phys.* **2001**, *114*, 10252-10264.
[283] Sala, A.; Marchetto, H.; Qin, Z. H.; Shaikhutdinov, S.; Schmidt, T.; Freund, H. J., Defects and Inhomogeneities in $Fe_3O_4$(111) Thin Film Growth on Pt(111). *Phys. Rev. B* **2012**, *86*, 155430.
[284] Kiejna, A.; Ossowski, T.; Pabisiak, T., Surface Properties of the Clean and Au/Pd Covered $Fe_3O_4$(111): DFT and DFT+U study. *Phys. Rev. B* **2012**, *85*, 125414.
[285] Parkinson, G. S., Iron Oxide Surfaces. *Surf. Sci. Rep.* **2016**, *71*, 272-365.
[286] Van Der Laan, G. P.; Beenackers, A. A. C. M., Kinetics and Selectivity of the Fischer–Tropsch Synthesis: A Literature Review. *Catal. Rev.-Sci. Eng.* **1999**, *41*, 255-318.
[287] de Smit, E.; Weckhuysen, B. M., The Renaissance of Iron-Based Fischer-Tropsch Synthesis: On the Multifaceted Catalyst Deactivation Behaviour. *Chem. Soc. Rev.* **2008**, *37*, 2758-2781.
[288] Freund, H.-J.; Pacchioni, G., Oxide Ultra-Thin Films on Metals: New Materials for the Design of Supported Metal Catalysts. *Chem. Soc. Rev.* **2008**, *37*, 2224-2242.
[289] Sun, Y. N.; Giordano, L.; Goniakowski, J.; Lewandowski, M.; Qin, Z. H.; Noguera, C.; Shaikhutdinov, S.; Pacchioni, G.; Freund, H. J., The Interplay between Structure and CO Oxidation Catalysis on Metal-Supported Ultrathin Oxide Films. *Angew. Chem. Int. Ed.* **2010**, *49*, 4418-4421.
[290] Casey, W. H.; Banfield, J. F.; Westrich, H. R.; McLaughlin, L., What Do Dissolution Experiments Tell Us About Natural Weathering? *Chem. Geol.* **1993**, *105*, 1-15.
[291] Ovcharenko, R.; Voloshina, E.; Sauer, J., Water Adsorption and O-defect Formation on $Fe_2O_3$(0001) surfaces. *Phys. Chem. Chem. Phys.* **2016**, *18*, 25560-25568.
[292] Lemire, C.; Meyer, R.; Henrich, V. E.; Shaikhutdinov, S.; Freund, H. J., The Surface Structure of $Fe_3O_4$(111) Films as Studied by CO Adsorption. *Surf. Sci.* **2004**, *572*, 103-114.
[293] Dementyev, P.; Dostert, K.-H.; Ivars-Barceló, F.; O'Brien, C. P.; Mirabella, F.; Schauermann, S.; Li, X.; Paier, J.; Sauer, J.; Freund, H.-J., Water Interaction with Iron Oxides. *Angew. Chem. Int. Ed.* **2015**, *54*, 13942-13946.

[294] Noh, J.; Osman, O. I.; Aziz, S. G.; Winget, P.; Brédas, J.-L., Magnetite $Fe_3O_4$(111) Surfaces: Impact of Defects on Structure, Stability, and Electronic Properties. *Chem. Mat.* **2015**, *27*, 5856-5867.
[295] Mantz, A. W.; Watson, J. K. G.; Rao, K. N.; Albritton, D. L.; Schmeltekorf, A. L.; Zare, R. N., Rydberg-Klein-Rees Potential for $X^1\,\Sigma^+$ State of CO Molecule. *J. Mol. Spectrosc.* **1971**, *39*, 180.
[296] Chatt, J.; Duncanson, L. A., Olefin Co-Ordination Compounds .3. Infra-Red Spectra and Structure - Attempted Preparation of Acetylene Complexes. *J. Chem. Soc.* **1953**, 2939-2947.
[297] Dewar, J. S., A Review of the π-Complex Theory. *Bull. Soc. Chim. Fr.* **1951**, *18*, C71-C79.
[298] Blyholder, G., Molecular Orbital View of Chemisorbed Carbon Monoxide. *J. Phys. Chem.* **1964**, *68*, 2772.
[299] Henrich, V. E.; Shaikhutdinov, S. K., Atomic Geometry of Steps on Metal-Oxide Single Crystals. *Surf. Sci.* **2005**, *574*, 306-316.
[300] Pacchioni, G.; Cogliandro, G.; Bagus, P. S., Characterization of Oxide Surfaces by Infrared-Spectroscopy of Adsorbed Carbon-Monoxide - A Theoretical Investigation of the Frequency-Shift of CO on MgO and NiO. *Surf. Sci.* **1991**, *255*, 344-354.
[301] Tosoni, S.; Sauer, J., Accurate Quantum Chemical Energies for the Interaction of Hydrocarbons With Oxide Surfaces: $CH_4$/MgO(001). *Phys. Chem. Chem. Phys.* **2010**, *12*, 14330-14340.
[302] Boese, A. D.; Sauer, J., Accurate Adsorption Energies of Small Molecules on Oxide Surfaces: CO-MgO(001). *Phys. Chem. Chem. Phys.* **2013**, *15*, 16481-16493.
[303] Pauling, L., The Principles Determining the Structure of Complex Ionic Crystals. *J. Am. Chem. Soc.* **1929**, *51*, 1010-1026.
[304] Fagiani, M. R.; Song, X.; Debnath, S.; Gewinner, S.; Schöllkopf, W.; Asmis, K. R.; Bischoff, F. A.; Müller, F.; Sauer, J., Dissociative Water Adsorption by $Al_3O_4^+$ in the Gas Phase. *J. Phys. Chem. Lett.* **2017**, *8*, 1272-1277.
[305] Moskovits, M., Surface selection rules. *J. Chem. Phys.* **1982**, *77*, 4408-4416.
[306] Greenler, R. G.; Snider, D.; Witt, D.; Sorbello, R., The metal-surface selection rule for infrared spectra of molecules adsorbed on small metal particles. *Surf. Sci.* **1982**, *118*, 415-428.
[307] Osawa, M.; Ataka, K.-I.; Yoshii, K.; Nishikawa, Y., Surface-enhanced infrared spectroscopy: the origin of the absorption enhancement and band selection rule in the infrared spectra of molecules adsorbed on fine metal particles. *Appl. Spectrosc.* **1993**, *47*, 1497-1502.
[308] Pearce, H.; Sheppard, N., Possible importance of a "metal-surface selection rule" in the interpretation of the infrared spectra of molecules adsorbed on particulate metals; infrared spectra from ethylene chemisorbed on silica-supported metal catalysts. *Surf. Sci.* **1976**, *59*, 205-217.
[309] Huggins, C. M.; Pimentel, G. C., Systematics of the infrared spectral properties of hydrogen bonding systems: frequency shift, half width and intensity. *J. Phys. Chem.* **1956**, *60*, 1615-1619.
[310] Yu, X.; Emmez, E.; Pan, Q.; Yang, B.; Pomp, S.; Kaden, W. E.; Sterrer, M.; Shaikhutdinov, S.; Freund, H.-J.; Goikoetxea, I.; Wlodarczyk, R.; Sauer, J., Electron stimulated hydroxylation of a metal supported silicate film. *Phys. Chem. Chem. Phys.* **2016**, *18*, 3755-64.

# Appendix

# P1

https://journals.aps.org/prl/abstract/10.1103/PhysRevLett.114.216101

# Surface Structure of $V_2O_3(0001)$ Revisited

Felix E. Feiten,[1] Jan Seifert,[1,2] Joachim Paier,[3,†] Helmut Kuhlenbeck,[1,*] Helmut Winter,[2] Joachim Sauer,[3] and Hans-Joachim Freund[1]

[1]*Fritz-Haber-Institut der Max-Planck-Gesellschaft, Faradayweg 4-6, 14195 Berlin, Germany*
[2]*Humboldt-Universität zu Berlin, Institut für Physik, Newtonstrasse 15, 12489 Berlin, Germany*
[3]*Humboldt-Universität zu Berlin, Institut für Chemie, Unter den Linden 6, 10099 Berlin, Germany*

(Received 20 January 2015; published 26 May 2015)

In a recent paper [A. J. Window *et al.*, Phys. Rev. Lett. 107, 016105 (2011)], it was proposed that $V_2O_3(0001)$ is terminated by the so-called $O_3$ termination, a reconstruction with a terminating distorted hexagonal oxygen layer. We show that the surface is terminated by vanadyl (V=O) groups instead. This conclusion is based on quantitative low-energy electron diffraction combined with scanning tunneling microscopy, fast atom scattering, and density functional theory employing the Heyd-Scuseria-Ernzerhof functional. New insights into the subsurface sensitivity of ion beam triangulation show that results previously interpreted in favor of the $O_3$ termination are reconcilable with vanadyl termination as well.

DOI: 10.1103/PhysRevLett.114.216101 PACS numbers: 68.35.B-, 61.05.jh, 68.47.Gh

Vanadium oxides find significant interest in basic research and are of technological importance because of their metal to insulator transitions and applications in oxygen transfer catalysis [1–5]. The surface termination is of decisive relevance for both classes of applications—this is obvious for the area of catalysis, but the influence on phase transitions, at least in near-surface layers, has also been shown [6]. For $V_2O_3(0001)$, a number of studies have been published, but there is still an ongoing debate about its termination [7–14].

For almost a decade, the $V_2O_3(0001)$ surface prepared under ultrahigh vacuum (UHV) conditions was assumed to be vanadyl terminated. This conclusion was based mainly on the presence of an intense vanadyl signal in vibrational spectra [7,8], but scanning tunneling microscopy (STM), X-ray photoelectron spectroscopy, and near edge X-ray absorption fine structure data also supported this view [7,8,15]. However, recent studies employing ion scattering and density functional theory (DFT) strongly favor the $O_3$ termination [9–11].

Motivated by this controversy, we have performed an extensive quantitative surface structure determination employing low-energy electron diffraction (LEED) and *I-V* LEED combined with STM, as well as fast atom scattering and DFT. Furthermore, we reinterpret the results of a previous ion scattering study [10].

The hexagonal bulk unit cell of $V_2O_3$ gives rise to three different possible terminations when cutting parallel to the 0001 plane: metal terminations with two vanadium atoms [double metal (DM)] ($\cdots O_3{-}V_2{-}O_3{-}V_2$) and one vanadium atom [single metal (SM)] ($\cdots O_3{-}V_2{-}O_3{-}V$) in the surface unit cell, respectively, and an oxygen termination ($\cdots O_3{-}V_2{-}O_3$). DFT calculations indicate that several reconstructions are energetically favorable over the bulk terminations [12,13]. At low oxygen chemical potential a vanadyl-covered surface ($\cdots O_3{-}V_2{-}O_3{-}V{=}O$) is thermodynamically stable, while at higher oxygen chemical potential incomplete V=O terminations form, with ordered superstructures at 2/3 and 1/3 of the full V=O coverage and finally an $O_3$ termination completely devoid of V=O groups. Compared to the bulklike, oxygen-terminated surface, this $O_3$ termination is reconstructed with each second V atom from the second layer moved up into the first layer ($\cdots O_3{-}V{-}O_3{-}V_3{-}O_3$) as shown in Fig. 1.

About 100 Å thick $V_2O_3(0001)$ films were prepared on Au(111) by deposition of vanadium from an *e*-beam evaporator with a rate of ~0.7 Å/ min in an $O_2$ ambience, followed by annealing in oxygen and finally in UHV for a short time. Some films were afterwards oxidized by annealing at elevated oxygen pressures. While films deposited at $1 \times 10^{-7}$ mbar$< p(O_2) < 1 \times 10^{-6}$ mbar show a $(1 \times 1)$ LEED pattern, a $(\sqrt{3} \times \sqrt{3})R30°$ superstructure appears after exposure to higher $O_2$ pressures. This is the first clear evidence that none of the prepared layers was $O_3$

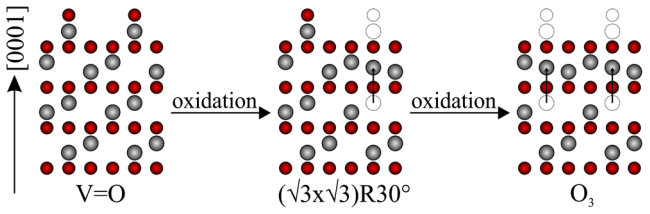


FIG. 1 (color online). Structural model (V gray and O red) of surface terminations predicted by DFT.

*Corresponding author.
kuhlenbeck@fhi-berlin.mpg.de
†To whom all correspondence regarding the density functional computations should be addressed.
joachim.paier@chemie.hu-berlin.de

 

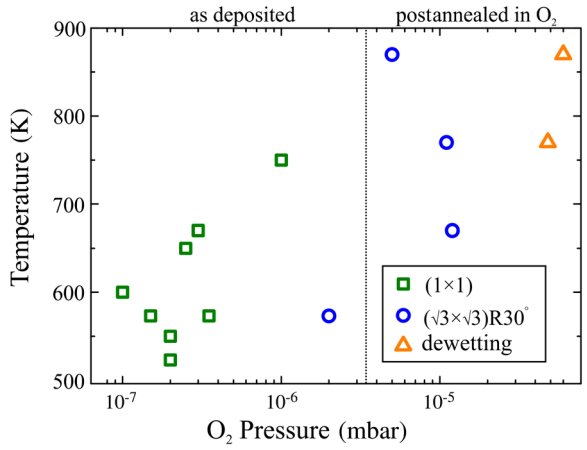


FIG. 2 (color online). Experimentally observed surface phases as a function of the preparation conditions.

terminated, since the oxygen content in the $O_3$ structure is higher than in the $(\sqrt{3} \times \sqrt{3})R30°$ phase. At even higher oxygen pressure, the film disappeared, probably through formation of $V_2O_5$, which sublimates at above ~800 K [16]. An overview of the observed phases is shown in Fig. 2.

While the $(\sqrt{3} \times \sqrt{3})R30°$ termination can easily be identified by LEED, both the V=O-covered surface and the $O_3$ termination exhibit identical reflex patterns. Thus, *I-V* LEED analysis was used to differentiate between these structures and to determine the positions of the atoms at the surface. For this study, the intensities of 32 diffraction spots were recorded. Averaging over symmetry equivalent spots and different domains yielded eight different beams over a combined energy range of 1819 eV. Beam damage was minimized by use of a LEED system with a microchannel plate detector, reducing electron currents to the surface to less than 10 nA. *I-V* curves were calculated with a modified version of the SATLEED package of Barbieri and van Hove [17]. The Pendry *R* factor [18] was used to quantify the agreement between theory and experiment—a smaller *R* factor means better agreement. The structures were refined by minimization of the *R* factor using a covariance matrix adaptation evolution strategy as implemented in the SHARK library [19]. Depending on the structural model, 15–17 atomic coordinates and three to five Debye temperatures as well as the imaginary and real parts of the inner potential and a linear background of the experimental data were selected as refinement parameters.

A total of 14 different structures with varying interlayer distances (five SM, five V=O, two DM, and two $O_3$ [11,12,20,21]) were selected as start structures for the refinement. Out of all models, coordinates published by Czekaj, Hermann, and Witko [20] for a V=O-terminated surface led to the smallest *R* factor after refinement ($R = 0.12$) [22]. In contrast, the smallest *R* factor for the $O_3$ termination is 0.36. The corresponding *I-V* curves shown in Fig. 3 visualize the good agreement between the

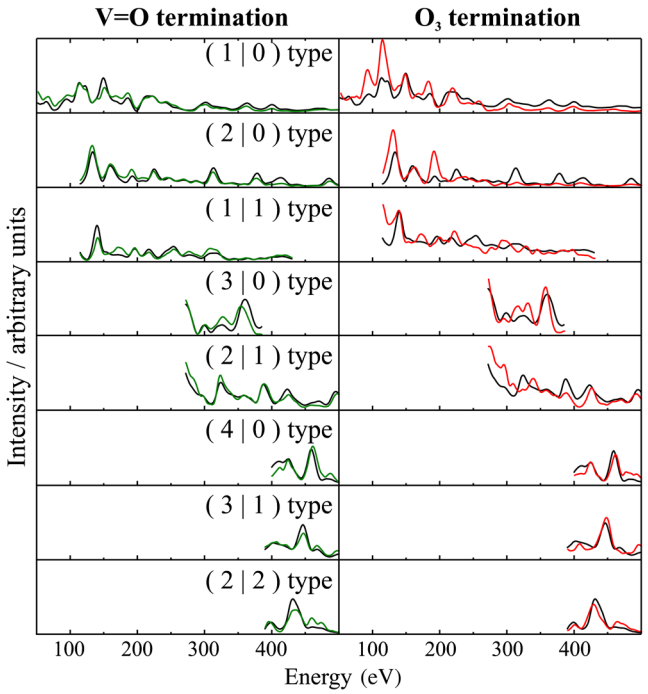


FIG. 3 (color online). Calculated *I-V* LEED curves (green and red) and experimental data (black) for the eight symmetry inequivalent beams.

V=O simulation and the experiment, while there are clear deviations from the experimental curves for the best-fit simulation of the $O_3$ termination.

STM images obtained for the $(1 \times 1)$ phase always show a hexagonal lattice (Fig. 4). This type of STM image is consistent with Tersoff-Hamann simulations for a fully vanadyl-covered surface, while the triangular features characteristic of an $O_3$ termination [11] or a bulklike oxygen termination [23] were never seen. Figure 4(a) shows an image taken directly after recording the *I-V* curves shown in Fig. 3. The bright triangular features are attributed to a slight reduction of the surface. In Fig. 4(b), a slightly oxidized surface is imaged. Herein dark depressions correspond to missing V=O groups [8].

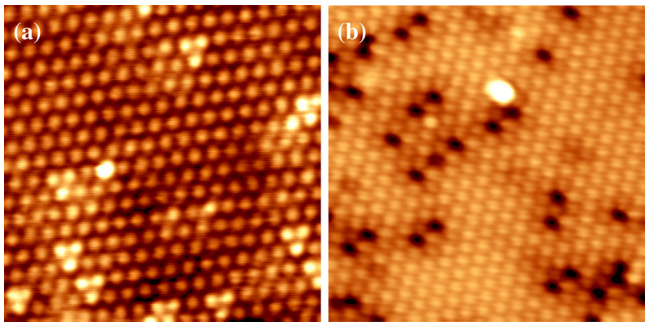


FIG. 4 (color online). Atomically resolved STM images of the $V_2O_3(0001)$ surface. (a) Slightly reduced layer; (b) slightly overoxidized layer. $10 \times 10$ nm$^2$, 2 V, and 0.1 nA.

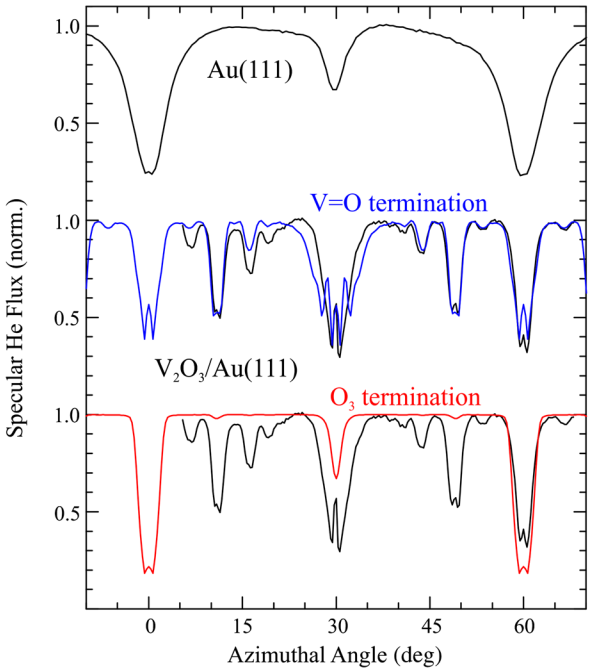


FIG. 5 (color online). Intensity of specularly reflected 2 keV He atoms (black curve) from Au(111) and a $V_2O_3(0001)$ thin film as a function of the azimuthal angle as well as simulations for the vanadyl (blue curve) and $O_3$ termination (red curve) of $V_2O_3(0001)$.

Further evidence is provided by grazing angle scattering of 2 keV He atoms. In this experiment the flux of specularly reflected He atoms was recorded as a function of the azimuthal rotation of the sample for a polar incidence angle of 1° with respect to the surface plane. Incidence along a principal axis, i.e., for scattering along a line of densely packed atoms, leads to a broadening of the angular distribution and thus to a reduction of the flux in the specular direction. In Fig. 5, this flux is plotted for Au(111) (upper panel) and a $V_2O_3(0001)$ film (lower panels). The data are compared with simulations based on classical trajectories using a superposition of atomic pair potentials as described elsewhere [24]. For the vanadyl termination (blue curve) good overall agreement is observed, whereas the close packing of surface oxygen atoms in the $O_3$ model (red curve) leads to narrow axial channels with little lateral deflection of scattered projectiles for most directions. The simulated curve deviates significantly from the experimental one.

This finding seems to be in conflict with a recent ion beam triangulation study [10] which favored the $O_3$ termination. In this study, electron emission following the grazing scattering from the surface of 25 keV H atoms was recorded as a function of the azimuthal surface orientation. For close-packed crystal surfaces, thin films, and adsorbate systems, a high surface sensitivity of ion beam triangulation has been demonstrated [25,26]. However, for one monolayer of the amino acid alanine on Cu(110) [24], a curve similar to that for the clean substrate was obtained, whereas from triangulation, based on the specular flux of 2 keV He atoms, information on the position of the topmost methyl groups is obtained. A similar issue may also be in effect for the $V_2O_3(0001)$ surface, where the relatively sparsely distributed vanadyl groups may affect the emission of electrons to a lesser extent than previously assumed.

Since DFT has been invoked to support the $O_3$ surface termination [9], we examine the sensitivity of DFT results with respect to the choice of the exchange-correlation functional, specifically with respect to Fock exchange. The screened hybrid functional after Heyd, Scuseria, and Ernzerhof (HSE) [27] with a range-separation parameter of 0.207 $Å^{-1}$ was used. Spin polarization was not included, because at ambient temperature $V_2O_3$ is a nonmagnetic metal crystallizing in the rhombohedral corundum structure. Our spin-unpolarized DFT calculations use the VASP code and employ projector-augmented plane waves (PAWs) up to a kinetic energy of 600 eV [28–30]. The electron-ion interaction was described by using PAW pseudopotentials with $3p^6 3d^3 4s^2$ and $2s^2 2p^4$ as valence electrons for V and O, respectively. Symmetric slab models of the primitive surface unit cell with a lattice constant of 4.933 Å (HSE equilibrium lattice constant) and 30 atomic layers were used, and a vacuum layer of approximately 10 Å was employed to separate periodic images of the slabs. To model the bulk, two innermost V atoms and one neighboring O trilayer per V were kept frozen at bulk positions. Forces acting on the atoms in the remaining 26 layers were relaxed to better than 0.05 eV/Å. To sample the surface Brillouin zone, Γ-centered Monkhorst-Pack meshes using $(2 \times 2)k$ points were used. Energies obtained by using a $(4 \times 4)k$ mesh (single points) consistently shifted the intercepts of the linear equations for surface energies by less than 6 meV/$Å^2$; thus, the results did not change qualitatively.

Schwingenschlögl and co-workers found that lowering the amount of Fock exchange (FX) from 25% to 10% in the HSE hybrid functional results in a more balanced description of the $VO_2$ bulk phases [31]. However, we found that HSE using the "as defined" amount of FX of 25% outperforms the Perdew-Burke-Ernzerhof (PBE) [32] functional, which is based on the generalized-gradient approximation (GGA) and does not include Fock exchange. HSE heats of formation for $V_2O_3$, $V_2O_4$, and $V_2O_5$ agree better with observed values than PBE results. Also, the oxidation of $V_2O_3$ to $V_2O_4$ is better described by using the HSE functional [33]. We do not claim that a simple hybrid functional like HSE consistently captures the complex physics of $V_2O_3$ mostly driven by Coulomb correlation effects, but based on the aforementioned thermochemical results we believe that HSE surface stabilities are more reliable than results obtained by using the PBE or the closely related Perdew-Wang 1991 GGA-type functionals used in earlier work [12]. Recent HSE results by Rubio

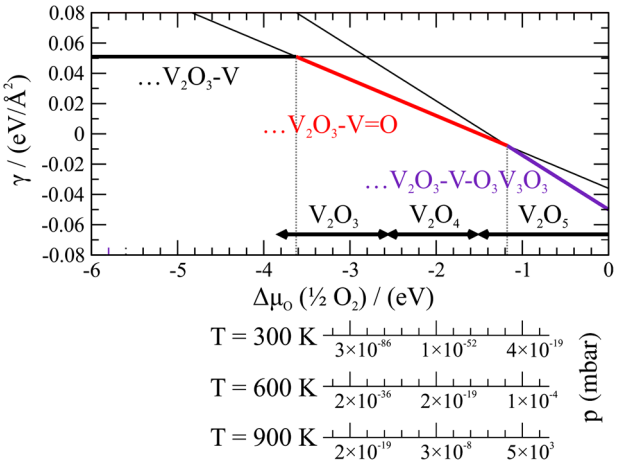


FIG. 6 (color online). Surface energy $\gamma$ as a function of the chemical potential $\Delta\mu_O$ for different terminations of the $V_2O_3(0001)$ surface. At the bottom, the chemical potential scale is transformed into $O_2$ pressure scales (mbar) for different temperatures. The stability ranges of the bulk phases are indicated by the horizontal black arrows.

and co-workers [34], which describe the metal-insulator transition in paramagnetic $V_2O_3$ correctly, provide further support for our findings.

When adding some FX to the GGA-based functional, the highest oxygen chemical potential, for which V=O termination is calculated to be thermodynamically favorable, increases from −2.3 (which is exactly the same as the PBE functional, i.e., no FX) through −1.9 (HSE with 10% FX) to −1.2 eV (HSE with 25% FX).

The phase diagram calculated with HSE is shown in Fig. 6. Phase diagrams for pure GGA as well as for 10% FX are provided in Supplemental Material [35]. The oxygen chemical potential $\Delta\mu_O(\frac{1}{2}O_2)$ uses half of the total energy of the $O_2$ molecule as a reference. Tabulated values for the enthalpy $H$ and entropy $S$ at the temperature $T$ were used [36]. Further details on the pressure and temperature dependence of $\Delta\mu_O$ can be found in Refs. [37,38]. Black arrows at the bottom refer to the stable bulk phases at the respective chemical potentials, while the bold lines above indicate the expected surface terminations. Figure 6 shows that the V=O termination is predicted to be thermodynamically stable over a wide range of oxygen chemical potentials. As also shown previously [12], the V=O termination cannot be reduced by heating in UHV, since the required potential is too negative to be realized experimentally. While conditions that would favor the $O_3$ termination are experimentally accessible, the stable bulk phase expected under these conditions is already $V_2O_5$, in agreement with the findings summarized in Fig. 2, which indicate that the oxide layer sublimates. We note that, according to the DFT calculations, $V_2O_3$ is not the equilibrium bulk phase for all preparation conditions employed in this study. This is a hint that the formation of higher oxides is just prevented by kinetic limitations.

In conclusion, we have shown that the $V_2O_3(0001)$ surface, prepared under standard UHV conditions, is terminated by vanadyl groups. *I-V* LEED measurements and fast atom scattering are clearly in favor of this termination, like the STM results. Recent ion beam triangulation results are also reconcilable with a vanadyl-terminated surface.

In a recent study, Window *et al.* [9] proposed that the surface might be terminated by an equilibrium mixture of $O_3$ and V=O areas with a small V=O contribution in order to explain the presence of the V=O stretching vibration in vibrational spectra. Neither our STM studies, which always show the presence of a single phase for well-prepared layers, nor our DFT calculations, which predict the vanadyl termination to be stable under the relevant conditions, support this conclusion. DFT shows that the $O_3$ termination is drastically destabilized. Even if one assumes an error of several hundred meV in the chemical potential of oxygen, which corresponds to several orders of magnitude of an error in the pressure, a phase equilibrium between V=O and $O_3$ with a noticeable contribution of the $O_3$ phase cannot be reached. This is in marked contrast to previous DFT studies [12,13] and can be attributed to the higher accuracy of the HSE hybrid functional as shown by, compared with experiment, improved formation enthalpies of bulk $V_xO_y$ phases [33].

This work was supported by the Deutsche Forschungsgemeinschaft (DFG) through their collaborative research center 546, "Transition Metal Oxide Aggregates." We also acknowledge support from the Fonds der Chemischen Industrie, the North-German Supercomputing Alliance in Berlin and Hannover (HLRN; grants for computing time), and thank Horst Niehus for helpful discussions.

*Corresponding author.
kuhlenbeck@fhi-berlin.mpg.de
†To whom all correspondence regarding the density functional computations should be addressed.
joachim.paier@chemie.hu-berlin.de

[1] K. Held, G. Keller, V. Eyert, D. Vollhardt, and V. I. Anisimov, Phys. Rev. Lett. **86**, 5345 (2001).
[2] S. Surnev, M. Ramsey, and F. Netzer, Prog. Surf. Sci. **73**, 117 (2003).
[3] G. Deo and I. E. Wachs, J. Catal. **146**, 323 (1994).
[4] G. C. Bond and S. F. Tahir, Appl. Catal. **71**, 1 (1991).
[5] D. Göbke, Y. Romanyshyn, S. Guimond, J. M. Sturm, H. Kuhlenbeck, J. Döbler, U. Reinhardt, M. V. Ganduglia-Pirovano, J. Sauer, and H.-J. Freund, Angew. Chem., Int. Ed. Engl. **48**, 3695 (2009).
[6] F. Pfuner, J. Schoiswohl, M. Sock, S. Surnev, M. G. Ramsey, and F. P. Netzer, J. Phys. Condens. Matter **17**, 4035 (2005).
[7] A.-C. Dupuis, M. Abu-Haija, B. Richter, H. Kuhlenbeck, and H.-J. Freund, Surf. Sci. **539**, 99 (2003).

[8] J. Schoiswohl, M. Sock, S. Surnev, M. Ramsey, F. Netzer, G. Kresse, and J. Andersen, Surf. Sci. **555**, 101 (2004).
[9] A. J. Window, A. Hentz, D. C. Sheppard, G. S. Parkinson, H. Niehus, D. Ahlbehrendt, T. C. Q. Noakes, P. Bailey, and D. P. Woodruff, Phys. Rev. Lett. **107**, 016105 (2011).
[10] J. Seifert, E. Meyer, H. Winter, and H. Kuhlenbeck, Surf. Sci. **606**, L41 (2012).
[11] A. J. Window, A. Hentz, D. C. Sheppard, G. S. Parkinson, D. P. Woodruff, W. Unterberger, T. C. Q. Noakes, P. Bailey, M. Ganduglia-Pirovano, and J. Sauer, Surf. Sci. **606**, 1716 (2012).
[12] G. Kresse, S. Surnev, J. Schoiswohl, and F. P. Netzer, Surf. Sci. **555**, 118 (2004).
[13] T. K. Todorova, M. V. Ganduglia-Pirovano, and J. Sauer, J. Phys. Chem. B **109**, 23523 (2005).
[14] I. Czekaj, K. Hermann, and M. Witko, Surf. Sci. **545**, 85 (2003).
[15] C. Kolczewski, K. Hermann, S. Guimond, H. Kuhlenbeck, and H.-J. Freund, Surf. Sci. **601**, 5394 (2007).
[16] S. Guimond, J. M. Sturm, D. Göbke, Y. Romanyshyn, M. Naschitzki, H. Kuhlenbeck, and H.-J. Freund, J. Phys. Chem. C **112**, 11835 (2008).
[17] A. Barbieri and M. van Hove, private communication, http://www.icts.hkbu.edu.hk/vanhove/.
[18] J. B. Pendry, J. Phys. C Solid State Phys. **13**, 937 (1980).
[19] C. Igel, V. Heidrich-Meisner, and T. Glasmachers, J. Mach. Learn. Res. **9**, 993 (2008).
[20] I. Czekaj, K. Hermann, and M. Witko, Surf. Sci. **525**, 33 (2003).
[21] E. A. Kröger, D. I. Sayago, F. Allegretti, M. J. Knight, M. Polcik, W. Unterberger, T. J. Lerotholi, K. A. Hogan, C. L. A. Lamont, and D. P. Woodruff, Surf. Sci. **601**, 3350 (2007).
[22] See Fig. S1 in Supplemental Material at http://link.aps.org/supplemental/10.1103/PhysRevLett.114.216101 for structural data of the best-fit models.
[23] S. Surnev, G. Kresse, M. Sock, M. G. Ramsey, and F. P. Netzer, Surf. Sci. **495**, 91 (2001).
[24] J. Seifert, M. Busch, E. Meyer, and H. Winter, Phys. Rev. B **89**, 075404 (2014).
[25] T. Bernhard, J. Seifert, and H. Winter, J. Phys. Condens. Matter **21**, 134001 (2009).
[26] J. Seifert and H. Winter, Nucl. Instrum. Methods Phys. Res., Sect. B **315**, 9 (2013).
[27] J. Heyd, G. E. Scuseria, and M. Ernzerhof, J. Chem. Phys. **118**, 8207 (2003); **124**, 219906 (2006).
[28] G. Kresse and J. Furthmüller, Phys. Rev. B **54**, 11169 (1996).
[29] G. Kresse and D. Joubert, Phys. Rev. B **59**, 1758 (1999).
[30] P. E. Blöchl, Phys. Rev. B **50**, 17953 (1994).
[31] H. Wang, T. A. Mellan, R. Grau-Crespo, and U. Schwingenschlögl, Chem. Phys. Lett. **608**, 126 (2014).
[32] J. P. Perdew, K. Burke, and M. Ernzerhof, Phys. Rev. Lett. **77**, 3865 (1996).
[33] See Tables S3 and S4 in Supplemental Material at http://link.aps.org/supplemental/10.1103/PhysRevLett.114.216101 for tables showing bulk heats of formation and heats of reactions.
[34] F. Iori, M. Gatti, and A. Rubio, Phys. Rev. B **85**, 115129 (2012).
[35] See Fig. S2 in Supplemental Material at http://link.aps.org/supplemental/10.1103/PhysRevLett.114.216101 for phase diagrams of pure GGA and 10% FX.
[36] *CRC Handbook of Chemistry and Physics*, edited by D. R. Lide and H. P. Frederiske, 76th ed. (CRC Press, Boca Raton, FL, 1995).
[37] K. Reuter and M. Scheffler, Phys. Rev. B **65**, 035406 (2001).
[38] M. V. Ganduglia-Pirovano and J. Sauer, Phys. Rev. B **70**, 045422 (2004).

# P2

https://link.springer.com/article/10.1007/s10562-016-1735-4

Catal Lett (2016) 146:861–885
DOI 10.1007/s10562-016-1735-4

P2

PERSPECTIVES

# Hybrid Density Functionals Applied to Complex Solid Catalysts: Successes, Limitations, and Prospects

**Joachim Paier**[1]

Received: 8 March 2016 / Accepted: 11 March 2016 / Published online: 26 March 2016


**Abstract** Density functional theory (DFT), employing semilocal approximations to describe electron exchange and correlation effects, tremendously advanced the research in the realm of computational catalysis. It allows to calculate atomic and electronic structure details of extended systems like bulk solids, surfaces or nanoparticles with reasonable accuracy at moderate computational cost. However, semilocal approximations suffer from shortcomings such as self-interaction errors (SIEs). This work discusses results obtained using two established and related approaches, namely DFT + U and orbital-dependent hybrid density functionals. Both methods partially alleviate some of the problems incurred by SIEs and are widely used in the computational community. We discuss four case studies involving reducible oxide materials: (i) the oxidative dehydrogenation of methanol at small vanadium oxide clusters supported on the $CeO_2(111)$ surface, (ii) the adsorption of Au atoms on the reduced $CeO_2(111)$ surface, (iii) stabilities of various terminations of the $V_2O_3(0001)$ surface, and (iv) the adsorption of water on the $Fe_3O_4(111)$ surface. Compared with semilocal functionals including DFT + U, we report substantial improvements in band gaps, defect formation energies, as well as activation barriers and emphasize the important role of state-of-the-art experiments for assessing DFT. Limitations of hybrid functionals due to the imposed computational workload and inherent functional approximations are discussed. To overcome these limitations, alternatives in terms of generalized RPA and embedded wavefunction-based methods are suggested.

**Graphical Abstract**

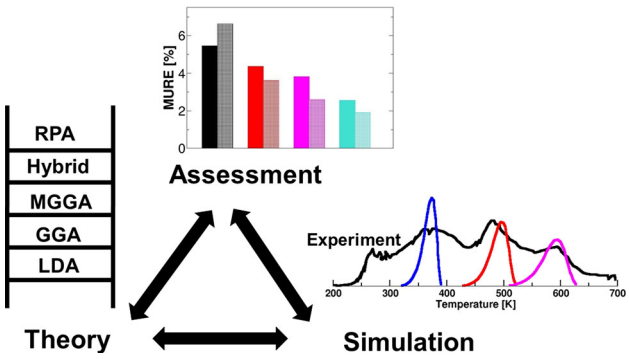


**Keywords** Density functional theory · Computational catalysis · Cerium oxide · Vanadium oxide · Methanol oxidation · Magnetite · Support effect · Gold adatoms · Electron transfer

## 1 Introduction

Density functional theory (DFT) after Kohn and Sham (KS) [1–3] based on the local density (LDA) or generalized-gradient approximation (GGA) to electron exchange and correlation (xc) is important in materials science and catalysis, because it provides atomic as well as electronic structure information of extended systems at a low computational cost. LDA was and very often is the favorite choice in the condensed matter community (e.g., [4]). The advent of GGA functionals and—few years later—the

✉ Joachim Paier
joachim.paier@chemie.hu-berlin.de

[1] Institut für Chemie, Humboldt-Universität zu Berlin, Unter den Linden 6, 10099 Berlin, Germany

introduction of orbital-dependent hybrid functionals convinced also the chemistry community to value DFT, as recently discussed by Walter Thiel [5]. With regard to molecular chemistry, LDA cannot be used, because of unacceptably large errors in binding or atomization energies [6, 7]. Conversely, errors in a number of solid-state properties obtained using LDA and GGA are comparable in magnitude. The sign of these errors may be opposite though [8].

GGA functionals provide fairly accurate molecular structures and structures of metal clusters [9, 10]. They offer sensible insights into basic material properties such as band structures and lattice parameters of simple metals, semiconductors, and insulators [11–13]. Total energy calculations employing GGA functionals are fast, and atomic forces can be evaluated at little extra computational cost. The numerical workload using GGA scales moderately with system size [14, 15], and convergence of the total energy with respect to the size of the employed basis set is easier to achieve compared to wavefunction-based methods (see, e.g., [16, 17]).

Supposed that all technical parameters employed in calculations have been converged, remaining errors are exclusively due to the approximate description of xc effects. In addition to the errors incurred by DFT (vide infra), the technical quality of selected structural models for extended systems may also affect the accuracy of results. For instance, single crystal surfaces or thin crystalline films may be modelled using clusters or slabs [18–20]. Cluster models offer the possibility to employ more accurate wavefunction-based approaches [21–23]. This allows to calculate local properties like adsorption energies with high accuracy. Slab models exploiting periodic boundary conditions may be more efficient in computing other properties like surface energies or band-structures. Finite size effects in both cluster and slab models prevent the system under study to relax or reconstruct appropriately, significantly affecting stability and reactivity.

LDA and GGA functionals suffer from so-called self-interaction errors (SIEs) [24, 25], which manifest themselves in overly delocalized orbitals and notoriously underestimated band gaps (see [26] and references therein). SIEs may drastically affect the accuracy of computational results, as discussed in many recent review articles focusing on reducible or semiconducting metal oxides [27–30]. GGAs underestimate activation barriers [31]. This is related to the fact, that a GGA functional does not correctly describe the "stretched bond" situation encountered in a transition state [32]. Related to a different type of error, GGAs fall short of correct dispersion-type van der Waals interactions [33]. The latter may substantially affect calculated adsorption energies, i.e. the stability of the adsorption complex [34]. Extensive methodologically motivated discussions on these shortcomings can be found in [35, 36] and [37].

Surfaces of reducible metal oxides are interesting model systems for oxidation reactions in catalysis [38, 39]. However, the accurate description of their physical and chemical properties by DFT represents a formidable task. The various 3d transition metal oxide phases of, e.g., vanadium, chromium, and iron as well as oxides of rare-earth metals like cerium featuring 4f orbitals represent particularly challenging systems from a computational point of view. As mentioned in [27, 29], cerium oxides (ceria) require methods that are capable to describe 4f orbitals involved in bonding as well as in the spatially localized (reduced) $Ce^{III}$. Oxides like $Fe_2O_3$, also known as Mott–Hubbard systems, have partially occupied d orbitals being subject to strong intra-atomic Coulomb correlation effects. A correct description of the latter is largely elusive to the GGA approximation [37, 40].

In catalysis, surface oxygen defects play a central role in the Mars-van Krevelen oxidation mechanism [41]. Oxygen defect formation energies are important descriptors to assess the activity of an oxide catalyst [42]. Formation of O defects in insulating reducible oxides incurs occupation of energetically low lying empty d or f orbitals, which implies formation of defect-induced electronic states below the conduction band minimum. Since GGA functionals substantially underestimate band gaps, electron occupation of the conduction band is energetically too facile. Instead of the formation of a defect state within the gap, the reduced system may spuriously metallize. The spatially localized nature of the defect state is lost, as shown for an O defect in the $CeO_2(111)$ surface (cf. Fig. 1a). Similar problems occur, if positively charged holes in the O 2p valence band are formed upon introduction of undervalent substitutional or interstitial cationic point defects (*p*-type doping) [43–45]. This shortcoming affects defect formation energies.

Hence, alleviating the band gap problem as well as overdelocalization may improve the accuracy in thermodynamic properties. However, we underline that a correct gap alone is not a sufficient condition for accurate thermodynamic predictions based on DFT [29].

Examining several case studies, this work provides evidence that hybrid functionals offer an improved description of reducible oxides for a number of properties including activation barriers as well as localization of charges and spins of electrons. With regard to defect formation energies, hybrid functionals outperform the commonly applied and less compute intensive DFT + U approach. We discuss (i) activation barriers in the oxidative dehydrogenation of methanol at small vanadium oxide clusters supported on the $CeO_2(111)$ surface, (ii) the adsorption of Au atoms on the reduced $CeO_2(111)$ surface, (iii) stabilities of various terminations of the $V_2O_3(0001)$ surface, and (iv) the adsorption

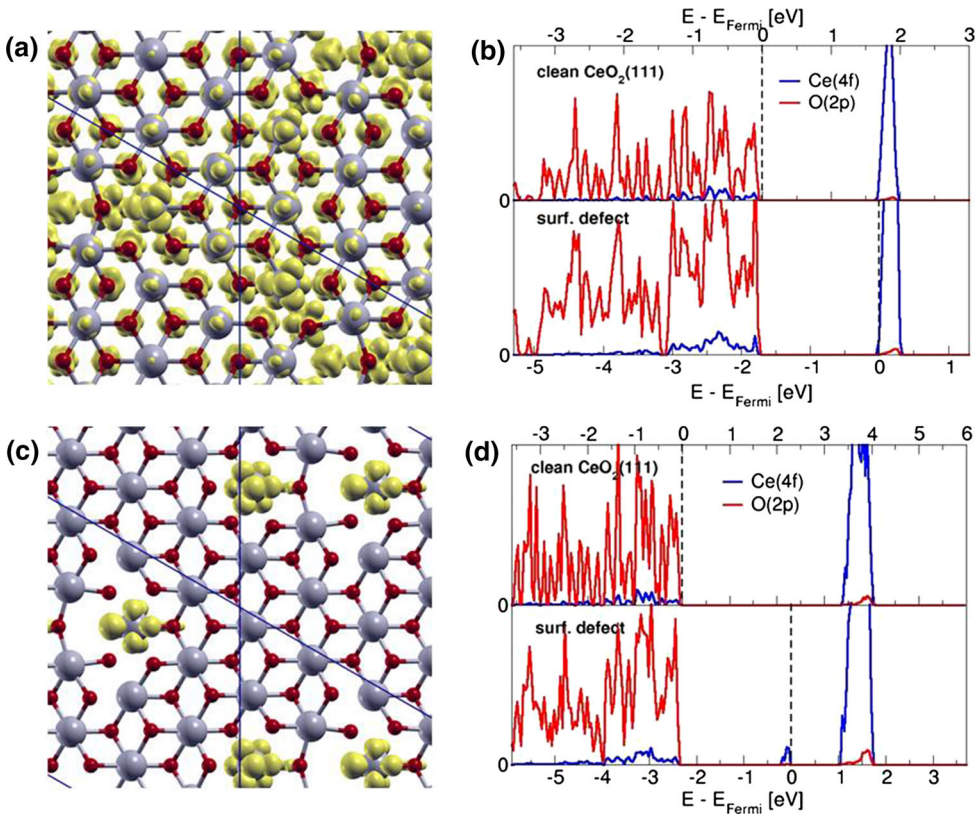


**Fig. 1** **a** Spin-densities (*yellow*) for a surface O defect in $CeO_2(111)$ obtained using PBE. **b** Corresponding PDOS for the clean surface (*top panel*) and O defect (*bottom panel*). *Blue lines* indicate the Ce 4f states, and *red lines* indicate O 2p states. **c** and **d** Analogous graphs showing spin-densities as well as PDOS obtained using the hybrid functional HSE (see below). For results on the (110) and (100) surfaces, see [46] and [47]. Reprinted and adapted with permission from [29]. Copyright (2013) American Chemical Society

of water on the $Fe_3O_4(111)$ surface. We survey limitations of hybrid functionals and conclude with final remarks on potential future developments.

### 1.1 Jacob's Ladder of Density Functional Approximations

It is frequently stated that DFT does not offer possibilities to systematically improve the accuracy of results in the way, e.g., wavefunction-based techniques do [48–57]. "Jacob's ladder of density functional approximations" [58, 59] is an attempt to introduce, at least to a certain extent, the aforementioned systematics. Currently the ladder comprises five rungs or classes of approximations. The underlying idea is that functionals accommodating a number of physical or exact constraints, e.g., meeting the uniform electron gas (UEG) limit for vanishing density gradients, are expected to be rather universally applicable and transferable. This means that the accuracy of results does neither critically depend on the material nor on the calculated property. The number of satisfied constraints or degree of complexity increases for higher rungs, but the amount of empiricism used for their construction should be minimal to avoid "overfitting" [60]. This way, the functionals' accuracies are expected to improve using higher rungs on the ladder.

LDA and GGA are known as the first and second rung on the ladder. The third rung refers to the meta-GGA approximation [61], which is on the point of becoming widely recognized in the catalysis community [62–66]. LDA, GGA, and meta-GGA are pooled by the term *semilocal* functionals, because of their dependence on the local electron density $\rho(\mathbf{r})$ as well as on derivatives of $\rho(\mathbf{r})$. While LDA only depends on $\rho$ (including spin-polarisation [67]), GGA also incorporates information on the reduced density gradient, which is proportional to $\frac{|\nabla\rho|}{\rho^{4/3}}$ [68–72]. A meta-GGA, in addition to its dependence on density and density gradient, includes information that originate from the kinetic energy density [73]. The information contained in the latter was shown to be almost equivalent to the one carried by the second derivative or the Laplacian of the density [74].

The fourth rung functionals contain also non-local information due to the explicit dependence on the occupied orbitals. In theory, this requires developing a generalization of KS-DFT [75]. In practice, this means that a fraction of non-local Fock exchange (FX) replaces the corresponding amount of semilocal exchange. The 'mixing ratio' is material-specific and hence a semi-empirical parameter [76–78]. Several hybrid functionals use 20–25 % of FX, which is a useful choice for many materials or systems of

interest. This choice was supported by non-empirical arguments [79], but they turned out to be imprecise [59].

The present work does not discuss hybrid functionals relying on many parameters [80, 81]. With regard to local hybrid functionals employing position dependent admixture of FX, we refer the interested reader to the literature (cf., e.g., [82–84]).

The generalized random-phase approximation (RPA) is the fifth rung on Jacob's ladder (cf., e.g., [17, 85–87]). This rung adds non-locality also in the correlation energy via dependence on occupied as well as virtual orbitals (and orbital energies). Thus, RPA is a fully non-local functional. RPA can be applied to small-gap and metallic systems, in contrast to double-hybrid functionals, which add a fraction of correlation energy based on second order Møller-Plesset perturbation theory (cf. [88–90]). Any 'order-by-order' perturbation theory breaks down when applied to systems with zero gap [91]. RPA describes dispersion-type van der Waals interactions correctly (e.g., [92, 93]). Up-to-date applications of RPA mostly use semilocal orbitals and orbital energies as input (e.g., [17, 94–99]. This also applies to the FX energy expression, which is then called exact exchange (EXX) energy. However, advantages by using the FX energy (i.e. using HF orbitals in the EXX energy expression) were reported by Xinguo Ren and coworkers [100, 101]. Throughout this work, we will not discriminate between EXX and FX. Self-consistent RPA calculations have not yet been applied to extended systems, although the number of recent publications indicate intense research activities [102–108].

## 2 Historic and Technical Remarks on Hybrid Functionals

Axel Becke introduced hybrid functionals in 1993 [109]. He used arguments based on the so-called adiabatic connection formula [110, 111] to theoretically motivate the employed mixing-ratio, i.e. 50 % of FX and 50 % of Slater-Dirac (LDA) exchange [112, 113]. This hybrid, known as the "Becke-Half-and-Half" (HH) functional, substantially outperformed both HF and LDA with respect to errors in molecular atomization energies. Moreover, the work reports improvements by employing two independent mixing parameters obtained from fitting against experimental data. The modified functional uses a smaller amount of FX (33 %) and sacrifices a constraint, namely the uniform electron gas (UEG) limit [109]. Despite its excellent performance in molecular atomization energies, this parametrization spoiled the accuracy in other properties such as proton affinities.

The three-parameter functional B3PW91 [114] was also introduced by Becke (Eq. 1).

$$E_{xc}^{B3PW91} = E_{xc}^{LDA} + a_0 \cdot \left(E_x^{FX} - E_x^{LDA}\right) + a_x \cdot \Delta E_x^{B88} + a_c \cdot \Delta E_c^{PW91} \quad (1)$$

It outperformes HH in terms of molecular atomization energies and preserves the UEG limit. The three parameters in Eq. 1 refer to the admixing factors for FX ($a_0 = 0.2$), the Becke-88 (B88) [115] gradient-correction to the LDA exchange ($a_x = 0.72$), and the Perdew–Wang-91 (PW91) [69, 116] gradient-correction to the LDA correlation energy ($a_c = 0.81$), respectively.

These parameters were fitted to minimize errors in calculated molecular properties such as atomization energies, ionization potentials, etc. Note that the popular B3LYP hybrid functional finds its origin in B3PW91, replacing LDA correlation together with PW91 gradient corrections by the Lee–Yang–Parr (LYP) correlation functional [117]. LYP consists of density dependent (local) terms as well as gradient-dependent (semilocal) contributions [118]. B3LYP was employed and published by Mike Frisch und coworkers for the first time in 1994 [119].

LYP is based on the Colle-Salvetti (CS) functional and does not fulfill the UEG limit. For vanishing density gradients, it lacks some of the correlation energy compared to LDA [120, 121]. As discussed in [122], electron correlation at the short range, i.e. small inter-electron distance, is less affected. However, at the long range, the effect of the aforementioned failure becomes noticeable. It is less problematic for calculations on atoms and molecules, but for solids errors may be significant. This shortcoming of LYP is nicely depicted in Fig. 5 of Ref. [120].

Figure 2 shows atomization energies for several archetypal metals, semiconductors, and insulators obtained with the Perdew, Burke, Ernzerhof (PBE) GGA [70] and the Heyd, Scuseria, Ernzerhof (HSE, vide infra), B3PW91, as well as B3LYP hybrid functionals [123]. The large negative relative errors illustrate the failure in LYP when

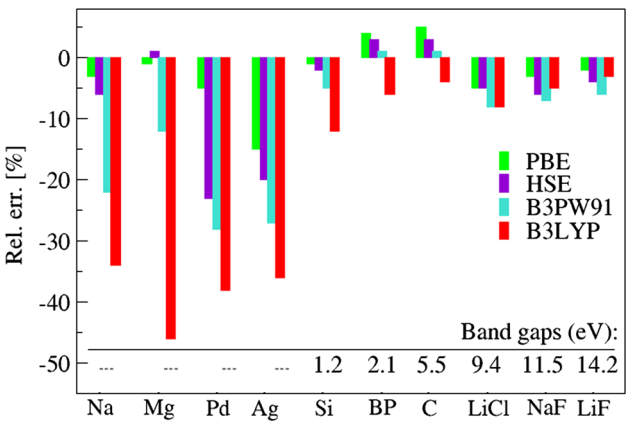


**Fig. 2** Relative errors in atomization energies (theory minus experiment) obtained using PBE (*green*), HSE (*violet*), B3PW91 (*light blue*), and B3LYP (*red*) [123]

applied to electron–gas-like systems, i.e. metals. The systematic underestimation of atomization energies can be readily understood. Supposed that the calculations for the atoms are reasonably accurate, the stability of the bulk material is underestimated by B3LYP, very likely due to the underestimation of correlation for the UEG described above. As indicated by the pronounced error bar for Si, problems also arise for small gap semiconductors, featuring delocalized orbitals or a slowly decaying density matrix [124]. For B3PW91, which fulfills the UEG limit, errors in metallic systems are substantially smaller compared to B3LYP [123]. Except for Na and Mg, B3PW91 and HSE perform similarly.

To avoid errors incurred by LYP and to single out the effect of admixed FX, it is advisable to compare the performance of PBE solely with B3PW91 and HSE. Both hybrids fulfill the UEG constraint. As shown in Fig. 2, admixture of FX yields suboptimal results for metallic systems. This finding is along the lines of, e.g., [65].

The UEG is the prototype model for metallic systems and applying HF to the UEG causes the electronic density of states to vanish logarithmically at the Fermi level [125, 126]. This artifact is a consequence of the long-range nature of the Coulomb $1/|\mathbf{r}_1 - \mathbf{r}_2| = 1/r_{12}$ interaction among electrons (cf. [124]). Two electrons at large distances do not feel the full $1/r_{12}$ potential, but a "screened" version due to the presence of, e.g., the other electrons as an intervening medium. So-called polarization or rearrangement effects of the electron gas cancel out the long-range part of the potential. Therefore, higher-order correlation effects, e.g., within the (non-local) RPA approximation, compensate this singular behavior of the potential [127]. Semilocal approximations to correlation employed in a hybrid functional insufficiently compensate the aforementioned singularity. A body of work in the literature points out the underperformance of hybrid functionals when applied to extended metallic systems [65, 77, 123, 128–130].

Summarizing the discussion on B3LYP, Fig. 2 shows a relation between B3LYP errors in atomization energies and the size of the band gap. Larger band gaps relate to smaller errors. Supposed that all of these functionals are comparably accurate for atoms, this finding is sensible, because the density matrix of wide-gap systems decays rapidly with the distance [15, 131]. It implies a high degree of localization in orbitals [132]. Apparently, the case involving a more localized scenario is unproblematic for the LYP functional. Recalling that B3LYP is plagued by two important shortcomings: (a) the long-range part of FX, which is problematic in metallic systems; (b) LYP does not describe long-range contributions of correlation effects in delocalized (metallic) states accurately. Using B3LYP, both shortcomings add up and lead to conspicuously large error bars for metallic systems as well as for small-gap semiconductors like Si.

In 1996, Becke introduced a simplified one-parameter hybrid functional shown in Eq. 2.

$$E_{xc}^{hybrid} = E_{xc}^{DFT} + a_0 \cdot \left(E_x^{FX} - E_x^{DFT}\right). \quad (2)$$

The admixing factor for FX, $a_0$, is usually small and varies between 0.16 and 0.28 depending on the GGA exchange functional used (i.e. $E_x^{DFT}$ in Eq. 2) [133]. The popular PBE0 or PBEh hybrid functional is based on the PBE GGA functional and uses 25 % of the FX energy ($E_x^{FX}$). It was introduced into the literature and independently assessed by Carlo Adamo and Vincenzo Barone [134] as well as Matthias Ernzerhof and Gustavo Scuseria [135]. Both groups reported high accuracy for a broad variety of molecules and their properties.

As mentioned before, the long-range asymptote of the Coulomb interaction (cf. Fig. 3a, black line) renders the application of hybrid functionals to metallic and semiconducting solids with a small band gap numerically difficult. As demonstrated in [77], the slow decay of $1/r_{12}$ with

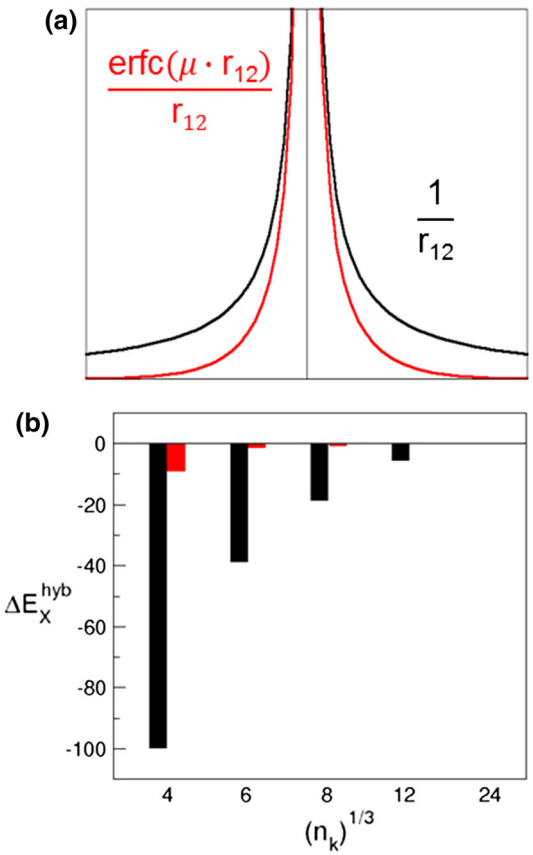


**Fig. 3** **a** Decay of a screened (*red*) and unscreened (*black*) Coulomb kernels. **b** Error in the exchange energy $\Delta E_X$ of fcc Al with (HSE, *red*) and without (PBE0, *black*) screening as a function of *k* points ($n_k \times n_k \times n_k$). See also [77]

distance requires dense *k*-point grids (or equivalently large supercells) to converge the FX energy.

To remedy this problem, one may resort to screening or range-separation of the Coulomb interaction. In molecular quantum chemistry, this technique was successfully applied to describe short-range correlation using DFT and long-range correlation effects using wavefunction-based methods [136]. In Fig. 3a the screened Coulomb interaction using the complementary error function is shown (Eq. 3).

$$\frac{1}{r_{12}} = \underbrace{\frac{\mathrm{erfc}(\mu \cdot r_{12})}{r_{12}}}_{\mathrm{SR}} + \underbrace{\frac{\mathrm{erf}(\mu \cdot r_{12})}{r_{12}}}_{\mathrm{LR}} \tag{3}$$

In principle, any functions summing up to 1/r are suitable for range separation. A screening based on the error function like in Eq. 3 is advantageous using GTOs or plane waves as a basis set [77, 137]. Historically, the first application of the error function dealt with efficient lattice summations of the long range electrostatic interactions in crystalline solids. It is commonly known as the Ewald technique [138]. The HSE or equivalently HSE06 hybrid functional, defined in Eq. 4, uses range separation in the exchange energy contribution according to Eq. 3 [137].

$$E_{HSE-X} = E_{PBE-X} + a_0\left(E_{FX}^{SR}(\mu) - E_{PBE-X}^{SR}(\mu)\right) \tag{4}$$

In Eq. 4, the superscript "SR" refers to "short-range" and $a_0$—similar to PBE0—amounts to 25 %. This means that the FX energy (or potential) is evaluated using the short-range kernel of the Coulomb interaction (cf. Fig. 3, red lines). The empirically set parameter μ amounts to 0.207 $\mathrm{Å}^{-1}$ and determines the length scale of the short-range and long-range interactions [139]. This offers substantial computational savings for metallic systems as shown in Fig. 3b [77]. The figure shows respective errors in the FX energy for the fcc bulk phase of Al with (red bars) and without (black bars) range separation as a function of the number *k* points. In other words, the figure compares the aforementioned convergence in the HSE and PBE0 exchange energies. Apparently, range-separation drastically enhances the technical convergence of the energy. HSE is very useful for treating metals and insulators on the same footing [26, 77, 140]. The high accuracy in band gaps obtained with HSE is amply discussed in recent review articles [26, 30, 141].

Hybrid functionals have been commonly used in the field of molecular quantum chemistry almost instantaneously after their introduction by Axel Becke. At the same time, they were offered to the computational solid state community by virtue of the CRYSTAL code [142] using Gaussian-type orbitals (GTOs) as a basis set to expand the crystal orbitals [143, 144]. GTOs are also used in the GAUSSIAN suite of programs [137, 145, 146]. Local (atom-centered) basis functions offer the possibility to treat all electrons, i.e. core as well as valence orbitals in the self-consistent field optimization. However, incompleteness or superposition errors [147, 148] have to be tackled by techniques like, e.g., the Boys-Bernardi counterpoise correction [149].

Hybrid functionals are implemented in many solid state electronic structure codes. The required FX energy can be computed employing various basis sets such as all-electron numeric (localized) orbitals as used in FHI-aims [150, 151] and full-potential linearized augmented plane waves as used in WIEN2K [152, 153] or Fleur [154, 155]). Moreover, projector-augmented pseudopotentials and plane waves are used in VASP [77, 156] or GPAW [157, 158], and mixed basis sets are employed in CP2K [159]. Pseudopotentials and plane waves are used in Quantum ESPRESSO [160, 161] or CASTEP [162–164]. Consequently, hybrid functionals are now accessible to a large manifold of computational communities.

## 3 Hybrid Functionals and the DFT + U Approach

Both, hybrid functionals as well as the DFT + U approach [165–168] assist in treating localized d or f electrons. The fraction of FX used in a hybrid functional partially alleviates one-electron SIEs in semilocal functionals, thus enhances localization.

Within DFT + U, the orbitals are subdivided into two groups, namely rather delocalized orbitals that form bands and spatially localized, atomic-like orbitals. These groups of orbitals are treated differently. This is justified by the assumption that semilocal functionals describe the band formation within s and p orbitals well, but corrections are required for the other case (d and f orbitals). The Mott–Hubbard theory [169–172] serves as the conceptual basis for DFT + U, relying on the idea of a hindered transfer of electrons among neighboring sites. The electron interaction is described by the Hubbard Hamiltonian involving effective Coulomb (U) and exchange (J) interactions. The meaning of U was extensively discussed by Herring [173]. For instance, in a 3d electron system with n electrons per atom, U is defined as the energy cost involving electron detachment at one site and attachment at a neighboring site, i.e. the 'redox' reaction energy.

Following [174], bypassing above mentioned deficiencies in LDA or GGA requires the introduction of a U-dependent correction to the total energy. The one-electron SIE-free HF theory is used as a reference. The correction to the DFT energy reads

$$\Delta E_{corr}[\{n_i\}] = E^{HF}[\{n_i\}] - E_{dd}^{DFT}[n_d], \tag{5}$$

with $E_{dd}^{DFT}[n_d]$ as the energy contribution stemming from the erroneous DFT description of interacting d electrons.

Equation 5 uses $n_i$ as the occupation number of orbital $i$ and $n_d$ refers to the total number of $d$ electrons, i.e. $n_d = \Sigma_i n_i$. The HF energy expression, with $E^{HF}[\{n_i\}]$ as a functional depending on the set of d orbitals, reads

$$E^{HF}[\{n_i\}] = \frac{e^2}{2}\sum_{i\neq j}(U_{ij} - J_{ij})n_i n_j, \tag{6}$$

with $U_{ij}$ and $J_{ij}$ as orbital-dependent Coulomb and exchange integrals. To illustrate the working principle, the electron exchange term J in Eq. 6 can be neglected [174], which leads to a simplified expression for the correction

$$\Delta E_{corr}[x] = -\frac{1}{2}Ux(x-1), \quad 0 \leq x \leq 1, \tag{7}$$

with $x$ as the variation of the total number of $d$ electrons [174]. This expression involves a $E_{dd}^{DFT}[n_d]$ of similar structure (see [174]). In consequence, the corresponding correction to the one-electron potential is equal to

$$\Delta V_{corr}[x] = \frac{d\Delta E_{corr}}{dx} = U\left(\frac{1}{2} - x\right). \tag{8}$$

Equations 7 and 8 convey the essential physics underlying the DFT + U approach. Supposing a half-filled d orbital, the correction to the total energy will result in a maximal increase in energy, whereas the correction to the Kohn–Sham eigenvalue vanishes. Conversely, integer occupation will be (variationally) preferred by the orbital-dependent DFT + U functional, which in turn leads to the opening of the band gap (Eq. 8). Unoccupied orbitals (x = 0) will be shifted by $+^1/_2$ U and occupied orbitals (x = 1) will be lowered by $-^1/_2$ U (cf. Fig. 4). Localization of d or f electrons is therefore inherent to DFT + U,

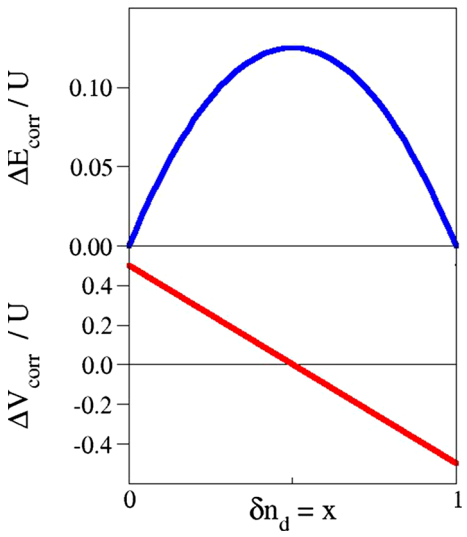


**Fig. 4** Correction to the total energy ($\Delta E_{corr}$, *blue line*) and the potential ($\Delta V_{corr}$, *red line*) within DFT + U as a function of the variation of *d* orbital occupation x. See also [174]

which incorporates orbital-dependence in a somewhat less rigorous manner compared to HF theory. Using a hybrid functional, all occupied orbitals are subject to the same generalized Kohn–Sham Hamiltonian [75], whereas in DFT + U only a subspace of orbitals is corrected in the aforementioned *ad hoc* manner. In practical applications, the size of U matters. It is usually chosen in a way to trade off the accuracy in the band gap against the accuracy reached for other system properties such as lattice parameters or reaction energies (e.g., [175–177]). Applying U together with semilocal functionals leads to increased lattice parameters. This is beneficial for LDA, because it underestimates lattice constants, but unfavorable for GGA functionals like PBE, which overestimate them [8]. For further discussions on DFT + U, we refer the interested reader to the literature [29, 178, 179].

## 4 Case Studies

### 4.1 Methanol Oxidation at Vanadia Supported on Ceria

Ceria as a support material for transition metal oxides like, e.g., vanadia has attracted much interest in the field of heterogeneous catalysis. Depositing vanadia on a ceria surface drastically increases turnover frequencies for the methanol oxidation to formaldehyde [180, 181]. The turnover frequencies for supported vanadia may vary within a range of three to four orders of magnitude depending on the nature of the support, i.e. its reducibility [29]. Importantly, it may also depend on the preparation of the catalyst (see, e.g., [182]). The vanadia coverage or loading also affects reactivity [183, 184]. Catalysts prepared by choosing amounts of vanadia lower than or equivalent to the so-called monolayer coverage are significantly more active than those with loadings large enough to form $V_2O_5$ nanoparticles [185, 186]. Precise atomic level details underlying the observed reactivity are generally missing, which induced a drive to generate these details by virtue of first-principles DFT studies.

In this section, we report the results of an extensive study on a $VO_x/CeO_2(111)$ catalytic model system [184, 187–190] examining the selective oxidation of methanol for low vanadia coverage on a ceria surface under dehydrated conditions. We compare kinetic results, i.e., intrinsic reaction barriers obtained using DFT + U and hybrid functionals with temperature-programmed spectroscopy (TPS) analyzed using Redhead's equation [191].

Previous collaborative efforts between the groups of Hajo Freund and Joachim Sauer in Berlin generated crucial insights into the atomic structure of the submonolayer vanadia catalyst deposited on a $CeO_2(111)$ surface [187]. These systems were investigated by applying surface

science techniques, such as atomically resolved scanning tunneling microscopy (STM), infrared absorption spectroscopy (IRAS), X-ray photoemission spectroscopy (XPS), TPS, as well as DFT. Vanadia was grown on a well characterized $CeO_2(111)$ film on a metal substrate by virtue of physical vapor deposition of metallic vanadium in an oxygen atmosphere. These studies give rise to the following main conclusions: (i) $VO_x$ wets the support in a two-dimensional manner (Fig. 5) according to the constant apparent height of the occupied state STM images as well as DFT calculations [188]. (ii) Each $VO_x$ cluster is terminated by V=O, i.e., vanadyl bonds as evidenced by IR and DFT. (iii) Larger $VO_x$ agglomerations such as trimers (Fig. 5b) are created upon sintering of larger amounts of vanadia at 700 K. (iv) V=O dipole moments couple within these clusters, leading to a blue shift of the IR-active resonance of the V=O stretching mode. This blue shift was reproduced by DFT calculations [187, 188]. A structure-IR relationship was corroborated by the computational results: the larger the $VO_x$ clusters, the larger the blue shift in IR wavenumbers. (v) XPS indicates occupied Ce 4f orbitals in agreement with DFT. Each $VO_x$ cluster at the $CeO_2(111)$ surface contains one tetrahedrally coordinated V atom in its highest oxidation state (+5). Ce atoms accommodate the 3d electrons of V in one of the 4f orbitals, i.e. upon V deposition and oxidation, some $Ce^{4+}$ ($4f^0$) ions are reduced, thereby creating $Ce^{3+}$ ($4f^1$) ions.

However, the composition of the $VO_x$ clusters at the $CeO_2(111)$ surface was unknown. This question could be successfully answered by DFT + U calculations combined with ab initio thermodynamics [192]. These calculations use the PBE GGA xc functional and a U parameter of 4.5 eV for the Ce 4f orbitals. This U value for Ce 4f was calculated self-consistently by Fabris et al. [193]. It was found that under the relevant, slightly reducing conditions, VO or $VO_2$ originating from the gas phase represent the prevalent surface species [189]. This finding was confirmed by Paier et al. [194] for low coverage using a larger surface unit cell than the one applied in [189].

Thermodynamic stabilities of various $VO_x$ oligomers and their respective reactivities were addressed by Penschke et al. using PBE + U [188]. The calculated structures of VO deposited at $CeO_2(111)$ as well as oligomers of $VO_2$ units on that surface are depicted in Fig. 6. This is the way how the $VO_x$ catalyst is modelled: uncharged VO with V featuring a $3d^3$ occupation, and $VO_2$ with V ($3d^1$) are put on the clean $CeO_2(111)$ surface. Figure 5 shows the optimized, minimum-energy structures, where the previous V 3d electrons are spontaneously transferred into Ce 4f orbitals. As a consequence, VO shows three $Ce^{3+}$ ions (dark blue), and $VO_2$ features one $Ce^{3+}$ in the surface. Note that the cutout in Fig. 6 does not show the $Ce^{3+}$, because it is located farther away from the $VO_2$ moiety [188].

Trimerization of VO monomers at the surface requires 333 kJ/mol (PBE + U). Thus, agglomeration of VO into $(VO)_3$ trimers is thermodynamically unfavorable. In contrast, deposited $VO_2$ monomers were found to trimerize pronouncedly exothermically releasing 162 kJ/mol. Experimentally, after slight sintering at higher loadings, trimers were found to be fairly abundant surface species [187]. This finding is consistent with the highly exothermic trimerization of $VO_2$. Calculated vibrational properties of $(VO_2)_3$ also agree with the observation. Particularly, the observed blue shift of of 27 $cm^{-1}$ for the V=O stretching mode agrees excellently with the calculated value (25 $cm^{-1}$). With regard to oxidation states, the remaining V ($3d^1$) electron of the $VO_2$ cluster is always transferred into a Ce 4f orbital upon adsorption on the surface. Therefore, a single $Ce^{3+}$ cation is created per $VO_2$ unit and V adopts its highest oxidation state +5. A minimum energy $VO_x/CeO_2(111)$ structure featuring (partially) reduced V could not be found [187–189, 194]. With respect to the oxidation state of vanadium, similar findings were obtained for mixed V/Ce-oxide clusters [195, 196]. Concerning surface structures, V is fourfold

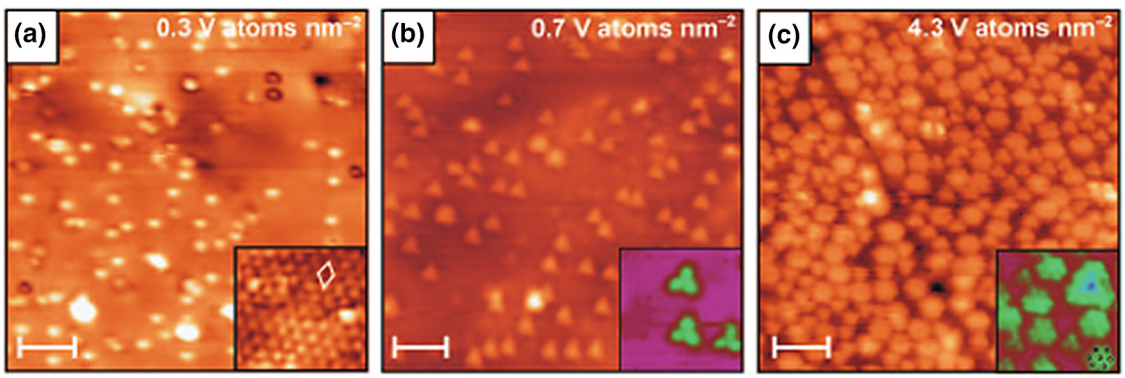


**Fig. 5** STM images of $VO_x$ species at the $CeO_2(111)$ surface showing **a** monomers, **b** trimers, and **c** larger oligomers for loadings corresponding to 0.3, 0.7, and 4.3 V atoms/$nm^2$, respectively. Adapted with permission from [187]. Copyright (2009) John Wiley and Sons

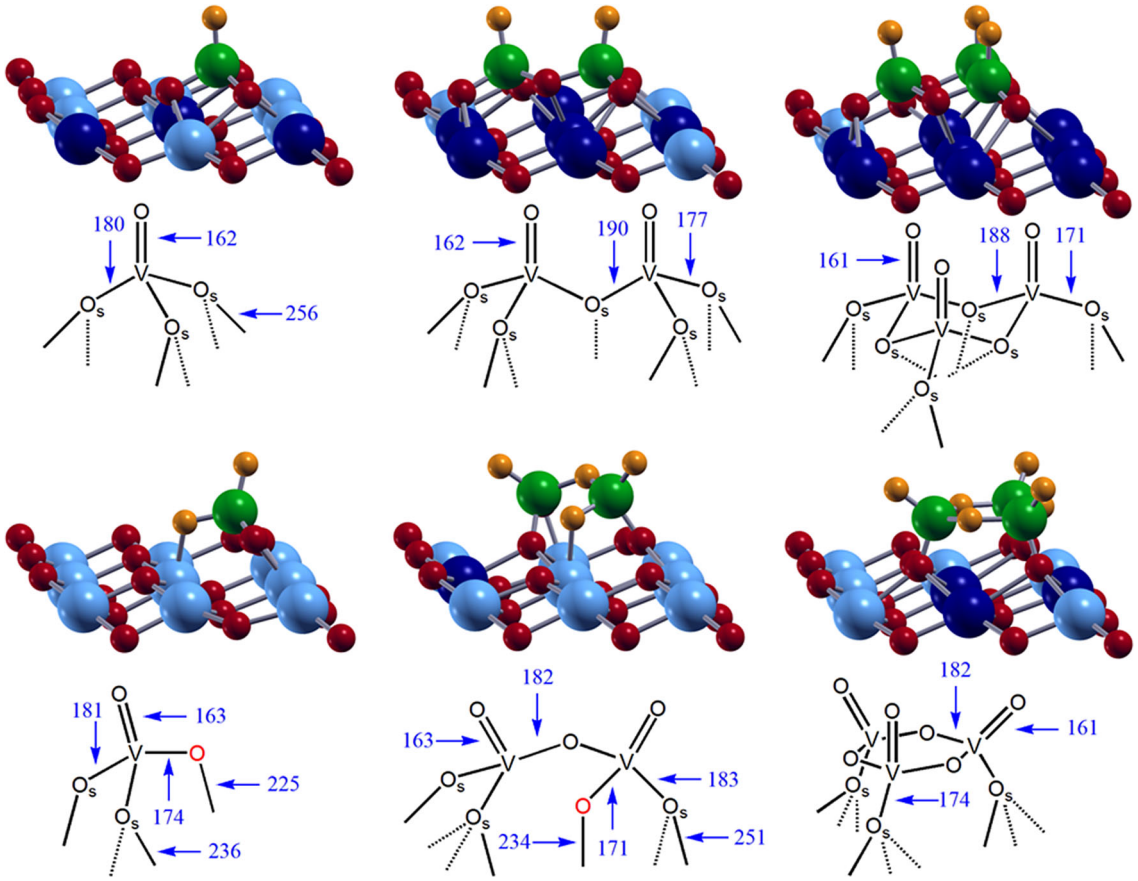


**Fig. 6** Minimum energy structures of VO (*top*) and $VO_2$ species (*bottom*) represented as ball and stick models. For clarity reasons only a (3 × 3) cutout of the first O–Ce–O trilayer is shown ($Ce^{4+}$ *light blue*, $Ce^{3+}$ *dark blue*, $V^{5+}$ *green*, $O^{2-}$ in the surface *red*, $O^{2-}$ from the *gas phase orange*). Corresponding schemes are given below with bond distances in pm. The "special" O atom in $VO_2$ and $V_2O_4$ is highlighted in *red* and "$O_s$" refers to a surface O. Adapted from [194]

coordinated by oxygen atoms resulting in a slightly distorted tetrahedron. To achieve this coordination for the $VO_2$ deposited on $CeO_2(111)$, two more oxygen ions from the terminating surface oxygen layer are needed.

But what about the reactivity of $VO_x/CeO_2(111)$? To answer this question, we focus on the TPS spectrum recorded for the oxidation of methanol to formaldehyde on mononuclear $VO_x$ species on ceria [184]. Formation of these surface species requires low V loadings (cf. STM shown in Fig. 7).

The TPS spectrum of $VO_x/CeO_2(111)$ is markedly different from the one of the clean surface. A so-called α peak of desorbing formaldehyde centers at about 370 K. This desorption temperature ($T_{des}$) is much lower than $T_{des}$ of the γ peak, which is characteristic for the clean $CeO_2(111)$ surface ($T_{des} \sim 570$ K). Employing the Redhead formula [191] based on a heating rate of 3 K $s^{-1}$ and a pre-exponential factor of $10^{13}$ $s^{-1}$, the corresponding desorption barriers for α and γ have been estimated and amount to 100 kJ/mol and 150–160 kJ/mol, respectively [184]. Thus, deposition of mononuclear vanadia clusters on $CeO_2(111)$ drastically enhances the dehydrogenation activity of the ceria support.

To understand this observation, individual mechanistic steps, i.e. possible minimum energy pathways for the dehydrogenation of methanol adsorbed on the clean $CeO_2(111)$ surface (fully oxidized and reduced) [197] and on the $VO_x/CeO_2(111)$ [190] system were studied with PBE + U and the HSE hybrid functional including the Grimme D2-type dispersion correction [198, 199]. For the $VO_x/CeO_2(111)$ surface additional calculations using the B3LYP hybrid functional were accomplished [190]. This was carried out having the well-defined surfaces under UHV conditions in mind. Prior to the TPS experiments, the surfaces were pre-saturated by dosing methanol. For low methanol coverage, dissociative adsorption occurs [197, 200]. Hence, observed desorption temperatures correspond to intrinsic barriers involved in the oxidation of the adsorbed methoxide. As a consequence, a comparison of theory with experimental results appears to be optimally suited to check whether observed and calculated activation barriers agree.

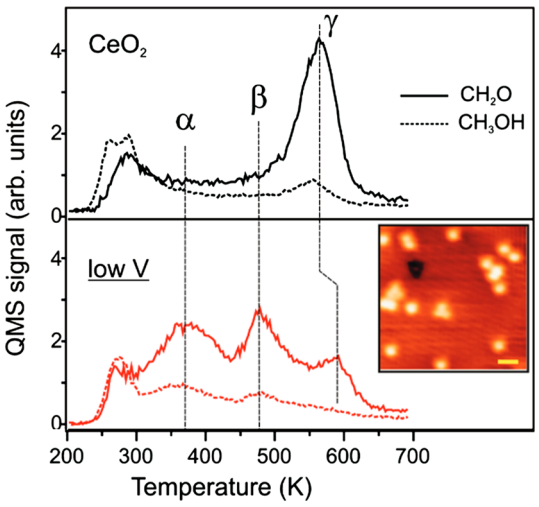


**Fig. 7** TPS for ~5 L of $CH_3OH$ adsorbed at 300 K on $CeO_2(111)$ (*upper panel*) and $VO_x/CeO_2(111)$ surfaces (*lower panel*) for a low loading of vanadia (<2 V/nm$^2$). The *inset* shows a typical STM image at the respective coverage. Reprinted and adapted with permission from [184]. Copyright (2010) American Chemical Society

Calculations for methanol adsorbed on the O-defect-free $CeO_2(111)$ surface suggest, that methanol prefers to desorb, instead of being oxidized to formaldehyde [197, 201, 202]. This is corroborated by the desorption energy of 88 kJ/mol compared with the substantially larger activation barrier for the oxidation step of 104 kJ/mol. In contrast, surface O-defects in $CeO_2(111)$ are reactive sites for the methanol oxidation. Here, the methoxy binds in the vacant site with 230 kJ/mol obtained using PBE + U + D. This value is slightly overestimated compared with the supposedly more accurate binding energy of 206 kJ/mol obtained using HSE + D. The PBE + U + D reaction barrier amounts to 129 kJ/mol, which is slightly higher than the barrier for the pristine surface. The HSE + D barrier at the defect is higher by only 10 kJ/mol. Given the strongly exothermic adsorption at the vacancy, this barrier can be easily overcome (cf. Fig. 5 in [197]).

Experimentally, it is known that the activity in TPS, i.e. peak intensity, increases with an increasing number of O defects in the surface [203, 204]. This is consistent with the findings given above: the more vacancies in the surface, the more methoxide will be converted to formaldehyde giving rise to higher intensities in TPS desorption peaks. The above mentioned HSE + D barrier of 139 kJ/mol agrees very well with the barrier suggested by TPS and Redhead analysis (~150 kJ/mol) [184].

To get fast insight into the reactivity of $VO_2$ on ceria, O-defect formation as well as hydrogenation energies were calculated [188]. As shown in [42] and [205], these are appropriate reactivity descriptors for reactions following a Mars-van Krevelen mechanism [41]. The O-defect formation energy, which corresponds to the overall reaction energy, and the hydrogenation energy, which relates to the barrier of the C–H bond breaking, are therefore valuable descriptors for the methanol oxidation on supported metal oxides. According to PBE + U results, a single $VO_2$ on the $CeO_2(111)$ surface is the most promising candidate for the active site.

It is interesting to compare results with vanadia deposited on a non-reducible silica support [206]. Previously, Joachim Sauer and coworkers studied the methanol oxidation step for vanadia supported on silica. In order to do that, silsesquioxane clusters were employed to model the silica surface. The transition state found involved the H-atom transfer from the methoxy towards the nearby V=O bond forming a five-membered ring, very similar to the analogue transition structure for vanadia on ceria (**TS1**, cf. Fig. 8). This work concludes that the reaction barrier obtained using B3LYP within the broken-symmetry approach [207], required for biradicaloid systems, is too high. This was shown by comparing results obtained with single-point energy calculations using CCSD(T) [208, 209] and B3LYP for the $O{=}V(OCH_3)_3$ molecule. The CCSD(T) correction to the B3LYP dehydrogenation barrier (191 kJ/mol, cf. Table 1) amounts to 16 kJ/mol. Hence, the B3LYP barrier corrected by the ΔCCSD(T) decrement is 175 kJ/mol. The above mentioned findings for the non-reducible silica support are instructive, because silica remains "electronically innocent" in the course of the reaction.

The same pathway (among others), i.e. H-atom transfer from the methyl group to the vanadyl O-atom, was studied for $VO_2/CeO_2(111)$ [190]. Similar to the transition state found for the silica support, no electrons were transferred to

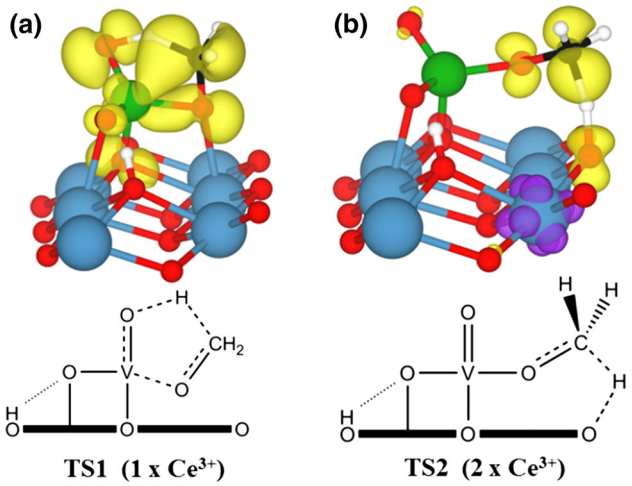


**Fig. 8** Electron and spin density (positive: *yellow*; negative: *purple*) contour plots at 0.01 Å$^{-3}$ showing the frontier orbitals involved in the formation of transition state **TS1 a** and **TS2 b**. Total number of $Ce^{3+}$ ions in the $CeO_2(111)$ surface is given in the schemes below. Reprinted and adapted with permission from [190]. Copyright (2014) American Chemical Society

**Table 1** Intrinsic barriers (kJ/mol) corresponding to transition states **TS1** and **TS2** (cf. Fig. 8) for the oxidation step of methoxide at vanadia/ceria and vanadia/silica, respectively

| | TS1 | | TS2 |
|---|---|---|---|
| | $VO_x/SiO_2$ | $VO_x/CeO_2$ | $VO_x/CeO_2$ |
| PBE + U | | 169[a] | 120[a] |
| HSE | | 177[a] | 150[a] |
| B3LYP | 191[b] | 198[a] | 149[a] |
| B3LYP + ΔCCSD(T) | 175[b] | 182[c] | |

[a] Ref. [190]

[b] Ref. [206]

[c] Obtained from the barrier in Ref. [190] subtracting ΔCCSD(T) = 16 kJ/mol as calculated in [206]

the surface, thus no additional $Ce^{3+}$ cations were formed upon H-abstraction. The electrons remained on the five-membered ring delocalized over its constituent atoms (**TS1**, Fig. 8) [190]. The barrier for the oxidation step found employing B3LYP subject to periodic-boundary conditions [123] amounts to 198 kJ/mol (cf. Table 1) and is very similar to the dehydrogenation barrier on a silica support. Subtracting the ΔCCSD(T) correction of 16 kJ/mol gives a barrier of 182 kJ/mol. This value agrees very well with the HSE barrier of 177 kJ/mol. Thus, we believe that the HSE barrier is accurate.

In contrast, the PBE + U barrier (169 kJ/mol) involving **TS1** having electrons delocalized over the five-membered ring, agrees fairly well with the HSE result. One may conclude that PBE + U performs well in case of rather nonpolar transition states involving a delocalized charge density.

For the $VO_x/CeO_2(111)$ system, a large number of distinct adsorption structures and pathways for the H-transfer in the oxidation step were studied [190]. One of them involves the methoxy bound to vanadium, i.e. the methoxide inserted into an "anchoring" V–O bond. This adsorption complex may be dehydrogenated passing through transition structures **TS1** or **TS2** (cf. Fig. 8). The H atom from the methyl group may be transferred to a surface oxygen, which leads to **TS2**. In this pathway, an electron localizes in Ce 4f orbitals close to the vanadia. In contrast to **TS1**, **TS2** shows a spin-density contour indicating a rather localized electronic structure. As outlined in Sect. 3, B3LYP is expected to perform well for situations involving localized charge densities. Indeed, B3LYP and HSE results are de facto identical for the **TS2** barrier. PBE + U is expected to suffer from SIEs in the "localized case". The conjecture is corroborated by the PBE + U barrier of 120 kJ/mol, which is too small compared with results obtained using HSE or B3LYP.

Eventually, the low temperature desorption (α) peak in the TPS shown in Fig. 7 remains to be understood. A pathway involving a low barrier of approximately 100 kJ/mol was reported in [190]. It requires adsorption of the methanol at the so-called pseudovacancy, i.e. a cavity opened in the $CeO_2(111)$ surface upon adsorption of $VO_2$ [188, 194]. In the oxidation step, the H atom from the methyl group is transferred to the V–O-Ce "interphase" oxygen atom connecting the $VO_2$ with the surface. The hybrid functional calculation on the corresponding transition structure was not done, but an error estimate from the difference in PBE + U and HSE barriers for **TS2** (i.e., "localized electrons") was computed. The correction amounts to 30 kJ/mol. Adding this correction to the PBE + U barrier of the aforementioned pathway yields a final barrier of 100 kJ/mol. This result agrees excellently with observation. We confirm what is known from molecular quantum chemistry but rarely achieved for reactions on crystalline surfaces due to the computational workload involved. Hybrid functionals clearly outperform DFT + U in terms of activation barriers.

### 4.2 Adsorption of Gold Atoms on Ceria Surfaces

Gold nanoparticles adsorbed on metal oxides have been intensely studied, since the days Haruta discovered their unexpectedly high activity in low-temperature CO oxidation [210, 211]. Generally, the atomic and electronic structure details of the interface between noble metals such as Au and Pt and the oxide support is crucial for understanding the activity of the catalyst [212–214]. One aspect of these details, so-called metal-support interactions, is of particular importance. These interactions may decisively determine reactivity, as reported in the literature [215–217].

Because of its high reducibility, ceria is a non-innocent support material for noble metals. Observed high catalytic activities were explained by two cooperative factors: (i) electron or charge transfer from the metal to the ceria support, and (ii) oxygen spillover from the support to the metal, i.e. oxidation of the metal [218]. Due to the propensity of ceria to form O defects [27, 29], these sites will play a role, particularly with respect to binding, e.g., single Au adatoms or Au atoms located on the rim of nanoparticles. Every (electroneutral) O defect in the surface is associated with two $Ce^{3+}$ ions. Thus, $Ce^{3+}$ is a mediator in electron transfer processes involved in metal-ceria support interactions. Consequently, polaron hopping can affect the electron-transfer mechanism (cf. [219] and references therein).

The interaction between Au atoms and the surface O vacancy in the $CeO_2(111)$ surface was profoundly studied by DFT + U [220–222] and amply reviewed by Zhang et al. [223]. It was found that the electron from neighboring $Ce^{3+}$ ions is spontaneously transferred into the Au 6s orbital, i.e. $Ce^{3+}$ is reoxidized and the $Au^0$ is reduced, thereby creating $Ce^{4+}$ and $Au^-$. The latter binds in the

vacancy with a large binding or adsorption energy of *ca.* 2.6 eV, because of attractive electrostatic interactions.

$Ce^{3+}$ ions were considered as potential adsorption sites for Au adatoms [224]. This was achieved by preparation of a reduced $CeO_2(111)$ surface containing O vacancies in subsurface position of the terminating O-Ce–O trilayer [224]. Annealing conditions, particularly the oxygen partial pressure, determine whether a surface or a subsurface O vacancy is created. After annealing to 1000 K, the density of subsurface defects was $\sim 5 \times 10^{12}$ $cm^{-2}$ [224]. Subsequent dosing of low amounts of Au by virtue of physical vapor deposition, induced the formation of pairs with Au–Au distances commensurate to the lattice of the $CeO_2(111)$ surface. 40 % of the pairs had a distance equal to twice the lattice parameter of the $CeO_2(111)$ surface unit cell ($\sim$7.6 Å, cf. Fig. 9a). The smallest Au–Au distance ($\sim$4.8 Å) was substantially larger than the distance typical of the $Au_2$ bond ($\sim$2.5 Å [225]). These Au pairs were metastable species, because a 3.0 V pulse via the STM tip rearranged them into upright standing $Au_2$ dimers. In some cases, the subsurface O vacancy in close proximity to Au was identified by its characteristic STM image (cf. Fig. 1 in [224]). Thus, it was conjectured that formation of the Au pairs is causally related to the $Ce^{3+}$ ions associated with subsurface O vacancies. Paired Au atoms as well as some of the isolated monomers, showed a halo-like contrast in STM images recorded at low bias. This contrast is typical of *charged* metal adatoms when adsorbed on metal oxides like, e.g., alumina [226] or magnesia [227].

Various adsorption configurations for an Au atom in the O-defective $p(2 \times 2)$ surface unit cell were studied using the HSE and B3LYP hybrid functionals (cf. Fig. 9b). The surface contained a single O vacancy in subsurface position, which corresponds to a defect concentration of *ca.* $200 \times 10^{12}$ $cm^{-2}$. Four adsorption structures were found. It was shown that electron transfer from a $Ce^{3+}$ $4f^1$ into $Au^0$ $6s^1$ leads to more stable structures relative to Au in O atop or bridging positions. The latter sites do not yield $Au^-$, but preserve the $Au^0$ oxidation state (cf. Fig. 10). The thermodynamic preference of $Au^-$ relative to $Au^0$ amounts to *ca.* 0.09 eV, when the $Ce^{3+}$ in subsurface position is reoxidized. This means that the final adsorption state is an $Au^-$ ion adsorbed on top of a $Ce^{3+}$ ion.

The stability of structures involving an $Au^-$ ion is caused by large relaxation effects upon oxidation of the $Ce^{3+}$. As discussed in [29], $Ce^{3+}$ has a larger ionic radius than the $Ce^{4+}$ cation and electron transfer from $Ce^{3+}$ to $Au^0$ relieves some of the surface strain induced upon O defect formation. Reoxidation of $Ce^{3+}$ to $Ce^{4+}$ involves pronounced stabilizing relaxation in the surface. $Au^-$ ions formed upon oxidation of $Ce^{3+}$ located in the surface or subsurface layer of the reduced $CeO_2(111)$ surface were recently confirmed [228] to be very stable species. The latter work also uses a $p(2 \times 2)$ cell and reports a fifth, distinct adsorption structure with Au located at the hollow site atop a subsurface O. Also for this configuration electron transfer from the $Ce^{3+}$ in subsurface position to $Au^0$ occurs and the $Au^-$ resides as a nearest neighbor to the surface $Ce^{3+}$. This structure is almost 0.5 eV more stable relative to the O-atop position [228].

In a next step, a number of $Ce^{3+}$ pair configurations in the larger $p(4 \times 4)$ surface unit cell of the $CeO_2(111)$ surface containing a single subsurface O vacancy were generated (cf. Fig. 9c). The structures were optimized using the HSE hybrid functional and corresponding defect formation energies are presented in Table 2. These results show that the stability of the O defect strongly depends on the particular $Ce^{3+}$ pair configuration. The nearest-neighbor sites of the vacancy, i.e. $\mathbf{a_1}$–$\mathbf{a_3}$ (cf. Fig. 9c), are thermodynamically unfavorable [229, 230]. In contrast, the $\mathbf{b_1}$–$\mathbf{b_3}$

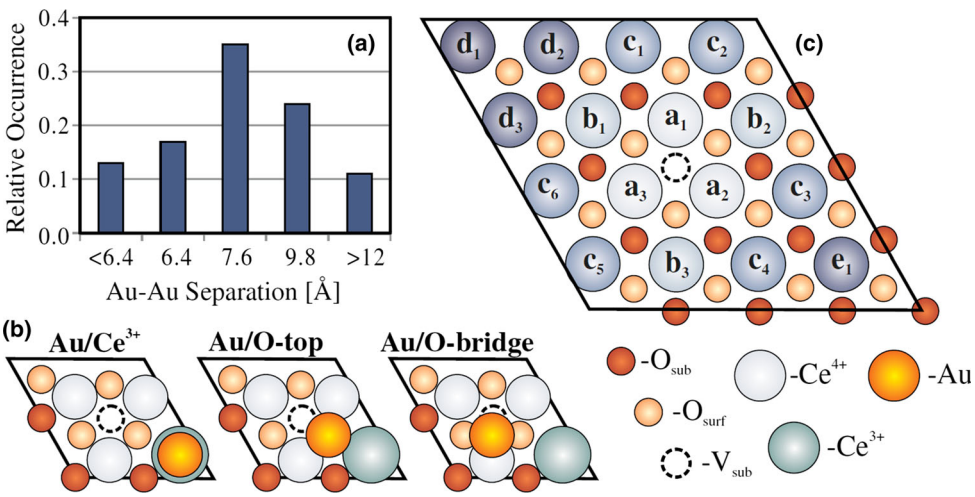


**Fig. 9** **a** Distance histogram determined for *ca.* 150 Au pairs on the ceria surface. **b** Configurations of a single Au adatom on reduced $CeO_2(111)$ containing a subsurface O vacancy in a $p(2 \times 2)$ unit cell. **c** Labels indicating the Ce coordination shells in a $p(4 \times 4)$ unit cell relative to the vacant site (cf. Table 2). Reprinted with permission from [224]. Copyright (2013) American Physical Society

**Table 2** Structure and vacancy formation energy ($E_{def}$) with respect to $^1/_2O_2$ for different subsurface O vacancy/$Ce^{3+}$ configurations obtained with HSE [224]

| $Ce^{3+}$ configuration | $Ce^{3+}$–$Ce^{3+}$ distance (Å) | $Ce^{3+}$-defect distances (Å) | $E_{def}$ ($^1/_2O_2$) (eV) | |
|---|---|---|---|---|
| | | | High spin | Low spin |
| $b_1$–$b_3$ | 7.67 | 4.41; 4.42 | 2.32 | 2.27 |
| $a_1$–$b_3$ | 6.77 | 2.33; 4.44 | 2.43 | 2.41 |
| $b_3$–$c_6$ | 6.65 | 4.41; 5.84 | 2.41 | |
| $a_3$–$b_3$ | 3.89 | 2.34; 4.43 | 2.50 | 2.54 |
| $b_3$–$d_3$ | 10.11 | 4.40; 7.94 | 2.47 | |
| $c_5$–$c_6$ | 3.88 | 5.84; 5.85 | 2.69 | |
| $c_1$–$c_6$ | 7.66 | 5.85; 5.84 | 2.66 | |
| $a_1$–$d_3$ | 7.63 | 2.35; 7.93 | 2.62 | |
| $a_3$–$c_5$ | 3.77 | 2.32; 5.86 | 2.63 | |
| $a_1$–$a_3$ | 4.08 | 2.37; 2.37 | 2.71 | 2.71 |

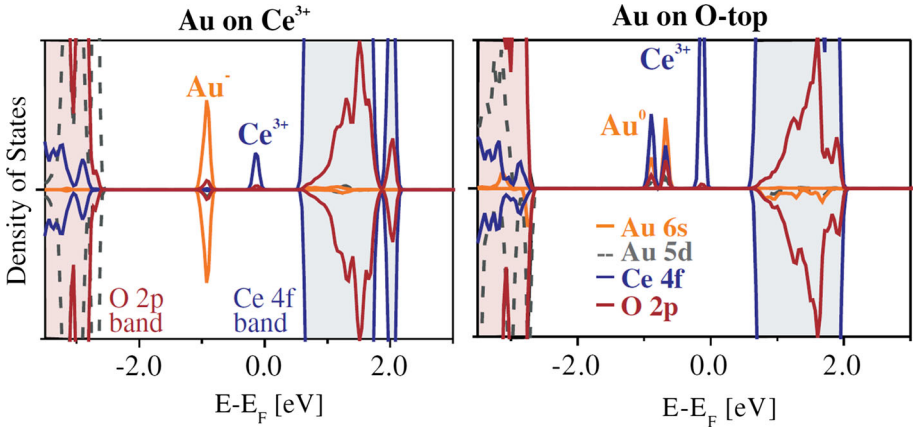


**Fig. 10** Respective projected local densities of states obtained with HSE for an $Au^-$ ion bound to a surface $Ce^{3+}$ (left) and to a $O^{2-}$ in atop position (right) in a $p(2 \times 2)$ cell of $CeO_2(111)$. Reprinted with permission from [224]. Copyright (2013) American Physical Society

configuration of two $Ce^{3+}$ ions (i.e., the second cationic shell with respect to the vacancy) is *ca.* 0.40 eV more stable than the $\mathbf{a_1}$–$\mathbf{a_3}$ configuration. The distance between $Ce^{3+}$ ions in $\mathbf{b_1}$–$\mathbf{b_3}$ is equal to two lattice parameters of the $CeO_2(111)$ surface unit cell. The low spin (antiferromagnetic) state is 0.05 eV more stable than the high spin (ferromagnetic) ordered $\mathbf{b_1}$–$\mathbf{b_3}$. Effects induced by the magnetic order are therefore considered as negligibly small. Thus, the favorable stability of $Au^-$ created upon electron transfer from surface or near-surface $Ce^{3+}$ together with the preferred $(2 \times 2)$ arrangement of $Ce^{3+}$ around the vacancy offers indeed a rationale for the Au pair formation.

However, we point out that the problem is complicated by several reasons. One complication arises because of the calculated, admittedly small energy differences. Francesc Illas and coworkers examined various theoretical models, including the HSE hybrid, to predict the oxidation state of Au adsorbed on the clean $CeO_2(111)$ surface as well as stabilities of the respective adspecies [231]. They concluded that the prediction of the oxidation state is fairly difficult using current DFT-based approaches, since solutions for the minimum energy structures for $Au^0$ or $Au^+$ are nearly degenerate in energy. It was found that GGA + U favors $Au^+/CeO_2(111)$ by 0.05 eV. In contrast, HSE predicts $Au^0/CeO_2(111)$ to be 0.15 eV more stable than the positively charged Au causing a $Ce^{3+}$ ion in the surface. This finding is consistent with a recent STM study, which concludes on close-to-neutral charge states for Au atoms adsorbed on defect-poor ceria surfaces [232].

For a ceria surface containing O defects, the complexity of the problem increases drastically and requires to address the influence of the defect concentration. Clearly, a large number of defects in the surface build up considerable amounts of strain due to the high $Ce^{3+}$ concentration. Thus, the thermodynamic driving force to reoxidize some of them to $Ce^{4+}$ is large when Au adatoms offer half-filled 6s orbitals for the redox process [224, 228]. As a consequence, the Au will titrate the $Ce^{3+}$. The effect of the defect concentration is supported by observation, because the STM revealed that the Au pairs did not homogenously cover the surface, but large variations in the abundance of pairs were observed. This suggests that the local degree of reduction affects the pairs [224]. Definitely, further research is required to get a more comprehensive picture.

### 4.3 Surface Structure of $V_2O_3$(0001)

Vanadia exists in many different oxide phases, because vanadium can accommodate a large number of oxidation states [233]. The oxidation states relate to varying occupations of the V 3d orbitals. For instance, the oxidation state of vanadium in VO is +2 featuring a (formal) $d^3$ electron occupation. In $V_2O_3$, the oxidation state is +3 ($d^2$), and $VO_2$ involves $V^{+4}$ ($d^1$). The highest oxidation state +5 is found in $V_2O_5$ featuring unoccupied V 3d orbitals.

The d electrons of the vanadium oxides are strongly affected by Coulomb correlation effects [234]. Especially in $V_2O_3$, correlation steers the subtle balance between localization and delocalization of electrons, giving rise to temperature-dependent metal-to-insulator phase transitions [235]. The latter involve concurrent structural changes. These phase transitions may be also induced by applying hydrostatic pressure [236] or, e.g., doping with Cr [237]. However, the underlying physics of these phase transitions is a much debated issue including surface effects [238, 239].

Concerning catalysis, vanadium oxides are major components of the active phases in many solid oxidation catalysts [180, 240, 241]. Thus, atomic level details of their surface structure is crucial for a rationale of reactivity. For an extensive review on selected case studies of vanadium oxide layers in model catalysis, we refer to [38].

Recent work combining results obtained using *I-V* LEED, atomically resolved STM, grazing angle He scattering, as well as DFT, elucidated the surface structure of $V_2O_3$(0001) [242]. This surface can be terminated by either one or two V atoms, or an $O_3$ layer. By virtue of DFT it was shown that surface reconstructions can be thermodynamically more stable than the bulk terminations [243, 244] (cf. Fig. 11). At low oxygen chemical potentials, a vanadyl (V=O) terminated surface was predicted to be the ground state. However, increasing the O chemical potential stabilizes ordered superstructures at $^2/_3$ or $^1/_3$ of full V=O coverage. Even higher chemical potentials of oxygen stabilize a reconstructed $O_3$ termination. As shown in Fig. 11, in this $O_3$ termination every other V atom from the second metal layer needs to move up into the first metal layer.

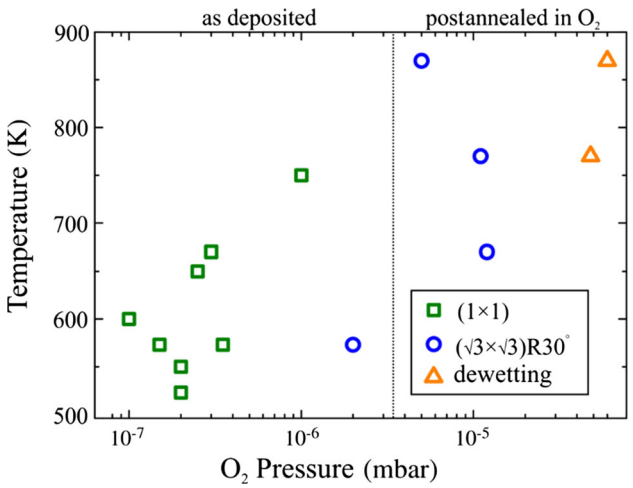


**Fig. 12** Experimentally observed surface phases as a function of preparation conditions. Reprinted with permission from [242]. Copyright (2015) American Physical Society

These aforementioned surface phases have been revisited [242, 245]. Fig. 12 shows them as a function of the preparation conditions. For the majority of experiments, a fully V=O covered surface was obtained. However, at higher $O_2$ pressures and temperatures, the $(\sqrt{3} \times \sqrt{3})R30^\circ$ surface, which is partially reconstructed and partially covered by V=O groups, was prepared. Increasing the oxygen partial pressure did not lead to further oxidation, but dewetting or sublimation of the oxide layer was observed instead.

The surface terminations of $V_2O_3$(0001) were intensively studied using semilocal functionals [243, 244, 246–248]. Recent experimental work [249] supported the $O_3$ termination invoking arguments based on DFT. Considering the shortcomings of the semilocal approximation, it appears worthwhile to check for robustness of results employing hybrid functionals. As discussed in Sect. 2, the amount of admixed FX is a material-specific quantity and may affect results. Hence, the question arises, whether results critically depend on the mixing ratio $a_0$ (cf. Eq. 4). We investigated the most important terminations of $V_2O_3$(0001) using PBE and HSE. In addition to the "as

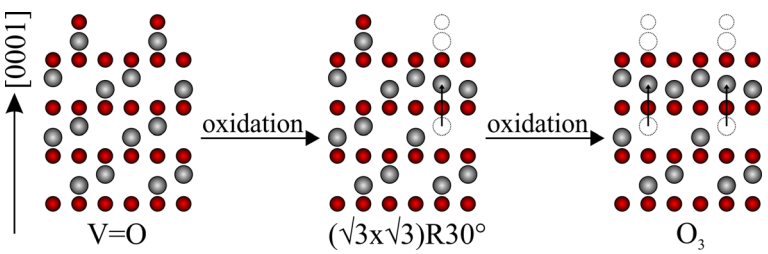


**Fig. 11** Structural models of $V_2O_3$(0001) surface terminations predicted by DFT. V atoms are depicted in *gray*, O atoms are *red*. Reprinted with permission from [242]. Copyright (2015) American Physical Society

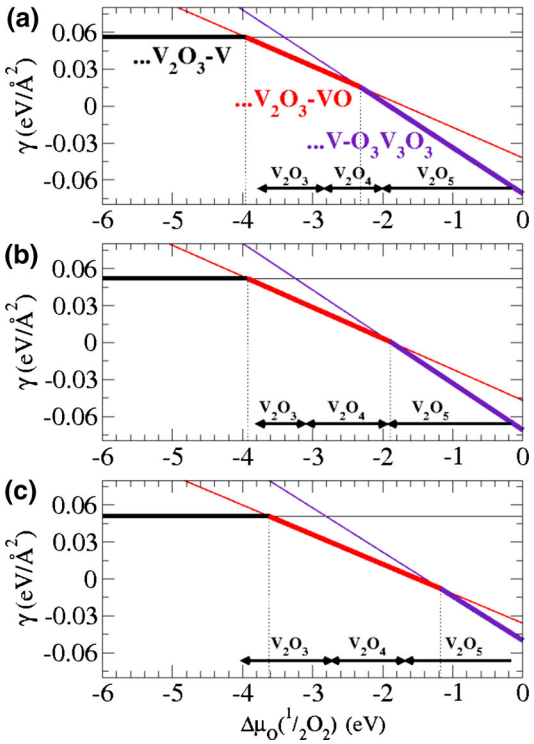


**Fig. 13** Surface energy $\gamma$ as a function of the chemical potential $\Delta\mu_O$ for the most relevant surface terminations obtained using **a** PBE, **b** HSE(10 % FX), and **c** HSE (25 % FX). Reprinted with permission from [242]. Copyright (2015) American Physical Society

defined" value $a_0 = 0.25$, we also used $a_0 = 0.10$, which was recently suggested for $VO_2$ [250].

The calculated phase diagrams obtained with PBE and HSE ($a_0 = 0.1$ and 0.25) are presented in Fig. 13. The black arrows at the bottom refer to the stable bulk phases at respective chemical potentials of oxygen. Our PBE results agree excellently with previously published results of Georg Kresse and coworkers obtained using the PW91 GGA functional [243]. PBE and PW91 [251, 252] are closely related in terms of their analytical forms. Hence, the agreement does not come as a surprise. Concerning HSE results, increasing $a_0$ shifts the boundary for the equilibrium between V = O and $O_3$ terminations towards more positive potentials, i.e. towards higher oxygen pressures for a given temperature. HSE ($a_0 = 0.25$) predicts a value for the phase equilibrium of −1.1 eV corresponding to—at 900 K—an oxygen pressure of about 1 mbar.

We do not claim that a simple hybrid functional like HSE describes the aforementioned Coulomb correlation effects in $V_2O_3$ correctly. Neither should the aforementioned results be interpreted quantitatively. Nonetheless, we believe that the PBE and the closely related PW91 functional overemphasize phase stability of the $O_3$ termination under reducing conditions, i.e. at low chemical potentials of oxygen. Note that the hybrid functionals only marginally modify the stability range for the bulk phase of $V_2O_5$ relative to PBE results. We learn from the phase diagram, that the $O_3$ termination is competing with the bulk phase of $V_2O_5$. This agrees with the observation, which indicates sublimation of the oxide layer (cf. Fig. 12).

Reliability of HSE for the vanadium sesquioxide is supported by theoretical work of Angel Rubio and coworkers [253]. They showed that HSE performs well for the paramagnetic phase of bulk $V_2O_3$. Our own work showed, that HSE outperforms PBE in terms of enthalpies of formation for the bulk phases of $V_2O_3$, $V_2O_4$, as well as $V_2O_5$ [242]. HSE results agree better with observed values (cf. Supporting Information of [242]).

In conclusion, HSE predicts the V=O termination to be stable under relevant experimental conditions and destabilizes the $O_3$ termination relative to the $V_2O_5$ bulk phase in agreement with observation. Conceding errors in the chemical potential of oxygen obtained, which may be as large as several hundred meV, translates to several orders of magnitude of an error in the pressure. Even within these uncertainties, the phase equilibrium between V=O and $O_3$ cannot be shifted in favor of the $O_3$ termination, i.e. the conditions cannot be reached experimentally. This result is in contrast to findings of previous studies [243, 244], which we attribute to the right balance between nonlocal and semilocal information contained in the HSE hybrid functional.

### 4.4 Adsorption of Water on the $Fe_3O_4$(111) Surface

Iron oxides represent an important class of materials, because of their widespread technical applications [254]. In catalysis, hematite ($Fe_2O_3$) and magnetite ($Fe_3O_4$), are used in the preparation of the iron catalyst employed in the Haber–Bosch process, i.e. the synthesis of $NH_3$ from $N_2$ and $H_2$ [233, 255]. Hematite is the most stable iron oxide phase under ambient conditions, however under more reducing conditions, i.e. high temperatures and low oxygen partial pressures, magnetite becomes the prevalent phase [256, 257].

At temperatures greater than the so-called Verwey transition temperature of *ca.* 122 K, magnetite crystallizes in a cubic, inverse spinel structure [234]. This means that tetrahedral (A) sites are occupied by $Fe^{3+}$ (high-spin $d^5$) and octahedral (B) sites are occupied by 50 % of $Fe^{2+}$ (high-spin $d^6$) and 50 % of $Fe^{3+}$, which are randomly distributed. It is a ferrimagnet, i.e. spins located at tetrahedral and octahedral iron sites are antiferromagnetically coupled. These local magnetic moments do not compensate each other, leading to a net magnetic moment of about 4 $\mu_B$ per $Fe_3O_4$ formula unit [258].

The predominant natural growth facet of magnetite is a surface in (111) orientation [259]. Hence, the (111) surface is relevant for studying ambient conditions.

We examined the adsorption of water at the $Fe_3O_4(111)$ surface using PBE + U(3.8) and the HSE hybrid to test for robustness of PBE + U results [260]. HSE is corrected for dispersion-type van der Waals interactions by a $c_6/r^6$ term as introduced by Stefan Grimme [198, 199, 261]. As discussed in [262], it is mandatory to use a sufficient number of layers in the slab model, because 3d electrons localize in subsurface iron layers upon ionic relaxation, which in turn incurs Jahn–Teller-type distortions. This effect is known as orbital or charge ordering [263, 264] and lowers the energy of the slab. To accommodate these aforementioned relaxation effects, the models used in [260] employ 12 atomic layers (cf. Fig. 14).

Table 3 presents local magnetic moments for the surface Fe ions obtained using PBE + U(3.8) and HSE + D, respectively. PBE + U values compare well with results given in [262]. Local magnetic moments of the octahedrally and tetrahedrally coordinated Fe ions in the bulk amount to 3.9 and −4.1 $\mu_B$, respectively. Smaller magnetic moments in surface ions indicate additional electron localization, i.e. a reduction of surface iron ions. HSE + D and PBE + U(3.8) results are de facto identical.

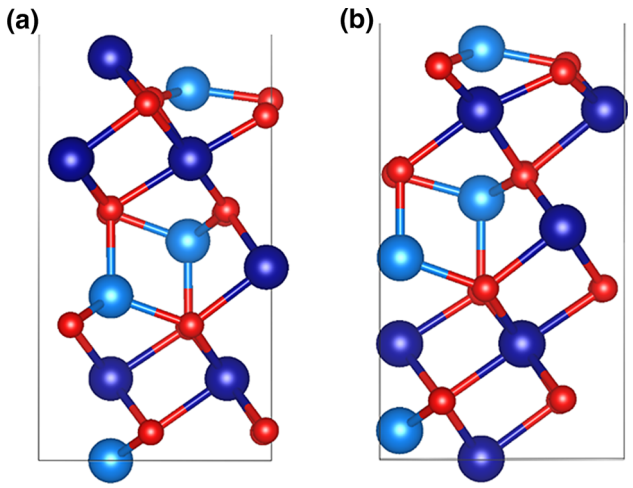


**Fig. 14** Relaxed slab models for **a** $Fe_{oct2}$ and **b** $Fe_{tet1}$ terminated $Fe_3O_4(111)$ surfaces. Octahedrally and tetrahedrally coordinated Fe ions are shown in *dark* and *light blue*, respectively. Reprinted with permission from [260]. Copyright (2016) American Chemical Society

**Table 3** Local magnetic moments ($\mu_B$) of surface iron ions in the $Fe_{oct2}$ and $Fe_{tet1}$ terminated $Fe_3O_4(111)$ surfaces obtained using PBE + U(3.8) and HSE + D

| Termination | Fe-oct2 | | Fe-tet1 |
|---|---|---|---|
| Surface ions | $Fe_{oct}$ | $Fe_{tet}$ | $Fe_{tet}$ |
| PBE + U(3.8)[a] | 3.58 | −3.58 | −3.51 |
| PBE + U(3.8) | 3.54 | −3.56 | −3.51 |
| HSE + D | 3.52 | −3.56 | −3.51 |

[a] Ref. [262]

From a practitioner's point of view, DFT + U suffers from many local minima on the corresponding potential energy surface. This hampers the determination of the electronic as well as magnetic ground state of $Fe_3O_4$. For example, after adsorption of an $H_2O$ molecule on the $Fe_3O_4(111)$ surface, the spin density or local magnetic moments per surface iron ion will be modified with respect to the clean surface. The precise value cannot be known a priori. Starting the HSE structure optimization on top of PBE + U(3.8) structures yields identical local magnetic moments and spin-orders as found by using the PBE + U(3.8) approach. This protocol turned out to be very robust and is suitable to confirm electronic and magnetic ground states of the hydrated surfaces. It appears that the problem of metastable minima plaguing the DFT + U approach is largely bypassed using a hybrid functional like HSE. This tremendously facilitates calculations.

Water adsorbed on the $Fe_3O_4(111)$ surface has been recently studied combining single crystal adsorption calorimetry (SCAC), infra-red spectroscopy, and DFT [265]. As shown in Fig. 15, the initial adsorption energy of water at temperatures greater than 120 K amounts to 100 kJ/mol. Figure 16a shows two IR bands at 2720 and 2695 $cm^{-1}$ using $D_2O$ adsorbed on $Fe_3O_4(111)$. These two bands are shifted by 18 and 16 $cm^{-1}$, respectively, when $^{18}O$ labeled water was dosed. Preparing the surface using $^{18}O$ and dosing $D_2^{16}O$ does not incur such an isotope shift. Thus, the observed OD stretching modes cannot involve O atoms originating from the surface.

Figure 16b shows that the modes involved in the two bands are coupled and cannot stem from spatially separated, individual OD groups. Dosing light water, the

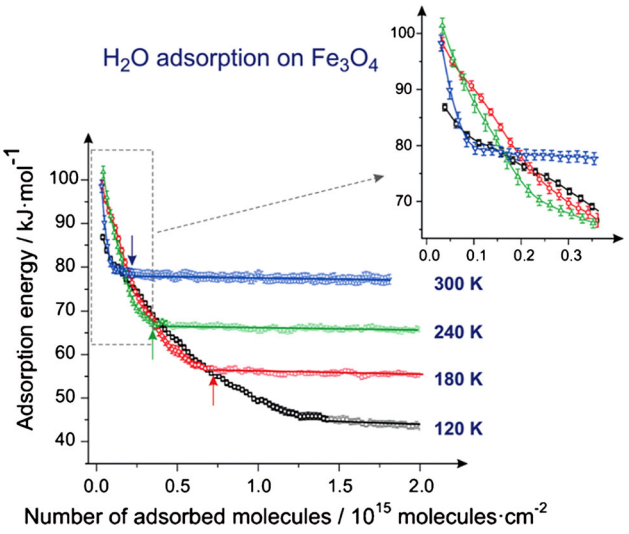


**Fig. 15** Adsorption energies of $H_2O$ on $Fe_3O_4(111)$ at different temperatures based on molecular beam techniques. Reprinted and adapted with permission from [265]. Copyright (2015) John Wiley and Sons

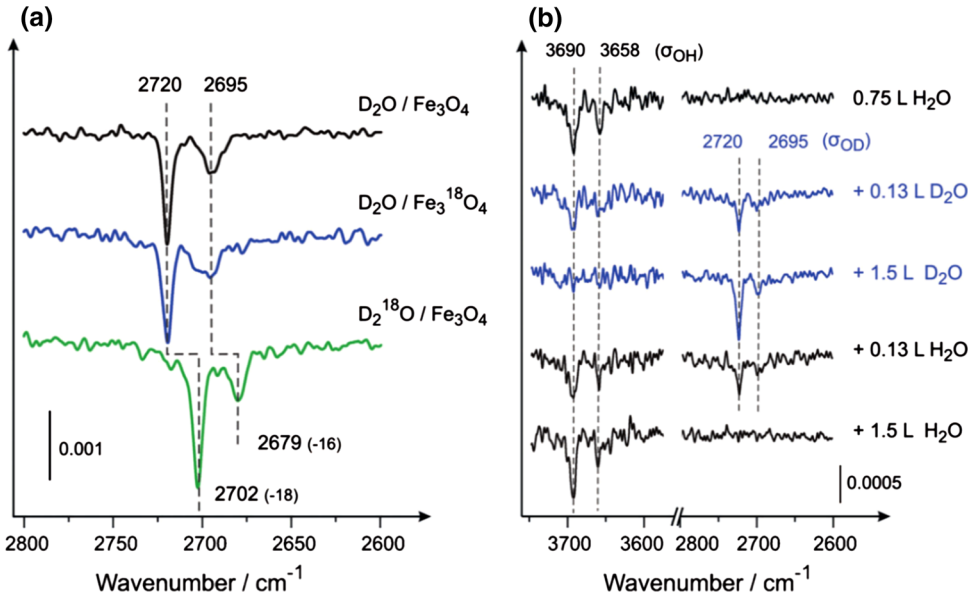


**Fig. 16** **a** IR spectra for $D_2O$ and $D_2^{18}O$ adsorbed on the $Fe_3O_4(111)$ surfaces prepared using $^{16}O$ and $^{18}O$ at a temperature of 300 K. **b** Series of IR spectra recorded at 300 K, when $H_2O$ was reversibly replaced by $D_2O$. Reprinted with permission from [265]. Copyright (2015) John Wiley and Sons

respective wavenumbers amount to 3690 and 3658 $cm^{-1}$, typical of OH stretching modes. Exposing the surface to some $D_2O$ results in decreased peak intensities and two bands at 2720 and 2695 $cm^{-1}$ appear. Upon further exposure to $D_2O$, the two peaks at around 3700 $cm^{-1}$ disappear and the two corresponding signals at 2700 $cm^{-1}$ appear with the same characteristic time constant. Hence, these IR signals originate from coupled modes.

Several minimum energy adsorption structures for one, two, and three water molecules at the $Fe_3O_4(111)$ surface were calculated using PBE + U(3.8) [260]. As discussed above, a single water molecule dissociatively adsorbed at the surface is not reconcilable with observed isotopic shifts. This is because of the formation of a surface OH group in case of dissociative adsorption, which would inevitably lead to a shift in one of the IR bands upon isotopic labeling of the surface. In case of molecular adsorption of water, one of the two (calculated) wavenumbers is substantially red-shifted and as a consequence their difference is much larger than the experimentally observed difference in bands (25 $cm^{-1}$, see also Fig. 8b in [260]).

Based on calculated adsorption energies and IR wavenumbers (including isotope shifts), only a water dimer-type species, involving a dissociated and an intact water molecule at the $Fe_{oct2}$ terminated $Fe_3O_4(111)$ surface, is reconcilable with experiment. The average PBE + U(3.8) adsorption enthalpy for this water dimer amounts to 109 kJ/mol, which agrees excellently with the observed value (100 kJ/mol; cf. Figure 15). Unscaled IR wavenumbers obtained using PBE + U(3.8) for the so-called terminal OD stretching modes of this adsorption complex amount to 2758 and 2728 $cm^{-1}$. Scaling of the wavenumbers with factors, that are either taken from the literature [266] or derived from the 'experiment/theory' ratio of respective averages between symmetric and antisymmetric stretching modes of molecular water [265, 267], leads to a 1 % decrease of PBE wavenumbers. Scaled wavenumbers agree better with observation. Similar successful scaling was applied to the stretching modes of terminal or "free" OH groups (cf. [34]) of hydroxylated silica surfaces using the B3LYP hybrid functional [268, 269].

## 5 Summary, Limitations, and Future Prospects

### 5.1 Summary

We learn from the case studies discussed in this work as well as from the work published in the literature, that hybrid functionals applied to semiconducting and insulating metal oxides outperform semilocal functionals in terms of (i) band gaps [128, 161, 270, 271], (ii) oxygen defect formation energies [230, 272], and (iii) activation barriers [97, 190, 197, 273]. Previously stated by Gianfranco Pacchioni, these improvements are closely connected to decreased SIEs and thereby enhanced charge as well as spin localization [28]. The admixture of non-local FX to semilocal exchange is beneficial for the "stretched-bond" situation in transition structures [60]. A quarter or 25 % of FX complemented by 75 % of semilocal exchange proved a good average for molecules (including transition metal oxides [274]) and semiconductors [270]. Metallic systems need less or no FX [77, 128]. A screened FX interaction, effective at shorter interelectron distances like in the HSE hybrid, yields very accurate 'medium sized' band gaps of (simple) semiconductors [275]. For other properties like magnetic exchange

couplings, FX effective on the long-range part of the Coulomb interaction was shown to yield more accurate results [276]. Details on magnetic properties obtained with hybrid functionals applied to extended systems can be found in the excellent review by Jean Paul Malrieu [277] or Francesc Illas [278]. Based on our practical experience, potential energy surfaces of hybrid functionals feature substantially fewer meta-stable local minima as encountered in DFT + U calculations. Thus, the likelihood of getting trapped in spurious minima in the course of electronic optimizations is substantially smaller. This enhances computational efficiency of calculations on magnetic systems like the magnetite surfaces discussed in Sect. 5 [260, 265]. Good performance of the B3PW91 hybrid functional applied to iron oxide has been reported in [279].

Oxygen defect formation energies are important descriptors to assess reactivity of oxidation catalysts [42]. Ceria is a reducible oxide with outstanding catalytic properties, because of its high reducibility [212, 280]. Accurate measurements of the O defect formation energy in ceria surfaces under well-defined conditions is difficult [281–283]. However, an estimate of 4.2 ± 0.3 eV corrected for the electron-hopping barrier was provided [29]. The error bar of 0.3 eV was estimated, and it may be even larger due to the reasons given in [29]. PBE + U using conventional values for U ranging between 4 and 6 eV [284] underestimates O vacancy formation energies by *ca.* 1.5 eV. A hybrid functional like HSE improves O vacancy formation energies significantly and underestimates them by *ca.* 0.8 eV.

Defects are commonly entangled with polaron formation. Hence, stabilization of the system by lattice distortions or relaxations plays a crucial role [285–287]. Consequently, high accuracy in lattice parameters as well as elastic constants is important for metal oxides [197]. For semiconductors and insulators in general and ceria in particular, the HSE or PBE0 hybrids perform with high accuracy [77, 175]. Results obtained using the B3LYP hybrid functional are slightly more off [123, 288]. Hybrid functionals benefit from the possibility to consistently optimize cells and atomic positions, because of available gradients and stress tensors (see, e.g., [30, 289, 290]) at affordable computational cost. Accomplishing hybrid functional calculations is the best a DFT practitioner can currently do, when dealing with insulating oxides like ceria, based on the fact that relaxation of atoms and cells can be *consistently* carried out.

### 5.2 Limitations

Global as well as range-separated hybrids run into problems, when applied to metallic systems [77, 128, 129]. The situation is particularly bad for transition metals, such as Fe or Cr, featuring so-called itinerant magnetism [65, 77, 291]. Ref. [291] reports, that HSE for Cr using the antiferromagnetically ordered state (cf. [292]) yields the lowest energy structure, however the equilibrium lattice constant is overestimated by 23 %. Similar findings are reported for the complex structure of Mn [291, 293]. The problem for these transition metals arises from overly localized orbitals using a hybrid functional. The metal is erroneously described as a so-called Hund's rule magnet featuring spatially too localized moments. This has been shown by the overestimated local magnetic moment of Fe compared to (e.g.) PBE results [77]. It appears plausible that for these systems the combination of non-local FX and semilocal correlation is unbalanced, and non-local correlation (e.g. based on the generalized RPA) is required. RPA lattice parameters for Fe, Co, and Ni were reported to be in good agreement with experiment [294].

Peter Feibelman's CO/Pt(111) puzzle offers another cautionary moment [295]. This problem deals with the preferred adsorption site of CO on the close packed Pt(111) surface, i.e., atop versus hollow positions, and the conflict between experiment and DFT results obtained with semilocal approximations. As described in [130, 296], hybrid functionals like HSE overestimate band widths of the d states in metallic surfaces, which results in adverse effects concerning the binding of CO, although the HOMO–LUMO gap in CO is properly described. The importance of the gap for CO adsorption on transition metals was shown in [297]. The adsorption energy differences for top and hollow sites amount to *ca.* 0.1 eV, which is a small value. Thus, the problem represents a veritable challenge for the computational modelling. Sure enough, the proper description of the electronic structure is important, but only one aspect of the entire problem. For instance, thermal effects may also play a role with regard to the aforementioned narrow energy range of 0.1 eV. We agree with the conclusions drawn in [298]. Whenever small energy differences or near-degeneracies require an evaluation or assessment, also other properties than mere energies need to be considered in order to provide a bigger picture.

Concerning CO adsorption, it appears that non-local correlation effects corresponding to dispersion-type van der Waals interactions are the clue underlying site preferences of CO on Pt(111) [95, 299, 300]. Additionally, the preference of CO to adsorb in atop position, e.g., on the Cu(111) surface was found using embedded, correlated wavefunction-based methods like configuration interaction [301], but also with a kinetic energy density functional approach [302].

Straightforward application of hybrids to the so-called strongly correlated vanadium oxides $VO_2$ and $V_2O_3$ may be problematic. These systems involve d states drastically changing character from rather band-like (delocalized) to atom-like (localized) depending on the crystal structure. The involved Coulomb correlation effects among electrons

are difficult to describe accurately within KS-DFT [37, 303, 304]. A profound discussion of a state-of-the-art description of the electronic properties of vanadium oxides is beyond the scope of the present work. We refer to the review article of Karsten Held and coworkers and therein cited references instead [305].

Recent computational studies applied hybrid functionals like HSE to $VO_2$ [163, 242, 250, 253, 306, 307]. While the situation is not that bad for paramagnetic $V_2O_3$ [163, 253], earlier HSE calculations using the "as defined" 25 % of FX, predicted a band gap for the metallic rutile $VO_2$ phase and magnetic ground states for both monoclinic and rutile phases, which are not observed [307]. Recent fixed-node diffusion quantum Monte Carlo (FN-DMC) results for $VO_2$ indicate that the ground state is spin polarized, because ferromagnetically and antiferromagnetically ordered spins provide lower total energies than the corresponding unpolarized result [308]. It is noteworthy that the FN-DMC uses PBE0 trial wavefunctions employing various FX admixing factors. Recently, it was shown that decreasing the amount of admixed FX to 10 % qualitatively improves HSE results for the $VO_2$ phases [250]. Similar problems have been reported for MnO phases [309].

The inevitable parameters used in a hybrid functional, such as the amount of FX and possible screening parameters, were shown to be material-specific (e.g. [76], [310], [271], [78], [311], [312]). The admixing ratio of FX can be physically motivated, because the generalized KS potential mimics the self-energy as amply discussed in [141]. Employing "dielectric adaptation of FX" or equivalently "statically screened exchange" (cf. [75], [313–315]), a series of successful calculations on complex semiconducting and insulating metal oxides like ZnO or $TiO_2$, but also on organic–inorganic perovskites like $CH_3NH_3PbI_3$ [316], could be accomplished. We emphasize that this adaptation is more than a mere fitting, it takes care of dielectric screening or equivalently some of the electron correlation effects. In light of the successes reported in the literature, potential limitations of hybrids incurred by a fixed amount of FX, which would naturally restrict their universal application, appear remediable though.

From a practitioner's point of view, the computational workload imposed by hybrid functionals is considerably larger compared with semilocal functionals. For instance, determining a transition structure for chemical reactions on surfaces is a non-trivial task involving high computational cost [190, 197]. Nonetheless, it is necessary to provide these benchmark results, not only for the sake of theory, but also to have reference values at hand, which can be compared with state-of-the-art experimental results. At the moment, the computational workload prevents, e.g., industrial research in catalysis relying on a screening of several thousand materials in short amount of time. With regard to academic research, hybrid functionals represent an important alternative to semilocal approximations, whenever there is need for results obtained with higher rung functionals of supposed higher accuracy. Standard optimizations are certainly feasible by nowadays technologies, either relying on in-house clusters of academic institutions or high-performance computer centers. Developments exploiting non-conventional computer architecture like graphical processing units (GPUs) promise to drastically enhance times spent to compute the FX energy [317] required for hybrid functionals. Additionally, software developments in terms of better exploitation of available high-performance resources is certainly prerequisite to efficient simulations on extended systems [318], particularly so for dynamics simulations [159, 319].

### 5.3 Prospects

Hybrid functionals have become a standard tool in computational catalysis or materials science and will enjoy widespread applications in the future. However, they do not represent a panacea in light of above mentioned shortcomings. This invites the question, how to do it better. If one adheres to DFT, developments in functionals of the fifth rung on Jacob's ladder, i.e. fully non-local hybrid functionals involving orbital dependence in the correlation energy, appears to be the logical step. Currently, RPA-based functionals are an active field of research (cf. [87] and therein cited references). It is expected that fifth rung functionals will overcome the limitations of conventional hybrid functionals. However, the generalized RPA involves an even higher computational workload, because it bears resemblance to wavefunction-based methods [86, 320, 321]. Developments with respect to computer hardware as well as algorithms used in the software will improve the situation (e.g. [106], [322], [323]). Related to extended systems, RPA-based functionals are not available self-consistently, i.e. orbitals and orbital energies need to be generated in a first step. KS-orbitals are conventionally used for that purpose. However, if semilocal approximations fail, e.g., to describe the band gap accurately, orbitals obtained using hybrid functionals represent a viable option (cf., e.g., [324, 325]).

Currently, there is a revived interest in embedding techniques (e.g., [326–333]). In order to save computing time, hybrids could be employed within an embedded framework, representing the so-called "high-level method". Alternatively, when doubts arise on the accuracy of the hybrid functional used, they could be employed to describe the "low-level domain", and more accurate generalized RPA or post-HF wavefunction-based methods can be used instead. Embedding hybrid functionals is certainly a way to render calculations more efficient. However,

technically this is not a trivial task, justifying the many promising research activities [334–337].

## 6 Final Remarks

A recent article by Axel Becke [338] nicely reviews the past fifty years of developments in DFT. It concludes with the interesting question, whether the efforts in making functionals more accurate will continue to satisfy DFT users in terms of speed. Semilocal functionals will remain a significant tool in computational chemistry and physics, because of the speed argument. Hybrid functionals represent an important step partially merging wavefunction-based theory (HF) with DFT (and vice versa). The additional non-local information originating from the one-electron density matrix required to compute the FX energy can substantially improve upon semilocal results for band gaps, defect formation energies, and activation barriers, but currently not for relatively low computational cost. *There ain't no such thing as a free lunch.*

If we want to compare computational results with observation, we need structural models to guarantee a well-defined scenario for both, experiment and theory [39]. For such an endeavor, we have to keep in mind merits and limits of the approximations involved in DFT, as well as of pros and cons of underlying structural models used in actual calculations. Hybrid functionals relying on a minimal number of physically motivated parameters represent a very useful rung on Jacob's ladder. Within their admitted limits, they offer a valuable way to check semilocal results including DFT + U. However, successful research in catalysis and materials science will continue to be pillared by DFT, wavefunction theory,[1] as well as state-of-the-art experiments employing several, possibly complementary techniques.

**Acknowledgments** I am indebted to Prof. Joachim Sauer for his continuous support and for many insightful discussions. I gratefully thank my ambitious coworkers Christopher Penschke, Thomas Kropp, and Xiaoke Li. I especially thank Thomas and Christopher for proofreading parts of the manuscript. I sincerely acknowledge the numerous fruitful collaborations and discussions with Prof. Hajo Freund (Fritz-Haber-Institut der Max-Planck-Gesellschaft), Prof. Niklas Nilius (Carl von Ossietzky Universität Oldenburg), and Prof. Swetlana Schauermann (Christian-Albrechts-Universität zu Kiel). These collaborative efforts generated decisive results, which form the basis for many conclusions drawn in this perspective article. I thank Prof. Christof Wöll (Karlsruher Institut für Technologie), Dr. M. Verónica Ganduglia-Pirovano (Instituto de Catálisis y Petroleoquìmica), Dr. Helmut Kuhlenbeck, and Dr. Shamil Shakhutdinov (Fritz-Haber-Institut der Max-Planck-Gesellschaft) for many fruitful and stimulating discussions. Several generous grants for computing time at the HLRN (North-German Supercomputing Alliance in Berlin and Hannover) and JUROPA (Forschungszentrum Jülich) are thankfully acknowledged. I owe tremendous thanks to Dr. Jens Döbler, Dr. Christian Tuma, and Dr. Stefan Wollny, representatives of the HLRN, for their continuous efforts. Financial support by the Deutsche Forschungsgemeinschaft within the Sonderforschungsbereich (SFB) 1109, the COST action CM1104, the Fonds der Chemischen Industrie (FCI), and the Stiftung Industrieforschung, Humboldt-Universität zu Berlin, are gratefully acknowledged.

[1] The term "wavefunction theory" is supposed to comprise higher-order density-matrix formalisms, Green function approaches, and Quantum Monte Carlo techniques, in addition to methods conventionally used in quantum chemistry (perturbation theory, configuration interaction, coupled-cluster).

## References

1. Kohn W, Sham LJ (1965) Phys Rev 140:1133
2. Dreizler RM, Gross EKU (1990) Density functional theory. Springer, Berlin
3. Jones RO, Gunnarsson O (1989) Rev Mod Phys 61:689
4. Grabowski B, Wippermann S, Glensk A, Hickel T, Neugebauer J (2015) Phys Rev B 91:201103
5. Thiel W (2014) Angew Chem Int Ed 53:8605
6. Curtiss LA, Raghavachari K, Redfern PC, Pople JA (1997) J Chem Phys 106:1063
7. Zhao Y, Truhlar DG (2005) J Phys Chem A 109:5656
8. Csonka GI, Perdew JP, Ruzsinszky A, Philipsen PHT, Lebegue S, Paier J, Vydrov OA, Ángyán JG (2009) Phys Rev B 79:155107
9. Rapps T, Ahlrichs R, Waldt E, Kappes MM, Schooss D (2013) Angew Chem Int Ed 52:6102
10. Koch W, Holthausen MC (2001) A chemist's guide to density functional theory. Wiley-VCH Verlag GmbH, Weinheim
11. Ozolins V, Körling M (1993) Phys Rev B 48:18304
12. Peverati R, Truhlar DG (2012) J Chem Theory Comput 8:2310
13. Kim Y-S, Marsman M, Kresse G, Tran F, Blaha P (2010) Phys Rev B 82:205212
14. Payne MC, Teter MP, Allan DC, Arias TA, Joannopoulos JD (1992) Rev Mod Phys 64:1045
15. Goedecker S (1999) Rev Mod Phys 71:1085
16. Jensen F (2002) J Chem Phys 116:7372
17. Furche F (2001) Phys Rev B 64:195120
18. Sauer J (1989) Chem Rev 89:199
19. Pacchioni G, Lomas JR, Illas F (1997) J Mol Catal A: Chem 119:263
20. Gillan MJ (1997) Contemp Phys 38:115
21. Pykavy M, Stämmler V, Seiferth O, Freund HJ (2001) Surf Sci 479:11
22. Schmitt I, Fink K, Stämmler V (2009) Phys Chem Chem Phys 11:11196
23. Müller C, Hermansson K, Paulus B (2009) Chem Phys 362:91
24. Perdew JP, Zunger A (1981) Phys Rev B 23:5048
25. Ruzsinszky A, Perdew JP, Csonka GI, Vydrov OA, Scuseria GE (2007) J Chem Phys 126:104102
26. Janesko BG, Henderson TM, Scuseria GE (2009) Phys Chem Chem Phys 11:443
27. Ganduglia-Pirovano V, Hofmann A, Sauer J (2007) Surf Sci Rep 62:219
28. Pacchioni G (2008) J Chem Phys 128:182505
29. Paier J, Penschke C, Sauer J (2013) Chem Rev 113:3949
30. Freysoldt C, Grabowski B, Hickel T, Neugebauer J, Kresse G, Janotti A, Van de Walle CG (2014) Rev Mod Phys 86:253
31. Zhao Y, Gonzalez-Garcia N, Truhlar DG (2005) J Phys Chem A 109:2012
32. Janesko BG, Scuseria GE (2008) J Chem Phys 128:244112

33. Kohn W, Meir Y, Makarov DE (1998) Phys Rev Lett 80:4153
34. Sauer J, Ugliengo P, Garrone E, Saunders VR (1994) Chem Rev 94:2095
35. Kümmel S, Kronik L (2008) Rev Mod Phys 80:3
36. Cohen AJ, Mori-Sanchez P, Yang W (2012) Chem Rev 112:289
37. Perdew JP, Ruzsinszky A, Constantin LA, Sun J, Csonka GI (2009) J Chem Theory Comput 5:902
38. Kuhlenbeck H, Shaikhutdinov S, Freund H-J (2013) Chem Rev 113:3986
39. Sauer J, Freund H-J (2015) Catal Lett 145:109
40. Jacob D, Haule K, Kotliar G (2008) EPL 84:57009
41. Mars P, van Krevelen DW (1954) Chem Eng Sci 3(Supplement 1):41
42. Sauer J, Döbler J (2004) Dalton Trans 19:3116
43. Keating PRL, Scanlon DO, Morgan BJ, Galea NM, Watson GW (2012) J Phys Chem C 116:2443
44. Pacchioni G, Freund H (2013) Chem Rev 113:4035
45. Solans-Monfort X, Branchadell V, Sodupe M, Sierka M, Sauer J (2004) J Chem Phys 121:6034
46. Nolan M (2010) Chem Phys Lett 499:126
47. Kropp T, Paier J (2015) J Phys Chem C 119:23021
48. Gillan MJ, Alfè D, De Gironcoli S, Manby FR (2008) J Comput Chem 29:2098
49. Pisani C, Maschio L, Casassa S, Halo M, Schütz M, Usvyat D (2008) J Comput Chem 29:2113
50. Nolan SJ, Gillan MJ, Alfè D, Allan NL, Manby FR (2009) Phys Rev B 80:165109
51. Paier J, Diaconu CV, Scuseria GE, Guidon M, VandeVondele J, Hutter J (2009) Phys Rev B 80:174114
52. Binnie SJ, Nolan SJ, Drummond ND, Alfè D, Allan NL, Manby FR, Gillan MJ (2010) Phys Rev B 82:165431
53. Voloshina E, Usvyat D, Schütz M, Dedkov Y, Paulus B (2011) Phys Chem Chem Phys 13:12041
54. Pisani C, Schütz M, Casassa S, Usvyat D, Maschio L, Lorenz M, Erba A (2012) Phys Chem Chem Phys 14:7615
55. Booth GH, Grüneis A, Kresse G, Alavi A (2013) Nature 493:365
56. Grüneis A (2015) J Chem Phys 143:102817
57. Grüneis A (2015) Phys Rev Lett 115:066402
58. Perdew JP, Schmidt K (2001) In: Van Doren VE, Van Alsenoy K, Geerlings P (eds) Density-functional theory and its applications to materials. American Institute of Physics, Melville
59. Perdew JP (2013) MRS Bull 38:743
60. Perdew JP, Staroverov VN, Tao J, Scuseria GE (2008) Phys Rev A 78:052513
61. Perdew JP, Kurth S, Zupan A, Blaha P (1999) Phys Rev Lett 82:2544; Erratum: (1999) ibid 82:5179
62. De Jong GT, Geerke DP, Diefenbach A, Sola M, Bickelhaupt FM (2005) J Comput Chem 26:1006
63. Sun J, Marsman M, Csonka GI, Ruzsinszky A, Hao P, Kim Y-S, Kresse G, Perdew JP (2011) Phys Rev B 84:035117
64. Sun J, Marsman M, Ruzsinszky A, Kresse G, Perdew JP (2011) Phys Rev B 83:121410
65. Janthon P, Luo SJ, Kozlov SM, Vines F, Limtrakul J, Truhlar DG, Illas F (2014) J Chem Theory Comput 10:3832
66. Maier TM, Boese AD, Sauer J, Wende T, Fagiani M, Asmis KR (2014) J Chem Phys 140:204315
67. Vosko SH, Wilk L, Nusair M (1980) Can J Phys 58:1200
68. Becke AD (1986) J Chem Phys 84:4524
69. Perdew JP, Wang Y (1992) Phys Rev B 45:13244
70. Perdew JP, Burke K, Ernzerhof M (1996) Phys Rev Lett 77:3865; Erratum: (1997) ibid 78:1396
71. Armiento R, Mattsson AE (2005) Phys Rev B 72:085108
72. Mattsson AE, Armiento R (2009) Phys Rev B 79:155101
73. Tao JM, Perdew JP, Staroverov VN, Scuseria GE (2003) Phys Rev Lett 91:146401
74. Perdew JP, Constantin LA (2007) Phys Rev B 75:155109
75. Seidl A, Görling A, Vogl P, Majewski JA, Levy M (1996) Phys Rev B 53:3764
76. Asmis KR, Santambrogio G, Brümmer M, Sauer J (2005) Angew Chem Int Ed 44:3122
77. Paier J, Marsman M, Hummer K, Kresse G, Gerber IC, Ángyán JG (2006) J Chem Phys 124:154709; Erratum: (2006) ibid 125:249901
78. Ramprasad R, Zhu H, Rinke P, Scheffler M (2012) Phys Rev Lett 108:066404
79. Perdew JP, Emzerhof M, Burke K (1996) J Chem Phys 105:9982
80. Zhao Y, Truhlar DG (2006) J Phys Chem A 110:13126
81. Zhao Y, Truhlar DG (2008) Theor Chem Acc 120:215
82. Jaramillo J, Scuseria GE, Ernzerhof M (2003) J Chem Phys 118:1068
83. Arbuznikov AV, Kaupp M (2007) Chem Phys Lett 440:160
84. Haunschild R, Janesko BG, Scuseria GE (2009) J Chem Phys 131:154112
85. Kurth S, Perdew JP (1999) Phys Rev B 59:10461; Erratum: (1999) ibid 60:11212
86. Grüneis A, Marsman M, Harl J, Schimka L, Kresse G (2009) J. Chem. Phys. 131:154115
87. Ren X, Rinke P, Joas C, Scheffler M (2012) J Mater Sci 47:7447
88. Zhao Y, Lynch BJ, Truhlar DG (2004) J Phys Chem A 108:4786
89. Schwabe T, Grimme S (2006) Phys Chem Chem Phys 8:4398
90. Karton A, Tarnopolsky A, Lamere J-F, Schatz GC, Martin JML (2008) J Phys Chem A 112:12868
91. Harris FE, Monkhorst HJ, Freeman DL (1992) Algebraic and diagrammatic methods in Many–Fermion theory. Oxford University Press, New York
92. Niquet YM, Fuchs M, Gonze X (2003) Phys Rev A 68:032507
93. Dobson JF, Gould T (2012) J Phys: Condens Matter 24:073201
94. Harl J, Kresse G (2008) Phys Rev B 77:045136
95. Ren X, Rinke P, Scheffler M (2009) Phys Rev B 80:045402
96. Ma J, Michaelides A, Alfè D, Schimka L, Kresse G, Wang E (2011) Phys Rev B 84:033402
97. Karlicky F, Lazar P, Dubecky M, Otyepka M (2013) J Chem Theory Comput 9:3670
98. Macher M, Klimes J, Franchini C, Kresse G (2014) J Chem Phys 140:084502
99. Bao JL, Yu HS, Duanmu K, Makeev MA, Xu X, Truhlar DG (2015) ACS Catal 5:2070
100. Ren X, Tkatchenko A, Rinke P, Scheffler M (2011) Phys Rev Lett 106:153003
101. Paier J, Ren X, Rinke P, Scuseria GE, Grüneis A, Kresse G, Scheffler M (2012) New J Phys 14:043002
102. Hellgren M, Rohr DR, Gross EKU (2012) J Chem Phys 136:034106
103. Jemai M, Delion DS, Schuck P (2013) Phys Rev C 88:044004
104. Bleiziffer P, Hesselmann A, Görling A (2013) J Chem Phys 139:084113
105. Ngoc Linh N, Colonna N, de Gironcoli S (2014) Phys Rev B 90:045138
106. Moussa JE (2014) J Chem Phys 140:014107
107. Hellgren M, Caruso F, Rohr DR, Ren X, Rubio A, Scheffler M, Rinke P (2015) Phys Rev B 91:165110
108. Bleiziffer P, Krug M, Görling A (2015) J Chem Phys 142:244108
109. Becke AD (1993) J Chem Phys 98:1372
110. Harris J, Jones RO (1974) J Phys F: Met Phys 4:1170
111. Langreth DC, Perdew JP (1977) Phys Rev B 15:2884
112. Dirac PAM (1929) Proc R Soc Lond A 123:714
113. Slater JC (1951) Phys Rev 81:385
114. Becke AD (1993) J Chem Phys 98:5648
115. Becke AD (1988) Phys Rev A 38:3098

116. Perdew JP (1991) In: Ziesche P, Eschrig H (eds) Electronic structure of solids. Akademie, Berlin
117. Lee CT, Yang WT, Parr RG (1988) Phys Rev B 37:785
118. Miehlich B, Savin A, Stoll H, Preuss H (1989) Chem Phys Lett 157:200
119. Stephens PJ, Devlin FJ, Chabalowski CF, Frisch MJ (1994) J Phys Chem 98:11623
120. Kurth S, Perdew JP, Blaha P (1999) Int J Quant Chem 75:889
121. Tao JM, Gori-Giorgi P, Perdew JP, McWeeny R (2001) Phys Rev A 63:032513
122. Caratzoulas S, Knowles PJ (2000) Mol Phys 98:1811
123. Paier J, Marsman M, Kresse G (2007) J Chem Phys 127:024103
124. Pisani C, Apra E, Causa M (1990) Int J Quant Chem 38:395
125. Gross EKU, Runge E (1986) Vielteilchentheorie. Teubner, Stuttgart
126. Ashcroft NW, Mermin ND (1976) Solid state physics. Saunders College Publishing, Orlando
127. Mahan GD (1990) Many-particle physics, 2nd edn. Plenum Press, New York
128. Cora F, Alfredsson M, Mallia G, Middlemiss DS, Mackrodt WC, Dovesi R, Orlando R (2004) The performance of hybrid density functionals in solid state chemistry. In: Kaltsoyannis N, McGrady JE (eds) Principles and applications of density in inorganic chemistry II, pp 171–232
129. Heyd J, Scuseria GE (2004) J Chem Phys 121:1187
130. Stroppa A, Kresse G (2008) New J Phys 10:063020
131. Kohn W (1995) Int J Quant Chem 56:229
132. Resta R (2006) J Chem Phys 124:104104
133. Becke AD (1996) J Chem Phys 104:1040
134. Adamo C, Barone V (1999) J Chem Phys 110:6158
135. Ernzerhof M, Scuseria GE (1999) J Chem Phys 110:5029
136. Leininger T, Stoll H, Werner HJ, Savin A (1997) Chem Phys Lett 275:151
137. Heyd J, Scuseria GE, Ernzerhof M (2003) J Chem Phys 118:8207
138. Ewald PP (1921) Ann Phys 64:253
139. Krukau AV, Vydrov OA, Izmaylov AF, Scuseria GE (2006) J Chem Phys 125:224106
140. Marsman M, Paier J, Stroppa A, Kresse G (2008) J Phys: Condens Matter 20:064201
141. Henderson TM, Paier J, Scuseria GE (2011) Phys Stat Solidi B 248:767
142. Dovesi R, Civalleri B, Orlando R, Roetti C, Saunders VR (2005) Ab initio quantum simulation in solid state chemistry. In: Lipkovitz KB, Thomas RL, Cundari TR (eds) Reviews in computational chemistry. Wiley-VCH, New York, p 1
143. Mackrodt WC, Harrison NM, Saunders VR, Allan NL, Towler MD, Apra E, Dovesi R (1993) Philos Mag A 68:653
144. Towler MD, Allan NL, Harrison NM, Saunders VR, Mackrodt WC, Apra E (1994) Phys Rev B 50:5041
145. Kudin KN, Scuseria GE, Martin RL (2002) Phys Rev Lett 89:266402
146. Frisch MJ, Trucks GW, Schlegel HB, Scuseria GE, Robb MA, Cheeseman JR, Scalmani G, Barone V, Mennucci B, Petersson GA, Nakatsuji H, Caricato M, Li X, Hratchian HP, Izmaylov AF, Bloino J, Zheng G, Sonnenberg JL, Hada M, Ehara M, Toyota K, Fukuda R, Hasegawa J, Ishida M, Nakajima T, Honda Y, Kitao O, Nakai H, Vreven T, Montgomery JA Jr, Peralta JE, Ogliaro F, Bearpark MJ, Heyd J, Brothers EN, Kudin KN, Staroverov VN, Kobayashi R, Normand J, Raghavachari K, Rendell AP, Burant JC, Iyengar SS, Tomasi J, Cossi M, Rega N, Millam NJ, Klene M, Knox JE, Cross JB, Bakken V, Adamo C, Jaramillo J, Gomperts R, Stratmann RE, Yazyev O, Austin AJ, Cammi R, Pomelli C, Ochterski JW, Martin RL, Morokuma K, Zakrzewski VG, Voth GA, Salvador P, Dannenberg JJ, Dapprich S, Daniels AD, Farkas Ö, Foresman JB, Ortiz JV, Cioslowski J, Fox DJ (2009) Gaussian 09, Gaussian 09. Gaussian Inc, Wallingford
147. VandeVondele J, Hutter J (2007) J Chem Phys 127:114105
148. Chalasinski G, Szczesniak MM (2000) Chem Rev 100:4227
149. Boys SF, Bernardi F (1970) Mol Phys 19:553
150. Blum V, Gehrke R, Hanke F, Havu P, Havu V, Ren X, Reuter K, Scheffler M (2009) Comput Phys Commun 180:2175
151. Ren X, Rinke P, Blum V, Wieferink J, Tkatchenko A, Sanfilippo A, Reuter K, Scheffler M (2012) New J Phys 14:053020
152. Tran F, Blaha P, Schwarz K, Novak P (2006) Phys Rev B 74:155108
153. Tran F, Blaha P (2011) Phys Rev B 83:235118
154. Betzinger M, Friedrich C, Blügel S (2010) Phys Rev B 81:195117
155. Friedrich C, Schindlmayr A, Blügel S (2009) Comput Phys Commun 180:347
156. Paier J, Hirschl R, Marsman M, Kresse G (2005) J Chem Phys 122:234102
157. Rostgaard C, Jacobsen KW, Thygesen KS (2010) Phys Rev B 81:085103
158. Yan J, Hummelshoj JS, Norskov JK (2013) Phys Rev B 87:075207
159. Guidon M, Hutter J, VandeVondele J (2010) J Chem Theory Comput 6:2348
160. Giannozzi P, Baroni S, Bonini N, Calandra M, Car R, Cavazzoni C, Ceresoli D, Chiarotti GL, Cococcioni M, Dabo I, Dal Corso A, de Gironcoli S, Fabris S, Fratesi G, Gebauer R, Gerstmann U, Gougoussis C, Kokalj A, Lazzeri M, Martin-Samos L, Marzari N, Mauri F, Mazzarello R, Paolini S, Pasquarello A, Paulatto L, Sbraccia C, Scandolo S, Sclauzero G, Seitsonen AP, Smogunov A, Umari P, Wentzcovitch RM (2009) J Phys Condens Matter 21:395502
161. Alkauskas A, Broqvist P, Pasquarello A (2011) Phys Stat Solidi B 248:775
162. Lee H-Y, Clark SJ, Robertson J (2012) Phys Rev B 86:075209
163. Guo Y, Clark SJ, Robertson J (2014) J Chem Phys 140:054702
164. Guo Y, Clark SJ, Robertson J (2012) J Phys: Condens Matter 24:325504
165. Anisimov VI, Zaanen J, Andersen OK (1991) Phys Rev B 44:943
166. Liechtenstein AI, Anisimov VI, Zaanen J (1995) Phys Rev B 52:R5467
167. Anisimov VI, Aryasetiawan F, Lichtenstein AI (1997) J Phys: Condens Matter 9:767
168. Dudarev SL, Botton GA, Savrasov SY, Humphreys CJ, Sutton AP (1998) Phys Rev B 57:1505
169. Mott NF (1961) Philos. Mag. 6:287
170. Mott NF (1956) Can J Phys 34:1356
171. Mott NF (1949) Proc Phys Soc Lond Sect A 62:416
172. Hubbard J (1964) Proc Phys Soc Lond Sect A 277:237; ibid 281:401
173. Herring C (1966) In: Rado GT, Suhl H (eds) Magnetism. Academic, New York
174. Solovyev IV, Dederichs PH, Anisimov VI (1994) Phys Rev B 50:16861
175. Da Silva JLF, Ganduglia-Pirovano MV, Sauer J, Bayer V, Kresse G (2007) Phys Rev B 75:045121
176. Lutfalla S, Shapovalov V, Bell AT (2011) J Chem Theory Comput 7:2218
177. Hu Z, Li B, Sun X, Metiu H (2011) J Phys Chem C 115:3065
178. Fabris S, Vicario G, Balducci G, de Gironcoli S, Baroni S (2005) J Phys Chem B 109:22860
179. Allen JP, Watson GW (2014) Phys Chem Chem Phys 16:21016
180. Deo G, Wachs IE (1994) J Catal 146:323
181. Wachs IE, Chen Y, Jehng JM, Briand LE, Tanaka T (2003) Catal Today 78:13

182. Beck B, Harth M, Hamilton NG, Carrero C, Uhlrich JJ, Trunschke A, Shaikhutdinov S, Schubert H, Freund H-J, Schlögl R, Sauer J, Schomäcker R (2012) J Catal 296:120
183. Feng T, Vohs JM (2004) J Catal 221:619
184. Ganduglia-Pirovano MV, Popa C, Sauer J, Abbott H, Uhl A, Baron M, Stacchiola D, Bondarchuk O, Shaikhutdinov S, Freund H-J (2010) J Am Chem Soc 132:2345
185. Kim T, Wachs IE (2008) J Catal 255:197
186. Wachs IE (2013) Dalton Trans 42:11762
187. Baron M, Abbott H, Bondarchuk O, Stacchiola D, Uhl A, Shaikhutdinov S, Freund H-J, Popa C, Ganduglia-Pirovano MV, Sauer J (2009) Angew Chem Int Ed 48:8006
188. Penschke C, Paier J, Sauer J (2013) J Phys Chem C 117:5274
189. Popa C, Ganduglia-Pirovano MV, Sauer J (2011) J Phys Chem C 115:7399; Erratum: (2012) ibid 116:18572
190. Kropp T, Paier J, Sauer J (2014) J Am Chem Soc 136:14616
191. Redhead PA (1962) Vacuum 12:203
192. Reuter K, Scheffler M (2001) Phys Rev B 65:035406
193. Fabris S, de Gironcoli S, Baroni S, Vicario G, Balducci G (2005) Phys Rev B 72:237102
194. Paier J, Kropp T, Penschke C, Sauer J (2013) Faraday Discuss 162:233
195. Burow AM, Wende T, Sierka M, Wlodarczyk R, Sauer J, Claes P, Jiang L, Meijer G, Lievens P, Asmis KR (2011) Phys Chem Chem Phys 13:19393
196. Jiang L, Wende T, Claes P, Bhattacharyya S, Sierka M, Meijer G, Lievens P, Sauer J, Asmis KR (2011) J Phys Chem A 115:11187
197. Kropp T, Paier J (2014) J Phys Chem C 118:23690
198. Grimme S (2006) J Comput Chem 27:1787
199. Kerber T, Sierka M, Sauer J (2008) J Comput Chem 29:2088
200. Beste A, Mullins DR, Overbury SH, Harrison RJ (2008) Surf Sci 602:162
201. Capdevila-Cortada M, García-Melchor M, López N (2015) J Catal 327:58
202. Yang C, Bebensee F, Nefedov A, Wöll C, Kropp T, Komissarov L, Penschke C, Moerer R, Paier J, Sauer J (2016) J Catal 336:116
203. Ferrizz RM, Wong GS, Egami T, Vohs JM (2001) Langmuir 17:2464
204. Vohs JM (2013) Chem Rev 113:4136
205. Rozanska X, Fortrie R, Sauer J (2007) J Phys Chem C 111:6041
206. Döbler J, Pritzsche M, Sauer J (2005) J Am Chem Soc 127:10861
207. Noodleman L (1981) J Chem Phys 74:5737
208. Hampel C, Peterson KA, Werner HJ (1992) Chem Phys Lett 190:1
209. Deegan MJO, Knowles PJ (1994) Chem Phys Lett 227:321
210. Haruta M, Kobayashi T, Sano H, Yamada N (1987) Chem Lett 16:405
211. Haruta M, Date M (2001) Appl Catal A Gen 222:427
212. Trovarelli A (2002) Catalysis by ceria and related materials. Catalytic science series, Hutchings, GJ. Imperial College Press, London
213. Fu Q, Saltsburg H, Flytzani-Stephanopoulos M (2003) Science 301:935
214. Rodriguez JA (2011) Catal Today 160:3
215. Haller GL, Resasco DE (1989) Adv Catal 36:173
216. Tauster SJ (1987) Acc Chem Res 20:389
217. Campbell CT (2012) Nat Chem 4:597
218. Vayssilov GN, Lykhach Y, Migani A, Staudt T, Petrova GP, Tsud N, Skala T, Bruix A, Illas F, Prince KC, Matolin V, Neyman KM, Libuda J (2011) Nat Mater 10:310
219. Plata JJ, Marquez AM, Fdez Sanz J (2013) J Phys Chem C 117:25497
220. Hernandez NC, Grau-Crespo R, de Leeuw NH, Sanz JF (2009) Phys Chem Chem Phys 11:5246
221. Chen Y, Hu P, Lee MH, Wang HF (2008) Surf Sci 602:1736
222. Camellone MF, Fabris S (2009) J Am Chem Soc 131:10473
223. Zhang CJ, Michaelides A, Jenkins SJ (2011) Phys Chem Chem Phys 13:22
224. Pan Y, Nilius N, Freund H-J, Paier J, Penschke C, Sauer J (2013) Phys Rev Lett 111:206101; Erratum: (2015) ibid 115:269901
225. Pyykkö P (2004) Angew Chem Int Ed 43:4412
226. Nilius N, Ganduglia-Pirovano MV, Brazdova V, Kulawik M, Sauer J, Freund HJ (2008) Phys Rev Lett 100:096802
227. Sterrer M, Risse T, Pozzoni UM, Giordano L, Heyde M, Rust H-P, Pacchioni G, Freund H-J (2007) Phys Rev Lett 98:096107
228. Kośmider K, Brázdová V, Ganduglia-Pirovano MV, Pérez R (2016) J Phys Chem C 120:927
229. Li H-Y, Wang H-F, Gong X-Q, Guo Y-L, Guo Y, Lu G, Hu P (2009) Phys Rev B 79:193401
230. Ganduglia-Pirovano MV, Da Silva JLF, Sauer J (2009) Phys Rev Lett 102:02610101
231. Branda MM, Castellani NJ, Grau-Crespo R, de Leeuw NH, Hernandez NC, Sanz JF, Neyman KM, Illas F (2009) J Chem Phys 131:094702
232. Pan Y, Cui Y, Stiehler C, Nilius N, Freund HJ (2013) J Phys Chem C 117:21879
233. Holleman AF, Wiberg E (1995) Lehrbuch der Anorganischen Chemie. Walter de Gruyter, Berlin
234. Imada M, Fujimori A, Tokura Y (1998) Rev Mod Phys 70:1039
235. Dernier PD, Marezio M (1970) Phys Rev B 2:3771
236. McWhan DB, Rice TM (1969) Phys Rev Lett 22:887
237. McWhan DB, Rice TM, Remeika JP (1969) Phys Rev Lett 23:1384
238. Held K, Keller G, Eyert V, Vollhardt D, Anisimov VI (2001) Phys Rev Lett 86:5345
239. Lantz G, Hajlaoui M, Papalazarou E, Jacques VLR, Mazzotti A, Marsi M, Lupi S, Amati M, Gregoratti L, Si L, Zhong Z, Held K (2015) Phys Rev Lett 115:236802
240. Surnev S, Ramsey MG, Netzer FP (2003) Prog Surf Sci 73:117
241. Göbke D, Romanyshyn Y, Guimond S, Sturm JM, Kuhlenbeck H, Döbler J, Reinhardt U, Ganduglia-Pirovano MV, Sauer J, Freund HJ (2009) Angew Chem Int Ed 48:3695
242. Feiten FE, Seifert J, Paier J, Kuhlenbeck H, Winter H, Sauer J, Freund H-J (2015) Phys Rev Lett 114:216101
243. Kresse G, Surnev S, Schoiswohl J, Netzer FP (2004) Surf Sci 555:118
244. Todorova TK, Ganduglia-Pirovano MV, Sauer J (2005) J Phys Chem B 109:23523
245. Feiten FE, Kuhlenbeck H, Freund H-J (2015) J Phys Chem C 119:22961
246. Czekaj I, Hermann K, Witko M (2003) Surf Sci 525:33; ibid 545:85
247. Czekaj I, Witko M, Hermann K (2003) Surf Sci 525:46
248. Window AJ, Hentz A, Sheppard DC, Parkinson GS, Woodruff DP, Unterberger W, Noakes TCQ, Bailey P, Ganduglia-Pirovano MV, Sauer J (2012) Surf Sci 606:1716
249. Window AJ, Hentz A, Sheppard DC, Parkinson GS, Niehus H, Ahlbehrendt D, Noakes TCQ, Bailey P, Woodruff DP (2011) Phys Rev Lett 107:016105
250. Wang H, Mellan TA, Grau-Crespo R, Schwingenschlögl U (2014) Chem Phys Lett 608:126
251. Wang Y, Perdew JP (1991) Phys Rev B 44:13298
252. Perdew JP, Chevary JA, Vosko SH, Jackson KA, Pederson MR, Singh DJ, Fiolhais C (1992) Phys Rev B 46:6671; Erratum: (1993) ibid 48:4978
253. Iori F, Gatti M, Rubio A (2012) Phys Rev B 85:115129

254. Cornell RM, Schwertmann U (2004) The iron oxides. Wiley-VCH, Weinheim
255. Schlögl R (2003) Angew Chem Int Ed 42:2004
256. Muan A (1958) Am J Sci 256:171
257. Ketteler G, Weiss W, Ranke W, Schlögl R (2001) Phys Chem Chem Phys 3:1114
258. Noh J, Osman OI, Aziz SG, Winget P, Bredas J-L (2014) Sci Technol Adv Mater 15:044202
259. Lennie AR, Condon NG, Leibsle FM, Murray PW, Thornton G, Vaughan DJ (1996) Phys Rev B 53:10244
260. Li X, Paier J (2016) J Phys Chem C 120:1056
261. Bucko T, Hafner J, Lebègue S, Ángyán JG (2010) J Phys Chem A 114:11814
262. Yu X, Huo C-F, Li Y-W, Wang J, Jiao H (2012) Surf Sci 606:872
263. Leonov I, Yaresko AN, Antonov VN, Korotin MA, Anisimov VI (2004) Phys Rev Lett 93:146404
264. Jeng HT, Guo GY, Huang DJ (2004) Phys Rev Lett 93:156403
265. Dementyev P, Dostert K-H, Ivars-Barceló F, O'Brien CP, Mirabella F, Schauermann S, Li X, Paier J, Sauer J, Freund H-J (2015) Angew Chem Int Ed 54:13942
266. Alecu IM, Zheng JJ, Zhao Y, Truhlar DG (2010) J Chem Theory Comput 6:2872
267. Yu X, Emmez E, Pan Q, Yang B, Pomp S, Kaden WE, Sterrer M, Shaikhutdinov S, Freund H-J, Goikoetxea I, Wlodarczyk R, Sauer J (2016) Phys Chem Chem Phys 18:3755
268. Ugliengo P, Sodupe M, Musso F, Bush IJ, Orlando R, Dovesi R (2008) Adv Mater 20:4579
269. Musso F, Sodupe M, Corno M, Ugliengo P (2009) J Phys Chem C 113:17876
270. Muscat J, Wander A, Harrison NM (2001) Chem Phys Lett 342:397
271. Oba F, Togo A, Tanaka I, Paier J, Kresse G (2008) Phys Rev B 77:245202
272. Di Valentin C, Pacchioni G, Selloni A (2006) Phys Rev Lett 97:166803
273. Kwapien K, Paier J, Sauer J, Geske M, Zavyalova U, Horn R, Schwach P, Trunschke A, Schlögl R (2014) Angew Chem Int Ed 53:8774
274. Furche F, Perdew JP (2006) J Chem Phys 124:044103
275. Heyd J, Peralta JE, Scuseria GE, Martin RL (2005) J Chem Phys 123:174101
276. Rivero P, Moreira IdPR, Scuseria GE, Illas F (2009) Phys Rev B 79:245129
277. Malrieu JP, Caballol R, Calzado CJ, de Graaf C, Guihery N (2014) Chem Rev 114:429
278. Moreira IPR, Illas F (2006) Phys Chem Chem Phys 8:1645
279. Eom T, Lim H-K, Goddard WA III, Kim H (2015) J Phys Chem C 119:556
280. Mullins DR (2015) Surf Sci Rep 70:42
281. Tuller HL, Nowick AS (1979) J Electrochem Soc 126:209
282. Panhans MA, Blumenthal RN (1993) Solid State Ionics 60:279
283. Gorte R (2010) AlChE J. 56:1126
284. Castleton CWM, Kullgren J, Hermansson K (2007) J Chem Phys 127:244704
285. Stoneham AM, Gavartin J, Shluger AL, Kimmel AV, Ramo DM, Ronnow HM, Aeppli G, Renner C (2007) J Phys: Condens Matter 19:255208
286. Deak P, Aradi B, Frauenheim T (2011) Phys Rev B 83:155207
287. Setvin M, Franchini C, Hao X, Schmid M, Janotti A, Kaltak M, Van de Walle CG, Kresse G, Diebold U (2014) Phys Rev Lett 113:086402
288. Graciani J, Marquez AM, Plata JJ, Ortega Y, Hernandez NC, Meyer A, Zicovich-Wilson CM, Sanz JF (2011) J Chem Theory Comput 7:56
289. Erba A, Mahmoud A, Belmonte D, Dovesi R (2014) J Chem Phys 140:124703
290. Knuth F, Carbogno C, Atalla V, Blum V, Scheffler M (2015) Comput Phys Commun 190:33
291. Chevrier VL, Ong SP, Armiento R, Chan MKY, Ceder G (2010) Phys Rev B 82:075122
292. Kübler J (1980) J Magn Magn Mater 20:277
293. Hobbs D, Hafner J, Spisak D (2003) Phys Rev B 68:014407
294. Schimka L, Gaudoin R, Klimes J, Marsman M, Kresse G (2013) Phys Rev B 87:214102
295. Feibelman PJ, Hammer B, Norskov JK, Wagner F, Scheffler M, Stumpf R, Watwe R, Dumesic J (2001) J Phys Chem B 105:4018
296. Schimka L, Harl J, Stroppa A, Grüneis A, Marsman M, Mittendorfer F, Kresse G (2010) Nat Mater 9:741
297. Kresse G, Gil A, Sautet P (2003) Phys Rev B 68:073401
298. Olsen RA, Philipsen PHT, Baerends EJ (2003) J Chem Phys 119:4522
299. Harl J, Kresse G (2009) Phys Rev Lett 103:056401
300. Lazic P, Alaei M, Atodiresei N, Caciuc V, Brako R, Blügel S (2010) Phys Rev B 81:045401
301. Huang C, Pavone M, Carter EA (2011) J Chem Phys 134:154110
302. Sharifzadeh S, Huang P, Carter E (2008) J Phys Chem C 112:4649
303. Scuseria GE, Jimenez-Hoyos CA, Henderson TM, Samanta K, Ellis JK (2011) J Chem Phys 135:124108
304. Tsuchimochi T, Scuseria GE (2011) J Chem Phys 134:064101
305. Held K, Nekrasov IA, Keller G, Eyert V, Blümer N, McMahan AK, Scalettar RT, Pruschke T, Anisimov VI, Vollhardt D (2006) Phys Stat Solidi B 243:2599
306. Eyert V (2011) Phys Rev Lett 107:016401
307. Grau-Crespo R, Wang H, Schwingenschlögl U (2012) Phys Rev B 86:081101
308. Zheng H, Wagner LK (2015) Phys Rev Lett 114:176401
309. Schrön A, Rödl C, Bechstedt F (2010) Phys Rev B 82:165109
310. Paier J, Marsman M, Kresse G (2008) Phys Rev B 78:121201
311. Seo D-H, Urban A, Ceder G (2015) Phys Rev B 92:115118
312. Gerosa M, Bottani CE, Caramella L, Onida G, Di Valentin C, Pacchioni G (2015) Phys Rev B 91:155201
313. Gygi F, Baldereschi A (1986) Phys Rev B 34:4405
314. Onida G, Reining L, Rubio A (2002) Rev Mod Phys 74:601
315. Pacchioni G (2014) Catal Lett 145:80
316. Menendez-Proupin E, Palacios P, Wahnon P, Conesa JC (2014) Phys Rev B 90:045207
317. Hutchinson M, Widom M (2012) Comput Phys Commun 183:1422
318. Orlando R, Delle Piane M, Bush IJ, Ugliengo P, Ferrabone M, Dovesi R (2012) J Comput Chem 33:2276
319. Guidon M, Schiffmann F, Hutter J, VandeVondele J (2008) J Chem Phys 128:214104
320. Scuseria GE, Henderson TM, Sorensen DC (2008) J Chem Phys 129:231101
321. Scuseria GE, Henderson TM, Bulik IW (2013) J Chem Phys 139:104113
322. Kaltak M, Klimes J, Kresse G (2014) Phys Rev B 90:054115
323. Del Ben M, Schuett O, Wentz T, Messmer P, Hutter J, VandeVondele J (2015) Comput Phys Commun 187:120
324. Bechstedt F, Fuchs F, Kresse G (2009) Phys Stat Solidi B 246:1877
325. Fuchs F, Furthmüller J, Bechstedt F, Shishkin M, Kresse G (2007) Phys Rev B 76:115109
326. Wesolowski TA, Warshel A (1993) J Phys Chem 97:8050
327. Ramo DM, Gavartin JL, Shluger AL, Bersuker G (2007) Phys Rev B 75:205336

328. Giordano L, Sushko PV, Pacchioni G, Shluger AL (2007) Phys Rev B 75:024109
329. Müller C, Hermansson K (2009) Surf Sci 603:3329
330. Burow AM, Sierka M, Döbler J, Sauer J (2009) J Chem Phys 130:174710
331. Boese AD, Sauer J (2013) Phys Chem Chem Phys 15:16481
332. Jacob CR, Neugebauer J (2014) WIREs Comput Mol Sci 4:325
333. Libisch F, Huang C, Carter EA (2014) Acc Chem Res 47:2768
334. Goodpaster JD, Barnes TA, Manby FR, Miller TF III (2012) J Chem Phys 137:224113
335. Manby FR, Stella M, Goodpaster JD, Miller TF III (2012) J Chem Theory Comput 8:2564
336. Goodpaster JD, Barnes TA, Manby FR, Miller TF III (2014) J Chem Phys 140:18A507
337. Yu K, Libisch F, Carter EA (2015) J Chem Phys 143:102806
338. Becke AD (2014) J Chem Phys 140:18A301

# P3

https://pubs.acs.org/doi/abs/10.1021/jp400520j

THE JOURNAL OF PHYSICAL CHEMISTRY C

Article

pubs.acs.org/JPCC

# Oligomeric Vanadium Oxide Species Supported on the $CeO_2(111)$ Surface: Structure and Reactivity Studied by Density Functional Theory

Christopher Penschke, Joachim Paier,* and Joachim Sauer

Institut für Chemie, Humboldt-Universität zu Berlin, Unter den Linden 6, 10099 Berlin, Germany

Supporting Information

**ABSTRACT:** We examine $(VO)_k$ and $(VO_2)_k$ ($k$ = 1, 2, 3) species supported on $CeO_2(111)$ by periodic density functional theory as models for ceria-supported vanadia catalysts. We use the PBE functional and correct for onsite Coulomb correlation (PBE+$U$). As reactivity descriptors, we calculate oxygen defect formation and hydrogenation energies. In agreement with experiment, our results suggest that vanadyl-terminated monomers, that is, $VO_2$, represent the most active species. This system has a remarkably low oxygen defect formation energy of 0.84 eV (clean surface: 1.84 eV), and hydrogenation proceeds more exothermic (−1.46 vs −1.07 eV for clean surface). The $VO_2$ dimer, preferring an open, chain-like structure at the $CeO_2(111)$ surface, is the only other system with a similarly high reactivity. The active species are thermodynamically less favored compared with the $VO_2$ trimer, which forms a ring structure and binds solely via vanadium atoms to $CeO_2(111)$. Thus, for this case, relaxation effects are minor. In contrast, the active species bind via oxygen atoms of the $VO_2$ moiety to surface Ce atoms necessitating substantial surface relaxation. Calculated IR vibrational spectra of the supported $VO_2$ monomer and trimer confirm the experimentally observed blue shift of the V═O stretching mode upon aggregation.

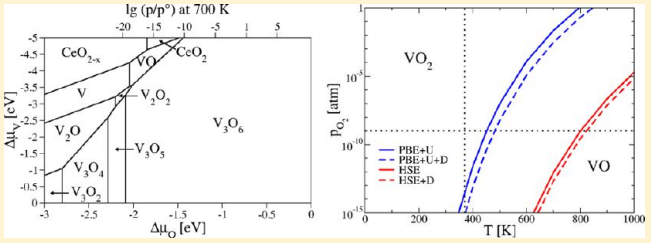


## I. INTRODUCTION

Supported vanadium oxides represent very active and selective catalysts for many reactions of industrial relevance. Important examples are the oxidation of *o*-xylene to phthalic anhydride, the selective catalytic reduction of $NO_x$ with ammonia, and the selective oxidation of methanol to formaldehyde.[1−5] The latter, a frequently studied model system for oxidative dehydrogenation (ODH) reactions, is a way to chemically activate and functionalize C−H bonds.[6] Selectivity of this process is indispensable due to the thermodynamic preference of combustion to $CO_2$ and $H_2O$.

However, activity and selectivity of the vanadium oxide catalyst are driven by several factors. First, they critically depend on the nature of the support material. Reducible oxides such as $TiO_2$ or $CeO_2$ perform significantly better than inert supports like $SiO_2$.[7−11] Note that reducibility of the support material plays a major role because hydrogen transfer, the rate-determining step in the ODH reaction,[12−14] leaves an electron on the supported vanadium oxide catalyst. Second, it is known experimentally that the vanadia catalyst exhibits only high activity when present as submonolayer or monolayer species on the support.[7,15,16]

Depositing vanadia on ceria leads to a particularly active catalytic system.[7,10,11] The high redox activity of ceria is explained by its ease to free and recapture oxygen,[17] but only recently a combined experimental and computational study of $VO{\cdot}CeO_2(111)$ and $VO_2{\cdot}CeO_2(111)$ has shown that this remarkable activity is due to the ability of ceria to easily accommodate electrons in localized Ce-4f orbitals.[12]

Several other studies have also addressed the partial reduction of the V,Ce-mixed metal oxide system.[18−22] Shapovalov and Metiu studied $VO_n$ clusters deposited on the $TiO_2(110)$ and $CeO_2(111)$ surfaces and applied density functional theory (DFT) within the generalized gradient approximation without correcting for onsite Coulomb correlation. They suggested $VO_3/VO_2$ as the active redox couple in oxidation reactions and found almost constant Bader charges for vanadium, which appeared to be insensitive to the support material supplied.[18] For $VO_n$ particles ($n$ = 0, 1) on a $CeO_2(111)$ surface, photoelectron spectroscopy in agreement with DFT+$U$ (i.e., DFT corrected for the Coulomb onsite correlation) demonstrated that vanadium becomes fully oxidized (+5 oxidation state), whereas reduced cerium (+3) is formed.[20] Furthermore, a direct relationship between the morphology of vanadia/ceria and the vanadyl frequency was found. Experimentally a blue shift of the vanadyl stretch frequency of ∼25 $cm^{-1}$ is observed, which could be attributed to the onset of dipole coupling between neighboring V═O groups. Calculation of the DFT harmonic frequencies for the $VO{\cdot}CeO_2(111)$ and $(VO)_3{\cdot}CeO_2(111)$ system could reproduce the blue shift.[20]

**Received:** January 16, 2013
**Revised:** February 12, 2013
**Published:** February 13, 2013

   dx.doi.org/10.1021/jp400520j | *J. Phys. Chem. C* 2013, 117, 5274−5285

DFT+$U$ calculations for crystalline $CeVO_4$ also found that the $Ce_2^{(+3)}O_3{\cdot}V_2^{(+5)}O_5$ form with the reduced Ce is more stable than $Ce^{(+4)}O_2{\cdot}V^{(+4)}O_2$ containing reduced V; that is, the extra electron prefers the Ce-4f states rather than the V-3d states.[19] Similar conclusions have been reached from IR vibrational predissociation experiments combined with hybrid DFT calculations on binary cerium−vanadium oxide gas-phase clusters. These studies have shown that the $Ce^{4+}(f^0)/V^{4+}(d^1)$ pair is more stable when the coordination numbers are high, as in the bulk solids or in aqueous solution, whereas in case of a low coordination of vanadium, the $Ce^{3+}(f^1)/V^{5+}(d^0)$ pair is preferred.[22] Lower coordination numbers for vanadium are found, for example, for vanadium in $CeVO_4$, for vanadia species on ceria supports[21] or for the aforementioned gas-phase clusters.

Popa et al.[21] have systematically studied monomeric $VO_n$ clusters ($n = 1 - 4$) on a $2 \times 2$ surface unit cell of $CeO_2(111)$. They predict $VO_2$ as the most stable species around 700 K in a pressure range from $10^{-1}$ to $10^6$ atm. Moreover, the striking conclusion has been reached that for all of the monomers studied ceria is the reduced component and stabilizes vanadium always in its highest oxidation state +5.

Atomistic understanding of the high activity of low-nuclearity vanadia catalysts on a ceria support for the ODH of alcohols has been generated to some extent;[12,23] however, reactivity studies on the larger aggregations, such as, dimers and trimers, have not been performed yet. Therefore, this work computationally studies structure and reactivity of VO and $VO_2$ monomers, dimers, and trimers deposited on the $CeO_2(111)$ surface. To test for reactivity of the combined $V_nO_m{\cdot}CeO_2(111)$ system, the oxygen defect formation energies in accord with the Mars−van Krevelen mechanism[24,25] have been calculated. The hydrogenation energy, relating to the energy barrier of the rate determining step,[13,14] was determined as well. Because dispersion may be important in reducible oxides,[26] we add to the DFT+$U$ energies and forces a semiempirical $C_6/R^6$ term suggested by Grimme.[27,28] The choice of parameters for Ce is discussed in Section II. In addition, thermodynamic stability of the various vanadium oxide species as a function of the oxygen partial pressure and temperature has been studied by DFT+$U$ combined with statistical thermodynamics. A few selected DFT+$U$ results have been checked by calculations with hybrid functionals including Fock exchange. Moreover, the vibrational spectra of VO and $VO_2$ species, in particular, the blue shift of the vanadyl stretching mode observed upon aggregation, have been investigated.

## II. COMPUTATIONAL DETAILS

**A. Methods.** Calculations were performed using the projector-augmented-wave (PAW) method[29,30] as implemented in the Vienna ab initio simulation package (VASP).[31−33] We take care of corrections for the onsite Coulomb correlation of occupied f orbitals via the DFT+$U$[34,35] approach based on the Perdew−Burke−Ernzerhof (PBE)[36] exchange-correlation functional, that is, PBE+$U$. The spin-polarized calculations employed a Hubbard $U$ parameter of 4.5 eV for the Ce f electrons, which has been calculated self-consistently by Fabris et al.[37] This parameter was successfully applied and tested by Ganduglia-Pirovano et al.[12,21] The plane-wave cutoff was set to 600 eV.

The PAW potential used to describe the electron-ion interaction for Ce comprises 12 valence electrons (Ce: [Xe] $5s^25p^64f^15d^16s^2$). Two partial waves were used for each orbital, and the cutoff radius for the partial waves amounted to 1.5 and 1.65 for 5s and 6s, 1.8 for 5p, 2.3 for 5d, and 2.57 au for the 6f states, respectively. For oxygen and vanadium, 6 ([He] $2s^22p^4$) and 11 ([Mg] $3p^64s^23d^3$) valence electrons were used, respectively. The respective partial wave cutoff radii amount to 1.2 and 1.52 au for 2s and 2p states in oxygen and 2.0, 2.3, and 2.3 au for the p, s, and d states in vanadium. For the 1s orbital of hydrogen, a partial wave cutoff radius of 1.10 au was employed.

Some selected results were obtained using the Heyd−Scuseria−Ernzerhof (HSE)[38] hybrid functional combined with a screening parameter of 0.207 $Å^{-1}$ (cf. ref 39). Structural optimizations were performed until all forces acting on the relaxed atoms were below 0.02 eV/Å. Vibrational frequencies use central differences for the force derivative with atomic displacements of ±0.015 Å. Only vanadium atoms and oxygen atoms bound to vanadium were included to build the partial Hessian, whereas all other atoms were kept fixed. Because of the relatively large unit cell used (see below), the sampling of the Brillouin zone was restricted to the Γ point. Convergence with respect to the plane-wave kinetic energy cutoff and $k$-point sampling was tested by (separate) calculations using a cutoff of 900 eV and a $(2 \times 2 \times 1)$ $k$ mesh. Both parameters affect relative energies by <60 meV.

**B. Models.** The "repeated slab" model for the $CeO_2$ surface was created by cutting the $CeO_2$ bulk cell (fluorite structure) optimized using PBE+$U$ along the (111) plane. A $(4 \times 4)(a_0/\sqrt{2})$ surface unit cell ($a_0$, the equilibrium lattice constant of ceria) with three (O−Ce−O)-trilayers was used consisting of 48 formula units of $CeO_2$. Only the upper two trilayers were allowed to relax, whereas the positions of the atoms in the bottom layer were kept fixed to simulate the bulk. The so-called vacuum layer of the surface unit cell was set to 10 Å. Various $VO_m$ units were deposited on the surface. Different starting structures were created for some of the systems by displacing the atoms of the $VO_m$ species including first two trilayers of the ceria surface randomly by up to 5% of their nearest-neighbor distances. All optimized structures were proved to be minima by the absence of imaginary vibrational frequencies. For consistency reasons, the supported vanadium oxides are labeled $V_nO_m$, with $n$ and $m$ corresponding to the content of the surface cell on V and O atoms in addition to the $CeO_2(111)$ surface. Note that $V_nO_m$ refers to $\{V_nO_m{\cdot}(CeO_2)_{48}\}_{CeO_2(111)}$.

**C. Determination of $C_6$ and $R_0$ Parameters for Ce.** The semiempirical damped $C_6/R^6$ term parametrized by Grimme[27] (so-called DFT-D2 scheme) has been implemented into *VASP* by Kerber et al. employing the Ewald summation technique[28] and by Bučko et al. employing a cutoff radius to the atom-pair interaction.[40] By virtue of careful tests, we found both approaches to give virtually identical results using a cutoff radius of 40 Å. To determine $C_6$ coefficients and the van der Waals radii $R_0$, we performed calculations on electrostatically embedded $Ce^{4+}$ and $Ce^{3+}$ ions following the protocol of Grimme.[27] To avoid rigorous refitting, we stay as closely as possible to the Grimme parameters; that is, $C_6$ and $R_0$ for V, O, and H are not varied, although many careful tests to check appropriateness have been made. This procedure suggested in ref 41 by Tosoni and Sauer for $Mg^{2+}$ yielded similar results for MgO as the approach suggested by Zhang et al.,[42] deriving a $C_6$ of ionic crystals from optical excitation spectra via the Clausius−Mossotti equation. Note that results including


dx.doi.org/10.1021/jp400520j | J. Phys. Chem. C 2013, 117, 5274−5285

dispersion effects are indicated by a "+D" throughout this work. Table 1 summarizes the parameters used in this work.

**Table 1. $C_6$ Parameters (J nm$^6$ mol$^{-1}$) and van der Waals Radii, $R_0$ (pm), Used in This Work**

| | $C_6$ | $R_0$ |
|---|---|---|
| Ce | 20.00 | 186.0 |
| V[a] | 10.80 | 156.2 |
| O[a] | 0.70 | 134.2 |
| H[a] | 0.14 | 100.1 |

[a]Ref 27.

## III. RESULTS AND DISCUSSION

**A. Structures of $\{V_nO_m\cdot(CeO_2)_{48}\}_{CeO_2(111)}$ ($n$ = 1−3; $m$ = $n$,2$n$).** The minimum energy structures of the species considered in this work are shown in Figure 1. As found in previous work,[12,20,21] the dominant structural motif is a slightly distorted vanadate tetrahedron with vanadium in the center, coordinated to four oxygen ligands, three V−O−M bonds (M = V or Ce), and a single vanadyl (V═O) bond. In agreement with experimental results,[20] vanadium accommodates the oxidation state +5, whereas, depending on the number of deposited VO and $VO_2$ units, several surface cerium atoms are reduced to $Ce^{3+}$. The oxidation states are easily ascertained by examining the total spin-density integrated within the atomic spheres determined by the PAW potentials (discrimination between d and f orbitals is possible due to projection of the spin-density on d- and f-type spherical harmonics). Note that one $Ce^{3+}$ cation is created per deposited $VO_2$ unit and three $Ce^{3+}$ cations per VO unit (indicated by dark blue spheres in Figure 1), which results in a large number of different structures. This is due to two factors: (i) different distributions of $Ce^{3+}$ ions among the Ce ions in the topmost layer and (ii) the various alignments of the f-electron spin in $Ce^{3+}$. Whereas there is no guarantee that the energy of optimized structures is minimal with respect to the observed $Ce^{3+}$ localization pattern, performing systematic calculations on each alignment is not feasible. However, test calculations on the $VO_2$ monomer, which used various sites for $Ce^{3+}$, found 310 meV as the maximum total energy difference. Keeping the site of $Ce^{3+}$ fixed but flipping spins of one ore more electrons incurred a maximum variation in the energy of ∼50 meV. We found defective VO as the only case with larger energy differences (discussed below). For consistency reasons, only ferromagnetic, that is, high spin, configurations are considered throughout this work, although in some cases antiferromagnetic alignments are preferred energetically by 40−50 meV. However, the energy differences we are aiming for, that is, defect formation, hydrogenation energy, and so on, are significantly larger than energy changes incurred by different localization patterns of $Ce^{3+}$ and different spin states; hence major trends derived from numerical results are unlikely to be biased.

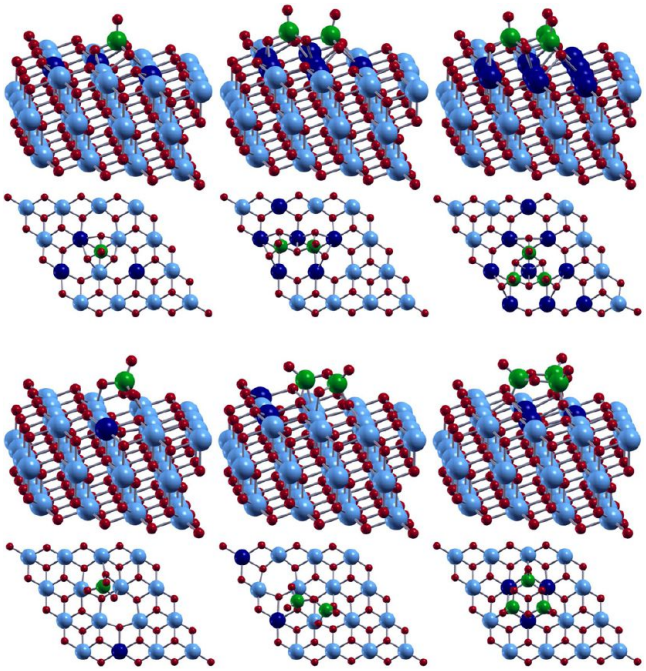

**Figure 1.** Structures of the VO (top) and $VO_2$ species (bottom) on the $CeO_2$(111) surface. The upper panels show the entire slab model used. The lower panels show a top view of the uppermost O−Ce−O layer rotated by 30°. Ce(IV) and Ce(III) cations are shown in light- and dark-blue, respectively. Vanadium and oxygen atoms are green and red, respectively. This color code is used throughout this work. All pictures were generated using the XCrySDen program.[46]

None of the $Ce^{3+}$ ions were found in subsurface positions; that is, it is energetically more favorable for $Ce^{3+}$ to occupy sites in the topmost layer. In most cases, electrons originating from $V_nO_m$ localize close to the adsorbate, that is, in f orbitals of Ce atoms residing in the first or second coordination shell of V. However, the $Ce^{3+}$ created upon adsorption of $VO_2$ and one out of the two $Ce^{3+}$ of the $V_2O_4$ system were found to localize farther away. (See Figure 1.) $Ce^{4+}$ in crystalline $CeO_2$ (bulk) is eight-fold coordinated, whereas in the surface layer of the pristine $CeO_2$(111) surface, cerium ions are seven-fold coordinated. Note that upon oxygen vacancy formation (see refs 43−45), $Ce^{3+}$ in nearest-neighbor position to the oxygen vacancy is six-fold coordinated. This rather low coordination number of cerium may also result upon $V_nO_m$ adsorption. Because of binding of surface oxygen atoms to the adsorbed vanadium and their induced rearrangement, which we denote in this work as *reconstruction*, some of the Ce atoms close to the adsorbate also become six-fold coordinated.

Dimers and trimers of $VO_2$ may form different structure isomers: a ring of alternating V−O−V motifs, also observed in the bulk phase of $V_2O_5$ or its easy cleavage (001) plane, and an open, chain-like structure. For $V_2O_4$, the chain isomer was found to be more stable than the ring by 0.11 eV only (+D: 0.17 eV). Therefore, both isomers of the $VO_2$ dimer were further investigated because they are close in energy. Unless mentioned otherwise, $V_2O_4$ corresponds to the chain structure. For $V_3O_6$, relative stabilities of ring and chain were found to be interchanged; that is, the $VO_2$ trimer in ring configuration is significantly more stable than its chain isomer by 1.74 eV (+D: 1.77 eV). Thus, this work considers only the ring structure of $V_3O_6$ and does not examine its chain-type isomer.

Importantly, the major difference between VO and $VO_2$ systems adsorbed on ceria is the way vanadium atoms are connected to build oligomers. The VO dimer and trimer use surface oxygen atoms for this purpose, whereas vanadium atoms of $V_2O_4$ and $V_3O_6$ are linked by the additional oxygen atoms stemming from the $VO_2$ species. In the $VO_2$ and $V_2O_4$ surface species, one of the "gas-phase $VO_2$" oxygen atoms connects a vanadium to a surface cerium atom, but this oxygen


dx.doi.org/10.1021/jp400520j | J. Phys. Chem. C 2013, 117, 5274−5285

atom is distinct from other anchoring O atoms of the corresponding system by its pronounced vertical displacement from the surface and the shorter V−O bond distance. Bond distances are depicted in Figure 2, whose values amount to 174

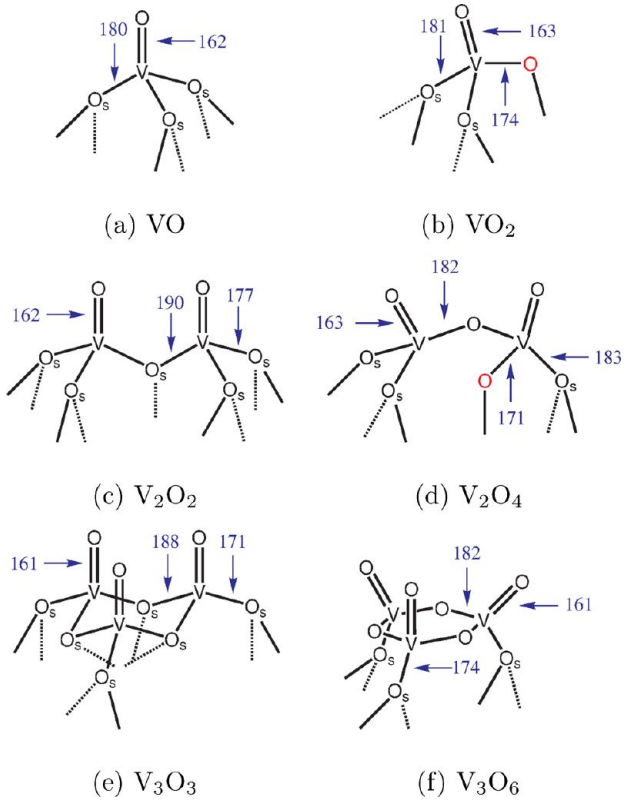


**Figure 2.** Schematic representation of the binding situation of the VO and $VO_2$ species with bond distances in picometers. Average values are given if there are multiple O atoms of one type, for example, anchoring atoms. The "special", anchoring O atom in $VO_2$ and $V_2O_4$ is shown in red.

and 171 pm for the special, "interphase" O atom of $VO_2$ and $V_2O_4$ compared with approximately 181 and 183 pm (on average) for the regular, anchoring ones. The vanadyl bond distance amounts to ∼162 pm (same for VO or $VO_2$ systems) and slightly decreases with increasing nuclearity. In VO oligomers, bonds between V and bridging O atoms (former surface atoms) are longer by 7 pm than corresponding bonds in $VO_2$ oligomers (for which bridging O atoms come from the $VO_2$ species). All structures were reoptimized using the dispersion term, but structural changes incurred by dispersion effects were negligible (smaller than 0.5 pm). Because the vanadium oxide units are strongly bound to the surface, the rather small influence of dispersion effects on bond distances appears to be plausible.

**B. Electronic Structure of Adsorbed $VO_m$ Aggregates.** The orbital projected, local densities of states (PDOS) for $VO_2$ and VO species are shown in Figure 3 and 4, respectively. $VO_2$ and $V_2O_4$-chain exhibit a characteristic peak at approximately −1 eV below the Fermi level compared with the PDOS of the ring-type structures. The largest contribution to the DOS in this region originates from p orbitals of oxygen bound to vanadium, especially the vanadyl O and the "special", anchoring O. These states are shifted to higher energies; that is, they are energetically destabilized compared with the PDOS of $V_2O_4$-ring and $V_3O_6$. As a consequence, the energy gap between O-2p orbitals at the valence band maximum and the occupied Ce-4f orbitals is reduced. The PDOS of VO aggregates on the one hand and $V_2O_4$-ring or $V_3O_6$ on the other hand are quite similar, where aforementioned O-2p states are found at lower energies (see green line in Figure 4) compared with the PDOS of O-2p belonging to the ceria surface. To test if this is an artifact of the PBE+*U* approach, we used the HSE hybrid functional to compute the PDOS of VO and $VO_2$ as well as $V_3O_6$. Although the little peak observed in panel a of Figure 3 vanishes when using HSE, comparing $VO_2$ with $V_3O_6$, the p states of oxygen atoms bound to V are still higher in energy than the p states of surface oxygens. Moreover, occupied Ce-4f states energetically overlap with the aforementioned O-2p states (see panels a and b of Figure 3), whereas for the ring structures, Ce-4f and O-2p states appear to be energetically well-separated. This is also confirmed by the PDOS obtained using the HSE hybrid. Thus, from a chemist's viewpoint, the valence band maximum can be interpreted as the frontier orbitals predominantly involved in chemical reactions; O-2p orbitals of $VO_2$ and $V_2O_4$-chain appear to be prone to be most likely involved in reduction and oxidation processes besides the Ce-4f states.

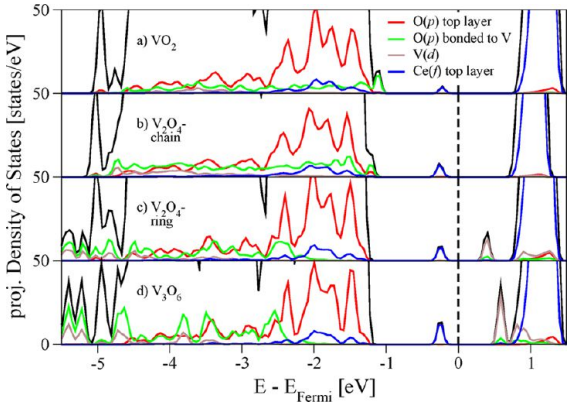


**Figure 3.** Orbital projected density of states (PDOS) of the $VO_2$ species. The dashed line marks the Fermi level.

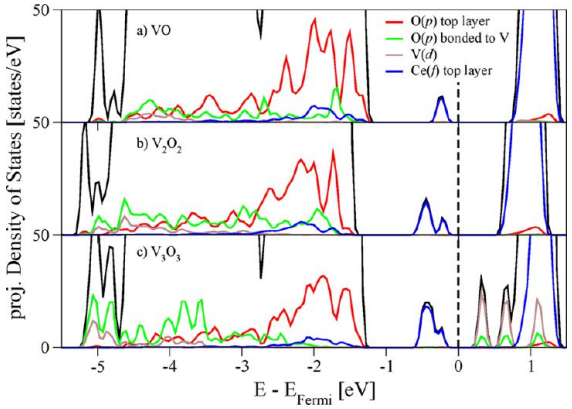


**Figure 4.** Orbital projected density of states (PDOS) of the VO species. The dashed line marks the Fermi level.

**C. Oxygen Defect Formation Energies.** The oxygen defect formation energy, a reactivity descriptor for reactions following the Mars−van Krevelen mechanism,[24,25] was calculated according to eq 1, and actual energies are shown in Table 2.


dx.doi.org/10.1021/jp400520j | J. Phys. Chem. C 2013, 117, 5274−5285

$$\{V_nO_m\cdot(CeO_2)_{48}\} \rightarrow \{V_nO_{m-1}\cdot(CeO_2)_{48}\} + \frac{1}{2}O_2 \quad (1)$$

**Table 2. Oxygen Defect Formation Energies before ($\Delta E_{Def,unrel}$) and after ($\Delta E_{Def}$) Relaxation and Including Dispersion Effects ($\Delta E_{Def}$+D) as well as Relaxation Energy $\Delta E_{Relax}$ in Electronvolts**

| | $\Delta E_{Def,unrel}$ | $\Delta E_{Relax}$ | $\Delta E_{Def}$ | $\Delta E_{Def}$ +D |
|---|---|---|---|---|
| $CeO_2$ | 3.80 | −1.96 | 1.84[a] | 2.00 |
| VO | 3.79 | −1.75 | 2.04[b] | 2.19 |
| $V_2O_2$ | 3.84 | −1.67 | 2.17 | 2.38 |
| $V_3O_3$ | 3.93 | −1.63 | 2.31 | 2.46 |
| $VO_2$ | 3.13[c] | −2.28 | 0.84[d] | 0.91 |
| $V_2O_4$-chain | 3.22 | −2.08 | 1.14 | 1.18 |
| $V_2O_4$-ring | 3.49 | −1.60 | 1.89 | 2.03 |
| $V_3O_6$ | 3.49 | −1.40 | 2.09 | 2.23 |

[a]Ref 21: 1.88 eV. [b]Ref 21: 2.19 eV. [c]Detaching the "special" anchoring O atom, a value of 3.88 eV is obtained. [d]Ref 21: 0.79 eV.

Near-surface oxygen defects in the clean $CeO_2$ surface obtained using a (4 × 4) cell will be discussed in depth in ref 47. In this work (see Table 2), the lowest defect formation energy for $CeO_2$ was 1.84 eV, which increases to 2.00 eV upon correcting for dispersion effects. Surface and subsurface oxygen defects were found to be, within the accuracy of the method used, de facto energetically degenerate. In agreement with previous findings, formation energies are minimal if the electrons left behind localize in Ce-4f states in next-nearest-neighbor position to the oxygen vacancy.[43−45]

For the $V_nO_m$ species studied in this work, the lowest oxygen defect formation energy was obtained for a surface oxygen vacancy close to the adsorbate. Removing an oxygen atom bound to vanadium, which corresponds to a lowering of its coordination number, required significantly more energy and led to a reduction of the vanadium atom due to the localization of the electrons left behind in V-3d states. As an example, the defect formation energy for the "special" anchoring oxygen atom of $VO_2$ is higher by 750 meV compared with the surface oxygen atom if the systems are not allowed to relax. Subsurface vacancies were found to be higher in energy than surface vacancies by at least 480 meV, except for the VO monomer, where the energy difference between surface and subsurface vacancy amounts to ∼200 meV only. In addition, for oxygen defects in VO, the energy differences between different spin-states (comparing high-spin with low-spin solutions) were determined to be as large as 370 meV. Note that this strong coupling of spins in VO is in stark contrast with the clean surface, where ferromagnetic (high-spin) and antiferromagnetic (low-spin) solutions were found to be virtually degenerate (cf. ref 45). Thorough investigations on this issue would lead beyond the scope of the present work, but the rather high DOS of occupied Ce-4f states close to the Fermi level (see Figure 4) compared to remaining systems as well as favorable overlap between the f-states (i.e., slightly broader bands, stronger delocalization) could be possible reasons. However, for the other systems such a strong dependence on the spin state has not been observed and for these systems the most important factor determining the defect formation energy was, whether a surface or a subsurface oxygen atom was removed in order to form the vacancy.

Defect formation in $(VO)_k$ species requires more energy than in the clean $CeO_2(111)$ surface and increases slightly with size. It costs ∼2.0 eV for the monomer and increases stepwise by ∼130 meV for dimer and trimer, respectively. Note that energy lowering induced by relaxation effects is significant. Roughly speaking, the relaxation contribution varies between −1.63 (trimer) and −1.75 (monomer) and adds to the unrelaxed defect formation energy of about 3.8 to 3.9 eV. The dispersion contribution renders defect formation energetically more difficult by ∼150 to 200 meV.

Contrary to the VO oligomers, oxygen defect formation energies in $VO_2$ oligomers vary much more strongly with the degree of aggregation. These species can be subdivided into two groups: (i) monomer and dimer-chain isomer of $VO_2$, whose defect formation energies are remarkably low (0.84 and 1.14 eV), whereas (ii) for the dimer-ring isomer and the trimer, they are about twice as large (1.89 and 2.09 eV). This suggests that $VO_2$ and $V_2O_4$ should be particularly active in Mars−van-Krevelen oxidation reactions.

The different behavior of monomer and chain-dimer of $VO_2$ is due to the very strong relaxation as well as reconstruction effects; see the substantial $\Delta E_{Relax}$ in Table 2. To illustrate this, Figure 5 shows top views on the surface cells of $VO_2$-based

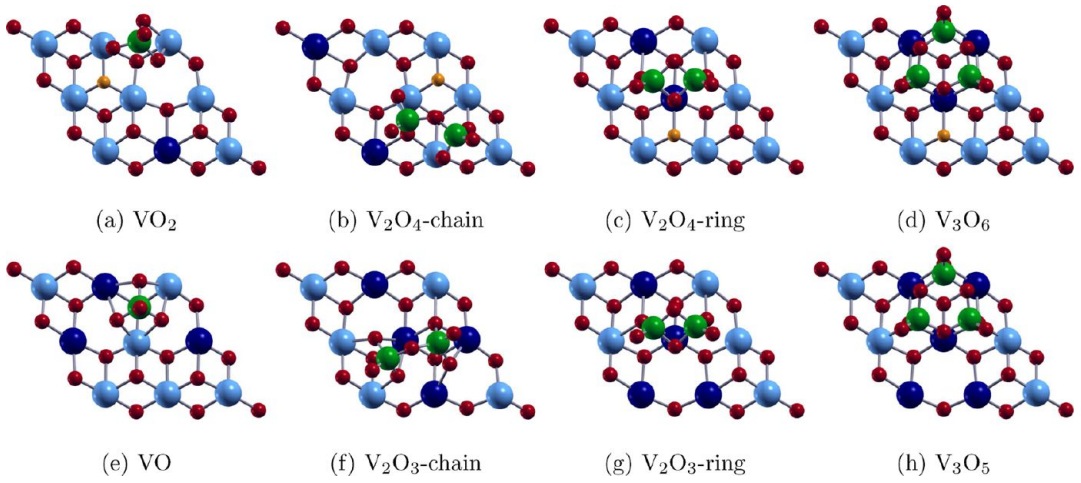


**Figure 5.** Comparison of the adsorbed $VO_2$ species without (upper row) and with (lower row) oxygen vacancy. Only important atoms of the surface unit cell are displayed. Color code as in Figure 1, except for the removed oxygen atom (orange).


dx.doi.org/10.1021/jp400520j | J. Phys. Chem. C 2013, 117, 5274−5285

structures (upper panel) as well as top views on their corresponding defect structures (lower panel). We consider the VO structure (see Figure 1) as the energetically most stable defect associated with $VO_2$; therefore, its energy represents the reference to calculate the defect formation energy of $VO_2$. The Figure clearly shows that upon removing an oxygen atom the ceria surface substantially reorganizes, but simultaneously the tetrahedral coordination of vanadium is preserved. From a different viewpoint, the vanadium oxide adsorbate rearranges to increase the coordination number of the cerium atoms at the vacancy; that is, the "special", anchoring oxygen atom (shown in red in Figure 2) heals the vacancy. As stated above, direct removal of this O atom requires more energy if the defective systems are not relaxed. However, from a purely thermodynamic point of view, both defects should undergo the above-mentioned reconstruction and therefore result in the same product, which means they have the same defect formation energy in the end. The kinetics, that is, the barriers, of these two paths are supposed to be different, though.

Another aspect is the localization of the $Ce^{3+}$, which sit rather compactly underneath the $V_2O_4$- and $V_3O_6$-rings (entirely from gas phase) and therefore only moderately "perturb" the ceria surface structure. Once the oxygen defect is formed, two $Ce^{4+}$ in nearest-neighbor position to the vacancy become reduced to $Ce^{3+}$, but apparently the structure of the ceria support is not much affected. This is in stark contrast with $VO_2$ or the chain isomer of $V_2O_4$. In these cases, minimum energy structures correspond to (at least) one $Ce^{3+}$ site farther away from the adsorbate, inducing rather pronounced relaxation of the support. It appears that the two $Ce^{3+}$ created after oxygen defect formation prefer (i) sites close to the adsorbate and (ii) attempt to aggregate; that is, they prefer to maximize connectivity. This leads to a rather open surface structure for the low nuclearity species of $VO_2$ due to the aforementioned relaxation and reconstruction effects demonstrated in Figure 5. Therefore, the stabilization of O defects in $VO_2$ and $V_2O_4$ is mainly due to the ceria surface, which tries to minimize stress–strain areas as described in ref 45 for the clean $CeO_2(111)$ surface. Thus, one may take the viewpoint of considering the defective systems as nondefective $V_nO_m$ on a defective $CeO_2$ surface instead of $V_nO_{m-1}$ on a pristine $CeO_2$ surface. Overall, taking clean surface, VO, as well as $VO_2$ species into consideration, the defect formation energy increases with an increasing number of $Ce^{3+}$ ions. This trend is reflected in "relaxed" energies and partially also in "unrelaxed" energies. (See Table 2.) It appears that the vanadium oxide units affect reactivity of the entire system in a more indirect way besides the aforementioned reconstruction effects in $VO_2$ and $V_2O_4$-chain.

As observed for VO, the dispersion correction yields larger defect formation energies; however, for $VO_2$ and $V_2O_4$-chain, it is less than half as large as for the remaining systems. Upon inclusion of the correction for dispersion effects, calculations showed that relative defect stabilities are unaltered when different oxygen defect positions are probed.

The oxygen defect formation energies of VO and $VO_2$ are in good agreement with previous results.[21] The differences of 0.05 and −0.15 eV for $VO_2$ and VO, respectively, are mainly due to the smaller surface unit cell (lateral interactions) as well as the smaller cutoff energy employed in ref 21 (400 vs 600 eV used in this work).

**D. Hydrogenation Energies.** Hydrogenation energies of the vanadium oxide aggregates relate to the energy barrier of the rate-determining step of ODH reactions[13,14] and therefore represent, in addition to the oxygen defect formation energies, a complementary descriptor to detect highly active catalysts. The reaction energies were calculated according to

$$\{V_nO_m\cdot(CeO_2)_{48}\} + \frac{1}{2}H_2 \rightarrow \{H\cdot V_nO_m\cdot(CeO_2)_{48}\} \quad (2)$$

and are presented in Table 3. Because of symmetry considerations for the clean $CeO_2(111)$ surface, there is only one distinct surface oxygen atom that may serve as an adsorption site. The corresponding reaction energy for its hydrogenation obtained using PBE+$U$ amounts to −1.07 eV. On passing, we note that hydrogenation of a subsurface oxygen atom in pristine $CeO_2(111)$ is an endothermic process. Remarkably, reaction 2 proceeds thermodynamically most favorable for surface oxygen atoms, whose defect formation energies are minimal. In contrast, hydrogenation of bridging, anchoring, or vanadyl oxygen atoms is generally less favorable by at least 520 meV, except for $VO_2$ and $V_2O_4$. Vanadyl-oxygen hydrogenation of these two species yields values rather close to these for the surface oxygens of the remaining vanadium oxide species, that is, about −1.2 to −1.3 eV.

**Table 3. Hydrogenation Energies without ($\Delta E_H$) and with Dispersion Effects ($\Delta E_H$ +D) in electronvolts**

| | surface O | | vanadyl O | |
|---|---|---|---|---|
| | $\Delta E_H$ | $\Delta E_H$ + D | $\Delta E_H$ | $\Delta E_H$ + D |
| $CeO_2$ | −1.07[a] | −1.11 | | |
| VO | −1.27[b] | −1.30 | −0.75[b] | −0.76 |
| $V_2O_2$ | −1.23 | −1.26 | −0.62 | −0.62 |
| $V_3O_3$ | −1.26 | −1.28 | −0.29 | −0.37 |
| $VO_2$ | −1.46[c] | −1.51 | −1.33[c] | −1.34 |
| $V_2O_4$ chain | −1.55 | −1.56 | −1.23 | −1.19 |
| $V_2O_4$ ring | −1.35 | −1.40 | −0.14 | −0.17 |
| $V_3O_6$ | −1.25 | −1.27 | −0.18 | −0.18 |

[a]Ref 21: −1.21 eV. [b]Ref 21: −1.09 and −0.62 eV for surface and vanadyl O, respectively. [c]Ref 21: −1.33 and −1.45 eV for surface and vanadyl O, respectively.

Contrary to the oxygen defect formation energies, all species, VO- as well as $VO_2$-based, exhibit a lower (more exothermic) hydrogenation energy than the clean $CeO_2(111)$ surface. No simple trends were found when relating hydrogenation energies to the degree of aggregation. This is probably due to the small differences in the reaction energies, especially in the case of $(VO)_k$, where actual values are within the range of the accuracy of the method. However, $VO_2$ and $V_2O_4$ were determined to be the most active species, in accord with findings presented in the previous section. For these two systems, hydrogenation proceeds strongly exothermic and the reaction energies for $VO_2$ and $V_2O_4$ amount to −1.46 and −1.55 eV, respectively. The hydrogenation for $V_3O_6$, that is, $VO_2$ trimer, has been found to be less exothermic by 210 meV compared with the hydrogenation of the monomer. We reiterate that reconstruction, that is, a pronounced reorganization of surface oxygen atoms upon defect formation, drives the system toward lower energies. Comparable effects do not occur in the course of hydrogen adsorption, but instead formation of a hydrogen bond to the special anchoring oxygen atom appears to be responsible for the noticeable stabilization of these structures. This is demonstrated in Figure 6, which shows the orientation of the adsorbed H atom toward the "special" anchoring O atom


dx.doi.org/10.1021/jp400520j | J. Phys. Chem. C 2013, 117, 5274−5285

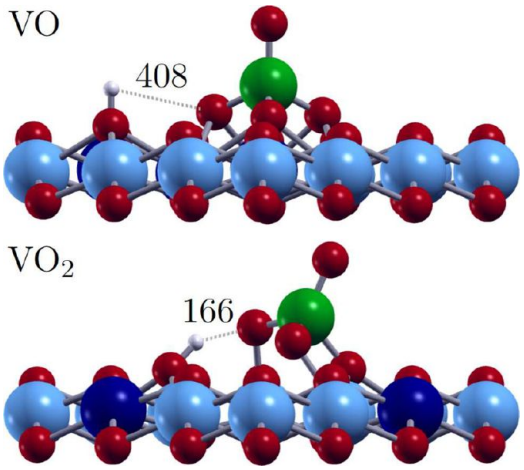


**Figure 6.** Different H-adsorption structures for VO (top) and $VO_2$ (bottom); the latter shows a potential hydrogen bond. Distances in picometers. Color code as in Figure 1 with hydrogen atoms shown in white.

of $VO_2$. The distance between this O atom and the H atom amounts to 166 pm, which is in the range of a typical hydrogen bond, for example, 174 pm for water.[48] These hydrogen bonds cannot be formed for the other systems because the above-mentioned oxygen is unique to $VO_2$ and $V_2O_4$-chain. Note that this applies to the surface oxygen atom only and does not apply to the remainder of potential hydrogen adsorption sites, also showing strongly exothermic hydrogenation. Thus, in addition to structural characteristics like the specially exposed O atom, also a large DOS of destabilized O-p "frontier orbitals" (see Section IIIB) appears to act as a driving force ("donor states"), contributing to the pronounced gain in energy upon hydrogen adsorption.

Hydrogenation of monomeric vanadium oxide units deposited on ceria was also studied in ref 21, predicting the hydrogenation of the clean surface to be thermodynamically more favorable than hydrogenation of VO (−1.21 vs −1.09 eV). Another discrepancy between ref 21 and our findings was spotted for $VO_2$. Whereas the hydrogenation energy (−1.45 eV) agrees well with this work, Popa et al. found the vanadyl-O to be the most stable adsorption site.

We briefly note that upon inclusion of dispersion effects, changes in the energies were determined to be very small. (See Table 3.) Neither the magnitude of energies for the various species studied nor the energetic ordering of adsorption sites are affected. As mentioned in the previous section, relative to the strong chemical bonding between the surface and the hydrogen as well as the vanadium oxide adsorbates, it appears that dispersion effects are too weak to have impact on the thermodynamic energy scale.

To succinctly present the differences in reactivity between the clean ceria surface and the $VO_2$ monomer, Figure 7 shows oxygen defect formation and hydrogenation energies together with the corresponding structures.

**E. Thermodynamic Stability.** This section aims at the identification of thermodynamically relevant vanadium oxide species adsorbed at the $CeO_2(111)$ surface in environments, that is, oxygen partial pressure and vanadium activity, that are typical for the experiments discussed in refs 12 and 20. We follow the common ab initio thermodynamics approaches published in the literature.[49,50]

As a first step, to evaluate relative stabilities of different vanadium oxide aggregates from PBE+$U$ total energies, we calculated corresponding agglomeration energies according to

$$a\{(VO)\cdot(CeO_2)_{48}\} + b\{(VO_2)\cdot(CeO_2)_{48}\} \rightarrow \{(V_{a+b}O_{a+2b})\cdot(CeO_2)_{48}\} + (a+b-1)\{(CeO_2)_{48}\} \quad (3)$$

In addition to the dimerization and trimerization of VO and $VO_2$, we also studied the formation of mixed aggregates using results for the oxygen defective systems. To give an example, VO and $VO_2$ may react to $V_2O_3$, which corresponds to defective $V_2O_4$. We reiterate (see Section IIIC) that $V_nO_m$, supposedly containing an oxygen defect, rather refers to $V_nO_{m+1}$ at the defective $CeO_2$ surface. The shorthand notation $V_nO_m$ solely indicates the cell content of vanadium and oxygen supplementary to the clean ceria surface (labeled as $CeO_2$) and *does not* contain any structural information. For the sake of completeness, we also performed calculations on the $V_3O_4$ system, which corresponds to the $VO_2$ trimer containing two (surface) oxygen vacancies.

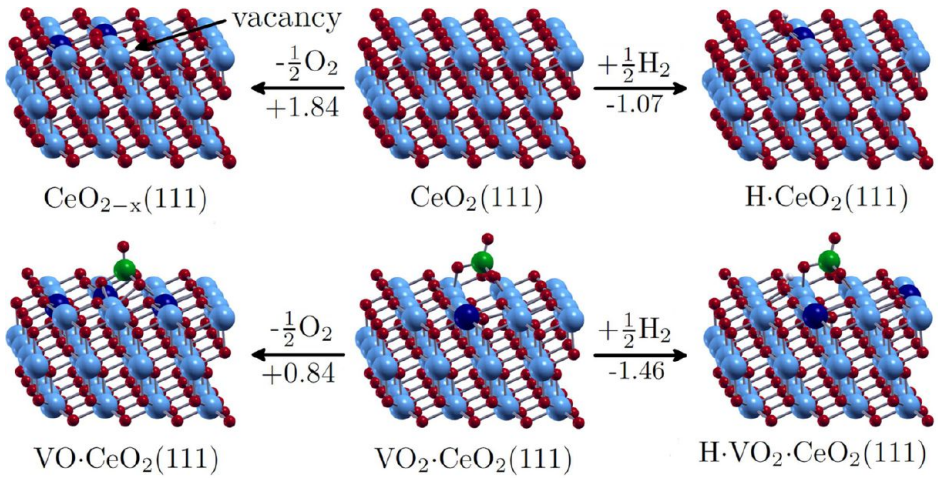


**Figure 7.** Reactivity of the clean $CeO_2(111)$ surface and the supported $VO_2$ system (energies in electronvolts). For details and color code, see Figure 1. Hydrogen atoms are shown in white.


dx.doi.org/10.1021/jp400520j | J. Phys. Chem. C 2013, 117, 5274−5285

Results for the "0 temperature, 0 pressure" agglomeration energies are presented in Table 4. Doubtlessly, the agglomeration of $VO_2$ units is thermodynamically favorable, whereas the agglomeration of VO units refers to a strongly endothermic process. This also holds for the formation of mixed clusters, whose stability increases with the amount of $VO_2$ units involved. Thus, stability is drastically improved by using oxygen atoms exclusively originating from $VO_2$ moieties instead of surface oxygen atoms to connect the vanadium atoms as, for example, in $V_3O_6$. Remarkably, VO and $VO_2$ may aggregate into $V_2O_3$ associated with a near-zero change in the total energy obtained using PBE+*U*. Admittedly, it challenges the overall accuracy of the method employed but at least indicates that the reaction energy is small. Recalling $\Delta G = \Delta H - T\Delta S$, the change in free energy for this reaction may therefore be strongly influenced by the $-T\Delta S$ term. We note that upon inclusion of dispersion effects, the oligomers formed become slightly stabilized.

**Table 4. Agglomeration Energies without ($\Delta E_{Agg}$) And with Dispersion Effects ($\Delta E_{Agg}$ + D) in electronvolts[a]**

| reactants | product | $\Delta E_{Agg}$ | $\Delta E_{Agg}$ + D |
|---|---|---|---|
| 2VO | $V_2O_2$ | 0.91 | 0.84 |
| 3VO | $V_3O_3$ | 3.45 | 3.13 |
| $2VO_2$ | $V_2O_4$ | −0.30 | −0.39 |
| $3VO_2$ | $V_3O_6$ | −1.68 | −1.99 |
| VO + $VO_2$ | $V_2O_3$ | 0.00 | −0.11 |
| 2VO + $VO_2$ | $V_3O_4$ | 1.00 | 0.84 |
| VO + $2VO_2$ | $V_3O_5$ | −0.44 | −0.66 |

[a]Note that in addition to the product presented here pristine surface unit cells are created (see eq 3).

To determine the most stable phases in thermodynamic equilibrium, we constructed a phase diagram using statistical thermodynamics.[51] Because the catalysts used in refs 12 and 20 are prepared via physical vapor deposition of vanadium on the ceria surface in a low-pressure oxygen ambient, the reactants are pristine $CeO_2$, bulk V, and gaseous $O_2$. These phases are supposed to be in equilibrium with the various $V_nO_m$ species. Within this framework, one may consider the stability of different adsorbates on the surface based on the surface free energy (eq 4) as a function of the Gibbs free energy. (For details, see ref 49.) The catalyst may also be synthesized by incipient wetness impregnation, which is a widely used technique.[2,52] In this case, different reactants are involved, and the approach used here would have to be modified. Because this is outside the scope of this article, we refer to a work by Hofmann et al.,[53] who used different reactants for a comparable system (vanadia and water on a zirconia support).

The change in the surface free energy was calculated according to

$$\Delta\gamma = \frac{1}{A}[\Delta E - n\Delta\mu_V - m\Delta\mu_O], \quad \text{with} \tag{4}$$

$$\Delta E = E(\{V_nO_m\cdot(CeO_2)_{48}\}_{CeO_2(111)}) - E(\{(CeO_2)_{48}\}_{CeO_2(111)}) - nE(V) - \frac{m}{2}E(O_2) \tag{5}$$

In eqs 4 and 5, $\Delta\gamma$ equals the variation in the surface free energy, $A$ is the area of the surface unit cell, $n$ and $m$ are the number of vanadium and oxygen atoms added to the surface, and $\mu_V$ and $\mu_O$ are the respective chemical potentials of vanadium and oxygen.

The dependence of eq 4 on the vanadium bulk chemical potential, $\mu_V(T, a_V)$, enters via

$$\Delta\mu_V = \mu_V(T, a_V) - E(V)$$

where $E(V)$ equals a carefully converged PBE total energy for metallic vanadium in the bcc (ground-state) crystal structure, and $a_V$ is the activity of vanadium in the bulk phase. Assuming oxygen as an ideal gas, the oxygen chemical potential depending on $p_{O_2}$, the partial pressure of oxygen, reads as

$$\Delta\mu_O = \frac{1}{2}[\mu_{O_2}(T, p_{O_2}) - E(O_2)] = \frac{1}{2}\left[H(T, p^\circ) - H(0K, p^\circ) - TS(T, p^\circ) + RT\ln\left(\frac{p_{O_2}}{p^\circ}\right)\right] \tag{6}$$

Using eq 6 together with tabulated values for the enthalpy and entropy of the $O_2$ molecule,[54] $\Delta\mu_O$ can be readily related to the oxygen partial pressure and the temperature. Entropic contributions from the solid phases and zero-point vibrations were neglected, which has been shown to be a valid approximation.[49] The most stable species, that is, species corresponding to minimal $\Delta\gamma$, was identified as a function of $\Delta\mu_O$ and $\Delta\mu_V$.

The phase diagram of the vanadium oxide aggregations calculated based on the aforementioned approach is shown in Figure 8. $V_3O_6$ dominates the diagram over a wide range of oxygen partial pressure and vanadium activity. At a rather high temperature of 700 K, it is the most stable species for oxygen pressures greater than $10^{-10}$ atm. Importantly, monomers and dimers of $VO_2$, which were identified as the most active phases by virtue of defect formation and hydrogenation energies, are not present in this phase diagram at all, implying lower stability than any of the remaining systems.

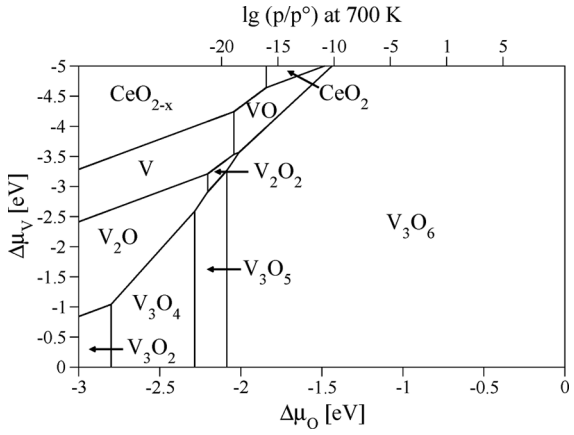


**Figure 8.** Phase diagram of various adsorbed vanadium oxide clusters. The Figure shows the most stable species as a function of $\Delta\mu_V$ and $\Delta\mu_O$. The latter has been translated into an oxygen pressure scale at 700 K.

At first glance, this finding is in contrast with experiment. STM measurements[12,20] conducted at conditions covered by


dx.doi.org/10.1021/jp400520j | J. Phys. Chem. C 2013, 117, 5274−5285

the ranges of oxygen partial pressure and vanadium activity shown in Figure 8 generated firm evidence that monomeric $VO_m$ species exist on the single-crystal ceria surface, but this conflict is easily resolved by taking kinetic effects into account. At low activities, once the vanadium is deposited onto the surface, metastable low-nuclearity vanadia species are formed, and kinetic effects such as very high energy barriers for migration prevent subsequent clustering as preliminary calculations for the $VO_2$ barrier of migration on the ceria surface have shown.[55]

Temperature -programmed desorption (TPD) experiments[12] to study the selective oxidation of methanol found a high activity for the aforementioned $VO_m$ monomers, indicated by a low-temperature formaldehyde desorption peak at 370 K and an oxygen pressure of $10^{-9}$ atm. To discriminate between VO and $VO_2$ under these conditions, the relative stability was computed using PBE+$U$ as well as HSE including the correction for dispersion effects. Figure 9 shows the resulting

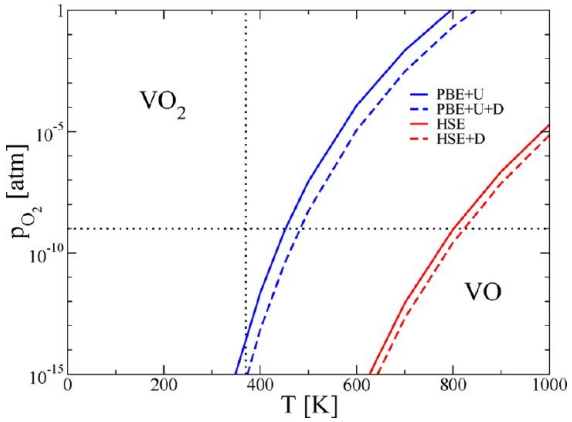


**Figure 9.** Phase diagram of VO and $VO_2$ monomers as a function of temperature $T$ and oxygen pressure $p_{O_2}$. The black dotted lines mark the experimental oxygen pressure and the corresponding formaldehyde desorption temperature at low vanadia coverage, that is, $10^{-9}$ atm and 370 K. (See ref 12.)

two-component phase diagram depending on temperature and oxygen pressure for the decomposition of $VO_2$ following $VO_2 \rightarrow VO + (1/2)O_2$, which is considered to be in thermodynamic equilibrium. According to PBE+$U$, $VO_2$ is the favored species below 450 K at the oxygen pressure of $10^{-9}$ atm. Upon inclusion of dispersion effects, this temperature is only moderately increased to 480 K due to the only moderate increase in the defect formation energy (see Table 2) by ~70 meV. To counter-check PBE+$U$, we repeated the above-mentioned calculations using the HSE hybrid functional. Because the defect formation energy for $VO_2$ obtained using HSE amounts to 1.57 eV, which is almost twice as large as the corresponding value obtained using PBE+$U$, the inferred transition temperature is much larger. Again, dispersion induces only a moderate shift toward a higher temperature. Notwithstanding the significant numerical discrepancy between PBE+$U$ and HSE results, however, they *consistently* suggest $VO_2$ to be the favored species under experimental conditions. On the basis of these findings together with results presented in previous sections, it appears that the $VO_2$ monomers are largely responsible for the low-temperature TPD peak observed.

We briefly mention previous studies[18] based on the GGA-PW91 functional refraining from a correction for Coulomb onsite correlations. These studies determined the $VO_3$ deposited on $CeO_2(111)$ as a very stable phase. Using PBE+$U$, however, the oxygen defect formation following $VO_3 \rightarrow VO_2 + (1/2)O_2$ amounts to −5 meV and is hence close to zero. Calculations using the HSE hybrid functional support this result, predicting an oxygen defect formation energy of only −20 meV. Upon inclusion of dispersion effects, the reaction becomes slightly endothermic. Thus, our findings predict the $VO_3$ species to be irrelevant by thermodynamic reasons.

**F. Vibrational Analysis.** Calculated IR frequencies for the vanadyl (V═O) stretching vibration, $\nu_{V=O}$, of the thermodynamically most relevant systems are shown in Table 5. (Spectra

**Table 5. Harmonic Frequencies of the V═O Stretching Vibration Given in Inverse Centimeters**

| $\nu_{V=O}$ | calculated | | exp.[20] |
|---|---|---|---|
| VO | 1029[a] | | |
| $VO_2$ | 1023[b] | | 1006 |
| $V_2O_4$-chain | 1015[c] | 1024[d] | |
| $V_2O_4$-ring | 1040[c] | 1058[d] | |
| $V_3O_6$ | 1048[c] | 1061[d] | 1033 |

[a]Ref 21: 1055 $cm^{-1}$. [b]Ref 21: 1046 $cm^{-1}$. [c]Asymmetric mode. [d]Symmetric mode.

are presented in the Supporting Information.) One may subdivide the various $VO_2$ species into two groups: (i) $VO_2$ and $V_2O_4$-chain, featuring the above-mentioned special anchoring O, and (ii) the vanadia clusters $V_2O_4$-ring and $V_3O_6$ featuring the ring motif. As expected, the V═O groups in the oligomers couple into an asymmetric and a symmetric mode. For clusters showing the ring motif, $\nu_{V=O}$ is significantly blue-shifted.

The frequency of the vanadyl stretching vibration has been measured for different vanadia coverages.[20] By increasing the amount of vanadia from 0.3 V atoms/$nm^{-2}$ to 0.7 V atoms/$nm^{-2}$, $\nu_{V=O}$ in the formed vanadia oligomers is blue-shifted from 1006 to 1033 $cm^{-1}$, that is, by 27 $cm^{-1}$, due to the coupling of individual V═O dipoles in larger agglomerates. The images obtained using STM of the single-crystal samples clearly show that predominantly monomeric $VO_x$ species are formed at lower V coverage, whereas trimeric species are mainly created at higher coverage. Hence, comparing $VO_2$ with $V_3O_6$, the computed blue shift (see Table 5) amounts to 25 $cm^{-1}$ in excellent agreement with experiment. However, absolute values for the frequencies obtained using PBE+$U$ overestimate the measured ones by ~16 $cm^{-1}$, but this is a well-known shortcoming of GGA-based functionals and well within expected error bars.

Jiang et al. calculated vibrational frequencies for cationic mixed cerium/vanadium oxide clusters using the B3LYP hybrid functional.[22] Interestingly, cluster **2A** presented in the above-mentioned article closely resembles the structural motif of the supported $V_2O_4$-ring, and cluster **3A** is structurally very similar to the adsorbed monomer. For example, symmetric and asymmetric $\nu_{V=O}$ for the adsorbed $V_2O_4$-ring isomer of 1058 and 1040 $cm^{-1}$, respectively, are in fair agreement with corresponding frequencies of 1040 and 1021 $cm^{-1}$ for the gas-phase cluster **2A**, although differences are due to different functionals as well as finite size effects in the cluster calculation, together with the positive charge applied in the latter. However, the splitting or coupling strength, $\Delta\nu$, agrees perfectly in both cases and amounts to 18 $cm^{-1}$ for the supported cluster and 19


dx.doi.org/10.1021/jp400520j | J. Phys. Chem. C 2013, 117, 5274−5285

$cm^{-1}$ for the gas phase cluster. Note that relative shifts in $\nu_{V=O}$ between monomer and the dimer species were found to agree remarkably well. Gas-phase cluster results predict a $\Delta\nu_{V=O}$ between "monomeric" **3A** and symmetric and asymmetric mode in the **2A** "dimer" of 35 and 16 $cm^{-1}$, respectively. Recalling the values for the adsorbed monomer $VO_2$ and the $V_2O_4$-ring species (see Table 5), $\Delta\nu_{V=O}$ amounts to 35 $cm^{-1}$ for the symmetric mode and 17 $cm^{-1}$ for the asymmetric mode, which is in perfect agreement with the cluster result. Taking the adsorbed VO monomer as a reference, these values would change to 29 $cm^{-1}$ as the relative shift to the symmetric mode and 11 $cm^{-1}$ as the relative shift to the asymmetric mode in $V_2O_4$-ring. Periodic calculations on the ceria supported monomers by Popa et al.[21] found a $\nu_{V=O}$ of 1055 and 1046 $cm^{-1}$ for VO and $VO_2$, respectively. The aforementioned work used more atoms (adsorbate plus first O− Ce− O trilayer) for the calculation of the force constant matrix than this work. This may explain the difference in the frequencies of ∼20 $cm^{-1}$ compared with this work; however, relative shifts are not noticeably affected. (See the discussion of experimentally observed blue shift upon aggregation.) Because the deviation is fairly small in terms of absolute numbers, the reduction of the number of considered atoms, which drastically decreases the computational workload, appears to be fully justified.

## IV. CONCLUSIONS

On the basis of oxygen defect formation energies, VO monomers, dimers, and trimers are significantly less reactive than analogous $VO_2$ aggregations and are even less reactive than the clean ceria surface. The oxygen defect formation energy for the $VO_2$ monomer is lower by 1 eV compared with the clean surface and thus indicates a significantly higher activity. For both types of oligomers, VO as well as $VO_2$, the O defect formation energy increases upon increasing nuclearity, and thus larger aggregations are less reactive. Alterations in hydrogenation energies are less pronounced for VO than for $VO_2$ aggregates; that is, they remain almost constant with increasing nuclearity. For $VO_2$, hydrogenation proceeds more exothermic by 210 meV compared with $VO_2$ trimer, indicating that reactivity decreases with degree of nuclearity, which is in accord with the trend observed for the O defect formation energies. However, the more active (small) species were found to be thermodynamically less favored; that is, there is an inverse proportionality between thermodynamic stability and reactivity. The monomeric vanadium oxide species observed on model catalyst surfaces[12,20] are not the thermodynamically most stable ones. The aggregation to oligomeric species such as $V_3O_6$ is hindered by substantial migration barriers for monomers. The experimentally observed blue shift due to the coupling of dipole moments in V═O bonds "perpendicular" to the surface has been confirmed for $VO_2$ trimerization by the DFT+*U* harmonic frequencies.

## ■ ASSOCIATED CONTENT

### Supporting Information

Concerning the semiempirical dispersion term, details of determination and assessment of $C_6$ and $R_0$ parameters for Ce are provided, and the influence of the global scaling parameter on PBE+*U*+D results is discussed. Vibrational spectra of $V_nO_m$ aggregations are shown. This material is available free of charge via the Internet at http://pubs.acs.org.

## ■ AUTHOR INFORMATION


### Corresponding Author

*E-mail: joachim.paier@chemie.hu-berlin.de.


### Notes

The authors declare no competing financial interest.

## ■ ACKNOWLEDGMENTS

This work was supported by the Deutsche Forschungsgemeinschaft (Sonderforschungsbereich 546, SFB 546). Grants for compute time at the high-performance computer clusters HLRN operated by The North-German Supercomputing Alliance (Berlin, Hannover) and JUROPA operated by the Supercomputer Centre at the Forschungszentrum Jülich are gratefully acknowledged. We thank C. Popa and M. V. Ganduglia-Pirovano for providing preliminary results on the same systems for a smaller cell. We also thank J. Döbler for insightful discussions on various DFT results studying vanadium oxide clusters.

## ■ REFERENCES

(1) Bond, G. C. Preparation and Properties of Vanadia/Titania Monolayer Catalysts . *Appl. Catal., A* **1997**, *157*, 91.
(2) Wachs, I.; Weckhuysen, B. Structure and Reactivity of Surface Vanadium Oxide Species on Oxide Supports. *Appl. Catal., A* **1997**, *157*, 67−90.
(3) Centi, G. Nature of Active Layer in Vanadium Oxide Supported on Titanium Oxide and Control of its Reactivity in the Selective Oxidation and Ammoxidation of Alkylaromatics. *Appl. Catal., A* **1996**, *147*, 267−298.
(4) Blasco, T.; Nieto, J. M. L. Oxidative Dehydrogenation of Short Chain Alkanes on Supported Vanadium Oxide Catalysts. *Appl. Catal., A.* **1997**, *157*, 117−142.
(5) Forzatti, P.; Tronconi, E.; Elmi, A. S.; Busca, G. Methanol Oxidation over Vanadia-based Catalysts. *Appl. Catal., A* **1997**, *157*, 387−408.
(6) Sauer, J. In *Computational Modeling for Homogeneous and Enzymatic Catalysis*; Morokuma, K., Musaev, J., Eds.; Wiley-VCH: Weinheim, Germany, 2008; p 231.
(7) Wachs, I. E. Recent Conceptual Advances in the Catalysis Science of Mixed Metal Oxide Catalytic Materials. *Catal. Today* **2005**, *100*, 79−94.
(8) Bañares, M. A. Supported Metal Oxide and Other Catalysts for Ethane Conversion: A Review. *Catal. Today* **1999**, *51*, 319−348.
(9) Khodakov, A.; Olthof, B.; Bell, A. T.; Iglesia, E. Structure and Catalytic Properties of Supported Vanadium Oxides: Support Effects on Oxidative Dehydrogenation Reactions. *J. Catal.* **1999**, *181*, 205−216.
(10) Dinse, A.; Frank, B.; Hess, C.; Habel, D.; Schomäcker, R. Oxidative Dehydrogenation of Propane over Low-loaded Vanadia Catalysts: Impact of the Support Material on Kinetics and Selectivity. *J. Mol. Catal. A: Chem.* **2008**, *289*, 28−37.
(11) Daniell, W.; Ponchel, A.; Kuba, S.; Anderle, F.; Weingand, T.; Gregory, D.; Knözinger, H. Characterization and Catalytic Behavior of $VO_x$-$CeO_2$ Catalysts for the Oxidative Dehydrogenation of Propane. *Top. Catal.* **2002**, *20*, 65−74.
(12) Ganduglia-Pirovano, M. V.; Popa, C.; Sauer, J.; Abbott, H.; Uhl, A.; Baron, M.; Stacchiola, D.; Bondarchuk, O.; Shaikhutdinov, S.; Freund, H. Role of Ceria in Oxidative Dehydrogenation on Supported Vanadia Catalysts. *J. Am. Chem. Soc.* **2010**, *132*, 2345−2349.
(13) Döbler, J.; Pritzsche, M.; Sauer, J. Oxidation of Methanol to Formaldehyde on Supported Vanadium Oxide Catalysts Compared to Gas Phase Molecules. *J. Am. Chem. Soc.* **2005**, *127*, 10861−10868.
(14) Rozanska, X.; Fortrie, R.; Sauer, J. Oxidative Dehydrogenation of Propane by Monomeric Vanadium Oxide Sites on Silica Support. *J. Phys. Chem. C* **2007**, *111*, 6041−6050.

(15) Feng, T.; Vohs, J. A TPD Study of the Partial Oxidation of Methanol to Formaldehyde on $CeO_2$-Supported Vanadium Oxide. *J. Catal.* **2004**, *221*, 619−629.
(16) Deo, G.; Wachs, I. Reactivity of Supported Vanadium Oxide Catalysts: The Partial Oxidation of Methanol. *J. Catal.* **1994**, *146*, 323−334.
(17) *Catalysis by Ceria and Related Materials*; Trovarelli, A., Hutchings, G. J., Eds.; Catalytic Science Series; Imperial College Press: London, 2002; Vol. 2.
(18) Shapovalov, V.; Metiu, H. $VO_x$ ($x$ = 14) Submonolayers Supported on Rutile $TiO_2$(110) and $CeO_2$(111) Surfaces: The Structure, the Charge of the Atoms, the XPS Spectrum, and the Equilibrium Composition in the Presence of Oxygen. *J. Phys. Chem. C* **2007**, *111*, 14179−14188.
(19) Da Silva, J. L. F.; Ganduglia-Pirovano, M. V.; Sauer, J. Formation of the Cerium Orthovanadate $CeVO_4$: DFT+U Study. *Phys. Rev. B* **2007**, *76*, 125117-1−125117-10.
(20) Baron, M.; Abbott, H.; Bondarchuk, O.; Stacchiola, D.; Uhl, A.; Shaikhutdinov, S.; Freund, H.-J.; Popa, C.; Ganduglia-Pirovano, M. V.; Sauer, J. Resolving the Atomic Structure of Vanadia Monolayer Catalysts: Monomers, Trimers and Oligomers on Ceria. *Angew. Chem., Int. Ed.* **2009**, *48*, 8006−8009.
(21) Popa, C.; Ganduglia-Pirovano, M. V.; Sauer, J. Periodic Density Functional Theory Study of $VO_n$ Species Supported on the $CeO_2$(111) Surface. *J. Phys. Chem. C* **2011**, *115*, 7399−7410; **2012**, *116*, 18572−18573 (Erratum)..
(22) Jiang, L.; Wende, T.; Claes, P.; Bhattacharyya, S.; Sierka, M.; Meijer, G.; Lievens, P.; Sauer, J.; Asmis, K. R. Electron Distribution in Partially Reduced Mixed Metal Oxide Systems: Infrared Spectroscopy of $Ce_mV_nO_o^+$ Gas-Phase Clusters. *J. Phys. Chem. A* **2011**, *115*, 11187−11192.
(23) Beck, B.; Harth, M.; Hamilton, N. G.; Carrero, C.; Uhlrich, J. J.; Trunschke, A.; Shaikhutdinov, S.; Schubert, H.; Freund, H.-J.; Schlögl, R.; Sauer, J.; Schomäcker, R. Partial Oxidation of Ethanol on Vanadia Catalysts on Supporting Oxides with Different Redox Properties Compared to Propane. *J. Catal.* **2012**, *296*, 120−131.
(24) Sauer, J.; Döbler, J. Structure and Reactivity of $V_2O_5$: Bulk Solid, Nanosized Clusters, Species Supported on Silica and Alumina, Cluster Cations and Anions. *Dalton Trans.* **2004**, *19*, 3116−3121.
(25) Kim, H. Y.; Lee, H. M.; Pala, R. G. S.; Shapovalov, V.; Metiu, H. CO Oxidation by Rutile $TiO_2$(110) Doped with V, W, Cr, Mo, and Mn. *J. Phys. Chem. C* **2008**, *112*, 12398−12408.
(26) Conesa, J. C. The Relevance of Dispersion Interactions for the Stability of Oxide Phases. *J. Phys. Chem. C* **2010**, *114*, 22718−22726.
(27) Grimme, S. Semiempirical GGA-type Density Functional Constructed with a Long-Range Dispersion Correction. *J. Comput. Chem.* **2006**, *27*, 1787−1799.
(28) Kerber, T.; Sierka, M.; Sauer, J. Application of Semiempirical Long-range Dispersion Corrections to Periodic Systems in Density Functional Theory. *J. Comput. Chem.* **2008**, *29*, 2088−2097.
(29) Blöchl, P. Projector Augmented-Wave Method. *Phys. Rev. B* **1994**, *50*, 17953−17979.
(30) Kresse, G.; Joubert, D. From Ultrasoft Pseudopotentials to the Projector Augmented-Wave Method. *Phys. Rev. B* **1999**, *59*, 1758−1775.
(31) Kresse, G.; Furthmüller, J. Efficient Iterative Schemes for *Ab Initio* Total-Energy Calculations Using a Plane-Wave Basis Set. *Phys. Rev. B* **1996**, *54*, 11169−11186.
(32) Kresse, G.; Furthmüller, J. Efficiency of Ab-Initio Total Energy Calculations for Metals and Semiconductors Using a Plane-Wave Basis Set. *Comput. Mater. Sci.* **1996**, *6*, 15−50.
(33) Bengone, O.; Alouani, M.; Blöchl, P.; Hugel, J. Implementation of the Projector Augmented-Wave LDA+U Method: Application to the Electronic Structure of NiO. *Phys. Rev. B* **2000**, *62*, 16392−16401.
(34) Anisimov, V. I.; Zaanen, J.; Andersen, O. K. Band Theory and Mott Insulators: Hubbard *U* Instead of Stoner *I*. *Phys. Rev. B* **1991**, *44*, 943−954.
(35) Liechtenstein, A. I.; Anisimov, V. I.; Zaanen, J. Density-Functional Theory and Strong Interactions: Orbital Ordering in Mott-Hubbard Insulators. *Phys. Rev. B* **1995**, *52*, R5467−R5470.
(36) Perdew, J. P.; Burke, K.; Ernzerhof, M. Generalized Gradient Approximation Made Simple. *Phys. Rev. Lett.* **1996**, *77*, 3865−3868; **1997**, *78*, 1396 (Erratum)..
(37) Fabris, S.; deGironcoli, S.; Baroni, S.; Vicario, G.; Balducci, G. Reply to "Comment on 'Taming Multiple Valency with Density Functionals: A Case Study of Defective Ceria'". *Phys. Rev. B* **2005**, *72*, 237102-1−237102-2.
(38) Heyd, J.; Scuseria, G. E. Hybrid Functionals Based on a Screened Coulomb Potential. *J. Chem. Phys.* **2003**, *118*, 8207−8215.
(39) Krukau, A. V.; Vydrov, O. A.; Izmaylov, A. F.; Scuseria, G. E. Influence of the Exchange Screening Parameter on the Performance of Screened Hybrid Functionals. *J. Chem. Phys.* **2006**, *125*, 224106-1−224106-5.
(40) Bučko, T.; Hafner, J.; Lebègue, S.; Ángyán, J. Improved Description of the Structure of Molecular and Layered Crystals: Ab Initio DFT Calculations with van der Waals Corrections. *J. Phys. Chem. A* **2010**, *114*, 11814−11824.
(41) Tosoni, S.; Sauer, J. Accurate Quantum Chemical Energies for the Interaction of Hydrocarbons with Oxide Surfaces: $CH_4$/MgO-(001). *Phys. Chem. Chem. Phys.* **2010**, *12*, 14330−14340.
(42) Zhang, G.; Tkatchenko, A.; Paier, J.; Appel, H.; Scheffler, M. van der Waals Interactions in Ionic and Semiconductor Solids. *Phys. Rev. Lett.* **2011**, *107*, 245501−1−245501−5.
(43) Li, H.-Y.; Wang, H.-F.; Gong, X.-Q.; Guo, Y.-L.; Guo, Y.; Lu, G.; Hu, P. Multiple Configurations of the two Excess 4f Electrons on Defective $CeO_2$(111): Origin and Implications. *Phys. Rev. B* **2009**, *79*, 193401-1−193401-4.
(44) Jerratsch, J.-F.; Shao, X.; Nilius, N.; Freund, H.-J.; Popa, C.; Ganduglia-Pirovano, M.; Burow, A.; Sauer, J. Electron Localization in Defective Ceria Films: A Study with Scanning-Tunneling Microscopy and Density-Functional Theory. *Phys. Rev. Lett.* **2011**, *106*, 246801-1−246801-4.
(45) Ganduglia-Pirovano, M. V.; Da Silva, J. L. F.; Sauer, J. Density-Functional Calculations of the Structure of Near-Surface Oxygen Vacancies and Electron Localization on $CeO_2$(111). *Phys. Rev. Lett.* **2009**, *102*, 026101-1−026101-4.
(46) Kokalj, A. Computer Graphics and Graphical User Interfaces as Tools in Simulations of Matter at the Atomic Scale. *Comput. Mater. Sci.* **2003**, *28*, 155−168.
(47) Paier, J.; Penschke, C.; Sauer, J., in preparation.
(48) Soper, A. K.; Benmore, C. J. Quantum Differences between Heavy and Light Water. *Phys. Rev. Lett.* **2008**, *101*, 065502-1−065502-4.
(49) Reuter, K.; Scheffler, M. Composition, Structure, and Stability of $RuO_2$(110) as a Function of Oxygen Pressure. *Phys. Rev. B* **2001**, *65*, 035406-1−035406-11.
(50) Raybaud, P.; Hafner, J.; Kresse, G.; Kasztelan, S.; Toulhoat, H. Ab Initio Study of the $H_2H_2S/MoS_2$ Gas Solid Interface: The Nature of the Catalytically Active Sites. *J. Catal.* **2000**, *189*, 129−146.
(51) Todorova, T. K.; Ganduglia-Pirovano, M. V.; Sauer, J. Vanadium Oxides on Aluminum Oxide Supports. 1. Surface Termination and Reducibility of Vanadia Films on alpha-$Al_2O_3$(0001). *J. Phys. Chem. B* **2005**, *109*, 23523−23531.
(52) Weckhuysen, B. M.; Keller, D. E. Chemistry, Spectroscopy and the Role of Supported Vanadium Oxides in Heterogeneous Catalysis. *Catal. Today* **2003**, *78*, 25−46.
(53) Hofmann, A.; Ganduglia-Pirovano, M. V.; Sauer, J. Vanadia and Water Coadsorption on Tetragonal Zirconia Surfaces. *J. Phys. Chem. C* **2009**, *113*, 18191−18203.
(54) NIST-JANAF Thermochemical Tables. http://kinetics.nist.gov/janaf/ (accessed February 2012).
(55) Paier, T.; Kropp, C.; Penschke, C.; Sauer, J. Stability and Migration Barriers of Small Vanadium Oxide Clusters on the $CeO_2$(111) Surface Studied by Density Functional Theory. Faraday Discussions: U.K., 2013, accepted.

## NOTE ADDED AFTER ASAP PUBLICATION

This paper was published on the Web on February 27, 2013, with an error to Figure 5. The corrected version was reposted on March 1, 2013.


dx.doi.org/10.1021/jp400520j | J. Phys. Chem. C 2013, 117, 5274−5285

# P4

https://pubs.rsc.org/en/content/articlehtml/2013/fd/c3fd00012e

# Stability and migration barriers of small vanadium oxide clusters on the $CeO_2(111)$ surface studied by density functional theory

**Joachim Paier,* Thomas Kropp, Christopher Penschke and Joachim Sauer**

*Received 12th February 2013, Accepted 26th February 2013*
**DOI: 10.1039/c3fd00012e**



By virtue of periodic density functional theory, we investigate structure and thermodynamic stability of $(VO)_k$ and $(VO_2)_k$ ($k = 1, 2, 3$) clusters deposited on the $CeO_2(111)$ surface, which serve as models for the very active sub-monolayer vanadia catalyst on a ceria support. We find V always completely oxidized (oxidation state +5) and coordinated to four O atoms. As a consequence, $Ce^{4+}$ is (partially) reduced to $Ce^{3+}$. Thus, localized Ce-4*f* states are populated, which requires an onsite U-term (PBE+U) to avoid over-delocalization of *f*-electrons. Importantly, trimers of $VO_2$ were found to be extraordinarily stable (agglomeration energy: −1.68 eV), whereas aggregation of VO species on $CeO_2(111)$ is thermodynamically clearly unfavourable (agglomeration energy: 3.45 eV). As a consequence a large area of the $V_nO_m$ phase diagram (for relevant temperatures) is dominated by the $VO_2$ trimer. The latter is less active towards reduction/oxidation than the active monomer and dimer of $VO_2$, which are not present in the phase diagram at all, although directly observed by recent STM measurements. This suggests that kinetic effects hinder $VO_2$ to grow into larger oligomers. The lowest migration energy barrier we found is as high as 1.95 eV, which indicates that adsorbed monomeric $VO_2$ is "kinetically locked" at low temperatures and explains why monomers are stabilized on the ceria surface.

## Introduction

Supported vanadium oxides represent very active and selective catalysts for many reactions of industrial relevance, as *e.g.* the oxidative dehydrogenation (ODH) of alcohols.[1–5] However, activity and selectivity of the vanadium oxide catalyst is strongly influenced by the rather complex interplay between several factors, most importantly (i) the nature of support material,[3,4,6,7] particularly its reducibility, as well as (ii) loading of the support.[8] On the one hand, reducible supporting oxides, such as ceria, titania, and zirconia exhibit much higher turn-over frequencies for ODH reactions than inert, irreducible oxides, as *e.g.* silica and alumina.[4,7] On the other hand, catalysts with loadings of vanadia corresponding to the so-called monolayer or sub-monolayer surface coverage are pronouncedly more active than crystalline $V_2O_5$ nanoparticles.[8]

For a structural characterization of coexisting monomeric and polymerized vanadia of the aforementioned monolayer species, which wet the support, predominantly Raman and UV/Vis spectroscopy,[3,5,9–12] as well as X-ray absorption spectroscopy have been used.[13,14] Various model systems of vanadia catalysts, as *e.g.* single

*Humboldt-Universität zu Berlin, Institut für Chemie, Unter den Linden 6, 10099 Berlin, Germany. E-mail: joachim.paier@chemie.hu-berlin.de*

crystals,[15,16] thin films,[17–19] and clusters supported on planar metal oxide substrates[20–25] have been extensively studied both experimentally and theoretically.[26–31]

Ceria is an easily reducible support material ideally suited for oxidation reactions following a Mars-van Krevelen mechanism.[32] From a surface science viewpoint, it is also perfectly suited for thin film experiments, since well defined surfaces can be grown on metal substrates.[33,34] The structure and reactivity of vanadia catalysts supported on $CeO_2$(111) has been studied using photoelectron spectroscopy and temperature-programmed desorption (TPD).[23–25] However, these studies could not resolve its atomic structure.

Recently, important structural as well as electronic structure details with respect to monolayer vanadia catalysts supported on ceria were published.[35–38] Employing density functional theory (DFT) combined with experimental results using scanning tunneling microscopy (STM), infrared reflection absorption spectroscopy (IRAS), and X-ray photo emission spectroscopy (XPS), Baron *et al.*[35] showed for the first time that $O{=}V^{5+}O_n$, *i.e.* vanadyl terminated species, are formed on the $CeO_2$(111) surface upon V deposition at various loadings. The nuclearity of vanadia species, which sintered into larger polymers upon annealing to 700 K, could be directly observed by STM and their vibrational properties could be monitored by IRAS.

Upon aggregation, the vanadyl stretching frequency was found to be blue-shifted by approximately 25 $cm^{-1}$ relative to the V=O stretching mode of the monomer. Furthermore, XPS of the vanadia/ceria samples revealed a Ce-4*f* peak indicating vanadium in its highest oxidation state (+5). These findings have been entirely supported by DFT, predicting V or any $VO_n$ species deposited onto $CeO_2$(111) to be stabilized in the +5 oxidation state.[37]

Reactivity towards ODH of methanol of these model catalysts was studied by TPD experiments.[36] At very low loadings of vanadium, at which predominantly monomeric vanadium oxide species were stabilized by $CeO_2$(111), an extraordinary increase of the methanol oxidation activity ("α-peak" at low desorption temperature) could be detected.[36,39] However, this low temperature TPD peak vanishes upon increasing the V loading on the ceria support inducing formation of trimers and larger oligomers. Thus, as mentioned in Ref. 35, reactivity of larger vanadia clusters shows strong similarity to the reactivity of vanadia clusters supported on alumina and silica.[20,22,39] DFT calculations generated clear evidence for a true cooperative effect between catalyst and support: Ceria is accommodating the electrons originating from V in its 4*f* states and vanadia is apparently releasing the oxygen atom, which is energetically more costly in pure ceria. More specifically, it could be shown that structure relaxation effects are largely responsible for the high reactivity, as demonstrated by reactivity descriptors such as oxygen defect formation energy[40] or hydrogenation energy.[41]

A comprehensive theoretical investigation of reactivity trends as a function of size of VO and $VO_2$ oligomers was performed by Penschke *et al.*[38] They confirmed the experimental observations, that larger species, specifically $VO_2$ oligomers, show significantly larger O defect formation energies and gain less energy upon hydrogenation than monomeric $VO_2$ at the $CeO_2$(111) surface. These findings indicate lower reactivity toward ODH reactions. Overall, they could establish (i) a direct relation between thermodynamic stability and nuclearity of the vanadia clusters, and (ii) an inversely proportional relation between stability and activity completely in line with experiment. The authors conjectured that stabilization of $VO_2$ monomers at the ceria surface is due to kinetic effects, *i.e.* large migration barriers, which fits the observation of a kinetically limited growth.[35]

Computation of these barriers, which has not been accomplished up to now, is central aspect of the present work. We will discuss DFT+U results of two migration pathways for monomeric $VO_2$ at the $CeO_2$(111) surface. We found that barriers are very large due to deformation of the very stable $O{=}VO_3$ tetrahedron as well as its reduction upon migration. The conjecture about kinetic effects stabilizing vanadia

 

monomers on ceria has therefore been confirmed by transition state theory (TST) based on DFT+U. Therein neglected temperature effects will certainly modify barrier heights quantitatively, but still we believe that TST provides a qualitatively correct picture.



## Computational details

Computational settings applied in this study follow closely those given in Ref. 38. Calculations were performed using the projector augmented-wave (PAW)[42,43] method as implemented in the Vienna *ab initio* simulation package (VASP).[44,45] We take care of corrections for the onsite Coulomb correlation of occupied f orbitals *via* the DFT+U approach based on the Perdew–Burke–Ernzerhof PBE exchange–correlation functional, *i.e.* PBE+U. The spin-polarized calculations employed a Hubbard U parameter of 4.5 eV for the Ce *f*-electrons. A kinetic energy cutoff of 600 eV for the plane-wave basis set was employed. Structural optimizations (including transition state structures) were performed until maximal forces acting on the relaxed atoms were smaller than 0.02 eV $Å^{-1}$. Vibrational frequencies use central differences for the force derivative with atomic displacements of $\pm 0.015$ Å.

We use a large $p(4 \times 4)$ surface unit cell employing a cell vector of 15.518 Å (lattice constant of 3.879 Å). The cell was cut in [111] orientation from the bulk phase of $CeO_2$ optimized using the PBE+U(4.5) method (see Da Silva *et al.*[46]). The present study uses two different slab models, one consisting of 9 atomic layers ($Ce_{48}O_{96}$) for calculations on thermodynamic stability, and a second one consisting of 6 atomic layers ($Ce_{32}O_{64}$) for the computationally more involved nudged elastic band (NEB) calculations as implemented in VASP following the algorithms discussed in Ref. 47 and 48. Refinement of transition state structures was accomplished by the so-called climbing image method as implemented by Henkelman and coworkers.[49] Sampling of the Brillouin zone was restricted to the Γ point. We use asymmetric slab models, *i.e.* atomic positions of the lowest lying trilayer were fixed in bulk positions. The vacuum layer was set to 10 Å. Careful tests showed that using six instead of nine layers results in an increased absolute value for the $VO_2$ adsorption energy by 0.12 eV only, *i.e.* 2.35%. Structural parameters are virtually identical.

All optimized structures were proved to be minima by the absence of imaginary vibrational frequencies. Similarly, transition state structures were identified by a single imaginary mode as well as by following along the normal mode eigenvector down-hill the internal reaction coordinate. Frequency calculations employ partial Hessians. For consistency reasons, the supported vanadium oxides are labeled $V_nO_m$, with $n$ and $m$ corresponding to the content of the surface cell on V and O atoms *in addition* to the $CeO_2$(111) surface. PBE+U corrected for dispersion effects use the method suggested by Grimme[50,51] (for the van der Waals parameters, *cf.* Ref. 38).

## Results

### Structural details of oligomeric VO and $VO_2$ at $CeO_2$(111)

Most important minimum energy structures of species considered in this work are shown in Fig. 1. As stated in previous work,[35–37] the essential structural motif is a slightly distorted vanadate tetrahedron having the vanadium atom in its center, coordinated to four oxygen ligands, *i.e.* three V–O–M bonds, with M being either V or Ce and a single vanadyl (V═O) bond. Importantly, per VO unit three surface $Ce^{4+}$ are reduced to $Ce^{3+}$, whereas per $VO_2$ only one $Ce^{3+}$ is formed (depicted as dark blue balls in Fig. 1). The influence on the total energy upon varying $Ce^{3+}$ sites at the surface as well as varying spin alignments, *i.e.* ferromagnetic *versus* antiferromagnetic states, was found to be small. For further discussions on this issue we refer

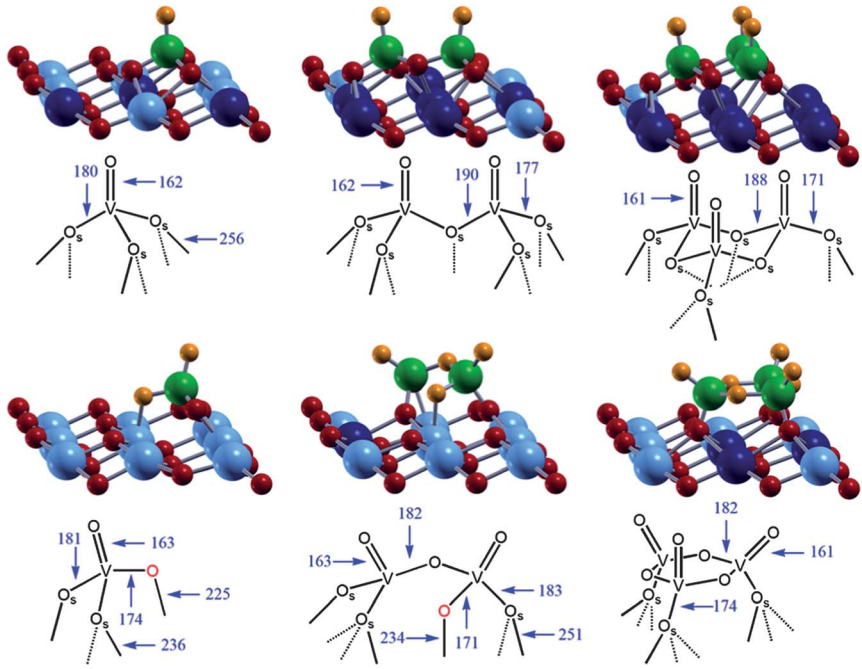


**Fig. 1** Minimum energy structures of VO (top) and $VO_2$ (bottom) species represented as ball and stick models. For clarity reasons, only a (3x3) cut-out of the first O–Ce–O trilayer is shown. Color code: $Ce^{4+}$: light blue; $Ce^{3+}$: dark blue; $V^{5+}$: green; surface $O^{2-}$: red; $O^{2-}$ originating from VO and $VO_2$: orange. Corresponding schematic representations are given below. Bond distances are given in pm. The "special" O atom in $VO_2$ and $V_2O_4$ is highlighted red and "$O_S$" refers to a surface oxygen atom. Ball-stick models were created using XCrysDen.[52]

to Ref. 38, but emphasize that changes in the energy due to the above mentioned effects were estimated to be smaller than 320 meV (= 30 kJ $mol^{-1}$).

Most important difference between VO- and $VO_2$-based systems adsorbed on $CeO_2(111)$ is the way how oligomers are built. The VO dimer and trimer exclusively use surface oxygen atoms for this purpose, whereas vanadium atoms in $V_2O_4$ and $V_3O_6$ are linked by the oxygen atoms of the $VO_2$ moieties. We emphasize the existence of a special, "interphase" oxygen atom in $VO_2$ and $V_2O_4$ distinct to other anchoring oxygen atoms. It connects vanadium to a surface cerium atom with a bond length of 225 pm. This special oxygen atom is vertically displaced from the surface and the associated V–O bond distance of 174 pm is shorter compared to the distance of V to a regular surface O atom (see Fig. 1).

Another structural characteristic of $VO_2$ monomer and dimer is a "pseudo-oxygen-vacancy" formed upon adsorption. The importance of this structural feature was revealed by mechanistic studies on the oxidation of methanol at the $VO_2 \cdot CeO_2(111)$ model catalyst.[53] The pseudo-vacancy is well seen in top-view representations of the surface cell (see M1 in Fig. 6 or Fig. 1 and 5 in Ref. 38). It is not related to the aforementioned special O atom, but results from a regular surface O atom coordinated to V. Upon formation of the $O{=}VO_3$ tetrahedron, the surface O needs to adopt a pronouncedly upraised position relative to the surface, which opens a "hole" in the hexagonal O–Ce–O surface network, which was also found for $V_2O_4$.

Concerning VO oligomers, the $O{=}VO_3$ tetrahedron is located such that V coordinates in hollow position relative to three surface oxygen atoms, which results in a trigonal local symmetry. As a consequence, V is approximately located atop a subsurface oxygen atom. In $V_3O_6$, the gas-phase $VO_2$ ad-species create a hexagonal

 

ring of three O–V (gas-phase) moieties (orange O atoms in Fig. 1), and V atoms directly bind to surface oxygen atoms. In this case no pseudo-vacancy is formed.

Simulations of STM images based on the Tersoff-Hamann[54,55] approximation are presented in Fig. 2. The images probe the occupied valence bands from −2.0 to −0.5 eV with respect to the Fermi level. As depicted in the densities of states (Fig. 3 and 4 in Ref. 38), these states predominantly consist of O-2*p* orbitals.

The images show VO and $VO_2$ units as bright blobs in agreement with experiment (*cf. e.g.* Ref. 35). VO clusters appear slightly smaller than $VO_2$ clusters. This effect is slightly more pronounced for respective dimers. In Fig. 2, surface oxygen atoms emerge as grey blobs, but these details are hardly resolved in experimental images (compare with Fig. 1a in Ref. 35). Note that the dark areas close to $VO_2$ and $V_2O_4$ indicate the above mentioned *missing* surface oxygen atom, which strongly reconstructs in order to coordinate to V, that is, it opens a "pseudo vacancy". Moreover, the experimentally observed distance of spots within trimers approximately equal to the lattice constant of $CeO_2$ is confirmed by the simulation. However, according to Fig. 2, unambiguous discrimination between VO and $VO_2$ species merely based on STM appears hardly possible.

## Thermodynamic stability

Relative stabilities of the various vanadium oxide clusters are obtained using PBE+U as well as dispersion-corrected PBE+U+D total energies. Agglomeration energies are obtained by virtue of eqn (1),

$$a\{VO\cdot(CeO_2)_{48}\} + b\{VO_2\cdot(CeO_2)_{48}\} \rightarrow \{V_{a+b}O_{a+2b}\cdot(CeO_2)_{48}\} + (a + b - 1)\,\{(CeO_2)_{48}\}, \quad (1)$$

and compiled in Table 1. The agglomeration of $VO_2$ units corresponds to an exothermic process and is therefore thermodynamically favourable (dimerization: −0.30 eV; trimerization: −1.68 eV). Correcting for dispersion effects lowers these energies by 90 and 310 meV, respectively. In contrast, agglomeration of VO units

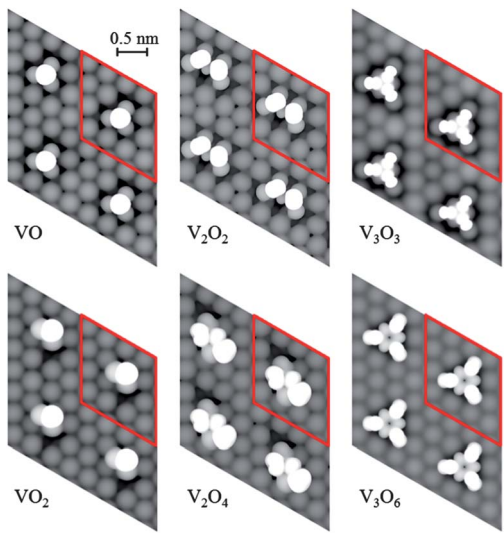


**Fig. 2** Simulated STM images of various adsorbed vanadium oxide clusters. The occupied states between −2 and −0.5 eV with respect to the Fermi level have been probed (mainly O-2*p*). The unit cell is represented by the red frame. The vanadia clusters are seen as bright blobs, whereas surface oxygen atoms emerge as grey blobs.

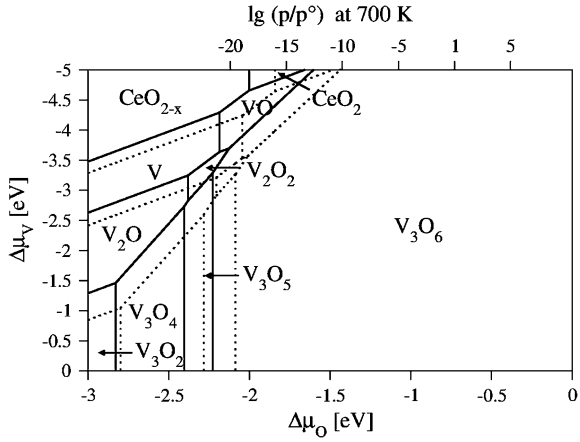


**Fig. 3** Phase diagram of various adsorbed vanadium oxide clusters, calculated with (full lines) and without (dotted lines) dispersion correction. The figure shows the most stable species as a function of $\Delta\mu_V$ and $\Delta\mu_O$, with the latter translated into a pressure scale for $T = 700$ K.

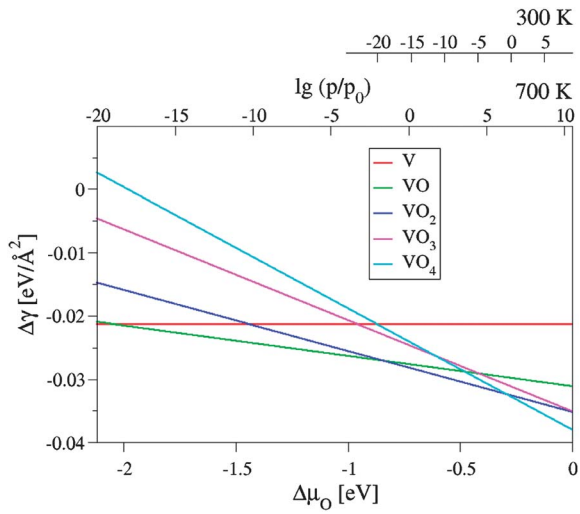


**Fig. 4** Variation in the surface free energy, $\Delta\gamma$, with respect to a varying oxygen chemical potential, $\Delta\mu_O$, for V (red), VO (green), $VO_2$ (blue), $VO_3$ (magenta), and $VO_4$ (cyan) deposited on $CeO_2$(111) using a (4x4) super cell. The scale opposite to the $\Delta\mu_O$-axis represents its translation into the corresponding partial pressure ($p/p_0$ with $p_0 = 1$ atm) at 700 as well as 300 K.

proceeds strongly endothermically. Dimerization requires 0.91 eV, whereas for the trimerization 3.45 eV are needed. Upon adding the correction for dispersion, these energies slightly decrease by 70 and 320 meV, respectively, hence energies decrease to a similar extent compared with dispersion-corrected results for $VO_2$. Sign and magnitude of agglomeration energies of "mixed" VO and $VO_2$ clusters depend on the mixing ratio of respective species. A single VO unit agglomerates with a single $VO_2$ with 0.0 eV as corresponding reaction energy, which decreases by 110 meV, *i.e.* becomes slightly exothermic, upon inclusion of dispersion effects. Depending on whether $VO_2$ or VO prevails, aggregation runs exothermic ($2VO_2$ + VO: −0.44 eV) or endothermic ($VO_2$ + 2VO: 1.00 eV; see Table. 1).

 

**Table 1** Agglomeration energies without ($\Delta E_{Agg}$) and with dispersion effects ($\Delta E_{Agg}$+D) given in eV

| Reactants | Product | $\Delta E_{Agg}$ | $\Delta E_{Agg}$+D |
|---|---|---|---|
| 2 VO | $V_2O_2$ | 0.91 | 0.84 |
| 3 VO | $V_3O_3$ | 3.45 | 3.13 |
| 2 $VO_2$ | $V_2O_4$ | −0.30 | −0.39 |
| 3 $VO_2$ | $V_3O_6$ | −1.68 | −1.99 |
| VO + $VO_2$ | $V_2O_3$ | 0.00 | −0.11 |
| 2 VO + $VO_2$ | $V_3O_4$ | 1.00 | 0.84 |
| VO + 2 $VO_2$ | $V_3O_5$ | −0.44 | −0.66 |

The phase diagram of $V_nO_m$ clusters deposited on $CeO_2$(111) is depicted in Fig. 3. $V_nO_m$ is supposed to be in equilibrium with the pristine surface, V bulk and $O_2$ (in gas phase). Within the framework of "*ab initio* thermodynamics"[56] stability of different adsorbates on a surface is based on the surface free energy, as a function of the Gibbs free energy. The variation of the surface free energy $\Delta\gamma$ is calculated according to

$$\Delta\gamma = \frac{1}{A}\cdot\Big[\Delta E_f - n\cdot\Delta\mu_V(a,T) - m\cdot\Delta\mu_O(p,T)\Big]. \quad (2)$$

$\Delta E_f$ is calculated according to

$$\Delta E_f = E(V_nO_m\cdot CeO_2) - E(CeO_2) - n\cdot E(V) - \frac{m}{2}\cdot E(O_2). \quad (3)$$

Eqn (2) and (3) use A as the area of the surface unit cell, $n$ and $m$ represent the number of vanadium and oxygen atoms added to the surface, $\Delta\mu_V$ and $\Delta\mu_O$ are the respective chemical potentials of vanadium and oxygen relative to the chemical potential at $T = 0$ K. The equations refer to solid V and gas-phase $O_2$. For solid V, the PBE total energy of metallic vanadium (bcc unit cell) was used (see also Ref. 38).

As shown in Fig. 3, $V_3O_6$ is the most stable species over a wide range of oxygen partial pressure and vanadium activity. At 700 K, the annealing temperature used in Ref. 35, $V_3O_6$ is the most stable phase for $p(O_2) > 10^{-10}$ atm. At strongly negative chemical potentials of oxygen, reduced species of $V_3O_6$ (*e.g.* $V_3O_5$ and $V_3O_4$) become more stable. As expected, under UHV (approximately $10^{-11}$ to $10^{-14}$ atm) and very low chemical potentials for V, the clean ceria surface is preferred thermodynamically. Most importantly, the active $VO_2$ species (monomer and dimer) are not visible on the diagram at all. This implies that these species have a significantly lower stability compared to the others. As stated in Ref. 38, correcting for dispersion effects does not incur qualitative changes in terms of relative stability of the $V_nO_m$ phases considered in this work, which is indicated in Fig. 3 by the full lines. However, upon inclusion of dispersion effects, it becomes slightly more difficult to create oxygen defective systems.

We re-visited the stability of the monomeric $VO_n$ ($n = 0 - 4$) species studied by Popa *et al.*[37] using a larger $p(4 \times 4)$ unit cell to study coverage induced effects, *i.e.* possible interactions between the adsorbates (see Fig. 4). We confirm the findings presented in Ref. 37. Interestingly, at low temperatures (see pressure scale for 300 K in Fig. 4) $VO_2$ is the most stable one, whereas for high temperatures its reduced form, VO, gains stability. Formally, at 700 K $VO_2$ is stable within a pressure range of $10^{-1}$ up to $10^{6}$ atm, and hence indicating that $VO_2$ is present under mildly reducing conditions. However, the upper boundary of this range represents very high pressures challenging the ideal gas assumption applied in *ab initio* thermodynamics.

### Migration pathways of $VO_2 \cdot CeO_2(111)$

**Path 1.** NEB calculations for the first migration pathway (M1 – TS2 – M3 – TS4, *cf.* Fig. 5 and 6) investigated in this work start out from the minimum energy structure found for $VO_2$ at the $CeO_2(111)$ surface (see Fig. 1). We will refer to this structure as M1 throughout this work. Relative energies and barriers reported in this section represent energy differences relative to M1.

NEB requires interpolation between two sets of coordinates corresponding to respective minimum energy structures. Therefore, to generate the structure of migrated $VO_2$, M1 was translated along one quarter of a cell vector. By virtue of subsequent NEB calculations, transition state structure TS2 was found. TS2 can be reached upon twisting the $VO_4$ tetrahedron of M1. Importantly, along this mode, it is the special, interphase oxygen, which is detached from the Ce atom. The rotational direction in M1 is indicated by an orange arrow at the special oxygen atom (*cf.* M1 in Fig. 6). The barrier of this step amounts to 0.77 eV (= 74 kJ $mol^{-1}$).

Relaxation of TS2 such that the special oxygen atom could fully re-establish its coordination at the "target" Ce atom yielded the local minimum M3, 0.22 eV (= 21 kJ $mol^{-1}$) higher in energy than M1. This small energy difference is plausible, since M3 is structurally closely related to M1. Upon formation of M3, the pseudo-vacancy as described in previous sections, is closed and re-created at a different position, as easily seen by comparing M1 with M3.

Running NEB on a number of images interpolating between M3 and the translated M1 structure, we found a transition state structure TS4 associated with a barrier of 1.95 eV (= 188 kJ $mol^{-1}$). Its imaginary mode is represented by inversion of the planar O═$VO_2$ moiety while the approaching/detaching surface oxygen atoms oscillate in the surface. Here, vanadium accommodates the oxidation state +4, as monitored by the projected spin-density ($V^{4+}$ coloured dark green in Fig. 6). Starting out from TS4, M1 can be reached by the neighbouring surface oxygen atom coordinating to the $VO_3$ moiety (indicated by orange arrows). This step recreates the pseudo-vacancy. In addition, an analogous local minimum M4 was found, which is similar to gas-phase $VO_3$ or $VO_3^+$, *i.e.* structurally related to an oxygen defective $VO_4$ tetrahedron forming a trigonal pyramid.[57] In TS4 and M4 the bond distance between V and the anchoring surface O is equal to 179 pm and the vanadyl bond is equal to 163 pm. In M4 the bond between V and the special O amounts to 171 pm and is therefore 1 pm shorter compared with the corresponding bond in TS4.

**Path 2.** For the second migration path, M1 was translated along a quarter of the second cell vector. We found a very symmetric transition state structure TS5, corresponding to a barrier of 2.73 eV (= 263 kJ $mol^{-1}$). The mode transforming M1 into TS5 (indicated by a purple arrow in M1) relates to a rocking mode of the $VO_2$ moiety

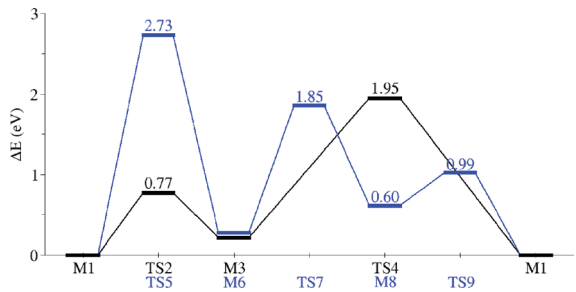


**Fig. 5** Proposed energy profile for two different migration pathways of $VO_2 \cdot CeO_2(111)$. Barrier heights are given in eV. Local minima on the PES are indicated with "M", whereas transition state structures are indicated with "TS".

 

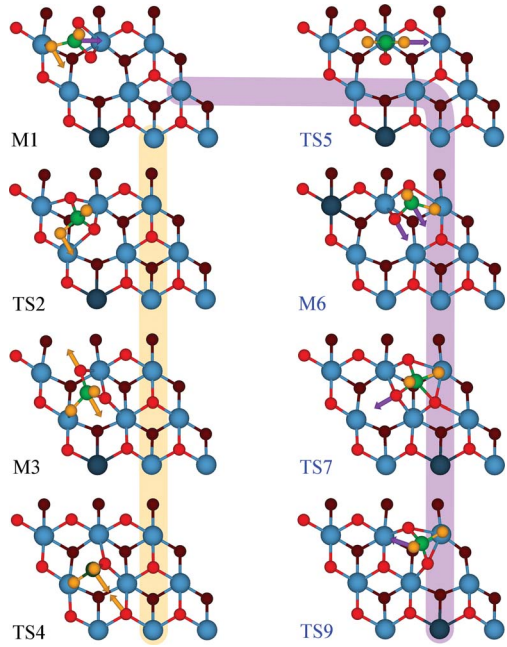


**Fig. 6** Top views of structures corresponding to the proposed migration pathways depicted in Fig. 5. Arrows (orange: pathway 1; purple pathway 2) indicate the direction of atomic motion creating the ensuing stationary point. Colour code similar to Fig. 1, except for $V^{4+}$ (dark green). Subsurface oxygen is shown in dark red and surface oxygen is shown in red. Ball-stick models were created using VESTA.[58]

(originally from gas phase). TS5 is reached by detaching the special anchoring O from Ce and a simultaneous flip of the vanadyl O atom towards the surface. In TS5, both aforementioned O atoms adopt a bond distance to V of 163 pm and can therefore be identified as V=O bonds. The O=V=O bond angle amounts to 110°. In fact, the species can be viewed as a (closed-shell) $VO_3^-$ (two vanadyl O, $V^{5+}$, $O^{2-}$ as anchoring oxygen). The corresponding imaginary mode consists of a rocking motion of the O=V=O group and simultaneous "asymmetric" movements of two surface O atoms underneath. When O=V=O tilts towards the surface, the nearby O approaches the V atom, while the other one moves back into the surface.

Upon relaxation of TS5, one of the vanadyl oxygen atoms coordinates to cerium, which re-establishes the $VO_4$ tetrahedron adopting the local minimum structure M6, 0.28 eV (= 27 kJ $mol^{-1}$) higher in energy than M1. Note that the site of $Ce^{3+}$ is altered compared to previous structures, but extensive test calculations showed that therefrom incurred variations in the total energy are small.[38] The tetrahedron moves along the surface as indicated by purple arrows. In addition, the $VO_4$ tetrahedron deforms, opening an additional coordination site at the V nucleus. A surface O atom binds to V creating the O=$VO_4$ motif of TS7 (fivefold coordinated V), resulting in a barrier of 1.58 eV (= 152 kJ $mol^{-1}$). It is noteworthy that the coordination pattern of V in TS7 is akin to the situation in solid $V_2O_5$, resulting in very similar V–O bond distances. The associated imaginary mode is represented by an asymmetric stretching motion of O–V–O, whereas the first O heals (see purple arrow in TS7) and the second one re-opens a pseudo-vacancy.

Relaxation of TS7 drives the system into M8, 0.60 eV (= 58 kJ $mol^{-1}$) higher in energy than M1. The rocking motion transforming M8 into M1 essentially preserves the structure of the $VO_4$ tetrahedron and is, therefore, only associated with a small barrier of 0.33 eV (= 32 kJ $mol^{-1}$). For this step the special oxygen detaches from the

Ce atom restoring V=O, whereas the former vanadyl oxygen coordinates to a neighbouring Ce atom, thereby re-creating the special, "interphase" oxygen atom (purple arrow in M8).

## Discussion

Based on the aforementioned findings, a rather clear-cut picture can be drawn. VO and $VO_2$ adsorb on the $CeO_2(111)$ surface such that V=O bonds are formed pointing away from the surface. Speaking in terms of a growth mode, $VO_2$ behaves distinctly from VO. Additional VO species just occupy a neighbouring trigonal surface oxygen hollow site. Thus, growing occurs rather regularly by placing one VO next to another. V=O bonds are oriented rather perpendicularly to the surface forming a flat sub-monolayer. In larger $VO_2$ units, connectivity changes qualitatively upon growth. The dimer shows a structurally similar characteristic compared with the monomer. Specifically it forms a rather open, chain-like structure, featuring a special oxygen atom as well as a pronouncedly lifted surface oxygen atom bound to V. The strong reorientation of the O atom, which binds to the V nucleus, opens a "pseudo-oxygen vacancy", and perturbs the regular Ce–O surface network significantly. However, for $V_3O_6$, the situation is entirely different. It is built from three gas-phase $VO_2$ units creating a ring with V atoms bridged by gas-phase oxygen atoms. None of the oxygen atoms coordinates to a surface Ce atom, as found for the monomer and the dimer. $V_3O_6$ binds *via* vanadium atoms to three surface oxygen atoms. As a consequence none of them needs to reorient or relax, *i.e.* the regular Ce–O network is largely preserved, and no pseudo-vacancies are formed. Although V=O bonds in $V_3O_6$ are rather tilted towards the surface, still it adopts a flat ring structure at the $CeO_2(111)$ surface. This flat growth mode of vanadia oligomers on the ceria surface was observed experimentally according to the apparent heights detected by STM for higher V coverage at $CeO_2(111)$.[35] Thus, our PBE+U results completely support this observation.

The experimentally observed blue-shift of the IR active vanadyl stretching frequency upon formation of larger $VO_n$ aggregations was studied by DFT for VO oligomers in Ref. 35 and for $VO_2$ oligomers in Ref. 38. Both calculated shifts, comparing VO and $VO_2$ monomers with respective trimers, fit very well to the observed value of 27 $cm^{-1}$, and hence based on the IR frequencies only, discrimination between VO and $VO_2$ is not possible.

However, larger VO and $VO_2$ species are very distinct in terms of stability. While aggregation of $VO_2$ moieties runs strongly exothermic, the aggregation of VO is thermodynamically not beneficial. Thus, as presented in Table. 1, DFT predicts deposited $VO_2$ to aggregate into very stable trimers, dominating the phase diagram for not too negative vanadium chemical potentials and for oxygen partial pressures greater than $10^{-11}$ atm (UHV) at elevated temperatures (700 K, the temperature applied to sinter vanadium oxide on $CeO_2(111)$, *cf.* Ref. 35).

However, as discussed by Penschke *et al.* in Ref. 38, the penalty for such a high stability of $V_3O_6$ is a loss in activity, which was also observed by TPD.[36] Our previous studies on activity clearly indicate that the $VO_2$ monomer and dimer are particularly active towards O defect formation and hydrogenation, a finding exactly matching the aforementioned TPD experiment. By virtue of STM applied to the catalyst at low coverage, monomers and dimers were observed as the predominant species, whereas for higher coverages larger oligomers, *e.g.* trimers and heptamers could be detected. A distinction between monomers and trimers can be easily made, since monomers appear as bright blobs, whereas trimers appear as trefoils, *i.e.* bright blobs in three-fold symmetry. The simulated STM images presented in this work perfectly agree with the observation (see Fig. 2).

The active $VO_2$ species (monomer and dimer), although observed experimentally, do not appear in the phase diagram at all. This is explained by kinetic effects, *i.e.* large migration barriers of $VO_2$. Two distinct migration pathways of a $VO_2$



 

monomer at the $CeO_2(111)$ surface were studied by means of NEB. Indeed, we were successful in locating required transition state structures and local minima, and we found extraordinarily high barriers preventing $VO_2$ to migrate and hence to dimerize, trimerize *etc.*

The first pathway investigated follows a two-step mechanism: (i) the $VO_4$ tetrahedron moves rather rigidly preserving its coordination sphere and the "special" O binds to a different surface Ce ion. Note that along this pathway the (previous) special oxygen atom remains always coordinated to V. This step is associated with a lower barrier of 0.77 eV. (ii) Subsequent stepwise substitution (O detachment/attachment) of anchoring surface oxygen atoms requires a very high activation energy of 1.95 eV (= 188 kJ $mol^{-1}$). In the second step $V^{5+}$ was reduced to $V^{4+}$. Note that initializing electron spin density at a nearby Ce atom in order to create the "missing" $Ce^{3+}$ in TS4/M4 always yields $V^{4+}(3d^1)$ and $Ce^{4+}(4f^0)$. The same was found upon slight distortion of the structures. Considering the findings of previous work on mixed metal V/Ce gas-phase clusters[59] and the DFT+U studies on bulk $CeVO_4$,[60] it is plausible that M4 or TS4 have to be high in energy, since the coordination number of V in M4/TS4 is low, but still V adopts oxidation state +4. Low coordinated V, as found in gas-phase clusters, solid $CeVO_4$ or vanadia clusters deposited on ceria, prefers the oxidation state +5. As shown by the aforementioned test calculations, TS4 and M4 do not represent artefacts, but appear to be robust even under structural distortion.

For the second pathway, the following sequence of steps was found: (i) First, the special O is detached from surface Ce creating a $VO_3$ species (TS5), but V remains in oxidation state +5. We found again that detachment of O from V is associated with a very high barrier, independent of the reduction of V as observed in the first pathway. (ii) Second, a re-coordination occurs, forming $O{=}VO_4$ and gaining 2.45 eV in energy with subsequent formation of a five-fold coordinated V (1.58 eV barrier). (iii) O coordinated to V detaches and heals the pseudo-vacancy. This re-coordination process has a high barrier, similar to the second step of the first mechanism. Subsequently, the $VO_4$ tetrahedron relaxes and re-opens the pseudo-vacancy and (iv) finally, a $VO_4$ rocking motion (presumably a step with a very low barrier, comparable to (i) of the first migration pathway) transforms the system back into the starting structure (M1).

Importantly, we emphasize that temperature effects, entirely neglected in our study, will certainly affect barriers. At elevated temperatures the oxygen ion mobility of the $CeO_2$ support is most likely sufficiently high to influence migration processes of vanadium oxide clusters deposited on it. Experimentally, monomeric vanadate species sinter upon heating to 700 K and ultimately form vanadia trimers, as observed by Baron *et al.* (see Fig. 1 in Ref. 35). We believe that under realistic conditions, the support "helps" the $O{=}VO_3$ tetrahedron to migrate, and therefore barriers should be substantially lower than our predictions, *i.e.* 1.86 eV. Nevertheless, the barriers obtained using PBE+U generate clear evidence for the previously conjectured kinetic hindrance of migrating vanadate tetrahedrons on the ceria surface. It is known that barriers obtained using GGA functionals are usually underestimated.[61,62] Thus, the energy barriers presented in this work most likely represent even lower boundaries to barriers obtained using *e.g.* hybrid functionals, which are expected to be more accurate.[63] However, it would be interesting to compare energy barriers with enthalpy barriers including temperature effects by virtue of harmonic frequencies, but we expect that the aforementioned effects do not alter our findings qualitatively.

We mention that current studies on the oxidation mechanism of methanol at the $VO_2{\cdot}CeO_2(111)$ interface,[53] provide strong evidence that the pseudo-vacancy plays an important role. We firmly believe that it is this very structural feature of the ceria surface, created upon adsorption/formation of vanadia, which drives the system towards the theoretically determined high activities in Mars-van Krevelen processes.

The large relaxation effects upon oxygen defect formation in the active, monomeric $VO_2$ species in fact heal the pseudo-vacancy.

## Summary

Based on TST using PBE+U, we found that small $VO_2$ species, although thermodynamically unstable, are stabilized at the $CeO_2$(111) surface, because of huge migration energy barriers. This is mainly due to (i) deformation of the vanadate tetrahedron as well as (ii) required re-coordination of O to V. Re-coordination was found to go along with activation energies as large as 2.73 eV (= 263 kJ mol$^{-1}$). However, the lowest energy barrier we found amounts to 1.95 eV (= 188 kJ mol$^{-1}$). Specifically, we studied two possible pathways: (i) V features threefold coordination with oxygen atoms, with or without simultaneous reduction of $V^{5+}$ to $V^{4+}$, or (ii) V adopts a fivefold coordination, with V in its highest oxidation state (+5). Intermediate steps, associated with rather rigid rotation or only slight deformation of the vanadate tetrahedron, correspond to moderate barriers of 0.77 eV (= 74 kJ mol$^{-1}$) only. Thus, it appears that any reaction steps involving detachment of O atoms coordinated to V are extremely unlikely.

## Acknowledgements

The authors are grateful for financial support from the Deutsche Forschungsgemeinschaft (DFG, SFB 546). Grants for compute time at the high-performance compute clusters HLRN (Berlin, Hannover) operated by the North-German Supercomputing Alliance and JUROPA operated by the Supercomputer Centre at the Forschungszentrum Jülich are gratefully acknowledged.

## References

1 I. E. Wachs and B. M. Weckhuysen, *Appl. Catal., A*, 1997, **157**, 67–90.
2 A. Khodakov, B. Olthof, A. T. Bell and E. Iglesia, *J. Catal.*, 1999, **181**, 205–216.
3 B. M. Weckhuysen and D. E. Keller, *Catal. Today*, 2003, **78**, 25–46.
4 I. E. Wachs, *Catal. Today*, 2005, **100**, 79–94.
5 B. Kilos, A. T. Bell and E. Iglesia, *J. Phys. Chem. C*, 2009, **113**, 2830–2836.
6 B. Olthof, A. Khodakov, A. T. Bell and E. Iglesia, *J. Phys. Chem. B*, 2000, **104**, 1516–1528.
7 M. A. Bañares, M. V. Martinez-Huerta, X. T. Gao, I. E. Wachs and J. L. G. Fierro, in *Stud. Surf. Sci. Catal.*, ed. A. Corma, F. V. Melo, S. Mendioroz and J. L. G. Fierro, Elsevier, Amsterdam, 2000, vol. 130D, p. 3125.
8 T. Kim and I. E. Wachs, *J. Catal.*, 2008, **255**, 197–205.
9 E. L. Lee and I. E. Wachs, *J. Phys. Chem. C*, 2008, **112**, 6487–6498.
10 H.-S. Kim, S. A. Zygmunt, P. C. Stair, P. Zapol and L. A. Curtiss, *J. Phys. Chem. C*, 2009, **113**, 8836–8843.
11 D. E. Keller, T. Visser, F. Soulimani, D. C. Koningsberger and B. M. Weckhuysen, *Vib. Spectrosc.*, 2007, **43**, 140–151.
12 M. A. Banares and G. Mestl, in *Advances in Catalysis, Vol 52*, ed. B. C. Gates and H. Knozinger, 2009, vol. 52, pp. 43–128.
13 D. E. Keller, S. M. K. Airaksinen, A. O. Krause, B. M. Weckhuysen and D. C. Koningsberger, *J. Am. Chem. Soc.*, 2007, **129**, 3189–3197.
14 M. Ruitenbeek, A. J. van Dillen, F. M. F. de Groot, I. E. Wachs, J. W. Geus and D. C. Koningsberger, *Top. Catal.*, 2000, **10**, 241–254.
15 K. Devriendt, H. Poelman and L. Fiermans, *Surf. Sci.*, 1999, **433**, 734–739.
16 R. P. Blum, H. Niehus, C. Hucho, R. Fortrie, M. V. Ganduglia-Pirovano, J. Sauer, S. Shaikhutdinov and H. J. Freund, *Phys. Rev. Lett.*, 2007, 99.
17 S. Surnev, M. G. Ramsey and F. P. Netzer, *Prog. Surf. Sci.*, 2003, **73**, 117–165.
18 H. Niehus, R. P. Blum and D. Ahlbehrendt, *Surf. Rev. Lett.*, 2003, **10**, 353–359.
19 A. C. Dupuis, M. Abu Haija, B. Richter, H. Kuhlenbeck and H. J. Freund, *Surf. Sci.*, 2003, **539**, 99–112.

 

20 N. Magg, B. Immaraporn, J. B. Giorgi, T. Schroeder, M. Baumer, J. Dobler, Z. L. Wu, E. Kondratenko, M. Cherian, M. Baerns, P. C. Stair, J. Sauer and H. J. Freund, *J. Catal.*, 2004, **226**, 88–100.
21 S. Kaya, Y. N. Sun, J. Weissenrieder, D. Stacchiola, S. Shaikhutdinov and H. J. Freund, *J. Phys. Chem. C*, 2007, **111**, 5337–5344.
22 Y. Romanyshyn, S. Guimond, H. Kuhlenbeck, S. Kaya, R. P. Blum, H. Niehus, S. Shaikhutdinov, V. Simic-Milosevic, N. Nilius, H. J. Freund, M. V. Ganduglia-Pirovano, R. Fortrie, J. Doebler and J. Sauer, *Top. Catal.*, 2008, **50**, 106–115.
23 G. S. Wong, M. R. Concepcion and J. M. Vohs, *J. Phys. Chem. B*, 2002, **106**, 6451–6455.
24 T. Feng and J. M. Vohs, *J. Catal.*, 2004, **221**, 619–629.
25 J. M. Vohs, T. Feng and G. S. Wong, *Catal. Today*, 2003, **85**, 303–309.
26 M. Calatayud, B. Mguig and C. Minot, *Surf. Sci.*, 2003, **526**, 297–308.
27 A. Vittadini, M. Casarin, M. Sambi and A. Selloni, *J. Phys. Chem. B*, 2005, **109**, 21766–21771.
28 T. K. Todorova, M. V. Ganduglia-Pirovano and J. Sauer, *J. Phys. Chem. C*, 2007, **111**, 5141–5153.
29 M. M. Islam, D. Costa, M. Calatayud and F. Tielens, *J. Phys. Chem. C*, 2009, **113**, 10740–10746.
30 J. Döbler, M. Pritzsche and J. Sauer, *J. Phys. Chem. C*, 2009, **113**, 12454–12464.
31 V. Shapovalov and H. Metiu, *J. Phys. Chem. C*, 2007, **111**, 14179–14188.
32 P. Mars and D. W. van Krevelen, *Chem. Eng. Sci.*, 1954, **3, Supplement 1**, 41–59.
33 D. R. Mullins, P. V. Radulovic and S. H. Overbury, *Surf. Sci.*, 1999, **429**, 186–198.
34 J. L. Lu, H. J. Gao, S. Shaikhutdinov and H. J. Freund, *Surf. Sci.*, 2006, **600**, 5004–5010.
35 M. Baron, H. Abbott, O. Bondarchuk, D. Stacchiola, A. Uhl, S. Shaikhutdinov, H.-J. Freund, C. Popa, M. V. Ganduglia-Pirovano and J. Sauer, *Angew. Chem., Int. Ed.*, 2009, **48**, 8006–8009.
36 M. V. Ganduglia-Pirovano, C. Popa, J. Sauer, H. L. Abbott, A. Uhl, M. Baron, D. Stacchiola, O. Bondarchuk, S. Shaikhutdinov and H.-J. Freund, *J. Am. Chem. Soc.*, 2010, **132**, 2345–2349.
37 C. Popa, M. V. Ganduglia-Pirovano and J. Sauer, *J. Phys. Chem. C*, 2011, **115**, 7399–7410; 2012, **116**, 18572–18573(Erratum).
38 C. Penschke, J. Paier and J. Sauer, *J. Phys. Chem. C*, 2013, **117**, 5274–5285.
39 B. Beck, M. Harth, N. G. Hamilton, C. Carrero, J. J. Uhlrich, A. Trunschke, S. Shaikhutdinov, H. Schubert, H.-J. Freund, R. Schlögl, J. Sauer and R. Schomäcker, *J. Catal.*, 2012, **296**, 120–131.
40 J. Sauer and J. Döbler, *Dalton Trans.*, 2004, 3116–3121.
41 X. Rozanska, R. Fortrie and J. Sauer, *J. Phys. Chem. C*, 2007, **111**, 6041–6050.
42 P. E. Blöchl, *Phys. Rev. B: Condens. Matter*, 1994, **50**, 17953–17979.
43 G. Kresse and D. Joubert, *Phys. Rev. B: Condens. Matter Mater. Phys.*, 1999, **59**, 1758–1775.
44 G. Kresse and J. Furthmuller, *Phys. Rev. B: Condens. Matter*, 1996, **54**, 11169–11186.
45 G. Kresse and J. Furthmuller, *Comput. Mater. Sci.*, 1996, **6**, 15–50.
46 J. L. F. Da Silva, M. V. Ganduglia-Pirovano, J. Sauer, V. Bayer and G. Kresse, *Phys. Rev. B: Condens. Matter Mater. Phys.*, 2007, **75**, 045121.
47 G. Mills, H. Jonsson and G. K. Schenter, *Surf. Sci.*, 1995, **324**, 305–337.
48 H. Jonsson, G. Mills and K. W. Jacobsen, in *Classical and Quantum Dynamics in Condensed Phase Simulations*, ed. J. Berne, G. Ciccotti and D. F. Coker, World Scientific, 1998.
49 G. Henkelman, B. P. Uberuaga and H. Jonsson, *J. Chem. Phys.*, 2000, **113**, 9901–9904.
50 S. Grimme, *J. Comput. Chem.*, 2006, **27**, 1787–1799.
51 T. Kerber, M. Sierka and J. Sauer, *J. Comput. Chem.*, 2008, **29**, 2088–2097.
52 A. Kokalj, *Comput. Mater. Sci.*, 2003, **28**, 155–168.
53 T. Kropp, J. Paier and J. Sauer, *in preparation*, 2013.
54 J. Tersoff and D. R. Hamann, *Phys. Rev. Lett.*, 1983, **50**, 1998–2001.
55 J. Tersoff and D. R. Hamann, *Phys. Rev. B*, 1985, **31**, 805–813.
56 K. Reuter and M. Scheffler, *Phys. Rev. B: Condens. Matter*, 2001, **65**, 035406.
57 A. Bande and A. Lüchow, *Phys. Chem. Chem. Phys.*, 2008, **10**, 3371–3376.
58 K. Momma and F. Izumi, *J. Appl. Crystallogr.*, 2011, **44**, 1272–1276.
59 L. Jiang, T. Wende, P. Claes, S. Bhattacharyya, M. Sierka, G. Meijer, P. Lievens, J. Sauer and K. R. Asmis, *J. Phys. Chem. A*, 2011, **115**, 11187–11192.
60 J. L. F. Da Silva, M. V. Ganduglia-Pirovano and J. Sauer, *Phys. Rev. B: Condens. Matter Mater. Phys.*, 2007, **76**, 125117.
61 Y. Zhao and D. G. Truhlar, *J. Phys. Chem. A*, 2005, **109**, 5656–5667.
62 Y. Zhao, N. Gonzalez-Garcia and D. G. Truhlar, *J. Phys. Chem. A*, 2005, **109**, 2012–2018.
63 K. Yang, J. J. Zheng, Y. Zhao and D. G. Truhlar, *J. Chem. Phys.*, 2010, 132.

# P5

https://pubs.acs.org/doi/abs/10.1021/ja508657c

JACS
JOURNAL OF THE AMERICAN CHEMICAL SOCIETY
Article
pubs.acs.org/JACS

# Support Effect in Oxide Catalysis: Methanol Oxidation on Vanadia/Ceria

Thomas Kropp, Joachim Paier, and Joachim Sauer*

Institut für Chemie, Humboldt-Universität zu Berlin, Unter den Linden 6, 10099 Berlin, Germany

Supporting Information

**ABSTRACT:** Density functional theory is used for periodic models of monomeric vanadia species deposited on the $CeO_2(111)$ surface to study dissociative adsorption of methanol and its subsequent dehydrogenation to formaldehyde. Dispersion-corrected PBE+U calculations are performed and compared with HSE and B3LYP results. Dissociative adsorption of methanol at different sites on $VO_2{\cdot}CeO_2(111)$ is highly exothermic with adsorption energies of 1.8 to 1.9 eV (HSE+D). Two relevant pathways for desorption of formaldehyde are found with intrinsic barriers for the redox step of 1.0 and 1.4 eV (HSE+D). The calculated desorption temperatures (370 and 495 K) explain the peaks observed in temperature-programmed desorption experiments. Different sites of the supported catalyst system are involved in the two pathways: (i) methanol can chemisorb on the $CeO_2$ surface filling a so-called pseudovacancy and the H atom is transferred to an V−O−Ce interphase bond or (ii) $CH_3OH$ may chemisorb at the V−O−Ce interphase bond and form a V−$OCH_3$ species from which H is transferred to the ceria surface, providing evidence for true cooperativity. In both cases, ceria is directly involved in the redox process, as two electrons are accommodated in Ce *f* states forming two $Ce^{3+}$ ions whereas vanadium remains fully oxidized ($V^{5+}$).

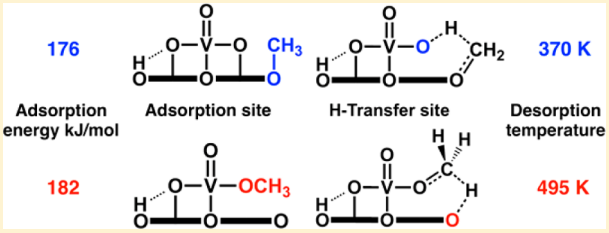


## 1. INTRODUCTION

Solid catalysts are complex systems with the active component dispersed on a supporting oxide. Heterogeneous catalysis provides ample evidence for the important role of the support for the activity and selectivity of a catalyst.[1,2] As a recent example, several orders of magnitude activity changes have been observed for CO oxidation on Pt nanoparticles supported on different oxides.[3] Here, we deal with transition metal oxides as industrially relevant catalysts that activate C−H bonds. Over more than a decade, evidence has been gathered[4−6] for a 3 to 4 orders of magnitude change in activity for, e.g., vanadium oxide supported on a broad variety of reducible and nonreducible oxides,[7] but an atomistic understanding has not yet been achieved. The reported results are for the partial oxidation of methanol to formaldehyde, but for the partial oxidation of ethanol and the oxidative dehydrogenation of propane the same observations have been made.[8,9] It has also been inferred that the support determines the type and distribution of the vanadia species and that these differences are the reason for the variation in turnover frequencies with the support for a given vanadium loading.[8,10]

Ceria-supported transition metal oxide catalysts are particularly active. Recent experimental and theoretical studies, including surface science experiments on model catalysts,[9,11−13] point to a very special role of this support.[14] It stabilizes the reduced state of the catalyst by accommodating electrons in the cerium *f* states, while vanadium remains in its highest oxidation state. This redox participation of the surroundings of an active M═O site in the C−H bond activation has also been found in enzymes. In cytochrome P450 which selectively oxidizes C−H bonds to C−OH bonds, the porphyrin ligand of the active $Fe^{IV}$═O species also participates in the redox reaction.[15] This may be considered a *unifying concept* in catalysis.

The above-mentioned and other results raise doubts about attempts[7,16] to ascribe the observed activity changes to the V−O−M interphase bond only (M − metal of the supporting oxide) and to map the support effect to one parameter such as Sanderson's electronegativity. While the higher activity of ceria-supported catalysts compared to nonreducible supports such as alumina and silica has been rationalized[9,13] by means of the energy of oxygen defect formation as a descriptor,[17,18] detailed information on how the support interferes with the elementary reaction steps is still missing. This is the subject of the present computational study. Specifically, for the methanol oxidation we will examine which of the available sites participate in the initial chemisorption step and in the hydrogen transfer step: the V═O site, the V−O−M interphase sites, or sites at the supporting oxides. To reduce complexity connected with varying size distribution for different supports,[8,10] in this study we focus on monomeric vanadia species and, hence, do not consider V−O−V sites. A previous study on silica-supported vanadia showed that larger species are more reactive,[19] whereas for vanadia on ceria the opposite was predicted.[20]

**Received:** August 22, 2014
**Published:** October 2, 2014

   dx.doi.org/10.1021/ja508657c | J. Am. Chem. Soc. 2014, 136, 14616−14625

For the vanadia/silica system[21] a previous computational study of monomeric sites (later confirmed and augmented)[22] has shown that first methanol chemisorbs on the V−O−Si interphase bond as also inferred from experiments.[23] Subsequently, a hydrogen atom is transferred from the methoxy group to the vanadyl (V═O) bond (see Figure 1). The latter is

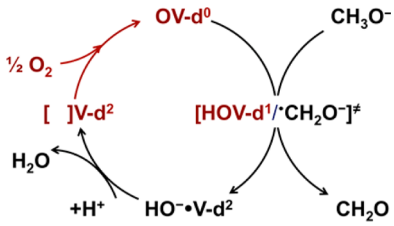


**Figure 1.** Mars−van Krevelen catalytic cycle for the methanol oxidation at a silica-supported vanadia species.

the rate-determining redox step involving a biradicaloid transition structure with vanadium in the +4 oxidation state ($d^1$ electron configuration on V). On release of $CH_2O$, another electron is transferred to vanadium, which acquires a $d^2$ electron configuration (+3 oxidation state). After water desorption, the reduced catalyst features an oxygen vacancy. The catalytic cycle is completed by a reoxidation step (Mars−van Krevelen),[24] the details of which have also been studied computationally.[25]

For monomeric vanadia species on ceria, we use a periodic model of $VO_2$ adsorbed on the $CeO_2(111)$ surface (see Figure 2). DFT+U calculations[26] showed that $VO_2$ is the most stable

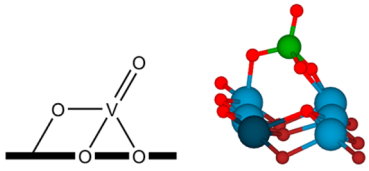

**Figure 2.** $VO_2$ deposited on the $CeO_2(111)$ surface. The ball and stick model (right) uses the following color code: $Ce^{4+}$ (blue), $Ce^{3+}$ (dark blue), O (red; subsurface dark red), and V (green).

$VO_n$ species under the slightly reducing conditions of the model catalyst experiments.[11] Vanadia is stabilized in its +5 oxidation state, and electrons are transferred to $CeO_2$ as indicated by DFT+U and XPS.[11] Therefore, our surface model features a $Ce^{3+}$ ion which is always present in addition to the one or two $Ce^{3+}$ ions formed in the catalytic cycle. It also features a cavity in the $CeO_2(111)$ surface, which we refer to as a pseudovacancy[27] and which turns out to be a strong adsorption site. Driven by the strong preference of vanadium for a tetrahedral coordination, the deposited $VO_2$ species pulls an oxygen ion out of the surface which creates the cavity.

We have found six different chemisorption structures for methanol. For two of the most stable adsorption structures that can form without a barrier we have studied possible reaction pathways. For each of them, two transition structures have been identified as well as a number of intermediates on the way to the final products. Similarly to results for vanadia supported on (reducible) titania[28] (see also refs 29−31), the pathways with the lowest apparent energy barriers directly involve the support. In the first one, methanol chemisorbs at the V−O−Ce interphase bond and forms a $V-OCH_3$ species whose hydrogen atom is transferred to the ceria surface. In the alternative pathway methanol chemisorbs on the ceria surface and the hydrogen atom is transferred to the V−O−Ce interphase bond. In both cases, the transition structure features a $Ce^{3+}$ ion (in addition to the one already present in $VO_2/CeO_2(111)$), while vanadium stays +5. In the fully reduced state of the catalyst, there are two additional $Ce^{3+}$ ions. Integration of the Polanyi−Wigner desorption equation for these two pathways using calculated desorption energies and pre-exponentials yields two peaks that explain the temperature-programmed desorption (TPD) features observed for the $VO_x/CeO_2(111)$ model catalyst.[13] We conclude that changing the support may change the active sites, and redox-active supports may be directly involved in the redox step.

Density functional theory (DFT) is applied with the Perdew−Burke−Ernzerhof functional[32] augmented by a dispersion term.[33,34] Attention is paid to the proper description of electrons in vanadium $d$ and cerium $f$ states ("DFT+U")[35,36] and to the possible existence of broken-symmetry open shell low-spin states as "biradicaloid" transition states. Comparison with hybrid functionals is also made.

## 2. COMPUTATIONAL DETAILS

Calculations were performed using the projector augmented wave (PAW) method[37,38] as implemented in the Vienna *ab initio* simulation package (VASP).[39,40] The onsite Coulomb correlation of occupied $f$ orbitals is corrected with the DFT+U[35,36] approach employing the exchange-correlation functional of Perdew, Burke, and Ernzerhof (PBE)[41] and an effective Hubbard-type U parameter of 4.5 eV for the Ce 4$f$ electrons, i.e. PBE+U. This U value was calculated self-consistently by Fabris et al.[42] A value between 3.0 and 5.5 eV leads to a proper localization of the two electrons left upon oxygen removal from $CeO_2$.[43] The specific implementation of DFT+U used in this work follows Dudarev et al.[44,45] Selected structures were also calculated using the hybrid functional by Heyd, Scuseria, and Ernzerhof (HSE)[46] as well as B3LYP.[47,48] A plane wave kinetic energy cutoff of 600 eV was used, and structure optimizations were performed until forces acting on the relaxed atoms were below 0.02 eV $Å^{-1}$ for PBE+U and 0.04 eV $Å^{-1}$ for hybrid functional calculations. The plane wave cutoff determining the Fourier grid for the Fock exchange related routines was set to $^9/_4$ times the cutoff for expanding the orbitals. The vanadium PBE pseudopotential includes the [Ar]-core 3$p$ states in the valence space. The semiempirical $C_6/R^6$ term by Grimme (DFT+D2) was added to correct for missing long-range dispersion-type interactions.[33,34] The required van der Waals parameters for Ce were taken from ref 20. The global scaling parameter $s_6$ was 0.75, 0.6, and 1.05 for PBE+U, HSE, and B3LYP, respectively. Based on the PBE+U results, dispersion correction affects structural parameters only to a minor degree. Thus, when HSE and B3LYP results are reported, these are results of single-point calculations for the respective DFT+D structures.

The oxygen-terminated $p(4 \times 4)$ surface unit cell was generated cutting bulk $CeO_2$ in (111) orientation with cell vectors that amount to 15.518 Å (PBE+U), 15.266 Å (HSE), and 15.452 Å (B3LYP), respectively. Our slab model consists of nine atomic layers ($Ce_{48}O_{96}$), where the bottom trilayer is frozen to simulate the bulk. The vacuum layer was set to 10 Å. Because of the large cell, sampling of the Brillouin zone was restricted to the Γ point.

Optimized structures using PBE+U were proven to be minima by the absence of imaginary vibrational frequencies. Calculations of harmonic frequencies include all atoms, but the frozen bottom trilayer. The force constants are calculated as numerical derivative of forces with atomic displacements of ±0.015 Å. Zero-point vibrational energy (ZPVE) contributions are calculated from these frequencies.

Transition structures were obtained by nudged elastic band (NEB) calculations[49,50] in combination with the so-called climbing image method[51] as implemented in VASP. The improved dimer method (IDM) was used to refine these structures.[52,53]


dx.doi.org/10.1021/ja508657c | J. Am. Chem. Soc. 2014, 136, 14616−14625

The ball-and-stick models in Figures 2, 3, and 6 were generated using VESTA[54] with the following color code: C (black), $Ce^{4+}$ (blue), $Ce^{3+}$ (dark blue), H (white), O (red; subsurface dark red), and V (green).

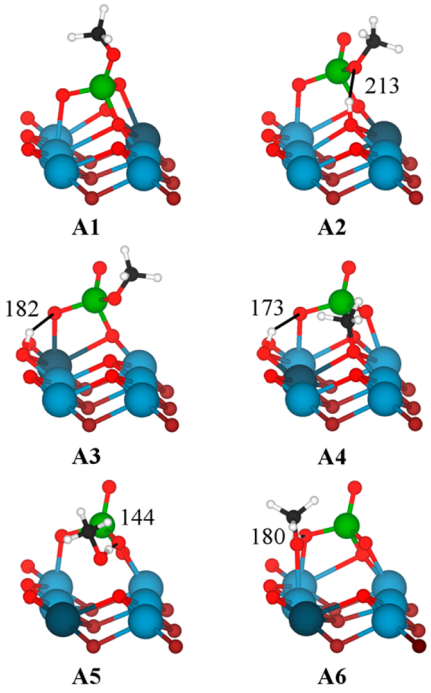


**Figure 3.** Adsorption structures **A1**−**A6** with hydrogen bond lengths in pm. Additional colors include C (black) and H (white).

## 3. RESULTS

**3.1. Methanol Adsorption.** Figure 2 shows the tetrahedral coordination of the monomeric vanadia surface species. It contains a vanadyl group ($r_{V=O}$ = 163 pm) and two different types of interphase oxygen atoms. One connects V to a surface cerium atom ($r_{V-O}$ = 174 pm), and two are surface oxygen atoms ($O_s$) to which $VO_2$ is attached with its V atom ($r_{V-O}$ = 181 pm). Methanol can adsorb by insertion into an interphase bond or into the pseudovacancy that opens in the surface when $VO_2$ is attached to the surface oxygen atoms. Figure 3 shows six different adsorption structures, and Table 1 lists their energies.

**Table 1. Adsorption Energies Including Zero-Point Vibrational Energies, $\Delta E_0$, for Methanol in eV**

| | PBE+U+D | D//PBE+U+D[a] |
|---|---|---|
| **A1** | −1.89 | −0.20 |
| **A2** | −1.72 | −0.27 |
| **A3** | −1.71 | −0.29 |
| **A4** | −1.77 | −0.32 |
| **A5** | −1.32 | −0.30 |
| **A6** | −0.95 | −0.15 |

[a]Dispersion contribution at the PBE+U+D structure.

Structure **A1** is formed by chemisorption of $CH_3OH$ onto a $V-O_{surface}$ bond. It is similar to the structure found by Sauer and co-workers[21] for silica-supported vanadia. Vanadium stays tetrahedrally coordinated, but the $VO_4$ tetrahedron moves 25 pm up. One of the surface O atoms is replaced by the oxygen atom in the methoxide, and the vanadyl oxygen atom attaches to a Ce surface atom. Hence, this structure does not contain a vanadyl V=O bond anymore. The two V−O (Ce) interphase bonds are shorter (171/167 pm) than in the surface vanadia species. Upon methanol adsorption, the $Ce^{3+}$ ion formed on $VO_2$ deposition[26] localizes next to the hydroxyl group located on the $CeO_2$ surface. The latter forms a hydrogen bond (172 pm) with the longer (171 pm) of the V−O interphase bond.

This structure is found to be the most stable one with an adsorption energy of −1.89 eV, but its formation requires significant structural rearrangements leading to a barrier of at least 0.6 eV as estimated by NEB runs.

Structure **A2** obtained by inserting methanol into a V−O interphase bond is slightly less stable (−1.71 eV). The methoxide replaces an anchoring oxygen atom, which relaxes into the pseudovacancy. The hydroxyl group, located next to the $Ce^{3+}$ site, forms a weak hydrogen bond with the methoxide oxygen atom with a H···O distance of 213 pm (see Figure 3). Structure **A3** is structurally and energetically very close to **A2**, although the sites for the $Ce^{3+}$ ion and the hydroxyl group are different. Conversion of both structures into each other appears to be easy with a low barrier of approximately 0.5 eV (see ref 55). It consists of a mere relocation of the hydroxyl H atom, which interacts with the interphase O atom (182 pm).

Structure **A4** is fundamentally different as methanol adsorbs into the pseudovacancy. Dispersion stabilizes this adsorption structure more than the other ones (Table 1), but the total adsorption energy (−1.77 eV) is comparable to the values for **A2** or **A3**. The methoxide oxygen atom is located 34 pm above the topmost surface layer, which is slightly higher than the hydroxyl oxygen atom (31 pm). $Ce^{3+}$ is located between the hydroxyl group and the methoxide. Whereas the V=O group is still present, similar to **A1**, two nearly equivalent interphase oxygen atoms are formed, one of which interacts with the hydroxyl H atom (173 pm).

In structure **A5**, methanol is molecularly adsorbed. It forms a hydrogen bond (136 pm) to the elevated anchoring oxygen atom of the $VO_2$ unit, and its oxygen is 89 pm above the pseudovacancy, which is thus partially healed. Although structure **A5** is the most stable molecular adsorption structure found, dissociation into **A4** is favored by 0.4 eV. Since the corresponding barrier is only 0.08 eV, molecular adsorption structures should not be present on a (dehydrated) catalyst.

A second molecular adsorption structure **A6** was found to be significantly less stable. Methanol adsorbs atop of a $Ce^{4+}$ ion with a hydrogen bond (171 pm) to an interphase oxygen atom, and stabilization by relaxation is minor.

**3.2. Formaldehyde Formation.** The most stable adsorption structures presented in the previous section are obvious starting points for various methanol oxidation pathways, and for each adsorption structure, multiple oxidation pathways are possible. Starting with **A1**, hydrogen transfer to one of the interphase oxygen atoms leads to intrinsic barriers greater than 2.0 eV and is, therefore, not relevant. Hydrogenation energies indicate that hydrogen transfer to surface oxygen atoms would be more favorable,[20] but these are too far away for this adsorption structure.

Starting with **A2** or **A3**, the hydrogen atom can either be transferred to the vanadyl group, the interphase oxygen atom, or a $CeO_2$ surface oxygen atom (**A3** only). In the present work, different hydrogen transfer pathways starting with **A3** (methoxide bonded to V) and **A4** (methoxide in pseudovacancy) are investigated using PBE+U and hybrid functionals. Reaction pathways starting with **A2** and **A3** feature similar


dx.doi.org/10.1021/ja508657c | J. Am. Chem. Soc. 2014, 136, 14616−14625

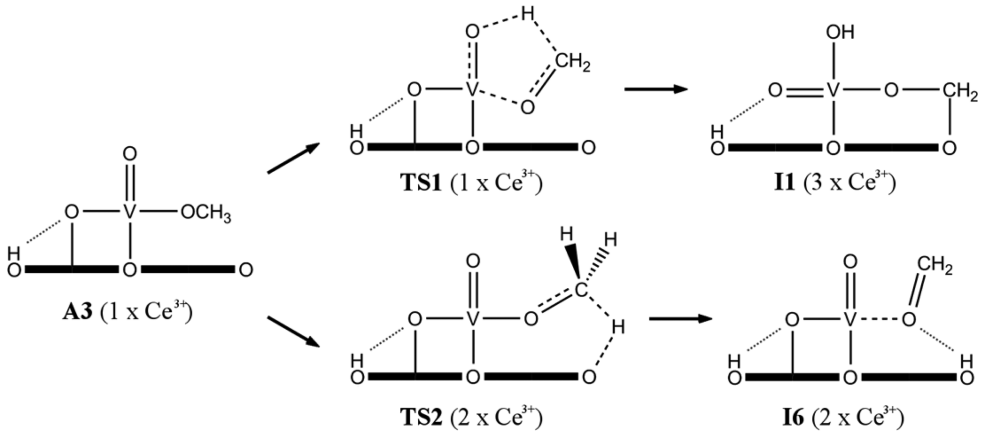


**Figure 4.** Hydrogen transfer step starting with **A3**. Top row: transfer to the vanadyl group; bottom row: transfer to a surface oxygen atom. Dotted lines represent hydrogen bonds, whereas dashed lines represent delocalized electrons.

transition structures, but the intrinsic barriers for **A2** are roughly 0.2 eV higher. Therefore, reaction channels involving **A2** will not be mentioned explicitly. Total energies discussed in this section are corrected for ZPVE and include dispersion (PBE+U+D). The ZPVE contributions decrease barriers by at most 0.2 eV, but do not affect reaction energies significantly.

*3.2.1. Vanadium-Bonded Methoxide (A3).* Figure 4 shows intermediates and transition structures for hydrogen transfer to the vanadyl group and to a $CeO_2$ surface oxygen atom starting with **A3**, and Table 2 reports selected bond distances. Figure 5

**Table 2. Selected Bond Distances (pm) for the Structures Shown in Figure 4 Obtained with PBE+U+D**

| bond | A3 | TS1 | I1 | TS2 | I6 | I3 |
|---|---|---|---|---|---|---|
| OH···O | 177 | 182 | 203 | 195 | 187 | 146 |
| V−O | 172 | 169 | 164 | 171 | 169 | 177 |
| V═O | 162 | 172 | 180 | 163 | 163 | 162 |
| V−OC | 183 | 188 | 181 | 185 | 196 | 186 |
| O−C | 143 | 141 | 147 | 137 | 129 | 141 |
| C−H | 110 | 153 | – | 139 | – | – |
| O−H | – | 128 | 97 | 121 | 97 | 97 |

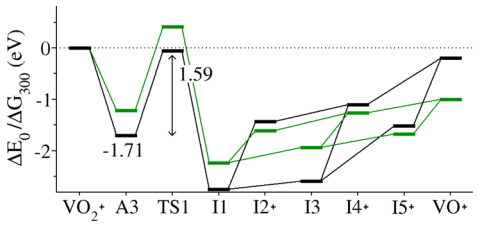


**Figure 5.** PBE+U+D reaction energy profile (ZPVE-corrected) with vanadyl O as the H-accepting atom and **A3** as the starting structure. Gibbs free energies (green) have been calculated for 300 K and 0.1 MPa. The plus sign after some structures indicates that the reported energies include gas phase molecules, e.g. $CH_3OH$ for $\mathbf{VO_2}$+ or $CH_2O$ for **I2**+.

shows the reaction energy profile for the hydrogen transfer to the vanadyl group. The transition structure **TS1** consists of a distorted five-membered ring. The imaginary mode (1502 $cm^{-1}$) shows that the hydrogen transfer is accompanied by planarization of the $CH_2O$ moiety, which then bends toward the ceria surface. The barrier of this step (1.65 eV) results in a slightly negative apparent barrier of −0.06 eV.

Structure **A3** features one unpaired electron (doublet state), the Ce *f* electron stemming from the deposition of $VO_2$. In the transition structure, this is the highest occupied orbital defining the Fermi level. A spin-unpolarized calculation with a pseudopotential excluding the Ce *f* states from the valence bands affects the barrier by less than 0.04 eV and thus proves the role of this $Ce^{3+}$ ion as an "innocent spectator" in this reaction. The second highest occupied orbital (2.0 eV below the Fermi level) is populated by two electrons of opposite spin. Its delocalization over the five-membered ring (see Figure 6)

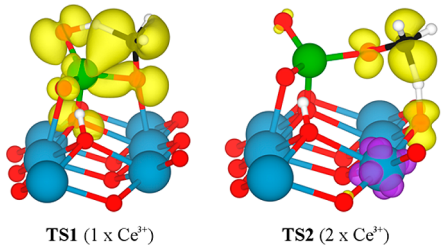


**Figure 6.** Electron density isocontour (0.01 $Å^{-3}$) for the second highest occupied orbital of **TS1** and spin density isocontour (0.01 $Å^{-3}$) for positive (yellow) and negative (purple) spin densities of **TS2**.

points to a concerted mechanism. The projected electron density shows that the vanadium $d_{yz}$ state is partially populated and overlaps with the $\pi^*$ orbital of the $CH_2O$ moiety. Since, for this transition structure, the ceria support is redox-innocent, it does not come as a surprise that the barrier coincides with the one reported by Sauer and co-workers[21] for the methanol oxidation on vanadia supported on the nonreducible silica.

Relaxation of **TS1** yields intermediate **I1**, which contains a V−O−$CH_2$−O−Ce moiety, i.e. formaldehyde coordinated to both $VO_X$ ($r_{V-O}$ = 181 pm) and the ceria support ($r_{C-O}$ = 138 pm). This structural motif is thermodynamically highly favored over V···O═$CH_2$ present in the vanadia/silica system. The oxidation step is strongly exothermic (−1.04 eV). Upon relaxation, both electrons occupying the delocalized orbital of the five-membered ring are transferred into Ce 4*f* states. Here, we see true cooperativity between vanadia and the support: the $CH_3O^-$ species formed in the chemisorption step has transferred a proton to the vanadyl group and two electrons to the ceria support.

The various pathways available for $CH_2O$ desorption are also shown in Figure 5, and the corresponding structural schemes


dx.doi.org/10.1021/ja508657c | J. Am. Chem. Soc. 2014, 136, 14616−14625

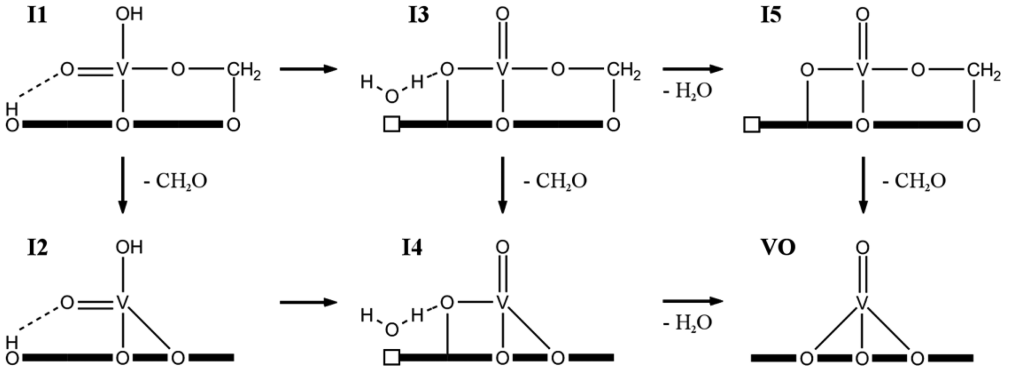


**Figure 7.** Elementary steps involved in water and formaldehyde desorption starting with **I1**. All these intermediates contain three $Ce^{3+}$ ions; no electron transfer between vanadia and ceria occurs during the desorption steps.

are presented in Figure 7. Each route contains the following elementary steps: formaldehyde desorption (**I1** → **I2**, **I3** → **I4**, **I5** → **VO**), water formation (**I1** → **I3**, **I2** → **I4**), and water desorption (**I3** → **I5**, **I4** → **VO**). None of these pathways seems to be favored over another, especially when considering free energies, and may occur simultaneously. The desorbing formaldehyde will contain either the methanol oxygen atom or a surface oxygen atom. The former pathway would require the formation of an under-coordinated vanadium, which involves very high barriers;[27] the desorbing formaldehyde is more likely to contain a surface oxygen atom. Such an oxygen exchange in the primary product of the methanol oxidation was observed by Romanyshyn et al. at the $V_2O_5(001)$ surface via isotope labeling.[56]

Figure 8 shows the reaction energy profile for hydrogen transfer to a $CeO_2$ surface oxygen atom starting from the same

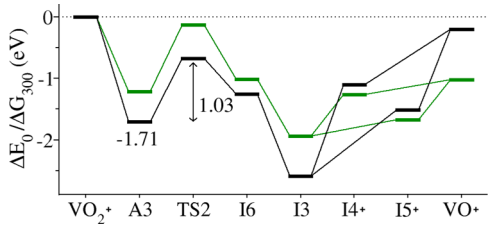


**Figure 8.** PBE+U+D reaction energy profile (ZPVE-corrected) with surface O as the H-accepting atom and **A3** as the starting structure. Gibbs free energies (green) have been calculated for 300 K and 0.1 MPa. For some structures, the plus sign indicates that the reported energies include gas phase molecules, e.g. $CH_3OH$ for $\mathbf{VO_2}$+.

adsorption structure (**A3**). Following the trend in hydrogenation energies, −1.34 eV for vanadyl groups and −1.51 eV for surface oxagen atoms,[20] the intrinsic barrier for **TS2** (1.03 eV) is much lower than that for **TS1**. The apparent barrier is as low as −0.68 eV. The imaginary mode belonging to the transition structure **TS2** (1464 $cm^{-1}$) also features the planarization of $CH_2O$ in addition to the hydrogen transfer.

In the **TS2** transition structure (Figure 4), the electron has been transferred into a Ce *f* orbital and the proton to a surface oxygen atom. The electronic structure corresponds to an antiferromagnetically coupled low-spin state (broken-symmetry solution). One of these orbitals (purple isocontour in Figure 6) is mostly Ce *f*, resulting in a second $Ce^{3+}$ ion in addition to the innocent one. The other state (yellow isocontour in Figure 6) corresponds to the $\pi^*$ orbital of formaldehyde, but also extends into the ceria surface. This is similar to what has been found for the H transfer to the vanadyl oxygen atom at silica-supported vanadia,[21] in which case the electron is transferred into a V *d* orbital, and the proton to the vanadyl oxygen atom. However, the intrinsic barrier is much lower. Obviously, accommodating electrons into Ce *f* states instead of vanadium *d* states is energetically more favorable, which is in agreement with previous findings.[13,26]

Relaxation of **TS2** leads to intermediate **I6**, which contains a partially reduced vanadium atom ($V^{+4}$) with some electron delocalization into the formaldehyde $\pi^*$ orbital (backbonding). This intermediate contains the above-mentioned V···O═$CH_2$ motif, while the stable V−O−$CH_2$−O−Ce structure is only formed upon water formation (intermediate **I3**, Figure 8). During this process, an electron moves from V *d* to Ce *f*, resulting in two $Ce^{3+}$ (plus one innocent one) compared to one $Ce^{3+}$ (plus one innocent one) in **I6**.

*3.2.2. Methoxide Bonded in the Pseudovacancy (**A4**).* Starting with methoxide bonded in the pseudovacancy (**A4**), hydrogen can be transferred to one of the interphase oxygen atoms or a $CeO_2$ surface oxygen atom. The latter was not investigated since this pathway is expected to be very similar to the oxidation of methanol adsorbed in an oxygen vacancy of $CeO_2(111)$ as described in ref 57. Figure 9 shows two pathways for hydrogen transfer which differ in the accepting interphase oxygen atom, more distant from the methoxide (**TS3**) or closer to it (**TS4**). Selected bond distances are given in Table 3.

The hydrogenation energy is the same in both cases,[20] and the lower barrier is obtained for the closer distance between hydrogen and the accepting oxygen atom. Here, the simple electronic reactivity descriptor that does not consider the local structure of the active site faces its limits.

Transition structure **TS3** is reached from **A4** upon rotation of the O═$VO_3$ tetrahedron toward the adsorbed methoxide species. Along this rotation, the more distant interphase oxygen atom detaches from the ceria surface inducing electron transfer into the Ce 4*f* states. Thus, a second $Ce^{3+}$ ion is created in the surface in addition to the one already present. The other unpaired electron (antiparallel spins) is delocalized over the interphase oxygen *p* state and the $CH_2O$ $\pi^*$ state. The imaginary mode (1501 $cm^{-1}$) involves planarization of $CH_2O$ as well as the H transfer. In addition, the hydrogen bond to the surface hydroxyl group is weakened as indicated by bond elongation (see Table 3). The apparent barrier and the reaction energy for **A4** → **I3** are −0.68 and −1.01 eV, respectively. Figure 10 shows the entire energy profile.

Structure **I3** is reached from **TS3** by hydrogen transfer to the surface hydroxyl group forming water (Figure 9). No local


dx.doi.org/10.1021/ja508657c | J. Am. Chem. Soc. 2014, 136, 14616−14625

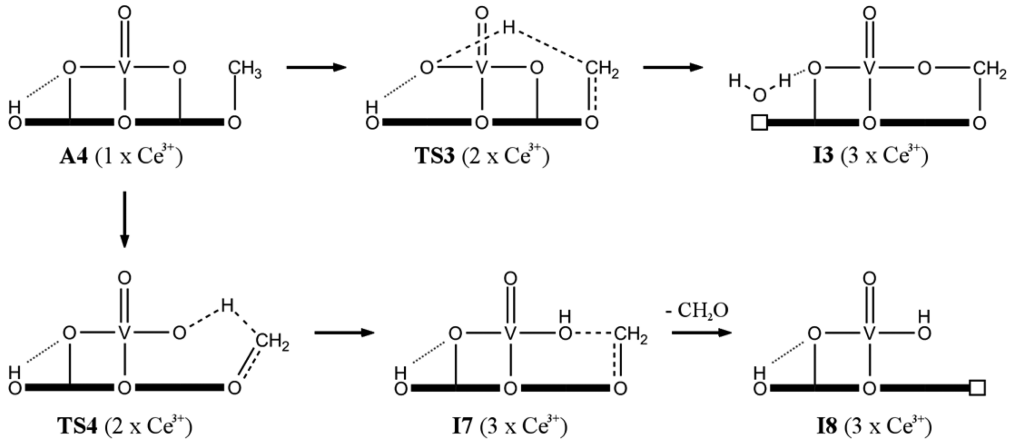


**Figure 9.** Reaction mechanisms for the hydrogen transfer step starting with **A4**. Top row: transfer to the more distant interphase oxygen atom; bottom row: transfer to the closer one. Dotted lines represent hydrogen bonds, whereas dashed lines represent delocalized electrons.

**Table 3. Selected Bond Distances (pm) for the Structures Shown in Figure 9 Obtained with PBE+U+D**

| bond | A4 | TS3 | I3 | TS4 | I7 |
|---|---|---|---|---|---|
| OH···O | 171 | 185 | 146 | 178 | 186 |
| V–O | 176 | 181 | 177 | 173 | 169 |
| V=O | 163 | 163 | 162 | 163 | 162 |
| V–OC | 175 | 172 | 186 | 181 | 195 |
| O–C | 143 | 139 | 141 | 137 | 127 |
| C–H | 110 | 139 | – | 137 | – |
| O–H | – | 126 | 97 | 119 | 98 |

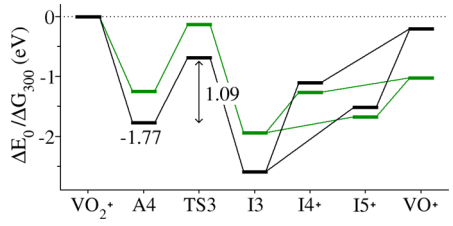


**Figure 10.** PBE+U+D reaction energy profile (ZPVE-corrected) for methanol oxidation from adsorption structure **A4** (methoxide in pseudovacancy). Gibbs free energies (green) have been calculated for 300 K and 0.1 MPa. For some structures, the plus sign indicates that the reported energies include gas phase molecules, e.g. $CH_3OH$ for $VO_2$+.

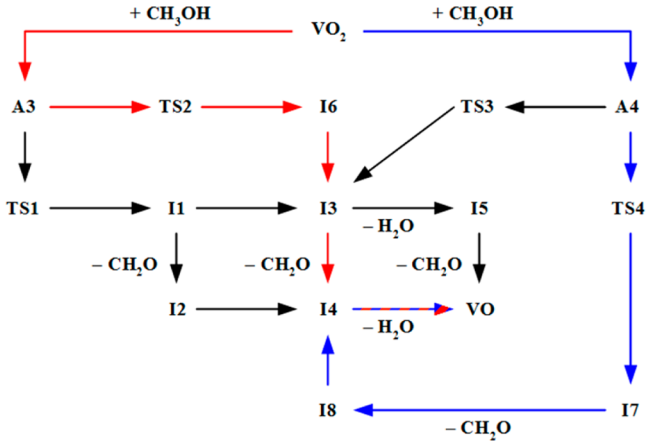


**Figure 11.** Reaction pathways for the ODH of methanol at $VO_2$·$CeO_2$(111).

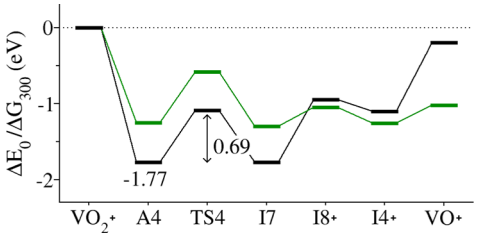


**Figure 12.** PBE+U+D reaction energy profile (ZPVE-corrected) for methanol oxidation from adsorption structure **A4** (methoxide in pseudovacancy). Gibbs free energies (green) have been calculated for 300 K and 0.1 MPa. For some structures, the plus sign indicates that the reported energies include gas phase molecules, e.g. $CH_3OH$ for $VO_2$+.

minimum structure was found for the corresponding dihydroxide, where the interphase oxygen atom is protonated instead. Intermediate **I3** is also accessible from **A3** via **TS2**.

Figure 11 provides an overview of the different intermediates that can be reached from **A3** or **A4** on different routes. For the routes passing through **A4** and **TS3**, the desorbing formaldehyde (**I3** → **I4**, **I3** → **I5** → **VO**) contains the methanol oxygen atom and not a surface oxygen atom. Hence, no oxygen isotope exchange will be observed.

The H transfer to the closer interphase O atom via **TS4** is preferred. The transition mode (1252 $cm^{-1}$) also involves planarization of the $CH_2O$ moiety. As with **TS3**, an electron is partially transferred into Ce *f* states. Figure 12 shows the reaction energy profile. Structures **A4**, **TS4**, and **I7** are very similar (see Table 3), and consequently, the intrinsic barrier is only 0.69 eV and the apparent barrier is particularly low (−1.08 eV).

Intermediate **I7** contains a bridged V–OH···$CH_2$–O–Ce motif with the $CH_2O$ fragment being structurally more similar to formaldehyde than that in **I3**. Therefore, the desorption energy amounts to 0.85 eV only. From **I7** the dihydroxyl species **I8** is reached (see Figure 9), which subsequently converts into the slightly more stable intermediate **I4** (Figure 7) via another proton transfer. The water desorption is strongly endothermic, but only mildly endergonic based on $\Delta G_{300}$.

**3.3. Hybrid Functionals.** For two adsorption structures, the vanadium methoxide structure **A3** and the pseudovacancy structure **A4**, we have performed calculations using hybrid


dx.doi.org/10.1021/ja508657c | J. Am. Chem. Soc. 2014, 136, 14616–14625

functionals and the results are included in Table 4. The total adsorption energies show only minor systematic deviations.

**Table 4. Comparison of Different Functionals for Adsorption Energies ($\Delta E_{ads}$) for A3 and A4 as well as Intrinsic Barriers ($\Delta E^{\ddagger}$), Apparent Barriers ($\Delta E^{\ddagger}_{app}$), and Reaction Energies ($\Delta E_{ox}$) for the Pathways Starting with A3 (All in eV)[a]**

| | PBE+U+D | HSE+D | B3LYP+D |
|---|---|---|---|
| $\Delta E_{ads}$ (**A3**) | −1.71 (−0.29) | −1.82 (−0.14) | −1.89 (−0.40) |
| $\Delta E_{ads}$ (**A4**) | −1.77 (−0.32) | −1.89 (−0.21) | −2.00 (−0.49) |
| $\Delta E^{\ddagger}$ (**TS1**) | 1.77 (+0.02) | 1.82 (−0.02) | 2.05 (0.00) |
| $\Delta E^{\ddagger}$ (**TS2**) | 1.20 (−0.04) | 1.53 (−0.03) | 1.49 (−0.05) |
| $\Delta E^{\ddagger}_{app}$ (**TS1**) | 0.06 (−0.27) | 0.00 (−0.12) | 0.16 (−0.40) |
| $\Delta E^{\ddagger}_{app}$ (**TS2**) | −0.51 (−0.33) | −0.29 (−0.11) | −0.40 (−0.35) |
| $\Delta E_{ox}$ (**I1**) | −1.04 (+0.01) | −0.63 (−0.03) | −0.65 (−0.02) |
| $\Delta E_{ox}$ (**I6**) | 0.45 (+0.04) | 0.86 (0.00) | 0.83 (0.01) |

[a]Dispersion contribution in parentheses.

HSE+D and B3LYP+D predictions are about 0.1 and 0.2 eV, respectively, more exothermic than the PBE+U+D values.

The varying amounts of dispersion (about 0.2 eV for HSE, 0.3 eV for PBE+U, and 0.5 eV for B3LYP) reflect the different global scaling parameters (cf. Section 2). The dispersion correction stabilizes **A4** more strongly than **A3**, independent of the functional used. This is reasonable, as **A4** consists of methanol in a binding pocket (pseudovacancy).

For structures starting from **A3**, Table 4 also compares PBE+U+D results for intrinsic barriers, apparent barriers, and reaction energies. As expected, PBE+U+D yields lower intrinsic barriers than the hybrid functionals. The difference is about 0.3 eV for B3LYP+D (both transition structures). For HSE+D the difference is smaller for **TS1** (0.05 eV) than for **TS2** (0.33 eV). PBE+U+D reaction energies for both oxidation steps are 0.4 eV more exothermic than hybrid functional results. Dispersion has only a small effect on calculated intrinsic barriers and reaction energies (less than 0.05 eV). Due to partial compensation with differences for the adsorption energies, the PBE+U+D apparent barriers are only 0.1 eV lower than the B3LYP+D barriers, and 0.06 or 0.22 eV lower than the HSE+D barriers for **TS1** and **TS2**, respectively.

Both hybrid functionals yield the same barriers for **TS2**, but the barrier toward **TS1** is 0.2 eV higher with B3LYP. We assign this to the failure of the LYP correlation functional to describe delocalized electronic states properly.[58,59] Sauer and co-workers[21] reported that B3LYP overestimates the intrinsic barrier for an equivalent transition state on a silica support by 0.17 eV compared to CCSD(T). Adding this CCSD(T) decrement to the B3LYP result for **TS1** yields a barrier very close to the HSE result. Therefore, we believe that HSE can be considered as accurate.

## 4. DISCUSSION

**4.1. Methanol Adsorption.** With −1.7 to −1.9 eV, adsorption of methanol on $VO_2$·$CeO_2$(111) is highly exothermic. This is easily understood when methanol adsorbs into the pseudovacancy (**A4**), but it is also the case when methanol binds to vanadium and replaces an anchoring surface oxygen atom, which in turn relaxes into the pseudovacancy (**A1**, **A2**, and **A3**). Our methanol chemisorption energies for vanadia/ceria are almost 1.1 eV higher than the values reported for vanadia/silica (based on B3LYP results, cf. Table 4).[21] They are also substantially higher than the −0.51 and −0.91 eV reported for vanadia/anatase[28] and pristine ceria,[57] respectively.

To the best of our knowledge, experimental adsorption energies are not available for the low vanadia loading studied here. For vanadia loadings of 6 wt % $V_2O_5$·$CeO_2$, which is equivalent to 11.3 V/nm$^2$ and substantially exceeds the loading corresponding to a monolayer,[60] Feng and Vohs determined a methanol desorption energy of 0.83 eV.[61] This value matches the DFT (PW91) adsorption energy of −0.64 eV for methanol on $V_2O_5$(001)[62] when adding the expected dispersion contribution of −0.2 eV (see Table 1).

The V═O stretching mode is one of the characteristic vibrations of vanadia surface species.[63] For **A2**, **A3**, and **A4**, a constant V═O bond distance of 163 pm was found. In contrast to the molecular adsorption structures **A5** and **A6**, in **A2**−**A4** the V═O bond is tilted toward the surface. In addition, the dipoles of the V═O and the O−H bonds are oppositely aligned and couple, which results in a substantial loss of intensity for the V═O stretching mode. This has been demonstrated by calculating IR intensities of a hydrogenated $VO_2$·$CeO_2$(111) surface model. We conclude that the extinction of the V═O stretching band upon methanol adsorption observed by Abbott et al.[12] is due to three effects: interaction with the $OCH_3$ dipole, tilting of V═O toward the surface (selection rule), and screening of the V═O dipole by the OH dipoles.

**4.2. Simulation of TPD Experiments.** Figure 11 shows four different pathways for the formation of formaldehyde. The calculated energy barriers in Table 5 indicate that only two may be relevant: From the vanadium methoxide chemisorption structure (**A3**) via **TS2** (H transfer to oxygen of the ceria surface) and from the chemisorption structure in the pseudovacancy of $CeO_2$ (**A4**) via **TS4** (H transfer to oxygen in the V−O−Ce interphase bond).

**Table 5. ZPVE- and Dispersion Corrected Intrinsic Barriers ($\Delta E^{\ddagger}$) in eV, Theoretical Desorption Temperatures $T_{des}$ in K, Pre-exponential Factors $A$ at $T_{des}$, and Kinetic Isotope Effects for the ODH of Methanol at $VO_2$·$CeO_2$(111)**

| | $\Delta E^{\ddagger}_{PBE+U+D}$ | $\Delta E^{\ddagger}_{HSE+D}$ | $A$ | $T_{des}$ | KIE |
|---|---|---|---|---|---|
| **TS1** | 1.65 | 1.70 | $2.8 \times 10^{12}$ | 640 | 2.2 |
| **TS2** | 1.03 | 1.36 | $3.0 \times 10^{12}$ | 495 | 3.2 |
| **TS3** | 1.09 | 1.4[a] (1.57)[b] | $8.3 \times 10^{12}$ | 510 | 2.3 |
| **TS4** | 0.69 | 1.0[a] (1.15)[b] | $2.2 \times 10^{13}$ | 370 | 6.1 |
| $CeO_2$[c] | 1.33 | 1.44 | $7.8 \times 10^{11}$ | 590 | 2.6 |

[a]Estimated by adding the HSE correction from **TS2** to the PBE+U value. [b]In parentheses: result of single-point HSE+D calculation. [c]Reference 57.

For a more detailed comparison with the experiments by the Freund group,[12,13] temperature-programmed desorption spectra have been simulated. Note that the experiments start from dissociatively adsorbed $CH_3OH$ at presaturated surfaces, i.e. in the high-coverage regime.[12,13] According to the reaction mechanisms discussed in the previous sections, the intrinsic barrier for the oxidation step $\Delta E^{\ddagger}_0$ is also the barrier for formaldehyde desorption. Assuming first-order kinetics, the desorption rate $dx/dt$ is given by


dx.doi.org/10.1021/ja508657c | J. Am. Chem. Soc. 2014, 136, 14616−14625

$$-\frac{dx}{dt} = \frac{k_B T}{h} \cdot \frac{q^{\ddagger}}{q} \cdot \exp\left(-\frac{\Delta E_0^{\ddagger}}{k_B T}\right) \cdot x$$

with coverage $x$ and temperature $T$ as time-dependent quantities. This differential equation was solved numerically with a (constant) heating rate of 3 K/s, which was also used in the experiment. The initial coverage for each pathway was set to $x_0 = 1$. Calculated (PBE+U+D) partition functions for transition state ($q^{\ddagger}$) and adsorption complex ($q$) are compiled in Table 5 for the reaction pathways studied. For the barriers we use ZPVE-corrected HSE+D values, estimated by adding the HSE corrections for **TS2** to the PBE+U+D results for **TS3** and **TS4**. This seems justified because the three transition states have similar electronic structures. We have also calculated the reaction rates for fully deuterated $CD_3OD$ in order to quantify the kinetic isotope effect KIE = $k_H/k_D$ for each oxidation pathway.

The predicted desorption temperatures in Table 5 confirm that from **A3** only the desorption pathway via **TS2** and from **A4** only the pathway via **TS4** are relevant. The resulting desorption rates are plotted in Figure 13 along with the TPD spectrum

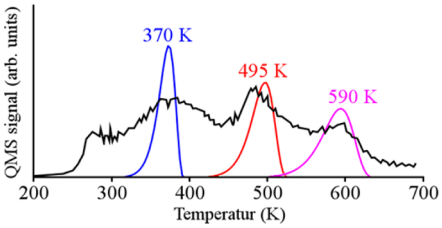


**Figure 13.** Experimental TPD spectrum[13] (black) along with the simulated $CH_2O$ desorption peaks via **TS4** (blue) and **TS2** (red). The third peak (purple) originates from the defective (= oxygen vacancy) $CeO_2(111)$ surface as shown in ref 57.

recorded for monomeric vanadia clusters as published in ref 13. At vanadia loadings of around 2.7 V/nm$^2$, the pristine $CeO_2(111)$ surface is exposed and may contribute to the formaldehyde formation as well. Therefore, we include the desorption peak resulting from the vanadia-free surface that is discussed in ref 57. These results suggest the following peak assignments: $\alpha$ peak—formaldehyde formation upon chemisorption into the pseudovacancy (**TS4**), $\beta$ peak—formaldehyde formation from methoxide at the vanadia surface species (**TS2**), and $\gamma$ peak—formaldehyde formation on the ceria support without vanadia participation.[57] The pathway via **TS4** has the highest KIE, which is plausible, as this pathway occurs at the lowest temperature. With fully deuterated $CD_3OD$, the $\alpha$ peak occurs at 390 K.

HSE barriers are in excellent agreement with experimental barriers, which were derived by assuming a constant pre-exponential factor of $10^{13}$ s$^{-1}$. DFT frequency calculations render a calculation of pre-exponentials possible. The pre-exponential factors compiled in Table 5 show that the conventional assumption of $10^{13}$ s$^{-1}$ is reasonable. In fact, we advise against blind fitting to experimental values, as it might introduce significant errors due to the simplicity of the Redhead model. For a $V_2O_5$·$CeO_2$ catalyst, Vohs et al.[64] fitted the formaldehyde desorption peak at 540 K with a pre-exponential factor of $2 \times 10^7$ s$^{-1}$ and a barrier of 84 kJ/mol, which is significantly lower than values reported in the present work. However, "static" transition state theory for simulating TPD spectra is, for example, not able to describe equilibria between different adsorption structures. This is expected to significantly broaden the peaks.

A mechanistic study of vanadia polymers and monolayer films on ceria is underway. TPD studies demonstrate that higher loadings behave differently from monomers. The missing low temperature peak[13,64] fits to the prediction of a lower activity of polymers based on oxygen defect formation energies.[20]

### 4.3. Cooperativity between Vanadia and the Support.

The partial oxidation of methanol on supported vanadia proceeds in three steps:

(1) heterolytic splitting of $CH_3OH$ and chemisorption of the methoxide anion,

$$HCH_2{-}OH \rightarrow HCH_2{-}O^-_{(s)} + H^+_{(s)}$$

(2) hydrogen abstraction from the methyl group,

$$HCH_2{-}O^-_{(s)} \rightarrow {}^{\bullet}CH_2{-}O^-_{(s)} + H^+_{(s)} + e^-_{(s)}$$

(3) formaldehyde release.

$${}^{\bullet}CH_2{-}O^-_{(s)} \rightarrow CH_2{=}O_{(s)} + e^-_{(s)}$$

Of the two hydrogen atoms that are removed from $CH_3OH$, one is decoupled into initial deprotonation (step 1) and final electron transfer on formation of molecular formaldehyde (step 3), whereas one is removed in a proton-coupled electron transfer step (PCET, step 2).

Different sites of the vanadia surface species are involved in the different steps. For monomeric vanadia species on silica, methanol chemisorbs at the V—O—Si interphase bond and forms a V—$OCH_3$ species, whereas the H atom is transferred to the V=O bond. In the transition structure, the proton is attached to the O atom, and the electron is accommodated in vanadium $d$ states, reducing vanadium from +5 to +4 (PCET). When $CH_2$=O is released, another electron is transferred to vanadium $d$ states, creating a $V^{+3}$ species.

For monomeric vanadia species on titania, both rutile[30,31] and anatase,[28] $CH_3OH$ also chemisorbs at the V—O—Ti interphase bond yielding a methoxide group attached to V and an OH group attached to the support. Hydrogen transfer is most favorable to the vanadyl O atom on the rutile support,[30,31] whereas a surface O atom is the best H acceptor for vanadia/anatase.[28] In the latter case, both electrons are transferred into subsurface Ti $d$ states.

For our vanadia/ceria system, the most favored pathway starts from methoxide adsorbed at the ceria surface in a pseudovacancy (**A4**) that is formed upon deposition of the monomeric vanadia species. When the H atom is transferred to the V—O—Ce interphase bond (**TS4**, −0.69 eV), the V—O bond gets protonated, whereas the electron is accommodated in Ce $f$ states, creating a $Ce^{3+}$ ion. An example with even more distant proton and electron accepting sites is selective oxidation of butane at vanadium phosphate oxide.[65,66] It has been found that the proton is transferred to P=O bonds, whereas the electron occupies vanadium $d$ states.

Methanol may also chemisorb at the V—O—Ce interphase bond and form a V—$OCH_3$ species (**A3**). For the hydrogen transfer there are two options. Similarly to vanadia/silica, the H atom can be transferred to the oxygen atom of the vanadyl bond (**TS1**), but H transfer to the ceria surface yields a lower


dx.doi.org/10.1021/ja508657c | J. Am. Chem. Soc. 2014, 136, 14616−14625

barrier (1.03 eV). In the transition structure (**TS2**) the proton binds to an oxygen ion of the ceria surface, and the electron is accommodated in a cerium *f* state, reducing cerium from +4 to +3. On rearrangement of the bridging V···O($CH_2$)···HO surface structure (**I6**) into molecularly adsorbed $CH_2O$ (**I3**), another electron is transferred into Ce *f* states.

In both cases, ceria is directly involved in the redox process, as two electrons are accommodated in Ce *f* states forming two $Ce^{3+}$ ions whereas vanadium remains fully oxidized ($V^{5+}$). In previous studies[11,13] we have shown, for vanadia supported on ceria and for vanadia−ceria gas phase clusters,[67] that vanadium is always stabilized in its highest oxidation state (+5) and a $Ce^{3+}/V^{5+}$ redox pair is always more stable than a $Ce^{4+}/V^{4+}$ redox pair. This is a consequence of the specific coordination of the ions at this interphase and the specific relaxation possibilities and is by no means trivial. In aqueous solution there is a preference for the $Ce^{3+}/V^{5+}$ redox pair, as the reduction potentials of 1.3−1.7 eV for $Ce^{4+}$ and 1.0 eV for $V^{5+}$ (in $VO_2^+$) indicate.[67] This is also the case for the bulk oxides as the reaction

$$CeO_2 + VO_2 \rightarrow \frac{1}{2}Ce_2O_3 + \frac{1}{2}V_2O_5 \quad (4)$$

is endothermic ($\Delta H^\circ$ = 1.1−1.3 eV), whereas the formation of $CeVO_4$ is exothermic ($\Delta H^\circ$ = −1.5 eV).[68,69] As a result, transition states with (partially) populated V *d* states such as **TS1** are disfavored over transition states with populated Ce *f* states (**TS2**−**TS4**).

On the vanadia-free ceria surface, the hydrogen atom is transferred to an oxygen of the ceria surface (as in **TS2**), but from a methoxy species that is also bound to the ceria surface which results in a higher intrinsic barrier (1.44 eV, Table 5) and a higher formaldehyde desorption temperature (590 K). Note that an oxygen vacancy is needed to bind methanol strong enough that it will not desorb before hydrogen transfer occurs.[57]

On the pure $V_2O_5$ surface, methanol adsorption also occurs on oxygen defects only,[62] and the barriers are expected to be similar to **TS1** and to the transition structure for the vanadia/silica system, which explains the higher temperatures at which formaldehyde formation is observed (400−550 K).[62]

## 5. CONCLUSIONS

Compared to the vanadia/silica system, the vanadia/ceria system is a more active catalyst both because methanol binds more strongly on the surface and the intrinsic barriers for the hydrogen transfer step are lower. The reason is the direct participation of ceria in the redox process. On nonreducible supports such as silica, vanadia is reduced, whereas ceria as a support stabilizes vanadium in its highest oxidation state. Our successful simulation of two peaks observed in temperature-programmed desorption experiments confirms the prediction of two low energy pathways that involve different surface sites in the adsorption and hydrogen transfer steps.

Vanadia/ceria is also a more active catalyst than ceria alone or vanadia alone where methanol adsorption occurs at oxygen vacancies and hydrogen is transferred to a neighbored site on the oxide surface.

We conclude that support effects are complex phenomena and the role of the support goes far beyond a mere electronic polarization, as captured by electronegativity scales. Different active sites may be involved for different supports. The support may also provide sites for binding the substrate molecules, and reducible supports may be involved in the redox process.

## ■ ASSOCIATED CONTENT

### Supporting Information

Simulated vibrational spectra for **A1**−**A4**, structures of intermediates, and a table with total energies. This material is available free of charge via the Internet at http://pubs.acs.org.

## ■ AUTHOR INFORMATION

### Corresponding Author

js@chemie.hu-berlin.de

### Notes

The authors declare no competing financial interest.

## ■ ACKNOWLEDGMENTS

This work has been supported by "Deutsche Forschungsgemeinschaft" (DFG) within the Cluster of Excellence "Unifying Concepts in Catalysis" and by the "Fonds der Chemischen Industrie" (FCI) as well as by grants for computing time at the high-performance computer centers HLRN (North-German Supercomputing Alliance in Berlin and Hannover) and JUROPA (Forschungszentrum Jülich). COST action CM1104, reducible oxide chemistry, structure and functions is gratefully acknowledged.

## ■ REFERENCES

(1) Somorjai, G. A.; Li, Y. *Introduction to Surface Chemistry and Catalysis*; John Wiley & Sons: Hoboken, NJ, 2010.
(2) Thomas, J. M.; Thomas, W. J. *Principles and Practice of Heterogeneous Catalysis*; Wiley: Weinheim, 1997.
(3) An, K.; Alayoglu, S.; Musselwhite, N.; Plamthottam, S.; Melaet, G.; Lindeman, A. E.; Somorjai, G. A. *J. Am. Chem. Soc.* **2013**, *135*, 16689.
(4) Deo, G.; Wachs, I. E. *J. Catal.* **1994**, *146*, 323.
(5) Wachs, I. E.; Deo, G.; Juskelis, M. V.; Weckhuysen, B. M. In *Dynamics of Surfaces and Reaction Kinetics in Heterogeneous Catalysis*; Froment, G. F., Waugh, K. C., Eds.; Elsevier: Amsterdam, 1997; p 305.
(6) Wachs, I. E.; Chen, Y.; Jehng, J.-M.; Briand, L. E.; Tanaka, T. *Catal. Today* **2003**, *78*, 13.
(7) Wachs, I. E. In *Catalysis*; Spivey, J. J., Ed.; The Royal Society of Chemistry: 1997; Vol. *13*, p 37.
(8) Khodakov, A.; Olthof, B.; Bell, A. T.; Iglesia, E. *J. Catal.* **1999**, *181*, 205.
(9) Beck, B.; Harth, M.; Hamilton, N. G.; Carrero, C.; Uhlrich, J. J.; Trunschke, A.; Shaikhutdinov, S.; Schubert, H.; Freund, H.-J.; Schlögl, R.; Sauer, J.; Schomäcker, R. *J. Catal.* **2012**, *296*, 120.
(10) Olthof, B.; Khodakov, A.; Bell, A. T.; Iglesia, E. *J. Phys. Chem. B* **2000**, *104*, 1516.
(11) Baron, M.; Abbott, H.; Bondarchuk, O.; Stacchiola, D.; Uhl, A.; Shaikhutdinov, S.; Freund, H.-J.; Popa, C.; Ganduglia-Pirovano, M. V.; Sauer, J. *Angew. Chem., Int. Ed.* **2009**, *48*, 8006.
(12) Abbott, H. L.; Uhl, A.; Baron, M.; Lei, Y.; Meyer, R. J.; Stacchiola, D. J.; Bondarchuk, O.; Shaikhutdinov, S.; Freund, H. J. *J. Catal.* **2010**, *272*, 82.
(13) Ganduglia-Pirovano, M. V.; Popa, C.; Sauer, J.; Abbott, H. L.; Uhl, A.; Baron, M.; Stacchiola, D.; Bondarchuk, O.; Shaikhutdinov, S.; Freund, H.-J. *J. Am. Chem. Soc.* **2010**, *132*, 2345.
(14) Paier, J.; Penschke, C.; Sauer, J. *Chem. Rev.* **2013**, *113*, 3949.
(15) McQuarters, A. B.; Wolf, M. W.; Hunt, A. P.; Lehnert, N. *Angew. Chem., Int. Ed.* **2014**, *53*, 4750.
(16) Wachs, I. E. *Catal. Today* **2005**, *100*, 79.
(17) Sauer, J.; Döbler, J. *Dalton Trans.* **2004**, *19*, 3116.
(18) Kim, H. Y.; Lee, H. M.; Pala, R. G. S.; Shapovalov, V.; Metiu, H. *J. Phys. Chem. C* **2008**, *112*, 12398.

(19) Rozanska, X.; Fortrie, R.; Sauer, J. *J. Am. Chem. Soc.* **2014**, *136*, 7751.
(20) Penschke, C.; Paier, J.; Sauer, J. *J. Phys. Chem. C* **2013**, *117*, 5274.
(21) Döbler, J.; Pritzsche, M.; Sauer, J. *J. Am. Chem. Soc.* **2005**, *127*, 10861.
(22) Bronkema, J. L.; Bell, A. T. *J. Phys. Chem. C* **2007**, *111*, 420.
(23) Burcham, L. J.; Wachs, I. E. *Catal. Today* **1999**, *49*, 467.
(24) Mars, P.; van Krevelen, D. W. *Chem. Eng. Sci.* **1954**, *3* (Supplement 1), 41.
(25) Rozanska, X.; Kondratenko, E. V.; Sauer, J. *J. Catal.* **2008**, *256*, 84.
(26) Popa, C.; Ganduglia-Pirovano, M. V.; Sauer, J. *J. Phys. Chem. C* **2011**, *115*, 7399.
(27) Paier, J.; Kropp, T.; Penschke, C.; Sauer, J. *Faraday Discuss.* **2013**, *162*, 233.
(28) Shapovalov, V.; Fievez, T.; Bell, A. T. *J. Phys. Chem. C* **2012**, *116*, 18728.
(29) Goodrow, A.; Bell, A. T. *J. Phys. Chem. C* **2008**, *112*, 13204.
(30) Kim, H. Y.; Lee, H. M.; Pala, R. G. S.; Metiu, H. *J. Phys. Chem. C* **2009**, *113*, 16083.
(31) Kim, H. Y.; Lee, H. M.; Metiu, H. *J. Phys. Chem. C* **2010**, *114*, 13736.
(32) Ernzerhof, M.; Scuseria, G. E. *J. Chem. Phys.* **1999**, *110*, 5029.
(33) Grimme, S. *J. Comput. Chem.* **2006**, *27*, 1787.
(34) Kerber, T.; Sierka, M.; Sauer, J. *J. Comput. Chem.* **2008**, *29*, 2088.
(35) Anisimov, V. I.; Zaanen, J.; Andersen, O. K. *Phys. Rev. B* **1991**, *44*, 943.
(36) Liechtenstein, A. I.; Anisimov, V. I.; Zaanen, J. *Phys. Rev. B* **1995**, *52*, R5467.
(37) Blöchl, P. E. *Phys. Rev. B* **1994**, *50*, 17953.
(38) Kresse, G.; Joubert, D. *Phys. Rev. B* **1999**, *59*, 1758.
(39) Kresse, G.; Furthmüller, J. *Phys. Rev. B* **1996**, *54*, 11169.
(40) Kresse, G.; Furthmüller, J. *Comput. Mater. Sci.* **1996**, *6*, 15.
(41) Perdew, J. P.; Ernzerhof, M.; Burke, K. *J. Chem. Phys.* **1996**, *105*, 9982.
(42) Fabris, S.; Vicario, G.; Balducci, G.; de Gironcoli, S.; Baroni, S. *J. Phys. Chem. B* **2005**, *109*, 22860.
(43) Castleton, C. W. M.; Kullgren, J.; Hermansson, K. *J. Chem. Phys.* **2007**, *127*, 244704.
(44) Dudarev, S. L.; Botton, G. A.; Savrasov, S. Y.; Humphreys, C. J.; Sutton, A. P. *Phys. Rev. B* **1998**, *57*, 1505.
(45) Bengone, O.; Alouani, M.; Blöchl, P.; Hugel, J. *Phys. Rev. B* **2000**, *62*, 16392.
(46) Heyd, J.; Scuseria, G. E.; Ernzerhof, M. *J. Chem. Phys.* **2003**, *118*, 8207.
(47) Becke, A. D. *J. Chem. Phys.* **1993**, *98*, 5648.
(48) Lee, C.; Yang, W.; Parr, R. G. *Phys. Rev. B* **1988**, *37*, 785.
(49) Mills, G.; Jonsson, H.; Schenter, G. K. *Surf. Sci.* **1995**, *324*, 305.
(50) Jonsson, H.; Mills, G.; Jacobsen, K. W. In *Classical and Quantum Dynamics in Condensed Phase Simulations*; Berne, J., Ciccotti, G., Coker, D. F., Eds.; World Scientific: Singapore, 1998; p 385.
(51) Henkelman, G.; Uberuaga, B. P.; Jonsson, H. *J. Chem. Phys.* **2000**, *113*, 9901.
(52) Henkelman, G.; Jonsson, H. *J. Chem. Phys.* **1999**, *111*, 7010.
(53) Heyden, A.; Bell, A. T.; Keil, F. J. *J. Chem. Phys.* **2005**, *123*, 224101.
(54) Momma, K.; Izumi, F. *J. Appl. Crystallogr.* **2011**, *44*, 1272.
(55) Watkins, M. B.; Foster, A. S.; Shluger, A. L. *J. Phys. Chem. C* **2007**, *111*, 15337.
(56) Romanyshyn, Y.; Guimond, S.; Kuhlenbeck, H.; Kaya, S.; Blum, R. P.; Niehus, H.; Shaikhutdinov, S.; Simic-Milosevic, V.; Nilius, N.; Freund, H. J.; Ganduglia-Pirovano, M. V.; Fortrie, R.; Döbler, J.; Sauer, J. *Top. Catal.* **2008**, *50*, 106.
(57) Kropp, T.; Paier, J. *J. Phys. Chem. C* **2014**, DOI: 10.1021/jp505088b.
(58) Kurth, S.; Perdew, J. P.; Blaha, P. *Int. J. Quantum Chem.* **1999**, *75*, 889.
(59) Paier, J.; Marsman, M.; Kresse, G. *J. Chem. Phys.* **2007**, *127*, 024103.
(60) Wachs, I. E. *Dalton Trans.* **2013**, *42*, 11762.
(61) Feng, T.; Vohs, J. M. *J. Catal.* **2004**, *221*, 619.
(62) Sturm, J. M.; Göbke, D.; Kuhlenbeck, H.; Döbler, J.; Reinhardt, U.; Ganduglia-Pirovano, M. V.; Sauer, J.; Freund, H. J. *Phys. Chem. Chem. Phys.* **2009**, *11*, 3290.
(63) Magg, N.; Immaraporn, B.; Giorgi, J. B.; Schroeder, T.; Bäumer, M.; Döbler, J.; Wu, Z. L.; Kondratenko, E.; Cherian, M.; Baerns, M.; Stair, P. C.; Sauer, J.; Freund, H. J. *J. Catal.* **2004**, *226*, 88.
(64) Wong, G. S.; Concepcion, M. R.; Vohs, J. M. *J. Phys. Chem. B* **2002**, *106*, 6451.
(65) Cheng, M.-J.; Nielsen, R. J.; Tahir-Kheli, J.; Goddard, W. A., III. *Phys. Chem. Chem. Phys.* **2011**, *13*, 9831.
(66) Cheng, M.-J.; Goddard, W. A., III. *J. Am. Chem. Soc.* **2013**, *135*, 4600.
(67) Jiang, L.; Wende, T.; Claes, P.; Bhattacharyya, S.; Sierka, M.; Meijer, G.; Lievens, P.; Sauer, J.; Asmis, K. R. *J. Phys. Chem. A* **2011**, *115*, 11187.
(68) Da Silva, J. L. F.; Ganduglia-Pirovano, M. V.; Sauer, J. *Phys. Rev. B* **2007**, *76*, 125117.
(69) Da Silva, J. L. F.; Ganduglia-Pirovano, M. V.; Sauer, J.; Bayer, V.; Kresse, G. *Phys. Rev. B* **2007**, *75*, 045121.

# P6

https://pubs.acs.org/doi/abs/10.1021/jp505088b

THE JOURNAL OF PHYSICAL CHEMISTRY C

Article

pubs.acs.org/JPCC

# Reactions of Methanol with Pristine and Defective Ceria (111) Surfaces: A Comparison of Density Functionals

Thomas Kropp and Joachim Paier*

Institut für Chemie, Humboldt-Universität zu Berlin, Unter den Linden 6, 10099 Berlin, Germany

Supporting Information

**ABSTRACT:** We study the dissociative adsorption and oxidative dehydrogenation of methanol at the pristine and O-defective ceria (111) surfaces to understand the role of surface oxygen vacancies. The accuracy of two density functional theory based approaches (PBE+U and the HSE hybrid functional) is assessed on available experimental data. In addition, the impact of dispersion correction and zero-point vibrational energy contributions is discussed. Calculated vibrational frequencies are compared with experimental IR spectra. Using dispersion-corrected PBE+U, we obtain comparably large intrinsic barriers for the oxidation step at the pristine (104 kJ/mol) and defective (119 kJ/mol) ceria surfaces. Compared to HSE+D, these barriers are underestimated by 20 kJ/mol. Adsorption energies for the pristine surface agree well between PBE+U+D (−88 kJ/mol) and HSE+D (−86 kJ/mol). However, adsorption energies for the defective surface vary by 25 kJ/mol (PBE+U+D: −231 kJ/mol; HSE+D: −206 kJ/mol). Nonetheless, adsorption into surface oxygen defects is thermodynamically highly favored. As a result, oxygen vacancies are preferred active sites for methanol oxidation in temperature-programmed desorption experiments.

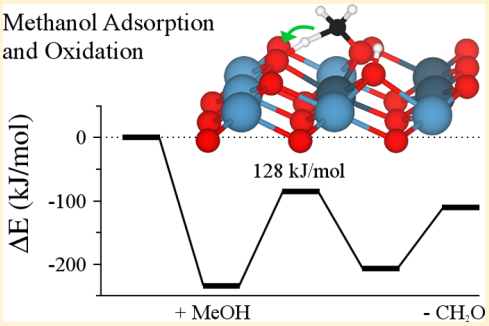


## 1. INTRODUCTION

Studying the interaction of alcohols with oxide surfaces is motivated by the importance of oxidizing alcohols to industrially valuable aldehydes. Furthermore, oxide catalysts can be used to reduce environmental pollution from volatile organic compounds (see, e.g., ref 1). In addition, the selective oxidation of methanol to formaldehyde (FA) has become an important model reaction to study C−H bond activation (see refs 2 and 3 and references therein). The site requirements for the interaction of oxygen-containing molecules, i.e. oxygenates, with various technologically important metal oxide surfaces are thoroughly discussed in a recent review article by Vohs.[4]

The rare-earth oxide ceria ($CeO_2$) represents a very active oxidation catalyst and is therefore widely used in catalysis.[5,6] Its outstanding oxygen storage capacity, which is related to relatively low oxygen vacancy formation energies, qualifies ceria for many applications such as exhaust catalysis[7] and solid-oxide fuel cells.[8] The oxidative dehydrogenation (ODH) of methanol to FA at the thermodynamically most stable $CeO_2(111)$ surface (see refs 9−12) of single crystals,[13] thin films,[14−16] and supported ceria nanoparticles,[17] preferentially exposing the (111) facet, has been studied experimentally by temperature-programmed desorption (TPD),[2,3,16] infrared reflection−absorption spectroscopy (IR-AS),[15] noncontact atomic force microscopy (NC-AFM),[18] and near-edge X-ray absorption fine structure spectroscopy (NEXAFS).[14]

The above-mentioned studies suggest that the formation of FA involves the following elementary steps: the dissociative adsorption of methanol leading to a methoxide and a hydroxyl group (proton transfer from the Brønsted acidic OH; heterolytic bond cleavage) and the supposedly rate-determining H-transfer from the methoxide to the surface, which results in FA and a second surface hydroxyl group (homolytic bond cleavage; redox step). The entire catalytic cycle proceeds according to the Mars−van Krevelen mechanism,[19] which involves water formation, desorption of FA and water (leading to a surface oxygen vacancy), and a fast reoxidation step by molecular oxygen. The present work focuses on the first two steps: methanol adsorption and H-transfer. Therefore, emphasis is implicitly put on respective low concentration limits of methanol and oxygen defects in $CeO_2(111)$. Other reaction channels such as the disproportionation of the adsorbed methoxide to FA and methanol are not considered in this computational study.

Concerning the methanol adsorption on ceria, there has been a debate on the importance of surface oxygen vacancies. There is experimental evidence as well as support by density functional theory (DFT) studies of Mei et al.[20] and Beste et al.[21] that methanol adsorbs dissociatively at low coverages regardless of the presence of vacancies. However, the fully oxidized $CeO_2(111)$ surface interacts rather weakly with methanol, and surface oxygen vacancies were found to be thermodynamically more favorable adsorption sites.[13,22] Beste et al.[21] also reported C−O stretching frequencies for their adsorption structures but did not comment on other vibrational modes. Accurate assignment of the vibrational modes to the

Received: May 23, 2014
Revised: August 25, 2014
Published: September 25, 2014





dx.doi.org/10.1021/jp505088b | J. Phys. Chem. C 2014, 118, 23690−23700

bands of the complex experimental IR spectra presented in refs 15 and 23 is still an open issue.

Carbon oxides are known side products[14] of the ODH of methanol; however, at the $CeO_2(111)$ surface, FA is the primary product. The activity, i.e., yield obtained in the TPD experiments, is known to increase with the number of defect sites.[4,13] Therefore, oxygen vacancies are expected to be the reactive sites. In the presence of molecular oxygen, the selectivity toward FA decreases.[24] The $CeO_2(100)$ surface is considered more active as well but has a lower selectivity toward FA.[16,25] Teng et al.[24] suggested a mechanism for the oxidation of FA to $CO_X$, but the atomic details for the initial oxidation step toward FA are not yet known.

From a computational perspective, creation of oxygen vacancies in the ceria surface poses challenges to DFT as discussed in ref 26: upon oxygen defect formation, the two remaining electrons localize in the Ce *f* states, consequently forming two $Ce^{3+}$ ions. Conventional functionals based on the generalized-gradient approximation (GGA) suffer from so-called self-interaction errors (SIE), which lead to completely delocalized excess electrons in the reduced surface. This failure of the GGA can be rectified with the DFT+U approach[27,28] or by use of hybrid functionals,[29] where the latter mix a certain amount of Fock exchange with GGA exchange. In calculations with hybrid functionals, SIE are partially alleviated. Both approaches describe the localization of the excess electrons correctly. However, accuracy of thermochemistry and kinetics of chemical reactions on surfaces needs further investigations.

Besides the erroneously delocalized excess electrons, it is well documented in the literature that GGA as well as conventional hybrids fall short of a proper description of long-ranged dispersion interactions.[30] However, the adsorption of molecules at surfaces is also influenced by van der Waals forces, most importantly dispersion interactions. Currently, many researchers have vivid interest in developing functionals that describe dispersion interactions correctly.[31−40] Admittedly, this type of interaction will be more important for physisorption of molecules at surfaces. They will be of lesser importance, though not entirely negligible, for chemisorption processes as discussed in the present work.

We report adsorption energies and barriers obtained using DFT+U based on the Perdew, Burke, and Ernzerhof[41−43] (PBE) GGA functional and the range-separated Heyd, Scuseria, and Ernzerhof[44,45] (HSE) hybrid functional employing periodic boundary conditions and plane waves as a basis set. Both methods will be systematically compared to show that the computationally less demanding PBE+U approach is reasonably accurate for this system. In addition, the influence of Grimme's dispersion correction[46] and the zero-point vibrational energy (ZPVE) will be discussed. Previous studies considered slab models with nine atomic layers to be converged (see ref 26 and references therein), though this proves to be challenging for transition state search algorithms, especially when using hybrid functionals. Because of that, a six-layer model is tested and compared to the nine-layer results. This work attempts to answer questions concerning the activity of pristine and defective $CeO_2(111)$ in the ODH of methanol by calculating barriers using PBE+U and HSE. By virtue of calculated harmonic IR frequencies and intensities, we endeavor to accurately assign IR modes to observed bands for the adsorbed methanol at both aforementioned ceria surfaces.

## 2. COMPUTATIONAL DETAILS

**Surface Model.** For PBE+U and HSE calculations subject to periodic boundary conditions, a $p(4 \times 4)$ surface unit cell was generated by cutting bulk $CeO_2$ in (111) orientation with cell vectors that amount to 15.518 and 15.266 Å, respectively. The cell vector in the *z*-direction was set to 17 Å for models using six atomic layers (6L $\triangleq$ $Ce_{32}O_{64}$) and 19 Å for nine atomic layers (9L $\triangleq$ $Ce_{48}O_{96}$) to avoid image interactions. Atomic positions of the lowest trilayer were kept frozen to simulate the bulk. Because of the large cell, sampling of the Brillouin zone was restricted to the Γ point. Unless specified otherwise, energies refer to the nine-layer slab.

**Electronic and Ionic Structure Optimizations.** Calculations were performed using the projector augmented wave method (PAW)[47,48] to describe the interaction between ionic cores and valence electrons as implemented in the Vienna *ab initio* simulation package (VASP).[49,50] The onsite Coulomb correlation of occupied Ce 4f orbitals is corrected via the DFT+U approach[27,28] employing the exchange-correlation functional by Perdew, Burke, and Ernzerhof (PBE)[51] and an *effective* Hubbard-type U parameter of 4.5 eV, i.e., PBE+U. The specific implementation of DFT+U used in this work follows Dudarev et al.[52,53] Selected structures were also obtained using the hybrid functional by Heyd, Scuseria, and Ernzerhof (HSE)[44] with a range-separation parameter of 0.207 $Å^{-1}$.[54] A plane-wave kinetic energy cutoff of 600 eV was used, and structure optimizations were performed until forces acting on the relaxed atoms were below 0.02 eV $Å^{-1}$. Optimized structures using PBE+U were proven to be minima by the absence of imaginary vibrational frequencies (see below). Oxygen defect formation energies vary by less than 0.04 eV, when the kinetic energy cutoff is changed from 400 to 600 eV. Therefore, the latter value provides technically converged energies. The plane-wave cutoff determining the Fourier grid for the Fock exchange related routines was set to 9/4 times the cutoff for expanding the orbitals (PRECFOCK = normal). O-defect formation energies obtained using a less accurate Fourier grid (PRECFOCK = fast) varied by less than 0.05 eV (including few further ionic optimization steps until force criterion was met).

Projected densities of states (DOS) and local magnetic moments at the $Ce^{3+}$ ions are obtained by projecting the spin density into spherical harmonics of *f* symmetry located in Ce-centered PAW spheres with a radius of 1.3 Å. Because the PAW spheres are not space-filling, a typical value for the local magnetic moment of $Ce^{3+}$ amounts to $\pm 0.96\ \mu_B$ for up and down spin, respectively.

**Dispersion Correction.** The semiempirical $C_6/R^6$ term by Grimme (DFT+D2) was added to correct for missing long-range dispersion-type interactions.[46,55,56] Required van der Waals parameters for Ce were derived and systematically tested in ref 57 (cf. Supporting Information of that reference). The parameters for Ce are $C_6$ = 20.0 J $nm^6$/mol and $R_0$ = 1.86 Å. The global scaling parameters $s_6$ used within the Grimme approach were set to 0.75 for PBE+U and 0.6 for HSE. For the PBE+U structures, respective global scaling parameters for PBE and PBE0 have been tested. Since both values lead to virtually identical structures and energy contributions, we decided to use the established parameter for PBE. For HSE, the global scaling parameter for PBE0 is used because the only difference between these functionals is the range separation. Thus, HSE and PBE0 are considered to perform rather similarly for


dx.doi.org/10.1021/jp505088b | J. Phys. Chem. C 2014, 118, 23690−23700

thermochemistry.[58] Therefore, it is appropriate to use similar scaling parameters for the dispersion contribution.

**Transition Structure Optimizations.** PBE+U transition structures were obtained using the nudged elastic bands (NEB) algorithm[59,60] in combination with the so-called climbing image method[61] as implemented in VASP. Eight images were used for each NEB calculation with a spring constant of 5 eV/Å$^2$. The improved dimer method (IDM) was used to refine these structures using the same convergence criteria and the same number of atomic degrees of freedom as employed in structure optimizations.[62,63] These structures were proven to be transition structures by the presence of a single imaginary mode (see below). HSE structures were generated by adding the scaled O−$CH_2$··H··O moiety of the PBE+U transition structure to the optimized HSE surface slab. A scaling factor of 0.983 was used, which corresponds to the ratio of the lattice constants. Thereafter, all degrees of freedom not associated with the imaginary mode were optimized.

**Harmonic Frequencies and IR Intensities.** Vibrational frequencies and normal modes were obtained by diagonalization of a partial, mass-weighted matrix of second derivatives with respect to each of the three Cartesian degrees of freedom for each atom. This "Hessian" matrix was obtained by finite differences of the gradients with displacements of ±0.015 Å (central differences). Frequencies for the ZPVE correction as well as the IR signals for methanol on the clean and defective ceria surface use the topmost three atomic layers including all adatoms. No scaling factors were employed for the harmonic frequencies. We consider the harmonic approximation as justified as calculated vibrations were larger than 70 cm$^{-1}$. Intensities were calculated using the approach described in ref 64. The IR intensity $I_m$ of a normal mode coordinate $Q_m$ is proportional to the square of the derivative of the dipole moment component $\mu_\perp$ perpendicular to the surface with respect to the normal mode (see eq 1). This derivative was calculated numerically for each normal mode coordinate.

$$I_m \propto \left(\frac{d\mu_\perp}{dQ_m}\right)^2 \tag{1}$$

IR spectra (harmonic frequencies and intensities) obtained using the HSE functional employ a 6L model and 30 degrees of freedom (10 atoms for the partial Hessian). As shown in previous work, we expect negligible influence on the admolecule's related frequencies.[57] We also tested the influence of the FFT grid density for the Fock exchange (PRECFOCK = fast vs normal) and found that the modes at about 3000 cm$^{-1}$ changed within 5 cm$^{-1}$ and some of the lower lying modes at about 1000 cm$^{-1}$ changed by at most 20 cm$^{-1}$. Hence, the coarser FFT grid gives *de facto* technically converged frequencies for these relatively stiff modes in the adsorbate.

## 3. RESULTS

**3.1. Accuracy of the Approach.** To study effects induced by a reduction of atomic layers from nine to six, we calculated the oxygen defect formation energies, $\Delta E_d(^1/_2O_2)$, for a topmost (surface) oxygen atom in the pristine (eq 2) and defective surfaces (eq 3; cf. Figure S2), respectively. We used PBE+U and HSE to detect possible differences. Both mono- and divacancy point defects will be relevant during methanol oxidation. For all structures, $Ce^{3+}$ localization patterns and spin orientations were kept identical for the 6L and 9L slab models.

$$Ce_nO_{2n}(111) \rightarrow Ce_nO_{2n-1}(111) + \frac{1}{2}O_2 \tag{2}$$

$$Ce_nO_{2n-1}(111) \rightarrow Ce_nO_{2n-2}(111) + \frac{1}{2}O_2 \tag{3}$$

Both the 6L model and HSE cause systematically larger defect formation energies independently (cf. Table 1). At the defective surface, subsurface oxygen atoms next to the defect are lifted by 16−18 pm, which causes strain in the 6L model as the next trilayer is fixed. This energy contribution is largely avoided in the 9L model because of further relaxation in the central trilayer. These lifted subsurface oxygen atoms were also reported by Ganduglia-Pirovano et al.[65] $Ce^{3+}$ ions in next-nearest-neighbor position to the vacancy are favored energetically and the least stable configuration features two nearest-neighbor $Ce^{3+}$ (first row in Table 1). Similar findings were reported for the subsurface O vacancy.[65−67]

**Table 1. Surface Oxygen Vacancy Formation Energies (Corrected for ZPVE Effects) in eV for the Six (6L) and Nine (9L) Layer Model**

| | PBE+U | | HSE | | |
|---|---|---|---|---|---|
| | 6L | 9L | 6L | 9L | obsd |
| | 2.23 | 2.01 | 2.99 | 2.74 | |
| eq 2[a] | | 1.86 | | 2.49 | 4.2[b] |
| | | 1.76 | | 2.44 | |
| eq 3 | 2.44 | 2.26 | 3.09[d] | 2.86[d] | |
| eq 4 | 0.04 | −0.18 | 0.73 | 0.23 | 1.7[c] |
| eq 5 | 2.23 | 2.12 | 2.38 | 2.04 | |

[a]Three different $Ce^{3+}$ patterns listed from top to bottom: $1_1-1_1$,$1_1-2_1$, and $2_1-2_1$, where $n_m$ denotes a cation position in the $n$th shell of cations surrounding the defect and $m$ is the cationic layer counted from the surface. [b]Reference 26. [c]The experimental formation enthalpy of water at 0 K is −2.48 eV.[68] [d]HSE single point at HSE+D structure.

For the formation of a second oxygen defect at the surface (eq 3), both slab models yield slightly higher defect formation energies compared to the monovacancy. Concerning HSE, the oxygen defect formation energy is 0.71 eV (0.76 eV) larger than the corresponding PBE+U result for the 9L (6L) model. For a smaller $p(2 \times 2)$ surface cell, a defect formation energy of 2.50 eV (3.30 eV) was reported for PBE+U (HSE),[65] which is in good agreement with results reported in this work.

Equation 2 corresponds to the conventional way of creating an oxygen vacancy in the ceria surface and refers to half the energy of the $O_2$ molecule to avoid errors in the O atom incurred by the approximate exchange-correlation functional. In order to avoid molecular oxygen in the reaction and the associated DFT errors, water formation can be treated instead (eq 4). Note that this pathway involves the desorption of a water molecule from a hydrogenated surface (eq 5).

$$Ce_nO_{2n}(111) + H_2 \rightarrow Ce_nO_{2n-1}(111) + H_2O \tag{4}$$

$$Ce_nO_{2n-2}(OH)_2(111) \rightarrow Ce_nO_{2n-1}(111) + H_2O \tag{5}$$

ZPVE-corrected formation energies, i.e. formation enthalpies, of water from hydrogen and oxygen obtained with PBE (−2.43 eV) and HSE (−2.54 eV) are both very close to the experimental value of −2.48 eV, and therefore reaction energies for eqs 2 and 4 deviate similarly from the experiment. However, only HSE predicts the expected sign for eq 4 correctly but still


dx.doi.org/10.1021/jp505088b | J. Phys. Chem. C 2014, 118, 23690−23700

underestimates the observed value by 1.5 eV. For eq 5, both functionals predict very similar results differing only by 0.05 eV.

**3.2. Methanol Adsorption.** This section summarizes results on the adsorption of methanol at the fully oxidized (**A1**) and the partially reduced (**A2**) ceria surfaces. The latter involves a single oxygen vacancy corresponding to 1/16 monolayer (= 0.48 $nm^{-2}$) of a defect concentration. Adsorption energies are given in Table 2, and both adsorption structures are shown in Figure 1.

**Table 2. Adsorption Energies for Methanol in eV Obtained Using Different Functionals for a 9L Slab Model**

| | PW91[a] | PBE+U | PBE+U+D | HSE[b] | HSE+D |
|---|---|---|---|---|---|
| **A1** | −0.84 | −0.69 | −0.91 | −0.71 | −0.89 |
| **A2** | −2.40 | −2.11 | −2.39 | −1.90 | −2.14 |

[a]Reference 21. [b]HSE single point at the HSE+D structure.

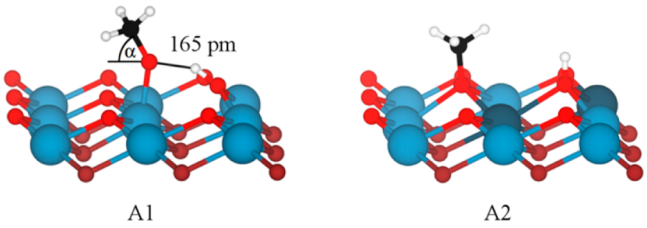


**Figure 1.** Adsorption structures with hydrogen bond lengths. The following color code is used throughout this work: C (black), $Ce^{4+}$ (blue), $Ce^{3+}$ (dark blue), H (white), O (red), and subsurface O (dark red). Figures were created using VESTA.[69]

*Pristine Surface.* **A1** is formed upon dissociative methanol adsorption at the $CeO_2(111)$ surface, i.e., no $Ce^{3+}$ ions are formed, in agreement with Beste et al.[21] The methoxide binds on top of a Ce atom with a Ce−O bond length of 221 pm, thus restoring the octahedral coordination of the $Ce^{4+}$. The structure is further stabilized by a hydrogen bond (165 pm, cf. Figure 1) to the hydroxyl group leading to a PBE+U adsorption energy of −0.69 eV. Dispersion correction results in a smaller tilting angle $\alpha$ of 59° instead of 65° (cf. Figure 1) between methoxide and the surface and stabilizes the adsorption by 0.22 eV (cf. Table 2). Similar tilting angles were found using HSE. The DFT total energies indicate a rather pronounced binding. However, the *free* adsorption energy based on the dispersion corrected PBE+U potential energy surface predicts weaker binding ($\Delta G$ = −0.44 eV at 300 K and the standard pressure of 0.1 MPa). This decrement of 0.47 eV is caused by the loss of entropy. Overall, results for the adsorption at the pristine surface predict comparable adsorption energies ranging between 0.69 and 0.91 eV. Vibrational frequencies for **A1** obtained using PBE+U and HSE are compiled in Table 3. Note that for HSE no intensities were calculated.

*Defective Surface.* **A2** refers to methanol adsorbed into the oxygen vacancy, leading to a methoxide anion in tridentate coordination to surface Ce ions. With a binding energy of −2.39 eV, **A2** is strongly favored over **A1** because the highly endothermic defect is (partly) healed. The resulting structure does not contain hydrogen bonds, and both the methoxide and the hydroxyl group are oriented almost perpendicularly to the surface. Both $Ce^{3+}$ ions (ferromagnetic spin order), caused by the electrons left behind after oxygen vacancy formation, are in next-nearest-neighbor position to the hydroxyl group. Dispersion correction does not affect structural parameters but stabilizes the adsorption by 0.28 eV.

**Table 3. Experimental and Calculated IR Frequencies for Methanol Adsorption Structures at $CeO_2(111)$ in $cm^{-1}$; Calculated Harmonic Frequencies for IR-Inactive Vibrations Are Given in Parentheses**

| | | $\nu_s(CH_3)$ | $r(CH_3)$ | $\nu_s(CO)$ |
|---|---|---|---|---|
| **A1** | PW91+U[a] | | | 1060 |
| | PBE+U | 2879 | 1130 | 1069 |
| | HSE[b] | 2994 | 1209 | 1142 |
| **A2** | PW91+U[a] | | | 1026 |
| | PBE+U | (2863) | (1136) | (1012) |
| | HSE | (2967) | (1227) | (1111) |
| obsd | ref 23[c] | 2803 | 1108, 1065, 1015 | |
| | ref 23[d] | 2808 | 1105, 1058, 1027 | |
| | ref 23[e] | | 1108, 1038 | |

[a]Reference 21 (no intensities given). [b]No intensities calculated. [c]Reference 23. [d]Reference 15. [e]Reference 17.

In the C−O stretching region, multiple peaks were observed experimentally. According to our calculations, **A2** does not show IR-active vibrations in this region. **A1** features two IR modes as the methyl rocking mode (1130 $cm^{-1}$) appears in this region as well. Observed and calculated frequencies (unscaled) are in fairly good agreement, though values obtained using PBE+U are approximately 1% too large. This is a known feature of GGA-type functionals (see, e.g., ref 70). HSE frequencies are rigidly blue-shifted compared to PBE+U results in accordance with scaling factors for harmonic frequencies obtained using PBE0 as shown in the aforementioned reference. Surface OH groups are predicted to be the only IR active species with obvious intensities (PBE+U+D and HSE+D intensities; cf. Supporting Information).

**3.3. Formaldehyde Formation.** Methanol can be oxidized upon adsorption at the pristine $CeO_2(111)$ surface (**A1**) or upon adsorption at a surface oxygen defect site (**A2**). Both pathways have been investigated, and the corresponding mechanisms are shown in Figure 2. Relevant structural parameters are compiled in Table 4.

*Pristine Surface.* Starting with **A1**, a H atom is transferred to a surface oxygen atom (homolytic bond breaking) and an electron is transferred to the $CeO_2$ surface. This leads to transition structure **TS1**. Along its imaginary mode (1143 $cm^{-1}$), the hydrogen transfer occurs and the $CH_2O$ moiety planarizes. Spin density and density of states (DOS) plotted in Figure 3 show a biradicaloid transition state with one electron (up spin) in the newly formed $\pi^*$ orbital of $CH_2O$ and the $\sigma$ orbital of the hydroxyl group (peak A in the local DOS represents both, cf. Figure 3b). Projection as described in section 2 indicates that the second electron occupies a hybrid orbital consisting of a Ce *f* state and the $\pi^*$ orbital (down spin). The *f* and $\pi^*$ orbitals interact and split into a bonding (peak B) and antibonding (peak C) orbital. These states form two peaks in the DOS located around the Fermi level. The local magnetic moment at the $Ce^{3+}$ ion amounts to −0.83 $\mu_B$ compared to the −0.96 $\mu_B$ for a complete electron transfer, which indicates the partial electron transfer in **TS1**. The barrier of this step amounts to 1.25 eV, resulting in an apparent barrier of 0.35 eV. The barrier decreases by 0.16 eV upon adding ZPVE.

Relaxation in the forward direction of **TS1** leads to the local minimum **I1** (cf. Figure 2), where FA is H-bonded between two surface hydroxyl groups. In this structure both unpaired


dx.doi.org/10.1021/jp505088b | J. Phys. Chem. C 2014, 118, 23690−23700

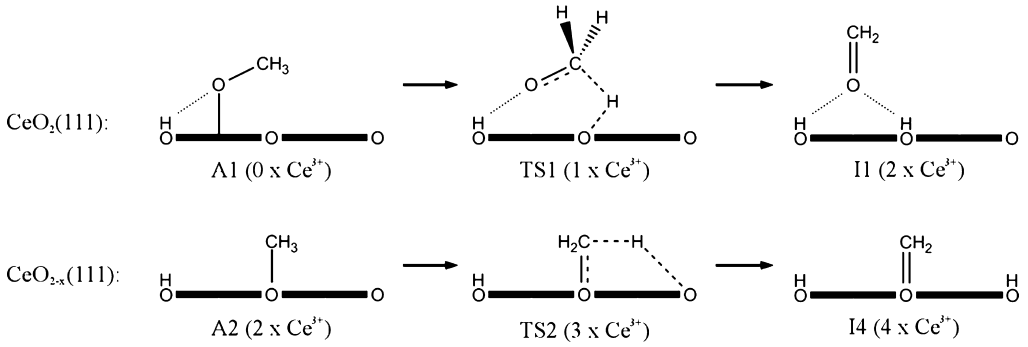


**Figure 2.** Reaction mechanism for the hydrogen transfer step at the pristine (upper part) and defective (lower part) $CeO_2(111)$ surface. Dotted lines represent hydrogen bonds, whereas dashed lines represent delocalized electrons.

**Table 4. Relevant Bond Lengths (pm) for the Structures Shown in Figure 2 Obtained Using Dispersion-Corrected PBE+U**

| | $Ce_nO_{2n}(111)$ | | | $Ce_nO_{2n-1}(111)$ | | |
|---|---|---|---|---|---|---|
| | **A1** | **TS1** | **I1** | **A2** | **TS2** | **I4** |
| $r_{OH\cdots O}$ | 168 | 162 | 253 | | | |
| $r_{O-C}$ | 141 | 133 | 123 | 143 | 140 | 127 |
| $r_{C-H}$ | 110 | 133 | | 110 | 145 | |
| $r_{O-H}$ | | 133 | 97 | | 129 | 97 |

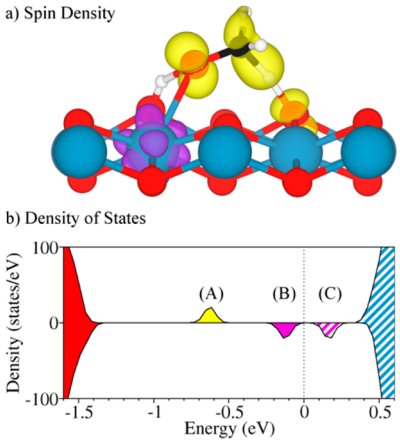


**Figure 3.** (a) Side view of **TS1** showing the spin density isocontour (0.01 $Å^{-3}$) for positive (yellow) and negative (purple) spin densities. (b) Projected local DOS for **TS1** around the Fermi level using the following color code: red (mostly O *p* states), yellow (formaldehyde $\pi^*$ state), purple (hybrid state), and blue (Ce *f* states). Shaded areas represent unoccupied states.

electrons occupy Ce *f* states. The hydrogen transfer is exothermic, resulting in a reaction energy of −0.76 eV. FA desorption leads to **I2** (cf. Supporting Information) and is slightly endothermic with a reaction energy of 0.27 eV. Thereafter, the two hydroxyl groups recombine to form water (**I3**), which leads to the surface defect $Ce_nO_{2n-1}$ upon water desorption. Water formation and desorption are both highly endothermic due to the large O defect formation energy in the $CeO_2(111)$ surface.

The FA desorption (**I1** → **I2**) competes with the formation of a bridging dioxymethylene species **I2′** (cf. Supporting Information), which is assumed to be the key intermediate for further oxidation.[14,24,71] The formation of **I2′** is highly exothermic (−0.81 eV), whereas FA desorption is endothermic by 0.35 eV, but favored in regard to a higher entropy contribution.

Dispersion correction stabilizes structures containing an $OCH_X$ moiety, and the surface oxygen defect is destabilized by 0.19 eV (see also ref 57). As a result, the intrinsic barrier decreases by 0.12 eV and the apparent barrier by 0.30 eV. Structural parameters are not significantly affected by the dispersion correction and change by no more than 1 pm (H bonds are most affected).

*Layer Convergence.* A slab model with six instead of nine atomic layers introduces small errors not higher than 0.2 eV (cf. Figure 4), and both models yield qualitatively similar results.

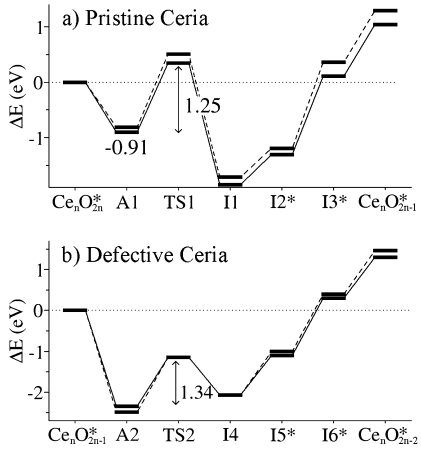


**Figure 4.** Energy profile for the ODH of methanol to FA at the pristine (a) and reduced (b) $CeO_2(111)$ surface. Total energies obtained using dispersion-corrected PBE+U at the six-layer (dashed line) and nine-layer slab (solid line) include gas phase molecules as indicated by an asterisk.

This model affects mostly the desorption steps, which are more endothermic at the smaller 6L model. The structural parameters of the surface layer are similar for both slab models, as relaxation mostly occurs in the subsurface oxygen layer. Using the 6L model for the transition state search algorithms and refining them afterward proved to be a very practicable approach.

*Defective Surface.* The ODH of methanol after adsorption at a surface oxygen defect site (**A2**; cf. Figure 1) occurs via transition structure **TS2** with an imaginary mode (1525 $cm^{-1}$) similar to **TS1**. This step has a slightly higher intrinsic barrier of 1.34 eV compared to the defect-free surface, but because of the high adsorption energy, its apparent barrier is strongly negative


dx.doi.org/10.1021/jp505088b | J. Phys. Chem. C 2014, 118, 23690−23700

and amounts to −0.95 eV. Note that a second transition state associated with a 0.10 eV higher barrier was found for PBE+U. The higher barrier is due to a nearest-neighbor $Ce^{3+}$ configuration in the surface, while in **TS2** these $Ce^{3+}$ are next-nearest neighbors, which features a lower energy (cf. section 3.1). Similar energy differences between different $Ce^{3+}$ localization patterns with respect to the vacancy have been found for minimum-energy structures with both functionals (cf. Table 1). ZPVE lowers the barrier by 0.11 eV. Dispersion correction lowers the apparent barrier by 0.30 eV because of the more exothermic adsorption energy. The four unpaired electrons form a (broken-symmetry) triplet state, which was found to be more stable than the high-spin quintet.

Relaxation in the forward direction of **TS2** leads to **I4**, where FA is adsorbed at the oxygen defect site and the populated Ce 4*f* states overlap with the $\pi^*$ orbital of FA. Because of that, the C═O bond length increases by 3% (cf. Table 4), and desorption of FA (**I4** → **I5*** in Figure 4b) appears to be thermodynamically disfavored with a desorption energy of 1.01 eV. The latter value will be lowered on a free energy surface due to the gain in entropy upon desorption. Again, formation of water (**I6**; cf. Supporting Information) from the two surface OH and water desorption represent highly endothermic processes.

*HSE Results.* The reaction energy obtained using HSE+D for FA formation at the pristine surface (**A1** → **I1**) amounts to −0.28 eV. For the reaction in the surface oxygen vacancy (**A2** → **I4**), HSE+D predicts an oxidation energy of +0.69 eV, which is more endothermic by 0.97 eV. The corresponding intrinsic barrier for the reaction in the defect is 1.55 eV. ZPVE correction decreases the HSE+D barrier to 1.44 eV. In addition, HSE predicts a stronger elongation of the C═O bond in **I4** (cf. Supporting Information) compared to gas phase FA (10%), which relates to a stronger binding of the intermediate.

## 4. DISCUSSION

**4.1. Accuracy of the Approaches: PBE+U vs HSE.** To satisfy the demands for accurate thermochemistry and kinetics, DFT-based methods have to meet two important requirements when applied to *reduced* ceria: first, the energy contribution of structure relaxation has to be captured properly, and second, the energetics of the system (bulk, surfaces, clusters) containing $Ce^{3+}$ has to be accurate. Both factors largely contribute to the overall stability of "reduced ceria" as shown in the literature.[9,11,72,73]

Concerning the relaxation energy contribution obtained from DFT, we consider—as a zero-order approximation—the calculated hardness or bulk modulus of the ceria lattice as a measure for the accuracy for this stabilizing energy contribution. As shown in ref 74, structural and elastic properties of ceria are acceptably accurate using PBE+U (cf. Table 5). Note that equilibrium lattice constants ($a_0$) and bulk moduli ($B_0$) are usually not corrected for zero-point energy and anharmonicity effects. These effects slightly increase $a_0$ (ca. +0.35%) and as a consequence decrease $B_0$.[75] HSE values are in better agreement with experiment. Note that there is quite a spread in the experimental bulk modulus of $CeO_2$ ranging between 204 and 230 GPa.[74]

**Table 5. Lattice Parameter $a_0$ (pm) and Bulk Modulus $B_0$ (GPa) for $CeO_2$ with Different Functionals and Relative Errors to Experimental Values**

| | PBE+U | PBE+U+D | HSE | HSE+D | obsd |
|---|---|---|---|---|---|
| $a_0$ | 549[a] | 548 | 540 | 539 | 541[b] |
| % error | +1.5 | +1.3 | −0.2 | −0.4 | |
| $B_0$ | 180[a] | 190 | 207 | 214 | 230[b] |
| % error | −21.7 | −17.4 | −10.0 | −7.0 | |

[a]Reference 74. [b]References 91 and 92.

The accurate description of the relaxation contribution to reaction energies is crucial, since the oxidation step of the methoxide species involves an electron transfer to form $Ce^{3+}$. Further relaxation in the lattice is due to the larger ionic radius of $Ce^{3+}$ compared to $Ce^{4+}$ as well as a larger $Ce^{3+}$−$O^{2-}$ bond distance. The energy gain upon relaxation is somewhat determined by the hardness of the material. Strongly underestimated bulk moduli as obtained using PBE+U indicate a too "flat" potential energy surface. As the HSE bulk modulus is in much better agreement with experiment, we believe relaxation effects are more accurately described using the hybrid functional.

To corroborate this conjecture, we compare $\Delta E_d(^1/_2O_2)$ for an unrelaxed surface oxygen vacancy (eq 2). The formation energy of a surface defect is calculated to be 3.69 eV by PBE+U and 4.45 eV with HSE, omitting relaxation. Note that for PBE+U the unrelaxed structure of the surface vacancy is difficult to converge electronically. Nevertheless, we are confident that the unrelaxed energies are reliable and a comparison with the lowest defect formation energy shown in Table 1 is worthwhile. We determined an upper boundary for the relaxation contribution, $\Delta E_d^{unrelaxed}(^1/_2O_2) - \Delta E_d^{relaxed}(^1/_2O_2)$, which amounts to 1.93 eV for PBE+U compared to 2.01 eV using HSE. Although the difference between the two approaches is small (0.08 eV), we find that PBE+U clearly underestimates relaxation effects compared to the HSE hybrid. The entanglement of this stabilizing energy contribution with electron transfer in reduced ceria has been recently discussed for the case of Au adatoms on a reduced $CeO_2(111)$ surface.[67]

The accuracy of the exchange-correlation functional naturally affects reaction energies as well as barriers. It is likely that the random-phase approximation (RPA)[76−80] or higher-order corrections to it[81] outperform conventional functionals like GGA(+U) or hybrids (PBE0 or HSE). However, the computational workload of RPA-based functionals is large, and structure optimizations using the RPA have become feasible only lately.[82]

Recent work suggests tuning the U-parameter employed in DFT+U such that important reaction energies involving the bulk phases of $CeO_2$ and $Ce_2O_3$ reasonably fit observed values.[83,84] In a similar spirit the amount of Fock exchange in hybrid functionals can be varied appropriately as done by Sanz and co-workers.[85] However, we try to avoid this approach. The present work uses PBE+U and (unmodified) HSE only. Both are based on the PBE exchange-correlation functional, which fulfills physical constraints and sum rules, e.g., capturing the uniform electron gas limit. The crucial difference is that the U is applied only to the Ce *f* states, while in the hybrid functional all occupied states are subject to the same (generalized) Kohn−Sham[86] Hamiltonian. This results in a partial correction for self-interaction because in HSE a quarter of Fock-type exchange is mixed with three-quarters of the PBE exchange energy.[44,45] This is in contrast to Hartree−Fock, which is completely (one-electron) self-interaction free.[87]

Discrepancies between PBE+U and HSE results can be essentially traced back to the more rigorous correction for SIE


dx.doi.org/10.1021/jp505088b | J. Phys. Chem. C 2014, 118, 23690−23700

using the hybrid functional. However, we emphasize that hybrid functionals still suffer from shortcomings, as seen in the accuracy obtained for heats of formation of bulk $CeO_2$ and $Ce_2O_3$.[74] For a systematic comparison of PBE+U and HSE applied to bulk ceria, we refer to ref 74. Some shortcomings of hybrids applied to other correlated oxides were recently discussed in the literature.[88,89]

*Dispersion Correction.* Concerning a description of dispersion effects within DFT, we are aware that many approaches could be used in principle (cf. section 1). However, as we are mainly interested in trends and relative energies, we believe that the simple $C_6/R^6$ term works reasonably well. This approach avoids other ambiguities, e.g., the inclusion of a large number of (semiempirical) parameters[32] or a strong dependence of results on the exchange-functional employed (see ref 90).

*Defect Formation Energies.* The conventional way to calculate $\Delta E_d(^1/_2O_2)$ follows eq 2. However, considering possible DFT errors in the total energy of the $O_2$ molecule (triplet ground state), eq 4 represents a viable alternative. This equation describes the formation of water from $H_2$ and the clean $CeO_2(111)$ surface. Table 1 shows that defect formation energies obtained using eq 4 consistently underestimate the observed reaction enthalpy of 1.7 eV. HSE correctly predicts an endothermic reaction, whereas PBE+U with 9L does not. However, as already stated in ref 26, the absolute error with respect to the experiment differs only marginally between both approaches.

Moreover, the defect formation energy can be calculated starting from a hydrogenated ceria surface (eq 5) containing two $Ce^{3+}$, one per H atom. In contrast to eqs 2 and 4, this does not involve reduction of the surface; i.e., it does not involve a change in the number of $Ce^{3+}$, but only desorption of a water molecule. Here, most likely a cancellation of errors in PBE+U as well as HSE leads to very similar defect formation energies differing only by 0.05 eV. It may be useful to distinguish between defect formation reactions involving reduction of the surface, i.e., creation of $Ce^{3+}$ ions, and reactions preserving the number of $Ce^{3+}$ ions, which corresponds to a mere desorption step as shown for eq 5. In contrast hydrogenation energies for the clean $CeO_2(111)$ surface (eq 6) differ strongly comparing PBE+U (−2.63 eV) with HSE (−1.90 eV). This energy can be obtained as the difference between results for eqs 4 and 5.

$$Ce_nO_{2n}(111) + H_2 \rightarrow Ce_nO_{2n-2}(OH)_2(111) \quad (6)$$

The PBE+U result for eq 6 is predicted to be more exothermic by 0.73 eV compared to HSE. Note that this discrepancy is similarly large for eq 2. The product in both reactions contains two $Ce^{3+}$ ions with the O vacancy being the only difference.

Equation 3 describes the formation of a divacancy. The layer converged defect formation energies obtained using PBE+U (2.26 eV) and HSE (2.86 eV) differ by 0.6 eV. This discrepancy is approximately 0.1 eV lower than corresponding values for the formation of a single O vacancy (eq 2). Although a systematic investigation of minimum-energy localization patterns of the four $Ce^{3+}$ ions in the surface layer (cf. Figure S2) has not been done, we believe that this is again an indication for the underestimation of relaxation contributions using the PBE+U approach. Our reasoning above appears to be supported by the following: while HSE predicts $\Delta E_d(^1/_2O_2)$ for eq 3 (2.86 eV) to be 0.42 eV more endothermic compared to eq 2 (2.44 eV), PBE+U predicts this step to be 0.50 eV more endothermic. The difference between 0.50 and 0.42 eV coincides with our estimate for the underestimation of relaxation effects by PBE+U using "unrelaxed" defect formation energies (see above).

**4.2. Methanol Adsorption.** Adsorption energies and structures of the methanol interacting with the pristine and defective $CeO_2(111)$ surface agree with the findings reported by Beste et al.[21] for the smaller $p(2 \times 2)$ cell. Surface oxygen vacancies represent thermodynamically more favorable adsorption sites, which is obtained using PBE+U as well as HSE. However, these two approaches perform qualitatively differently comparing the methoxide formation at the pristine and the defective surfaces.

For **A1**, adsorption energies using PBE+U and HSE are virtually identical at −0.69 and −0.71 eV, respectively (cf. Table 2). Note that the aforementioned HSE result refers to the HSE single-point energy at the HSE+D structure. However, optimization using HSE affected the adsorption energy by only 0.01 eV. The dispersion correction stabilizes the adsorbate by about 0.2 eV. The ZPVE effects for adsorption at the pristine surface were found to be negligibly small (0.004 eV) because contributions of reactants and the product *de facto* cancel each other. For **A2**, however, ZPVE effects are approximately 1 order of magnitude larger (−0.04 eV), leading to a net stabilization. At the defective surface, PBE+U and HSE perform very differently. Adsorption at the defect is predicted to be pronouncedly exothermic. This is not surprising, as the oxygen defect is (partly) healed; however, this is not a redox reaction as the number of $Ce^{3+}$ ions before and after methanol adsorption does not change. The adsorption energy obtained using PBE+U amounts to −2.11 eV, whereas HSE predicts −1.90 eV, which is less exothermic by 0.21 eV.

The $CH_3O^-$ and the positively charged oxygen vacancy interact attractively, mainly because of electrostatic interactions. Here, SIE in PBE+U contribute to a spurious overbinding of the methoxide. This is very likely because of the SIE-induced overdelocalization of charge, which in turn leads to a more attractive electrostatic interaction (see also ref 93). Since SIE are reduced in HSE, the interaction is smaller. In addition, this is supported by the smaller distance between the methoxide oxygen atom and the surface $Ce^{4+}$ layer obtained using PBE+U (117 pm) compared to HSE (123 pm). The overbinding is rather pronounced for the methoxide at the tridentate defect site, however smaller at the pristine surface, where the methoxide binds atop a $Ce^{4+}$. In other words, the interaction of the methoxide with the vacancy (3-fold coordinated to Ce) is stronger, as overdelocalization errors become more effective at the higher coordinated site. It is noteworthy that the parameters used for dispersion correction, i.e., different global scaling factors, appear to be reasonable as PBE+U and HSE predict very similar dispersion contributions for both **A1** and **A2**.

The existence of multiple IR peaks in the C−O stretching region was previously attributed to multiple adsorption structures (atop, bridging, and tridentate),[23] though Abbott et al.[3] only reported two peaks for methanol on the pristine $CeO_2$ (111) surface. These signals were attributed to the C−O stretching modes of atop and tridentate methanol.[21] However, the adsorption structure in the surface defect (**A2**, tridentate methoxide) does not possess IR-active vibrations in this region, whereas **A1** features two IR-active modes according to our calculations. Therefore, we assign the experimental peak at 1038 $cm^{-1}$ to the C−O stretching mode of "atop methanol" (**A1**) and the peak at 1104 $cm^{-1}$ to the methyl rocking mode of this adsorption structure.


dx.doi.org/10.1021/jp505088b | J. Phys. Chem. C 2014, 118, 23690−23700

**4.3. Formaldehyde Formation.** Similar to eqs 2 and 4, the oxidation of methanol to FA involves the reduction of the surface, and according to the above-mentioned arguments, discrepancies between PBE+U and HSE are expected. However, these discrepancies may be estimated using the Brønsted−Evans−Polanyi (BEP) principle. Knowing the HSE reaction energy suffices to estimate the corresponding reaction barrier: the hybrid functional predicts more endothermic reaction energies for the steps **A1** → **I1** and **A2** → **I4** compared to PBE+U. For the defective surface (**A2** → **I4**), the difference between PBE+U+D and HSE+D reaction energies ($\Delta E_{reac}$ = +0.32 eV; cf. Table 6) as well as barriers ($\Delta E^{\ddagger}$ = +0.21 eV) were calculated (cf. Figure 5). These differences agree well with the BEP principle. We emphasize that this estimate works surprisingly well for PBE+U and HSE as both functionals are conceptually related, but there is no guarantee that it will work when other less similar functionals are employed.

**Table 6. ZPVE-Corrected Adsorption ($\Delta E_{ads}$) and Reaction ($\Delta E_{reac}$) Energies as Well as Intrinsic Barriers ($\Delta E^{\ddagger}$) in eV**

| | PBE+U+D | HSE+D |
|---|---|---|
| | pristine | |
| $\Delta E_{ads}$ | −0.91 | −0.89 |
| $\Delta E_{reac}$ | −0.76 | −0.28 |
| $\Delta E^{\ddagger}$ | 1.08 | |
| | defective | |
| $\Delta E_{ads}$ | −2.39 | −2.14 |
| $\Delta E_{reac}$ | 0.37 | 0.61 |
| $\Delta E^{\ddagger}$ | 1.23 | 1.44 |

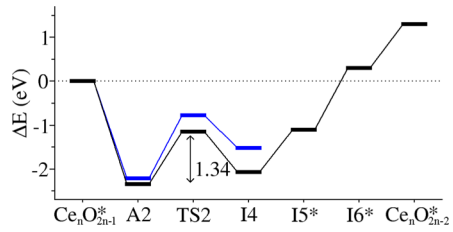


**Figure 5.** Energy profile for the ODH of methanol to FA at the reduced $CeO_2(111)$ surface. Total energies obtained using dispersion-corrected PBE+U (black line) and HSE (blue line) include gas phase molecules as indicated by an asterisk.

TPD experiments predict an intrinsic barrier of approximately 1.5 eV.[2] The ZPVE-corrected HSE+D barrier of 1.44 eV is closer to the observed value than the PBE+U+D result (1.23 eV). On the basis of that comparison, we believe that HSE+D outperforms PBE+U+D. This result is not surprising since GGA functionals generally underestimate barriers compared to hybrid functionals.[94,95]

Pristine ceria surfaces are rather inactive,[13] whereas partially reduced surfaces catalyze the oxidation of $CH_3OH$ to $CH_2O$ and $CO_X$. The selectivity toward $CO_X$ increases with the degree of reduction.[96] At the pristine surface, the desorption energy for methanol is significantly smaller than the intrinsic barrier for the oxidation step. Therefore, methanol desorption is favored. FA formation occurs at the oxygen defects with an intrinsic barrier of 1.44 eV. These results explain the methanol desorption peak at 0.8 eV (270 K; cf. Figure 5 in ref 3) and the FA desorption peak of 1.5 eV (610 K) as observed in TPD experiments.[2,3,16,96]

As stated by Beste et al., the reported increase in the activity upon reduction of the ceria surface is actually an increase in the FA *yield*, while the desorption temperature remains unchanged. This observation fully agrees with our model (low methanol coverage at low O defect concentration) for the surface reaction considering the adsorbed methoxide in the vacancy reacting to FA by H-transfer to the surface. The model reflects the experimental TPD conditions starting from a presaturated surface. As a consequence the yield of FA will be directly proportional to the defect concentration.

Instead of creating water, two hydroxyl groups might also recombine into $H_2$ in order to avoid the formation of the endothermic oxygen vacancy. At the $CeO_2(111)$ surface, this pathway (2.30 eV; PBE+U desorption energy in Table 1) is slightly less favored compared to water desorption (2.12 eV; PBE+U). HSE predicts the opposite: $H_2$ evolution (1.81 eV) is favored over water desorption (2.04 eV). However, both desorption routes require high temperatures and do not occur below 800 K.[16] At the $CeO_2(100)$ surface, water and hydrogen desorption occur already at 600 K due to the lower defect formation energies.[16,25]

In the presence of water, the O-defect site is likely to be occupied, and therefore, less exothermic adsorption enthalpies should be expected. Note that this work focuses on the intrinsic barriers that are obtained via TPD experiments.

## 5. CONCLUSIONS

This work predicts surface oxygen defects to be the reactive site in methanol oxidation at the $CeO_2(111)$ surface under TPD conditions because the intrinsic barrier obtained using ZPVE-corrected HSE+D (139 kJ/mol) is lower than the corresponding methanol desorption energy (206 kJ/mol). This barrier is considered very accurate as it agrees well with that reported by Freund and co-workers derived from TPD using Redhead analysis (∼150 kJ/mol).[2] Therefore, differences in TPD spectra for the methanol oxidation at the clean and $Ar^+$-sputtered $CeO_2(111)$ surface as reported by Ferrizz et al.[13] can be explained: The more reactive sites, i.e., number of O defects on the surface, the more formaldehyde is created, causing a larger TPD peak. However, we clearly state that our work does not allow for conclusions at higher defect concentrations as it studies the isolated point defect only. Also, other reaction channels which are likely to become effective at higher methanol loadings, e.g., recombination of two methoxides into methanol and formaldehyde, were not investigated.

The adsorption structure of methoxide in the O defect has no IR-active C−O stretching mode according to our calculations. The adsorption structure at the pristine surface features two IR-active modes at around 1100 $cm^{-1}$: a C−O stretching and a $CH_3$ rocking mode. On the pristine surface, the less strongly bonded methoxide is more likely to desorb than to be oxidized. This is shown by comparing the ZPVE-corrected PBE+U+D adsorption energy (−88 kJ/mol) with the intrinsic barrier (104 kJ/mol). Importantly, the adsorption energy on the pristine surface is less affected by self-interaction errors as the ZPVE-corrected HSE+D result amounts to −86 kJ/mol, which is only slightly lower. The PBE+U approach predicts the reactive site correctly but overestimates the adsorption energy at the defect by 20 kJ/mol and underestimates the intrinsic barrier by the same amount compared to HSE. Related to the partial correction of self-interaction errors, this behavior has been expected. Overall, the computationally less expensive PBE+U results agree reasonably well with the HSE results.


dx.doi.org/10.1021/jp505088b | J. Phys. Chem. C 2014, 118, 23690−23700

Compared to pristine $CeO_2(111)$, the reduced surface is, however, the less effective oxidant (higher intrinsic barrier for the oxidation step), which is plausible from a chemical viewpoint.

## ■ ASSOCIATED CONTENT

### Supporting Information

Simulated vibrational spectra for methanol, **A1** and **A2**; structures of intermediates; table of total energies; figure showing the topview on surface layer of $Ce_nO_{2n-2}$; Cartesian coordinates of transition structures. This material is available free of charge via the Internet at http://pubs.acs.org.

## ■ AUTHOR INFORMATION

### Corresponding Author

*Phone +(49)-30-2093-7139; e-mail joachim.paier@chemie.hu-berlin.de.

### Notes

The authors declare no competing financial interest.

## ■ ACKNOWLEDGMENTS

We owe thanks to Prof. Joachim Sauer for support, insightful discussions, and comments on the manuscript. We also thank the reviewers, whose comments were particularly useful and helped us to improve the manuscript. We are grateful to Dr. Brian Solis for proofreading the manuscript. This work has been supported by grants for computing time at the high-performance computer centers HLRN (North-German Supercomputing Alliance in Berlin and Hannover) and JUROPA (Forschungszentrum Jülich). We acknowledge support from COST action CM1104. J.P. is grateful for financial support by the Fonds der Chemischen Industrie, FCI.

## ■ REFERENCES

(1) Álvarez-Galván, M. C.; Pawelec, B.; de la Peña O'Shea, V. A.; Fierro, J. L. G.; Arias, P. L. Formaldehyde/Methanol Combustion on Alumina-Supported Manganese-Palladium Oxide Catalyst. *Appl. Catal., B* **2004**, *51*, 83.

(2) Ganduglia-Pirovano, M. V.; Popa, C.; Sauer, J.; Abbott, H. L.; Uhl, A.; Baron, M.; Stacchiola, D.; Bondarchuk, O.; Shaikhutdinov, S.; Freund, H.-J. Role of Ceria in Oxidative Dehydrogenation on Supported Vanadia Catalysts. *J. Am. Chem. Soc.* **2010**, *132*, 2345.

(3) Abbott, H. L.; Uhl, A.; Baron, M.; Lei, Y.; Meyer, R. J.; Stacchiola, D. J.; Bondarchuk, O.; Shaikhutdinov, S.; Freund, H. J. Relating Methanol Oxidation to the Structure of Ceria-Supported Vanadia Monolayer Catalysts. *J. Catal.* **2010**, *272*, 82.

(4) Vohs, J. M. Site Requirements for the Adsorption and Reaction of Oxygenates on Metal Oxide Surfaces. *Chem. Rev.* **2012**, *113*, 4136.

(5) Gorte, R. Ceria in Catalysis: From Automotive Applications to the Water-Gas Shift Reaction. *AlChE J.* **2010**, *56*, 1126.

(6) Trovarelli, A. *Catalysis by Ceria and Related Materials*; Imperial College Press: London, 2002.

(7) Peng, Y.; Liu, Z. M.; Niu, X. W.; Zhou, L.; Fu, C. W.; Zhang, H.; Li, J. H.; Han, W. Manganese Doped $CeO_2$-$WO_3$ Catalysts for the Selective Catalytic Reduction of $NO_x$ with $NH_3$: An Experimental and Theoretical Study. *Catal. Commun.* **2012**, *19*, 127.

(8) Steele, B. C. H.; Heinzel, A. Materials for Fuel-Cell Technologies. *Nature* **2001**, *414*, 345.

(9) Fronzi, M.; Soon, A.; Delley, B.; Traversa, E.; Stampfl, C. Stability and Morphology of Cerium Oxide Surfaces in an Oxidizing Environment: A First-Principles Investigation. *J. Chem. Phys.* **2009**, *131*, 104710.

(10) Skorodumova, N. V.; Baudin, M.; Hermansson, K. Surface Properties of $CeO_2$ from First Principles. *Phys. Rev. B* **2004**, *69*, 075401.

(11) Yang, Z. X.; Woo, T. K.; Baudin, M.; Hermansson, K. Atomic and Electronic Structure of Unreduced and Reduced $CeO_2$ Surfaces: A First-Principles Study. *J. Chem. Phys.* **2004**, *120*, 7741.

(12) Branda, M. M.; Loschen, C.; Neyman, K. M.; Illas, F. Atomic and Electronic Structure of Cerium Oxide Stepped Model Surfaces. *J. Phys. Chem. C* **2008**, *112*, 17643.

(13) Ferrizz, R. M.; Wong, G. S.; Egami, T.; Vohs, J. M. Structure Sensitivity of the Reaction of Methanol on Ceria. *Langmuir* **2001**, *17*, 2464.

(14) Mullins, D. R.; Robbins, M. D.; Zhou, J. Adsorption and Reaction of Methanol on Thin-Film Cerium Oxide. *Surf. Sci.* **2006**, *600*, 1547.

(15) Siokou, A.; Nix, R. M. Interaction of Methanol with Well-Defined Ceria Surfaces: Reflection/Absorption Infrared Spectroscopy, X-Ray Photoelectron Spectroscopy, and Temperature-Programmed Desorption Study. *J. Phys. Chem. B* **1999**, *103*, 6984.

(16) Albrecht, P. M.; Mullins, D. R. Adsorption and Reaction of Methanol over $CeO_x(100)$ Thin Films. *Langmuir* **2013**, *29*, 4559.

(17) Uhlrich, J.; Yang, B.; Shaikhutdinov, S. Methanol Reactivity on Silica-Supported Ceria Nanoparticles. *Top. Catal.* **2014**, DOI: 10.1007/s11244.

(18) Namai, Y.; Fukui, K.; Iwasawa, Y. The Dynamic Behaviour of $CH_3OH$ and $NO_2$ Adsorbed on $CeO_2(111)$ Studied by Noncontact Atomic Force Microscopy. *Nanotechnology* **2004**, *15*, S49.

(19) Mars, P.; van Krevelen, D. W. Oxidations Carried out by Means of Vanadium Oxide Catalysts. *Chem. Eng. Sci.* **1954**, *3* (Suppl. 1), 41.

(20) Mei, D.; Deskins, N. A.; Dupuis, M.; Ge, Q. Methanol Adsorption on the Clean $CeO_2(111)$ Surface: A Density Functional Theory Study. *J. Phys. Chem. C* **2007**, *111*, 10514.

(21) Beste, A.; Mullins, D. R.; Overbury, S. H.; Harrison, R. J. Adsorption and Dissociation of Methanol on the Fully Oxidized and Partially Reduced (111) Cerium Oxide Surface: Dependence on the Configuration of the Cerium 4f Electrons. *Surf. Sci.* **2008**, *602*, 162.

(22) Overbury, S. H.; Mullins, D. R.; Huntley, D. R.; Kundakovic, L. Chemisorption and Reaction of NO and $N_2O$ on Oxidized and Reduced Ceria Surfaces Studied by Soft X-Ray Photoemission Spectroscopy and Desorption Spectroscopy. *J. Catal.* **1999**, *186*, 296.

(23) Badri, A.; Binet, C.; Lavalley, J. C. Use of Methanol as an IR Molecular Probe to Study the Surface of Polycrystalline Ceria. *J. Chem. Soc., Faraday Trans.* **1997**, *93*, 1159.

(24) Teng, B. T.; Jiang, S. Y.; Yang, Z. X.; Luo, M. F.; Lan, Y. Z. A Density Functional Theory Study of Formaldehyde Adsorption and Oxidation on $CeO_2(111)$ Surface. *Surf. Sci.* **2010**, *604*, 68.

(25) Li, M. J.; Wu, Z. L.; Overbury, S. H. Surface Structure Dependence of Selective Oxidation of Ethanol on Faceted $CeO_2$ Nanocrystals. *J. Catal.* **2013**, *306*, 164.

(26) Paier, J.; Penschke, C.; Sauer, J. Oxygen Defects and Surface Chemistry of Ceria: Quantum Chemical Studies Compared to Experiment. *Chem. Rev.* **2013**, *113*, 3949.

(27) Liechtenstein, A. I.; Anisimov, V. I.; Zaanen, J. Density-Functional Theory and Strong-Interactions - Orbital Ordering in Mott-Hubbard Insulators. *Phys. Rev. B* **1995**, *52*, R5467.

(28) Anisimov, V. I.; Zaanen, J.; Andersen, O. K. Band Theory and Mott Insulators - Hubbard-U Instead of Stoner-I. *Phys. Rev. B* **1991**, *44*, 943.

(29) Becke, A. D. A New Mixing of Hartree-Fock and Local Density-Functional Theories. *J. Chem. Phys.* **1993**, *98*, 1372.

(30) Kohn, W.; Meir, Y.; Makarov, D. E. Van der waals Energies in Density Functional Theory. *Phys. Rev. Lett.* **1998**, *80*, 4153.

(31) Tkatchenko, A.; Scheffler, M. Accurate Molecular van der Waals Interactions from Ground-State Electron Density and Free-Atom Reference Data. *Phys. Rev. Lett.* **2009**, *102*.

(32) Grimme, S.; Antony, J.; Ehrlich, S.; Krieg, H. A Consistent and Accurate Ab Initio Parametrization of Density Functional Dispersion Correction (DFT-D) for the 94 Elements H-Pu. *J. Chem. Phys.* **2010**, *132*, 154104.

(33) Zhao, Y.; Truhlar, D. G. Applications and Validations of the Minnesota Density Functionals. *Chem. Phys. Lett.* **2011**, *502*, 1.

(34) Kannemann, F. O.; Becke, A. D. Van der Waals Interactions in Density-Functional Theory: Rare-Gas Diatomics. *J. Chem. Theory Comput.* **2009**, *5*, 719.
(35) Becke, A. D.; Johnson, E. R. Exchange-Hole Dipole Moment and the Dispersion Interaction Revisited. *J. Chem. Phys.* **2007**, *127*.
(36) Tao, J. M.; Perdew, J. P.; Ruzsinszky, A. Long-Range van der Waals Interaction. *Int. J. Mod. Phys. B* **2013**, *27*.
(37) Lebegue, S.; Harl, J.; Gould, T.; Angyan, J. G.; Kresse, G.; Dobson, J. F. Cohesive Properties and Asymptotics of the Dispersion Interaction in Graphite by the Random Phase Approximation. *Phys. Rev. Lett.* **2010**, *105*.
(38) Klimes, J.; Bowler, D. R.; Michaelides, A. Chemical Accuracy for the van der Waals Density Functional. *J. Phys.: Condens. Matter* **2010**, *22*.
(39) Eshuis, H.; Furche, F. A Parameter-Free Density Functional That Works for Noncovalent Interactions. *J. Phys. Chem. Lett.* **2011**, *2*, 983.
(40) Dion, M.; Rydberg, H.; Schroder, E.; Langreth, D. C.; Lundqvist, B. I. Van Der Waals Density Functional for General Geometries. *Phys. Rev. Lett.* **2004**, *92*.
(41) Perdew, J. P.; Burke, K.; Ernzerhof, M. Generalized Gradient Approximation Made Simple. *Phys. Rev. Lett.* **1996**, *77*, 3865.
(42) Perdew, J. P.; Burke, K.; Ernzerhof, M. Generalized Gradient Approximation Made Simple (1996, Vol. 77, p 3865). *Phys. Rev. Lett.* **1997**, *78*, 1396.
(43) Perdew, J. P.; Burke, K.; Ernzerhof, M. Comment on "Generalized Gradient Approximation Made Simple" - Reply. *Phys. Rev. Lett.* **1998**, *80*, 891.
(44) Heyd, J.; Scuseria, G. E.; Ernzerhof, M. Hybrid Functionals Based on a Screened Coulomb Potential. *J. Chem. Phys.* **2003**, *118*, 8207.
(45) Heyd, J.; Scuseria, G. E.; Ernzerhof, M. Hybrid Functionals Based on a Screened Coulomb Potential (2003, Vol. 118, p 8207). *J. Chem. Phys.* **2006**, *124*, 219906.
(46) Grimme, S. Semiempirical GGA-Type Density Functional Constructed with a Long-Range Dispersion Correction. *J. Comput. Chem.* **2006**, *27*, 1787.
(47) Blöchl, P. E. Projector Augmented-Wave Method. *Phys. Rev. B* **1994**, *50*, 17953.
(48) Kresse, G.; Joubert, D. From Ultrasoft Pseudopotentials to the Projector Augmented-Wave Method. *Phys. Rev. B* **1999**, *59*, 1758.
(49) Kresse, G.; Furthmüller, J. Efficient Iterative Schemes for Ab Initio Total-Energy Calculations Using a Plane-Wave Basis Set. *Phys. Rev. B* **1996**, *54*, 11169.
(50) Kresse, G.; Furthmüller, J. Efficiency of Ab-Initio Total Energy Calculations for Metals and Semiconductors Using a Plane-Wave Basis Set. *Comput. Mater. Sci.* **1996**, *6*, 15.
(51) Perdew, J. P.; Ernzerhof, M.; Burke, K. Rationale for Mixing Exact Exchange with Density Functional Approximations. *J. Chem. Phys.* **1996**, *105*, 9982.
(52) Dudarev, S. L.; Botton, G. A.; Savrasov, S. Y.; Humphreys, C. J.; Sutton, A. P. Electron-Energy-Loss Spectra and the Structural Stability of Nickel Oxide: An LSDA+U Study. *Phys. Rev. B* **1998**, *57*, 1505.
(53) Bengone, O.; Alouani, M.; Blochl, P.; Hugel, J. Implementation of the Projector Augmented-Wave LDA+U Method: Application to the Electronic Structure of NiO. *Phys. Rev. B* **2000**, *62*, 16392.
(54) Krukau, A. V.; Vydrov, O. A.; Izmaylov, A. F.; Scuseria, G. E. Influence of the Exchange Screening Parameter on the Performance of Screened Hybrid Functionals. *J. Chem. Phys.* **2006**, *125*, 224106.
(55) Kerber, T.; Sierka, M.; Sauer, J. Application of Semiempirical Long-Range Dispersion Corrections to Periodic Systems in Density Functional Theory. *J. Comput. Chem.* **2008**, *29*, 2088.
(56) Bučko, T.; Hafner, J.; Lebegue, S.; Angyan, J. G. Improved Description of the Structure of Molecular and Layered Crystals: Ab Initio DFT Calculations with van der Waals Corrections. *J. Phys. Chem. A* **2010**, *114*, 11814.
(57) Penschke, C.; Paier, J.; Sauer, J. Oligomeric Vanadium Oxide Species Supported on the $CeO_2$(111) Surface: Structure and Reactivity Studied by Density Functional Theory. *J. Phys. Chem. C* **2013**, *117*, 5274.
(58) Paier, J.; Marsman, M.; Hummer, K.; Kresse, G.; Gerber, I. C.; Angyan, J. G. Screened Hybrid Density Functionals Applied to Solids. *J. Chem. Phys.* **2006**, *124*, 154709.
(59) Mills, G.; Jonsson, H.; Schenter, G. K. Reversible Work Transition-State Theory - Application to Dissociative Adsorption of Hydrogen. *Surf. Sci.* **1995**, *324*, 305.
(60) Jonsson, H.; Mills, G.; Jacobsen, K. W. Nudged Elastic Band Method for Finding Minimum Energy Paths of Transitions. In *Classical and Quantum Dynamics in Condensed Phase Simulations*; Berne, J., Ciccotti, G., Coker, D. F., Eds.; World Scientific: Singapore, 1998.
(61) Henkelman, G.; Uberuaga, B. P.; Jonsson, H. A Climbing Image Nudged Elastic Band Method for Finding Saddle Points and Minimum Energy Paths. *J. Chem. Phys.* **2000**, *113*, 9901.
(62) Henkelman, G.; Jonsson, H. A Dimer Method for Finding Saddle Points on High Dimensional Potential Surfaces Using Only First Derivatives. *J. Chem. Phys.* **1999**, *111*, 7010.
(63) Heyden, A.; Bell, A. T.; Keil, F. J. Efficient Methods for Finding Transition States in Chemical Reactions: Comparison of Improved Dimer Method and Partitioned Rational Function Optimization Method. *J. Chem. Phys.* **2005**, *123*, 224101.
(64) Porezag, D.; Pederson, M. R. Infrared Intensities and Raman-Scattering Activities within Density-Functional Theory. *Phys. Rev. B* **1996**, *54*, 7830.
(65) Ganduglia-Pirovano, M. V.; Da Silva, J. L. F.; Sauer, J. Density Functional Calculations of the Structure of Near-Surface Oxygen Vacancies and Electron Localization on $CeO_2$(111). *Phys. Rev. Lett.* **2009**, *102*, 026101.
(66) Li, H.-Y.; Wang, H.-F.; Gong, X.-Q.; Guo, Y.-L.; Guo, Y.; Lu, G.; Hu, P. Multiple Configurations of the Two Excess 4f Electrons on Defective $CeO_2$(111): Origin and Implications. *Phys. Rev. B* **2009**, *79*, 193401.
(67) Pan, Y.; Nilius, N.; Freund, H.-J.; Paier, J.; Penschke, C.; Sauer, J. Titration of $Ce^{3+}$ Ions in the $CeO_2$(111) Surface by Au Adatoms. *Phys. Rev. Lett.* **2013**, *111*, 206101.
(68) Chase, M. W., Jr. *NIST-JANAF Thermochemical Tables*; AIP: New York, 1998.
(69) Momma, K.; Izumi, F. Vesta 3 for Three-Dimensional Visualization of Crystal, Volumetric and Morphology Data. *J. Appl. Crystallogr.* **2011**, *44*, 1272.
(70) Alecu, I. M.; Zheng, J. J.; Zhao, Y.; Truhlar, D. G. Computational Thermochemistry: Scale Factor Databases and Scale Factors for Vibrational Frequencies Obtained from Electronic Model Chemistries. *J. Chem. Theory Comput.* **2010**, *6*, 2872.
(71) Mei, D.; Aaron Deskins, N.; Dupuis, M. A Density Functional Theory Study of Formaldehyde Adsorption on Ceria. *Surf. Sci.* **2007**, *601*, 4993.
(72) Nolan, M.; Parker, S. C.; Watson, G. W. The Electronic Structure of Oxygen Vacancy Defects at the Low Index Surfaces of Ceria. *Surf. Sci.* **2005**, *595*, 223.
(73) Fabris, S.; Vicario, G.; Balducci, G.; de Gironcoli, S.; Baroni, S. Electronic and Atomistic Structures of Clean and Reduced Ceria Surfaces. *J. Phys. Chem. B* **2005**, *109*, 22860.
(74) Da Silva, J. L. F.; Ganduglia-Pirovano, M. V.; Sauer, J.; Bayer, V.; Kresse, G. Hybrid Functionals Applied to Rare Earth Oxides: The Example of Ceria. *Phys. Rev. B* **2007**, *75*, 045121.
(75) Csonka, G. I.; Perdew, J. P.; Ruzsinszky, A.; Philipsen, P. H. T.; Lebegue, S.; Paier, J.; Vydrov, O. A.; Angyan, J. G. Assessing the Performance of Recent Density Functionals for Bulk Solids. *Phys. Rev. B* **2009**, *79*.
(76) Furche, F. Molecular Tests of the Random Phase Approximation to the Exchange-Correlation Energy Functional. *Phys. Rev. B* **2001**, *64*, 195120.
(77) Ren, X. G.; Rinke, P.; Scheffler, M. Exploring the Random Phase Approximation: Application to CO Adsorbed on Cu(111). *Phys. Rev. B* **2009**, *80*, 045402.

(78) Mittendorfer, F.; Garhofer, A.; Redinger, J.; Klimes, J.; Harl, J.; Kresse, G. Graphene on Ni(111): Strong Interaction and Weak Adsorption. *Phys. Rev. B* **2011**, *84*, 201401.
(79) Casadei, M.; Ren, X.; Rinke, P.; Rubio, A.; Scheffler, M. Density-Functional Theory for F-Electron Systems: The Alpha-Gamma Phase Transition in Cerium. *Phys. Rev. Lett.* **2012**, *109*, 146402.
(80) Göltl, F.; Grüneis, A.; Bučko, T.; Hafner, J. Van Der Waals Interactions between Hydrocarbon Molecules and Zeolites: Periodic Calculations at Different Levels of Theory, from Density Functional Theory to the Random Phase Approximation and Møller-Plesset Perturbation Theory. *J. Chem. Phys.* **2012**, *137*, 114111.
(81) Grüneis, A.; Marsman, M.; Harl, J.; Schimka, L.; Kresse, G. Making the Random Phase Approximation to Electronic Correlation Accurate. *J. Chem. Phys.* **2009**, *131*.
(82) Burow, A. M.; Bates, J. E.; Furche, F.; Eshuis, H. Analytical First-Order Molecular Properties and Forces within the Adiabatic Connection Random Phase Approximation. *J. Chem. Theory Comput.* **2014**, *10*, 180.
(83) Lutfalla, S.; Shapovalov, V.; Bell, A. T. Calibration of the DFT/GGA+U Method for Determination of Reduction Energies for Transition and Rare Earth Metal Oxides of Ti, V, Mo, and Ce. *J. Chem. Theory Comput.* **2011**, *7*, 2218.
(84) Hu, Z.; Li, B.; Sun, X.; Metiu, H. Chemistry of Doped Oxides: The Activation of Surface Oxygen and the Chemical Compensation Effect. *J. Phys. Chem. C* **2011**, *115*, 3065.
(85) Graciani, J.; Marquez, A. M.; Plata, J. J.; Ortega, Y.; Hernandez, N. C.; Meyer, A.; Zicovich-Wilson, C. M.; Sanz, J. F. Comparative Study on the Performance of Hybrid Dft Functionals in Highly Correlated Oxides: The Case of $CeO_2$ and $Ce_2O_3$. *J. Chem. Theory Comput.* **2011**, *7*, 56.
(86) Seidl, A.; Görling, A.; Vogl, P.; Majewski, J. A.; Levy, M. Generalized Kohn-Sham Schemes and the Band-Gap Problem. *Phys. Rev. B* **1996**, *53*, 3764.
(87) Ruzsinszky, A.; Perdew, J. P.; Csonka, G. I.; Vydrov, O. A.; Scuseria, G. E. Density Functionals That Are One- and Two- Are Not Always Many-Electron Self-Interaction-Free, as Shown for $H_2^+$, $He_2^+$, $LiH^+$, and $Ne_2^+$. *J. Chem. Phys.* **2007**, *126*, 104102.
(88) Grau-Crespo, R.; Wang, H.; Schwingenschloegl, U. Why the Heyd-Scuseria-Ernzerhof Hybrid Functional Description of $VO_2$ Phases Is Not Correct. *Phys. Rev. B* **2012**, *86*.
(89) Iori, F.; Gatti, M.; Rubio, A. Role of Nonlocal Exchange in the Electronic Structure of Correlated Oxides. *Phys. Rev. B* **2012**, *85*.
(90) Klimes, J.; Bowler, D. R.; Michaelides, A. Van der Waals Density Functionals Applied to Solids. *Phys. Rev. B* **2011**, *83*.
(91) Duclos, S. J.; Vohra, Y. K.; Ruoff, A. L.; Jayaraman, A.; Espinosa, G. P. High-Pressure X-Ray-Diffraction Study of $CeO_2$ to 70 GPa and Pressure-Induced Phase-Transformation from the Fluorite Structure. *Phys. Rev. B* **1988**, *38*, 7755.
(92) Gerward, L.; Olsen, J. S.; Petit, L.; Vaitheeswaran, G.; Kanchana, V.; Svane, A. Bulk Modulus of $CeO_2$ and $PrO_2$ - an Experimental and Theoretical Study. *J. Alloys Compd.* **2005**, *400*, 56.
(93) Hansen, N.; Kerber, T.; Sauer, J.; Bell, A. T.; Keil, F. J. Quantum Chemical Modeling of Benzene Ethylation over H-ZSM-5 Approaching Chemical Accuracy: A Hybrid MP2:DFT Study. *J. Am. Chem. Soc.* **2010**, *132*, 11525.
(94) Zhao, Y.; Truhlar, D. G. Design of Density Functionals That Are Broadly Accurate for Thermochemistry, Thermochemical Kinetics, and Nonbonded Interactions. *J. Phys. Chem. A* **2005**, *109*, 5656.
(95) Zhao, Y.; Gonzalez-Garcia, N.; Truhlar, D. G. Benchmark Database of Barrier Heights for Heavy Atom Transfer, Nucleophilic Substitution, Association, and Unimolecular Reactions and Its Use to Test Theoretical Methods. *J. Phys. Chem. A* **2005**, *109*, 2012.
(96) Feng, T.; Vohs, J. M. A TPD Study of the Partial Oxidation of Methanol to Formaldehyde on $CeO_2$-Supported Vanadium Oxide. *J. Catal.* **2004**, *221*, 619.

# P7

https://pubs.acs.org/doi/abs/10.1021/acs.jpcc.5b07186

THE JOURNAL OF PHYSICAL CHEMISTRY C

Article

pubs.acs.org/JPCC

# Activity versus Selectivity of the Methanol Oxidation at Ceria Surfaces: A Comparative First-Principles Study

Thomas Kropp and Joachim Paier*

Institut für Chemie, Humboldt-Universität zu Berlin, Unter den Linden 6, 10099 Berlin, Germany

Supporting Information

**ABSTRACT:** Ceria nanoparticles may expose (100) and (111) facets depending on the preparation method. Motivated by that, we study the reactions of methanol with the $CeO_2$(100) surface using dispersion-corrected PBE+U subject to periodic boundary conditions and compare with results for the $CeO_2$(111) surface. At (100) facets, the oxidative dehydrogenation of methanol to formaldehyde occurs with an intrinsic barrier of only 0.94 eV (91 kJ/mol), which is significantly lower than the corresponding barrier of 1.23 eV (119 kJ/mol) at the (111) surface. The lower barrier maps to lower formaldehyde desorption temperatures as observed in temperature-programmed desorption spectroscopy. The higher activity is in accordance with predicted lower oxygen defect formation energy in the (100) surface. Thus, defect formation energies are valid reactivity descriptors for oxidation reactions following a Mars-van Krevelen mechanism. At both surfaces, formaldehyde either desorbs or forms a bridging dioxymethylene intermediate, which can be further oxidized into carbon oxides. However, formaldehyde desorption from the (100) surface is significantly more endothermic. Thus, methanol oxidation at the (100) surface is predicted to yield both formaldehyde and carbon oxides, whereas at the (111) surface, formaldehyde can easily desorb. Therefore, the desorption step appears to be the key to the selectivity of methanol oxidation to formaldehyde.

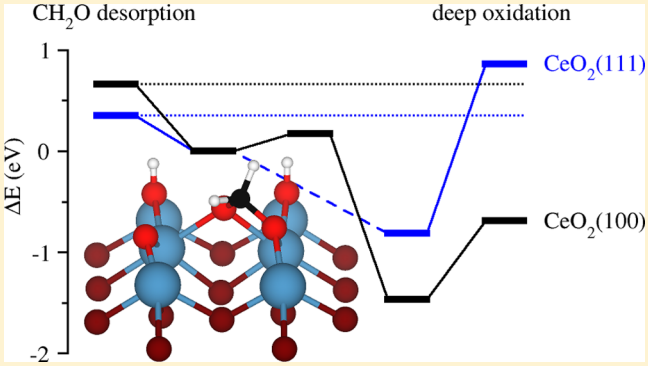


## 1. INTRODUCTION

The oxidation of methanol on metal oxides plays a crucial role in several applications related to energy conversion, such as steam reforming[1] or so-called direct methanol fuel cells.[2] By virtue of heterogeneous catalysis, metal oxides are used to convert methanol via oxidative dehydrogenation (ODH) to formaldehyde,[3] which is the parent compound for many fine chemicals and pharmaceuticals.

Besides their technical relevance, methanol adsorption and oxidation also represent a highly sensitive probe with high specificity to the active sites, which has been extensively reviewed by Tatibouët.[4] It gives experimentalists the opportunity to quantitatively determine the number of active surface sites, which is required for quantifying turnover frequencies, as stated by Wachs and co-workers.[5] Overall, methanol oxidation turned out to be very useful for characterizing supported oxide catalysts that activate C−H bonds,[6−10] where it was found that transition metal oxides supported on ceria ($CeO_2$) are particularly active catalysts. Recent experimental and theoretical studies including surface science experiments on model catalysts highlighted the very special role of this easily reducible support.[11−14]

The outstanding role of ceria can be explained by its ability to act as an oxygen buffer; that is, it enables facile and reversible detachment from, as well as incorporation of oxygen into, its crystal lattice. In other words, oxygen defects form easily.[15,16] This is a consequence of particularly low oxygen vacancy formation energies and accessible Ce 4f states, which become occupied by remaining excess electrons once an (overall electroneutral) oxygen vacancy in the $O^{2-}$ lattice is formed. Occupation of Ce 4f states leads to the formation of atom-like split-off states in the band gap.[17] In fully oxidized ceria with cerium in its highest oxidation state +4, two $Ce^{4+}$ ions are reduced to $Ce^{3+}$ upon creating a single O vacancy. Reoxidation of $Ce^{3+}$ to $Ce^{4+}$ (e.g., by replenishing the vacancy with ambient oxygen) is similarly easy.

As mentioned above, alcohol oxidation proceeds at ceria catalysts via dehydrogenation. This involves the heterolytic dissociation of methanol into a methoxide and a proton on the surface and the homolytic C−H bond breaking (oxidation step). During the ODH following a Mars-van Krevelen mechanism,[18] two electrons will be transferred from methanol to the surface. In the case of ceria-based catalysts, these electrons will reduce two $Ce^{4+}$ ions to $Ce^{3+}$ per methanol. As stated by Tatibouët,[4] on redox active catalysts like ceria, methanol is dehydrogenated to formaldehyde, whereas on catalysts with basic sites oxidation to $CO_2$ occurs. Catalysts with Brønsted or Lewis acid sites yield primarily dimethyl ether.

**Received:** July 24, 2015
**Revised:** September 9, 2015
**Published:** September 16, 2015





DOI: 10.1021/acs.jpcc.5b07186
J. Phys. Chem. C 2015, 119, 23021−23031

In real-world applications, (supported) metal oxides are commonly used in the form of polycrystalline powders that are comprised of nanocrystallites with exposed surfaces of different orientations depending on the preparation conditions, especially temperature. Additionally, defects and many low-coordinated sites (e.g., steps, kinks, and corners) may be involved. Particularly for ceria, surface properties vary drastically with surface orientation. Furthermore, it is well-established that defects are strongly involved in the surface chemistry of reducible oxides.[19,20]

From a theoretical point of view, the thermodynamically stable low-index ceria surfaces with (111), (110), and (100) orientations have been extensively studied,[21−23] though (100) surfaces have been studied less compared to other orientations. An important result of density functional theory (DFT) studies is the increase of their respective surface energies according to (111) < (110) < (100). Conventionally employed models for the (100) surface are oxygen terminated, however, characterizations of the $CeO_2$(100) surface have not been definitive.[24−30] Due to its inherent polarity, mechanisms that compensate for the surface dipole moment are required.[31,32] Furthermore, (100) is the least stable surface orientation for cubic ceria. References 22 and 33 suggest that ceria (100) might feature a variety of terminations in constant flux rather than a "static" one. This is corroborated by the small surface energy differences (including defective structures) found by Pan et al.[30]

Not surprisingly, formation energies of oxygen defects in (100) surfaces are lower compared to (111) and (110) surfaces, which leads to high activities for oxidation or ODH reactions. This high activity comes with a higher degree of coordinative unsaturation of surface oxygen atoms (see, e.g., Mullins[33]). It has also been suggested that this difference in oxygen defect formation energies is responsible for different catalytic behavior: the (111) surface catalyzes predominantly hydrogenation reactions, while the (100) surface catalyzes oxidation reactions.[34]

Most experimental studies on alcohol oxidation at clean or reduced ceria considered the thermodynamically most stable (111) surface.[35−38] The methanol adsorption on fully oxidized or reduced $CeO_2$(111)[39−41] as well as (110)[42] has been studied using DFT. Also, reactions of its dehydrogenation product formaldehyde have been studied.[43,44] Experimentally, methanol adsorption and dehydrogenation on $CeO_2$(100) have been examined by Albrecht and Mullins.[45] The surface structure dependence of ethanol oxidation on variously faceted ceria nanocrystals has been studied by Li et al.[46]

Recently, adsorption and oxidation of methanol on (111), (110), and (100) surfaces of ceria have been studied by López and co-workers by virtue of DFT+U.[47] The authors report the lowest barriers for oxidation steps at the (100) surface, but in contrast to the present work, they found carbon monoxide to be the sole product of methanol oxidation at the (100) surface. This finding conflicts with the experimentally observed product ratio of formaldehyde, CO, and $CO_2$.[45] We resolve this discrepancy by providing a different mechanism for the deep oxidation. In addition, the competing water desorption and hydrogen evolution reactions are discussed. Furthermore, we present formation energies of oxygen defects in the (100) surface using two different approaches, DFT+U and the HSE hybrid functional, to address questions concerning the accuracy of DFT. Defect formation energies have been shown to be useful reactivity descriptors.[48] To study the low methanol coverage limit, a large $c(2 \times 2)$ surface unit cell was used as recently suggested by Pan et al.[30] Overall, this work provides details about methanol oxidation at ceria surfaces guided by three well-known concepts: the coordinative unsaturation, the reducibility, and the degree of reduction.[49]

## 2. COMPUTATIONAL DETAILS

Calculations were performed using the projector augmented wave method (PAW)[50,51] as implemented in the Vienna ab initio simulation package (VASP).[52,53] The onsite Coulomb correlation of occupied f orbitals is corrected via the DFT+U approach[54,55] employing the generalized gradient-corrected exchange-correlation functional by Perdew, Burke, and Ernzerhof (PBE)[56] and an effective Hubbard-type U parameter of 4.5 eV for the Ce 4f electrons, i.e., PBE+U (cf. ref 17). The specific implementation of DFT+U used in this work follows Dudarev et al.[57,58] A plane wave kinetic energy cutoff of 600 eV was used and structure optimizations were performed until forces acting on the relaxed atoms were below 0.02 eV $Å^{-1}$. Dipole moments perpendicular to the surface are corrected with the approach presented in ref 59. To compute integrals over $k$ space, the Brillouin zone was sampled with a mesh of $2 \times 2 \times 1$ $k$ points. Optimized structures using PBE+U were proven to be minima by the absence of imaginary vibrational frequencies. O defect formation energies were also calculated using the screened hybrid functional after Heyd, Scuseria, and Ernzerhof (HSE).[60,61] HSE uses identical settings except for structure optimizations, which employ the PRECFOCK = fast Fourier grid for Fock-exchange related routines. HSE results reported in this work are single points at optimized structures using the dense PRECFOCK = normal Fourier grid. This is a valid and accurate procedure, which was extensively tested in previous work (see refs 41 and 62).

Harmonic vibrational frequencies and their corresponding normal modes were obtained by diagonalizing a partial, mass-weighted matrix of second derivatives with respect to each of the three Cartesian degrees of freedom per atom. This "Hessian" matrix was obtained by finite-differences of the gradients with displacements of ±0.015 Å (central differences). Zero-point vibration energy (ZPVE) corrections as well as IR frequencies use the topmost three atomic layers including all adatoms.

The semiempirical $C_6/R^6$ term by Grimme (DFT+D2) was added to total energies and forces to correct for missing long-range dispersion-type interactions with a global scaling factor of 0.75 that was fitted for the PBE functional.[63,64] Required van der Waals parameters for Ce were derived and tested in ref 65 (cf. the Supporting Information (SI) of that reference).

Transition structures were obtained by nudged elastic bands (NEB) calculations[66,67] in combination with the so-called climbing image method[68] as implemented in VASP. Eight images were used for each NEB calculation with a spring constant of 5 eV/$Å^2$. The improved dimer method (IDM) was later used to refine these structures using the same convergence criteria as employed in structure optimizations.[69,70]

The $c(2 \times 2)$ surface unit cell was generated by cutting bulk $CeO_2$ in (100) orientation with a cell vector that amounts to 10.980 Å (HSE: 10.802 Å). The slab model consists of 8 $CeO_2$ units in the surface layer and 11 atomic layers keeping atomic positions of the lowest three layers frozen to simulate the bulk (cf. Figure 1). Both surfaces are oxygen-terminated, but only 50% of the lattice positions are occupied in order to maintain stoichiometry (cf. Figure 2c of ref 22). The vacuum layer in $z$-


DOI: 10.1021/acs.jpcc.5b07186
J. Phys. Chem. C 2015, 119, 23021−23031

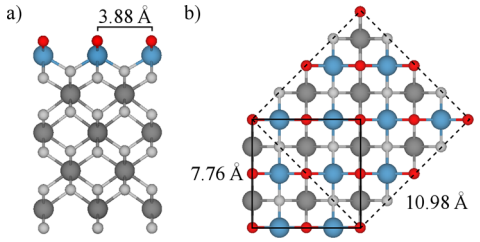


**Figure 1.** Side view (a) of the slab model used in this work as well as a top view (b) that compares a $p(2 \times 2)$ surface cell (solid line) with a $c(2 \times 2)$ surface cell (dashed line). The following color code is used: $Ce^{4+}$ (dark gray; surface blue), O (light gray; surface red). VESTA is used for visualizing structural models.[71]

direction was set to 8 Å, which after testing was found to be sufficient to avoid interactions between replicated images.

## 3. RESULTS

**3.1. Layer Convergence.** Previous studies considered symmetrical slab models (i.e., both slab surfaces can relax) with nine atomic layers.[21,72,73] However, increasing the number of atomic layers from nine to 11 increases the relaxation contribution ($\Delta_{relax} = \gamma_{relax} - \gamma_0$, cf. Table 1) to the surface energy from −0.64 to −0.67 J/m$^2$ (cf. Figure 2). An asymmetrical slab model (i.e., positions of atoms in one surface are fixed to simulate the bulk) with the same number of atomic layers decreases the surface energy even further (−0.71 J/m$^2$ relaxation contribution). Adding more atomic layers does not affect the surface energy significantly, which is why we consider 11 layers to be converged. The hybrid functional predicts a lower surface relaxation energy of −0.88 J/m$^2$, but the corresponding surface energy is nevertheless higher (1.72 J/m$^2$ compared to 1.44 J/m$^2$ with PBE+U). Dispersion contributions only marginally affect surface energies. These results are compiled in Table 1.

**Table 1. Surface Energies as well as Surface Oxygen Defect Formation Energies Obtained with Symmetrical (s) and Asymmetrical (as) Slab Models**[a]

| | surface energy [J/m$^2$] | | | defect formation [eV] | | |
|---|---|---|---|---|---|---|
| | unrelaxed | relaxed | $\Delta_{relax}$ | unrelaxed | relaxed | $\Delta_{relax}$ |
| PW91+U (s)[b] | 2.05 | 1.41 | −0.64 | | 2.27 | |
| PW91+U (s)[c] | 2.39 | 1.65 | −0.74 | | | |
| PBE+U (s, 11L) | 2.15 | 1.48 | −0.67 | 2.39 | 1.49 | −0.90 |
| PBE+U (as, 11L) | 2.15 | 1.44 | −0.71 | 2.39 | 1.28 | −1.11 |
| PBE+U+D (as, 11L) | 2.15 | 1.44 | −0.71 | 2.50 | 1.38 | −1.12 |
| HSE (as, 11L) | 3.40 | 1.72 | −0.88 | 2.70 | 1.56 | −1.14 |
| $CeO_2$(111), PBE+U | 0.69 | 0.68 | −0.01 | 3.80[d] | 1.84[d] | −1.96[d] |
| $CeO_2$(111), HSE | | 0.82 | | 4.44 | 2.44 | −2.00 |
| Bulk, PBE+U[e] | | | | 4.22 | 2.76 | −1.46 |
| Bulk, HSE[e] | | | | 4.96 | 3.78 | −1.18 |

[a]Bulk ceria defect formation energies are stated for comparison. [b]Reference 21. [c]Reference 23. [d]Reference 65. [e]Values refer to a $Ce_{32}O_{64}$ supercell.

**3.2. Surface Oxygen Defects.** Using eq 1, the PBE+U formation energy for the most stable surface oxygen defect amounts to $\Delta E_d(1/2\ O_2)$ = 1.28 eV (cf. Table 1), which includes −1.11 eV relaxation contribution and 0.05 eV dipole corrections.

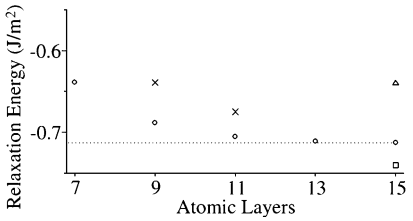


**Figure 2.** DFT+U relaxation contributions $\Delta_{relax}$ to the surface energies $\gamma$ in J/m$^2$ for symmetrical (×) and asymmetrical (o) slab models. The latter include dipole corrections. References 21 (Δ) and 23 (□) report values obtained with PW91+U for symmetrical slab models.

$$[2Ce^{4+}, 4O^{2-}] \rightarrow [2Ce^{3+}, 3O^{2-}, V_O] + 1/2O_2 \quad (1)$$

This value is significantly lower than the surface oxygen defect formation energy obtained for a symmetrical slab model with the same number of layers (1.49 eV) due to the different relaxation contributions $\Delta_{relax}$ as shown in Table 1, which is a strong indication that symmetrical slab models with 11 atomic layers are not converged with respect to the number of atomic layers. The discrepancy in $\Delta E_d(1/2\ O_2)$ of 0.21 eV is caused by relaxation, because it is equal to the difference in $\Delta_{relax}$ (cf. Table 1). Dispersion correction increases the defect formation energy to 1.38 eV (+0.10 eV). The hybrid functional HSE predicts a defect formation energy of 1.56 eV, which is 0.28 eV larger compared to PBE+U.

For the most stable surface oxygen defect, both $Ce^{3+}$ ions (5-fold coordinated) are in nearest neighbor position with respect to the oxygen vacancy as shown in Figure 3a. Specific relaxations of individual atoms are discussed in the SI. $Ce^{3+}$ configurations with one nearest neighbor and one next-nearest neighbor regarding the vacancy are 0.06 and 0.25 eV less stable, respectively. The energy difference between 3b and 3c illustrates that larger $Ce^{3+}$−$Ce^{3+}$ distances are preferred energetically. Configurations with subsurface $Ce^{3+}$ ions lead to defect formation energies greater than 1.5 eV, and subsurface oxygen vacancies (3.13 eV) are even less stable than bulk defects (2.76 eV; unit cell with 96 atoms).

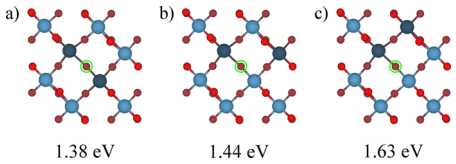


**Figure 3.** Top view on different $Ce^{3+}$ configurations at surface oxygen defects (green circle) along with the PBE+U+D defect formation energies in eV. The following color code is used throughout this work: $Ce^{3+}$ (dark blue), $Ce^{4+}$ (blue), and O (red; subsurface dark red).

Oxygen defects discussed in this work use high-spin configurations, which were found to be energetically favored over low-spin configurations. The nearest neighbor configuration shown in Figure 3a is particularly destabilized in the low-spin case (1.74 eV), i.e., antiferromagnetic order. At the ceria (111) surface, high- and low-spin configurations were found to be similar in energy.[74]

**3.3. Methanol Adsorption.** Methanol adsorbs dissociatively at the $CeO_2$(100) surface with an adsorption energy of


DOI: 10.1021/acs.jpcc.5b07186
J. Phys. Chem. C 2015, 119, 23021−23031

−1.94 eV, which includes −0.25 eV dispersion correction. The most stable adsorption structure **A** ($\theta$ = 0.125, i.e., 1 methanol per 8 surface Ce ions) is shown in Figure 4 and relevant bond

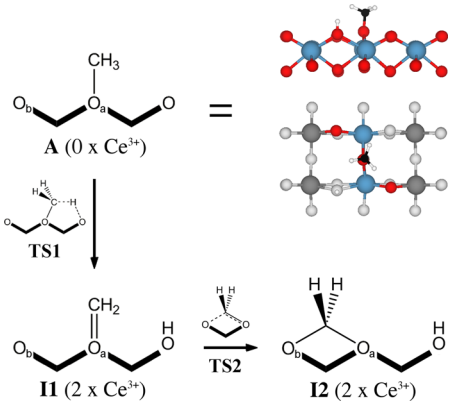


**Figure 4.** Thermodynamically favored methanol adsorption structure **A** at the $CeO_2$(100) surface (side and top view as well as a schematic stick figure representation) along with the oxidation products **I1** and **I2** that are reached via transition structures **TS1** and **TS2**.

**Table 2. Selected Bond Lengths (pm) for the Structures Shown in Figure 4 (A, TS1, I1, TS2, and I2) Obtained with Dispersion-Corrected PBE+U**

| | A | TS1 | I1 | TS2 | I2 |
|---|---|---|---|---|---|
| C−H | 110 | 147 | | | |
| $C-O_a$ | 142 | 139 | 123 | 129 | 143 |
| $C-O_b$ | | | | 255 | 141 |
| O−H | | 118 | 97 | 97 | 97 |

lengths are given in Table 2. Figure 4 also introduces a schematic stick representation to illustrate the local structure around the adsorbed methoxy species. Note that the stick figure corresponds to all colored atoms shown in the top view and each apex between two bold lines indicates a corresponding Ce ion in the surface.

Here, the methoxide binds to the surface by bridging two Ce ions and a nearest neighbor oxygen ion is protonated. Prior to the methanol adsorption, this oxygen ion is located at an equidistant site between two Ce ions ($r_{Ce-O}$ = 220 pm), but after protonation it is lifted by 15 pm and moves closer to one of the aforementioned Ce ions ($r_{Ce-OH}$ = 240 and 251 pm) and the methoxide moves toward the same Ce ion. Protonation of a next-nearest neighbor oxygen atom is 0.06 eV less stable as the aforementioned relaxation does not occur. Vibrational frequencies of **A** are discussed in section 4.2.

**3.4. Methanol Oxidation.** Starting with **A**, a hydrogen atom can be transferred to a neighboring surface oxygen atom. Except for their relative position to the hydroxyl group, these oxygen atoms are symmetrically equivalent (cf. top view in Figure 4). Because of that, reaction barriers are expected to be similar and only one pathway via transition structure **TS1** will be investigated. Intermediate and transition structures are shown in Figure 4, and the PBE+U+D reaction profile is shown in Figure 5.

Along the imaginary mode of **TS1** (1274 $cm^{-1}$), the hydrogen atom is transferred to a surface oxygen atom and the $CH_2O$ moiety planarizes with an intrinsic barrier of 1.09 eV.

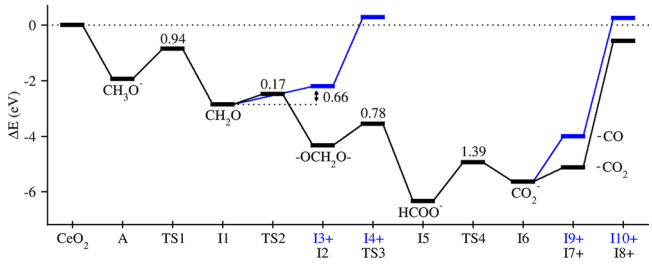


**Figure 5.** Energy profile for the oxidation of methanol at the $CeO_2$(100) surface. Total energies obtained using dispersion-corrected PBE+U include gas phase molecules as indicated by a plus sign. Intrinsic barriers are given in eV.

Dispersion does not affect this barrier, but ZPVE corrections decrease the barrier to 0.94 eV. The density of states of **TS1** as well as an electron density isocontour plot of the highest occupied crystal orbital (HOCO) is depicted in Figure 6. The HOCO is occupied by two electrons and consists of the formaldehyde $\pi^*$ orbital and the f orbitals of three Ce ions.

Forward relaxation of **TS1** leads to the metastable **I1**, which consists of formaldehyde adsorbed 82 pm above the hydrogenated $Ce_{40}O_{78}(OH)_2$ surface. Both electrons are now localized in surface Ce f states. The reaction energy for the oxidation step **A** → **I1** amounts to −0.91 eV. Starting with **I1**, two pathways are considered: further relaxation toward **I2** and formaldehyde desorption.

Formation of **I2**, which contains a bridging $-O-CH_2-O-$ motif, is highly exothermic with a reaction energy of −1.47 eV. This intermediate may lead to the formation of carbon oxides, and its formation occurs via transition structure **TS2** (cf. Figure 4) with an intrinsic barrier of 0.17 eV. Along the imaginary mode of **TS2** (222 $cm^{-1}$), the C═O bond becomes longer as the carbon atom approaches the surface oxygen atom.

Desorption of the loosely bonded formaldehyde, on the other hand, is expected to occur barrierless with a desorption energy of 0.66 eV, which includes 0.2 eV dispersion contributions. This reaction pathway leading to $Ce_{40}O_{78}(OH)_2$ (**I3**) is furthermore favored by a gain in entropy. An estimate for the entropy contribution would be the value at the (111) surface, which amounts to $-T\Delta S$ = −0.56 eV (300 K, 0.1 MPa).[41] In contrast, water desorption leading to $Ce_{40}O_{79}$ (**I4**) is highly endothermic (2.48 eV) due to the creation of a surface oxygen defect.

**3.5. Formation of Carbon Oxides.** Starting with **I2**, further oxidation occurs via transition structure **TS3** (see Figure 6b). Along its imaginary mode (521 $cm^{-1}$), a hydrogen atom is transferred to a neighboring surface oxygen atom and the $HCOO^-$ moiety planarizes as the C−O bonds are contracted. This is depicted in Figure 7 and structural parameters are compiled in Table 3. **TS3** contains two $Ce^{3+}$ ions in the surface Ce layer and one $Ce^{3+}$ ion in the subsurface layer (not shown in Figure 6b). A fourth unpaired electron is delocalized in the formate $\pi^*$ orbital and a surface oxygen p orbital, thus forming a broken-symmetry singlet state. The intrinsic barrier for this elementary step is only 0.78 eV.

Forward relaxation of **TS3** leads to intermediate structure **I5**, which consists of a formate anion adsorbed at a $Ce_{40}O_{77}(OH)_3$ slab. The newly formed hydroxyl group is tilted toward another surface oxygen atom and forms a weak hydrogen bond (223 pm). All four unpaired electrons are now localized in surface Ce f states, i.e., half of the Ce ions of the surface layer. The reaction energy for this oxidation step amounts to −2.40 eV, thus


DOI: 10.1021/acs.jpcc.5b07186
J. Phys. Chem. C 2015, 119, 23021−23031

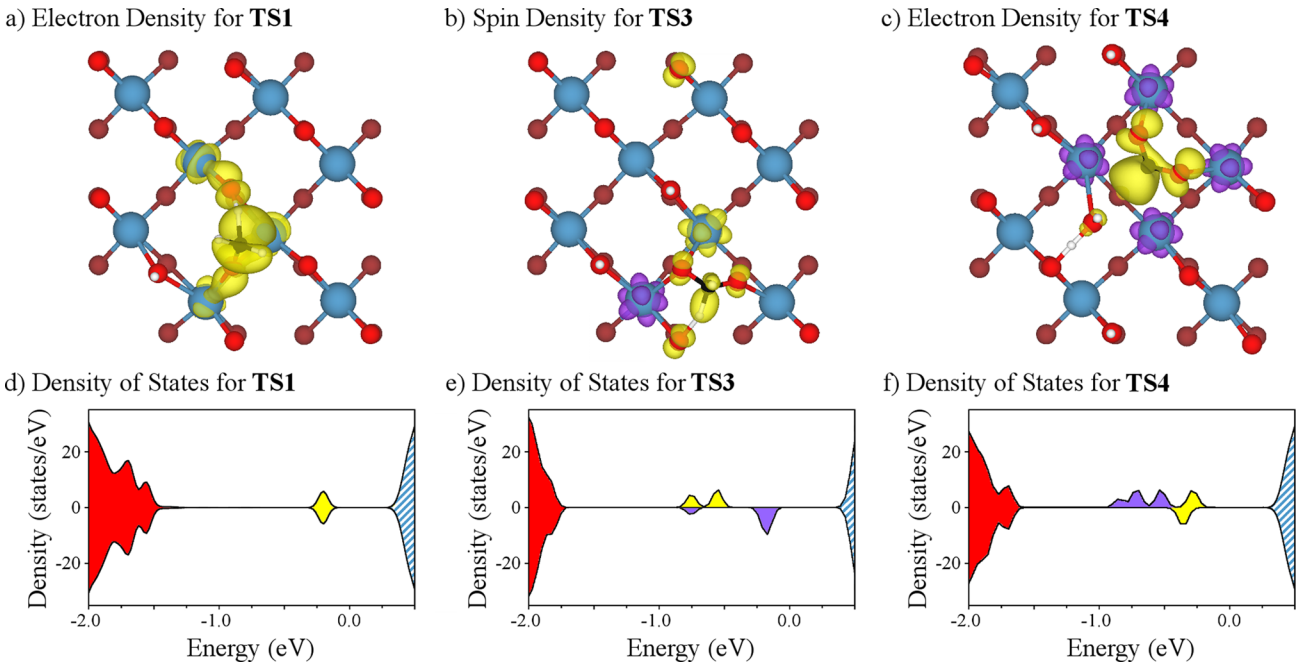


**Figure 6.** Electron and spin density isocontours (0.01 Å$^{-3}$) for the highest occupied bands of **TS1** (a), **TS3** (b), and **TS4** (c) as well as respective projected local densities of states (d–f; topmost six atomic layers) around the Fermi level using the following color code: red (mostly O p states), yellow/purple (hybridized state depicted above), and blue (unoccupied Ce f states).

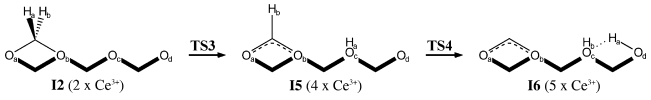


**Figure 7.** Reaction pathways for the oxidation of formaldehyde at the $CeO_2$(100) surface. Top views of these structures are shown in the SI (cf. Figure S2).

**Table 3. Relevant PBE+U+D Bond Lengths (pm) for the Intermediate Structures Shown in Figure 7 and the Corresponding Transition Structures**

| | I2 | TS3 | I5 | TS4 | I6 | $CO_2$ |
|---|---|---|---|---|---|---|
| C–$H_a$ | 111 | 122 | | | | |
| C–$H_b$ | 111 | 111 | 111 | 300 | | |
| C–$O_a$ | 143 | 137 | 128 | 131 | 125 | 118 |
| C–$O_b$ | 141 | 138 | 127 | 130 | 125 | 118 |
| $O_c$–$H_a$ | | 150 | 98 | 124 | 185 | |
| $O_c$–$H_b$ | | | | 98 | 97 | |
| $O_d$–$H_a$ | | | 223 | 119 | 98 | |

making **I5** the most stable intermediate along the reaction coordinate shown in Figure 5.

Via transition structure **TS4** (cf. Figure 6c), the formate anion (**I5**) can be converted into a carbon dioxide anion (**I6**). The intrinsic barrier for this elementary step amounts to 1.39 eV. Along the imaginary mode of **TS4** (1127 cm$^{-1}$), the $HCO_2^-$ moiety is rotated toward the surface, the hydrogen is transferred to a hydroxyl oxygen atom, while the hydroxyl proton is transferred to the neighboring oxygen atom along the former hydrogen bond. Electronically, **TS4** can be considered a quintet state (high-spin) with all four Ce f electrons in $\alpha$ spin. The formate $\pi$ orbital is doubly occupied and slightly exchange-splitted most likey due to interactions with the occupied Ce f states (see Figure 6f).

Forward relaxation of **TS4** leads to the intermediate **I6**, which consists of a negatively charged carbon dioxide adsorbed at a $Ce_{40}O_{76}(OH)_4$ slab—the charge is compensated by a $Ce^{4+}$ counterion. This oxidation step is endothermic with a reaction energy of 0.69 eV. Five unpaired electrons are localized in Ce f states and one electron is localized at the $CO_2^-$ moiety within the $6a_1$ orbital (see Figure 1 of ref 75). As a result, the C═O bonds of **I6** are 7 pm longer compared to gas phase $CO_2$ (see Table 3) and the molecule is bent (132°, $C_{2v}$ symmetry). It binds through both oxygen atoms, which occupy sites in the surface oxygen lattice.

Starting with **I6**, both CO and $CO_2$ can desorb with respective desorption energies of 1.63 and 0.51 eV. Carbon dioxide desorption leads to the formation of an additional $Ce^{3+}$ (6 in total, $\theta$ = 0.75), whereas carbon monoxide desorption oxidizes the surface (4 $Ce^{3+}$ ions, $\theta$ = 0.5). Note that $\theta$ = 1.0 refers to a fully reduced surface $Ce_2O_3$ layer. As shown in Figure 5, carbon dioxide desorption (**I7+**) is favored. Water desorption (**I7** → **I8**, **I9** → **I10**) is highly endothermic with desorption energies of 2.29 and 2.13 eV per water molecule, respectively.

## 4. DISCUSSIONS

**4.1. Surface Properties.** Nolan et al.[21,76] studied the $CeO_2$(100) surface using PW91+U with a U parameter of 5.0 eV, which is expected to yield similar results compared with the PBE+U approach used in this work. For a symmetric slab model with 15 atomic layers, they reported a surface energy of 1.41 J/m$^2$ that includes −0.64 J/m$^2$ relaxation contributions. This agrees well with the results presented in section 3.1 (1.44 J/m$^2$ surface energy and −0.67 J/m$^2$ relaxation contributions). Results discussed in ref 23 differ by 10%. As previously reported for the (111) and (110) surfaces,[77] HSE also leads to a higher surface energy (1.72 J/nm$^2$) for the (100) orientation compared with PBE+U (1.44 J/nm$^2$).

Using an asymmetrical slab model with 11 atomic layers, a defect formation energy of 1.28 eV is obtained (cf. Table 4). This is significantly lower than the value reported in ref 21



DOI: 10.1021/acs.jpcc.5b07186
J. Phys. Chem. C 2015, 119, 23021–23031

**Table 4. (Sub-)Surface Oxygen Defect Formation Energies in eV Obtained with PBE+U and HSE**

| | defect formation [eV] | | |
|---|---|---|---|
| | unrelaxed | relaxed | $\Delta_{relax}$ |
| $CeO_2$(100), PBE+U | 2.39 | 1.28 | −1.11 |
| → subsurface | 4.80 | 3.13 | −1.67 |
| $CeO_2$(100), HSE | 2.70 | 1.56 | −1.14 |
| $CeO_2$(111), PBE+U[a] | 3.80 | 1.84 | −1.96 |
| → subsurface | 3.80 | 1.81 | −1.99 |
| $CeO_2$(111), HSE | 4.44 | 2.44 | −2.00 |
| → subsurface[b] | 4.51 | 2.26 | −2.25 |
| bulk, PBE+U[c] | 4.22 | 2.76 | −1.46 |
| bulk, HSE[c] | 4.96 | 3.78 | −1.18 |

[a]Reference 65. [b]Reference 78. [c]Values refer to a $Ce_{32}O_{64}$ supercell.

(2.27 eV), which was obtained using a symmetrical slab model with 9 atomic layers. Since this value is close to the unrelaxed defect formation energy (2.39 eV), it can be concluded that the smaller model is not converged with respect to the number of atomic layers. In addition, the ceria (100) defect formation energy reported in ref 21 is actually larger than the value for the (111) surface reported in ref 65 (1.84 eV), which does not follow the trend predicted by DFT surface energies in refs 21−23. This further indicates that 9 atomic layers are not sufficient for modeling the ceria (100) surface.

At the (100) surface, $\Delta E_d(1/2\ O_2)$ is lower than the defect formation energy at the more stable (111) surface obtained with the same methodology and settings (1.84 eV in ref 65), which correlates with lower coordination numbers of the surface oxygen ions at the (100) surface (CN = 2 compared to CN = 3 at the (111) surface). At the (111) surface, two next-nearest neighbor $Ce^{3+}$ ions are favored,[41] but at the (100) surface two nearest neighbor $Ce^{3+}$ ions are favored (cf. Figure 3). The significantly less stable low-spin configuration of the most stable defect at the (100) surface infers interactions between the neighboring $Ce^{3+}$ ions ($r_{Ce-Ce}$ = 440 pm).

Furthermore, surface and subsurface defect formation energies are similar in the (111) surface (cf. Table 4) but in the (100) surface, oxygen defects in surface position are highly favored over defects in subsurface position. The subsurface defect formation energy at the (100) surface (3.13 eV; two nearest neighbor $Ce^{3+}$) is even larger than the bulk defect formation energy (2.76 eV). The stronger binding of the subsurface oxygen atom in the (100) surface is due to electrostatic interaction as reflected by a lower Madelung potential at the subsurface vacancy (−2.3 V) compared with the surface vacancy (±0.0 V). For ceria (111), the Madelung potential at the surface vacancy (−1.7 V) is lower than at the subsurface vacancy (−1.2 V) due to relaxation.[74] This is further supported by experimental findings. At fully oxidized ceria (100) films, acetaldehyde is oxidized to water and carbon oxides, whereas partially reduced ceria (100) films yield $H_2$ and carbon deposits.[79] These findings indicate that subsurface defects are significantly more difficult to form in the (100) surface. In contrast, upon adsorption on a reduced ceria (111) film, acetaldehyde desorbs without decomposition.[80]

The unpaired electrons of minimum energy structures are all localized in cubic f states of $f_{x(y^2-z^2)}$ symmetry, which were found to be more stable than $f_{z^3}$ states in the cubic lattice of $CeO_2$ by Allen and Watson.[81] Only transition structure **TS1** contains occupied $f_{z^3}$ states (cf. Figure 6a).

HSE yields a significantly higher defect formation energy (1.56 eV) than PBE+U, which has also been reported for the (111) surface.[41,74] Note that relaxation contributions are slightly larger using HSE (−1.14 eV) compared with PBE+U (−1.11 eV). The same is observed for the (111) surface, but PBE+U yields a significantly higher relaxation contribution for bulk defects (cf. Table 4) most likely because of the overestimated lattice parameter and the strongly underestimated bulk modulus.[82] The PBE+U bulk defect formation energy agrees well with the value reported in ref 83.

**4.2. Methanol Adsorption.** At the $CeO_2$(100) surface, methanol adsorbs with −1.94 eV. This corresponds to a methanol coverage of $\theta$ = 0.125. This is significantly more exothermic than at the pristine $CeO_2$(111) surface (−0.91 eV in ref 41), but less exothermic than the adsorption in a surface oxygen vacancy (−2.39 eV in ref 41). This correlates with the number of Ce ions coordinated to the methoxide as shown in Table 5. Upon neglect of dispersion corrections, ref 47 reports a virtually identical adsorption energy of ca. −1.6 eV.

**Table 5. Number of Ce Ions Coordinating the Methoxide (CN), Methanol Adsorption Energies ($E_{ads}$), and Vibrational Frequencies for the $H_3C-O$ Rocking ($r$) and the C−O Stretching ($\nu$) Modes in $cm^{-1}$ Obtained with Dispersion-Corrected PBE+U[a]**

| | CN | $E_{ads}$ (eV) | $r(CH_3)$ | $\nu$(CO) |
|---|---|---|---|---|
| $CH_3OH$ | | | 1132, 1001 | 1050 |
| (111)[b] | 1 | −0.91 (−0.22) | 1130, 1125 | 1069 |
| (100) | 2 | −1.94 (−0.25) | 1140, 1116 | 1035 |
| (111)[b] | 3 | −2.39 (−0.28) | 1136 | 1012 |

[a]The dispersion correction included in the previous value is given in parentheses. [b]Reference 41.

The C−O stretching frequency of the monodentate methoxide (CN = 1) at the ceria (111) surface is blue-shifted by +19 $cm^{-1}$ compared to gas phase methanol. The stretching frequencies of the bridging (**A**, cf. Figure 4) and tridentate methoxide are red-shifted compared to gas phase methanol by −15 and −38 $cm^{-1}$, respectively. At the (111) surface, the $OCH_3$ rocking modes have similar frequencies due to the high symmetry of the surface, but at the (100) surface the difference amounts to 24 $cm^{-1}$ as one mode occurs within and one perpendicular to the $Ce-O_{Me}-Ce$ plane. However, all rocking modes occur at frequencies that are typically assigned to C−O stretching modes (see, e.g., ref 84). The entire vibrational spectrum of **A** is given in the SI.

**4.3. Methanol Oxidation.** The oxidation of methanol to formaldehyde involves the reduction of the surface. Since PBE+U yields a lower defect formation energy compared to HSE, it likely underestimates the intrinsic barriers for the oxidation of methanol. It is known that GGA functionals typically underestimate barriers,[85,86] and for methanol oxidation at the ceria (111) surface PBE+U underestimates the HSE barrier by 0.11 eV.[41]

According to the energy profile shown in Figure 5, the initial oxidation step (**A** → **I1**) involves the highest barrier in the formation of formaldehyde and is considered as rate-determining. This was, e.g., also concluded by Wachs and co-workers, when he found an almost perfect correlation of the turnover frequency for the methanol oxidation with the decomposition temperature for various metal oxides.[5] However, from a theory point of view, more definite conclusions would


DOI: 10.1021/acs.jpcc.5b07186
J. Phys. Chem. C 2015, 119, 23021−23031

require a microkinetic simulation (see, e.g., ref 87). Using the computational scheme described in ref 62, a TPD spectrum can be simulated for this reaction pathway. The harmonic frequencies of **A** and **TS1** translate into a pre-exponential factor of $1.7 \times 10^{12}$ $s^{-1}$, which leads to a formaldehyde desorption peak at 430 K assuming an intrinsic barrier of 1.05 eV, i.e. 0.94 eV PBE+U barrier corrected by 0.11 eV (difference between the intrinsic barrier at the (111) surface obtained with PBE+U and HSE). At ceria (100) films, formaldehyde desorption was observed at higher temperatures between 480−650 K (see, e.g., ref 45). This exceptionally broad temperature range might indicate a superposition of multiple desorption peaks possibly caused by defects in the thin films. These defects may have formed during the methanol oxidation. Taking this into account, the predicted desorption temperature of 430 K agrees reasonably well. The low methanol coverage of $\theta = 0.125$ used in this work might represent another reason for the discrepancy between theory and observation. Further TPD experiments using ceria nanoparticles on a silica support yielded two distinct formaldehyde desorption peaks at 435 and 590 K.[88] The second peak was attributed to (111) facets, and the peak at 435 K could either originate from edges or (100) facets. Our calculations support the interpretation that the peak at 435 K is caused by (100) facets. Methanol conversion at about this temperature range is also supported by Li et al.,[89] who observed formation of formates from methanol at polycrystalline ceria between 373 and 473 K using infrared spectroscopy.

The formation of a bridging dioxymethylene (**I1** → **I2**) proceeds exothermically by −1.47 eV with a small intrinsic barrier of 0.17 eV. Again, this barrier is likely underestimated by the PBE+U approach. This pathway leads to the formation of carbon oxides. Formaldehyde desorption (**I1** → **I3**) on the other hand is endothermic by 0.66 eV, but favored in regard to a higher entropy contribution. At the (111) surface, entropy contributions for this reaction amount to $-T\Delta S = -0.56$ eV (300 K, 0.1 MPa).[41] These two competitive pathways give rise to different products, but computation of their precise ratio is beyond the scope of the present work. This would require accurate desorption barriers that include temperature effects. However, it can be inferred with certainty from present results that methanol oxidation at the ceria (100) surface yields both formaldehyde and carbon oxides, which is in agreement with experimental results (see, e.g., ref 45).

For the conversion of **A** into **I2**, ref 47 suggests a direct route with an intrinsic barrier of 0.89 eV (compared to 0.94 eV via **TS1**), and intermediate **I1** is not reported. As a result, further oxidation steps are highly favored over formaldehyde desorption. In contrast to the present work, CO is predicted to be the exclusive product.

The dioxymethylene **I2** can be converted into the formate **I5** via transition structure **TS3** with an intrinsic barrier of 0.78 eV for the proton-coupled electron transfer (PCET). Two out of three surface oxygen ions next to the O−$CH_2$−O moiety are already protonated, which reflects the increasing degree of surface reduction. As a result, only one O ion of **I2** can accept the proton to form **I5**. One of the $Ce^{3+}$ ions of **TS3** is located in a subsurface Ce layer. Such localization patterns are about 0.1 eV less favored for surface oxygen defects (see section 3.2). Therefore, a transition structure **TS3′** with three $Ce^{3+}$ ions in the topmost cationic layer should exist, which might slightly decrease the intrinsic barrier for this step. This assumption is further supported by the fact that the highest occupied band of **TS3** originates from the subsurface $Ce^{3+}$ ion (cf. Figure 6e). However, a highly accurate barrier for this reaction step is not needed as it is not supposed to be rate-determining.

The bidentate formate **I5** was found to be the most stable intermediate and as such, it is expected to be the most abundant one. Using infrared spectroscopy, Li et al.[89] studied the thermal decomposition of methanol at polycrystalline ceria: formate formation is observed at 473 K, and no methanol could be detected after heating to 573 K. Interestingly, formaldehyde deposition at 300 K leads to an immediate formation of formates. This supports our finding that the initial methanol oxidation step is rate-determining. All other intrinsic barriers along the pathways **I1** → **I5** are lower than the barrier for the first C−H bond breaking in methoxide, and formates may be formed at relatively lower temperatures. Reference 89 also suggests that formates may be formed via disproportionation of two formaldehyde molecules ("Cannizzaro reaction"). However, bimolecular reaction mechanisms, i.e., higher orders, are beyond the scope of the present work.

Further oxidation of the formate occurs via **TS4** with an intrinsic barrier of 1.39 eV. Here, the H atom has to be transferred to a neighboring hydroxyl group since all O ions in the vicinity of the formate are already protonated due to the high degree of surface reduction. The barrier for this H transfer is significantly higher than the barriers calculated for H transfers to surface O ions. The hydrogen atom of that hydroxyl group originating from PCET is subsequently transferred to another surface oxygen atom. The high density of surface hydroxyl groups ($\theta = 0.5$) along with a O−O distance of only 280 pm enables this Grotthuss-like mechanism.

This leads to the intermediate **I6** that contains a negatively charged $CO_2^-$ moiety—the charge is compensated by a $Ce^{4+}$ counterion. In contrast to molecular $CO_2$, the anion is bent (132°) and the C═O bonds are elongated (125 instead of 118 pm) resulting in $C_{2v}$ symmetry. This change in geometry lowers the $6a_1$ orbital ($\triangleq 2\pi_u$ in linear $CO_2$), which accommodates the 23rd electron, as shown in the Walsh diagram given in ref 75. In **I6**, the $CO_2^-$ moiety is bonded through both oxygen atoms, which occupy surface oxygen positions.

Upon transferring an electron into the Ce f states, $CO_2$ can desorb (0.51 eV). The resulting $Ce_{40}O_{75}(OH)_4$ slab contains six $Ce^{3+}$ and two $Ce^{4+}$ ions in the surface layer, which is close to a $Ce_2O_3$ surface layer. Based on dispersion-corrected PBE+U energies, this pathway is favored over the CO desorption (1.63 eV), which results in a $Ce_{40}O_{76}(OH)_4$ slab with only four $Ce^{3+}$ ions in the surface layer. However, these values do not include temperature effects, which are known to affect the equilibrium between $CO_2$ and CO.

Ref 47 also reports the formate **I5** to be the most stable intermediate, but for the following oxidation steps López and co-workers report different intermediates. Instead of the $CO_2^-$ moiety **I6**, molecularly adsorbed carbon monoxide was obtained with a reaction energy of +1.3 eV, which is significantly less stable than **I6** (0.69 eV). $CO_2$ formation was not considered in ref 47. Note that their smaller $p(2 \times 2)$ surface unit cell can only accommodate 4 $Ce^{3+}$ ions in the surface layer, but $CO_2$ formation yields in total 6 $Ce^{3+}$ ions. Therefore, strain contributions strongly affect the reaction energy because at least 2 $Ce^{3+}$ ions have to be located in subsurface positions, which are known to be less favored (see section 3.2).

Reference 90 reports that $CO_2$ adsorbs at pristine and oxygen-defective ceria (100) surfaces forming a flat $CO_3^-$


DOI: 10.1021/acs.jpcc.5b07186
J. Phys. Chem. C 2015, 119, 23021−23031

species by reacting with a surface oxygen ion. With an adsorption energy of −1.93 eV (PBE+U), this carbonate structure is significantly more stable than **I6** (−0.51), though **I6** cannot be easily converted into such a carbonate since all neighboring surface O ions are protonated due to the previous dehydrogenation reactions.

**4.4. Comparison to the (111) Surface.** At the pristine $CeO_2$ (111) surface, methanol adsorbs with an adsorption energy of −0.91 eV, and the adsorption at defective sites such as oxygen vacancies is significantly more exothermic (−2.39 eV).[41] The adsorption energy at the pristine (100) surface (−1.94 eV) adopts a value in between those for the fully oxidized and reduced (111) surfaces, which correlates with the number of Ce ions coordinated to the methoxide as shown in Table 5. Methanol adsorption at the pristine (111) surface is less exothermic than at the (100) surface. The reason is the higher degree of coordinative unsaturation of ions in the (100) surface compared to (111). However, dissociative adsorption is favored over molecular adsorption in all cases at low methanol coverage.

The intrinsic barriers for the methanol oxidation at the (111) surface are 1.08 and 1.23 eV for pristine and the partially reduced surfaces, respectively.[41] At the (100) surface, the barrier is slightly lower (0.94 eV). This reaction pathway is also the most exothermic one (−0.91 eV), as expected from the Bell−Evans−Polanyi (BEP) principle. The initial oxidation step at the pristine (111) surface is slightly less exothermic (−0.71 eV) and its intrinsic barrier is 0.12 eV higher. At the partially reduced (111) surface, this oxidation runs endothermically by 0.37 eV, and the intrinsic barrier is 1.23 eV. The lower barrier at the (100) surface also correlates with lower oxygen defect formation energies (cf. Table 1), which further supports the hypothesis stated in ref 48 that oxygen defect formation energies can be used to efficiently compare the reactivity of different surfaces with respect to ODH reactions.

Albrecht and Mullins studied the ODH of methanol at both surfaces using TPD experiments. While the (111) surface has a high selectivity toward formaldehyde, the (100) surface yields both formaldehyde and carbon oxides in similar amounts.[45] Figure 8 compares the energy profiles for the relevant elementary steps at these surfaces. Values for the reactions at the (111) surface are taken from refs 41 (formaldehyde desorption) and 44 (oxidation to $CO_X$).

The initial methanol oxidation yields molecularly adsorbed formaldehyde (**I1**) that can either desorb via **I3** or form the bridging dioxymethylene **I2** that can be further oxidized to a formate via **TS3**. At the (111) surface (blue line in Figure 8), the desorption energy amounts to 0.35 eV, and the conversion of **I1** into **I2** proceeds exothermically with a reaction energy of −0.81 eV.[41] The associated barrier is expected to be small and has not been calculated. For the onward oxidation of **I2**, an intrinsic barrier of 1.71 eV was reported,[44] which suggests that formaldehyde desorption is more likely to occur under these conditions. A similar barrier was reported in ref 47. In contrast, at the (100) surface, desorption of formaldehyde is by 0.31 eV more endothermic (0.66 eV) as indicated by an arrow at **I3** in Figure 8, and the formation of **I2** is significantly more exothermic (−1.47 eV). The intrinsic barrier of the oxidation step is also lower (0.78 eV). As a result, the formation of **I2** via **TS2** becomes the decisive step for the selectivity of the methanol oxidation at this surface orientation. As mentioned above, we avoid calculating the exact ratio of formaldehyde to carbon oxides, but these results suggest that both products may form at the ceria (100) surface.

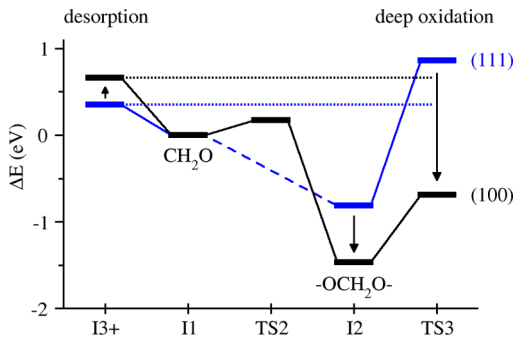


**Figure 8.** Reaction profiles for the desorption (**I1** → **I3**) and oxidation (**I2** → **TS3**) of formaldehyde at different ceria surfaces: $CeO_2$(100) − black, $CeO_2$(111) − blue. The values for the ceria (111) surface are taken from refs 41 and 44.

Differences in reactivity between both surface orientations are caused by the lower coordination number of Ce and O ions at the (100) surface. This leads to more endothermic formaldehyde desorption energies and more exothermic dehydrogenation reactions with lower barriers in agreement with the BEP principle. The same has been reported by López and co-workers.[47] A correlation between high activity and low coordination numbers was also recently discussed by Vohs.[91]

**4.5. Water Desorption versus $H_2$ Evolution.** Two surface hydroxyl groups can either form water (eq 2) or molecular hydrogen (eq 3). Water desorption does not change the degree of surface reduction, i.e., the number of $Ce^{3+}$ ions, while $H_2$ evolution oxidizes the surface.

$$[2Ce^{3+}, 2O^{2-}, 2OH^{-}] \rightarrow [2Ce^{3+}, 3O^{2-}, V_O] + H_2O \quad (2)$$

$$[2Ce^{3+}, 2O^{2-}, 2OH^{-}] \rightarrow [2Ce^{4+}, 4O^{2-}] + H_2 \quad (3)$$

At the ceria (111) surface, PBE+U and HSE predict similar water desorption energies (2.12 and 2.04 eV in ref 41), but $H_2$ desorption energies vary drastically (2.30 and 1.81 eV in ref 41). As a result, water desorption is favored when using PBE+U, and $H_2$ evolution is favored when using the HSE hybrid functional.[41] This is caused by too low oxygen defect formation energies obtained with PBE+U (cf. Table 1) implying too high reducibility of the surface. Because HSE results agree better with observation (see, e.g., ref 16), they are considered more accurate. Therefore, $H_2$ evolution is expected to occur. The free desorption energies (HSE energies, 600 K, and 0.1 MPa) for water and hydrogen amount to 0.99 and 0.70 eV, respectively. This shows that the picture is not changed upon inclusion of temperature effects. However, the low conversion of methanol to formaldehyde on the (111) surface prevents the detection of either $H_2$ or $H_2O$ in TPD experiments.[45]

At the (100) surface, water desorption (2.33 eV, **I3** → **I4**) is also favored over $H_2$ evolution (3.51 eV) when using PBE+U. Due to the lower oxygen defect formation energy at (100), this preference is significantly more pronounced than at the (111) surface. PBE+U and HSE yield similar defect formation energies at the (100) surface, i.e., similar reducibility (cf. Table 1). Thus, we infer that water will preferentially desorb independent of the functional used. However, this preference depends on the degree of surface reduction: in the presence of two additional oxygen defects (**I7**), water formation (2.29 eV)


DOI: 10.1021/acs.jpcc.5b07186
J. Phys. Chem. C 2015, 119, 23021−23031

is less favored over $H_2$ evolution (2.79 eV). While water desorption energies are only mildly affected, $H_2$ evolution becomes thermodynamically more favorable with an increasing degree of reduction. Albrecht and Mullins[45] observed both water and $H_2$ in TPD experiments at fully oxidized ceria films, whereas reduced ceria films only produced $H_2$. The aforementioned results are consistent with these observations and indicate rather high degrees of surface reduction during the TPD experiments.

## 5. CONCLUSIONS

The surface energy of the ceria (100) surface involves large relaxation effects, which is why large slab models with at least 11 atomic layers are required to accurately account for relaxation. The oxygen defect formation energy at the (100) surface (1.56 eV, HSE) is markedly lower than the defect formation energy at the (111) surface (2.44 eV, HSE), and subsurface defects are significantly less stable than surface defects. The lower oxygen defect formation energies at the (100) surface are caused by the coordinative unsaturation making it the more reducible surface, i.e., the better oxidant. Likewise, methanol adsorbs very exothermically (−1.94 eV, PBE+U) at the (100) surface and reacts to formaldehyde with an intrinsic barrier of only 0.94 eV (PBE+U). This study shows that formaldehyde desorption appears to be key to selectivity. The resulting formaldehyde either desorbs or further reacts to a bridging dioxymethylene species, which leads to deep oxidation. Methanol conversion to formaldehyde as well as deep oxidation at the (111) surface involves larger barriers. Thus, formaldehyde desorption is favored over further oxidation on this surface, which is consistent with observation, and renders $CeO_2$(111) the more selective but less active catalyst. At low methanol coverage on the (100) surface, deep oxidation yields $CO_2$ and water, but with an increasing degree of surface reduction, $H_2$ and CO will preferentially form. This work illustrates the influence of the three well-known concepts on the oxidation of methanol at reducible ceria surfaces: (i) the coordinative unsaturation, (ii) the reducibility, and (iii) the degree of reduction.

## ■ ASSOCIATED CONTENT

### Supporting Information

The Supporting Information is available free of charge on the ACS Publications website at DOI: 10.1021/acs.jpcc.5b07186.

Relaxation patterns at surface defects; simulated vibrational spectrum for **A**; top views on structures **I2**, **I5**, **I6**, **TS3**, and **TS4**; table of total energies (PDF)

## ■ AUTHOR INFORMATION

### Corresponding Author

*Phone +(49)-30-2093-7139. E-mail joachim.paier@chemie.hu-berlin.de.

### Notes

The authors declare no competing financial interest.

## ■ ACKNOWLEDGMENTS

We wish to thank Prof. Joachim Sauer for his continuous support and many fruitful discussions. This work has been supported by the "Fonds der Chemischen Industry (FCI)" as well as by grants for computer time at the high-performance computer centers HLRN (North-German Supercomputing Alliance in Berlin and Hannover). COST action CM1104 (Reducible Oxide Chemistry, Structure, and Function) is gratefully acknowledged. We thank Dr. Brian Solis for proofreading the manuscript.

## ■ REFERENCES

(1) Purnama, H.; Ressler, T.; Jentoft, R. E.; Soerijanto, H.; Schlögl, R.; Schomäcker, R. CO formation/selectivity for steam reforming of methanol with a commercial $CuO/ZnO/Al_2O_3$ catalyst. *Appl. Catal., A* **2004**, *259*, 83−94.

(2) Campos, C. L.; Roldan, C.; Aponte, M.; Ishikawa, Y.; Cabrera, C. R. Preparation and methanol oxidation catalysis of Pt-$CeO_2$ electrode. *J. Electroanal. Chem.* **2005**, *581*, 206−215.

(3) Bahmanpour, A. M.; Hoadley, A.; Tanksale, A. Critical review and exergy analysis of formaldehyde production processes. *Rev. Chem. Eng.* **2014**, *30*, 583−604.

(4) Tatibouët, J. M. Methanol oxidation as a catalytic surface probe. *Appl. Catal., A* **1997**, *148*, 213−252.

(5) Badlani, M.; Wachs, I. E. Methanol: a "smart" chemical probe molecule. *Catal. Lett.* **2001**, *75*, 137−149.

(6) Deo, G.; Wachs, I. E. Reactivity of supported vanadium-oxide catalysts - the partial oxidation of methanol. *J. Catal.* **1994**, *146*, 323−334.

(7) Wachs, I. E.; Deo, G.; Juskelis, M. V.; Weckhuysen, B. M. Methanol Oxidation. In *Dynamics of surfaces and reaction kinetics in heterogeneous catalysis*; Froment, G. F., Waugh, K. C., Eds.; Elsevier: Amsterdam, 1997; pp 305−314.

(8) Wachs, I. E.; Chen, Y.; Jehng, J.-M.; Briand, L. E.; Tanaka, T. Molecular structure and reactivity of the group V metal oxides. *Catal. Today* **2003**, *78*, 13−24.

(9) Wachs, I. E. Molecular engineering of supported metal oxide catalysts: oxidation reactions over supported vanadia catalysts. In *Catalysis*; Spivey, J. J., Ed.; The Royal Society of Chemistry: London, 1997; Vol. *13*, pp 37−54.

(10) Ganduglia-Pirovano, V. The non-innocent role of cerium oxide in heterogeneous catalysis: A theoretical perspective. *Catal. Today* **2015**, *253*, 20−32.

(11) Beck, B.; Harth, M.; Hamilton, N. G.; Carrero, C.; Uhlrich, J. J.; Trunschke, A.; Shaikhutdinov, S.; Schubert, H.; Freund, H.-J.; Schlögl, R.; Sauer, J.; Schomäcker, R. Partial oxidation of ethanol on vanadia catalysts on supporting oxides with different redox properties compared to propane. *J. Catal.* **2012**, *296*, 120−131.

(12) Baron, M.; Abbott, H.; Bondarchuk, O.; Stacchiola, D.; Uhl, A.; Shaikhutdinov, S.; Freund, H.-J.; Popa, C.; Ganduglia-Pirovano, M. V.; Sauer, J. Resolving the atomic structure of vanadia monolayer catalysts: monomers, trimers, and oligomers on ceria. *Angew. Chem., Int. Ed.* **2009**, *48*, 8006−8009.

(13) Abbott, H. L.; Uhl, A.; Baron, M.; Lei, Y.; Meyer, R. J.; Stacchiola, D. J.; Bondarchuk, O.; Shaikhutdinov, S.; Freund, H. J. Relating methanol oxidation to the structure of ceria-supported vanadia monolayer catalysts. *J. Catal.* **2010**, *272*, 82−91.

(14) Ganduglia-Pirovano, M. V.; Popa, C.; Sauer, J.; Abbott, H. L.; Uhl, A.; Baron, M.; Stacchiola, D.; Bondarchuk, O.; Shaikhutdinov, S.; Freund, H.-J. Role of ceria in oxidative dehydrogenation on supported vanadia catalysts. *J. Am. Chem. Soc.* **2010**, *132*, 2345−2349.

(15) Ganduglia-Pirovano, V.; Hofmann, A.; Sauer, J. Oxygen Vacancies in transition metal and rare earth oxides: Current state of understanding and remaining challenges. *Surf. Sci. Rep.* **2007**, *62*, 219−270.

(16) Paier, J.; Penschke, C.; Sauer, J. Oxygen defects and surface chemistry of ceria: quantum chemical studies compared to experiment. *Chem. Rev.* **2013**, *113*, 3949−3985.

(17) Fabris, S.; Vicario, G.; Balducci, G.; de Gironcoli, S.; Baroni, S. Electronic and atomistic structures of clean and reduced ceria surfaces. *J. Phys. Chem. B* **2005**, *109*, 22860−22867.

(18) Mars, P.; van Krevelen, D. W. Oxidations carried out by means of vanadium oxide catalysts. *Chem. Eng. Sci.* **1954**, *3* (Supplement 1), 41−59.



DOI: 10.1021/acs.jpcc.5b07186
*J. Phys. Chem. C* 2015, 119, 23021−23031

(19) Trovarelli, A. *Catalysis by ceria and related materials*; Imperial College Press: London, 2002.
(20) Jupille, J.; Thornton, G. *Defects at Oxide Surfaces*; Springer: Heidelberg, 2015.
(21) Nolan, M.; Grigoleit, S.; Sayle, D. C.; Parker, S. C.; Watson, G. W. Density functional theory studies of the structure and electronic structure of pure and defective low index surfaces of ceria. *Surf. Sci.* **2005**, *576*, 217−229.
(22) Skorodumova, N. V.; Baudin, M.; Hermansson, K. Surface properties of $CeO_2$ from first principles. *Phys. Rev. B: Condens. Matter Mater. Phys.* **2004**, *69*, 075401.
(23) Marrocchelli, D.; Yildiz, B. First-principles assessment of $H_2S$ and $H_2O$ reaction mechanisms and the subsequent hydrogen absorption on the $CeO_2$(111) surface. *J. Phys. Chem. C* **2012**, *116*, 2411−2424.
(24) Overbury, S. H.; Huntley, D. R.; Mullins, D. R.; Ailey, K. S.; Radulovic, P. V. Surface studies of model supported catalysts: NO adsorption on Rh/$CeO_2$(001). *J. Vac. Sci. Technol., A* **1997**, *15*, 1647−1652.
(25) Herman, G. S. Surface structure determination of $CeO_2$(001) by angle-resolved mass spectroscopy of recoiled ions. *Phys. Rev. B: Condens. Matter Mater. Phys.* **1999**, *59*, 14899−14902.
(26) Nörenberg, H.; Harding, J. H. The surface structure of $CeO_2$(001) single crystals studied by elevated temperature STM. *Surf. Sci.* **2001**, *477*, 17−24.
(27) Yang, F.; Choi, Y.; Agnoli, S.; Liu, P.; Stacchiola, D.; Hrbek, J.; Rodriguez, J. A. $CeO_2 \leftrightarrow CuO_x$ interactions and the controlled assembly of $CeO_2$(111) and $CeO_2$(100) nanoparticles on an oxidized Cu(111) substrate. *J. Phys. Chem. C* **2011**, *115*, 23062−23066.
(28) Stetsovych, O.; Beran, J.; Dvořák, F.; Mašek, K.; Mysliveček, J.; Matolín, V. Polarity driven morphology of $CeO_2$(100) islands on Cu(111). *Appl. Surf. Sci.* **2013**, *285* (Part B), 766−771.
(29) Lin, Y.; Wu, Z.; Wen, J.; Poeppelmeier, K. R.; Marks, L. D. Imaging the atomic surface structures of $CeO_2$ nanoparticles. *Nano Lett.* **2014**, *14*, 191−196.
(30) Pan, Y.; Nilius, N.; Stiehler, C.; Freund, H.-J.; Goniakowski, J.; Noguera, C. Ceria nanocrystals exposing wide (100) facets: Structure and polarity compensation. *Adv. Mater. Interfaces* **2014**, *1*, 1400404.
(31) Rohr, F.; Wirth, K.; Libuda, J.; Cappus, D.; Baumer, M.; Freund, H. J. Hydroxyl-driven reconstruction of the polar NiO(111) surface. *Surf. Sci.* **1994**, *315*, L977−L982.
(32) Goniakowski, J.; Finocchi, F.; Noguera, C. Polarity of oxide surfaces and nanostructures. *Rep. Prog. Phys.* **2008**, *71*, 016501.
(33) Mullins, D. R. The surface chemistry of cerium oxide. *Surf. Sci. Rep.* **2015**, *70*, 42−85.
(34) Vile, G.; Colussi, S.; Krumeich, F.; Trovarelli, A.; Perez-Ramirez, J. Opposite face sensitivity of $CeO_2$ in hydrogenation and oxidation catalysis. *Angew. Chem., Int. Ed.* **2014**, *53*, 12069−12072.
(35) Siokou, A.; Nix, R. M. Interaction of methanol with well-defined ceria surfaces: Reflection/absorption infrared spectroscopy, X-ray photoelectron spectroscopy, and temperature-programmed desorption study. *J. Phys. Chem. B* **1999**, *103*, 6984−6997.
(36) Ferrizz, R. M.; Wong, G. S.; Egami, T.; Vohs, J. M. Structure sensitivity of the reaction of methanol on ceria. *Langmuir* **2001**, *17*, 2464−2470.
(37) Mullins, D. R.; Robbins, M. D.; Zhou, J. Adsorption and reaction of methanol on thin-film cerium oxide. *Surf. Sci.* **2006**, *600*, 1547−1558.
(38) Matolín, V.; Libra, J.; Skoda, M.; Tsud, N.; Prince, K. C.; Skála, T. Methanol adsorption on a $CeO_2$(1 1 1)/Cu(1 1 1) thin film model catalyst. *Surf. Sci.* **2009**, *603*, 1087−1092.
(39) Mei, D.; Deskins, N. A.; Dupuis, M.; Ge, Q. Methanol adsorption on the clean $CeO_2$(111) surface: A density functional theory study. *J. Phys. Chem. C* **2007**, *111*, 10514−10522.
(40) Beste, A.; Mullins, D. R.; Overbury, S. H.; Harrison, R. J. Adsorption and dissociation of methanol on the fully oxidized and partially reduced (111) cerium oxide surface: Dependence on the configuration of the cerium 4*f* electrons. *Surf. Sci.* **2008**, *602*, 162−175.
(41) Kropp, T.; Paier, J. Reactions of methanol with pristine and defective ceria (111) surfaces: A comparison of density functionals. *J. Phys. Chem. C* **2014**, *118*, 23690−23700.
(42) Mei, D.; Deskins, N. A.; Dupuis, M.; Ge, Q. F. Density functional theory study of methanol decomposition on the $CeO_2$(110) surface. *J. Phys. Chem. C* **2008**, *112*, 4257−4266.
(43) Mei, D.; Aaron Deskins, N.; Dupuis, M. A density functional theory study of formaldehyde adsorption on ceria. *Surf. Sci.* **2007**, *601*, 4993−5001.
(44) Teng, B. T.; Jiang, S. Y.; Yang, Z. X.; Luo, M. F.; Lan, Y. Z. A density functional theory study of formaldehyde adsorption and oxidation on $CeO_2$(111) surface. *Surf. Sci.* **2010**, *604*, 68−78.
(45) Albrecht, P. M.; Mullins, D. R. Adsorption and reaction of methanol over $CeO_X$(100) thin films. *Langmuir* **2013**, *29*, 4559−4567.
(46) Li, M. J.; Wu, Z. L.; Overbury, S. H. Surface structure dependence of selective oxidation of ethanol on faceted $CeO_2$ nanocrystals. *J. Catal.* **2013**, *306*, 164−176.
(47) Capdevila-Cortada, M.; García-Melchor, M.; López, N. Unraveling the structure sensitivity in methanol conversion on $CeO_2$: A DFT+*U* study. *J. Catal.* **2015**, *327*, 58−64.
(48) Sauer, J.; Döbler, J. Structure and reactivity of $V_2O_5$: Bulk solid, nanosized clusters, species supported on silica and alumina, cluster cations and anions. *Dalton Transactions* **2004**, *19*, 3116−3121.
(49) Barteau, M. A. Organic reactions at well-defined oxide surfaces. *Chem. Rev.* **1996**, *96*, 1413−1430.
(50) Blöchl, P. E. Projector augmented-wave method. *Phys. Rev. B: Condens. Matter Mater. Phys.* **1994**, *50*, 17953−17979.
(51) Kresse, G.; Joubert, D. From ultrasoft pseudopotentials to the projector augmented-wave method. *Phys. Rev. B: Condens. Matter Mater. Phys.* **1999**, *59*, 1758−1775.
(52) Kresse, G.; Furthmüller, J. Efficient iterative schemes for ab initio total-energy calculations using a plane-wave basis set. *Phys. Rev. B: Condens. Matter Mater. Phys.* **1996**, *54*, 11169−11186.
(53) Kresse, G.; Furthmüller, J. Efficiency of ab-initio total energy calculations for metals and semiconductors using a plane-wave basis set. *Comput. Mater. Sci.* **1996**, *6*, 15−50.
(54) Liechtenstein, A. I.; Anisimov, V. I.; Zaanen, J. Density functional theory and strong-interactions - orbital ordering in Mott-Hubbard insulators. *Phys. Rev. B: Condens. Matter Mater. Phys.* **1995**, *52*, R5467−R5470.
(55) Anisimov, V. I.; Zaanen, J.; Andersen, O. K. Band theory and Mott insulators - Hubbard-U instead of Stoner-I. *Phys. Rev. B: Condens. Matter Mater. Phys.* **1991**, *44*, 943−954.
(56) Perdew, J. P.; Burke, K.; Ernzerhof, M. Generalized gradient approximation made simple. *Phys. Rev. Lett.* **1996**, *77*, 3865−3868.
(57) Dudarev, S. L.; Botton, G. A.; Savrasov, S. Y.; Humphreys, C. J.; Sutton, A. P. Electron-energy-loss spectra and the structural stability of nickel oxide: A LSDA+U study. *Phys. Rev. B: Condens. Matter Mater. Phys.* **1998**, *57*, 1505−1509.
(58) Bengone, O.; Alouani, M.; Blöchl, P.; Hugel, J. Implementation of the projector augmented-wave LDA+U method: application to the electronic structure of NiO. *Phys. Rev. B: Condens. Matter Mater. Phys.* **2000**, *62*, 16392−16401.
(59) Makov, G.; Payne, M. C. Periodic boundary-conditions in ab-initio calculations. *Phys. Rev. B: Condens. Matter Mater. Phys.* **1995**, *51*, 4014−4022.
(60) Heyd, J.; Scuseria, G. E.; Ernzerhof, M. Hybrid functionals based on a screened Coulomb potential. *J. Chem. Phys.* **2003**, *118*, 8207−8215.
(61) Krukau, A. V.; Vydrov, O. A.; Izmaylov, A. F.; Scuseria, G. E. Influence of the exchange screening parameter on the performance of screened hybrid functionals. *J. Chem. Phys.* **2006**, *125*, 224106.
(62) Kropp, T.; Paier, J.; Sauer, J. Support effect in oxide catalysis: methanol oxidation on vanadia/ceria. *J. Am. Chem. Soc.* **2014**, *136*, 14616−14625.
(63) Grimme, S. Semiempirical GGA-type density functional constructed with a long-range dispersion correction. *J. Comput. Chem.* **2006**, *27*, 1787−1799.


DOI: 10.1021/acs.jpcc.5b07186
*J. Phys. Chem. C* 2015, 119, 23021−23031

(64) Kerber, T.; Sierka, M.; Sauer, J. Application of semiempirical long-range dispersion corrections to periodic systems in density functional theory. *J. Comput. Chem.* **2008**, *29*, 2088−2097.
(65) Penschke, C.; Paier, J.; Sauer, J. Oligomeric vanadium oxide species supported on the $CeO_2(111)$ surface: Structure and reactivity studied by density functional theory. *J. Phys. Chem. C* **2013**, *117*, 5274−5285.
(66) Mills, G.; Jonsson, H.; Schenter, G. K. Reversible work transition-state theory - application to dissociative adsorption of hydrogen. *Surf. Sci.* **1995**, *324*, 305−337.
(67) Jonsson, H.; Mills, G.; Jacobsen, K. W. Nudged elastic band method for finding minimum energy paths of transitions. In *Classical and quantum dynamics in condensed phase simulations*; Berne, J., Ciccotti, G., Coker, D. F., Eds.; World Scientific: Singapore, 1998.
(68) Henkelman, G.; Uberuaga, B. P.; Jonsson, H. A climbing image nudged elastic band method for finding saddle points and minimum energy paths. *J. Chem. Phys.* **2000**, *113*, 9901−9904.
(69) Henkelman, G.; Jonsson, H. A dimer method for finding saddle points on high dimensional potential surfaces using only first derivatives. *J. Chem. Phys.* **1999**, *111*, 7010−7022.
(70) Heyden, A.; Bell, A. T.; Keil, F. J. Efficient methods for finding transition states in chemical reactions: comparison of improved dimer method and partitioned rational function optimization method. *J. Chem. Phys.* **2005**, *123*, 224101.
(71) Momma, K.; Izumi, F. VESTA 3 for three-dimensional visualization of crystal, volumetric and morphology data. *J. Appl. Crystallogr.* **2011**, *44*, 1272−1276.
(72) Nolan, M.; Fearon, J. E.; Watson, G. W. Oxygen vacancy formation and migration in ceria. *Solid State Ionics* **2006**, *177*, 3069−3074.
(73) Nolan, M. Hybrid density functional theory description of oxygen vacancies in the $CeO_2$ (110) and (100) surfaces. *Chem. Phys. Lett.* **2010**, *499*, 126−130.
(74) Ganduglia-Pirovano, M. V.; Da Silva, J. L. F.; Sauer, J. Density functional calculations of the structure of near-surface oxygen vacancies and electron ocalization on $CeO_2(111)$. *Phys. Rev. Lett.* **2009**, *102*, 026101.
(75) Freund, H. J.; Roberts, M. W. Surface chemistry of carbon dioxide. *Surf. Sci. Rep.* **1996**, *25*, 225−273.
(76) Nolan, M.; Parker, S. C.; Watson, G. W. The electronic structure of oxygen vacancy defects at the low index surfaces of ceria. *Surf. Sci.* **2005**, *595*, 223−232.
(77) Nolan, M. Enhanced oxygen vacancy formation in ceria (111) and (110) surfaces doped with divalent cations. *J. Mater. Chem.* **2011**, *21*, 9160−9168.
(78) Pan, Y.; Nilius, N.; Freund, H.-J.; Paier, J.; Penschke, C.; Sauer, J. Titration of $Ce^{3+}$ Ions in the $CeO_2(111)$ Surface by Au Adatoms. *Phys. Rev. Lett.* **2013**, *111*, 206101.
(79) Mullins, D. R.; Albrecht, P. M. Acetaldehyde adsorption and reaction on CeO2(100) thin films. *J. Phys. Chem. C* **2013**, *117*, 14692−14700.
(80) Chen, T. L.; Mullins, D. R. Adsorption and reaction of acetaldehyde over $CeO_X(111)$ thin films. *J. Phys. Chem. C* **2011**, *115*, 3385−3392.
(81) Allen, J. P.; Watson, G. W. Occupation matrix control of *d* and *f* electron localisations using DFT + U. *Phys. Chem. Chem. Phys.* **2014**, *16*, 21016−21031.
(82) Da Silva, J. L. F.; Ganduglia-Pirovano, M. V.; Sauer, J.; Bayer, V.; Kresse, G. Hybrid functionals applied to rare earth oxides: the example of ceria. *Phys. Rev. B: Condens. Matter Mater. Phys.* **2007**, *75*, 045121.
(83) Murgida, G. E.; Ferrari, V.; Veronica Ganduglia-Pirovano, M.; Llois, A. M. Ordering of oxygen vacancies and excess charge localization in bulk ceria: a DFT plus U study. *Phys. Rev. B: Condens. Matter Mater. Phys.* **2014**, *90*, 115120.
(84) Nakanishi, K. *Infrared Absorption Spectroscopy - Practical*; Holden-Day: San Francisco, 1962.
(85) Zhao, Y.; Truhlar, D. G. Design of density functionals that are broadly accurate for thermochemistry, thermochemical kinetics, and nonbonded interactions. *J. Phys. Chem. A* **2005**, *109*, 5656−5667.
(86) Zhao, Y.; Gonzalez-Garcia, N.; Truhlar, D. G. Benchmark database of barrier heights for heavy atom transfer, nucleophilic substitution, association, and unimolecular reactions and its use to test theoretical methods. *J. Phys. Chem. A* **2005**, *109*, 2012−2018.
(87) Rozanska, X.; Fortrie, R.; Sauer, J. Size-dependent catalytic activity of supported vanadium oxide species: oxidative dehydrogenation of propane. *J. Am. Chem. Soc.* **2014**, *136*, 7751−7761.
(88) Uhlrich, J.; Yang, B.; Shaikhutdinov, S. Methanol reactivity on silica-supported ceria nanoparticles. *Top. Catal.* **2014**, *57*, 1229−1235.
(89) Li, C.; Domen, K.; Maruya, K.-i.; Onishi, T. Spectroscopic identification of adsorbed species derived from adsorption and decomposition of formic acid, methanol, and formaldehyde on cerium oxide. *J. Catal.* **1990**, *125*, 445−455.
(90) Albrecht, P. M.; Jiang, D.-e.; Mullins, D. R. $CO_2$ adsorption as a flat-lying, tridentate carbonate on $CeO_2(100)$. *J. Phys. Chem. C* **2014**, *118*, 9042−9050.
(91) Vohs, J. M. Site requirements for the adsorption and reaction of oxygenates on metal oxide surfaces. *Chem. Rev.* **2013**, *113*, 4136−4163.


DOI: 10.1021/acs.jpcc.5b07186
*J. Phys. Chem. C* 2015, 119, 23021−23031

# P8

https://pubs.acs.org/doi/abs/10.1021/cr3004949

CHEMICAL REVIEWS

Review

pubs.acs.org/CR

# Oxygen Defects and Surface Chemistry of Ceria: Quantum Chemical Studies Compared to Experiment

Joachim Paier, Christopher Penschke, and Joachim Sauer*

Institut für Chemie, Humboldt Universität, 10099 Berlin, Germany

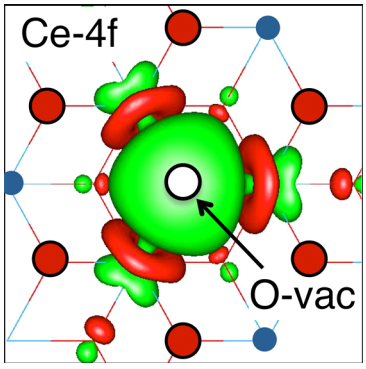


## CONTENTS



## 1. INTRODUCTION

As one of the most significant rare earth oxides, ceria ($CeO_2$) has attracted much interest over the past decades. In catalysis,[1,2] $CeO_2$ serves as a widely used support material and as such helps to improve mechanical and thermal stability as well as activity and selectivity of catalysts. These catalysts may be either one of the late transition metals, like Pd, Rh, Pt, etc., or a transition metal oxide (V, Mn, or Cu). Technologically, ceria is relevant in treatment of toxic emissions, for removal of soot from diesel engine exhaust, for removal of organics in wastewater, as an additive for combustion catalysts, and in redox and electrochemical reactions and last but not least represents an integral part of car exhaust catalysts. Moreover, due to its relatively high oxygen ion conductivity at intermediate temperatures (800–1100 K), ceria is an interesting material as an electrolyte in solid oxide fuel cells.[1] This widespread applicability mainly originates from the outstanding oxygen storage capacity of ceria, i.e., its ability to repeatedly pass through redox cycles rapidly. This is

Special Issue: 2013 Surface Chemistry of Oxides

Received: December 14, 2012
Published: May 7, 2013

   dx.doi.org/10.1021/cr3004949 | Chem. Rev. 2013, 113, 3949–3985

causally related to the ease in forming and repairing oxygen vacancies at the surface of solid ceria.

Much effort has been spent to study the role of ceria in well-established industrial processes such as fluid catalytic cracking and processes occurring in three-way automotive catalysts. Ceria-based oxides have become very interesting candidates for $H_2$ production within a two-step water-splitting redox reaction (see, e.g., ref 3). Remarkably, this material not only serves as a "driving component" in redox chemistry but may also play a role in acid−base chemistry due to OH groups on the surface. Note that the OH groups are of basic character, but due to $Ce^{4+}$ ions, both Brønsted as well as Lewis type sites occur.[1]

The recent review by Gorte[2] represents a valuable source of technologically relevant experimental results on ceria. As far as computational studies are concerned, we start from the review by Ganduglia-Pirovano, Hofmann, and Sauer,[4] hereafter abbreviated GHS, which discusses oxygen vacancies in transition metal and rare earth oxides, specifically vanadia, titania, zirconia, and ceria. In another recent account of potential problems related to electronic structure theory applied to transition metal oxides, Pacchioni underlines the strengths of Kohn−Sham and hybrid density functional theory (DFT) in terms of computed materials properties but also emphasizes the notorious problem of DFT related to electron and, hence, spin localization.[5] The review articles of Kilner and Shoko and others amply discuss theoretical modeling of the conductivity and transport phenomena in ceria.[6,7]

Prerequisite to the design of ceria-based materials, in general, and catalysts and catalytic processes with improved activity, in particular, is an atomistic understanding of the catalyst structure and of the elementary catalytic steps. Whereas this information is needed for the "material in action", i.e., the working catalyst under realistic conditions, the complexity of the problem requires an approach that departs from characterization of well-defined surfaces with surface science techniques, often under ultra-high-vacuum (UHV) conditions. Theory and computational simulation techniques have become an integral part of this approach. Not only do computational techniques help to assign spectroscopic signals (IR, NMR) and topographic images (STM) to specific atomic structures, they also help to bridge the 'materials gap' between single-crystal studies and real powder catalysts and the 'pressure gap' between UHV conditions and the pressure in a reactor. This together with advances in theoretical methods and the impressive progress in computational technology induced a boost in computational studies of the surface chemistry of ceria over the past decade, often in close collaboration with experiments.

Here, we will review theoretical studies of the surface chemistry of ceria of the past decade. Experimental studies will only be mentioned if there is a direct relation to a computational study. We will focus on the redox properties and oxygen-defect formation, because they are essential toward a detailed understanding of the reactivity of ceria-based systems. Oxygen-defect formation is accompanied by localization of the electrons left behind in Ce 4f states, leading to formation of two $Ce^{3+}$ ions. For a long time common opinion has been that Ce cations in the nearest neighbor position to the oxygen defect become reduced. Recent computations related to the site preference of $Ce^{3+}$ upon oxygen removal generated firm evidence that the $Ce^{3+}$ resulting from formation of an oxygen vacancy is located at sites farther away from the vacancy position.[8−10]

In insulating rare earth oxides, accurately accounting for the oxygen-defect formation computationally represents a formidable task. Any electronic structure method of value has to be able to localize the electrons left upon oxygen removal. Therefore, we devote the first section to the methods that have been (or should be) applied. The following section focuses on oxygen-defect formation as well as the reducibility of ceria surfaces. Subsequent sections are topically organized discussing the interaction of polar molecules (section 4), ceria as a support for other oxides (section 5), ceria as a support for metals (section 6), some selected ceria-based catalysts, and catalytic reactions (section 7). Conclusions are drawn in section 8.

## 2. METHODS AND COMPUTATIONAL APPROACHES

We focus on quantum mechanical methods and consider both wave-function-based techniques and density functional theory (DFT). Parameterized force fields, which benefit from low computational cost but suffer from limited transferability among different systems, will not be discussed. We mention just one study on ceria nanoclusters,[11] which reports good agreement between DFT and interionic potential functions for the energy ordering of different isomers and trends in the atomic structure.

### 2.1. Modeling the Solid State

**2.1.1. Periodic Boundary Conditions.** Making use of the translational symmetry of infinite crystalline solids, Born−von-Karmán periodic boundary conditions (PBC)[12] capture the bulk properties by performing simulations on a single (primitive) unit cell but for different points in reciprocal space. For PBC computations of the electronic and geometric structure, plane-wave basis sets in conjunction with effective core potentials or pseudopotentials are the most natural choice. Working in reciprocal or momentum space, use is made of highly optimized and efficient fast Fourier transform (FFT) techniques, see ref 13 and references therein. The basis set quality is controlled by one parameter, the kinetic energy cutoff, but for a given cutoff the number of plane waves depends on the size of the simulation cell. Differently from basis sets of atom-centered functions, there is no basis set superposition error (BSSE) in plane wave calculations. However, the BSSE is generally smaller for Kohn−Sham (KS) DFT[14] than for techniques using correlated wave functions, see below.

When employing PBC for systems that are not periodic in all three dimensions, e.g., molecules, clusters, defects in solids, polymer chains, or crystalline surfaces, rather large supercells are required to minimize spurious image−image interactions. The system of interest, which is aperiodic in at least one spatial direction (e.g., a slab of a surface), is still treated as translation symmetric in all three spatial dimensions. The corresponding unit cell of a surface is built such that some extra empty space separates the periodic replicas along the directions in which the system is considered as finite.

Charged systems are notoriously problematic in PBC computations due to a divergent electrostatic energy. Conventionally, a charge-neutrality condition is imposed, which implicitly introduces an artificial homogeneous and oppositely charged ("jellium") background.[15,16] Computation of, e.g., bulk defect formation energies in the dilute limit are computationally demanding because large unit cells are required, and the true limit remains practically inaccessible. Recently, Hellman et al. suggested a promising approach to simulate the dilute defect limit via depopulation of defect states in the band gap.[17]


dx.doi.org/10.1021/cr3004949 | Chem. Rev. 2013, 113, 3949−3985

Table 1. Lattice Parameters (pm) and Energies (kJ/mol) of Formation for $CeO_2$ and $Ce_2O_3$ and Energies of Reduction (eqs 2.1 and 2.2) Obtained with Different Methods[53,71,80]

| | $Ce_2O_3$ | | | $CeO_2$ | | eq 2.1 | eq 2.2 | |
|---|---|---|---|---|---|---|---|---|
| | $a_0$ | $c_0$ | $\Delta E_f$ | $a_0$ | $\Delta E_f$ | $\Delta_r E$ | $\Delta_r E$ | ref |
| obsd | 389 | 606 | −1793 | 540.6[a] | −1090 | 388[b] | 149[c] | |
| obsd | | | | 541.1[d] | | | | |
| HSE/pw+D | 385 | 608 | −1850 | 539 | −1089 | 327 | 75 | 80 |
| PBE0/pw+D | 386 | 607 | −1873 | 539 | −1100 | 327 | 75 | 80 |
| HSE/pw | 387 | 608 | −1819 | 540 | −1061 | 305 | 53 | 53 |
| PBE0/pw | 387 | 607 | −1850 | 539 | −1076 | 303 | 51 | 53 |
| PBE0/GTO | 386 | 604 | | 540 | | 353 | | 71 |
| B3LYP/GTO | 389 | 617 | | 547 | | 340 | | 71 |
| PBE+$U$(4.5)/pw | 392 | 618 | −1435[e] | 549 | −834[e] | 221 | −20 | 53 |
| PBE/pw[f] | 383 | 608 | −1573 | 547 | −988 | 403 | 162 | 53 |
| PBE/pw[g] | 385 | 604 | −1589 | 547 | −999 | 409 | 168 | 53 |

[a]Reference 81. [b]Zero-point vibrational energy and thermal contributions to the heats of formation are very small (2.1 and 1.4 kJ/mol for $CeO_2$ and $Ce_2O_3$, respectively) and even smaller for reaction 2.1 (0.8 kJ/mol). Therefore, we use $\Delta E_{f,r} \approx \Delta H_{f,r}^0$ (values from Table 2). [c]Experimental formation enthalpy of water at 0 K (−239 kJ/mol) has been taken from the literature.[82] [d]Reference 63. [e]Reference 80. Since GGA+$U$ yields only the less stable $\gamma$ phase of cerium, the energy difference between $\alpha$ and $\gamma$ phase (−3 kJ/mol) has been added to the heats of formation. [f]PAW ansatz to describe the electron−ion interaction using plane waves. [g]LAPW+LO ansatz to describe the electron−ion interaction using plane waves, which can be considered as the benchmark method in the solid-state community. Both, PAW and LAPW are so-called full-potential methods.

**2.1.2. Embedded Cluster Methods.** The alternative strategy of treating local features in extended systems limits treatment to finite size models (cluster models) of the chemically interesting subsystem (defect, reaction site) that is embedded into the "chemically innocent" bulk part.[18−21] Among the different approaches, electrostatic embedding, based on a periodic array of point charges,[22] is the most straightforward way which, in the case of ionic solids, only requires a plausible choice of point charges. To avoid spilling out of electron density, the quantum mechanically treated ions are surrounded by a shell of full-ion effective core or pseudopotentials, see, e.g., ref 22. For ceria-based systems, the embedded cluster approach[23−25] also enables application of computationally more demanding wave-function-based methods,[23,26] e.g., Møller−Plesset (MP) perturbation theory and coupled-cluster (CC) methods, or of molecular dynamics simulations.[27]

## 2.2. Solving for the Electronic Structure

**2.2.1. Wave Function-Based Techniques.** There are very few applications of wave-function-based techniques like HF, MP2, or CC methods to cluster models of bulk ceria or ceria surfaces. Early calculations on bulk and surface properties have been performed by Catlow and co-workers using HF within a local, atom-centered basis implementation.[28a] Voloshina and Paulus performed CCSD and CCSD(T) calculations on embedded $Ce_4O_7$ clusters and compared the lattice constant as well as the atomization energy of the $CeO_2$ bulk phase with GGA.[28b] They found that CCSD overestimates the experimental lattice constant (not corrected for zero-point anharmonic expansion effects) by less than 1%, whereas the bulk modulus, which was evaluated at the experimental lattice constant, overshoots experiment by approximately 8%. The latter studies employed electrostatic embedding of the cerium oxide clusters together with the method of increments to calculate the correlation energy. For the studies devoted to adsorption of CO and $N_2O$ on the (111) and (110) surfaces of ceria, we refer to section 4 of this work.[24−26,29]

**2.2.2. Density Functional Theory.** Most frequently applied to extended systems is Kohn−Sham density functional theory (KS-DFT)[30,31] because the results are reasonably accurate and calculations can be done at moderate computational cost. However, assuming convergence of the technical parameters such as basis set expansion of the orbitals, number of k points, the accuracy is determined by the chosen exchange-correlation (xc) energy functional.

Whereas the local density approximation (LDA)[31] suffers from unacceptably large errors for molecular binding energies, drastic improvements are achieved with functionals based on the generalized-gradient approximations (GGA), see, e.g., refs 32, 33, and 34. Hybrid Hartree−Fock(HF)/DFT functionals[35] include a varying fraction of the *nonlocal* orbital-dependent Fock exchange. They are also known as *generalized* KS-DFT functionals.[33] For more detailed discussions, including applications of hybrid functionals to solids, we refer the reader to available review articles.[36−41]

Explicit dispersion-type interaction terms are missing in conventional xc functionals. Whereas some short-range dispersion may be effectively included, long-range dispersion-type interactions are not properly captured by conventional KS-DFT due to the exponential decay of the electron density and, hence, xc potential. Over the years it has become well established that dispersion may be important for solid state and adsorption problems.[42−44] Conesa pointed out the important role of dispersion for the relative stability of different polymorphs of oxides.[45] He showed that the reversed stability of the $TiO_2$ phases rutile and anatase obtained using GGA (a longstanding issue) is repaired upon inclusion of dispersion effects. This remarkable finding suggests that dispersion effects may influence other properties such as oxygen-defect formation energies in reducible oxides.

Principally, two different approaches are currently pursued by functional developers: (i) addition of a $C_6/R^6$ dispersion term evaluated as a sum over atom-pair contributions to the KS-DFT energy (see, e.g., refs 46 and 47) or (ii) evaluation of correlation energy contributions within the so-called random-phase approximation (RPA).[48] The first approach has been followed for calculation of dispersion-corrected hybrid results shown in Table 1. Whereas approach (i) offers a de facto zero additional cost strategy (compared to the DFT self-consistent field calculation), (ii) induces a significantly larger computa-


dx.doi.org/10.1021/cr3004949 | Chem. Rev. 2013, 113, 3949−3985

tional workload. However, applications to surface science problems appear to be feasible by recent implementations.[49−52]

The shortcomings of approximate xc functionals mentioned above become obvious when modeling, e.g., complex materials such as the defective bulk phase of ceria or defective ceria surfaces using KS-DFT (see also ref 4). Ceria with all cerium ions in oxidation state +4 and, thus, having all 4f orbitals empty does not represent a serious problem for semilocal functionals aiming, e.g., at the equilibrium lattice constant or the density of states, see, e.g., ref 53. The problem sets in when $Ce^{4+}$ is reduced to $Ce^{3+}$, and as a consequence, atom-like rather localized 4f orbitals become populated with electrons. This happens, e.g., upon formation of oxygen defects. The problems are due to the self-interaction error (SIE)[54] intrinsic to semilocal functionals. Whereas in HF theory the 'self-interaction Coulomb term' is exactly canceled by the analogous self-exchange term, in DFT this cancellation is incomplete due to the approximate gradient-corrected exchange interaction. The SIE tends to overdelocalize electrons.[55] It is also responsible for systematic underestimation of energy barriers for chemical reactions,[56] which is also observed in surface reactions, see, e.g., ref 57.

In the case of the oxygen monovacancy formation in ceria, SIE prevents the electrons left behind to localize on two cerium atoms, i.e., they do not populate Ce 4f states with integer occupation. Instead, the spin density is spread out leading to fractional occupation of 4f states on in fact all cerium atoms (see also Figure 3 a). Furthermore, due to the spurious self-interaction, band gaps obtained using GGA may be underestimated by approximately 50%, which sometimes even leads to an artificial metallization of semiconductors (cf. ref 33 and references therein). This error conveys into an underestimation of the energetic cost to occupy conduction bands, which in turn sullies the energy cost for removing an oxygen atom, i.e., it artificially lowers the defect formation energy, see, e.g., refs 4 or 58.

For total energy calculations on complex transition metal and rare earth compounds, two remedies to the aforementioned shortcomings exist: (i) DFT corrected for on-site Coulomb correlation effects by a Hubbard-type $U$ term, known as the DFT+$U$ approach,[59,60] and (ii) hybrid functionals, which add a certain fraction[35,61] of the Fock exchange energy to the remainder of (gradient-corrected) DFT exchange energy. For completeness, we mention the self-interaction correction (SIC) scheme for GGA functionals after Perdew and Zunger,[54] but only a few applications of this SIC scheme to ceria have appeared to date.[62,63]

Many workers assessed the strengths and weaknesses of approaches (i) and (ii).[53,64−72] They all caution against nonuniversality of the DFT+$U$ approach, i.e., the rather strong dependence of band gap, lattice constant, etc., on the value of $U$. For example, calculated oxygen-defect formation energies depend on the $U$ parameter employed. Whereas Huang and Fabris find that $U$ = 2 eV is required to obtain the adsorption energy for CO at ceria that is comparable to experiment,[73] consistent description of the electronic structure of ceria needs a $U$ between 4.5 and 6 eV.[53,58,64,67,74,75] As will be demonstrated in section 3.4, where defect formation energies in low-index ceria surfaces will be discussed, ambiguities in total energies obtained using DFT+$U$ have to be considered, because numerical results may strongly depend on actual implementation of the required projector functions (see also ref 76). This would be a minor issue if *relative* energies or trends in energies were unaffected, but we will discuss examples showing that quantitative changes may be non-negligible. Concerning the diversity of implementations of the DFT+$U$ approach, we note that most DFT+U results discussed in this work are based on the rotationally invariant approach after Dudarev et al. employing a $U$ parameter that effectively takes care of both the on-site Coulomb repulsion and the exchange effects.[77]

Another warning example is the work of Branda et al.,[78] who found that the oxidation state of Au on $CeO_2(111)$ critically depends on the value chosen for $U$ and that changes in the total energy upon changing the oxidation state of Au are on the order of only several 10 meV (∼1 kJ/mol) for both DFT+$U$ as well as hybrid functionals. Watson and co-workers showed that application of a $U$ for oxygen 2p states is mandatory to effectively correct for their self-interaction error, which favors a proper localization of oxygen hole states.[79] Sanz and co-workers applied $U$ parameters to both Ce 4f and O 2p states and achieved moderate improvements of lattice constants, band gaps, and formation and reduction energies for $CeO_2$ and $Ce_2O_3$.[69]

Recently, Sanz and co-workers[71] examined the performance of various hybrid functionals for the difficult case of ceria. Their study aims at a balanced description of materials properties of ceria such as cell parameters, band gaps, and reaction energies (cf. Table 1). Specifically, it considers reaction energies for reduction of $CeO_2$ to $Ce_2O_3$, releasing molecular oxygen

$$2CeO_2 \rightarrow Ce_2O_3 + \frac{1}{2}O_2 \tag{2.1}$$

The accurate thermochemical description of reaction 2.1 is of particular interest not only because it is part of many oxidation reactions that use $CeO_2$, e.g., oxidation of CO to $CO_2$, but also because it involves the cerium oxidation states +4 and +3. Recall that formation of one or several oxygen vacancies at a ceria surface also involves the $Ce^{4+}/Ce^{3+}$ redox couple. Thus, the heat of reaction of eq 2.1 is related to the oxygen vacancy formation and most likely represents an upper bound to it. Alternatively, reduction of $CeO_2$ can also be achieved by hydrogenation according to

$$2CeO_2 + H_2 \rightarrow Ce_2O_3 + H_2O \tag{2.2}$$

Following this equation, errors incurred by an inaccurate DFT description of $O_2$ are bypassed. Table 2 presents observed heats of formation of $Ce_2O_3$ and $CeO_2$ as well as the enthalpy of reduction corresponding to eqs 2.1 and 2.2. Gibbs free energy values are also given.

Five hybrid density functionals have been applied to the $CeO_2$ and $Ce_2O_3$ bulk phases:[71] Becke's half and half functional (BHLYP),[88] PBE0,[89] B3LYP,[90] and the recently introduced B1-WC hybrid functional. The latter uses the modified gradient-

**Table 2. Observed Heats of Formation of $Ce_2O_3$ and $CeO_2$, $\Delta H_f^\circ$, and Reduction Enthalpies, $\Delta H_r^0$ (eq 2.1), at $T$ = 298 K**

| $-\Delta H_f^\circ$ | | | | |
|---|---|---|---|---|
| $CeO_2$ | $Ce_2O_3$ | $\Delta H_r^\circ$ | $T$/K | ref |
| 1090.4[a] | 1792.4 | 388.4[b] | 298 | 2006, Zinkevich et al.[83] |
| 1089 (1025)[c] | 1796 (1708)[c] | 382 (344)[c] | 298 | 2002, Trovarelli[84,85] |
| 1088.7 | 1796.2 | 381.2[b] | 298 | 1993, Lide[86] |

[a]Reference 87., cf. ref 83. [b]Calculated from heats of formation. [c]In parentheses $-\Delta G^\circ$ values.


dx.doi.org/10.1021/cr3004949 | Chem. Rev. 2013, 113, 3949−3985

corrected exchange functional of Wu and Cohen (WC).[91] Remarkably, all of them predict much improved structural parameters compared to GGA, i.e., errors are smaller than 2−3%. For lattice parameters, the PBE0 functional performs best.

Band gaps, specifically the O(2p)−Ce(5d) as well as the O(2p)−Ce(4f) gap in $CeO_2$ and the Ce(4f)−Ce(5d) gap in $Ce_2O_3$, have also been calculated and compared to experiment. In addition, the amount of Fock exchange has been systematically varied to study the dependence of the gap on the percentage of Fock exchange added to the remainder of the semilocal exchange energy. Overall, the authors found an overestimation of the three band gaps studied, which diminishes as the amount of Fock exchange in the functional gets smaller. In contrast, the reaction energies studied are underestimated by the hybrid functionals. For the reduction energy (eq 2.1) significant differences are found between PBE0 results obtained with plane wave and GTO basis sets. The GTO result is 50 kJ/mol larger than the plane wave result (see Table 1). A comparison of total energies[92] and calculation of bond dissociation (atomization) energies for the $O_2$ molecule points to the deficiencies of the basis set used for $O_2$ in ref 71. The general experience with GTO calculations is that hybrid functionals are more demanding as far as basis sets are concerned than GGA functionals. Using a high-quality GTO basis set, a quadruple-$\zeta$ valence polarization (QZVP) basis set ("def2" in the Turbomole library),[93] the dissociation energy becomes 43 kJ/mol lower, which compares very well to the observed energy difference of 50 kJ/mol between plane wave and GTO reduction energies for PBE0 in Table 1.

In addition, Table 1 shows lattice parameters, energies of formation for $CeO_2$ and $Ce_2O_3$, and energies of reduction (eq 2.1) obtained with different methods taken from the literature[53,71] and from additional calculations for this review (HSE+D and PBE0+D).[80] In Table 1 and throughout this work we indicate the actual value for the effective $U$ parameter for Ce 4f in eV given in parentheses after the $U$. For instance, PBE +$U$(4.5) means that an effective $U$ parameter of 4.5 eV has been used. Calculated reduction energies can be directly compared with observed enthalpies at 298 K because contributions of zero-point vibrational energies and thermal effects are negligible, see footnote b of Table 1. PBE+$U$(4.5) underestimates the bulk reduction energy of $CeO_2$ by as much as 167 kJ/mol, whereas hybrid functionals yield significantly better results, but still underestimate the experimental values by about 80 kJ/mol. Adding a dispersion term to the hybrid functionals (PBE0+D and HSE+D) improves the reduction energies by about 20 kJ/mol, and the PBE0 and HSE results are both 60 kJ/mol smaller than the experimental value. Utilization of eq 2.2, i.e., adding the energy of formation of water to the reduction energy of ceria, does not improve results compared to $^1/_2O_2$ as reference.

PBE as a conventional GGA functional seems to perform surprisingly well. Reaction energies in Table 1 are only 15−21 and 13−19 kJ/mol larger than the experimental values for reactions 2.1 and 2.2, respectively. This is due to a fortuitous error cancellation that is seen when the energies of formation are considered. Deviations for $Ce_2O_3$ and $CeO_2$ (two formula units as in eq 2.1) are 220 and 204 kJ/mol, respectively, whereas for PBE0 they are −57 and +48 kJ/mol, respectively, and for HSE+D −57 and +2 kJ/mol, respectively. For PBE +$U$(4.5) the errors in the heat of formation are +358 and +512 kJ/mol for $Ce_2O_3$ and $2CeO_2$, respectively. We note that the reference for the heats of formation is the metallic $\alpha$ phase of cerium. There exits also a $\gamma$ phase, which is only 2−3 kJ/mol less stable. Whereas PBE yields the $\alpha$ phase as the only stable phase, hybrid functionals yield both phases but artificially overstabilize the $\gamma$ phase, see ref 94. PBE+$U$ yields only the $\gamma$ phase, and we add −3 kJ mol, i.e., the experimental difference between $\alpha$ and $\gamma$ phase, to the PBE+$U$(4.5) formation energy to obtain the values listed in Table 1.

From a methodological point of view, on one hand it is appealing that the xc potential used in hybrid functionals is consistently applied to all atomic species of a system as well as to all orbitals, contrary to DFT+$U$, where $U$ is applied to orbitals of a certain angular momentum of a particular atomic species only. On the other hand, a hybrid functional, such as, e.g., B3LYP,[90] PBE0,[89,95] or HSE,[96,97] contains parameters that fix the amount of Fock exchange. Results will depend on these parameters, and different problems may require different parameter choices. A typical problem is creation of an electron hole in or addition of an electron to a system in which nearly equivalent sites are available and the hole/electron can either localize (and break the symmetry) or delocalize.[98] Proper description always requires hybrid functionals, but the amount of Fock exchange to achieve even a qualitatively correct description may vary. While for the correct description of the size-dependent localization of the additional electron in vanadium oxide gas-phase clusters the 20% Fock exchange in the B3LYP functional was sufficient,[99] for localization of an electron hole in silicates (an abundant defect) a 50% Fock exchange (BHLYP functional) is required.[100]

Doubtlessly, the biggest hurdle for applications of hybrid functionals to extended systems is the computational workload and resulting computing times involved. In particular, the gain in computational efficiency when using plane wave instead of atom-centered GTO basis sets is lost when passing from GGA functionals to hybrid functionals. Application of hybrid functionals to systems with very small or even vanishing band gaps, i.e., metallic systems,[101,102] is problematic, which is due to the erroneous description of metals by Hartree−Fock, see, e.g., ref 103. Closely related to this issue is the question about performance of hybrid functionals applied to ceria-supported metal nanoparticles. Although to our knowledge computational results still have to be awaited, depending on the gap size of the nanoparticle, the reliability of hybrid functionals may be questionable in this special case.

**Summary.** We conclude that GGA+$U$ (PBE+$U$) provides the proper electron localization but describes energy differences only qualitatively right. Hybrid functionals (HSE) are a better choice, but the high computational cost limits their application to selected problems. With GGA+$U$ the heat of reduction is 1.7 eV too low, whereas hybrid functionals underestimate the heat of reduction by 0.9 eV (Table 1).

**2.2.3. Spin States.** The two electrons left behind on creation of an oxygen vacancy may be ferromagnetically (triplet) or antiferromagnetically (singlet) coupled.[104] Within KS-DFT only the high-spin state can be straightforwardly tackled, while low-spin states require additional approximations such as the broken symmetry approach[105,106] that has become a standard tool in DFT, see, e.g., ref 107. For oxygen vacancies, singlet and triplet states are virtually degenerate; the energy differences are on the order of 0.05 eV.[8,108] To reduce complexity one often starts with high-spin states and checks for low-spin states once the high-spin structures have been obtained. With the presence of transition metal dopants (section 3.7) or other surface species that have open electron


dx.doi.org/10.1021/cr3004949 | Chem. Rev. 2013, 113, 3949−3985

shells (e.g., VO or $VO_2$ in section 5), the number of spins to consider increases. As an extreme case, an energy difference between high-spin and low-spin solutions as large as 0.37 eV has been reported[108] for the oxygen vacancy in the $VO/CeO_2$ system which features five electrons in V-d states and Ce-f states.

When considering surface reactions several spin states may be involved and the reactivity may be different for different spin states. This is a quite general phenomenon with transition metal compounds for which the term "two-state reactivity" has been coined.[109] Then the question appears whether spin is conserved (which some researchers prefer as first approximation) or spin crossing is so easy (large spin−orbit coupling constants) that the system crosses to another potential energy surface whenever it is energetically possible.[110] Since potential energy surfaces are multidimensional objects, determination of minimum energy crossing points requires special algorithms that have become standard tools. At these points the crossing probability may be calculated using the spin−orbit coupling matrix elements.[110] To the authors knowledge, such calculations have not yet been performed for reactions on cerium oxide surfaces.

## 3. STABILITY AND REDUCIBILITY OF CERIA SURFACES (O-DEFECT FORMATION)

The energetic cost to form an oxygen vacancy in ceria is relatively low, and this makes ceria an interesting candidate for an active catalyst in Mars−van Krevelen-type oxidation−reduction reactions[111] or an appropriate electrolyte in solid oxide fuel cells. Recently, Gorte and co-workers discussed factors different to mere "oxygen binding energies", which may also be important for a more profound understanding of catalytic properties of ceria, as, e.g., the actual atomic structure at the catalytic site.[112,113] They pointed out that thermodynamic data cannot answer each and every question on the activity of ceria, but it provides an important starting point for mechanistic reasoning. Having theoretical means at hand, which are able to reliably predict thermodynamic properties such as the stability of various surface terminations or the energy required to form an oxygen defect at a ceria surface, is of value for a rational design of its properties.

Before presenting the more recent theoretical studies on the reducibility of ceria surfaces (section 3.4 in this work, for earlier studies see GHS[4]), we explain how we understand "reducibility" of an oxide (section 3.2) and summarize basic properties of the most important low-index surfaces of ceria (section 3.1) for which most of the calculations are done. This can only be a first step, and more realistic surface models should also include morphological defects such as steps and corners. Section 3.3 discusses available experimental information on surface reducibility. An alternative way to reduce a ceria surface is its hydrogenation, which will be discussed in section 3.5. Section 3.6 sheds some light on defect healing or reoxidation of reduced ceria surfaces via interaction with oxygen. Effects of dopants will be briefly discussed in section 3.7.

### 3.1. Low-Index Surfaces of Ceria

For ceria, surfaces with (111), (110), and (100) orientation are commonly studied, because these are thermodynamically most stable. The surface energies (cf. Table 3) increase following (111) < (110) < (100). A common feature of (111) and (100) is a terminating oxygen layer (topmost or first layer), and Ce atoms are located in a second layer underneath the surface O atoms. At the surface, the respective coordination numbers (CN) of Ce and O atoms are lower than the corresponding CNs in the bulk phase. Bulk $CeO_2$ has a fluorite-type (face-centered cubic) structure, and the Ce and O atoms are 8- and 4-fold coordinated, respectively. Indicative for stability, surface relaxation effects are smallest for the (111) surface but more pronounced for (110) and (100) correlating with the smaller CNs (cf. Table 3).

**Table 3. Basic Information on the Clean Low-Index Ceria Surfaces**

| | 111 | 110 | 100 |
|---|---|---|---|
| first layer, coordination numbers | 3 (O) | 6(Ce), 3(O) | 2(O) |
| second layer | 7 (Ce) | | 6(Ce) |
| surface energy ($J/m^2$), calcd HSE[116] | 0.81 | 0.91 | |
| surface energy ($J/m^2$), calcd PBE0[118] | 0.73 | 0.81 | |
| surface energy ($J/m^2$), calcd PW91[114,116] | 0.68 | 1.05 | 1.41 |
| relaxation energy ($J/m^2$) | 0.01 | 0.20 | 0.65 |
| relaxation Ce (pm) | 1 | −25 | |
| relaxation O (pm) | 3[a] | −8 | |
| surface energy ($J/m^2$), calcd PW91+$U$(5)[74] | 0.68 | 1.01 | 1.41 |
| relaxation energy ($J/m^2$) | 0.01 | 0.25 | 0.64 |
| surface energy ($J/m^2$), calcd PW91+$U$(5)[119] | 0.64 | 1.39 | 1.65 |
| relaxation energy ($J/m^2$) | 0.04 | 0.24 | 0.74 |

[a]Relaxation effects are maximal for the third O layer (compared to bulk position). Positive sign indicates outward relaxation; negative sign indicates inward relaxation.

Skorodumova et al.[114] employed the (GGA-type) PW91 functional to study geometric structure and stability as well as density of states (DOS) of the clean (111), (110), and (100) low-index surfaces. Later, their results were confirmed by Yang et al.[115] (PW91) and Nolan et al.[74] (PW91+$U$(5)). However, the HSE hybrid functional predicts a smaller energy difference between (111) and (110) surface energies.[116] Fronzi et al. applied the PBE functional to study stabilities and morphologies of various $CeO_2$ surface terminations in terms of the surface free energy.[117] One has to keep in mind that the problems like, e.g., overdelocalization and metallization incurred by the SIE inherent to any GGA functional most likely bias results obtained for reduced and metal-terminated surfaces. For the latter a reconstruction into a $Ce_2O_3(0001)$-like surface was observed by the aforementioned authors.

### 3.2. How to Define Reducibility?

We ask two questions: what is reducibility and when is an oxide material considered to be easily reducible? Certainly, a clear-cut definition is not possible since thermodynamically any oxide is reduced, i.e., oxygen defects will be created, at low enough oxygen partial pressures and high enough temperatures. For some oxides, oxygen defects can be formed under mild conditions. For these materials, required temperatures are moderate and pressures are technically accessible by virtue of appropriate vacuum techniques.

To illustrate, we calculated oxygen-defect formation energies using DFT for two so-called "reducible" oxides, specifically for the surface oxygen defect at $CeO_2(111)$ and the bridging oxygen defect at $TiO_2(110)$ and for two "non-reducible oxides", namely, $Al_2O_3(0001)$ and MgO(001). Calculations have been performed for defect concentrations ($\Theta$) of $^1/_4$ for $CeO_2(111)$, $^1/_2$ for $TiO_2(110)$, $^1/_3$ for $Al_2O_3(0001)$, and $^1/_2$ for MgO, and


dx.doi.org/10.1021/cr3004949 | Chem. Rev. 2013, 113, 3949−3985

defect formation energies of 1.8, 3.2, 5.6, and 6.2 eV, respectively, were obtained.

Starting from these energies, it is readily possible to calculate phase diagrams by statistical thermodynamics (for early applications to surface problems, see, e.g., refs 120−123). For the O defect formation reaction

$$\text{Surf} \rightarrow \text{Surf}{-}V_O + \frac{1}{2}O_2 \tag{3.1}$$

the Gibbs free reaction energy equals

$$\Delta G_d(\frac{1}{2}O_2) = -G(\text{Surf}) + G(\text{Surf}{-}V_O) + \frac{1}{2}G(O_2) \tag{3.2}$$

Applying total energies for the oxides instead of Gibbs free energies corresponds to neglecting finite temperature and pressure effects and was shown to be a valid approximation, see footnote b of Table 1 and ref 124. Starting out from

$$\frac{1}{2}G(O_2) = \frac{1}{2}E(O_2) + \Delta\mu(O) \tag{3.3}$$

one obtains

$$\Delta G_d(\frac{1}{2}O_2) = \Delta E_d(\frac{1}{2}O_2) + \Delta\mu(O) \tag{3.4}$$

with

$$\Delta E_d(\frac{1}{2}O_2) = -E(\text{Surf}) + E(\text{Surf}{-}V_O) + \frac{1}{2}E(O_2) \tag{3.5}$$

For the stoichiometric and reduced oxide in equilibrium, $\Delta G_d(^1/_2O_2) = 0$, hence

$$\Delta\mu(O) = -\Delta E_d(\frac{1}{2}O_2)$$

i.e., the change in the oxygen chemical potential is equal to the negative oxygen-defect formation energy.

We use DFT for calculating the defect formation energies but rely on experimental values[82] for enthalpy and entropy changes of $\Delta\mu(O)$ for a given temperature $T$ and pressure $p$, according to

$$\Delta\mu(O) = \frac{1}{2}[H(T, p^\circ) - H(0K, p^\circ) - TS(T, p^\circ) + RT\cdot\ln(p/p^\circ)] \tag{3.6}$$

Problems related to the fact that the calculated energy of the oxygen molecule enters $\Delta E_d(^1/_2O_2)$ will be discussed later.

Figure 1 shows the phase-separating equilibrium conditions (black lines) as a function of $O_2$ partial pressure and temperature for the pristine and defective oxide surfaces. (The O particle reservoir is in equilibrium with $O_2$ assuming an ideal gas.) These lines indicate the zero value for the Gibbs free (surface) energy change of eq 3.1 ($V_O$ indicates the oxygen vacancy). Decreasing the pressure at a given temperature (moving downwards parallel to the ordinate axis in Figure 1) or increasing the temperature at a given pressure (moving from left to right in the figure) shifts the equilibrium of eq 3.1 from left to right. To avoid the large error in the total energy for the O atom incurred by DFT, vacancy formation energies are commonly computed referring to one-half of the energy of the $O_2$ molecule. Throughout this work the O-defect formation energy calculated this way is denoted $\Delta E_d(^1/_2O_2)$. Still, the deviation of the PBE $O_2$ dissociation energy from experiment is

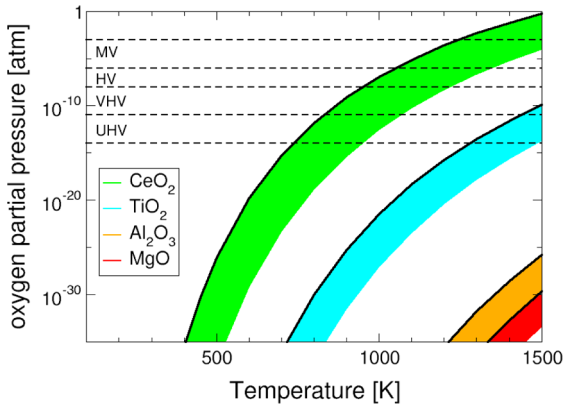


**Figure 1.** $p(O_2)$ vs $T$ (atm vs K) phase diagram showing transition curves for pristine and defective surfaces in thermodynamic equilibrium. Two oxide surfaces considered as "reducible", $CeO_2(111)$ (green) and $TiO_2(110)$ (blue), as well as two systems considered as "non-reducible", $Al_2O_3(0001)$ (orange) and MgO(001) (red), are depicted. Graph is based on PBE+$U$(4.5) calculations for $CeO_2(111)$ and PBE calculations for $TiO_2(110)$, $Al_2O_3(0001)$, and MgO(001) surfaces. Range of the respective colored areas is defined by the error in the $O_2$ molecule incurred by the PBE xc functional (about 1 eV with respect to experiment). Dashed horizontal lines indicate, as a guide to the eye, various vacuum pressures commonly applied in surface science experiments.

on the order of +1 eV (+96 kJ/mol), i.e., the $O_2$ molecule is predicted to be too stable compared to two individual O atoms. As a consequence, the surface defect is artificially stabilized relative to the clean surface. To give an estimate for this error, the black lines in Figure 1 are bounded defined by the experimental $O_2$ dissociation energy (green area). Similarly, blue, orange, and red areas refer to analogous equilibria for $TiO_2(110)$, $Al_2O_3(0001)$, and MgO(001), respectively.

Clearly, Figure 1 confirms that the $CeO_2(111)$ and $TiO_2(110)$ surfaces may be considered as easily *reducible*. For these surfaces, defect formation is thermodynamically favored at technically accessible oxygen partial pressures. In contrast, $Al_2O_3(0001)$ and MgO(001) (cf. Figure 1, orange and red areas) are considered as *nonreducible* oxides. In Figure 1 calculations use a $U$ parameter for ceria only, because in O-defective titania electrons localize properly at Ti sites using the PBE functional, see also GHS.[4] According to Figure 1, the error in the $O_2$ binding energy is apparent and incurs deviations in the oxygen partial pressure of a few orders of magnitude. However, the qualitative picture is not changed, i.e., one can clearly discriminate between reducible and nonreducible oxides. As discussed in later sections (see, e.g., section 6), complex problems such as adsorption of metal atoms on ceria surfaces may suffer from inaccuracies incurred by the approximations within DFT or DFT+$U$, and thermochemical results may be even qualitatively incorrect.

This review puts emphasis on the thermodynamic point of view, but we are well aware that kinetic phenomena may also play a role. Hence, in experimental studies even of reducible oxides, defects are frequently generated by special means such as electron bombardment, see, e.g., ref 10.

Regarding the electronic structure, reducible oxides could also be defined as oxides with low-lying empty electronic states, which accommodate the two electrons that are left behind when an O atom leaves the ionic material. For $CeO_2$ these are the Ce 4f states, and transition metal oxides such as $TiO_2$ or


dx.doi.org/10.1021/cr3004949 | Chem. Rev. 2013, 113, 3949−3985

Table 4. Heats of O-Defect Formation, $\Delta H_d°(^1/_2O_2)$, from Different sources

| | T/K | kJ/mol | eV | ref |
|---|---|---|---|---|
| crystalline $CeO_2$ | 1150−1400 | 321[a] | 3.33[a] | 1971, Steele[125] |
| conductivity, oxygen diffusion[b] | | 323 ± 45[b] | 3.35 ± 0.47[b] | |
| nonstoichiometric $CeO_{2-x}$ Conductivity, electronic | 1100 | 418 ± 33[c] | 4.34 ± 0.33[c] | 1993, Panhans[130] |
| coulometric titration | 873−973 | 387 ± 13 | 4.02 ± 0.13 | 2010, Gorte[2] |

[a]See p 67 of ref 125. [b]Adopting values between 17.4 ± 1.9 and 21.3 ± 0.6 kcal/mol for oxygen vacancy migration barriers and values between 48.5 and 50.7 kcal/mol for activation energies for conductivity; see Table 1 and p 64 of ref 125, respectively. [c]Assuming a polaron hopping barrier of 0.40 eV.[131]

$V_2O_5$[4] have 3d states available. On the contrary, so-called excess electrons in simple metal oxides (MgO, $Al_2O_3$) localize in the vacancy and are stabilized by electrostatic effects only.

### 3.3. Available Experimental Data

**3.3.1. Energies.** Experimental energies for O-vacancy formation according to

$$[2Ce^{4+}, O^{2-}] \rightarrow [2Ce^{3+}, V_O] + \frac{1}{2}O_2 \qquad (3.2)$$

with $V_O$ abbreviating the O vacancy are most often derived from conductivity data. However, the temperature dependence of the latter depends on both formation of defects and their migration. The conductivity model applied suggests the following temperature coefficient

$$\frac{2}{5}\Delta H_d\left(\frac{1}{2}O_2\right) + \Delta H^{‡}_{ion}$$

Here, $\Delta H_d(^1/_2O_2)$ is the defect formation energy according to eq 3.2 and $\Delta H^{‡}_{ion}$ is the activation energy for migration of the defect.[125] Note that the prefactor of $^2/_5$ is twice the factor given by Steele and Floyd due to a different reference ($^1/_2O_2$ in our case).

Oxygen diffusion experiments on single crystals[125] yield a migration barrier of 50 ± 16 kJ/mol for $CeO_{1.92}$ and values between 73 ± 8 and 104 ± 15 kJ/mol for defect concentrations below 0.02%. Note that the experimental values are heats of activation for temperatures between 1150 and 1450 K. These results are by and large supported by DFT+$U$ calculations, which yield an energy barrier of 51 kJ/mol for oxygen vacancy migration,[126] whereas earlier DFT calculations[127,128] report values between 44 and 104 kJ/mol depending on the defect concentration. Molecular dynamics simulations based on interatomic potentials found an activation energy of 56 kJ/mol for $CeO_{1.8778}$ (simulation $T$ = 800−2200 K).[129]

From the reported activation energy for conductivity (50.7 kcal/mol)[125] and an average value of 20 kcal/mol for the activation enthalpy for the motion of oxygen ions a defect formation enthalpy of 76.7 kcal/mol is derived by Steele and Floyd, Table 4.[125] If we consider the range of measured values with their error bars mentioned above (Table 1 in ref 125) and the range of activation energies for conductivity mentioned on p 64 of that paper (48.5−50.7 kcal/mol), we obtain 77.3 ± 10.8 kcal/mol. Note that these values also refer to rather high temperatures (1150−1400 K).

In ceria, conductivity is determined not only by ion mobility but also by electronic conduction. Electrons left behind on O-vacancy formation are "self-trapped" at $Ce^{4+}$ sites, forming $Ce^{3+}$ ions, and conductivity is of the "small polaron" type (see, e.g., ref 7). From the temperature dependence of n-type conductivity at fixed $p(O_2)$, Panhans and Blumenthal[130] obtained a temperature coefficient of 2.57 ± 0.33 eV, which according to their model corresponds to

$$\frac{1}{2}\Delta H_d\left(\frac{1}{2}O_2\right) + \Delta H^{‡}_{polaron}$$

The barrier for polaron hopping, $\Delta H^{‡}_{polaron}$, i.e., for electron transfer from one $Ce^{3+}$ ion to a neighboring $Ce^{4+}$ ion, has very recently been calculated by Sanz et al.[132] following earlier work of Deskins et al. on $TiO_2$.[133] A barrier of 0.48 eV was obtained for the bulk, which supports the experimental value of 0.40 eV of Tuller and Nowick[131] but not the value of 0.21 eV[134] cited in ref 130. With a hopping barrier of 0.40 eV, $\Delta H_d(^1/_2O_2)$ = 2(2.57 − 0.40) = 4.34 eV is obtained for the O-vacancy formation energy.

O-defect formation energies derived from ion conductivity measurements by Steele and Floyd[125] are about 1 eV (ca. 100 kJ/mol) lower than the later data, derived from electron conductivity[130] and Coulometric titration.[2] With 418 ± 33 and 387 ± 13 kJ/mol, the latter are also close to the heat of reduction for the bulk oxides, 389 ± 7 kJ/mol (cf Table 2), and we consider them as the more reliable data. Hence, the best estimate from experiment[2,130] is 4.2 ± 0.3 eV (402 ± 28 kJ/mol). However, the true uncertainty may be much larger than indicated by the error bars. Conductivity measurements may be affected by impurities and grain boundary effects, whereas Coulometric titration experiments face problems of establishing equilibrium and measuring very small oxygen partial pressures.

**3.3.2. Structure.** The O-vacancy defect is defined by three points in the structure, the missing oxygen site and the two cerium sites at which the two electrons left behind have localized. Localization of excess electrons in defective ceria films was recently studied by STM/STS in combination with PBE+$U$ calculations (Figure 2).[10] Although the precise sites of the two $Ce^{3+}$ ions could not be revealed, it was shown that both $Ce^{3+}$ ions (Figure 2 c) or at least one (Figure 2 d) are not neighboring the O-vacancy site. Experiments show that defect formation is connected with substantial lattice distortion.[10,135,136] For a surface vacancy Esch et al.[135] found that six $O^{2-}$ ions move outward (8−9 pm) and laterally away from the closest Ce ions, creating dumbbell-shaped pairs (Figure 2 b). These substantial lattice distortions, which are connected with the fact that $Ce^{3+}$ is bigger than $Ce^{4+}$ (see also Table 12), also relate to the space-charge-induced surface stresses discussed by Sheldon and Shenoy.[137]

These relaxation effects are also intimately connected with the localization of the two electrons on two Ce ions. When PBE+$U$(4.5) calculations are performed for the O vacancy with the unrelaxed structure of the clean surface,[8] the two electrons are delocalized over all three (surface defect) or four (subsurface defect) nearest neighbor Ce ions.


dx.doi.org/10.1021/cr3004949 | Chem. Rev. 2013, 113, 3949−3985

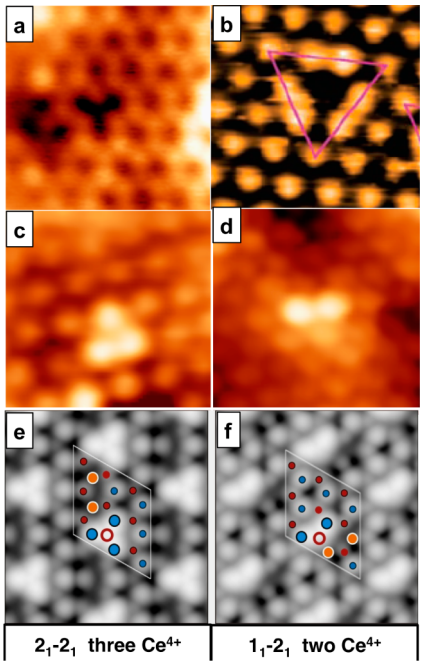


**Figure 2.** STM images of O vacancies on the $CeO_2(111)$ surface. (a and b) Images of the O sublattice from refs 10 and 135, respectively. (c and d) Images of the Ce sublattice (ref 10) with three and two $Ce^{4+}$ ions surrounding the defect site. Simulations by PBE+$U$(4.5) (e and f, respectively) show that $Ce^{4+}$ appears bright (blue, filled circles), whereas $Ce^{3+}$ appears dark (orange, filled circles).[10] (b) Reprinted with permission from ref 135. Copyright 2005 American Association for the Advancement of Science.

### 3.4. Calculations of O-Defect Formation Energies

We focus on the formation energies of a single O defect at the $CeO_2(111)$ surface. Figure 3 illustrates some of the problems related to the GGA approximation. For an O surface vacancy, Figure 3a shows a totally delocalized spin density, characteristic of a metallized defective surface. However, when a hybrid functional like HSE is applied the self-interaction error, which overdelocalizes the electrons, is sufficiently reduced and the electrons occupy two Ce 4f states close to the vacancy (see Figure 3c and 3d). Importantly, the energy gap between occupied O 2p and unoccupied Ce 4f states for the clean surface is significantly larger applying HSE instead of PBE, which in turn conveys into larger O-defect formation energies (see Tables 5 and 6).

**3.4.1. Location and configuration of Defects.** DFT+$U$ is the most frequently applied electronic structure method when periodically repeated slab models together with plane wave basis sets are used. Its computational workload is de facto identical to KS-DFT using a conventional GGA. Table 5 compiles defect formation energies obtained using PBE+$U$ (plane wave basis sets) for oxygen atoms in the surface layer and varying sites of the two $Ce^{3+}$ ions. For a long time it has been believed that these $Ce^{3+}$ ions are located in nearest neighbor positions to the defect site. Ganduglia-Pirovano, Da Silva, and Sauer[8] and Li et al.[9] have independently shown that this is not the case. Within a range of a few tenths of electronvolts, i.e., very similar stabilities, there are multiple configurations of the two $Ce^{3+}$ ions with respect to the coordination shell around the defect site and the layer of ions counted from the surface. For example, "$1_1-3_1$" in Table 5 means that both $Ce^{3+}$ ions are located in the surface layer. Furthermore, one is sitting in the first coordination shell and the second one in the third shell. Later, in conjunction with

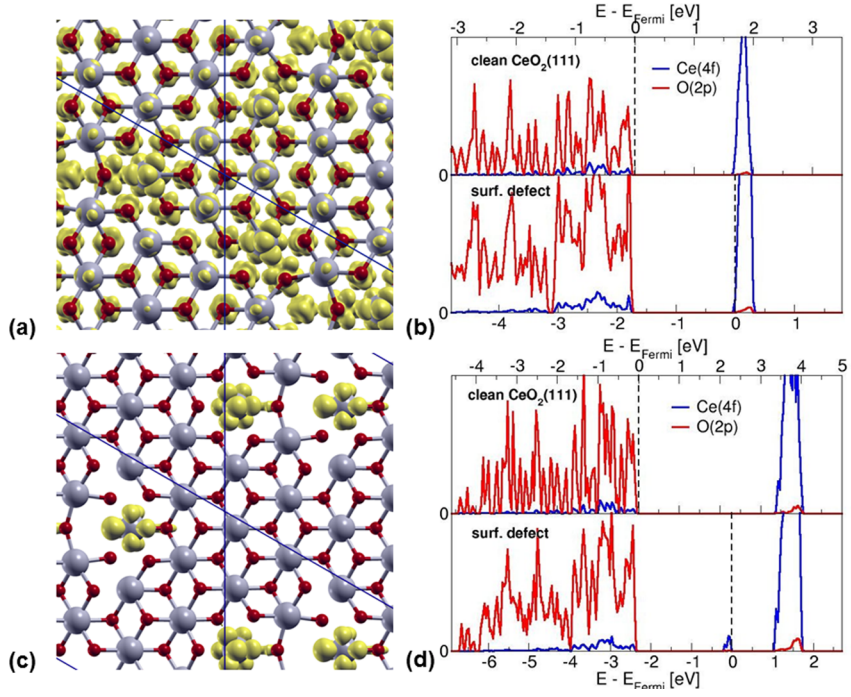


**Figure 3.** (a) Spin density (yellow) for a surface oxygen vacancy in $CeO_2(111)$ obtained using PBE. (b) Corresponding projected electronic DOS for the clean surface (top panel) and oxygen vacancy (bottom panel) obtained using PBE. Blue lines indicate Ce 4f states, and red lines indicate O 2p states. Note that the system is metallic, i.e., Ce 4f states slightly below the Fermi level become occupied. (c and d) Analogous graphs for the spin density as well as projected DOS obtained using the hybrid functional HSE. Surfaces have been rendered using the XCrySDen program.[138]


dx.doi.org/10.1021/cr3004949 | Chem. Rev. 2013, 113, 3949−3985

**Table 5. Formation Energies, $\Delta E_d(^1/_2O_2)$, for Oxygen Defects in the $CeO_2(111)$ Surface Layer Obtained with PBE+$U$ for Different Defect Configurations; Distance between the Two $Ce^{3+}$ Ions and between Each of the $Ce^{3+}$ ions and the Vacancy Site $V_O$, Their Coordination Numbers, CN, and Splitting of the Two Occupied f States (energies in eV, distances in pm)**

| | $p(4\times4)^b$ | $p(3\times4)^c$ | $p(3\times3)^d$ | | | | |
|---|---|---|---|---|---|---|---|
| $Ce^{3+}$ positions[a] | $\Delta E_d(^1/_2O_2)$ | $\Delta E_d(^1/_2O_2)$ | $\Delta E_d(^1/_2O_2)$ | $Ce^{3+}$– $Ce^{3+}$ | $Ce^{3+}$–$V_O$ | CN | f splitting |
| $2_1$–$2_1$ | 1.76 | 2.13 | 2.06 | 391 | 452; 452 | 7; 7 | 0.00 |
| $1_1$–$2_1$ | 1.86 | 2.20 | 2.16[e] | 390 | 254; 453 | 6; 7 | 0.05 |
| $1_1$–$1_1$ | 2.01[d] | 2.31 | 2.22[e] | 417 | 254; 254 | 6; 6 | 0.00 |
| $1_1$–$3_1$ | 2.15 | 2.46 | 2.28 | 374 | 254; 595 | 6; 7 | 0.10 |
| $1_1$–$4_2$ | | | 2.45 | 543 | 254; 708 | 6; 8 | 0.47 |
| $2_2$–$4_2$ | | | 2.59 | 390 | 447;708 | 8; 8 | 0.06 |

[a]The notation $n_m$ implies a cation position in the $n$th shell of cations surrounding the defect, and $m$ is the cationic layer counted from the surface. [b]Reference 139. Cutoff 900 eV; Γ point; $U$ = 4.5 eV. [c]Reference 9. Cutoff 500 eV; Γ point; $U$ = 5.0 eV; additional results 2.35 ($1_1$–$4_1$), 2.35 ($2_2$–$2_1$), 2.43 ($2_2$–$1_2$). [d]References 8 and 10. Cutoff 400 eV; 2 × 2 × 1 $k$ points; $U$ = 4.5 eV. [e]For a 2 × 2 cell (3 × 3 × 1 $k$ points) 2.34 and 2.22 eV, respectively, have been obtained before, ref 8. [f]A value of 2.23 eV has been reported in ref 140, cutoff 400 eV; 2 × 2 × 1 $k$ points; $U$ = 5.0 eV.

**Table 6. Oxygen-Defect Formation Energies (eV) for Subsurface (Subs) and Surface (Surf) Sites Obtained Using the HSE Hybrid Functional As Well As PBE+$U$ (corrected for dispersion, +D) for a p(2 × 2), p(3 × 3), and p(4 × 4) Surface Unit Cell Corresponding to a Defect Concentration, Θ, of $^1/_4$,[a] $^1/_9$,[b] and $^1/_{16}$[c] Monolayer of Oxygen Atoms[d]**

| | | Θ = $^1/_4$[a] | Θ = $^1/_{16}$[c] | | Θ = $^1/_4$[a] | Θ = $^1/_9$[b] | Θ = $^1/_{16}$[c] | Θ = $^1/_{16}$[c] |
|---|---|---|---|---|---|---|---|---|
| defect site | $Ce^{3+}$ [e] | HSE | HSE | HSE+D | | PBE+$U$(4.5) | | PBE+$U$(4.5)+D |
| Subs | $1_1$–$1_1$ | 3.21[a] | 2.70 | 2.83 | 2.38 | | 1.96 | 2.12 |
| Subs | $1_1$–$2_1$ | 2.79[a] | 2.49 | 2.61 | 2.00 | | 1.84 | 2.01 |
| Subs | $2_1$–$2_1$ | | 2.26 | 2.38 | | | 1.84 | 1.97 |
| Surf | $1_1$–$1_1$ | 3.30[a] | 2.74 | 2.85 | 2.50 | 2.22[b,f] | 2.01 | 2.14 |
| Surf | $1_1$–$2_1$ | 3.10[a] | 2.49 | 2.61 | 2.34 | 2.16[b,f] | 1.86 | 1.98 |
| Surf | $2_1$–$2_1$ | | 2.44 | 2.57 | | 2.06[b,f] | 1.76 | 1.91 |

[a]Reference 8. [b]Reference 10. [c]Reference 139. [d]Observed $\Delta H_{298}^\circ$ = 4.0 ± 0.1 eV, ref 112. [e]The notation $n_m$ implies a $Ce^{3+}$ position in the $n$th shell of cations surrounding the defect in the $m$th cationic layer counted from the surface. [f]Similar values have been obtained in ref 9 for Θ = $^1/_{12}$.

STM (see section 3.3), it could be proven that at least one of the excess electrons localizes in a Ce ion that is not adjacent to the O vacancy.[10]

Table 5 provides further structure details of the different defect configurations: the coordination numbers of the two ions which differ between 6 (surface, neighbored to the vacancy) and 8 (bulk, away from the vacancy), the distance between the two $Ce^{3+}$ ions, and the distances for each of the $Ce^{3+}$ ions to the vacancy site. The splitting of the two f states is a signature of the difference between the two coordination spheres, also known as crystal field splitting. The splitting is zero if both $Ce^{3+}$ ions have the same coordination number and the same distance to the vacancy ($1_1$–$1_1$; $2_1$– $2_1$). Splitting is largest for two $Ce^{3+}$ ions with coordination numbers 6 and 8 and very different distances to the vacancy site. Scanning tunneling spectroscopy of filled f states indeed yields two types of spectra, one with a single peak and another with two peaks.[10] The latter are observed only for those defects with just one $Ce^{3+}$ ion next to the vacancy site and the other away from it so that these ions feel a different, local crystal field.

The defect formation energies for the different $Ce^{3+}$ configurations vary over a few tenths of electronvolts. In detail, they also depend on two technical factors: (i) size of the surface cell and (ii) value for $U_{eff}$ applied. The lesson learned from these[8−10] and subsequent studies on defective ceria is that there are many local minima for both the positions of the ions and the local structure, which makes it difficult to converge to the most stable solution and easy to overlook a low-energy structure.

Table 6 compares O-defect formation energies, $\Delta E_d(^1/_2O_2)$, calculated using the HSE hybrid functional as well as PBE+$U$ for both surface and subsurface vacancies with $Ce^{3+}$ at different crystallographic sites at various distances to the vacancy. We adopt the notation[10] used in Table 5, where $n_m$ denotes a $Ce^{3+}$ sitting in the $n$th shell of cations (with respect to the vacancy site) of the $m$th cationic layer. For illustration, Figure 4 shows the structures of the $1_1$–$1_1$, $1_1$–$2_1$, and $2_1$–$2_1$ $Ce^{3+}$ configurations for both surface and subsurface defects. The topmost three layers of a $p(4\times4)$ surface unit cell of $CeO_2(111)$ obtained using HSE are shown, and the $Ce^{3+}$ ions are indicated as dark blue spheres.

We discuss three important aspects.

(i) Accuracy of PBE+$U$ judged on the supposedly more accurate HSE results. In section 2 we concluded that PBE+$U$(4.5) underestimates the reduction energy of $CeO_2$ (388 kJ/mol) by as much as 167 kJ/mol, whereas HSE underestimates it by 85 kJ/mol only (Table 1). Table 6 also shows that the HSE results are 0.4−0.7 eV larger than the PBE+$U$(4.5) results (Θ = $^1/_{16}$). Recalling the best estimate for the O-defect formation energy from experiment, 4.2 ± 0.3 eV per $^1/_2O_2$ (section 3.3), HSE values are closer to experiment than corresponding PBE +$U$ results. Adding a dispersion term shifts HSE results about 0.12 eV toward experiment. This shift amounts to 0.15 eV for PBE+$U$. In absolute terms the deviation between theory and experiment for the lowest defect concentration studied (Θ = $^1/_{16}$) is still very large, about 1.7 eV for HSE+D and 2.2 eV for PBE+$U$(4.5)+D. Similar to the reduction energy of bulk ceria, which can be described by either eq 2.1 or eq 2.2, we recalculate the defect formation energies for the most stable defects obtained using PBE+$U$ and HSE. The experimental


dx.doi.org/10.1021/cr3004949 | Chem. Rev. 2013, 113, 3949−3985

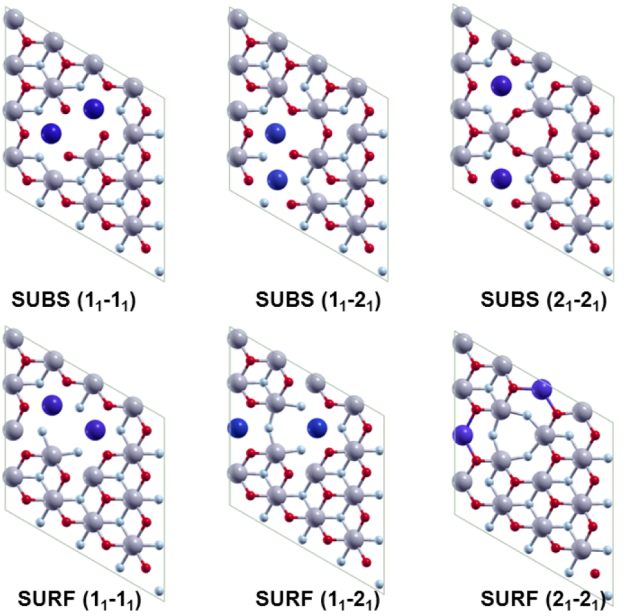


**Figure 4.** Top views of oxygen defects relaxed using HSE. First O−Ce−O trilayer in $CeO_2(111)$ is shown: (top row) subsurface defects; (bottom row) surface defects; (dark blue spheres) $Ce^{3+}$, (gray spheres) $Ce^{4+}$, (red spheres) surface oxygen atoms, (light blue spheres) subsurface oxygen atoms. Relative position of $Ce^{3+}$ is represented by $n_m$, i.e., $n$th cation shell around the vacancy in the $m$th cationic layer counting from the topmost layer. Surfaces rendered using XCrySDen.[138]

formation energy of 4.2 eV changes to 1.72 eV. Respective deviations compared with experiment in defect formation energies obtained using PBE+$U$ (−0.74 eV, i.e., 2.46 eV less than obsd.) and HSE (−0.35 eV, i.e., 2.07 eV less than obsd.) are comparable to results relative to $^1/_2O_2$.

(ii) Dependence on the defect concentration, Θ. Table 6 gives defect formation energies for three different values of Θ, namely, $^1/_4$, $^1/_9$, and $^1/_{16}$ monolayer of O ions. Due to the net positive charge of the vacancy and simulations via PBC, defect−defect interactions destabilize the O defect relative to the clean surface. In addition, so-called elastic contributions must not be forgotten. The defect formation energy $\Delta E_d(^1/_2O_2)$ for, e.g., the $1_1$−$1_1$ surface defect decreases for both PBE+$U$ and HSE comparing Θ = $^1/_4$ with Θ = $^1/_{16}$. On passing we mention that for Θ = $^1/_{16}$, the most stable defects have the $Ce^{3+}$ located in the topmost cationic surface layer, i.e., $Ce^{3+}$ in lower layers were always found to be energetically less stable.

(iii) Relative stabilities of surface and subsurface defects. Generally, HSE and PBE+$U$ predict the $2_1$−$2_1$ configuration as the most stable one for surface as well as subsurface defect. However, the $1_1$−$2_1$ and $2_1$−$2_1$ configurations have almost the same energy using PBE+$U$. The hybrid functional predicts the subsurface defect to be more stable by 0.18 eV relative to the surface defect (HSE, Θ = $^1/_{16}$). PBE+$U$ predicts the surface defect to be slightly more stable (0.08 eV). Including dispersion-type interactions does not alter the qualitative picture. However, defect formation energies generally increase by 4−9%.

Concerning structural aspects, $Ce^{3+}$ prefers a more open structure due to its larger ionic radius associated with a (preferred) lower CN (7, in $Ce_2O_3$) compared to the $Ce^{4+}$ ions, which prefer a higher CN (8 in $CeO_2$), see refs 8 and 10. A more thorough discussion will be given elsewhere.[139] Different preference of CNs for $Ce^{3+}$ and $Ce^{4+}$ sites and their implications on structural modifications similar to the surface model have also been found for ceria nanoclusters by DFT calculations[58,141−143] (see ref 144 for tests on the dependence of vacancy formation energies on $U$). The energies for O-vacancy formation in $Ce_nO_{2n}$ gas-phase clusters have been investigated by PBE+$U$(5).[145]

Conesa[146] studied the mutual interaction of O vacancies on $CeO_2(111)$ and found that dimerization of two monovacancies as well as trimerization of monomer and dimer are processes uphill in terms of energy (+0.34 eV per monomer). For divacancies, where relaxation within a surface cell is substantial, numerical estimates on elastic effects due to the restrictions on cell size have to our knowledge not been presented in the literature yet. Hermansson and co-workers[147] reported on vacancy pairs on the (110) surface.

**3.4.2. Dependence on Methodology and Technical Parameters.** Table 7 presents defect formation energies obtained with various techniques and electronic structure methods. We start our discussion with pure DFT (LDA/GGA) results, continue with strengths and weaknesses of DFT+$U$ and hybrid functionals, and compare with results for embedded cluster models obtained with computationally more demanding wave-function-based methods.

Hermansson and co-workers[115] performed periodic slab calculations using the PW91 functional, which is a conventional GGA functional. The problem of overdelocalization of excess electrons upon defect formation, i.e., metallization, has already been discussed in this section (see also section 6.3.1 of GHS[4]). This is connected with the finding that relaxation does not lead to the rather asymmetrically distorted structure at the vacant site. Recall that $Ce^{3+}$ ions have a larger atomic radius than $Ce^{4+}$, which certainly affects Ce−O bond distances. $\Delta E_d(^1/_2O_2)$ values obtained for surface and subsurface O defects in $CeO_2(111)$ amount to 3.39 and 3.21 eV, respectively (Θ = $^1/_4$). Although, for Θ = $^1/_2$ absolute values increase by about 0.6 eV, subsurface defects remain more stable than surface defects. For the $CeO_2(110)$ surface, subsurface defects were found about 0.5 (Θ = $^1/_2$) and 0.9 eV (Θ = $^1/_4$) less stable than surface defects. The (110) surface is more active than the (111) surface, i.e., it is easier to form O defects, which is due to low-coordinated $Ce^{4+}$ ions (cf. Table 3). For bulk $CeO_2$, a defect formation energy of 4.73 eV was obtained (cf. Table 7, 1 × 1 × 1 cell, $Ce_4O_8$). Thus, according to ref 115, oxygen defects are predicted to be more stable at low-index surfaces than in the bulk.

Fabris et al.[76] applied LDA+$U$ and PBE+$U$ to the (111) and (110) facets of ceria and also calculated the formation energy for the bulk oxygen defect. For a detailed discussion we refer to section 6.3.2 of GHS.[4] However, we want to point out that the DFT+$U$ approach used in the work of Fabris et al. is based either on projector functions derived from Ce 4f atomic orbitals, as solutions of the KS atomic Schrödinger equation in the reference configuration [Xe] $4f^1$ $5d^1$ $6s^2$ (see ref 42 in Fabris et al.[76]), or localized Wannier functions[149] derived from self-consistent Ce 4f bands. To check for robustness of the approach, the authors calculated the energy of reduction for $CeO_2$ bulk (see eq 2.1 in this work) and showed that results based on Wannier−Boys projector functions are essentially independent of the $U$ value employed. On the contrary,


dx.doi.org/10.1021/cr3004949 | Chem. Rev. 2013, 113, 3949−3985

**Table 7. Oxygen-Defect Formation Energies, $\Delta E_d(^1/_2O_2)$ in eV, for $CeO_2$ Obtained by Different Methods and Technical Parameters**

| method | cut off (eV) | core | | slab | cell | $\Theta_{def}$ | $\Delta E_d(^1/_2O_2)$ surf/subsurf | spin state | refs |
|---|---|---|---|---|---|---|---|---|---|
| HF/DZ(Ce)8−51G(O) | | Ce:ECP | (110) | C | | | 1.70/− | T | 2005, Herschend[23] |
| MP2 | | | | | | | 3.26/− | | |
| PBE0/DZVP | | Ce:ECP-46 | bulk (111) | C | | | 3.00 | T | 2009, Burow[22] |
| | | | | | | | 3.30/3.33 | T/S | |
| HSE | 400 | PAW | bulk | | $Ce_{32}O_{64}$ | $CeO_{1.969}$ | 3.78 | T | 2012, Paier |
| | 400 | | bulk | | $Ce_{64}O_{128}$ | $CeO_{1.984}$ | 3.74 | T | 2012, Paier |
| | 400 | | (111) | 9L | $p(2 \times 2)$ | $^1/_4$ | 3.10/2.79[a] | | 2009, Pirovano[8] |
| | 600 | | (111) | 9L | $p(4 \times 4)$ | $^1/_{16}$ | 2.44/2.26 | | 2012, Paier |
| PBE+$U$(4.5) | 400 | PAW | bulk | | $Ce_{32}O_{64}$ | $CeO_{1.969}$ | 2.84 | T | 2012, Paier |
| | 400 | PAW | (111) | | $p(2 \times 2)$ | $^1/_4$ | 2.34/2.00 | T | 2009, Pirovano[8] |
| | 900 | PAW | | 9L | $p(4 \times 4)$ | $^1/_{16}$ | 1.76/1.84 | | 2012, Paier |
| LDA+$U$(4.5) | 400 | PAW | (111) | | $p(2 \times 2)$ | $^1/_4$ | 3.2$^1/_3$.08 | T | 2009, Pirovano[8] |
| PW91+$U$(5.0) | 500 | PAW | bulk | | $Ce_8O_{16}$ | $CeO_{1.875}$ | 3.39 | T | 2006, Nolan[126] |
| | | | (111) | 4L | $p(2 \times 2)$ | $^1/_4$ | 2.60/− | T | 2005, Nolan[74,148] |
| | | | (110) | 7L | $p(1 \times 2)$ | $^1/_4$ | 1.99/− | T | |
| | | | (100) | 3L | $p(2 \times 2)$ | $^1/_4$ | 2.27/− | T | |
| PBE+$U$(4.5) | 408 | US-PP | bulk | | $Ce_8O_{16}$ | $CeO_{1.875}$ | 5.55[b] | S | 2005, Fabris[76] |
| | | | | | | | 2.58[c] | | |
| | | | (111) | 9L | $p(2 \times 2)$ | $^1/_4$ | 4.95/4.81[b] | S | |
| | | | (110) | 6L | $p(2 \times 2)$ | $^1/_8$ | 2.15/1.89[c] | | |
| | | | | | | | 4.42[b]/− | T | |
| | | | | | | | 1.57[c]/− | | |
| LDA+$U$(5.3) | | | bulk | | $Ce_8O_{16}$ | $CeO_{1.875}$ | 6.74[b] | | 2005, Fabris[76] |
| | | | | | | | 3.45[c] | S | |
| | | | (111) | 9L | $p(2 \times 2)$ | $^1/_4$ | 6.10/6.25[b] | | |
| | | | | | | | 2.92/2.95[c] | T | |
| | | | (110) | 6L | $p(2 \times 2)$ | $^1/_8$ | 5.50[b]/− | | |
| | | | | | | | 2.33[c]/− | | |
| PW91 | 400 | PAW | bulk | | $Ce_4O_8$ | $CeO_{1.75}$ | 4.73 | | 2004, Yang[115] |
| | | | (111) | 4L | $p(\sqrt{3} \times 1)$ | $^1/_2$ | 3.98/3.80 | S | |
| | | | | | $p(\sqrt{3} \times 2)$ | $^1/_4$ | 3.39/3.21 | | |
| | | | (110) | 5L | $p(1 \times 2)$ | $^1/_4$ | 3.17/3.66 | T | |
| | | | | | $p(2 \times 2)$ | $^1/_8$ | 2.48/3.39 | | |

[a]Defect formation energy corresponds to a $Ce^{3+}$ configuration, where both $Ce^{3+}$ cations are located in the surface layer. We take this value for consistency reasons, although for the $p(2 \times 2)$ cell, $Ce^{3+}$ in subsurface position appears to be energetically favorable by 0.14 eV. [b]Calculation uses projectors based on localized Wannier orbitals (see eq 3 in ref 76). [c]Calculation uses projectors based on the "generic" atomic orbitals within the applied US-PP approach.

agreement of the calculated reduction energy with the observed value has been fair (theoretical 4.8 vs observed 4.0 eV). However, employing different projectors strongly affected $\Delta E_d(^1/_2O_2)$, which varied within a range of about 3.2 eV (cf. Table 7). The latter result refers to the surface defect at $CeO_2(111)$. This is a rather unsettling situation. Furthermore, discussing the relative stability of surface and subsurface O defect at the (111) surface, one realizes that the stabilization energy varies by about 10% depending on the type of projectors used, e.g., for a 9L slab and a p(2 × 2) surface cell, PBE+$U$(4.5) formation energies of Fabris using atomic projectors results in 2.15 eV for the surface and 1.89 eV for the subsurface defect. This means the subsurface defect is stabilized by 12% relative to the surface defect. However, using Wannier-type projectors, defect formation energies increase drastically resulting in a surface defect formation energy of 4.95 eV. Compared to that, creating a subsurface defect requires 4.81 eV. This means the subsurface defect is stabilized by 2.8% relative to the surface defect. Apparently, the type of projectors employed does not change the qualitative picture, but quantitatively these variations are non-negligible. Taking the good agreement of the bulk reduction energy into account as well as results obtained using a hybrid functional (Table 6), we consider these findings as strong support for the energetic near-degeneracy of surface and subsurface O defect at the (111) surface.

Nolan et al.[74,148] considered O-defect formation at (111), (110), and (100) consistently for a defect concentration of $\Theta = {}^1/_4$ using the PW91+$U$(5.0) approach. They confirmed the findings of other workers,[76,115] i.e., the $CeO_2(110)$ surface defect is easier to create than a corresponding oxygen defect at $CeO_2(111)$. Regarding formation of an O defect in the bulk, Hermansson and co-workers obtain 4.73 eV using PW91. This value is 39% larger than the defect formation energy at the (111) surface. Nolan et al., using PW91+$U$(5.0), predict a bulk defect formation energy larger by 30% compared with the defect at the (111) surface. Admittedly, the largest scatter is reported in ref 76 by Fabris et al. Depending on the xc functional and projector type applied, the bulk defect is 10−20% more difficult to create than the aforementioned surface O defect [PBE+$U$(4.5), atomic projectors 20%; Wannier-type


dx.doi.org/10.1021/cr3004949 | Chem. Rev. 2013, 113, 3949−3985

projectors 12%; LDA+$U$(5.3), atomic projectors 10%, Wannier-type projectors 18%]. Note that the spin state reported is an open-shell singlet (i.e., antiferromagnetic coupling), whereas most of the other results are reported for the triplet state (i.e., ferromagnetic coupling).

Comparing the defect formation energies obtained using HSE, we find broad agreement with previous work. In Table 7 $\Delta E_d(^1/_2O_2)$ obtained using HSE for the bulk amounts to 3.74 eV using a 4 × 4 × 4 supercell ($Ce_{64}O_{128}$) with respect to the primitive bulk cell. For the smaller $Ce_{32}O_{64}$ supercell one obtains 3.78 eV, which can be consistently compared with PBE+$U$(4.5). This defect formation energy amounts to 2.84 eV. Compared to the best experimental estimate, HSE underestimates defect formation energies by approximately 0.5 eV, whereas PBE+$U$(4.5) underestimates them by approximately 1.4 eV.

Burow et al.[22] calculated $\Delta E_d(^1/_2O_2)$ for ceria bulk as well as for the $CeO_2$(111) surface defect using the hybrid functional PBE0 employing electrostatically embedded clusters subject to PBC. The authors predicted that the defect in the bulk is easier to form than the defect at (111) by 0.3 eV, which corresponds to stabilization of the bulk defect relative to the surface by about 9%. The HF and MP2 calculations on embedded cluster models by Herschend et al.[23] have been analyzed by GHS,[4] and no important differences compared to DFT+$U$ have been found.

**3.4.3. Summary.** Upon creation of an oxygen vacancy in ceria (bulk as well as surfaces), the two electrons left behind localize in two cerium ions, reducing them from $Ce^{4+}$ to $Ce^{3+}$.[150] The existence of multiple configurations of $Ce^{3+}$ ions has been predicted by DFT[8,9] and confirmed by STM, which provided evidence for $Ce^{3+}$ ions in different coordination environments.[10] The self-interaction error inherent in GGA-type functionals such as PBE or PW91 prevents electrons left behind after oxygen-defect formation to localize properly at the two Ce sites altering their oxidation state from +4 to +3. The DFT+$U$ ansatz rectifies the erroneous delocalization but describes energy differences only qualitatively right. Hybrid functionals such as HSE are a better choice, but the high computational cost limits their application to selected problems. Compared to the best experimental estimate of 4.2 ± 0.3 eV,[2,130] HSE underestimates defect formation energies by about 0.5 eV, whereas PBE+$U$(4.5) underestimates them by about 1.4 eV.

### 3.5. Surface Reduction by Hydrogenation

Reduction of $CeO_2$ without formation of an O vacancy is possible by adsorption of an H atom[151−153] (or by adsorption of an $H_2$ molecule and subsequent dissociation[154]),

$$[2Ce^{4+}, O^{2-}] + H \rightarrow [Ce^{4+}, Ce^{3+}, O^{2-}]H^{+} \quad (3.3)$$

The hydrogenation energy has been used as an activity descriptor for catalysts in oxidative dehydrogenation reactions, e.g., for $CH_4$ activation on Li-doped MgO[155] but also for methanol oxidation on $VO_x/CeO_2$.[156]

Table 8 shows results obtained with different methods. Pure GGA functionals (PBE, PW91) yield significantly smaller values, indicating lower reducibility. The effect of doping can be different for reduction by O-defect formation and by hydrogenation. For doping with Pt, Tang et al. found that $Pt^{4+}$ is reduced on oxygen-vacancy formation (based on Bader charges) but do not find participation of Pt when the surface is hydrogenated upon $CH_4$ adsorption.[157]

**Table 8. Energy of Hydrogenation (per $^1/_2H_2$ as well as H atom) of the $CeO_2$(111) Surface**

| | $-E_H$ ($^1/_2H_2$) | $-E_H$ (H) | refs |
|---|---|---|---|
| PBE+$U$(4.5) | 1.21 (0.91)[a] | 3.47[b] | Popa, 2011[151] |
| PW91+$U$(5) | | 3.48 | Gordon, 2009[158] |
| PW91 | | 2.99 | |
| PBE+$U$(5)//LDA[c] | | 3.14 | Joshi, 2009[159] |
| | | 1.86[d] | |
| PW91+$U$(7) | 1.41[e,f] | | Chen, 2007[154] |
| PW91+$U$(5) | | 3.50[g] | Watkins, 2007[160] |
| PBE | 0.65 | | Fronzi, 2009[152] |
| PW91 | 0.43[h] | 2.69 | Chafi, 2009[153] |

[a]Surface with an O vacancy. [b]Calculated from the hydrogenation energy per $^1/_2H_2$ and one-half of the $H_2$ dissociation energy (2.26 eV, PBE, calculated for this review). [c]"//LDA" at the LDA-optimized structure [d]W-doped ceria [e]Adsorption of $H_2$ with formation of two OH groups. Energy given per $^1/_2H_2$. [f]$CeO_2$(110) Surface: 1.77 eV. [g]The number in Table 4 of ref 160 is different because it does not include $E$(H) = 1.1 eV (personal communication). [h]Calculated from the hydrogenation energy per hydrogen atom and $^1/_2$ of the $H_2$ dissociation energy (2.26 eV, PBE, calculated for this review).

### 3.6. Interaction with Oxygen

Understanding formation of activated oxygen species is crucial for an understanding of catalytic properties as well as oxygen exchange mechanisms of ceria, e.g., in the context of its ability to easily store and release oxygen. Because of increasing bond distances compared to $O_2$ and the corresponding O−O stretching frequency shift, superoxo, $O_2^{\bullet-}$, and peroxo, $O_2^{2-}$, surface species can be identified experimentally by vibrational spectroscopy (infrared or Raman, see, e.g., ref 161). Evidence for the presence of paramagnetic superoxide, $O_2^{\bullet-}$, can also be obtained by EPR (see, e.g., ref 162). Huang and Fabris[163] studied the adsorption of $O_2$ on the clean $CeO_2$(111) surface (cf. Table 9), where it would bind essentially by dispersion,

**Table 9. $O_2$ Adsorption Energies (eV) for Different Oxygen Vacancies (eV)**

| | | $E_{ads}$ | | |
|---|---|---|---|---|
| | | surface−$V_O$ peroxo | subsurface−$V_O$ superoxo | refs |
| clean | PBE+$U$(4.5)[a] | 1.72 | | Huang and Fabris[163] |
| clean | PBE+$U$(5) | 1.89 | 0.37 | Li et al.[9] |
| | | | La−$V_O$ | |
| | PBE+$U$(4.5) | 2.10 | 1.40 | Conesa[146] |

[a]PAW approach using atomic orbitals as projectors for the PBE+$U$ calculations. Note that a larger $p(2\sqrt{3} \times 2\sqrt{3})$ supercell was used. Slab thickness: $6L$ = 2 $CeO_2$-trilayers.

which was not included in the PBE+$U$(4.5) calculations. The calculated binding energy is negligible. Adsorption of $O_2$ into a surface defect releases 1.72 eV and yields a peroxo species as the calculated bond distance (144 pm) shows,

$$[2Ce^{3+}, V_O] + O_2 \rightarrow [2Ce^{4+}, O_2^{2-}] \quad (3.3)$$

This defect healing process is involved in reoxidation of $CeO_2$ in catalytic oxidation processes. The surface peroxo species is a stronger oxidant. Releasing an oxygen atom from this species costs only 2.6 eV, whereas releasing an oxygen atom from the clean surface and forming a vacancy is almost


dx.doi.org/10.1021/cr3004949 | Chem. Rev. 2013, 113, 3949−3985

twice as costly, 5.1 eV (assuming a PBE value of 3.2 eV for the $O_2$ dissociation energy this would translate into $\Delta E_d(^1/_2O_2)$ = 1.9 for the clean surface and −0.6 for the surface peroxo species).

Later, Hu and co-workers[9] confirmed the result for $O_2$ adsorption into a surface vacancy and found that on a subsurface vacancy only one electron is transferred from a $Ce^{3+}$ ion to $O_2$, yielding a superoxo species (bond distance 133.5 pm),

$$[2Ce^{3+}, V_O] + O_2 \rightarrow [Ce^{4+}, Ce^{3+}, O_2^{\bullet -}] \quad (3.4)$$

Conesa also confirmed peroxo formation for the surface vacancy and found formation of a superoxo when a trivalent dopant is present and there is only one $Ce^{3+}$ ion connected with the vacancy site. Therefore, only one electron is available for transfer to the $O_2$ unit,

$$[Ce^{3+}, M^{3+}, V_O] + O_2 \rightarrow [Ce^{4+}, M^{3+}, O_2^{\bullet -}] \quad (3.5)$$

EPR experiments indeed detect (paramagnetic) $O_2^{\bullet -}$ species when $O_2$ is adsorbed on activated high surface area $CeO_2$ samples, see, e.g., ref 164. Preda et al.[165] studied the interaction of $O_2$ with ceria nanoparticles of up to 1.5 nm in size by virtue of hybrid DFT using the B3LYP functional. They showed that the superoxide $O_2^{\bullet -}$ radical forms upon direct interaction of $O_2$ with *low-coordinated* $Ce^{3+}$ ions on the reduced ceria nanoparticles.

As part of the reoxidation step in the catalytic cycle of CO oxidation on $CeO_2$(111), Figure 5 (cf. section 4) shows

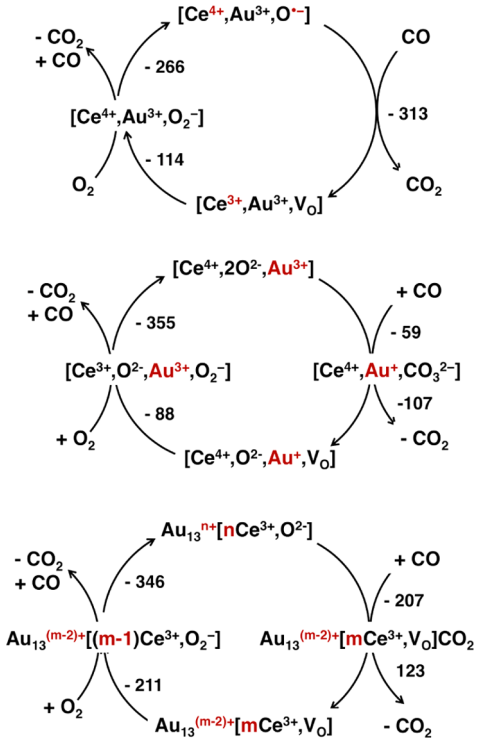


**Figure 5.** Catalytic cycle for CO oxidation on Au-doped ceria and Au clusters on ceria (energies in kJ/mol). (Top) Cycle involving a $Ce^{4+}$, $O^{\bullet -}/Ce^{3+}$,$V_O$ redox couple, PBE+$U$(4.5) calculations.[167] (Middle) Cycle involving the $Au^+/Au^{3+}$ redox couple in the presence of a $Ce^{3+}/CO_3^{2-}$ spectator species, rPBE;[209,210] calculations of Shapovalov and Metiu.[166] (Bottom) Cycle in the presence of a $Au_{13}$ cluster that has partially reduced the surface.[168]

formation of superoxo species related to adsorption of $O_2$ into an O-vacancy site in the presence of a Au dopand[166,167] or an adsorbed Au cluster.[168] The role of Ag doping in ceria on the interaction with $O_2$ was studied by Preda and Pacchioni[169] and Wang et al.[170] The impact of doping ceria with Fe, Ru, Os, Sm, and Pu was studied by means of PW91+$U$(6.3).[171] Diffusion of oxygen and involved reduction mechanisms were studied by Chen et al.[172] employing PW91+$U$ with $U$ = 0.7 eV and $J$ = 0.7 eV.

### 3.7. Doping

Many recent studies demonstrated the effect of transition metal, noble metal, and rare earth metal doping induced lowering of defect formation energies. Dopants may tune the surface activity in oxidation catalysis or ionic conductivity in solid oxide fuel cells. For instance, Hermansson and co-workers found that Pd doping lowers the surface oxygen vacancy formation energy from 3.0 to 0.6 eV.[173,174] Kinetic lattice Monte Carlo studies on the oxygen vacancy diffusion in Prasaeodymium-doped[175,176] as well as Gadolinium-doped[177] $CeO_2$ were carried out by Dholabhai et al. The impact of transition metal, noble metal, and rare earth metal doping on the oxygen storage capacity has been investigated by Gupta et al. using LDA.[178]

Nolan discusses the healing of the surface oxygen vacancy in ceria.[179] Furthermore, he studied the interaction of atomic and molecular oxygen as well as $NO_2$ with oxygen vacancies on gold-doped (110) and (100) surfaces using DFT+$U$. One of his major findings is that irrespective of doping, ceria surfaces will undergo vacancy healing. This means that the key step in the activation of ceria is formation of the active oxygen vacancy. However, the question remains how cation dopants influence vacancy formation energy and if dopants can be used to improve the activity of ceria in catalysis. Nolan and Watson performed elastic band simulations to determine activation energies for oxygen-vacancy migration in ceria.[126]

Comparison of oxygen-defect formation energies obtained using periodic DFT with results obtained using calculations on nanoparticles appears to be vital for understanding the materials gap between single crystals and powder catalysts. The work of Migani et al.[58] used PBE+$U$ and the screened hybrid functional HSE to study the dependence of oxygen vacancy formation energies on the size of ceria nanoclusters.

Hu and Metiu[180] analyze the effects responsible for lowering the O-vacancy formation energy for doped ceria (see also section 4.2 of this review). They discriminate local and global effects of dopants. Structure relaxation or effects modulating the chemical bonding between oxygen and cerium ions are considered as local, whereas global effects refer to the global electronic structure. This can be creation of O 2p hole states in the valence band maximum. Suppose ceria is doped using La, which prefers the oxidation state +3, according to

$$[2Ce^{4+}, O^{2-}, O^{2-}] \rightarrow [Ce^{4+}, M^{3+}, O^{\bullet -}, O^{2-}] \quad (3.6)$$

Upon O-defect formation, one of the two created electrons will occupy the hole state created by La doping and the other electron will occupy a Ce 4f state,

$$[Ce^{4+}, M^{3+}, O^{\bullet -}, O^{2-}] \rightarrow [Ce^{3+}, M^{3+}, O^{2-}, V_O] + \frac{1}{2}O_2 \quad (3.7)$$


dx.doi.org/10.1021/cr3004949 | Chem. Rev. 2013, 113, 3949−3985

Table 10. Interaction of CO with Different $CeO_2$ Surfaces[a]

| surface | | $-\Delta E_a$ | $E_d$ ($^1/_2O_2$) | $\Delta E_r$ $V_O$ + $CO_2$(g) | ref |
|---|---|---|---|---|---|
| (111)[b] | CCSD(T)//B3LYP | 27.3 ($Ce^{4+}$) | | | 2009, Müller[26] |
| | MP2//B3LYP[c] | 31.3 ($Ce^{4+}$) | | | |
| (110)[b] | CCSD(T)//B3LYP | 19.9 ($Ce^{4+}$) | | | 2008, Müller[25] |
| | MP2//B3LYP[c] | 23.6 ($Ce^{4+}$) | | | |
| (110) | B3LYP/[ecp, 4s, | 9.6 ($Ce^{4+}$) | | | 2006, Herschend[24] |
| | 4p,2d,2f/8−411G][d] | 205 ($CO_3^{2-}$) | | | |
| (110) | HF, (B3LYP)[b] | 11.6 ($Ce^{4+}$) | | | 2005, Müller[29] |
| | emb. cluster[e] | | | | |
| (111) | PBE+$U$(5) | 17.6 ($Ce^{4+}$) | | | 2011, Yang[190] |
| (110) | | 17.4 ($Ce^{4+}$) | | | 2008, Yang[191] |
| | | 357 ($CO_3^{2-}$) | | | |
| (110) | PBE+$U$(5) | 342 ($CO_3^{2-}$) | 1.61 | −1.63 | 2009, Scanlon[192] |
| (111) | PW91+$U$(5) | 25.1 ($Ce^{4+}$) | 2.60 | −0.56 | 2006, Nolan[189,193,194] |
| (110) | | 188 ($CO_3^{2-}$) | 1.99 | −1.16 | |
| (100) | | 309 ($CO_3^{2-}$) | 2.27 | −0.88 | |
| (111) | PW91/pw(408) | 16.4 ($Ce^{4+}$) | | | 2004, Yang[188] |
| (110) | | 17.4 ($Ce^{4+}$) | | | |
| | | 189 ($CO_3^{2-}$) | | | |

[a]Binding energy given in kJ/mol. $\Delta E_r$ (eV) refers to desorption of $CO_2$, leaving an oxygen vacancy. [b]Structure not relaxed. [c]Basis sets: Ce (46-ecp,4s, 4p, 2d, 2f), O (3s, 2p), CO (aug-cc-pVTZ). [d]Basis sets: Ce (46-ecp, VDZ),O (8−411G), CO (cc-pVDZ). [e]Constraint relaxation.

Since the hole states are energetically lower than the Ce 4f "gap states" (cf. GHS[4]), La doping *lowers* the O-vacancy formation energy, and Metiu considered this behavior as a global effect.[180]

In section 4.2, we take a different point of view, namely, that the vacancy is created at the $O^{\bullet-}$ position,

$$[Ce^{4+}, M^{3+}, O^{\bullet-}] \rightarrow [Ce^{3+}, M^{3+}, V_O] + \frac{1}{2}O_2 \qquad (3.8)$$

In this case, only one electron is left behind, which localizes in a single Ce ion. This and the fact that the electrostatic contribution to the lattice energy is significantly smaller for a monovalent anion than for a divalent anion explains the significantly lower O-vacancy formation energies.

To analyze individual electronic (global) or structure relaxation (local) contributions, one may consider electronically inert or nonreducible dopants, such as, e.g., Zr. Table 1 in ref 180 lists the vacancy formation energy in doped $CeO_2$(111) as well as the work function for vacancies created near the dopant and far from it. $Zr^{4+}$ is associated with a CN of 6 and is smaller than $Ce^{4+}$ (72 vs 87 pm, cf. Table 12). It is nonreducible; thus, structure relaxation effects are driving the lowering of the defect formation energy. Clearly, the clean ceria surface becomes energetically destabilized by doping; therefore, the energies of the defective surface and the doped surface approach each other. For this case, $\Delta E_d(^1/_2O_2)$ is lowered by almost 0.80 eV. However, the work function as a measure for the long-ranged or global impact on the electronic structure of a surface remains de facto unaltered for the Zr doping. Reducible dopants such as Ru have an impact on a local as well as on a global scale. Nolan also discusses the role of the ionic radius of dopants in ceria.[181] The large relaxation energy of about 2 eV for O-vacancy formation on the pure $CeO_2$ surface,[108] see Figure 9, underlines the high potential for lowering the defect formation by doping with nonreducible isovalent dopants.

**Summary.** O-vacancy formation energies can be lowered by different types of dopants. Isovalent nonreducible dopants ($Zr^{4+}$) affect the relaxation energy due to their different size, whereas trivalent cations ($La^{3+}$) create $O^{\bullet-}$ oxygen radical species that are easier to remove for electrostatic reasons.

## 4. INTERACTION WITH SMALL MOLECULES

Detailed understanding of the adsorption of polar molecules such as CO, $NO_x$, $SO_x$, and $H_2O$ on ceria is important because such species are involved in catalytic reactions on ceria or on catalysts with ceria as support. Oxidation of CO to $CO_2$ and reduction of $NO_x$ to $N_2$ are key targets of three-way catalysts, one of the main applications of $CeO_2$. Industrially, water adsorption represents an elementary step of the water−gas shift reaction, which in turn is of paramount importance for production of CO-free hydrogen. Adsorption of alcohols is the first step in their selective oxidation, e.g., selective oxidation of methanol to formaldehyde may be catalyzed by vanadium oxide supported on ceria.[183]

### 4.1. Adsorption and Oxidation of CO

It has been found by infrared (IR) spectroscopy, e.g., refs 182 and 184, that CO may adsorb molecularly in vertical orientation as it does on other oxides such as MgO but may also interact strongly, i.e., react chemically to carbonate-like or carboxylate-like complexes even at room temperature. Other experimental studies negate the aforementioned findings or at least indicate the need for surface pretreatment to render carbonate formation possible.[185−187] These ambiguous findings certainly call for independent information from calculations based on first principles.

Yang, Woo, and Hermansson[188] examine CO adsorption on the clean (111) and (110) surfaces of ceria by DFT and apply the (GGA-type) PW91 xc functional. As model systems, periodically repeated slabs with $p(\sqrt{3} \times 1)$ and $p(1 \times 2)$ surface unit cells, respectively, have been adopted. The slab for the (111) surface was built from 12 atomic layers, whereas the slab for the (110) surface was set up using 5 atomic layers. CO adsorption at the (111) surface was found to be weak with an adsorption energy of 16.4 kJ/mol only, whereas at the (110) surface also another, more favorable binding site was found, at which CO may chemisorb on an O-bridging position and form carbonate-like, $CO_3^{2-}$, structures. At the (111) surface CO adsorbs C down on $Ce^{4+}$ in an upright position ($R$(Ce−C) = 288 pm, $R$(C−O) = 116 pm). The adsorption energy for this


dx.doi.org/10.1021/cr3004949 | Chem. Rev. 2013, 113, 3949−3985

Table 11. Defect Formation Energies, $\Delta E_d(^1/_2O_2)$ (eV), CO Binding Energies in Different Modes, $-\Delta E_a$ (kJ/mol), and Reaction Energies, $\Delta E_r$ (kJ/mol), for the Interaction of CO with Surfaces of Doped and Undoped $CeO_2$

| | | | | $-\Delta E_a$ | | | | $-\Delta E_r$ | $-\Delta E_r$[a] | |
|---|---|---|---|---|---|---|---|---|---|---|
| surface | | | $\Delta E_d(^1/_2O_2)$ | CO | $CO_2$ | $CO_2^-$ | $CO_3^{2-}$ | $CO_2(g) + V_O$ | eq 4.2 | |
| (111) | $CeO_2$ | PBE+$U$(5) | 2.87 | 18 | | −57 | | 40 | 317 | 2011, Yang[190,200] |
| | $Zr_{0.25}Ce_{0.75}O_2$ | | 2.35 | | 77 | | | (50)[b] | (277)[b] | |
| | | | | | | | | 105 | 331 | |
| | $La_xCe_{1-x}O_2$ | PW91+$U$(5) | 0.90 | | 94 | | | | | 2009, Yeriskin[201] |
| | $CeO_2$ | rPBE | 3.01 | | | | 40 | 15 | 305 | 2007, Shapovalov[166] |
| | $Au_{0.06}Ce_{0.94}O_2$ | | −0.36 | | | | 427 | 166[d] | 304[d] | |
| | | | 1.46[c] | | | | 59 | | | |
| | $CeO_2$ | PBE+$U$(4.5) | 2.15 | | | | | (75) | (282) | 2009, Camellone[167] |
| | $Au_xCe_{1-x}O_2$ | | 0.32 | | | | | 313 | 282 | |
| | | | 1.61[e] | | | | | 223[e] | | |
| | $Cu_{0.08}Ce_{0.92}O_2$ | PBE+$U$(5) | 0.04 | | 338 | | 443 | 314 | 318 | 2010, Yang[202] |
| | | | 2.17 | | | | | | | |
| | $CeO_2$ | PBE+$U$(6.3) | 2.08 | | | | | | | |
| | $Ru_{0.125}Ce_{0.875}O_2$ | PBE+$U$(6.3) | 0.87 | | | 223 | 264 | 235 | 319 | 2012, Chen[199] |
| | $Fe_{0.125}Ce_{0.875}O_2$ | PBE+$U$(6.3) | 0.68 | | 279 | | 372 | 249 | 315 | 2011, Chen[203] |
| (110) | $CeO_2$ | PBE+$U$(5) | 2.30 | | | | 357 | 101 | 323 | 2008, Yang[191,204] |
| | $Zr_{0.25}Ce_{0.75}O_2$ | | 0.94 | | | | | (21) | (112) | |
| | | | | | 299 | 96[d] | 395 | 226 | 317 | |
| | $CeO_2$ | PBE+$U$(5) | 1.99 | | | | 188 | | | 2009, Nolan[198] |
| | $Ti_{0.04}Ce_{0.96}O_2$ | | 0.31 | | | | 415 | | | |
| | $Zr_{0.04}Ce_{0.96}O_2$ | | 0.48 | | | | 416 | | | |
| | $Hf_{0.04}Ce_{0.96}O_2$ | | 0.36 | | | | 396 | | | |
| | $La_xCe_{1-x}O_2$ | PW91+$U$(5) | 0.64 | | | | 233 | | | 2009, Yeriskin[201] |
| | $CeO_2$ | PBE+$U$(5) | 2.07 | | | | 188 | | | 2008, Nolan[205] |
| | $Au_xCe_{1-x}O_2$ | | −0.08 | | | | 454 | | | |
| (100) | $Au_xCe_{1-x}O_2$(100) | PBE+$U$(5) | | | 376 | | | | | 2008, Nolan[205] |

[a]Observed −283 kJ/mol, ref 206. [b]There seems to be a problem with the numbers in Figure 4a of ref 190. When subtracting the defect formation energy (2.35 eV) from the energy for reaction 4.1, 18.5 − 6.5 = 12.0 kcal/mol, the energy of oxidation of CO in the gas phase should be obtained. The result, 277 kJ/mol, is different from the result obtained in the same way for $CeO_2$(111) in the same paper (317 kJ/mol). We suspect that $CO_2$ desorption from the bent $CO_2$ structure is 6.5 kcal exothermic, not endothermic as shown in Figure 4a of ref 190. [c]Second vacancy. [d]In the presence of a carbonate-like spectator species. [e]Creation of a second vacancy and chemisorption of a second CO molecule.

site at the (110) surface amounts to 17.4 kJ/mol, slightly larger than the corresponding adsorption energy computed for the (111) surface. Formation of upright and tilted carbonate-like structures at (110) is accompanied by adsorption energies of 181 and 189 kJ/mol, respectively. Importantly, the corresponding vibrational spectra are in fair agreement with experiment. In the molecular (weak) adsorption model the calculated vibrational frequencies are slightly blue shifted, whereas the frequencies for the carbonate-type species are significantly red shifted. The authors correctly pointed out that defects in the $CeO_2$(111) surface, like step edges, oxygen vacancies, as well as partial surface reconstructions, may also induce formation of surface carbonates.

DFT using GGA-type functionals is adequate for nonreduced $CeO_2$ with empty Ce 4f states; application of conventional GGA becomes questionable once the Ce 4f states start to get populated, i.e., ceria is partially reduced (see sections 2 and 3). The DOSs depicted in Figure 3 of ref 188 suffer from that very problem. A partially occupied Ce 4f peak crosses the Fermi level (metallization), which indicates that $Ce^{4+}$ has been reduced to $Ce^{3+}$ upon $CO_3^{2-}$ formation at the $CeO_2$(110) surface. Within DFT, partial reduction of ceria can be treated using the ad hoc DFT+$U$ approach employing a Hubbard-type $U$ to open the band gap (section 2.2). Using PW91+U(5), Nolan and Watson[189] were able to confirm the PW91 results for molecular adsorption of CO atop Ce sites at the (111) surface and formation of $CO_3^{2-}$ species involving partial reduction of ceria at the (110) surface. They also examined adsorption on the more reactive (100) surface and found also formation of $CO_3^{2-}$ with an even larger chemisorption energy of 309 kJ/mol compared to the aforementioned 189 kJ/mol. Huang and Fabris investigated the dependence of adsorption energies on $U$ based on PBE calculations. For PBE+$U$(2), they obtained virtually the same results for molecular adsorption of CO atop Ce on the (110) and (111) surface as Yang et al., who employed pure PW91, whereas their chemisorption energy is about 10% larger than the PW91 and PW91+$U$(5) results.

As discussed in section 2, hybrid functionals or Hartree−Fock followed by wave-function-based correlation methods like MP2 or coupled cluster appear to be well suited to cope with reduction processes in ceria but are computationally also more demanding. The Hermansson group applied such methods to embedded cluster models (cf. Table 10).[24−26,29]

In their Hartree−Fock study, Müller et al.[29] compared clusters embedded in approximately 30 000 point charges (formal charges of +4 and −2 for Ce and O ions) with slab models (PBC). A $Ce_6O_{12}$ cluster represented the domain of atoms, which was treated quantum mechanically. The point charge array together with the cluster along the direction perpendicular to the surface consisted of nine atomic layers, similar to the periodic slab model employed. For Ce, the so-called SBKJC effective core potential was employed ([Kr]4d[10]


dx.doi.org/10.1021/cr3004949 | Chem. Rev. 2013, 113, 3949−3985

treated as core, i.e., 46 electrons are described by the ECP) together with a corresponding SBKJC basis set expanding the remaining 12 electrons using a (6s6p3d7f) → [4s4p2d2f] Gaussian-type basis set.[195]

The authors found two structures. In the first one, CO adsorbs atop Ce (C-end toward surface) with a tilting angle of 33°, whereas for the second structure the CO is located between two cerium ions and two oxygen ions in the second layer with a tilting angle of 77°. The BSSE-corrected HF adsorption energies amount to 11.6 and 21.2 kJ/mol, respectively. For the structure adsorbed on the cerium ion, the CO stretch frequency has been found to be blue shifted by 20 $cm^{-1}$ compared to the free molecule. The most severe limitation of this study was the constrained structure of the slab, i.e., relaxation of atomic positions on CO adsorption was not allowed. It is therefore not surprising that formation of surface carbonate or carboxylate structures, which involves major structure relaxation, was not found.

Subsequent work by Herschend et al.[24] applies the B3LYP hybrid functional to the $CO/CeO_2(110)$ system, also within the embedded cluster approach. The largest cluster used was $Ce_{12}O_{24}$. For Ce and O, the aforementioned SBKJC valence double-$\zeta$ (46e-ECP) and 8-411G basis sets were applied, respectively, whereas for the CO molecule the cc-pVDZ basis set was used. Since some of the cluster ions have been allowed to relax, in agreement with the PW91 calculations of ref 188, formation of a carbonate-type species was observed. The B3LYP adsorption energy of 205 kJ/mol is insignificantly larger by 16 kJ/mol than the corresponding energy obtained using PW91.

Calculations on molecular adsorption of CO at the (110) surface identified a single minimum energy structure. CO adsorbs atop Ce, yielding 9.5 kJ/mol. Since dispersion, which is not properly accounted for in B3LYP, may contribute significantly to the interaction with the surface, MP2 calculations have been performed at the B3LYP structure, which yield 21 kJ/mol. This adsorption energy is more than twice as large compared with the B3LYP result.

Two recent articles apply CCSD(T) to molecular CO adsorption on the (110)[25] and (111)[26] surfaces. The embedded-clusters CCSD(T) single-point calculations at structures optimized using B3LYP employ the incremental approach. CCSD(T) predicts CO to adsorb more strongly on the (111) than on the more open (110) surface, with 31 kJ/mol compared to 24 kJ/mol. The authors have shown that large parts of the electron correlation contribution to the binding energy are due to the interaction between CO and the O atoms in the topmost surface layer. For $CO/CeO_2(111)$ 85% of the correlation energy originates from surface oxygen atoms proximate to CO. The MP2 binding energy is approximately 17% larger than the one obtained using CCSD(T) for $CO/CeO_2(110)$ and 11% larger for $CO/CeO_2(111)$.

## 4.2. Vacancy Formation and CO Adsorption on Doped Ceria Surfaces

Formation of O vacancies according to eq 3.2 may become less endothermic when coupled with an exothermic oxidation reaction, such as CO oxidation,

$$CO(g) + [2Ce^{4+}, O^{2-}] \rightarrow CO_2(g) + [2Ce^{3+}, V_O] \quad (4.1)$$

The experimental values for the enthalpies of defect formation, $\Delta H_d(^1/_2O_2) = 403 \pm 39$ kJ/mol (section 3.3, Table 4), and CO oxidation in the gas phase,

$$CO + \frac{1}{2}O_2 \rightarrow CO_2 \quad (4.2)$$

$\Delta H_r$ (ox) = −283 kJ/mol[196] yield $\Delta H$ = 120 kJ/mol for eq 4.1, substantially smaller than the defect formation enthalpy without CO but still endothermic.

Table 11 shows that exothermicity can be reached for reaction 4.1 by appropriate doping, which lowers the defect formation energy. Besides the O-vacancy formation energies, Table 11 includes energies for formation of different types of chemisorbates, $CO_2$, $CO_2^-$, $CO_3^{2-}$, as well as molecular CO adsorption. With one exception, these studies use DFT+$U$(Ce). Previous GGA-based studies on the same systems,[197] very often done by the same groups, are not listed in Table 11. From the reported defect formation energies and energies for reaction 4.1 one can calculate the energy of reaction 4.2. We did it as a consistency check and list the corresponding values in Table 11.

The effect of doping has already been discussed in section 3.7 for O-vacancy formation. Here, we consider the effect of doping on vacancy formation by reduction with CO.

**4.2.1. Doping with Zr Atoms.** In contrast to $Ce^{4+}$, the isovalent $Zr^{4+}$ dopant is not reducible and therefore cannot accept electrons on O-defect formation. This leads to a different excess electron localization pattern in the lattice.[191] Another difference is the smaller size of the $Zr^{4+}$ ion (72 pm compared to 87 pm for $Ce^{4+}$, see Table 12) affecting structure relaxation.[191] As a result, the O-vacancy formation energy decreases by about 0.5 eV for the (111) surface and by 1.36 eV for the more flexible (110) surface. On the latter, carbonate formation is 38 kJ/mol more favorable than on the undoped surface and $CO_2$ desorption needs only 163 kJ/mol instead of 256 kJ/mol. Overall, O-vacancy formation by reduction with CO is 131 kJ/mol more favorable on the Zr-doped (110) surface. Atop of O atoms, CO adsorbs molecularly on the undoped (110) surface, whereas at the Zr-doped surface, an anionic chemisorbed $CO_2^-$ species is formed,

**Table 12. Ionic Radii (pm)[207] of Several Rare Earths and Transition Metals for Various Coordination Numbers (subscript) and Oxidation States**

| $Ce^{3+}$ | $La^{3+}$ | $Ce^{4+}$ | $Zr^{4+}$ | $Fe^{2+/3+}$ | $Ni^{2+}$ | $Cu^{2+}$ | $Au^{3+/+}$ |
|---|---|---|---|---|---|---|---|
| $101_6$ | $103_6$ | $87_6$ | $72_6$ | $78^{2+}{}_6$ | $55_{4\text{-tetr}}$ | $57_4$ | $137^+{}_6$ |
| | $116_8$ | | $59_4$ | $65^{3+}{}_6$ | $69_6$ | $46_7$ | $68^{3+}{}_4$ |
| | | | | $Ru^{3+}$ | $Pt^{4+}$ | | |
| | | | | $68_6$ | $63_6$ | | |

$$CO(g) + [Zr^{4+}, Ce^{4+}, O^{2-}] \rightarrow [Zr^{4+}, Ce^{3+}, CO_2^-] \quad (4.3)$$

On the doped (111) surface,[190] an adsorbed $CO_2$ molecule is directly formed, which needs only 22 kJ/mol to desorb (according to these calculations, which do not include dispersion contributions). The whole reaction according to eq 4.1 is exoenergetic, but this is found even for undoped $CeO_2$, because the DFT O-defect formation energies in Table 11 may be about 1 eV lower than the experimental values as comparison of the experimental estimates in Table 4 with calculated bulk values (Table 7) shows. On the same surface orientation (undoped), creation of a bent $CO_2^-$ species is reported[190] but rather as a transition structure, 57 kJ/mol above the CO molecule separated from the surface.


dx.doi.org/10.1021/cr3004949 | Chem. Rev. 2013, 113, 3949−3985

Studies on the (110) surface doped with Ti, Zr, and Hf have been performed. As expected, the dopants are not involved in the reduction of the surface, on O-defect formation, or CO adsorption.[198]

**4.2.2. Doping with Ru and Pt Atoms.** Similarly to Zr, Ru is also isovalent with Ce, but differently from Zr, it is reducible and the $Ru^{4+}/Ru^{3+}$ redox couple could compete with the $Ce^{4+}/Ce^{3+}$ redox couple. PW91+$U$(6.3) calculations for the $CeO_2$(111) surface[199] show that the Ru dopant is not involved in the O-vacancy formation or CO oxidation. The author concludes "...substitution with Ru metal ions activates lattice oxygen by the creation of longer Ce−O and Ru−O bonds (...) compared to those in $CeO_2$ and $RuO_2$ metal oxides".[199]

The O defect in $Ru_{0.125}Ce_{0.875}O_2$ binds $O_2$ molecules as peroxo species (−114 kJ/mol),

$$[2Ce^{3+}, V_O] + O_2 \rightarrow [2Ce^{4+}, O_2^{2-}] \quad (4.4)$$

The peroxo species oxidizes CO in a direct exothermic process (−211 kJ/mol) in which the defect is healed and the catalyst regenerated,

$$[2Ce^{4+}, O_2^{2-}] + CO(g) \rightarrow [2Ce^{4+}, O^{2-}] + CO_2 \quad (4.5)$$

Also when doping $CeO_2$ with Pt, Pt is found to stay in its +4 oxidation state[157] and does not spontaneously form O vacancies as divalent dopants do, cf. eq 4.14 below. The authors rationalize the lowering of the O-defect formation energy from 3.0 eV for the undoped (111) surface to 2.15 eV for the Pt-doped surface (LDA+$U$(5.5))[157] with the reduction of Pt indicated by smaller Bader charges on Pt. They also find smaller Bader charges on some Ce ions, and because they do not analyze possible occupation of Ce 4f states, it remains unsettled whether Pt is reduced from 4+ to 2+ or from 4+ to 3+ and one Ce ion (on average) is reduced from $Ce^{4+}$ to $Ce^{3+}$.

**4.2.3. Doping with Trivalent Metal Atoms.** Oxygen radical anion species are formed according to

$$[Ce^{4+}, O^{2-}, O^{2-}] \rightarrow [M^{3+}, O^{\bullet -}, O^{2-}] \quad (4.6)$$

When the vacancy is created at the $O^{\bullet -}$ position,

$$[Ce^{4+}, M^{3+}, O^{\bullet -}] \rightarrow [Ce^{3+}, M^{3+}, V_O] + \frac{1}{2}O_2 \quad (4.7)$$

only one electron is left behind, which localizes on one Ce ion. This and the fact that the electrostatic contribution to the lattice energy is significantly smaller for a monovalent anion than for a divalent anion leads to significantly lower O-vacancy formation energies.

In the case of La doping, the O-vacancy formation energies are about 2.0 and 1.7 eV smaller for the (111) and (110) surfaces, respectively (Table 11). Note that the specific computational model includes two substitutional sites, and the defect is formed according to

$$[Ce^{4+}, 2La^{3+}, 2O^{\bullet -}] \rightarrow [Ce^{3+}, 2La^{3+}, O^{\bullet -}, V_O] + \frac{1}{2}O_2 \quad (4.8)$$

with one spin at the reduced cerium ion and the other still as an oxygen hole state.[208] The authors employed a $U$(7) to correct for the SIE in O 2p states (see also refs 79 and 69, where bulk Ce defects, which create holes in the valence band, were modeled using a $U$(5.5) and $U$(5), respectively, for O 2p).

Interaction of CO with the La-doped (110) surface can yield carbonate species,

$$CO(g) + [Ce^{4+}, O^{2-}, La^{3+}, O^{\bullet -}] \rightarrow [Ce^{3+}, La^{3+}, CO_3^{2-}] \quad (4.9a)$$

but this is less favorable than on the undoped surface,

$$CO(g) + [2Ce^{4+}, 2O^{2-}] \rightarrow [2Ce^{3+}, CO_3^{2-}] \quad (4.9b)$$

On the La-doped (111) surface formation of strongly adsorbed $CO_2$ is found (94 kJ/mol),

$$CO(g) + [Ce^{4+}, La^{3+}, O^{\bullet -}] \rightarrow [Ce^{3+}, La^{3+}, CO_2] \quad (4.10)$$

whereas on the undoped surface, CO adsorbs molecularly with 25 kJ/mol.[189]

In the case of doping the (111) surface with Fe atoms, the O-vacancy formation energy is as low as 0.68 eV,[203] 1.4 eV lower than for the undoped surface. In the most stable defect configuration, iron remains in its +3 oxidation state, see eq 4.7, and one $Ce^{3+}$ ion is formed.

On CO adsorption carbonate formation is reported to occur with formation of two $Ce^{3+}$ ions (372 kJ/mol, CI3 in Figures 6 and 7 of ref 203). This would imply that the oxygen hole state accompanying the trivalent dopant persists,

$$CO(g) + [2Ce^{4+}, 2O^{2-}, Fe^{3+}, O^{\bullet -}] \rightarrow [2Ce^{3+}, Fe^{3+}, O^{\bullet -}, CO_3^{2-}] \quad (4.11)$$

The configuration with one $Ce^{3+}$ and $Fe^{2+}$ is 111 kJ/mol less stable (CI2 in Figures 6 and 7 of ref 203). A CO molecule placed on top of surface O ions next to the $Fe^{3+}$ site, spontaneously formed $CO_2$ and an O vacancy (−253 to −279 kJ/mol),[203]

$$CO(g) + [Ce^{4+}, O^{2-}, Fe^{3+}, O^{\bullet -}] \rightarrow [Ce^{3+}, Fe^{2+}, O^{\bullet -}, CO_2] \rightarrow [Ce^{3+}, Fe^{2+}, O^{\bullet -}] + CO_2(g) \quad (4.12)$$

Desorption of $CO_2$ requires between 17 and 43 kJ/mol.

Also here analysis of the authors based on Bader charges seems to indicate that a $Ce^{3+}$ and an $Fe^{2+}$ ion are formed, which again would imply that the oxygen hole state ($O^{\bullet -}$) persists. This is in apparent contradiction to the statement of the authors: "For the reduced ceria, the Fe neighboring the O vacancy was still in the 3+ oxidation state, whereas the $Ce^{4+}$ ion neighboring the O vacancy was reduced to $Ce^{3+}$". This contradiction can only be resolved assuming that different O-vacancy sites around the Fe dopant ion lead to different localization of the electrons left behind on O-vacancy formation. The authors conclude that the $Fe^{3+}/Fe^{2+}$ redox couple participates in the CO oxidation. We note that oxidation states cannot be unambiguously assigned based on Bader charges. This cannot replace a determination of the d-electron configuration on Fe and the f-band occupation on Ce. Note that this work does not use a $U$ parameter for the O 2p orbitals but does employ a $U$(6.3) for the Ce 4f states only.

**4.2.4. Doping with Au Atoms.** DFT calculations have shown that also for Au doping all cerium ions remain $Ce^{4+}$ ions and an $Au^{3+}$,$O^{\bullet -}$ ion pair is formed, cf. eq 4.6.[166,167] Note that the PBE+$U$(4.5) calculations of Camellone and Fabris[167] indicate some delocalization of the spin density over several oxygen atoms and the Au atom; however, a different result may be obtained with hybrid functionals.


dx.doi.org/10.1021/cr3004949 | Chem. Rev. 2013, 113, 3949−3985

Table 13. O-Vacancy Formation Energy for $CeO_2$ Surfaces with Divalent Dopants[116]

| | | Pd | Ni | Cu[a] | Cu[b] | undoped |
|---|---|---|---|---|---|---|
| HSE | (111) | −2.21 | −2.77 | | | |
| PW91+$U$(5) | (111) first | −0.97 | −0.93 | 0.04[a] | −0.46[b] | |
| | (111) second | 1.32 | 1.45 | 2.17[a] | 2.61[b] | 2.6 |
| | (110) first | −1.17 | −0.27 | | | |
| | (110) second | 1.36 | 1.30 | | | 2.0 |

[a]PBE+$U$(5), ref 202. [b]PBE+$U$(5), ref 211.

Table 14. Interaction of $H_2O$ and $CH_3OH$ with the (111) Surface of $CeO_2$; $H_2O$ or $CH_3OH$ Binding Energies (eV) for Molecular and Dissociative Adsorption on Defect-Free Surfaces and Surfaces with an O Vacancy[a]

| | | | | defect free | | O-vacancy present | | | |
|---|---|---|---|---|---|---|---|---|---|
| system | method | surface cell | $\theta$ | molecular | dissociation | $\Delta E_d(^1/_2O_2)$ | molecular | dissociation | ref |
| $H_2O/CeO_2$ | PW91+$U$(4), | 2 × 2 | $^1/_4$ | 0.52 | 0.38 | | | | Fuente, 2012[220] |
| | vdW-PBE+$U$(4.5) | 3 × 3 | $^1/_9$ | 0.67 | 0.67 | | | | Fernandez-Torre, 2012[213] |
| | | 2 × 2 | $^1/_4$ | 0.67 | 0.61 | | | | |
| | PBE+$U$(5) | 2 × 3 | $^1/_6$ | 0.58 | 0.59 | 2.01[b] | 0.82 | 2.12[b] | Molinari, 2012[218] |
| | | | 1 | 0.57 | 0.15 | | | | |
| | PW91+$U$(5) | 2 × $\sqrt{3}$ | $^1/_4$ | 0.51 | 0.37 | 2.53 | 0.8 | 2.2 | Marrocchelli, 2012[119] |
| | | | 1 | 0.55 | | | | | |
| | PBE+$U$(5) | 2 × 2 | $^1/_4$ | 0.57 | 0.55 | 2.65 | 0.54 | 2.11 | Yang, 2010[221] |
| | PBE | 2 × 2 | $^1/_4$ | 0.49 (Ce) | 0.33 | 3.03 | 1.28 | 1.40 | Fronzi, 2009[152] |
| | | 2 × 1 | $^1/_2$ | 0.50 | | | | | |
| | PBE+$U$(7) | | | 0.52 | | (3.87)[c] | 0.49 | 2.66 | Chen, 2007[154] |
| | PW91+$U$(5) | 2 × $\sqrt{2}$ | | 0.35 | 0.65 | 2.62 | 0.8 | 2.45 | Watkins, 2007[160] |
| | | 2 × 1 | $^1/_2$ | 0.58 | | 3.36 | 0.64[d] | | Kumar, 2006[212] |
| | | 2 × 1 | 1 | 0.56 | | | | | |
| $H_2O/Zr_{0.25}Ce_{0.75}O_2$ | PBE+$U$(5) | 2 × 2 | $^1/_4$ | 0.72 | 1.06 | 2.80 | | 2.33 | Yang, 2011[222] |
| | | | | | | 2.15 | | 1.41 | |
| $H_2O/Cu_{0.08}Ce_{0.92}O_2$ | PBE+$U$(5) | 2 × 2 | $^1/_4$ | 0.88 | 1.90 | | 1.66 | 2.57 | $Cu_{0.08}Ce_{0.92}O_2$ Yang, 2011[211] |
| $CH_3OH$ | PW91+$U$(5) | 2 × 2 | $^1/_4$ | 0.76 | 0.84 | 3.17 | 1.22 | 2.60 | Beste, 2008[223] |

[a]$E_d$ ($^1/_2O_2$) is the defect formation energy. [b]In the presence of a $H_2O$ molecule, the defect formation energy is 0.48 eV. [c]Bulk defect [d]For a defect in the third layer instead of the first layer, the $H_2O$ binding energy is 0.72 kJ/mol.

Defect formation according to eq 4.7 with Au remaining in its +3 oxidation state requires little energy (0.32 eV)[167] or is even exoenergetic (−0.36 eV).[166] A second O vacancy can be formed with a lower energy (1.61 eV) than for undoped ceria (2.15 eV) accompanied by reduction of $Au^{3+}$ to $Au^+$,[167]

$$[Ce^{3+}, Au^{3+}, O^{2-}, V_O] \rightarrow [Ce^{3+}, Au^{+}, 2V_O] + \frac{1}{2}O_2 \quad (4.13)$$

Shapovalov and Metiu[166] found that $CeO_2$ doped with Au at Ce lattice positions forms very stable carbonate species on the (111) surface when CO adsorbs on an O ion next to the Au dopant. This reaction is exothermic with 427 kJ/mol, and the $Ce^{3+}/CO_3^{2-}$ species is a spectator in a catalytic cycle for CO oxidation that involves a $Au^+/Au^{3+}$ redox couple (Figure 5, middle). Camellone and Fabris[167] found a different cycle involving a $Ce^{4+},O^{\bullet-}/Ce^{3+},V_O$ redox couple (Figure 5, top).

**4.2.5. Doping with Divalent Metal Atoms.** The negative O-vacancy formation energies in Table 13 show that doping with Pd and Ni leads to spontaneous O-vacancy formation, i.e., a $Ce^{4+}O^{2-}$ pair is replaced by $M^{2+}$,

$$[Ce^{4+}, O^{2-}] \rightarrow [M^{2+}, V_O] + \frac{1}{2}O_2 \quad (4.14)$$

To characterize the activity of such a surface, formation of an O vacancy in addition to the $[M^{2+}, V_O]$ site should be considered,

$$[2Ce^{4+}, O^{2-}, M^{2+}, V_O] \rightarrow [2Ce^{3+}, M^{2+}, 2V_O] + \frac{1}{2}O_2 \quad (4.15)$$

The numbers in Table 13 indicate that O-defect formation according to eq 4.15 needs significantly less energy than for an undoped surface. For Cu doping, O-vacancy formation according to eq 4.14 is found to be spontaneous (−0.46)[211] or nearly spontaneous (0.04 eV)[202] and formation of a second vacancy (eq 4.15) needs about 0.4 eV less energy than on the undoped surface (Table 13).

### 4.3. Summary: CO Adsorption

Adsorption of CO at $CeO_2$(111) is weak, and formation of surface carbonate species, a strongly exothermic process, was found for the (110) and (100) orientations only. Similar to O-vacancy formation, DFT+$U$ predicts reduction of ceria too exothermic and oxidation reactions too endothermic. On doped $CeO_2$ surfaces, the dopant may or may not be involved in the redox process, depending on its nature.

### 4.4. Adsorption of $H_2O$ and $CH_3OH$

Water adsorption is ubiquitous with oxide surfaces, as water is always present either as a reactant or as just an "innocent


dx.doi.org/10.1021/cr3004949 | Chem. Rev. 2013, 113, 3949−3985

**Table 15. Experimental Results Compared to an Estimate Obtained Using DFT on Adsorption of Water on $CeO_2(111)$ Surfaces**

| $\Delta H$ (kJ/mol) | $\Theta$ (ML) | | $T_p$ | rate (K/s) | log ($\nu$/s$^{-1}$) | ref |
|---|---|---|---|---|---|---|
| 80 | 1 | TPD | 271 | 2 | 14.6[a] | Matolin, 2012[217] |
| 49 → 53 | 1 | | 185 → 170 | | 14.4−14.3[a] | |
| ≥95 | | scanning force microscopy | | | | Gritschneder, 2007[224] |
| 80 → 97 | | TPD | 320 → 265 | 1 | 14.7−14.6[a] | Henderson, 2003[216] |
| 57 → 61 | | | 207 → 195 | | 14.4[a] | |
| 80 → 72 | | TPD | 265 → 240 | 1 | 14.6−14.5[a] | $CeO_{1.98}$, Henderson, 2003[216] |
| 56 | | | 190 | | 14.4[a] | |
| 85 | 0.04−0.07 | TPD | 320 | 1 | 13[b] | ref 213, data ref 216 |
| 212 | | DFT | 650 | | 13[b] | Estimate, see text |

[a]See ref 215 for how $\Delta H$ is derived. [b]Pre-exponential assumed in Redhead analysis.

spectator". Adsorption of alcohols is chemically related; however, for (lower) alcohols it is predominantly the selective oxidation driven by ceria or supported catalysts, which renders alcohol adsorption interesting. Therefore, the adsorption mechanism and wetting behavior are usually driven by a complex interplay of several factors, such as the surface structure, thermodynamics, as well as kinetic phenomena associated with adsorption.

DFT with GGA-type functionals (PW91, PBE) has been used to examine water adsorption on the clean and reduced $CeO_2(111)$ surfaces.[152,212] As on other oxides, on the clean surface $H_2O$ molecules can adsorb on top of a $Ce^{4+}$ cation either molecularly or dissociatively,

$$H_2O(g) + [2Ce^{4+}, O^{2-}] \rightarrow [2Ce^{4+}, O^{2-}]H_a^{+}, OH_a^{-} \quad (4.17)$$

with $H_a$ as the adsorbed proton, which results in surface hydroxylation due to heterolytic water splitting.

Fernández-Torre et al.[213] showed that both structures are stabilized by a hydrogen bond and differ in energy by a few kJ/mol only (Table 14). They are easily interconverted with barriers below 14 kJ/mol. The authors further showed that apparent discrepancies between previous calculations as far as the relative stability of molecular and dissociated adsorption structures is concerned are due to incomplete exploration of the potential energy surface of water on $CeO_2(111)$. Use of a hybrid functional (HSE) or PBE+$U$(4.5) did not change the conclusions. The same is true for van der Waals functionals, which uniformly increase the binding energies by about 15−65 kJ/mol (optPBE-vdW+$U$).[213] Adding a typical value[214] of about 5 kJ/mol for the difference between the enthalpy and the calculated energy, one gets about 60 kJ/mol for the enthalpy of adsorption, still significantly smaller than the 80−100 kJ/mol derived by Campbell and Sellars[215] from TPD data of refs 216 and 217 (cf. Table 15). These TPD spectra exhibit a second peak at lower temperature from which Campbell and Sellars[215] derive enthalpies of 50−60 kJ/mol, which better fits the calculated values. The experiments refer to loadings of about one monolayer and below. The DFT(+$U$) results (including some improvements by virtue of incorporating van der Waals interactions), which have been performed for loadings below one monolayer (one $H_2O$ molecule per $Ce^{4+}$ surface ion), do not provide an explanation for two distinct adsorption states with about 30−40 kJ/mol difference in binding energies. For molecular adsorption, the binding energies hardly vary when the coverage varies between $^1/_6$ and 1[218] or between $^1/_4$ and 1.[119] There is limited knowledge about the coverage dependence for the dissociated structure.

We believe that the potential energy surface for the $H_2O/CeO_2(111)$ system for loadings around and below one ML has been insufficiently explored. Fernandez-Torre et al. did their best for low loadings ($^1/_9$ and $^1/_4$) to find the global minimum. However, this can probably not be achieved without a global optimization tool, as the example of the apparently simple $H_2O/MgO(100)$ system tells us.[219]

On a defective surface, dissociative adsorption, i.e., heterolytic water splitting, is expected to be more favorable, because the $OH^-$ formed is more stable in an oxygen surface position,

$$H_2O(g) + [2Ce^{3+}, Ce^{4+}, O^{2-}, V_O] \rightarrow [2Ce^{3+}, Ce^{4+}, OH_a^{-}, OH^{-}] \quad (4.18)$$

than on top of a $Ce^{4+}$ surface ion (eq 4.17). Figure 6 shows different states of water adsorption on the clean and O-defective $CeO_2(111)$ surface. The black lines are the plain PBE results of Fronzi et al.,[152] who found a substantial barrier for dissociation of $H_2O$ on the surface with an O defect. This was in contradiction to the earlier PBE+$U$(5) results of Watkins et al.,[160] shown in red in Figure 6, who did not find a substantial barrier ("...dissociation was found to occur within 100 fs") and predicted a much stronger dissociative adsorption (236 kJ/mol) than on the clean surface (63 kJ/mol). Recent results of Molinari et al.[218] and Marrocchelli and Yildiz[119] (205 and 212 kJ/mol, respectively) confirm these results.

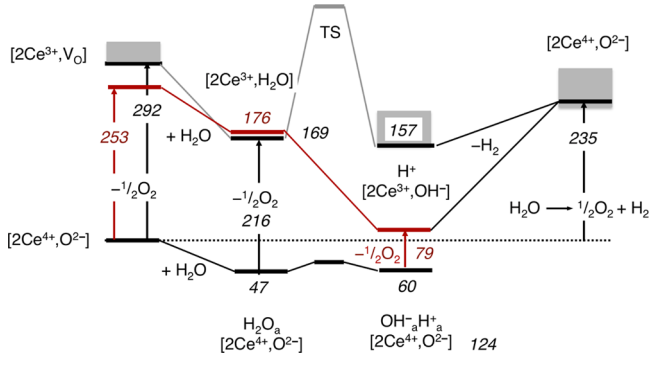


**Figure 6.** Adsorption of $H_2O$ on the clean and O-defective $CeO_2(111)$ surface according to refs 152 (black) and 160 (red), see also text.

Large binding energies for $H_2O$ on the defective surface also fit the observation of Matolin et al.[217] that some water (hydroxyl groups) stays till very high temperatures on the surface. For the desorption peak at 320 K, the Redhead equation with a pre-exponential of $10^{13}$ s$^{-1}$ and a heating rate of


dx.doi.org/10.1021/cr3004949 | Chem. Rev. 2013, 113, 3949−3985

1 K·s$^{-1}$ yields a desorption energy of 85 kJ/mol. Assuming a linear function $E_d = f(T_p)$ the desorption temperature predicted for a desorption energy of 212 kJ/mol is around 650 K.

Adsorption of $H_2O$ molecules has also been investigated by atomic force microscopy.[224,225a] From the barrier of movements between different $Ce^{4+}$ adsorption sites, it has been concluded that the lower bound for the adsorption energy should be 95 kJ/mol,[224] slightly larger than 80−97 kJ/mol derived from the high-temperature TPD peaks of ref 216, see Table 15. Using noncontact atomic force microscopy, Torbrügge et al. were able to show tip-induced diffusion of a water molecule around a surface oxygen vacancy at 80 K.[225a] Contrary to what has been found in the calculations, water does not seem to fill the vacancy site neither as $H_2O$ nor as $OH^-$. It is unclear if this raises questions about the interpretation/assignment of the observed force patterns or about the calculations. Also, in the AFM experiments no indications have been found that water would form monolayer-like hydrogen-bonded networks; rather it has been found that it is easy to dissociate water dimers on the $CeO_2(111)$ surface by action of the tip.[225a]

Water molecules binding more strongly on O vacancies than on the defect-free surface means that the presence of water on the surfaces reduces the defect formation energy and enhances the reducibility,

$$H_2O(g) + [2Ce^{4+}, 2O^{2-}] \rightarrow [2Ce^{3+}, OH^-, O^{2-}]H_a^+ + \frac{1}{2}O_2 \quad (4.19)$$

PBE+$U$ calculations predict that the O-defect formation energy is substantially lowered, from 2.62 eV for the dry surface to 0.82 eV for the surface with adsorbed water molecules.[160]

The diagram in Figure 6 further shows dehydrogenation of the hydrated defective surface which is connected with healing the defect (reoxidizing the reduced surface),

$$[2Ce^{3+}, OH^-, O^{2-}]H_a^+ \rightarrow [2Ce^{4+}, 2O^{2-}] + H_2 \quad (4.20)$$

The sum of the energies for defect formation, water adsorption, and dehydrogenation should yield the energy of the overall reaction

$$H_2O \rightarrow \frac{1}{2}O_2 + H_2$$

which we used as a consistency check for the results reported in the literature. Our PBE result (large basis set) is −240 kJ/mol, very close to the observed value[206] of −242 kJ/mol. The reverse reaction, reduction of the $CeO_2(111)$ surface by $H_2$,

$$[2Ce^{4+}, 2O^{2-}] + H_2 \rightarrow [2Ce^{3+}, OH^-, O^{2-}]H_a^+ \rightarrow [2Ce^{3+}, O^{2-}] + V_O + H_2O(g)$$

has been studied by Chen et al.[154] by PBE+$U$ with a parameter $U$ = 7 eV being larger than usually applied.

It has been suggested that water adsorption itself leads to formation of $Ce^{3+}$ species, i.e., reduces the $Ce^{4+}$ surface and becomes oxidized,[216,217] e.g., according to

$$[Ce^{4+}, O^{2-}]OH^-_aH^+_a \rightarrow [Ce^{3+}, O^{2-}]OH_aH^+_a$$

The problem reduces to the question if an extra electron in the $Ce^{4+}OH^-_a$ species stays on the hydroxyl anion or if it localizes in cerium 4f states leaving a hole in the O (or OH) 2p states ($Ce^{3+}OH_a$). In none of the calculations such an electronic structure has been found, neither do the redox potentials in solution, 1.3−1.7 eV[225b] for

$$Ce^{IV}{}_{aq} + e^- \rightarrow Ce^{III}{}_{aq}$$

and 1.8 eV[225c] for

$$OH^-{}_{aq} \rightarrow e^- + {}^{\bullet}OH_{aq}$$

support it. The latter yield an energy of 3.1−3.5 eV for the related reaction

$$\{Ce^{4+}\}_{aq} + \{OH^-\}_{aq} \rightarrow \{Ce^{3+}\}_{aq} + \{{}^{\bullet}OH\}_{aq}$$

We conclude that neither the DFT calculations for surface reactions nor the experimental results for fully hydrated ions support the conclusion of ref 217 that the number of $Ce^{3+}$ ions with occupied f states is increased in multilayer water adsorption on $CeO_2(111)$ surfaces. We rather believe that the authors of ref 217 are right when they offer the explanation "This can be caused by a more effective screening of the $Ce^{4+}$ photoemission signal by the water overlayer compared to the $Ce^{3+}$ signal".

**Summary.** For $H_2O$ adsorption on the nondefective $CeO_2(111)$ surface, the potential energy surface has been insufficiently explored for loadings up to one monolayer, and there is currently no explanation for the observed[215] two distinct adsorption states with about 30−40 kJ/mol difference in binding energies. There is no doubt, however, that $H_2O$ molecules strongly and dissociatively bind on O-vacancy sites.[119,160,218]

### 4.5. Adsorption of $H_2S$

Reduction of the $CeO_2$ surface by $H_2S$ is more likely than by $H_2O$ for which computations did not find evidence that this might happen. The PW91+$U$ studies by Chen et al.[226] and Marrocchelli and Yildiz,[119] see Table 16, agree in the observation that on the clean $CeO_2(111)$ surface $H_2S$ can adsorb either molecularly or dissociatively according to

$$H_2S(g) + [2Ce^{4+}, O^{2-}] \rightarrow [2Ce^{4+}, O^{2-}]H^+_a, SH^-_a$$

**Table 16. Interaction of $H_2S$ with the (111) Surface of $CeO_2$[a]**

| | PW91+$U$(7), Chen, 2007[226] | PW91+$U$(5), Marrocchelli, 2012[119] |
|---|---|---|
| surface cell | $\sqrt{3} \times 2$ | $2 \times \sqrt{3}$ |
| molecular adsorption | −15 | −17 (−53)[b] |
| dissociative adsorption | −19 | −32 (−183)[b] |
| S−H dissociation | −125 | −116 |
| apparent barrier | 16 | 51 |
| $H_2(g)$ formation | 85 | 116 |
| apparent barrier | 108 | 280 |
| $H_2$ desorption | 3 | |
| $H_2O(g)$ formation | 7 | 80 (−15)[b] |
| apparent barrier | (16)[c] | 193 (−53)[b] |
| $H_2O$ desorption | 57 | 106 (183)[b] |
| $SO_2(g)$ formation | −38 | 89 |
| apparent barrier | (16)[c] | (51)[c] |
| $SO_2$ desorption | 90 | 190 |

[a]Energies are given in kJ/mol with respect to $H_2S$ in the gas phase. [b]At the defective surface. [c]This is the barrier for formation of the [2$Ce^{3+}$, O−$S^{2-}$, 2$O^{2-}$] 2$H^+_a$ intermediate.


dx.doi.org/10.1021/cr3004949 | Chem. Rev. 2013, 113, 3949−3985

In principle, a partial reduction could happen already in this step according to

$$[Ce^{4+}]SH^-_a \rightarrow [Ce^{3+}]SH_a$$

but this has not been reported.

The two studies further agree that the second step involves dehydrogenation of the $SH^-$ group and formation of a peroxo-like $O-S^{2-}$ species (bond distance 172 pm), which necessitates formation of two $Ce^{3+}$ ions according to

$$[2Ce^{4+}, 3O^{2-}]H^+_a, SH^-_a \rightarrow [2Ce^{3+}, O-S^{2-}, 2O^{2-}]2H^+_a$$

The apparent energy barriers and stabilities with respect to $H_2S$ in the gas phase are given in Table 16. Chen et al. report 16 and 125 kJ/mol, respectively, whereas Marrocchelli and Yildiz[119] obtained 51 and 116 kJ/mol, respectively.

Formation of $H_2$, $H_2O$, and $SO_2$ from this common intermediate was considered in the two studies, but very different energy profiles were obtained. Even the energies for the total reactions

$$H_2S(g) + [2Ce^{4+}, O^{2-}] \rightarrow H_2(g) + [2Ce^{4+}, O-S^{2-}]$$

$$H_2S(g) + [2Ce^{4+}, 2O^{2-}] \rightarrow H_2O(g) + [2Ce^{3+}, O-S^{2-}] + V_O$$

$$H_2S(g) + [6Ce^{4+}, 4O^{2-}] \rightarrow SO_2(g) + [6Ce^{3+}, 2O^{2-}]2H^+_a + 2V_O$$

differ by 31, 73, and 127 kJ/mol, respectively. Since in these reactions none, one, and two O vacancies are formed, the increasing difference may be due to a difference in the O-vacancy formation energy.

Neither of the calculations is in agreement with the observations of Mullins et al.,[227] who found that (besides $H_2S$ at 155 K) only $H_2O$ desorbs from the nondefective surface between 200 and 450 K. Both calculations predict that $SO_2$ should form as easily as $H_2O$ or easier. The likely reason that it is not observed is the large desorption energy which is significantly larger than the $H_2O$ desorption energy according to both calculations, although the absolute values again differ substantially between the two calculations. In disagreement with the observed $H_2O$ desorption, calculations of Marrocchelli and Yildiz[119] predict a high barrier for water formation, 193 kJ/mol above $H_2S(g) + CeO_2(111)$—much higher than the barrier for S−H dissociation to form the $[2Ce^{3+}, O-S^{2-}, 2O^{2-}]2H^+_a$ intermediate. On the contrary and in agreement with the observed $H_2O$ desorption, Chen et al.[226] found a much lower barrier 20 kJ/mol below the $H_2S(g) + CeO_2(111)$ level, so that the apparent barrier for formation of the $[2Ce^{3+}, O-S^{2-}, 2O^{2-}]2H^+_a$ intermediate (16 kJ/mol) becomes decisive.

On a surface with O defects when about 20% of $Ce^{4+}$ ions are reduced to $Ce^{3+}$ ions, water is produced, which desorbs at higher temperatures (580 K). This supports the calculations of Marrocchelli and Yildiz on defective surfaces, who find that formation of $H_2O(g)$ is exothermic (−15 kJ/mol), but desorption needs more energy (183 kJ/mol) than on the defect-free surface (106 kJ/mol).

Although some features of the reactions following $H_2S$ adsorption on the $CeO_2(111)$ surface are understood, the two computational studies available clearly show that converged results have not been obtained yet, even at the PBE+*U* level. These reactions are of interest for desulfurization processes, e.g., after gasification of biomass to syngas to avoid potential poisoning of catalysts and $SO_x$ production. Since reaction temperatures are rather high and may be well above 800 K (see refs 228 and 229 and references therein), considering free energies instead of the total electronic energy obtained by DFT as shown in Table 16 appears to be indispensable. This is well demonstrated by Mayernick et al.,[228,229] who computed Gibbs free energies at 1100 K and partial pressures for $H_2$, $H_2S$, as well as $H_2O$ of 0.35, $10^{-2}$, and 0.03 atm, respectively. Importantly, the partial pressure of oxygen may be very low ($<10^{-20}$ atm) under "catalytic conditions" in a gasifier. The low oxygen pressure together with the aforementioned elevated temperatures favors formation of oxygen vacancies. The role of these vacancies in the adsorption and dissociation processes of $H_2S$ on $CeO_2(111)$ as well as on La and Tb mixed-oxide surfaces created by systematic substitution of $Ce^{4+}$ ions by $La^{3+}$ or $Tb^{3+}$ was also investigated in ref 229.

Table 17 shows selected results for dissociative adsorption of $H_2S$ forming SH*+H* and for deposition of sulfur, releasing $H_2$ into the gas phase, S* + $H_2$(g). Oxygen vacancies formed at the surface play an important role. Sulfur formation becomes thermodynamically favorable only when vacancies are formed on the surface. For the $La_{0.25}Ce_{0.75}O_{1.25}$ mixed-oxide surface, the effect is significantly stronger, i.e., vacancy formation lowers the Gibbs free energies of sulfur formation by 3.54 eV, compared to 2.51 eV for pure $CeO_2$. The authors conclude from their joined computational−experimental study that the sulfur adsorption process occurs via $H_2S$ adsorption (rate limiting) and dissociation over oxygen vacancies.

**Table 17. Gibbs Free Energy Differences (eV) for O-Vacancy Formation[a] and Adsorption of $H_2S$ on the Pure and La-Mixed $CeO_2(111)$ Surface[228]**

| | surface | SH* + H* | S* + $H_2$(g) |
|---|---|---|---|
| $CeO_2(111)$ | 0.0 | 4.34 | 2.12 |
| $V_O-CeO_2(111)$ | −1.03[a] | 1.11 | −0.39 |
| 2 $V_O-CeO_2(111)$ | −1.81[a] | 0.25 | −1.30 |
| $La_{0.25}Ce_{0.75}O_{1.25}$ | 0.0 | 4.26 | 3.59 |
| $V_O-La_{0.25}Ce_{0.75}O_{1.25}$ | −0.74 | 1.47 | 0.05 |

[a]The free energy of $O_2$, $G_{O2}$, has been determined by $G_{O2} = (G_{H2O} - G_{H2}) \times 2$.

**Summary.** Reactions involving $H_2S$ adsorbed on ceria are distinct from the $H_2O/CeO_2$ system because of possible reduction of the surface. Reactions following $H_2S$ adsorption can lead to reduction of the $CeO_2$ surface, but the two PBE+*U* studies[119,226] have not yet led to converged results.

### 4.6. Adsorption of Other (Small) Molecules

Table 18 lists computational studies of the interaction of other small molecules with ceria surfaces. We begin with a discussion of ref 230. The O ends of the adsorbed NO molecules fill the oxygen vacancies, and the N−O bonds are elongated. If two such adsorbed NO molecules meet from neighboring sites, their N ends will form a strong N−N bond with little or no barrier. This is an intermediate step toward dissociation of free $N_2$.

Scanlon et al.[192] examined reduction (O-defect formation) of the (110) surface by CO and subsequent reoxidation of the defective surface with $NO_2$. Both steps are exothermic. $NO_2$


dx.doi.org/10.1021/cr3004949 | Chem. Rev. 2013, 113, 3949−3985

**Table 18. Interaction with Other Small Molecules**

| system | method | remark | ref |
|---|---|---|---|
| $N_2O/CeO_2(111)$ | CCSD(T) | | Müller, 2009[232] |
| $NO_2/CeO_2(111)$, (110), (100) | GGA+$U$ | $NO_2$ adsorption on and reoxidation of O-defective surfaces | Galea, 2009[233] |
| CO, $NO_2/CeO_2(110)$ | PBE+$U$(5) | reduction by CO, reoxidation by $NO_2$ | Scanlon, 2009[192] |
| CO, NO/Ti,Zr,Hf-doped-$CeO_2(110)$ | PBE+$U$(5) | | Nolan, 2009[198] |
| $NO_2/CeO_2$ (111),(110),(100) | PW91+$U$(5) | $NO_2^-$ formation on the O-defective surfaces | Nolan, 2006[234] |
| $NO_2$, $NO/CeO_2$ (111),(110),(100) | PW91+$U$(5) | reduction energies on defective surfaces | Nolan, 2006[194] |
| $NO_2/CeO_2$ | GGA | adsorption and nitrate formation | Rodriguez, 2000[235] |
| $NO/CeO_2$ (111),(110) | PBE | NO binds O down on O defects | Yang, 2006[230] |
| $SO_2/CeO_2$ | DFT+$U$ | sulfate formation | Lu, 2011[236] |
| $Cl_2$, $Br_2/CeO_2(111)$ | LDA+$U$(5.5) | Heterolytic dissociation | Hu, 2012[231] |
| $CH_4/CeO_2(111)$ | LDA+$U$(5.5) | $^{\bullet}CH_3$(gas) formation | Hu, 2012[231] |
| $CH_4$/Pt-$CeO_2$ | LDA+$U$(5.5) | $^{\bullet}CH_3$(gas) formation | Tang, 2010[157] |
| $NH_3$/(W-doped)−$CeO_2(111)$ | PW91 | clean and hydrogenated surface | Joshi, 2009[159] |
| | PW91+$U$(5) | | |
| HCOOH/$CeO_2(111)$ | PW91 | formation of different formate species | Gordon, 2009[158] |
| | PW91+$U$(5) | | |
| 1,3-butanediol/$CeO_2(111)$ | PBE//LDA[a] | adsorption on clean and O-defect surfaces | Ichikawa, 2006[237] |

[a]PBE single-point calculations at LDA-optimized structures.

adsorbs in two modes on the defective surface, where both involve reoxidation of one of the $Ce^{3+}$ ions to $Ce^{4+}$ and a $NO_2^-$ adspecies.

In a joined computational−experimental study Tang et al.[157] used LDA+$U$(5.5) to examine the homolytic C−H bond dissociation of $CH_4$ on the $CeO_2(111)$ surface. H and $CH_3$ bond to surface O atoms, yielding OH and $OCH_3$ groups. On the undoped surface the energy barrier is 1.29 eV, and 1.67 eV are needed to get $CH_3$ into the gas phase (both with respect to $CH_4$(g) and the clean surface).[157] Doping by $Pt^{4+}$ weakens the bonds to oxygen as indicated by the lowering of the O-defect formation energy from 3.0 to 2.15 eV. Accordingly, the barrier for C−H bond splitting and the energy for desorbing the $CH_3$ radical into the gas phase are lowered by 0.21 and 0.35 eV, respectively.[157] The $Pt^{4+}$ dopant does not seem to be involved in the accompanying reduction of the $CeO_2$, while it is involved in the O-vacancy formation (see section 4.2).

The situation is different for La-doped $CeO_2(111)$, for which a more dramatic lowering of the reaction energy to 0.01 eV is calculated.[231] Doping by the trivalent La ion creates $O^{\bullet-}$ sites according to eq 4.6, and it is the $O^{\bullet-}$ radical site that abstracts a hydrogen atom from the $CH_4$ molecule,

$$[Ce^{4+}, La^{3+}, O^{\bullet-}] + H - CH_3 \rightarrow [Ce^{4+}, La^{3+}, H] + {}^{\bullet}CH_3$$

Gordon et al. examined the fate of adsorbed formic acid on increasing temperature by reflection−absorption IR spectroscopy in combination with DFT calculations.[158] For the defect-free surface, they observed heterolytic splitting into proton and formate species. On the defective surface, formic acid adsorbs with one of its O atoms into the defect site, closely related to water adsorption as shown in Figure 6. It illustrates the conclusion from the above-mentioned work for defective (top) and defect-free (bottom) $CeO_2(111)$.

Hu and Metiu show that halogen molecules split heterolytically on the $CeO_2(111)$ surface in a Lewis acid−base reaction with a $Ce^{4+}/O^{2-}$ pair of sites.[231]

## 5. CERIA AS SUPPORT FOR OTHER OXIDES (VANADIA)

Supported vanadium oxides are widely used in heterogeneous catalysis. One frequently studied model reaction is the oxidative dehydrogenation (ODH) of methanol, in which vanadium oxide supported on reducible oxides like ceria is more active than on inert supports like silica.[156,183,238,239]

While there are many computational studies of vanadia on various supports, interest in ceria as support for other oxides seems to have been limited to vanadia. However, Rodriguez and co-workers[240−242] examined cerium oxide nanoparticles deposited on the $TiO_2(110)$ rutile surface. It was shown that in $CeO_x/TiO_2(110)$ Ce prefers the oxidation state +3 over +4, which was in stark contrast to $TiO_x/TiO_2(110)$ creating $Ti^{4+}$ exclusively. This was rationalized by strongly destabilized Ti d states. Moreover, it was shown experimentally that the Ce/Ti mixed-metal oxide surface supporting Au, Cu, and Pt admetal atoms at low coverages (ca. 0.15 ML) leads to excellent activities toward the WGS reaction.[241] The support effect of nonreducible oxide surfaces like $ZrO_2(111)$ and $\gamma$-$Al_2O_3(100)$ acting on small $Ce_2O_4$ clusters has been recently studied by Cheng et al.[243]

### 5.1. Structure and Electron Distribution

Monomeric $VO_n$ clusters ($n$ = 1−4) on a 3 × 3 surface cell of $CeO_2(111)$ have been studied with PW91[244] and on a 2 × 2 cell with PBE+$U$(4.5).[151] More recent PBE+$U$(4.5) calculations used a 4 × 4 surface cell.[108] Figure 7 shows the structures found for the different $VO_n$ species. For $VO_3$ there is an additional flat structure with all three O atoms in one plane and V slightly

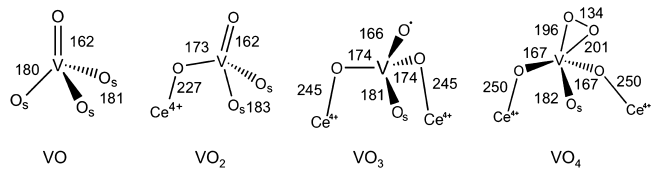


**Figure 7.** Structures of the most stable $VO_n$·$CeO_2(111)$ species. $O_S$ denotes surface O atoms (after Figure 1 of ref 151, see also Figure 7 of ref 244).


dx.doi.org/10.1021/cr3004949 | Chem. Rev. 2013, 113, 3949−3985

Table 19. Oxygen-Defect Formation Energies with Respect to $^1$·surface unit cell. For results obtained using $a_2O_2$ (eV) for Ceria-Supported $VO_n$ Species[a]

| method | $U_{eff}$(Ce) | $U_{eff}$(V) | cell | $CeO_2$ | VO | $VO_2$ | difference[b] | $VO_3$ | $VO_4$ | refs |
|---|---|---|---|---|---|---|---|---|---|---|
| PBE+$U$ | 4.5 | 0 | 4 × 4 | 1.84 (3.80) | 2.04 | 0.84 (3.88) | 1.00 (−0.06) | 0.00 | | 108 |
| PBE+$U$ | 4.5 | 0 | 2 × 2 | 1.87 (3.93) | 2.19 | 0.79 (3.99) | 1.08 (−0.06) | 0.25 | 0.40 | 151 |
| | 5.2 | 0 | | 1.53 | | 0.57 | 0.96 | | | |
| | 4.5 | 2.0 | | 1.87 | | 1.60 | 0.27 | | | |
| | 4.5 | 4.5 | | 1.87 | | 1.58 | 0.29 | | | |
| HSE | | | 2 × 2 | 2.69 | | 1.61 | 1.08 | | | |
| PW91 | | | 3 × 3 | | | 2.34 | | 1.14 | 0.48 | 244 |

[a]In parentheses values for unrelaxed structures. [b]Difference in $\Delta E_d(^1/_2O_2)$ for $VO_2/CeO_2(111)$ and the clean surface.

closer to the surface. PW91 predicts it to be 0.07 eV more stable,[244] whereas with PBE+$U$(4.5) it is found to be 0.17 eV less stable.[151] Shapovalov and Metiu[244] did not find the superoxo structure shown in Figure 7 for $VO_4$. In their PW91 calculation $VO_4$ always dissociated into $VO_3$ and a surface O species.

As for O-defect formation energies (cf. Table 5), PBE+$U$ yields smaller energies for release of oxygen from a given $VO_n$ surface species. This results in different conclusions about the dominating species under experimentally relevant conditions. Whereas PW91 predicts $VO_3$ to be the dominant species above 500 K at ambient pressure (0.21 atm),[244] PBE+$U$ predicts $VO_2$ as the most stable species around 700 K in a pressure range from $10^{-1}$ to $10^6$ atm.[245]

From analysis of the occupation of V-d states and Ce-f states in the $VO_n$·$CeO_2$ systems ($n$ = 1−4) the striking conclusion has been reached that ceria is the reduced component and stabilizes vanadium always in its highest oxidation state +5. This explains the nearly constant Bader charges found for all surface species[244] that already surprised Shapovalov and Metiu. (Note that the absolute values of Bader charges are not expected to agree with the formal oxidation state.) This means that deposition of vanadium oxide species on ceria leads to a partial reduction of the surface. The vanadium electron configuration in isolated V, VO, and $VO_2$ is $d^3s^2$, $d^3$, and $d^1$, respectively. On formation of the surface species, V is always $d^0$, whereas 5, 3, and 1 $Ce^{3+}$ ions, respectively, can be identified.[151]

This is in agreement with UHV experiments on a $CeO_2(111)$ thin film, in which formation of V═O species as evidenced by IR spectroscopy was accompanied by a Ce 4f XPS peak.[246] It also fits with an earlier PBE+$U$(4.5) calculation on crystalline $CeVO_4$ for which, in agreement with XANES studies,[247] a $Ce^{(+3)}(f^1)V^{(+5)}(d^0)$ electronic structure was found instead of $Ce^{(+4)}(f^0)V^{(+4)}(d^1)$.[248]

As already mentioned in section 2, DFT+$U$ results depend on the choice of the effective $U$ parameter. The only way to ascertain numerical results obtained using the DFT+$U$ approach is careful testing. From the first two rows of Table 19 we gather that the cell size does not have a large influence on $\Delta E_d(^1/_2O_2)$ for the clean and $VO_2$-carrying $CeO_2(111)$ surface. However, upon application of a $U$ parameter for the V 3d states of 2.0 eV, $\Delta E_d(^1/_2O_2)$ increases significantly for $VO_2$·$CeO_2$. This diminishes the difference between $VO_2$·$CeO_2$ and the clean $CeO_2$ surface significantly. Note that for the various $U$ applied $U$(Ce) = 4.5 and $U$(V) = 0 matches the HSE result for the difference between $VO_2$·$CeO_2$ and $CeO_2$ perfectly, but the individual defect formation energies are 0.8 eV too low. Qualitatively, however, the picture does not change: $VO_2/CeO_2$ is always found easier to reduce than the bare ceria surface, see refs 108 , 151, and 156.

The $Ce^{(+3)}(f^1)V^{(+5)}(d^0)$ preference for $VO_n$·$CeO_2$ species is by no means trivial. For example, it is in contrast to the $Ce^{(+4)}(f^0)V^{(+4)}(d^1)$ preference inferred from both of the reduction potentials in aqueous solution (1.3−1.7 eV for $Ce^{(+4)}$ depending on pH and 1.0 eV for $V^{(+5)}$ in $VO_2^+$) and the heats of formation for the bulk oxides.[249] The latter yield endothermicity ($\Delta H_{298}^\circ$ = 1.1−1.3 eV) for the reaction

$$CeO_2 + VO_2 \rightarrow \frac{1}{2}Ce_2O_3 + \frac{1}{2}V_2O_5$$

PBE+$U$(4.5) calculations also show that the above reaction is unfavorable ($\Delta H_0^\circ$ = 0.25 eV), whereas the reaction yielding bulk $Ce(f^1)VO_4$,

$$CeO_2 + VO_2 \rightarrow CeVO_4$$

is strongly exothermic, $\Delta H_0^\circ$ = −1.53 eV.[248] What is different in $CeVO_4$ compared to $Ce_2O_3 + V_2O_5$ is the coordination of the ions and the average distance to the oxygen ligands which determine the splitting and hence the stability of f states with respect to d states.

Additional evidence for the interplay of Ce(f)/V(d) preference and geometric structure comes from gas-phase IR spectroscopy on mixed-metal oxide clusters.[249] For the $CeV_2O_6^+$ species, which can also be written as $(CeVO_4)$-$(V^VO_2)^+$, the same question arises as for crystalline $CeVO_4$: Is the Ce 4f or the V 3d state populated with an electron,

$$Ce^{IV}(f^0)O_2\cdot V^{IV}(d^1)O_2\cdot V^V(d^0)O_2^+ \text{ or } [Ce^{III}(f^1)O]^+\cdot V^V(d^0)_2O_5$$

and does this lead to geometrically different isomers? Figure 8 shows that in the cage-type isomer the electron is preferentially located in Ce f states, whereas in the chain isomer it is located in the V d states. Comparison with the experimental IR photon dissociation spectrum shows unequivocally that the cage isomer is observed, and we may safely conclude that this is the most stable isomer as the DFT calculations predict.

### 5.2. Reactivity

The oxygen-defect formation energy has been used as reactivity parameter (cf. section 3) when discussing the activity of vanadia supported on ceria and other oxides in methanol oxidation.[151,156] The PBE+$U$(4.5) value of 0.79 eV (Table 19) for the most likely monomeric surface species $VO_2$·$CeO_2$ is much lower than the PBE value of 3.91 eV (ref 250) for the most likely monomeric species on a silica support $VO_{2.5}$·$SiO_2$. On both surfaces there is a tetrahedral O═V(O−)$_3$ species, but in the former case an "interphase" O atom (V−O−Ce bond) is removed and two $Ce^{4+}$ ions are reduced to $Ce^{3+}$ ions, whereas on the nonreducible $SiO_2$ support the vanadyl oxygen is removed from the terminal O═V bond, and $V^{5+}$ is reduced to


dx.doi.org/10.1021/cr3004949 | Chem. Rev. 2013, 113, 3949−3985

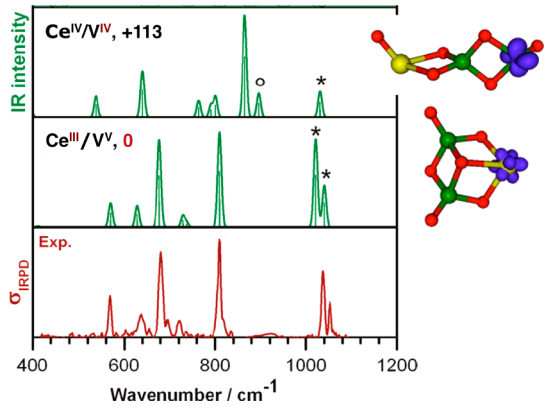


**Figure 8.** Two different $CeV_2O_6^+$ isomers, their relative energies (kJ/mol), and their IR spectra predicted by DFT (B3LYP hybrid functional) and compared to experiment.[249]

$V^{3+}$. This explains the higher activity of ceria-supported catalysts compared to silica- or alumina-supported catalysts in the oxidation of methanol,[239,246,251] ethanol,[183] and propane,[183,252] not only for powder catalysts but also for thin film model catalysts on which temperature-programmed desorption of aldehydes from an alcohol-covered surface has been studied.[156]

The reactivity increase of supported vanadia species when passing from the nonreducible silica or alumina support to the reducible ceria support is rationalized by the ease of accommodating electrons in Ce 4f states. More surprising, however, is the finding that O-defect formation on $VO_2/CeO_2(111)$ species is easier than defect formation on the clean $CeO_2$ surface, see Figure 9 and Table 19. Defect formation is easier in the combined system than in either vanadium oxide or cerium oxide itself. This is not primarily an electronic effect but rather a structure (relaxation) effect. Defect formation energies are almost the same for both cases (0.06 eV difference only) if structure relaxation is not allowed ("unrelaxed" in Figure 9). The relaxation energy is much larger (3.04 eV!) for $VO_2{\cdot}CeO_2(111)$ than for $CeO_2(111)$ (1.98 eV).

Structure relaxation is accompanied by electronic relaxation. For the clean ceria surface, structure relaxation is connected with localization of the two electrons left behind upon O removal on two instead of four Ce ions. In the unrelaxed structure of $VO_2{\cdot}CeO_2(111)$ only one of the two electrons is located on a Ce ion and the other on a vanadium ion (see Figure 9). During relaxation a $V^{IV}(d^1)Ce^{IV}(f^0)$ pair is converted into a $V^{V}(d^0)Ce^{III}(f^1)$ pair. The effect of the local structure on the relative stability of such pairs has already been discussed above. There is a true cooperative effect: Ceria is accommodating the electrons in its 4f states, and vanadia is releasing the oxygen atom, which is more difficult in pure ceria. This is reminiscent of the effect of dopants on O-vacancy formation energies, see section 3. Low-valent dopants lower the defect formation energies because they have already accepted one or two electrons that otherwise would reduce $Ce^{4+}$ to $Ce^{3+}$, whereas inert isovalent dopants like Zr modify the geometric structure and make it easier to release the O atom.

Vanadium oxide species of different size have been identified by STM. This is a very important achievement because for powder catalysts it is usually not possible to distinguish species of different size. The observed direct relationship between the nuclearity of these clusters and their V=O frequency has been reproduced by PBE+$U$(4.5) calculations.[108,139,253]

Figure 10 shows that $VO_2$ supported on ceria becomes less reactive (higher O-defect formation energies, less energy gain on hydrogenation) when the $VO_2$ species get larger, from monomeric to dimeric and trimeric species. However, the more active species were found to be thermodynamically less favored, i.e., there is an inverse proportionality between thermodynamic stability and reactivity (see Figure 10).[139] Due to the stabilization of monomeric species in thin film experiments it was possible to observe an extraordinary increase of the methanol oxidation activity for very low vanadium loading ("$\alpha$ peak" at low desorption temperature).[156,254]

An experimental study by Wu et al.[255] showed that the shape of the ceria support influences the termination, which in turn affects the oxygen-defect formation energy. Rods, terminated mainly by (110) and (100) facets, result in a lower activation energy in the ODH of isobutene than octahedra, terminated mainly by (111) facets.

**Summary.** Depositing vanadium oxides on ceria leads to a high improvement of the catalytic activity in ODH reactions

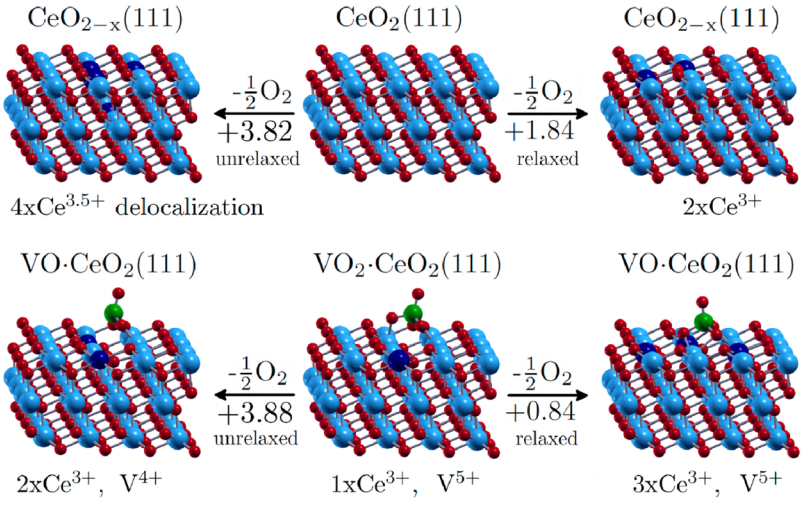


**Figure 9.** O-defect formation energy for $VO_2{\cdot}CeO_2(111)$ compared to $CeO_2(111)$ using a $p(4 \times 4)$ surface unit cell. For results obtained using a $p(2 \times 2)$ cell, see Figure 11 in ref 151.


dx.doi.org/10.1021/cr3004949 | Chem. Rev. 2013, 113, 3949−3985

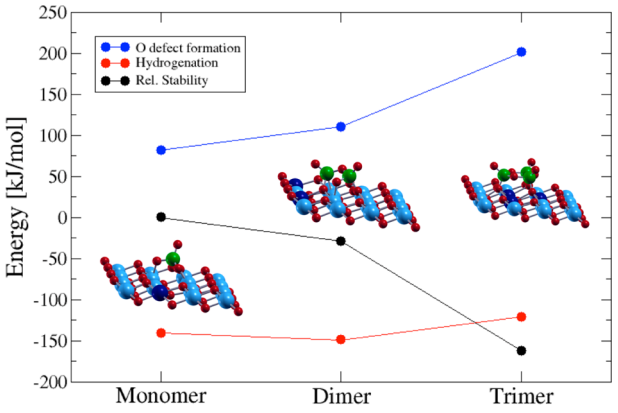


**Figure 10.** Relative stability, O-defect formation energy (with respect to $^1/_2O_2$), and hydrogenation energy (with respect to $^1/_2H_2$) of $VO_2$ aggregates supported on $CeO_2(111)$.[108]

compared to the pure oxides, in particular for the smallest species. Both structural relaxation effects as well as the availability of Ce 4f states in the reduction process contribute to the overall reactivity of this very special support system.

## 6. CERIA AS SUPPORT FOR METALS

Ceria is widely used as support for active metal nanoparticles,[256] even though it is a good catalyst on its own. Deposition of metals on the surface, ranging from single adatoms and small clusters up to monolayers or larger films, is one way to tune the reducibility and thereby the activity of ceria surfaces. The topic of so-called inverse model catalysts, i.e., ceria particles on a metal surface, is not within the scope of this review. We refer the interested reader to articles published by Suchorski et al.[257] on the reactivity of $CeO_x$/Pt(111) toward CO oxidation (experimental study) and Spiel et al.[258] about a ceria monolayer on Pt(111) (calculations use DFT+$U$). Campbell recently commented on the use of the term "strong metal support interaction" to describe the migration of the (ceria) support on the active metal surface.[259] Here we report on computational studies for atoms and small metal clusters and on ceria−metal interfaces.

Due to their flexibility concerning oxidation states, transition metals like Pd, Pt, and Au deposited on the $CeO_2(111)$ surface have been most intensively studied. Nolan[260] did a comprehensive study on metal atoms supported on $CeO_2(110)$. All of the tested metal atoms are oxidized, creating $Ce^{3+}$ and distorting the surface structure. Au, Ag, and Cu transfer one electron, Ga, In, and Fe two electrons, and Al, La, Ce, V, and Cr three electrons.

### 6.1. Au

Gold clusters supported on ceria represent a very special catalytic system that attracts a lot of interest of both theoreticians and experimentalists. A perspective article by Zhang, Michaelides, and Jenkins[261] that appeared early in January 2011 reviews the "theory of gold on ceria" up to 2010. It is based on several original articles of this group of authors.[168,262,263]

**6.1.1. Au Atoms and Clusters.** Table 20 summarizes the findings on which different authors agree for adsorption of a single Au atom on the $CeO_2(111)$ surface. The binding is much stronger at an O-defect site than on the defect-free surface. At the O-defect site an electron is transferred from one of its $Ce^{3+}$ ions to the Au atom, which becomes negatively charged,

**Table 20. Results for a Single Au Atom Adsorbed on a Defect-Free $CeO_2(111)$ Surface and on an O Defect**

| | defect free | O defect |
|---|---|---|
| adsorption energy, eV | 1.15−1.18 | 2.58 |
| site | O−O bridge | O-defect site |
| Bader charge on Au | 0.32−0.34 | −0.6 to −0.62 |
| oxidation state (f occupation) | $Ce^{3+}/Au^+$ | $Ce^{3+}$, $Ce^{4+}/Au^-$ |
| PBE+$U$(5) | Zhang et al. 2008,[264] Hernandez et al. 2009,[265] Branda et al. 2010[266] | |
| PBE+$U$(4.5) | Camellone and Fabris 2009[167] | |

$$[2Ce^{3+}, V_O] + Au \rightarrow [Ce^{3+}, Ce^{4+}, Au^-]$$

This state is electrostatically stabilized because $Au^-$ occupies the position of an $O^{2-}$ ion in the defect-free surface,

$$[2Ce^{4+}, O^{2-}] \rightarrow [Ce^{3+}, Ce^{4+}, Au^-]$$

Evidence comes from the density of states projected onto states with f symmetry, which shows two electrons in f states for the O vacancy and one when Au is filling the vacancy site.[264]

On the defect-free surface, on the contrary, a $Ce^{4+}$ ion accepts an electron from the ad-Au atom, which becomes positively charged,

$$[2Ce^{4+}, O^{2-}] + Au \rightarrow [Ce^{3+}, Ce^{4+}, O^{2-}]Au^+$$

Hernandez et al.[265] have shown that this electron transfer is coupled to the bridging adsorption structure between two surface O ions. $Au^+$ is known to prefer 2-fold coordination.[264] We reiterate that, in general, Bader charges cannot be used to determine the oxidation state unequivocally, but as Table 20 shows they indicate the same trend as the oxidation state derived from f-state occupation.

All of the studies cited so far use PBE+$U$ with $U$ = 5.0 or 4.5 eV. Branda et al.[78,266] examined Au adsorption on the nondefective surface and found a strong dependence of the Au oxidation state on the method. In particular, the relative stability of the $Ce^{4+}/Au$ and $Ce^{3+}/Au^+$ adsorption states depends on the functional (GGA vs LDA), the value of $U$, the lattice parameter of ceria (for which PBE+$U$ yields a much larger value than experiment), and the starting structure. Even the HSE hybrid functional did not provide a definitive answer. Their main conclusion is as follows: "In any case, the very small energy difference between neutral and cationic Au adsorbed at the surface strongly suggests the presence of a statistical distribution of the two species at the most stable adsorption sites of the $CeO_2(111)$ surface as a function of temperature. Thus, practical applications especially at elevated temperature should definitely take into account this unusual and interesting interplay of the $Ce^{3+}/Au^+$ and $Ce^{4+}/Au^0$ states even in the absence of defects on the $CeO_2(111)$ surface.[78]

The next obvious questions to be addressed by computational studies is how larger clusters grow and which structure they have. The abundance of O defects on the $CeO_2(111)$ surface and the stronger binding of Au atoms on defect sites compared to clean surface sites suggest that cluster growth starts on defect sites. Zhang et al.[263] examined clusters up to $Au_{11}$. They were specifically interested in the growth mode and found that multilayer (3D) clusters are more stable than monolayer (2D) clusters. From the data in their Figure 2 one can calculate the energy for adding an isolated Au atom on the surface (not trapped at a defect) to an existing $Au_n$ cluster at an O-defect site,


dx.doi.org/10.1021/cr3004949 | Chem. Rev. 2013, 113, 3949−3985

$$[Ce^{4+}, Ce^{3+}, Au^{-}]Au_{n-1} + [Ce^{4+}, O^{2-}]Au \rightarrow [Ce^{4+}, Ce^{3+}, Au^{-}]Au_n + [Ce^{4+}, O^{2-}]$$

The energy for the above reaction is always negative and, as expected, becomes smaller from $n + 1 = 2$ (−0.39 eV/Au atom) to $n + 1 = 11$ (−0.17 eV/Au atom). This implies an unlimited cluster growth, and the average particle size will be given by the ratio of the number of Au atoms available and the number of O defects at which the clusters can anchor.

The electronic structure of the adsorbed cluster is peculiar because adsorption at the defect site diminishes the number of $Ce^{3+}$ ions from two to one, whereas adsorption of the additional cluster atoms on the surface may result in electron transfer from Au to $Ce^{4+}$ according to

$$[Ce^{4+}, Ce^{3+}, Au^{-}]\cdot[Ce^{3+}]_{m-1}(Au^{+})_{m-1} \times Au_{n-m}$$

yielding a total number of $m$ $Ce^{3+}$ ions for a cluster of $n$ Au atoms. Zhang et al.[263] found 1, 2, 3, 4, and 5 $Ce^{3+}$ ions for $n = 3$, 4, 5, 6−10, and 11 Au atoms, respectively.

For $Au_{13}$ on an O-defect Kim et al.[168] also find electron transfer from Au atoms to cerium ions. The most stable structure is, as expected, 3D, but the 2D structure predicted for the gas-phase $Au_{13}$ cluster may be incorrect due to use of the PBE functional. The binding energy for the $Au_{13}$ cluster increases if more O defects are involved: −3.15 (no defect), −3.35 (one O missing), −3.78 (two O defects), and −4.11 eV (3 O defects in a row).

From gold clusters on thin oxide films[267] and gas-phase gold clusters[268,269] we know that charge affects the cluster structure. This will be also the case on the ceria surface with additional constraints imposed by the adatom−surface binding energy. For anionic gas-phase clusters, the transition from 2D structures to 3D structures occurs at a cluster size of $n = 12$ Au atoms as consistently found by trapped ion electron diffraction and ion mobility studies.[268] GGA functionals such as PBE are found to be biased toward 2D structures, whereas meta-GGAs like TPSS[270] yield results in agreement with the experimental findings and CCSD(T). Whereas for anions $Au_{12}^{-}$ is the largest cluster predicted to be planar by TPSS, for cationic gold it is $Au_8^{+}$. Therefore, it would not come as a surprise if dications or even higher charged cations form 3D species for even smaller cluster sizes. Indeed, gold clusters attached to an oxygen-defect site, which may be considered as $Au_4^{2+}$, $Au_5^{3+}$, $Au_6^{3+}$, and $Au_7^{3+}$ attached to a $[Ce^{3+}, Au^{-}]$ substitution species, are all found to be 3D species. It would be interesting to search for the global minimum structures of these gas-phase polycations. Since $Au^{+}$ is isoelectronic with Pt, comparison of $Au_n$ with $Pt_mAu_{n-m}$ gas-phase clusters[271,272] could provide some insight. Whereas for pure $Au_n$ clusters, 2D structures are found significantly less stable, for $Pt_{n/2}Au_{n/2}$ 2D and 3D structures are about of the same stability (investigated up to $n = 10$ by DFT, PW91 functional). Moreover, Pt and Au atoms are found to segregate in a cluster. This would be compatible with the observation of 3D clusters on the surface and all $Au^{+}$ species in the bottom layer.[168,263]

Our own experience and experience documented in the literature tells us that in redox systems involving ceria, be it an oxygen defect or adsorbed Au atoms, there are many local minima on the potential energy surface and there are many different electronic solutions. Hence, it is very difficult to determine precisely the lowest energy geometric structure of an Au cluster and to find the lowest energy electron distribution, as for example expressed by the number of $Ce^{3+}$ ions for a given cluster size even if a genetic algorithm or another global optimization scheme will be applied. Zhu et al.[273] examined the adsorption of $Au_3$ clusters on the (111), (110), and (100) surfaces of $CeO_2$ by GGA+$U$(5) and calculated binding energies of 1.02, 1.09, and 1.24 eV/atom with respect to the Au trimer in the gas phase. In all three cases, one electron was transferred to ceria converting one $Ce^{4+}$ ion into a $Ce^{3+}$ ion. Different $Ce^{3+}$ sites showed little energy differences.

**6.1.2. Comparison with Au Dopants.** Au atoms can be present not only as adsorbed species but also as dopants as discussed in section 4.2 for $Au^{3+}$ replacing $Ce^{4+}$. Tibiletti et al.[274] suggested that Au clusters nucleate on such Au cations on cerium positions.

Table 21 shows that removing $Ce^{4+}$ and replacing it with $Au^{3+}$ is exoenergetic,

**Table 21. Stability of Au in O-Defect Sites and Ce-Defect Sites[a]**

| | Zhang 2009[275] | Zhang 2008[264] | Camellone and Fabris[167] |
|---|---|---|---|
| surface cell | 4 × 4 | 3 × 5 | 2 × 2 |
| $U$ | 5[b] | 5[b] | 4.5[c] |
| $E_d(^1/_2O_2)$ | 2.23 | 2.26 | 2.15 |
| $E_a$(Au) | −2.28 | −2.42 | −2.29 |
| $E_d(^1/_2O_2) + E_a$(Au) | −0.05[d] | −0.16 | −0.14 |
| $E_d$(Ce) | 4.67 | 4.85 | |
| $E_a$(Au) | −5.97[d] | −5.88 | −5.68 |
| $E_d$(Ce) + $E_a$(Au) | −1.30[d] | −1.02 | |
| $E_a$(no defect) | −1.16[d] | −1.14 | −1.18 |

[a]Defect formation energies, $E_d$, and adsorption energy into the defect site, $E_a$, as well as their sum is given in eV. [b]PW91 xc functional. [c]PBE xc functional. [d]Cohesive energy of gold is used (3.03 eV) to convert the numbers in Table 1 of ref 275 to the usual reference of one Au atom in the gas phase.[276]

$$E_d(Ce) + E_a(Au) < 0$$

and that Au adsorption on the nondefective surface is only a few tenths of electronvolts more favorable. In contrast, creating an O defect and filling it with a Au atom,

$$E_d\left(\frac{1}{2}O_2\right) + E_a(Au) < 0$$

is about 1 eV less favorable. What is more stable under real conditions depends on the thermodynamic conditions, i.e., temperature, activity of Au, oxygen partial pressure. Zhang et al. used PW91+$U$ to calculate the thermodynamic stability.[275] They found that at oxygen chemical potentials typical for water−gas shift conditions Au adsorbed in a (created) O vacancy is more stable than on the clean surface, whereas it is significantly less stable when adsorbed in a created $Ce^{4+}$ site. This, however, does not say anything about the kinetic stability of an Au dopant prepared under different conditions.

**6.1.3. CO Oxidation on Au/$CeO_2$.** Table 22 shows results for the interaction of CO with Au on the $CeO_2$(111) surface. A single Au atom on the defect-free $CeO_2$(111) surface binds CO very strongly, and the energy for O-vacancy formation is less than one-half of that for a clean $CeO_2$ surface. This is due to a very special structure of the $O^{2-}CeO_2$−Au−CO complex.[167] The final structure is an Au atom adsorbed into the O-vacancy site, whose stability prevents further reactions with CO.


dx.doi.org/10.1021/cr3004949 | Chem. Rev. 2013, 113, 3949−3985

Table 22. Defect Formation Energies, $\Delta E_d(^1/_2O_2)$, Binding Energies, $\Delta E_a$, and Reaction Energies, $\Delta E_r$, for Interaction of CO with Different Gold Species on the $CeO_2(111)$ Surface[a]

| | | $\Delta E_d(^1/_2O_2)$ | $-\Delta E_a$, CO | $\Delta E^{\ddagger}_{int}$ | $-\Delta E_a$, $CO_2$ | $-\Delta E_r$, $CO_2$(g)+$V_O$ | $-\Delta E_r$,[b] eq 4.2 | |
|---|---|---|---|---|---|---|---|---|
| | | a | b | | c | d | e | ref |
| $CeO_2$ | PBE+$U$(4.5) | 2.15 | | | | (0.78) | | 2009, Camellone[167] |
| $Au/CeO_2$ | | 1.04[c] | 2.48 | 0.86[d] | 2.24 | 2.50 | 3.54[e] | |
| $Au_{13}/CeO_2$ | PBE+$U$(5) | (2.06)[f] | 1.28 | 0.47 | 2.14 | 0.87 | | 2011, Kim[168] |
| $Au_{13}/3V_O,CeO_2$ | | (2.32)[f] | 1.13 | 0.01 | 2.78 | 0.61 | | |
| $Au_{13}/CeO_2,O_2-V_O$[g] | | (1.10)[f] | 0.98 | 0.22 | 1.63 | 3.46 | | |
| $O_2-Au_{13}/3V_O,CeO_2$ | | (0.60)[f] | 0.90 | 0.08 | 2.55 | 2.33 | | |
| $Au_{13}/3V_O,CeO_2,O_2-V_O$[g] | | (−0.40)[f] | 0.87 | 0.32 | 3.86 | 3.33 | | |
| $O_2{\cdot}Au_{13}/CeO_2$[h] | | (−0.33)[f] | 1.05 | 0.14 | 3.25 | 3.26 | | |
| $O_2{\cdot}Au_{13}/3\ V_O,CeO_2$[h] | | (−0.27)[f] | 1.18 | 0.33 | 3.30 | 3.20 | | |

[a] $\Delta E^{\ddagger}_{int}$ is the (intrinsic) barrier for $CO_2$ formation from adsorbed CO. Energies given in eV. [b] Experimental value: 2.93 eV. [c] From Table 1 of ref 167. [d] CO "spillover" from on-top Au onto $CeO_2$. [e] From Figure 8 of ref 167. [f] Estimated from the experimental gas-phase reaction energy for CO + $^1/_2O_2$ → $CO_2$; (column e, −2.93 eV) and column d. [g] Second half of CO oxidation according to a Mars−van Krevelen mechanism [h] Coadsorption of CO and $O_2$ on the $Au_{13}$ adcluster

However, ref 167 does not consider reoxidation by $O_2$ and a second CO oxidation step as Kim et al.[168] did for the $Au_{13}$ adcluster. Binding of CO on the latter is only one-half as strong as on a single Au adatom.

Kim et al. examine different scenarios for two different catalyst models: $Au_{13}$ on a defect-free $CeO_2(111)$ surface and on a linear trimer of O defects (3 $V_O$). For these catalysts a Mars−van-Krevelen-type mechanism (first CO oxidation, reoxidation with $O_2$, second CO oxidation) is compared with coadsorption of CO and $O_2$ on the $Au_{13}$ adcluster. Adsorption of $O_2$ at a Au−$Ce^{3+}$ bridge site at the rim of the adcluster is also considered, but $O_2$ adsorption is weaker (0.62 eV) than on an O-vacancy site next to the cluster (2.58 eV). Figure 5 (bottom) compares the catalytic cycle for CO oxidation by $Au_{13}/CeO_2(111)$ with the one for Au-doped ceria.

Figure 11 shows a generic reaction energy diagram. The first step of the Mars−van-Krevelen mechanism, releasing $CO_2$ into the gas phase and forming the O vacancy, is endothermic. If further oxygen species are added, e.g., for the second Mars−van-Krevelen oxidation step (after reoxidation of the surface), the reaction is exothermic or thermoneutral.

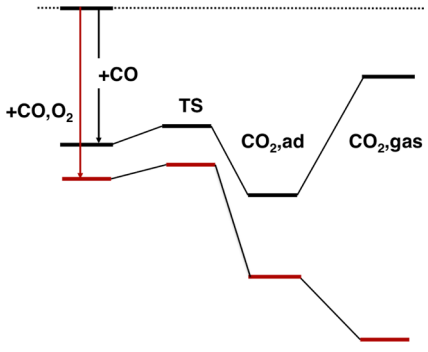


**Figure 11.** Reaction energy diagram for CO oxidation on different Au/$CeO_2(111)$ species.

Intrinsic reaction barriers for converting adsorbed CO into $CO_2$ surface species are small. For the first step of the Mars−van Krevelen mechanism, desorbing $CO_2$ is energetically more difficult. For all other cases the intrinsic barriers do not exceed 0.33 eV, whereas apparent barriers are all significantly below zero, which means that the surface concentration of the different species involved becomes important. For comparison with experiment, microkinetic simulations become mandatory.

According to the PBE+$U$(4.5/5) calculations listed in Table 22 the overall reaction is always exothermic. However, O-defect formation energies calculated with PBE+$U$(4.5/5) may be about 1.8 eV too low, see sections 2.2 and 3.4. This means that the whole energy diagram may change, and realistic results cannot be expected from a simulation using PBE+$U$ energies as input for elementary steps.

**6.1.4. Summary.** Au clusters when supported on $CeO_2$ are oxidized and $CeO_2$ is reduced,[261] i.e., $Ce^{4+}$ ions are converted into $Ce^{3+}$ ions. However, when a Au atom fills an O vacancy it attracts an electron from one of the two $Ce^{3+}$ ions,[261] which can also be understood as substitution of $Ce^{4+}/O^{2-}$ by $Ce^{3+}/Au^-$. For Au clusters anchored on O vacancies, this leads to varying net charge transfer. Multilayer 3D structures are found to be preferred over 2D monolayers. Replacing Ce with Au also appears to be thermodynamically favorable. Relevant to the water−gas shift reaction, adsorption of Au activates ceria toward CO oxidation. However, the reaction energies obtained by DFT+$U$ are affected by significantly (1.4 eV) underestimated defect formation energies.

## 6.2. Ag and Cu

When comparing adsorption of different coinage metals on $CeO_2(111)$ using three different DFT+$U$ approaches, Branda et al.[266] could firmly establish the sequence Cu > Ag > Au for the adsorption energy. Because of the lower ionization potentials, Cu and Ag are found to be always oxidized, whereas the oxidation state of Au remained uncertain in their previous study.[78] Two of the three methods used LDA+$U$(5) to optimize both lattice parameters and fractional coordinates, whereas the energies and properties were calculated with PBE+$U$(3) or LDA+$U$(5). This was compared with PBE+$U$(5) throughout including optimization of lattice parameters and fractional coordinates.

In a combined experimental and theoretical study Luches et al.[277] observed a reduction of Ce after Ag deposition (formation of $Ce^{3+}$ ions) and discuss two possible mechanisms. According to their PW91+$U$(3−4) results (structures have been optimized with PW91+$U$(5)) for $Ag_5$ and $Ag_{10}$ clusters on (3 × 3) and (4 × 4) surface cells, direct electron transfer from Ag to Ce is favorable compared to oxygen reverse spillover from the support to the Ag nanoparticle. In addition, the latter


dx.doi.org/10.1021/cr3004949 | Chem. Rev. 2013, 113, 3949−3985

is not predicted to depend on the particle size, in contrast to the experimental finding of increasing $Ce^{3+}$ concentration with larger particle size.

Yang et al.[278] investigated the growth of small $Cu_n$ clusters ($n$ = 1−4) on $CeO_2(111)$ and water dissociation on the $Cu_4/CeO_2(111)$ catalyst. The competition between the Cu−O and the Cu−Cu interactions, which are of comparable strength, affects the structure of the cluster. The observed charge transfer from Cu 3d and 4s states to Ce 4f states (for the $Cu_4$ cluster, two cerium ions become $Ce^{3+}$) increases the electrostatic interaction between Cu sites and $H_2O$ compared to unsupported $Cu_4$. This in turn leads to a small $H_2O$ dissociation barrier on the catalyst, with Cu/O interface sites as the active centers. The authors conclude that the ceria support not only acts as electron acceptor and donor to activate Cu but also participates in the dissociation reaction at the Cu/O interface.

Szabová et al.[279] performed calculations on the Cu/ceria system, investigating supported Cu adatoms, solid solutions with Cu as substitutional point defect, and the $Cu(111)/CeO_2(111)$ interface. While incorporation of Cu into the ceria surface does not lead to the presence of reduced Ce atoms, they occur in the other two cases, with a complete reduction of the ceria trilayer at the interface.

### 6.3. Pt, Pd, and Rh Clusters

Heyden and co-workers[280] studied $Pt_n$ clusters ($n$ = 1−10) on stoichiometric and partially reduced ceria using DFT+$U$ and a 4 × 4 surface unit cell. They found a cubic-close metal packing for $Pt_{10}$ and identified (111) facets on the cluster, which is the most stable Pt surface. Their results indicated an increased reducibility of ceria in the presence of adsorbed Pt. This is illustrated in Table 23, which compares the oxygen-defect formation energies of a single Pt adatom with the defect formation energy of the $Pt_{10}$ cluster. Furthermore, they evaluated the stability of various phases by a constrained ab initio thermodynamic simulation. Furthermore, they studied the interaction of the catalyst with oxygen and hydrogen atoms as well as CO molecules, since these are the important reactants for the WGS. Under experimentally relevant temperatures and partial pressures, $H_2$ is more likely to adsorb at the three-phase boundary (metal−oxide−gas phase) than CO. The latter, which adsorbs preferably at Pt atoms not in contact with the ceria surface, has little effect on the redox behavior but increases the $H_2$ surface coverage. For smaller clusters ($Pt_4$) studied on a 2 × 2 cell the bridge site was found to be the most stable CO adsorption site.[281] This investigation also included $Pd_4$. Note that a positive charge was found for both metal clusters. However, the local density of states is high enough to donate electrons, and thereby $Pd_4$ or $Pt_4$ activates CO more strongly than the clean ceria surface.

**Table 23. Oxygen-Defect Formation Energies with Respect to $^1/_2$ $O_2$ (eV) for $Pt_n$ Clusters Supported on $CeO_2(111)$ Obtained with PBE+$U$**

| $n$ | cell | $k$ mesh | $U$ | cut off | $E_{def}(^1/_2O_2)$ | ref |
|---|---|---|---|---|---|---|
| 1 | 2 × 2 | 4 × 4 × 1 | 5 | 408 | 1.83 | 283 |
| 1 | 4 × 4 | 2 × 2 × 1 | 5 | 500 | 2.03 | 280 |
| 10 | 4 × 4 | 2 × 2 × 1 | 5 | 500 | 1.59 | 280 |

Vayssilov et al.[282] performed DFT+$U$ calculations on $Pt_8$ on a 3 × 4 surface unit cell as well as $Pt_8$ on a $Ce_{40}O_{80}$ nanoparticle. They found (i) electron transfer from Pt to the ceria support and (ii) transfer of activated oxygen from ceria to Pt. While electron transfer is favorable on both systems, oxygen transfer requires nanostructured ceria. Yang et al. studied the effect of Pt on the reducibility of ceria using a 2 × 2 cell.[283] They relate the lower oxygen vacancy formation energy to partially occupied metal-induced gap states. The reported defect formation energy is given in Table 23.

Platinum clusters on ceria (modeled as $Pt_8$ on a 3 × 4 cell) may also enhance water adsorption and dissociation compared to a pure Pt(111) surface.[284] This is attributed to electronic perturbations, see also ref 259, in particular the much smaller density of Pt 5d states close to the Fermi level of the supported system compared with bulk Pt. Reported experimental results indicate a high catalytic activity toward formation of hydrogen for Pt on a $CeO_x/TiO_2(110)$ mixed-metal oxide system.

Mayernick and Janik[285] evaluated the stability of Pd, $Pd_4$, and $PdO_x$ adsorbed on the (111), (110), and (100) surfaces of ceria using ab initio thermodynamics. Ceria support shifts transitions between formal oxidation states of Pd relative to bulk Pd. Stabilization of individual oxidation states depends on temperature, oxygen partial pressure, and cell potential. The latter is important since the authors model a solid oxide fuel cell. Moreover, different terminations of ceria surfaces stabilize certain oxidized Pd species. A combined experimental and theoretical study on Pd supported on $CeO_{2-x}(111)$ was published by Wilson et al.[286] They found an increase in $Ce^{3+}$ concentration caused by Pd nanoparticles. PW91+$U$(5) calculations confirmed reduction of $Ce^{4+}$ to $Ce^{3+}$ by virtue of the integrated spin density of Ce 4f electrons within the atomic spheres determined by the PAW pseudopotential.

Alfredsson and Catlow[287] studied the properties of Pd and Pt monolayers on $CeO_2(111)$ and on c-$ZrO_2(111)$ and found much higher adsorption energies for Pt than for Pd. According to their results, the electronic structure of the support dictates the geometrical structure of the interface and electrostatics makes the main contribution to the bonding between the metal adlayers and the oxide support. The metal/ceria interfaces have metallic properties due to metal-induced gap states, while the metal/zirconia interfaces feature a small band gap.

Loffreda and Delbecq[288] studied the growth of a multilayered Pt film on $CeO_2(111)$. Since Pt−Pt bonds are stronger than Pt−O bonds, the stability decreases in the order 3D films > 2D films > clusters > isolated atoms. Compared to the Pt bulk structure, Pt−Pt distances in the films are shorter to match the ceria lattice. The difference in catalytic activity between the interface and the single-crystal surfaces is attributed to changes in shape and energy in the density of Pt 5d states.

Lu and Yang[289] compared single Pd, Pt, and Rh adatoms with corresponding four-membered clusters deposited on a 2 × 2 $CeO_2(111)$ cell. Calculated adsorption energies obtained using PBE+$U$(5) were maximal for Rh (3.72 eV), followed by Pt (2.91 eV), while the energy was found to be smallest for Pd (1.78 eV). Bader-type charge analysis showed that charge transfer from the metal to cerium ions occurs for all of these systems, creating a $Ce^{3+}$ ion. Adsorption energies for $Rh_4$ (4.10 eV), $Pt_4$ (4.06 eV), and $Pd_4$ (2.47 eV) clusters are systematically larger and follow the same trend as observed for the single adatoms. Bader charges of the three metal atoms binding to the surface were determined to be positive, while the top metal atom is negatively charged. The authors report on formation of one or two $Ce^{3+}$ ions. For the Rh system, they stated a dependence of electron localization, energetic, and


dx.doi.org/10.1021/cr3004949 | Chem. Rev. 2013, 113, 3949−3985

structural properties on the value of *U*, while (Bader) charges appear to be rather insensitive.

Chen et al.[290] studied the $Rh_4/CeO_2(111)$ system in the context of the water−gas shift reaction. According to this work, formation of a cluster is favored compared to separate Rh adatoms. CO and $H_2O$ adsorb preferably on top of one of the Rh atoms. The authors suggest that the carboxyl mechanism is the predominant process among the possible reaction pathways (cf. section 7). All intermediates and transition structures found in this work are below the energy reference ($CO(g) + H_2O(g)$ + clean ceria surface). Therefore, the authors suggest that the reactions run without thermal activation.

### 6.4. Other Metals

Nolan et al.[291] reported experimental and computational results on Mg supported on $CeO_2(111)$. While adsorption leads to creation of $Ce^{3+}$, incorporation at a Ce site leads to spontaneous oxygen-vacancy formation. In addition, formation of a catalytically active second oxygen vacancy requires less energy than vacancy formation at the clean ceria surface. The authors performed corresponding calculations for the (110) surface and obtained results that suggest a similar behavior for Mg.

Zhao et al.[292] studied Sn on $CeO_2(111)$. Adsorption of this metal leads to an electron transfer to Ce and a partial activation of surface O. In addition, the strong Sn−ceria interaction facilitates CO adsorption.

Chafi, Keghouche, and Minot[293] investigated the influence of Ni atoms on bulk ceria as well as (111) and (110) surfaces. Insertion of Ni into the ceria lattice has a reaction energy that is similar to that of adsorption on the surface. The authors of the aforementioned work suggest that formation of an alloy is possible after insertion due to the low Ni−Ce distance. The interaction between Ni and ceria is stronger for the (110) compared with the (111) surface.

## 7. CERIA-BASED CATALYSTS AND CATALYTIC REACTIONS

This section deals with DFT simulations on the following chemical processes: (i) water−gas shift reaction,[294−296] (ii) selective reduction of $NO_x$ with $NH_3$,[297] and (iii) methanation of $CO_2$.[298] Desulfurization reactions have been discussed in section 4.4. They are important for gasification of biomass to syngas, from which $H_2S$ needs to be removed before further processing to avoid potential poisoning of catalysts and $SO_x$ production.

### 7.1. Water−Gas Shift Reaction

During the past 15 years the water−gas shift (WGS) reaction has attracted much interest of both theorists as well as experimentalists since it offers a way to produce hydrogen from carbon monoxide and water according to

$$CO + H_2O \rightarrow H_2 + CO_2 \quad (7.1)$$

Technologically important, eq 7.1 offers a way to remove traces of CO in the $H_2$-rich feed gas for polymer electrolyte membrane fuel cells, which would poison the Pt catalyst otherwise. Chen et al. examined two of the predominantly discussed reaction mechanisms for the WGS reaction, namely, the redox and formate mechanism on $Au/CeO_2$.[296] Therein, the redox mechanism on $Au/CeO_2(111)$ is discussed in terms of the following elementary steps

$$CO(g) + \bullet_{Me} \rightarrow CO_{Me} \quad (7.2)$$

$$H_2O(g) + V_O \rightarrow H_2O_V \quad (7.3)$$

$$H_2O_V + \bullet_{Me} \rightarrow OH_V + H_{Me} \quad (7.4)$$

$$CO_{Me} + O_V \rightarrow CO_2(g) + V_O + \bullet_{Me} \quad (7.5)$$

$$H_{Me} + OH_V \rightarrow H_2(g) + O_V + \bullet_{Me} \quad (7.6)$$

$$H_{Me} + H_{Me} \rightarrow H_2(g) + 2\bullet_{Me} \quad (7.7)$$

where $\bullet_{Me}$ indicates a free adsorption site on the metal cluster and $V_O$ represents an O vacancy in the oxide. Note that in eqs 7.2−7.7 a subscript generally refers to the corresponding adsorption site.

Two interesting reaction channels for H formation and O reproduction have been studied in ref 296 and follow

$$OH_V + \bullet_{Me} \rightarrow H_{Me} + O_V \quad (7.8)$$

$$OH_V + OH_V \rightarrow H_2(g) + 2O_V \quad (7.9)$$

Key steps in the redox mechanism outlined above are (i) dissociation of the water molecule (eq 7.4) and (ii) breaking of the OH bond (eqs 7.6, 7.8, and 7.9; cf. Figure 12). OH

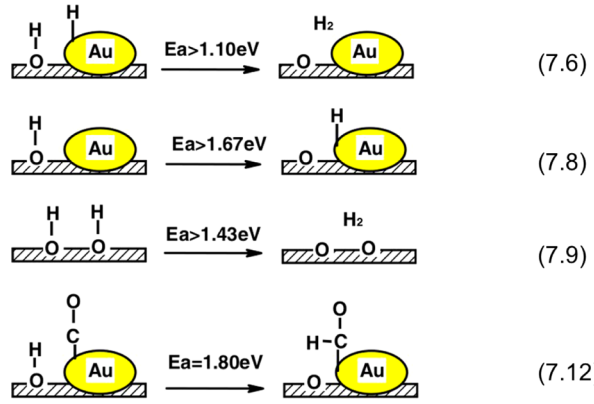


**Figure 12.** To regenerate surface oxygen from water, the corresponding OH group needs to dissociate. Potential steps involve activation energies significantly larger than 1 eV. Reprinted with permission from ref 296. Copyright 2008 Elsevier.

dissociation restores the surface oxygen needed to oxidize CO to $CO_2$. The formate mechanism can be denoted as follows

$$CO + HO_{ad}-CeO_{2-x} \rightarrow HCOO_{ad}-CeO_{2-x} \quad (7.10)$$

$$HCOO_{ad}-CeO_{2-x} + H_2O \rightarrow HO_{ad}-CeO_{2-x} + CO_2 + H_2 \quad (7.11)$$

Note that these reactions do not represent elementary steps; instead, as described in ref 296, the reaction circle for the formate mechanism consists of the following.

(i) Water adsorbs at the oxygen vacancy near a Au cluster under concomitant dissociation to OH and H.
(ii) Subsequently, CO adsorbs on Au or atop a surface oxygen.
(iii) Formate is created via two main channels: (a) CO insertion into OH and (b) adsorbed CO reacts with OH or $H_2O$.
(iv) Decomposition of the formate to $CO_2$.
(v) Au-adsorbed H atoms pair up to form $H_2$.


dx.doi.org/10.1021/cr3004949 | Chem. Rev. 2013, 113, 3949−3985

The pathway for formate formation is still a matter of debate. Chen et al. emphasize the following elementary steps

$$OH_V + CO_{Me} \rightarrow HCO_{Me} + O_V \quad (7.12)$$

$$HCO_{Me} + O_V \rightarrow HCOO_V + \bullet_{Me} \quad (7.13)$$

The work of Chen et al. substantiates important criticism about the redox and formate mechanism. The key step in both is oxygen regeneration on the ceria surface. Concerning the redox mechanism, surface oxygen atoms are responsible for CO oxidation to $CO_2$ (eq 7.5), whereas in the formate mechanism the surface O adsorbs CHO to form formate (eq 7.13).

As shown in Figure 12, to regenerate surface oxygen from water the corresponding OH needs to dissociate. Potential steps involve activation energies significantly larger than 1 eV (after Chen et al., ref 296); thus, OH cannot easily dissociate. They correctly concluded that a low rate for oxygen regeneration will limit CO oxidation as well as formation of formate. This is an important finding and constructively contributes to the debate on the WGS mechanism.

Although "inverse" catalysts with exposed oxide nanoparticles on metallic surfaces are beyond the scope of this review, we mention two studies[299,300] that demonstrate the pronounced ability of $CeO_x$/Cu(111) to oxidize CO even at low temperatures, where pure (and rather expensive) noble metals like, e.g., Rh(111), Pd(110), or Pt(100) are hardly active. DFT calculations could unravel this high activity by elucidating the unique reduction/oxidation properties of $CeO_x$ deposited on the copper surface.

### 7.2. Selective Reduction of $NO_x$ with $NH_3$

Selective reduction of $NO_x$ is important for its removal from diesel exhaust and coal power plants. For this purpose, a $CeO_2$–$WO_3$ catalyst has been shown to perform with high activity for selective catalytic reduction and to benefit from a high $N_2$ selectivity and $SO_2$ durability at medium temperatures between 250 and 350 °C.[297] However, Peng et al. point out that for this catalyst improvements below 200 °C are still needed. Therefore, they investigated the Mn-doped $CeO_2$–$WO_3$ catalyst by experimental as well as theoretical means.[297] However, we have to underline that the aforementioned authors applied the conventional PBE functional to describe, e.g., formation of O vacancies in $CeO_2$(110). Unfortunately, the remainder of models for the investigated systems are not unequivocally defined by Peng et al., rendering analysis of discrepancies compared to the literature difficult, e.g., they find an oxygen-vacancy formation energy, $E_{def}(^1/_2O_2)$, of 3.14 eV for the surface vacancy in $CeO_2$(110), which is in stark contrast to the work by Scanlon et al.[192] [1.61 eV, PBE+$U$(5)] and Fabris et al.[76] [1.57 eV, PBE+$U$(4.5)].

### 7.3. Methanation of $CO_2$

We briefly mention the findings of Sharma et al., who studied $CO_2$ methanation on Ru-doped ceria.[298] Reaction of interest reads as

$$CO_2 + 4H_2 \rightarrow CH_4 + 2H_2O \quad (7.14)$$

Equation 7.14 is technologically of great relevance, since it enables conversion of hydrogen to methane, which is easy to store and can be efficiently transported in conventional pipelines. The latter is very involved or even impossible in the case of $H_2$. Computationally, a rather established approach, namely, PAW employing the LDA+$U$(5.5) method, was used. A $p(3 \times 3)$ surface unit cell together with a $2 \times 2 \times 1$ $k$-point mesh and a 400 eV plane wave cutoff was employed. The results show that $Ce_{1-x}Ru_xO_2$ accommodates the minimum energy structure when Ru is located in the second Ce layer in the slab model for $CeO_2$(111). As a consequence, assuming Ru is close to chemical equilibrium, it segregates at the surface. Furthermore, CO binding at the defective Ru-doped ceria surface was investigated with the aim in mind to rationalize an IR frequency of approximately 2000 $cm^{-1}$ as observed in experiment. Although favorable binding of CO was found ($\Delta E_r$ = −3.41 eV relative to the gas-phase molecule and the defective $Ce_{1-x}Ru_xO_2$ surface), corresponding harmonic frequencies (1476 and 1276 $cm^{-1}$ for symmetric and antisymmetric O−C−O stretching modes, respectively) obtained using LDA+$U$ are significantly different compared with observed ones. Therefore, CO as an intermediate in the methanation reaction could be safely excluded.

## 8. CONCLUSIONS

On formation of an oxygen vacancy in ceria, the two electrons left behind localize on two cerium ions, reducing them from $Ce^{4+}$ to $Ce^{3+}$.[150] Oxygen-vacancy defects are therefore characterized by three points in the structure: the missing oxygen site and the two $Ce^{3+}$ sites. Probing the oxygen lattice (occupied states), STM has identified the missing oxygen site and, supported by DFT calculations, shown that vacancy formation is connected with substantial structure relaxation (Figure 2). Probing the cerium lattice (unoccupied states) with STM, $Ce^{3+}$ ions were not visible, but DFT calculations showed that $Ce^{4+}$ ions surrounding an O vacancy will appear brighter than $Ce^{4+}$ ions away from the surface vacancy.[10] The conclusion has been reached that both or at least one of the $Ce^{3+}$ ions is not neighboring the O-vacancy site. The existence of multiple configurations of $Ce^{3+}$ ions has been predicted before by DFT[89] and confirmed by tunneling spectroscopy (STS), which provided evidence for $Ce^{3+}$ ions in different coordination environments.[10]

Defect formation energies are not precisely known from experiment. The best estimate from different sources[2,130] is 4.2 ± 0.3 eV, which is close to the best estimate of the heat of reduction of bulk $CeO_2$ to bulk $Ce_2O_3$, 4.0 eV.[83]

Dopants can facilitate defect formation in different ways. Lattice relaxation substantially reduces the defect formation energy as predicted by DFT[151] by as much as 2–2.9 eV (Figure 9).[139] This explains the finding (DFT) that an isovalent redox-inert dopant like $Zr^{4+}$, due to its different (smaller) size, can lower the defect formation energy by 0.5–0.8 eV.[180,191] Doping with trivalent metal cations, e.g., $La^{3+}$, creates an oxygen radical anion species, $O^{\bullet-}$, i.e., an electron hole in the highest occupied states, which will accept one of the two electrons on O-vacancy formation, and only one $Ce^{3+}$ species is formed. Hu and Metiu[180] discussed the different possibilities in terms of local and global effects.

Density functional theory needs hybrid functionals that include some Fock exchange such as PBE0 or HSE to get the proper localization of the two electrons left behind on O-vacancy formation along with the corresponding structure distortion. Hybrid functionals underestimate the heat of reduction by 0.9 eV (Table 1) and, judged on bulk defects for large enough cells, the defect formation energy by 0.5 eV (Table 7). Given the uncertainty of the experimental value this calls for application of improved quantum chemical methods.

Hybrid functionals are computationally very demanding, and such calculations on ceria can be completed only as


dx.doi.org/10.1021/cr3004949 | Chem. Rev. 2013, 113, 3949–3985

benchmarks in a few cases. The localization problem of the standard functionals for large-scale solid state applications ("generalized gradient approximation") is rectified in the DFT +$U$ approach without a noticeable increase in computational expense. However, as far as energy is concerned, DFT+$U$ is far less satisfactory. The heat of reduction is 1.7 eV too low (Table 1), and (bulk) defect formation energies are 1.4 eV lower than experiment (Tables 4 and 7).

The largest share of DFT calculations researched for this review used DFT+$U$, and valuable insight into many problems has been gained. However, there are two problems one has to be aware of:

(i) The energy diagrams for catalytic reactions of ceria will be too exothermic when ceria is reduced and too endothermic when ceria is reoxidized. For the example of CO oxidation by $CeO_2$, the experimental estimate for the heat of reaction is +1.2 eV, whereas the PBE+$U$ result is −0.4 eV (Table 11). This large energy difference will also affect barrier heights.

(ii) For a vacancy in $CeO_2$ there are many different possibilities—surface, subsurface, bulk—all with different configurations of the $Ce^{3+}$ ions, but there are also many different ways of performing the calculation—cell/surface cell size, number of $k$ points, value of the effective $U$ parameter, etc. Even for a given set of parameters it is not easy to converge the electronic solution (localization of electrons at a certain site) and reach the global minimum structure in configurational space since the latter two are closely coupled. Very often one will end up with a solution that is not the lowest energy solution. Needless to say, even more possibilities exist when dopants are involved.

On one hand, this explains the differences between different calculations on the same problem in the literature and in this review because really converged calculations are difficult to achieve and rarely available. On the other hand, this tells us something about the nature of O vacancies in ceria; there are many different minima within a narrow energy range which may play a role when finite temperatures and gas pressures are taken into account.

For $H_2O$ adsorption on the nondefective $CeO_2(111)$ surface we conclude that the potential energy surface has been insufficiently explored for loadings up to one monolayer, and there is currently no explanation for the observed[215] two distinct adsorption states with about 30−40 kJ/mol difference in binding energies. On the contrary, there is no doubt that $H_2O$ molecules strongly and dissociatively bind on O-vacancy sites.[119,160,218] The predicted desorption temperature of 650 K fits to the observation that some hydroxyl groups stay on the $CeO_2(111)$ surface up to high temperatures.[217] Reactions following $H_2S$ adsorption can lead to a reduction of the $CeO_2$ surface, but the two PBE+$U$ studies[119,226] have not yet lead to converged results, most likely due to the multiminima problem mentioned above.

When $CeO_2$ is used as support for small vanadium oxide species the latter are always stabilized in their highest oxidation state because the Ce-$f^1$/V-$d^0$ electron configuration is more stable than the Ce-$f^0$/V-$d^1$ configuration.[151,246] O-defect formation on $VO_2/CeO_2(111)$ species is easier than defect formation on either vanadium oxide or cerium oxide itself, which primarily is a structure (relaxation) effect.[151] This explains the observed high activity in the oxidative dehydrogenation of alcohols by vanadia supported on ceria compared to other (nonreducible) supports.[156,254]

When $CeO_2$ serves as support for metal clusters, frequently the metal cluster is oxidized and $CeO_2$ is reduced,[260] i.e., $Ce^{4+}$ ions are converted into $Ce^{3+}$ ions. This is also true for Au clusters.[261] However, when a Au atom fills an O vacancy, it attracts an electron from one of the two $Ce^{3+}$ ions,[261] which can also be understood as substitution of $Ce^{4+}/O^{2-}$ by $Ce^{3+}/Au^-$. For Au clusters anchored on O vacancies, this leads to varying net charge transfer. More calculations are needed to clarify how this affects the structure of the Au clusters on the $CeO_2(111)$ surface with defects.[168,263]

## AUTHOR INFORMATION

### Corresponding Author

*E-mail: js@chemie.hu-berlin.de.

### Notes

The authors declare no competing financial interest.

### Biographies

Joachim Paier studied Chemistry at the University of Graz, Austria, where he received his Master of Science degree in 2002. He joined the Faculty of Physics (Prof. Dr. Georg Kresse) and the Center for Computational Materials Science at the University of Vienna in 2003. He was awarded his Ph.D. degree in 2008. After a postdoctoral year with Prof. Kresse he joined the group of Prof. Dr. Gustavo E. Scuseria at Rice University, Houston, TX, in 2009. Since 2010 he has been performing research in the group of Prof. Dr. Joachim Sauer.

Christopher Penschke studied Chemistry at the Humboldt-Universität in Berlin, where he graduated in 2012 and started his Ph.D. studies in the research group of Prof. Dr. Joachim Sauer. His Diploma thesis dealt with structure and reactivity of ceria-supported vanadium oxide

catalysts. His research interests focus on transition metal oxides and rare earth oxides in heterogeneous catalysis.

Joachim Sauer received the Dr. rer. nat. degree in Chemistry from Humboldt University in Berlin in 1974 and the Dr. sc. nat. degree from the Academy of Sciences in (East) Berlin in 1985. Since 1993 he has been Professor of Theoretical Chemistry at Humboldt University in Berlin, and since 2006 he has been an external member of the Fritz Haber Institute (Max Planck Society). He is member of the Berlin-Brandenburg (formerly Prussian) Academy of Sciences, the German National Academy Leopoldina, and the Academia Europaea. His research has explored the application of quantum chemical methods in chemistry, with emphasis on surface science, particularly adsorption and catalysis. He has published more than 300 research papers, notably in the area of modeling the structure and reactivity of transition metal oxide catalysts and zeolites, and he has given more than 330 invited lectures. From 1999 to 2011 he was chairman of the Collaborative Research Center of the German Research Foundation (DFG) "Aggregates of transition metal oxides – Structure, dynamics, reactivity" and is cofounder and principal investigator of the DFG-funded Cluster of Excellence UNICAT in Berlin.

## ACKNOWLEDGMENTS

We would like to thank Javier Fernández Sanz, Stephen Jenkins, Roy Johnston, Allesandro Trovarelli, and Bilge Yildiz for providing us with further details on published results or copies of their papers. The Deutsche Forschungsgemeinschaft (Collaborative Research Centre 546, Center of Excellence UNICAT) and the Fonds der Chemischen Industrie (FCI) are acknowledged for financial support. Grants for compute time at the high-performance compute clusters HLRN operated by The North-German Supercomputing Alliance (Berlin, Hannover) and JUROPA operated by the Supercomputer Centre at the Forschungszentrum Jülich are gratefully acknowledged.

## ACRONYMS

| | |
|---|---|
| BSSE | basis set superposition error |
| B3LYP | Becke 3-parameter hybrid functional |
| CASSCF | complete active space self-consistent field |
| CC | coupled cluster (method) |
| CCSD(T) | coupled cluster including single, double, and perturbative triple substitutions |
| CI | configuration interaction |
| CN | coordination number |
| DFT | density functional theory |
| DOS | density of states |
| FFT | fast Fourier tranformation |
| GGA | generalized gradient approximation |
| GTO | Gaussian-type orbitals |
| HF | Hartree–Fock |
| BHLYP | Becke's half and half hybrid functional using the LYP correlation functional |
| HSE | Heyd–Scuseria–Ernzerhof hybrid functional |
| IR | infrared |
| KS | Kohn and Sham |
| LAPW+LO | linearized augmented plane waves with local orbitals |
| LDA | local density approximation |
| LYP | Lee–Yang–Parr correlation energy functional |
| MCSCF | multiconfiguration self-consistent field |
| meta-GGA | GGA augmented with a term that depends on the kinetic energy density of electrons |
| MP2 | Møller–Plesset perturbation theory to second order |
| NMR | nuclear magnetic resonance |
| ODH | oxidative dehydrogenation |
| PAW | projector-augmented wave method |
| PBC | periodic boundary conditions |
| PBE | Perdew–Burke–Ernzerhof GGA |
| PBE0 | Perdew–Burke–Ernzerhof hybrid functional |
| PDOS | projected density of states |
| PW91 | Perdew–Wang 91 functional |
| QM/MM | quantum mechanics/molecular mechanics (embedding technique) |
| revPBE | revised Perdew–Burke–Ernzerhof GGA after Zhang and Yang |
| rPBE, RPBE | revised PBE corrected for the local Lieb–Oxford bound after Hammer, Hansen, Nørskov |
| SCF | self-consistent field |
| SIE | self-interaction error |
| STM | scanning tunneling microscopy |
| TPSS | meta-GGA after Tao, Perdew, Staroverov, and Scuseria |
| UHV | ultrahigh vacuum |
| US-PP | ultrasoft pseudopotentials |
| WC | Wu–Cohen GGA for exchange |
| WGS | water–gas shift reaction |
| XC | exchange and correlation (energy functional) |

## REFERENCES

(1) Trovarelli, A. *Catalysis by Ceria and Related Materials*; Imperial College Press: London, 2002.
(2) Gorte, R. *AlChE J.* **2010**, *56*, 1126.
(3) Abanades, S.; Legal, A.; Cordier, A.; Peraudeau, G.; Flamant, G.; Julbe, A. *J. Mater. Sci.* **2010**, *45*, 4163.
(4) Ganduglia-Pirovano, V.; Hofmann, A.; Sauer, J. *Surf. Sci. Rep.* **2007**, *62*, 219.
(5) Pacchioni, G. *J. Chem. Phys.* **2008**, *128*, 182505.
(6) Kilner, J. A. *Chem. Lett.* **2008**, *37*, 1012.
(7) Shoko, E.; Smith, M. F.; McKenzie, R. H. *J. Phys. Chem. Solids* **2011**, *72*, 1482.
(8) Ganduglia-Pirovano, M. V.; Da Silva, J. L. F.; Sauer, J. *Phys. Rev. Lett.* **2009**, *102*, 02610101.
(9) Li, H.-Y.; Wang, H.-F.; Gong, X.-Q.; Guo, Y.-L.; Guo, Y.; Lu, G.; Hu, P. *Phys. Rev. B* **2009**, *79*, 193401.
(10) Jerratsch, J. F.; Shao, X.; Nilius, N.; Freund, H.-J.; Popa, C.; Ganduglia-Pirovano, M. V.; Burow, A. M.; Sauer, J. *Phys. Rev. Lett.* **2011**, *106*, 246801.
(11) Migani, A.; Neyman, K. M.; Illas, F.; Bromley, S. T. *J. Chem. Phys.* **2009**, *131*, 064701.
(12) Ashcroft, N. W.; Mermin, N. D. *Solid State Physics*; Saunders College Publishing: Orlando, 1976.

(13) Martin, R. M. *Electronic Structure: Basic Theory and Practical Methods*; Cambridge University Press: New York, 2004.
(14) Perdew, J. P.; Schmidt, K. In *Density Functional Theory and Its Application to Materials*; VanDoren, V., VanAlsenoy, C., Geerlings, P., Eds.; American Institute Physics: Melville, 2001; Vol. *577*.
(15) Leslie, M.; Gillan, M. J. *J. Phys. C: Solid State Phys.* **1985**, *18*, 973.
(16) Makov, G.; Payne, M. C. *Phys. Rev. B* **1995**, *51*, 4014.
(17) Hellman, O.; Skorodumova, N. V.; Simak, S. I. *Phys. Rev. Lett.* **2012**, *108*, 135504.
(18) Sauer, J. *Chem. Rev.* **1989**, *89*, 199.
(19) Sauer, J.; Sierka, M. *J. Comput. Chem.* **2000**, *21*, 1470.
(20) Huang, P.; Carter, E. A. In *Annual Reviews in Physical Chemistry*; Annual Reviews: Palo Alto, 2008; Vol. *59*.
(21) Müller, C.; Hermansson, K. *Surf. Sci.* **2009**, *603*, 3329.
(22) Burow, A. M.; Sierka, M.; Döbler, J.; Sauer, J. *J. Chem. Phys.* **2009**, *130*, 174710.
(23) Herschend, B.; Baudin, M.; Hermansson, K. *Surf. Sci.* **2005**, *599*, 173.
(24) Herschend, B.; Baudin, M.; Hermansson, K. *Chem. Phys.* **2006**, *328*, 345.
(25) Müller, C.; Herschend, B.; Hermansson, K.; Paulus, B. *J. Chem. Phys.* **2008**, *128*, 214701.
(26) Müller, C.; Paulus, B.; Hermansson, K. *Surf. Sci.* **2009**, *603*, 2619.
(27) Herschend, B.; Baudin, M.; Hermansson, K. *J. Chem. Phys.* **2007**, *126*, 234706.
(28) (a) Gennard, S.; Cora, F.; Catlow, C. R. A. *J. Phys. Chem. B* **1999**, *103*, 10158. (b) Voloshina, E.; Paulus, B. *J. Chem. Phys.* **2006**, *124*, No. 234711.
(29) Müller, C.; Freysoldt, C.; Baudin, M.; Hermansson, K. *Chem. Phys.* **2005**, *318*, 180.
(30) Hohenberg, P.; Kohn, W. *Phys. Rev. B* **1964**, *136*, B864.
(31) Kohn, W.; Sham, L. J. *Phys. Rev.* **1965**, *140*, 1133.
(32) Marx, D.; Hutter, J. *Ab initio Molecular Dynamics*; Cambridge University Press: Cambridge, 2009.
(33) Seidl, A.; Gorling, A.; Vogl, P.; Majewski, J. A.; Levy, M. *Phys. Rev. B* **1996**, *53*, 3764.
(34) Goedecker, S. *Rev. Mod. Phys.* **1999**, *71*, 1085.
(35) Becke, A. D. *J. Chem. Phys.* **1993**, *98*, 5648.
(36) Cora, F.; Alfredsson, M.; Mallia, G.; Middlemiss, D. S.; Mackrodt, W. C.; Dovesi, R.; Orlando, R. In *Principles and Applications of Density in Inorganic Chemistry II*; Kaltsoyannis, N., McGrady, J. E., Eds.; Springer-Verlag: Berlin, 2004; Vol. *113*.
(37) Perdew, J. P.; Ruzsinszky, A.; Constantin, L. A.; Sun, J. W.; Csonka, G. I. *J. Chem. Theory Comput.* **2009**, *5*, 902.
(38) Perdew, J. P.; Ruzsinszky, A. *Int. J. Quantum Chem.* **2010**, *110*, 2801.
(39) Kummel, S.; Kronik, L. *Rev. Mod. Phys.* **2008**, *80*, 3.
(40) Janesko, B. G.; Henderson, T. M.; Scuseria, G. E. *Phys. Chem. Chem. Phys.* **2009**, *11*, 443.
(41) Henderson, T. M.; Paier, J.; Scuseria, G. E. *Phys. Status Solidi B: Basic Solid State Phys.* **2011**, *248*, 767.
(42) Kerber, T.; Sierka, M.; Sauer, J. *J. Comput. Chem.* **2008**, *29*, 2088.
(43) Civalleri, B.; Middlemiss, D. S.; Orlando, R.; Wilson, C. C.; Ugliengo, P. *Chem. Phys. Lett.* **2008**, *451*, 287.
(44) Tosoni, S.; Sauer, J. *Phys. Chem. Chem. Phys.* **2010**, *12*, 14330.
(45) Conesa, J. C. *J. Phys. Chem. C* **2010**, *114*, 22718.
(46) Grimme, S. *J. Comput. Chem.* **2006**, *27*, 1787.
(47) Grimme, S.; Antony, J.; Ehrlich, S.; Krieg, H. *J. Chem. Phys.* **2010**, *132*, 154104.
(48) Furche, F. *Phys. Rev. B* **2001**, *64*, 195120.
(49) Ren, X. G.; Rinke, P.; Scheffler, M. *Phys. Rev. B* **2009**, *80*, 045402.
(50) Schimka, L.; Harl, J.; Stroppa, A.; Gruneis, A.; Marsman, M.; Mittendorfer, F.; Kresse, G. *Nat. Mater.* **2010**, *9*, 741.
(51) Mittendorfer, F.; Garhofer, A.; Redinger, J.; Klimes, J.; Harl, J.; Kresse, G. *Phys. Rev. B* **2011**, *84*, 201401.
(52) Göltl, F.; Grüneis, A.; Bucko, T.; Hafner, J. *J. Chem. Phys.* **2012**, *137*, 114111.
(53) Da Silva, J. L. F.; Ganduglia-Pirovano, M. V.; Sauer, J.; Bayer, V.; Kresse, G. *Phys. Rev. B* **2007**, *75*, 045121.
(54) Perdew, J. P.; Zunger, A. *Phys. Rev. B* **1981**, *23*, 5048.
(55) Mori-Sanchez, P.; Cohen, A. J.; Yang, W. T. *Phys. Rev. Lett.* **2008**, *100*, 146401.
(56) Zhao, Y.; Truhlar, D. G. *J. Phys. Chem. A* **2005**, *109*, 5656.
(57) Svelle, S.; Tuma, C.; Rozanska, X.; Kerber, T.; Sauer, J. *J. Am. Chem. Soc.* **2009**, *131*, 816.
(58) Migani, A.; Vayssilov, G. N.; Bromley, S. T.; Illas, F.; Neyman, K. M. *J. Mater. Chem.* **2010**, *20*, 10535.
(59) Anisimov, V. I.; Zaanen, J.; Andersen, O. K. *Phys. Rev. B* **1991**, *44*, 943.
(60) Liechtenstein, A. I.; Anisimov, V. I.; Zaanen, J. *Phys. Rev. B* **1995**, *52*, R5467.
(61) Perdew, J. P.; Ernzerhof, M.; Burke, K. *J. Chem. Phys.* **1996**, *105*, 9982.
(62) Petit, L.; Svane, A.; Szotek, Z.; Temmerman, W. M. *Phys. Rev. B* **2005**, *72*, 205118.
(63) Gerward, L.; Olsen, J. S.; Petit, L.; Vaitheeswaran, G.; Kanchana, V.; Svane, A. *J. Alloys Compd.* **2005**, *400*, 56.
(64) Fabris, S.; de Gironcoli, S.; Baroni, S.; Vicario, G.; Balducci, G. *Phys. Rev. B* **2005**, *71*, 041102.
(65) Kresse, G.; Blaha, P.; Da Silva, J. L. F.; Ganduglia-Pirovano, M. V. *Phys. Rev. B* **2005**, *72*, 237101.
(66) Fabris, S.; de Gironcoli, S.; Baroni, S.; Vicario, G.; Balducci, G. *Phys. Rev. B* **2005**, *72*, 237102.
(67) Castleton, C. W. M.; Kullgren, J.; Hermansson, K. *J. Chem. Phys.* **2007**, *127*, 244704.
(68) Lutfalla, S.; Shapovalov, V.; Bell, A. T. *J. Chem. Theory Comput.* **2011**, *7*, 2218.
(69) Plata, J. J.; Marquez, A. M.; Sanz, J. F. *J. Chem. Phys.* **2012**, *136*, 041101.
(70) Kullgren, J.; Castleton, C. W. M.; Muller, C.; Ramo, D. M.; Hermansson, K. *J. Chem. Phys.* **2010**, *132*, 054110.
(71) Graciani, J.; Marquez, A. M.; Plata, J. J.; Ortega, Y.; Hernandez, N. C.; Meyer, A.; Zicovich-Wilson, C. M.; Sanz, J. F. *J. Chem. Theory Comput.* **2011**, *7*, 56.
(72) Hay, P. J.; Martin, R. L.; Uddin, J.; Scuseria, G. E. *J. Chem. Phys.* **2006**, *125*, 034712.
(73) Huang, M.; Fabris, S. *J. Phys. Chem. C* **2008**, *112*, 8643.
(74) Nolan, M.; Grigoleit, S.; Sayle, D. C.; Parker, S. C.; Watson, G. W. *Surf. Sci.* **2005**, *576*, 217.
(75) Nolan, M. *Chem. Phys. Lett.* **2010**, *499*, 126.
(76) Fabris, S.; Vicario, G.; Balducci, G.; de Gironcoli, S.; Baroni, S. *J. Phys. Chem. B* **2005**, *109*, 22860.
(77) Dudarev, S. L.; Botton, G. A.; Savrasov, S. Y.; Humphreys, C. J.; Sutton, A. P. *Phys. Rev. B* **1998**, *57*, 1505.
(78) Branda, M. M.; Castellani, N. J.; Grau-Crespo, R.; de Leeuw, N. H.; Hernandez, N. C.; Sanz, J. F.; Neyman, K. M.; Illas, F. *J. Chem. Phys.* **2009**, *131*, 094702.
(79) Keating, P. R. L.; Scanlon, D. O.; Morgan, B. J.; Galea, N. M.; Watson, G. W. *J. Phys. Chem. C* **2012**, *116*, 2443.
(80) Paier, J. Personal communication, 2012.
(81) Duclos, S. J.; Vohra, Y. K.; Ruoff, A. L.; Jayaraman, A.; Espinosa, G. P. *Phys. Rev. B* **1988**, *38*, 7755.
(82) Chase, M. W., Jr. *NIST-JANAF Thermochemical Tables*; AIP: New York, 1998.
(83) Zinkevich, M.; Djurovic, D.; Aldinger, F. *Solid State Ionics* **2006**, *177*, 989.
(84) Trovarelli, A. In *Catalysis by Ceria and Related Materials*; Trovarelli, A., Ed.; Imperial College Press: London, 2002.
(85) Morss, L. R. *Handbook on the Physics and Chemistry of Rare Earths*; Elsevier Science: New York, 1994.
(86) Lide, D. R. *CRC Handbook of Chemistry and Physics*, 74th ed.; CRC Press: New York, 1993.
(87) Cordfunke, E. H. P.; Konings, R. J. M. *Thermochim. Acta* **2001**, *375*, 65.

(88) Becke, A. D. *J. Chem. Phys.* **1993**, *98*, 1372.
(89) Adamo, C.; Barone, V. *J. Chem. Phys.* **1999**, *110*, 6158.
(90) Stephens, P. J.; Devlin, F. J.; Chabalowski, C. F.; Frisch, M. J. *J. Phys. Chem.* **1994**, *98*, 11623.
(91) Wu, Z. G.; Cohen, R. E. *Phys. Rev. B* **2006**, *73*, 235116.
(92) Sanz, J. F. 2012.
(93) Weigend, F.; Ahlrichs, R. *Phys. Chem. Chem. Phys.* **2005**, *7*, 3297.
(94) Casadei, M.; Ren, X.; Rinke, P.; Rubio, A.; Scheffler, M. *Phys. Rev. Lett.* **2012**, *109*, 146402.
(95) Ernzerhof, M.; Scuseria, G. E. *J. Chem. Phys.* **1999**, *110*, 5029.
(96) Heyd, J.; Scuseria, G. E.; Ernzerhof, M. *J. Chem. Phys.* **2003**, *118*, 8207.
(97) Heyd, J.; Scuseria, G. E.; Ernzerhof, M. *J. Chem. Phys.* **2006**, *124*, 219906.
(98) Sodupe, M.; Bertran, J.; Rodriguez-Santiago, L.; Baerends, E. J. *J. Phys. Chem. A* **1999**, *103*, 166.
(99) Asmis, K. R.; Santambrogio, G.; Brümmer, M.; Sauer, J. *Angew. Chem.* **2005**, *117*, 3182.
(100) Solans-Monfort, X.; Branchadell, V.; Sodupe, M.; Sierka, M.; Sauer, J. *J. Chem. Phys.* **2004**, *121*, 6034.
(101) Paier, J.; Marsman, M.; Hummer, K.; Kresse, G.; Gerber, I. C.; Angyan, J. G. *J. Chem. Phys.* **2006**, *124*, 154709.
(102) Paier, J.; Marsman, M.; Kresse, G. *J. Chem. Phys.* **2007**, *127*, 024103.
(103) Pisani, C.; Apra, E.; Causa, M. *Int. J. Quantum Chem.* **1990**, *38*, 395.
(104) Daul, C. A.; Ciofini, I.; Bencini, A. In *Reviews of Modern Quantum Chemistry*; Sen, K. D., Ed.; World Scientific, 2002.
(105) Noodleman, L. *J. Chem. Phys.* **1981**, *74*, 5737.
(106) Noodleman, L.; Baerends, E. J. *J. Am. Chem. Soc.* **1984**, *106*, 2316.
(107) Illas, F.; Moreira, I. D. R.; de Graaf, C.; Barone, V. *Theor. Chem. Acc.* **2000**, *104*, 265.
(108) Penschke, C.; Paier, J.; Sauer, J. *J. Phys. Chem. C* **2013**, *117*, 5274.
(109) Schröder, D.; Shaik, S.; Schwarz, H. *Acc. Chem. Res.* **2000**, *33*, 139.
(110) Harvey, J. N. *Phys. Chem. Chem. Phys.* **2007**, *9*, 331.
(111) Mars, P.; van Krevelen, D. W. *Chem. Eng. Sci.* **1954**, *3* (Suppl 1), 41.
(112) Zhou, G.; Shah, P. R.; Montini, T.; Fornasiero, P.; Gorte, R. J. *Surf. Sci.* **2007**, *601*, 2512.
(113) Zhou, G.; Shah, P. R.; Kim, T.; Fornasiero, P.; Gorte, R. J. *Catal. Today* **2007**, *123*, 86.
(114) Skorodumova, N. V.; Baudin, M.; Hermansson, K. *Phys. Rev. B* **2004**, *69*, 075401.
(115) Yang, Z. X.; Woo, T. K.; Baudin, M.; Hermansson, K. *J. Chem. Phys.* **2004**, *120*, 7741.
(116) Nolan, M. *J. Mater. Chem.* **2011**, *21*, 9160.
(117) Fronzi, M.; Soon, A.; Delley, B.; Traversa, E.; Stampfl, C. *J. Chem. Phys.* **2009**, *131*, 104710.
(118) Desaunay, T.; Ringuede, A.; Cassir, M.; Labat, F.; Adamo, C. *Surf. Sci.* **2012**, *606*, 305.
(119) Marrocchelli, D.; Yildiz, B. *J. Phys. Chem. C* **2012**, *116*, 2411.
(120) Raybaud, P.; Hafner, J.; Kresse, G.; Kasztelan, S.; Toulhoat, H. *J. Catal.* **2000**, *189*, 129.
(121) Reuter, K.; Scheffler, M. *Phys. Rev. B* **2001**, *65*, 035406.
(122) Finnis, M. W. *Phys. Status Solidi A* **1998**, *166*, 397.
(123) Sauer, J.; Zahradník, R. *Int. J. Quantum Chem.* **1984**, *26*, 793.
(124) Reuter, K.; Scheffler, M. *Phys. Rev. B* **2002**, 65.
(125) Steele, B. C. H.; Floyd, J. M. *Proc. Br. Ceram. Soc.* **1971**, *19*, 55.
(126) Nolan, M.; Fearon, J. E.; Watson, G. W. *Solid State Ionics* **2006**, *177*, 3069.
(127) Frayret, C.; Villesuzanne, A.; Pouchard, M.; Matar, S. *Int. J. Quantum Chem.* **2005**, *101*, 826.
(128) Andersson, D. A.; Simak, S. I.; Skorodumova, N. V.; Abrikosov, I. A.; Johansson, B. *Proc. Natl. Acad. Sci. U.S.A.* **2006**, *103*, 3518.
(129) Gotte, A.; Spangberg, D.; Hermansson, K.; Baudin, M. *Solid State Ionics* **2007**, *178*, 1421.
(130) Panhans, M. A.; Blumenthal, R. N. *Solid State Ionics* **1993**, *60*, 279.
(131) Tuller, H. L.; Nowick, A. S. *J. Electrochem. Soc.* **1979**, *126*, 209.
(132) Sanz, J. F. P. Personal communication, 2012.
(133) Deskins, N. A.; Dupuis, M. *Phys. Rev. B* **2007**, *75*, 195212.
(134) Mason, M. J. Personal communication, Marquette University, 1979.
(135) Esch, F.; Fabris, S.; Zhou, L.; Montini, T.; Africh, C.; Fornasiero, P.; Comelli, G.; Rosei, R. *Science* **2005**, *309*, 752.
(136) Torbrügge, S.; Reichling, M.; Ishiyama, A.; Morita, S.; Custance, O. *Phys. Rev. Lett.* **2007**, *99*, 07543301.
(137) Sheldon, B. W.; Shenoy, V. B. *Phys. Rev. Lett.* **2011**, *106*, 216104.
(138) Kokalj, A. *Comput. Mater. Sci.* **2003**, *28*, 155.
(139) Paier, J.; Penschke, C.; Sauer, J. In preparation.
(140) Zhang, C.; Michaelides, A.; King, D. A.; Jenkins, S. J. *Phys. Rev. B* **2009**, *79*, 075433.
(141) Loschen, C.; Bromley, S. T.; Neyman, K. M.; Illas, F. *J. Phys. Chem. C* **2007**, *111*, 10142.
(142) Loschen, C.; Migani, A.; Bromley, S. T.; Illas, F.; Neyman, K. M. *Phys. Chem. Chem. Phys.* **2008**, *10*, 5730.
(143) Migani, A.; Vayssilov, G. N.; Bromley, S. T.; Illas, F.; Neyman, K. M. *Chem. Commun.* **2010**, *46*, 5936.
(144) Inerbaev, T. M.; Seal, S.; Masunov, A. E. *J. Mol. Model.* **2010**, *16*, 1617.
(145) Mei, D. H.; Ge, Q. F. *Comput. Theor. Chem.* **2012**, *987*, 25.
(146) Conesa, J. C. *Catal. Today* **2009**, *143*, 315.
(147) Yang, Z. X.; Yu, X. H.; Lu, Z. S.; Li, S. F.; Hermansson, K. *Phys. Lett. A* **2009**, *373*, 2786.
(148) Nolan, M.; Parker, S. C.; Watson, G. W. *Surf. Sci.* **2005**, *595*, 223.
(149) Marzari, N.; Vanderbilt, D. *Phys. Rev. B* **1997**, *56*, 12847.
(150) Skorodumova, N. V.; Simak, S. I.; Lundqvist, B. I.; Abrikosov, I. A.; Johansson, B. *Phys. Rev. Lett.* **2002**, *89*, 166601.
(151) Popa, C.; Ganduglia-Pirovano, M. V.; Sauer, J. *J. Phys. Chem. C* **2011**, *115*, 7399.
(152) Fronzi, M.; Piccinin, S.; Delley, B.; Traversa, E.; Stampfl, C. *Phys. Chem. Chem. Phys.* **2009**, *11*, 9188.
(153) Chafi, Z.; Keghouche, N.; Minot, C. In *Proceedings of the Jmsm 2008 Conference*; Cheikhrouhou, A., Ed.; Elsevier Science Bv: Amsterdam, 2009; Vol. 2.
(154) Chen, H. T.; Choi, Y. M.; Liu, M. L.; Lin, M. C. *ChemPhysChem* **2007**, *8*, 849.
(155) Kwapien, K.; Sierka, M.; Döbler, J.; Sauer, J. *ChemCatChem* **2010**, *2*, 819.
(156) Ganduglia-Pirovano, M. V.; Popa, C.; Sauer, J.; Abbott, H. L.; Uhl, A.; Baron, M.; Stacchiola, D.; Bondarchuk, O.; Shaikhutdinov, S.; Freund, H.-J. *J. Am. Chem. Soc.* **2010**, *132*, 2345.
(157) Tang, W.; Hu, Z. P.; Wang, M. J.; Stucky, G. D.; Metiu, H.; McFarland, E. W. *J. Catal.* **2010**, *273*, 125.
(158) Gordon, W. O.; Xu, Y.; Mullins, D. R.; Overbury, S. H. *Phys. Chem. Chem. Phys.* **2009**, *11*, 11171.
(159) Joshi, A.; Rammohan, A.; Jiang, Y.; Ogunwumi, S. *THEOCHEM: J. Mol. Struct.* **2009**, *912*, 73.
(160) Watkins, M. B.; Foster, A. S.; Shluger, A. L. *J. Phys. Chem. C* **2007**, *111*, 15337.
(161) Pushkarev, V. V.; Kovalchuk, V. I.; d'Itri, J. L. *J. Phys. Chem. B* **2004**, *108*, 5341.
(162) Choi, Y. M.; Abernathy, H.; Chen, H. T.; Lin, M. C.; Liu, M. L. *ChemPhysChem* **2006**, *7*, 1957.
(163) Huang, M.; Fabris, S. *Phys. Rev. B* **2007**, *75*, 081404.
(164) Soria, J.; Martinezarias, A.; Conesa, J. C. *J. Chem. Soc., Faraday Trans.* **1995**, *91*, 1669.
(165) Preda, G.; Migani, A.; Neyman, K. M.; Bromley, S. T.; Illas, F.; Pacchioni, G. *J. Phys. Chem. C* **2011**, *115*, 5817.
(166) Shapovalov, V.; Metiu, H. *J. Catal.* **2007**, *245*, 205.
(167) Camellone, M. F.; Fabris, S. *J. Am. Chem. Soc.* **2009**, *131*, 10473.

(168) Kim, H. Y.; Lee, H. M.; Henkelman, G. *J. Am. Chem. Soc.* **2011**, *134*, 1560.
(169) Preda, G.; Pacchioni, G. *Catal. Today* **2011**, *177*, 31.
(170) Wang, J. H.; Liu, M. L.; Lin, M. C. *Solid State Ionics* **2006**, *177*, 939.
(171) Chen, H. L.; Chang, J. G.; Chen, H. T. *Chem. Phys. Lett.* **2011**, *502*, 169.
(172) Chen, H. T.; Chang, J. G.; Chen, H. L.; Ju, S. P. *J. Comput. Chem.* **2009**, *30*, 2433.
(173) Yang, Z. X.; Luo, G. X.; Lu, Z. S.; Hermansson, K. *J. Chem. Phys.* **2007**, *127*, 074704.
(174) Yang, Z.; Zhansheng, L. A.; Luo, G.; Hermansson, K. *Phys. Lett. A* **2007**, *369*, 132.
(175) Dholabhai, P. P.; Anwar, S.; Adams, J. B.; Crozier, P.; Sharma, R. *J. Solid State Chem.* **2011**, *184*, 811.
(176) Dholabhai, P. P.; Adams, J. B.; Crozier, P.; Sharma, R. *J. Chem. Phys.* **2010**, *132*, 094104.
(177) Dholabhai, P. P.; Adams, J. B.; Crozier, P.; Sharma, R. *Phys. Chem. Chem. Phys.* **2010**, *12*, 7904.
(178) Gupta, A.; Waghmare, U. V.; Hegde, M. S. *Chem. Mater.* **2010**, *22*, 5184.
(179) Nolan, M. *J. Chem. Phys.* **2009**, *130*, 144702.
(180) Hu, Z. P.; Metiu, H. *J. Phys. Chem. C* **2011**, *115*, 17898.
(181) Nolan, M. *J. Phys. Chem. C* **2011**, *115*, 6671.
(182) Binet, C.; Badri, A.; Boutonnet-Kizling, M.; Lavalley, J. C. *Faraday Trans.* **1994**, *90*, 1023.
(183) Khodakov, A.; Olthof, B.; Bell, A. T.; Iglesia, E. *J. Catal.* **1999**, *181*, 205.
(184) Descorme, C.; Madier, Y.; Duprez, D. *J. Catal.* **2000**, *196*, 167.
(185) Berner, U.; Schierbaum, K.; Jones, G.; Wincott, P.; Haq, S.; Thornton, G. *Surf. Sci.* **2000**, *467*, 201.
(186) Bensalem, A.; Bozonverduraz, F.; Delamar, M.; Bugli, G. *Appl. Catal. A: Gen.* **1995**, *121*, 81.
(187) Street, S. C.; Xu, C.; Goodman, D. W. *Annu. Rev. Phys. Chem.* **1997**, *48*, 43.
(188) Yang, Z. X.; Woo, T. K.; Hermansson, K. *Chem. Phys. Lett.* **2004**, *396*, 384.
(189) Nolan, M.; Watson, G. W. *J. Phys. Chem. B* **2006**, *110*, 16600.
(190) Yang, Z. X.; Fu, Z. M.; Zhang, Y. N.; Wu, R. Q. *Catal. Lett.* **2011**, *141*, 78.
(191) Yang, Z. X.; Fu, Z. M.; Wei, Y. W.; Lu, Z. S. *J. Phys. Chem. C* **2008**, *112*, 15341.
(192) Scanlon, D. O.; Galea, N. M.; Morgan, B. J.; Watson, G. W. *J. Phys. Chem. C* **2009**, *113*, 11095.
(193) Nolan, M.; Parker, S. C.; Watson, G. W. *Surf. Sci.* **2006**, *600*, L175.
(194) Nolan, M.; Parker, S. C.; Watson, G. W. *Phys. Chem. Chem. Phys.* **2006**, *8*, 216.
(195) Cundari, T. R.; Stevens, W. J. *J. Chem. Phys.* **1993**, *98*, 5555.
(196) Wachs, I. E. *Catal. Today* **2005**, *100*, 79.
(197) Yang, Z.; Woo, T. K.; Hermansson, K. *J. Chem. Phys.* **2006**, *124*, 224704.
(198) Nolan, M. *J. Phys. Chem. C* **2009**, *113*, 2425.
(199) Chen, H. T. *J. Phys. Chem. C* **2012**, *116*, 6239.
(200) Yang, Z. X.; Wei, Y. W.; Fu, Z. M.; Lu, Z. S.; Hermansson, K. *Surf. Sci.* **2008**, *602*, 1199.
(201) Yeriskin, I.; Nolan, M. *J. Chem. Phys.* **2009**, *131*, 244702.
(202) Yang, Z. X.; He, B. L.; Lu, Z. S.; Hermansson, K. *J. Phys. Chem. C* **2010**, *114*, 4486.
(203) Chen, H. T.; Chang, J. G. *J. Phys. Chem. C* **2011**, *115*, 14745.
(204) Yang, Z. X.; Fu, Z. M.; Wei, Y. W.; Hermansson, K. *Chem. Phys. Lett.* **2008**, *450*, 286.
(205) Nolan, M.; Verdugo, V. S.; Metiu, H. *Surf. Sci.* **2008**, *602*, 2734.
(206) Linstron, P. J.; Mallard, W. G. *NIST Chemistry WebBook*; National Institute of Standards and Technology: Gaithersburg, MD, 2001.
(207) Periodensystem der Elemente nach Fluck und Heumann. Verlagsgesellschaft: Weinheim, 1989.
(208) Yeriskin, I.; Nolan, M. *J. Phys.: Condens. Matter* **2010**, *22*, 135004.
(209) Hammer, B.; Hansen, L. B.; Norskov, J. K. *Phys. Rev. B* **1999**, *59*, 7413.
(210) Zhang, Y. K.; Yang, W. T. *Phys. Rev. Lett.* **1998**, *80*, 890.
(211) Yang, Z. X.; Wang, Q. G.; Wei, S. Y. *Phys. Chem. Chem. Phys.* **2011**, *13*, 9363.
(212) Kumar, S.; Schelling, P. K. *J. Chem. Phys.* **2006**, *125*, 204704.
(213) Fernández-Torre, D.; Kosmider, K.; Carrasco, J.; Ganduglia-Pirovano, M. V.; Pérez, R. *J. Phys. Chem. C* **2012**, *116*, 13584.
(214) Tuma, C.; Sauer, J. *Chem. Phys. Lett.* **2004**, *387*, 388.
(215) Campbell, C. T.; Sellars, J. R. V. *Chem. Rev.* **2013**, submitted for publication.
(216) Henderson, M. A.; Perkins, C. L.; Engelhard, M. H.; Thevuthasan, S.; Peden, C. H. F. *Surf. Sci.* **2003**, *526*, 1.
(217) Matolin, V.; Matolinova, I.; Dvorak, F.; Johanek, V.; Myslivecek, J.; Prince, K. C.; Skala, T.; Stetsovych, O.; Tsud, N.; Vaclavu, M.; Smid, B. *Catal. Today* **2012**, *181*, 124.
(218) Molinari, M.; Parker, S. C.; Sayle, D. C.; Islam, M. S. *J. Phys. Chem. C* **2012**, *116*, 7073.
(219) Wlodarczyk, R.; Sierka, M.; Kwapień, K.; Sauer, J.; Carrasco, E.; Aumer, A.; Gomes, J. F.; Sterrer, M.; Freund, H.-J. *J. Phys. Chem. C* **2011**, *115*, 6764.
(220) Fuente, S.; Branda, M. M.; Illas, F. *Theor. Chem. Acc.* **2012**, *131*, 1190.
(221) Yang, Z. X.; Wang, Q. G.; Wei, S. Y.; Ma, D. W.; Sun, Q. A. *J. Phys. Chem. C* **2010**, *114*, 14891.
(222) Yang, Z. X.; Wang, Q. G.; Wei, S. Y. *Surf. Sci.* **2011**, *605*, 351.
(223) Beste, A.; Mullins, D. R.; Overbury, S. H.; Harrison, R. J. *Surf. Sci.* **2008**, *602*, 162.
(224) Gritschneder, S.; Reichling, M. *Nanotechnology* **2007**, *18*, 044024.
(225) (a) Torbrügge, S.; Custance, O.; Morita, S.; Reichling, M. *J. Phys.: Condens. Matter* **2012**, *24*, 084010. (b) Cotton, F. A.; Wilkinson, G. Advanced Inorganic Chemistry. Interscience Publishers: New York; 1962. (c) Koppenol, W. H.; Liebman, J. F. *J. Phys. Chem.* **1984**, *88*, 99.
(226) Chen, H. T.; Choi, Y. M.; Liu, M. L.; Lin, M. C. *J. Phys. Chem. C* **2007**, *111*, 11117.
(227) Mullins, D. R.; McDonald, T. S. *Surf. Sci.* **2007**, *601*, 4931.
(228) Mayernick, A. D.; Li, R.; Dooley, K. M.; Janik, M. J. *J. Phys. Chem. C* **2011**, *115*, 24178.
(229) Mayernick, A. D.; Janik, M. J. *J. Catal.* **2011**, *278*, 16.
(230) Yang, Z. X.; Woo, T. K.; Hermansson, K. *Surf. Sci.* **2006**, *600*, 4953.
(231) Hu, Z. P.; Metiu, H. *J. Phys. Chem. C* **2012**, *116*, 6664.
(232) Müller, C.; Hermansson, K.; Paulus, B. *Chem. Phys.* **2009**, *362*, 91.
(233) Galea, N. M.; Scanlon, D. O.; Morgan, B. J.; Watson, G. W. *Mol. Simul.* **2009**, *35*, 577.
(234) Nolan, M.; Parker, S. C.; Watson, G. W. *J. Phys. Chem. B* **2006**, *110*, 2256.
(235) Rodriguez, J. A.; Jirsak, T.; Sambasivan, S.; Fischer, D.; Maiti, A. *J. Chem. Phys.* **2000**, *112*, 9929.
(236) Lu, Z. S.; Muller, C.; Yang, Z. X.; Hermansson, K.; Kullgren, J. *J. Chem. Phys.* **2011**, *134*, 184703.
(237) Ichikawa, N.; Sato, S.; Takahashi, R.; Sodesawa, T.; Fujita, H.; Atoguchi, T.; Shiga, A. *J. Catal.* **2006**, *239*, 13.
(238) Wachs, I. E.; Deo, G.; Juskelis, M. V.; Weckhuysen, B. M. In *Dynamics of Surfaces and Reaction Kinetics in Heterogeneous Catalysis*; Froment, G. F., Waugh, K. C., Eds.; Elsevier: Amsterdam, 1997.
(239) Vining, W. C.; Strunk, J.; Bell, A. T. *J. Catal.* **2012**, *285*, 160.
(240) Park, J. B.; Graciani, J.; Evans, J.; Stacchiola, D.; Ma, S.; Liu, P.; Nambu, A.; Sanz, J. F.; Hrbek, J.; Rodriguez, J. A. *Proc. Natl. Acad. Sci. U.S.A.* **2009**, *106*, 4975.
(241) Park, J. B.; Graciani, J.; Evans, J.; Stacchiola, D.; Senanayake, S. D.; Barrio, L.; Liu, P.; Sanz, J. F.; Hrbek, J.; Rodriguez, J. A. *J. Am. Chem. Soc.* **2010**, *132*, 356.
(242) Graciani, J.; Plata, J. J.; Sanz, J. F.; Liu, P.; Rodriguez, J. A. *J. Chem. Phys.* **2010**, *132*, 104703.

(243) Cheng, L.; Mei, D. H.; Ge, Q. F. *J. Phys. Chem. C* **2009**, *113*, 18296.
(244) Shapovalov, V.; Metiu, H. *J. Phys. Chem. C* **2007**, *111*, 14179.
(245) Popa, C.; Ganduglia-Pirovano, M. V.; Sauer, J. *J. Phys. Chem. C* **2012**, *116*, 18572.
(246) Baron, M.; Abbott, H.; Bondarchuk, O.; Stacchiola, D.; Uhl, A.; Shaikhutdinov, S.; Freund, H.-J.; Popa, C.; Ganduglia-Pirovano, M. V.; Sauer, J. *Angew. Chem., Int. Ed.* **2009**, *48*, 8006.
(247) Reidy, R. F.; Swider, K. E. *J. Am. Ceram. Soc.* **1995**, *78*, 1121.
(248) Da Silva, J. L. F.; Ganduglia-Pirovano, M. V.; Sauer, J. *Phys. Rev. B* **2007**, *76*, 125117.
(249) Jiang, L.; Wende, T.; Claes, P.; Bhattacharyya, S.; Sierka, M.; Meijer, G.; Lievens, P.; Sauer, J.; Asmis, K. R. *J. Phys. Chem. A* **2011**, *115*, 11187.
(250) Sauer, J.; Döbler, J. *Dalton Trans.* **2004**, *19*, 3116.
(251) Wachs, I. E.; Chen, Y.; Jehng, J.-M.; Briand, L. E.; Tanaka, T. *Catal. Today* **2003**, *78*, 13.
(252) Daniell, W.; Ponchel, A.; Kuba, S.; Anderle, F.; Weingand, T.; Gregory, D. H.; Knozinger, H. *Top. Catal.* **2002**, *20*, 65.
(253) Baron, M.; Abbott, H. L.; Bondarchuk, O.; Stacchiola, D.; Uhl, A.; Shaikhutdinov, S.; Freund, H.-J.; Popa, C.; Ganduglia-Pirovano, M. V.; Sauer, J. *Angew. Chem., Int. Ed.* **2009**, *48*, 8006.
(254) Beck, B.; Harth, M.; Hamilton, N. G.; Carrero, C.; Uhlrich, J. J.; Trunschke, A.; Shaikhutdinov, S.; Schubert, H.; Freund, H.-J.; Schlögl, R.; Sauer, J.; Schomäcker, R. *J. Catal.* **2012**, *296*, 120.
(255) Wu, Z. L.; Schwartz, V.; Li, M. J.; Rondinone, A. J.; Overbury, S. H. *J. Phys. Chem. Lett.* **2012**, *3*, 1517.
(256) Bernal, S.; Calvino, J. J.; Gatica, J. M.; Cartes, C. L.; Pintado, J. M. In *Catalysis by Ceria and Related Materials*; Trovarelli, A., Ed.; Imperial College Press: London, 2002.
(257) Suchorski, Y.; Wrobel, R.; Becker, S.; Weiss, H. *J. Phys. Chem. C* **2008**, *112*, 20012.
(258) Spiel, C.; Blaha, P.; Suchorski, Y.; Schwarz, K.; Rupprechter, G. *Phys. Rev. B* **2011**, *84*, 045412.
(259) Campbell, C. T. *Nat. Chem.* **2012**, *4*, 597.
(260) Nolan, M. *J. Chem. Phys.* **2012**, *136*, 134703.
(261) Zhang, C. J.; Michaelides, A.; Jenkins, S. J. *Phys. Chem. Chem. Phys.* **2011**, *13*, 22.
(262) Liu, Z. P.; Jenkins, S. J.; King, D. A. *Phys. Rev. Lett.* **2005**, *94*, 196102.
(263) Zhang, C. J.; Michaelides, A.; King, D. A.; Jenkins, S. J. *J. Am. Chem. Soc.* **2010**, *132*, 2175.
(264) Zhang, C.; Michaelides, A.; King, D. A.; Jenkins, S. J. *J. Chem. Phys.* **2008**, *129*, 194708.
(265) Hernandez, N. C.; Grau-Crespo, R.; de Leeuw, N. H.; Sanz, J. F. *Phys. Chem. Chem. Phys.* **2009**, *11*, 5246.
(266) Branda, M. M.; Hernandez, N. C.; Sanz, J. F.; Illas, F. *J. Phys. Chem. C* **2010**, *114*, 1934.
(267) Pacchioni, G.; Freund, H.-J. *Chem. Rev.* **2013**, accepted for publication.
(268) Johansson, M. P.; Lechtken, A.; Schooss, D.; Kappes, M. M.; Furche, F. *Phys. Rev. A* **2008**, *77*, 053202.
(269) Ferrighi, L.; Hammer, B.; Madsen, G. K. H. *J. Am. Chem. Soc.* **2009**, *131*, 10605.
(270) Tao, J. M.; Perdew, J. P.; Staroverov, V. N.; Scuseria, G. E. *Phys. Rev. Lett.* **2003**, *91*, 146401.
(271) Logsdail, A.; Paz, B.; n, L. O.; Johnston, R. L. *J. Comput. Theor. Nanosci.* **2009**, *6*, 857.
(272) Leppert, L.; Kümmel, S. *J. Phys. Chem. C* **2011**, *115*, 6694.
(273) Zhu, W. J.; Zhang, J.; Gong, X. Q.; Lu, G. Z. *Catal. Today* **2011**, *165*, 19.
(274) Tibiletti, D.; Amieiro-Fonseca, A.; Burch, R.; Chen, Y.; Fisher, J. M.; Goguet, A.; Hardacre, C.; Hu, P.; Thompsett, A. *J. Phys. Chem. B* **2005**, *109*, 22553.
(275) Zhang, C.; Michaelides, A.; King, D. A.; Jenkins, S. J. *J. Phys. Chem. C* **2009**, *113*, 6411.
(276) Jenkins, S. J. Personal communication, 2012.
(277) Luches, P.; Pagliuca, F.; Valeri, S.; Illas, F.; Preda, G.; Pacchioni, G. *J. Phys. Chem. C* **2012**, *116*, 1122.
(278) Yang, Z. X.; Xie, L. G.; Ma, D. W.; Wang, G. T. *J. Phys. Chem. C* **2011**, *115*, 6730.
(279) Szabova, L.; Camellone, M. F.; Huang, M.; Matolin, V.; Fabris, S. *J. Chem. Phys.* **2010**, *133*, 234705.
(280) Aranifard, S.; Ammal, S. C.; Heyden, A. *J. Phys. Chem. C* **2012**, *116*, 9029.
(281) Jung, C.; Tsuboi, H.; Koyama, M.; Kubo, M.; Broclawik, E.; Miyamoto, A. *Catal. Today* **2006**, *111*, 322.
(282) Vayssilov, G. N.; Lykhach, Y.; Migani, A.; Staudt, T.; Petrova, G. P.; Tsud, N.; Skala, T.; Bruix, A.; Illas, F.; Prince, K. C.; Matolin, V.; Neyman, K. M.; Libuda, J. *Nat. Mater.* **2011**, *10*, 310.
(283) Yang, Z. X.; Lu, Z. S.; Luo, G. X. *Phys. Rev. B* **2007**, *76*, 075421.
(284) Bruix, A.; Rodriguez, J. A.; Ramirez, P. J.; Senanayake, S. D.; Evans, J.; Park, J. B.; Stacchiola, D.; Liu, P.; Hrbek, J.; Illas, F. *J. Am. Chem. Soc.* **2012**, *134*, 8968.
(285) Mayernick, A. D.; Janik, M. J. *J. Chem. Phys.* **2009**, *131*, 084701.
(286) Wilson, E. L.; Grau-Crespo, R.; Pang, C. L.; Cabailh, G.; Chen, Q.; Purton, J. A.; Catlow, C. R. A.; Brown, W. A.; de Leeuw, N. H.; Thornton, G. *J. Phys. Chem. C* **2008**, *112*, 10918.
(287) Alfredsson, M.; Catlow, C. R. A. *Phys. Chem. Chem. Phys.* **2002**, *4*, 6100.
(288) Loffreda, D.; Delbecq, F. *J. Chem. Phys.* **2012**, *136*, 044705.
(289) Lu, Z. S.; Yang, Z. X. *J. Phys.: Condens. Matter* **2010**, *22*, 475003.
(290) Chen, H. L.; Peng, W. T.; Ho, J. J.; Hsieh, H. M. *Chem. Phys.* **2008**, *348*, 161.
(291) Nolan, M.; Lykhach, Y.; Tsud, N.; Skala, T.; Staudt, T.; Prince, K. C.; Matolin, V.; Libuda, J. *Phys. Chem. Chem. Phys.* **2012**, *14*, 1293.
(292) Zhao, Y.; Teng, B. T.; Yang, Z. X.; Zhao, L. H.; Luo, M. F. *J. Phys. Chem. C* **2011**, *115*, 16461.
(293) Chafi, Z.; Keghouche, N.; Minot, C. *Surf. Sci.* **2007**, *601*, 2323.
(294) Chen, Y.; Wang, H. F.; Burch, R.; Hardacre, C.; Hu, P. *Faraday Discuss.* **2011**, *152*, 121.
(295) Teng, B. T.; Jiang, S. Y.; Yang, Z. X.; Luo, M. F.; Lan, Y. Z. *Surf. Sci.* **2010**, *604*, 68.
(296) Chen, Y.; Cheng, J.; Hu, P.; Wang, H. F. *Surf. Sci.* **2008**, *602*, 2828.
(297) Peng, Y.; Liu, Z. M.; Niu, X. W.; Zhou, L.; Fu, C. W.; Zhang, H.; Li, J. H.; Han, W. *Catal. Commun.* **2012**, *19*, 127.
(298) Sharma, S.; Hu, Z. P.; Zhang, P.; McFarland, E. W.; Metiu, H. *J. Catal.* **2011**, *278*, 297.
(299) Rodriguez, J. A.; Graciani, J.; Evans, J.; Park, J. B.; Yang, F.; Stacchiola, D.; Senanayake, S. D.; Ma, S.; Perez, M.; Liu, P.; Sanz, J. F.; Hrbek, J. *Angew. Chem., Int. Ed.* **2009**, *48*, 8047.
(300) Yang, F.; Graciani, J.; Evans, J.; Liu, P.; Hrbek, J.; Sanz, J. F.; Rodriguez, J. A. *J. Am. Chem. Soc.* **2011**, *133*, 3444.

# P9

https://journals.aps.org/prl/abstract/10.1103/PhysRevLett.111.206101

# Titration of $Ce^{3+}$ Ions in the $CeO_2(111)$ Surface by Au Adatoms

Yi Pan,[1] Niklas Nilius,[1,2,*] Hans-Joachim Freund,[1] Joachim Paier,[3,†] Christopher Penschke,[3] and Joachim Sauer[3]

[1]*Fritz-Haber-Institut der MPG, Faradayweg 4-6, 14195 Berlin, Germany*

[2]*Carl von Ossietzky Universität Oldenburg, Institut für Physik, D-26111 Oldenburg, Germany*

[3]*Humboldt-Universität zu Berlin, Unter den Linden 6, 10099 Berlin, Germany*

(Received 23 August 2013; revised manuscript received 19 September 2013; published 12 November 2013)

The role of surface and subsurface O vacancies for gold adsorption on crystalline $CeO_2(111)$ films has been investigated by scanning tunneling microscopy and density functional theory. Whereas surface vacancies serve as deep traps for the Au atoms, subsurface defects promote the formation of characteristic Au pairs with a mean atom distance of two ceria lattice constants (7.6 Å). Hybrid density functional theory calculations reveal that the pair formation arises from a titration of the two $Ce^{3+}$ ions generated by a single O vacancy. The Au-$Ce^{3+}$ bond forms due to a strain effect, as the associated charge transfer from the spacious $Ce^{3+}$ into the adgold enables a substantial relaxation of the ceria lattice. Also the experimentally determined Au-pair length is reproduced in the calculations, as we find a $Ce^{3+}$-$Ce^{3+}$ spacing of two ceria lattice parameters to be energetically preferred. Single Au atoms can thus be taken as position markers for $Ce^{3+}$ ion pairs in the surface, providing unique information on electron-localization phenomena in reduced ceria.

DOI: 10.1103/PhysRevLett.111.206101 PACS numbers: 68.37.Ef, 71.15.Mb, 73.20.Hb, 73.61.Ng

Ceria in combination with precious metals (Pt, Au) features outstanding properties in a variety of catalytic processes, such as the water-gas-shift reaction and the low-temperature CO oxidation [1–3]. The high catalytic activity was interpreted as a cooperative effect of charge donation from the metal, resulting in $Ce^{3+}$ formation, and oxygen spillover from the ceria lattice [4]. Although circumstantial evidence could be provided in support of this scenario, an atomistic verification of the mechanism, especially of the metal-oxide charge transfer, could not be given so far. In fact, even fundamental questions, such as the charge state of individual metal atoms on ideal and defective $CeO_2(111)$ surfaces lack definite answers.

From a theoretical point of view, there is agreement in the nature of Au binding to surface O defects, as being mediated by a charge transfer from adjacent $Ce^{3+}$ ions into the adatom [5,6]. In contrast, formation of both neutral and positively charged gold is proposed on ideal surfaces, and no consensus has been reached on the preferred Au binding site that is either a surface $O^{2-}$ or an O-O bridge site [5–7]. Moreover, possible $Ce^{3+}$ adsorption sites have not been considered by theory so far.

The experimental situation for the Au/ceria system is even less satisfactory. In nonlocal X-ray spectroscopy studies, formation of $Ce^{3+}$ species has been observed upon Au dosing onto $CeO_2(111)$; however, the charge state of the gold was not determined [8]. Other studies reported the formation of positively charged gold, but could not connect this data to the presence of specific defects in the surface [9,10]. The main reason for this uncertainty is the lack of atomic-scale information that is however of pivotal importance to accurately describe the Au-ceria redox properties. Direct correlation between a predominant Au adsorption scheme and the defect topology requires a local view onto the surface, as provided by scanning tunneling microscopy (STM). Examples for a successful elucidation of charge-transfer processes on ideal and defective oxides are the Au adsorption studies on alumina, magnesia, and vanadia films [11,12]. For ceria, the experiments mainly focused on defects in the uncovered surface so far [13–15].

In this Letter, we analyze the interaction of Au atoms with O vacancies in the $CeO_2(111)$ surface. From the abundance of atom pairs observed upon low-temperature gold deposition, we conclude that Au is able to decorate the $Ce^{3+}$ ions generated by oxygen removal from the lattice. Our density-functional theory (DFT) calculations attribute this unusual binding behavior to a reduction of lattice strain induced by spacious $Ce^{3+}$ ions in the oxide surface [16]. By transferring the extra charges into the Au atoms, the surface tension is reduced, which in turn reinforces the Au-Ce bond.

The experiments were performed with an ultrahigh-vacuum STM operated at liquid helium temperature. Ceria films of 5–8 trilayer thickness were prepared by cerium deposition onto a sputtered and annealed Ru(0001) single crystal in $5 \times 10^{-7}$ mbar $O_2$ at room temperature. To promote long-range ordering, the oxide was annealed to 1000 K until a sharp hexagonal spot pattern became visible in low-energy electron diffraction, indicative for the presence of wide $CeO_2(111)$ patches. The quality of our films was confirmed by STM images that showed atomically flat terraces with triangular or hexagonal shapes and diameters as large as 50 nm [Fig. 1(a)]. The oxide defect structure was found to depend on the final annealing step. While annealing in $O_2$ triggered the formation of subsurface vacancies ($V_{sub}$), appearing as

 

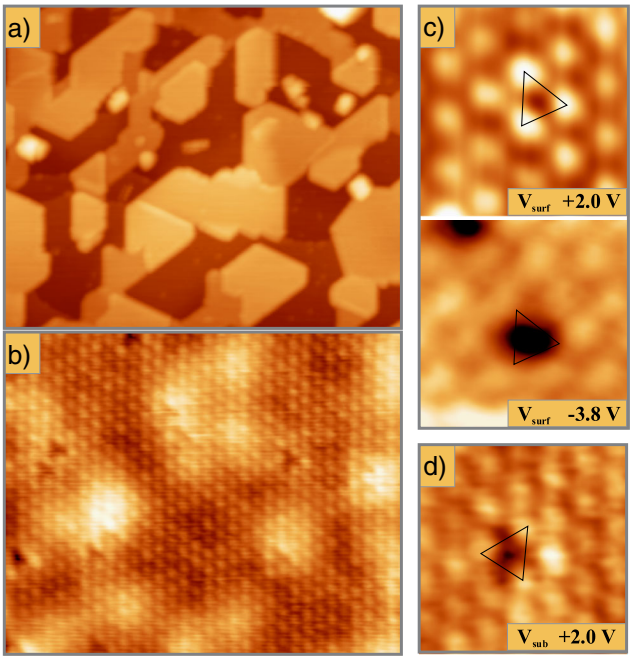


FIG. 1 (color online). (a) Overview ($120 \times 100$ nm$^2$) and (b) atomically resolved STM image ($10.5 \times 8.5$ nm$^2$) of a five trilayer thick $CeO_2(111)$ film grown on Ru(0001) ($U_s = +2.0$ V). The defects in (b) are mainly subsurface O vacancies. (c),(d) High resolution images of surface ($V_{surf}$) and subsurface O vacancies ($V_{sub}$) measured at positive and negative sample bias ($2 \times 2$ nm$^2$). All STM data have been obtained at 25 pA current.

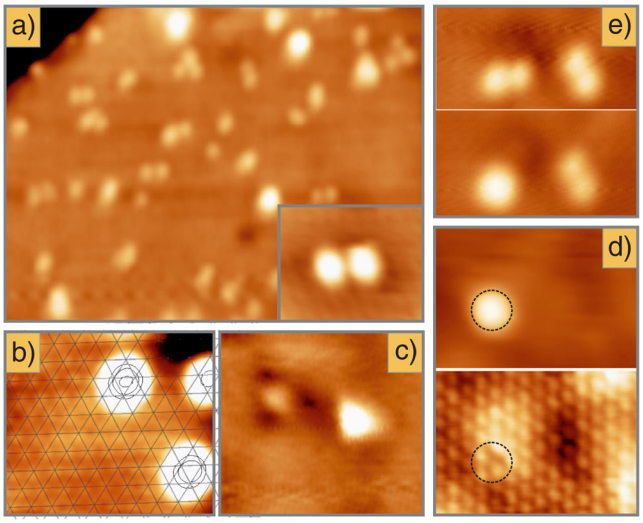


FIG. 2 (color online). (a) Ceria surface after dosing 0.05 ML of Au at 10 K (2.5 V, $26 \times 20$ nm$^2$). Note the abundance of atom pairs on the surface. The pair in the inset shows a pronounced sombrero shape, indicating its charged nature. (b) STM image showing the Ce sub-lattice and three Au atoms bound to regular O-top sites. (c) Au atoms sitting in a $V_{surf}$ defect (left) and a regular lattice site (right) (both $3.8 \times 3.0$ nm$^2$). (d) Au adatom bound to a subsurface defect, as deduced from the atomically resolved image taken after atom removal with the tip (both $4.2 \times 3.0$ nm$^2$). (e) Transformation of an Au atom pair into an upright standing dimer via a tip-voltage pulse ($5.5 \times 3.0$ nm$^2$).

trifoliate depressions in empty-state (positive bias) images, vacuum annealing mainly produced surface defects ($V_{surf}$) [13,14]. The $V_{surf}$ showed up as holes and twofold or threefold maxima in filled and empty-state images, respectively [Fig. 1(c)]. The specific positive-bias contrast relates to the spill-out of $4f$ orbitals of adjacent $Ce^{4+}$ ions, while $Ce^{3+}$ species next to the vacancy appear slightly darker in the STM images [15]. The defect density was determined to be $\sim 5 \times 10^{12}$ cm$^{-2}$ for $V_{sub}$ at $O_2$-rich preparation conditions, and $\sim 5 \times 10^{13}$ cm$^{-2}$ for $V_{surf}$ defects formed upon 1000 K vacuum annealing [Fig. 1(b)].

Small quantities of gold were dosed from a tungsten filament directly onto the cryogenic sample at 10 K. The arriving atoms had only limited transient mobility and mainly remained isolated on the surface [Fig. 2(a)]. At positive sample bias, Au monomers were imaged as simple protrusions with 1.5 Å height and 10 Å diameter, while Au aggregates featured larger heights of 3–5 Å [17]. The role of lattice defects in the adsorption behavior was derived from a closer inspection of appearance and binding position of the Au atoms. The STM image in Fig. 2(b), taken on an ideal oxide region, shows the atomically resolved Ce sublattice with three Au atoms bound atop. The position of the surface and subsurface O sites in the lattice was determined by evaluating the orientation of nearby equilibrium step edges, as displayed in Fig. 1. Based on geometrical considerations discussed in Ref. [18], the downward pointing triangles in Fig. 2(b) correspond to O-top positions, while the upright triangles mark the subsurface $O^{2-}$ ions. This assignment was cross-checked against the position of surface and subsurface O defects that were indeed found at the expected lattice sites. With this input, the O-top position was identified as preferred Au adsorption site on the ideal $CeO_2(111)$ surface, although O-O bridge sites have been detected as well.

Further binding geometries emerged in the presence of lattice defects. As expected, surface vacancies turned out to be effective traps for the Au atoms, from which they could not be removed with the STM tip anymore [Fig. 2(c)] [5,6]. Such defect-bound species served as nucleation centers for incoming Au atoms and governed the aggregation processes on the surface [17]. However, also subsurface defects, more precisely the $Ce^{3+}$ ions associated with them, were found to modify the adsorption behavior. Experimental evidence came from the unusual arrangement of Au atoms on oxide films with a high density of $V_{sub}$ defects. At low exposure, up to 40% of the Au species appeared as characteristic pairs with a mean atom distance of 7.6 Å (two $CeO_2$ lattice parameters) [Fig. 2(a)]. Note that even the shortest pair length of 4.8 Å observed here would be too large to enable direct Au-Au coupling [Fig. 3(a)]. We therefore suggest that this unusual atom

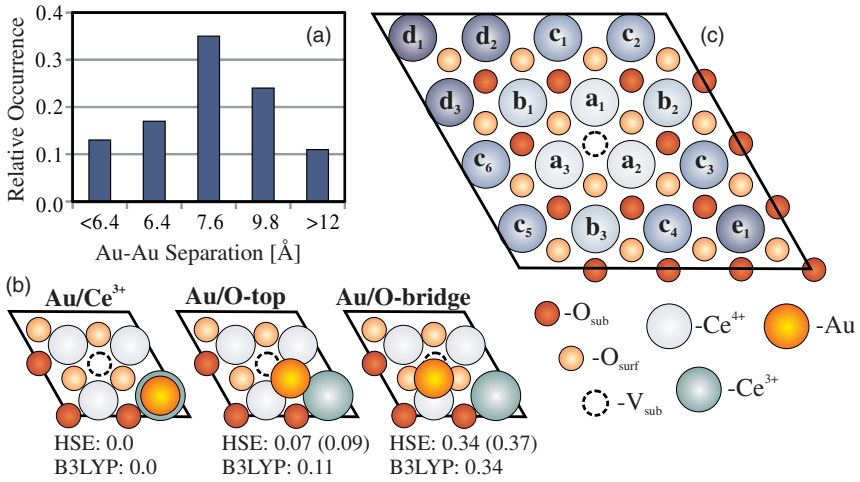


FIG. 3 (color online). (a) Distance histogram determined for ~150 Au pairs on the ceria surface. (b) Relative energies [eV] obtained using HSE (optimized) and B3LYP (single point) for three relevant Au adsorption sites (Values in parenthesis include dispersion effects). (c) $p(4 \times 4)$ unit cell with the notation of different Ce coordination shells around the $V_{sub}$ defect, as used in Table I.

distribution is governed by defects in the ceria lattice. The atom pairs were found to be metastable, as they could be assembled to a single upright $Au_2$ dimer with a 3.0 V tip pulse [Fig. 2(e)]. Further manipulation experiments enabled us to determine the binding sites of the paired atoms by desorbing them via high bias scanning. In a few successful examples, we could identify a subsurface vacancy in close vicinity to the Au pair, suggesting an involvement of this defect type in the pair formation [Fig. 2(d)]. This idea is supported by a statistical analysis of our data that revealed a direct dependence of the number of Au pairs on the $V_{sub}$ concentration in the surface [19]. Finally, all atoms in paired configurations but also a couple of isolated monomers featured a specific contrast in low bias images, characterized by a dark ring around the actual maximum [Fig. 2(a), inset]. In earlier experiments on alumina [11] and magnesia films [20], such sombrero shapes were associated with charges on the adatoms, inducing a local bending of the surrounding oxide bands. We thus conclude that $V_{sub}$ defects are not only responsible for the pair formation, but induce a charge transfer into the Au atoms as well. As a working hypothesis, we propose that the Au pairs result from a titration of the $Ce^{3+}$ surface species created by oxygen removal from the ceria lattice.

To corroborate this scenario, we have performed spin-polarized DFT calculations as implemented in VASP [21]. The electron-ion interaction was described with the projector augmented wave method, including scalar relativistic corrections and a kinetic energy cutoff of 600 eV [22]. To simulate isolated $V_{sub}$ defects at high and low concentrations, we used a $p(2 \times 2)$ and a $p(4 \times 4)$ unit cell comprising three O-Ce-O trilayers, respectively. The Brillouin zone was sampled on a $2 \times 2$ $k$-point grid and the $\Gamma$ point for the two models. To overcome shortcomings of conventional GGA + $U$, all calculations were performed with the screened hybrid functional HSE [23,24]. Dispersion effects were included by using a pairwise summed $C_6/R^6$ term [25], parameterized with values for Au and Ce from the literature [26,27]. To demonstrate the robustness of our conclusions, we reproduced selected data points using the B3LYP hybrid functional.

In a first approach, we have explored the adsorption energies of Au atoms in the presence of subsurface O defects in a $p(2 \times 2)$ configuration [19]. Depending on the functional, the $Ce^{3+}$ position was found to be preferred by 70–110 meV with respect to the O-top site, while O-O bridge positions were pronouncedly less stable [Fig. 3(b)]. The adsorption energies for Au slightly varied with the alignment of the two $Ce^{3+}$ spins, with a ferromagnetic coupling [Fig. 3(b)] being 30 meV lower in energy than an antiferromagnetic one. In the preferred binding position, the $4f$ electron of $Ce^{3+}$ gets transferred into the Au $6s$ orbital, generating a $Ce^{4+}$ and an $Au^-$. The charge transfer is possible, because the Au $6s$ orbital is energetically close to the occupied $4f$ orbital of $Ce^{3+}$ (Fig. 4). Already these findings are able to explain the effect of $Ce^{3+}$ titration and the sombrero shape that can

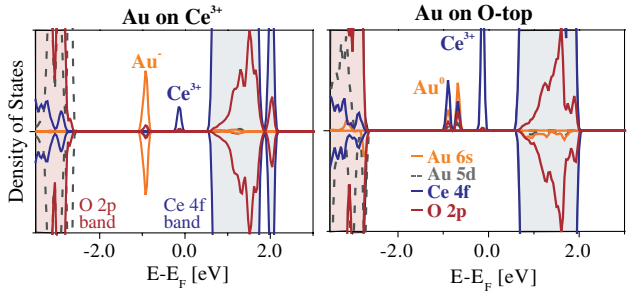


FIG. 4 (color online). Projected local density of states (with HSE) for an Au atom bound to a $Ce^{3+}$ and an $O^{2-}$-top site in a $p(2 \times 2)$ cell.

be taken as experimental fingerprint for charged Au species on the ceria surface.

In a next step, we have analyzed the origin of the Au-$Ce^{3+}$ binding preference, in particular the role of lattice strain in reduced $CeO_2(111)$. For this purpose, we used the larger $p(4 \times 4)$ cell to simulate the $V_{sub}$ defect. In the dilute limit, the energetic ordering for Au adsorption reversed and binding to O-top sites became favorable by 70 meV with respect to the $Ce^{3+}$ sites. Moreover, only a partial electron transfer occurred when fixing the Au on top of $Ce^{3+}$ and the resulting electron configuration was closer to $Ce^{3+}(4f^1)/Au^0(6s^1)$. This difference reflects the impact of surface tension in reduced ceria on the Au adsorption behavior. Given the large ion radius of $Ce^{3+}$ compared to $Ce^{4+}$ (1.01 versus 0.87 Å), a substantial lattice strain builds up when reducing the oxide film [16]. Electron transfer from surface $Ce^{3+}$ to the Au atoms now provides an effective means to release this strain, which in turn stabilizes the Au-Ce bond. The effect of $Ce^{3+}$ titration is therefore expected to occur only in regions with a high number of reduced Ce species. Although we cannot pinpoint the critical $Ce^{3+}$ density at which the Au adsorption swaps from $Ce^{3+}$ to O-top sites, we want to emphasize that large variations were observed in the abundance of Au-atom pairs, suggesting a decisive influence of the local oxide reduction state.

To further support the $Ce^{3+}$ titration scenario, we compared the experimentally determined Au-Au pair distances [Fig. 3(a)] with the equilibrium separation of the two $Ce^{3+}$ created by a single O subsurface defect. For this purpose, the $Ce^{3+}$-$V_{sub}$ configuration as well as the $Ce^{3+}$ pair distance were varied systematically within the $p(4 \times 4)$ cell [19]. In extension to earlier data [15,16,28], we found not only a preference for electron localization away from the $V_{sub}$ defect, but determined the optimum arrangement of the associated $Ce^{3+}$ ions (Table I). The lowest defect formation energy, as calculated with respect to $\frac{1}{2}O_2$, was revealed when both $Ce^{3+}$ sit in the 2nd coordination shell of the defect and are 7.6 Å apart [Fig. 3(c), ($b_1$–$b_3$) configuration]. This value agrees well with the maximum in the Au pair length derived from experiment. When moving one $Ce^{3+}$ into the 1st coordination shell, the formation energy rises by 160 meV if both $Ce^{3+}$ ions are opposite to each other ($a_1$-$b_3$) and by 230 meV if they locate on neighboring sites ($a_3$-$b_3$). All other configurations have even higher formation energies, in particular when the $Ce^{3+}$ pair occupies nearest neighbor sites to the $V_{sub}$ ($a_1$-$a_3$). Apparently, the $Ce^{3+}$ repel each other and prefer configurations, in which both ions sit in the 2nd coordination shell of the defect and are spaced by two lattice constants.

In summary, we have demonstrated that Au adatoms are able to titrate $Ce^{3+}$ ions in a reduced $CeO_2(111)$ surface. The associated charge transfer into the gold is promoted by the release of lattice strain, as spacious $Ce^{3+}$ transform into small $Ce^{4+}$ species. The Au decoration effect can be exploited to determine the position of $Ce^{3+}$ ions at the atomic scale, addressing the essential question of electron localization in defective ceria.

TABLE I. Structure and vacancy formation energy ($E_{def}$) with respect to $\frac{1}{2}O_2$ for different subsurface O vacancy/$Ce^{3+}$ configurations obtained with HSE.

| $Ce^{3+}$ configuration | $Ce^{3+}$-$Ce^{3+}$ distance [Å] | $Ce^{3+}$-defect distances [Å] | $E_{def}(\frac{1}{2}O_2)$ [eV] | |
|---|---|---|---|---|
| | | | High spin | Low spin |
| $b_1$–$b_3$ | 7.67 | 4.41; 4.42 | **2.26** | 2.34 |
| $a_1$–$b_3$ | 6.77 | 2.33; 4.44 | 2.42 | 2.41 |
| $b_3$–$c_6$ | 6.65 | 4.41; 5.84 | 2.48 | |
| $a_3$–$b_3$ | 3.87 | 2.34; 4.42 | 2.49 | 2.55 |
| $b_3$–$d_3$ | 10.11 | 4.40; 7.94 | 2.51 | |
| $c_5$–$c_6$ | 3.88 | 5.84; 5.85 | 2.60 | |
| $c_1$–$c_6$ | 7.65 | 5.85; 5.84 | 2.61 | |
| $a_1$–$d_3$ | 7.63 | 2.35; 7.93 | 2.62 | |
| $a_3$–$c_5$ | 3.77 | 2.32; 5.86 | 2.63 | |
| $a_1$–$a_3$ | 4.09 | 2.37; 2.37 | 2.71 | 2.70 |

The DFG excellence cluster 'UNICAT', the COST action CM1104, the HLRN cluster of the North-German Supercomputing Alliance, and the JUROPA cluster (Jülich) are acknowledged for support.

*Note added in proof.*—We recently found another structure for Au bound atop $Ce^{3+}$, where charge-transfer occurs from $Ce^{3+}$ in a subsurface position to the ad-gold. The energy of this structure is even lower by 120 meV than the one shown in Fig. 3(b).

*Corresponding author.
nilius@fhi.mpg-berlin.de
†Corresponding author.
joachim.paier@chemie.hu-berlin.de

[1] A. Trovarelli, *Catalysis by Ceria and Related Materials* (Imperial College Press, London, 2002).
[2] Q. Fu, H. Saltsburg, and M. Flytzani-Stephanopoulos, Science **301**, 935 (2003).
[3] J. Rodriguez, Catal. Today **160**, 3 (2011).
[4] G. N. Vayssilov *et al.*, Nat. Mater. **10**, 310 (2011).
[5] C. J. Zhang, A. Michaelides, and S. J. Jenkins, Phys. Chem. Chem. Phys. **13**, 22 (2011).
[6] J. Paier, C. Penschke, and J. Sauer, Chem. Rev. **113**, 3949 (2013).
[7] M. Nolan, S. C. Parker, and G. W. Watson, Surf. Sci. **595**, 223 (2005); C. Loschen, A. Migani, S. T. Bromley, F. Illas, and K. M. Neyman, Phys. Chem. Chem. Phys. **10**, 5730 (2008); M. M. Branda, N. J. Castellani, R. Grau-Crespo, N. H. de Leeuw, N. C. Hernandez, J. F. Sanz, K. M. Neyman, and F. Illas, J. Chem. Phys. **131**, 094702 (2009).
[8] M. Škoda, M. Cabala, I. Matolínová, K. C. Prince, T. Skála, F. Šutara, K. Veltruská, and V. Matolín. J. Chem. Phys. **130**, 034703 (2009).

[9] Q. Fu, W. Deng, H. Saltsburg, and M. Flytzani-Stephanopoulos, Appl. Catal., B **56**, 57 (2005); R. Si, J. Tao, J. Evans, J. B. Park, L. Barrio, J. C. Hanson, Y. Zhu, J. Hrbek, and J. A. Rodriguez. J. Phys. Chem. C **116**, 23 547 (2012).

[10] M. Baron, O. Bondarchuk, D. Stacchiola, S. Shaikhutdinov, and H.-J. Freund, J. Phys. Chem. C **113**, 6042 (2009); K. Naya, R. Ishikawa, and K. Fukui, J. Phys. Chem. C **113**, 10 726 (2009).

[11] N. Nilius, M. V. Ganduglia-Pirovano, V. Brázdová, M. Kulawik, J. Sauer, and H.-J. Freund, Phys. Rev. Lett. **100**, 096802 (2008).

[12] N. Nilius, V. Brázdová, M.-V. Ganduglia-Pirovano, V. Simic-Milosevic, J. Sauer, and H.-F. Freund, New J. Phys. **11**, 093007 (2009).

[13] F. Esch, S. Fabris, L. Zhou, T. Montini, C. Africh, P. Fornasiero, G. Comelli, and R. Rosei, Science **309**, 752 (2005).

[14] S. Torbrügge, M. Reichling, A. Ishiyama, S. Morita, and Ó. Custance, Phys. Rev. Lett. **99**, 056101 (2007).

[15] J.-F. Jerratsch, X. Shao, N. Nilius, H.-J. Freund, C. Popa, M. V. Ganduglia-Pirovano, A. M. Burow, and J. Sauer, Phys. Rev. Lett. **106**, 246801 (2011).

[16] M. V. Ganduglia-Pirovano, J. L. F. Da Silva, and J. Sauer, Phys. Rev. Lett. **102**, 026101 (2009).

[17] Y. Pan, Y. Cui, N. Nilius, and H.-J. Freund, J. Phys. Chem. C **117**, 21879 (2013).

[18] N. Nilius, S. M. Kozlov, J.-F. Jerratsch, M. Baron, X. Shao, S. Shaikhutdinov, H.-J. Freund, F. Viñes, and K. M. Neyman, ACS Nano **6**, 1126 (2012).

[19] See Supplemental Material at http://link.aps.org/supplemental/10.1103/PhysRevLett.111.206101 for statistical analysis of defect versus Au-pair numbers, computational details, and atomic coordinates used in the calculations.

[20] M. Sterrer, T. Risse, U. Martinez Pozzoni, L. Giordano, M. Heyde, H.-P. Rust, G. Pacchioni, and H.-J. Freund, Phys. Rev. Lett. **98**, 096107 (2007).

[21] G. Kresse and J. Furthmüller, Comput. Mater. Sci. **6**, 15 (1996).

[22] P. E. Blöchl, Phys. Rev. B **50**, 17 953 (1994); G. Kresse and D. Joubert, Phys. Rev. B **59**, 1758 (1999).

[23] J. Heyd, G. E. Scuseria, and M. Ernzerhof, J. Chem. Phys. **118**, 8207 (2003).

[24] A. V. Krukau, O. A. Vydrov, A. F. Izmaylov, and G. E. Scuseria, J. Chem. Phys. **125**, 224106 (2006).

[25] S. Grimme, J. Comput. Chem. **27**, 1787 (2006).

[26] K. Tonigold and A. Gross, J. Chem. Phys. **132**, 224701 (2010).

[27] C. Penschke, J. Paier, and J. Sauer, J. Phys. Chem. C **117**, 5274 (2013).

[28] H. Y. Li, H. F. Wang, X. Q. Gong, Y. L. Guo, Y. Guo, G. Lu, and P. Hu, Phys. Rev. B **79**, 193401 (2009).

# Erratum: Titration of $Ce^{3+}$ Ions in the $CeO_2(111)$ Surface by Au Adatoms [Phys. Rev. Lett. 111, 206101 (2013)]

Yi Pan, Niklas Nilius, Hans-Joachim Freund, Joachim Paier, Christopher Penschke, and Joachim Sauer

(Received 1 December 2015; published 23 December 2015)

DOI: 10.1103/PhysRevLett.115.269901 PACS numbers: 68.37.Ef, 71.15.Mb, 73.20.Hb, 73.61.Ng, 99.10.Cd

Because of an error in some of the routines of VASP.5.2.12 ("Γ point only" version, release 26May11) [1], the O defect formation energies in the subsurface position of the $CeO_2(111)$ surface had to be recalculated. For this purpose, VASP.5.3.5 (release 31Mar14) was used. Results are shown in Table I. The adjustments of the previously published formation energies are within 0.07 eV. The conclusions of the Letter are not affected.

TABLE I. Structure and vacancy formation energy ($E_{def}$) with respect to ½$O_2$ for different subsurface O vacancy/$Ce^{3+}$ configurations obtained with HSE.

| | | | $E_{def}$(½$O_2$) [eV] | |
|---|---|---|---|---|
| $Ce^{3+}$ configuration | $Ce^{3+} - Ce^{3+}$ distance [Å] | $Ce^{3+}$—defect distances [Å] | High spin | Low spin |
| $b_1 - b_3$ | 7.67 | 4.41; 4.42 | **2.32** | 2.27 |
| $a_1 - b_3$ | 6.77 | 2.33; 4.44 | 2.43 | 2.41 |
| $b_3 - c_6$ | 6.65 | 4.41; 5.84 | 2.41 | |
| $a_3 - b_3$ | 3.89 | 2.34; 4.43 | 2.50 | 2.54 |
| $b_3 - d_3$ | 10.11 | 4.40; 7.94 | 2.47 | |
| $c_5 - c_6$ | 3.88 | 5.84; 5.85 | 2.69 | |
| $c_1 - c_6$ | 7.66 | 5.85; 5.84 | 2.66 | |
| $a_1 - d_3$ | 7.63 | 2.35; 7.93 | 2.62 | |
| $a_3 - c_5$ | 3.77 | 2.32; 5.86 | 2.63 | |
| $a_1 - a_3$ | 4.08 | 2.37; 2.37 | 2.71 | 2.71 |

We thank Dr. Doris Vogtenhuber for helpful discussions. We cordially thank representatives of the HLRN (North-German Supercomputing Alliance), Dr. Jens Döbler and Dr. Stefan Wollny, for a straightforward supply of sufficient amounts of computing time.

[1] See www.vasp.at.

 

# P10

https://pubs.rsc.org/en/content/articlehtml/2017/cp/c7cp01785e

PCCP

PAPER

View Article Online
View Journal | View Issue





Cite this: *Phys. Chem. Chem. Phys.*, 2017, **19**, 12546

# Reduction and oxidation of Au adatoms on the $CeO_2$(111) surface – DFT+*U versus* hybrid functionals†

Christopher Penschke and Joachim Paier *

Received 20th March 2017,
Accepted 24th April 2017

DOI: 10.1039/c7cp01785e

rsc.li/pccp

Recently we showed that Au atoms may titrate $Ce^{3+}$ ions in near-surface layers of reduced $CeO_2$(111). This surface contained oxygen vacancies in subsurface position within the topmost O–Ce–O trilayer [Pan *et al.*, *Phys. Rev. Lett.*, 2013, **111**, 206101.]. The present work builds upon these findings and discusses additional results obtained using PBE+*U* and hybrid functionals. These approaches do not predict the same relative stabilities for the various adsorption sites of a single Au adatom at an O-defect concentration of a $\frac{1}{4}$ ML or 1.984 $nm^{-2}$. We attribute this discrepancy to a different alignment within the O 2p–Ce 4f gap, *i.e.* a different order by energy of partially occupied Ce 4f and Au 6s orbitals. The energy offset of these orbitals matters, because the adsorption of $Au^0(6s^1)$ atop $Ce^{3+}(4f^1)$ or atop a subsurface oxygen atom in the first coordination shell of a $Ce^{3+}(4f^1)$ involves creation of $Au^-(6s^2)$ and $Ce^{4+}(4f^0)$ ions. The electron transfer to Au is coupled to stabilizing ionic relaxation in the lattice, commonly known as polaronic distortion, reinforcing the Au–Ce bond. The order of 4f and 6s orbitals depends on the density functional approximation and is also strongly influenced by the oxygen defect concentration.

## 1. Introduction

The pioneering work of Haruta on metal oxide supported Au nanoparticles revealed that these catalysts are highly active in many oxidation reactions[1–4] and drastically modified the view on noble metals in catalysis. Platinum or gold deposited on a reducible oxide support like ceria ($CeO_2$) form particularly active catalysts important in many technological processes, such as the water-gas shift reaction or low-temperature CO oxidation.[5–7] Atomistic insight is indispensable in order to understand the reasons for the observed catalytic activity, but disentangling individual relevant effects involved in a specific reaction is a formidable task. Especially metal–support interactions are complex, because many factors, such as binding site, size of metal clusters, support morphology (extended surface *versus* confined nanoparticle), and the distribution of charges may impact reactivity.[8–10]

Recently, Campbell emphasized the role of the so-called electronic metal–support interaction (EMSI), which conveys into strong chemical bonding between transition metal atoms and ceria.[11] EMSI involves electron transfer between metal ad-species and the ceria support, implying its partial reduction as indicated by the presence of $Ce^{3+}$ ions.[12,13] This effect occurs independently of the present ceria nanostructure. In contrast, morphology of the ceria support plays a decisive role in the interaction with surface oxygen atoms. For ceria nanoparticles oxygen spill-over from the support to the metal, necessitating formation of oxygen defects, is reported by Vayssilov *et al.*[13] However, this does not occur at perfectly ordered extended surfaces.

In addition to the metal ad-species, also oxygen defects may influence the charge or oxidation state of $Ce^{4+}$ ions in ceria. Upon removal of an oxygen atom, the two remaining electrons easily occupy localized Ce 4f states creating two $Ce^{3+}$ ions. Surface oxygen vacancies are important adsorption sites for noble metal atoms as found experimentally by Flytzani-Stephanopoulos and co-workers[6] as well as by Freund and co-workers.[14,15] Additionally, surface O vacancies were identified as deep effective traps for Au atoms using density functional theory (DFT). Depending on details of the approach, the adsorption energy of Au in the vacant site varies within −2.29 and −2.75 eV.[16–18]

From a theory point of view, the workhorse method for calculations on simple oxides is DFT employing conventional exchange–correlation (xc) functionals as, *e.g.*, the local density (LDA) or generalized-gradient approximation (GGA). Despite their successes, these functionals are unable to correctly describe the aforementioned localized Ce 4f states due to self-interaction and related delocalization errors.[19–23] The DFT+*U* approach is commonly used to rectify this failure and to properly localize

*Institut für Chemie, Humboldt-Universität zu Berlin, Unter den Linden 6, 10099 Berlin, Germany. E-mail: joachim.paier@chemie.hu-berlin.de*

† Electronic supplementary information (ESI) available: Details of GW calculations, lattice parameters and bulk moduli of $CeO_2$, and total energies. See DOI: 10.1039/c7cp01785e

defect states. The method involves a Hubbard-type $U$ term applied to the supposedly spatially confined, atom-like orbitals.[24,25] The $U$ parameter can be chosen such that calculated band gaps[26] or reaction energies[27,28] agree with experiment, but also other methods exist to calculate $U$ by virtue of first principles (see, *e.g.*, ref. 29 and 30).

Hybrid functionals, which replace a certain fraction of the GGA exchange with orbital-dependent Fock exchange (FX), represent an alternative to DFT+$U$ to at least partially rectify self-interaction errors.[31,32] For hybrids, the increase in the computational workload compared to GGA may be substantial.[33–35] Nevertheless, Da Silva *et al.* conclude that hybrid functionals yield a more balanced description of the bulk properties of ceria compared with DFT+$U$.[21] Similar conclusions were drawn by Sanz and co-workers, who explored varying the amount of admixed FX in a hybrid functional when applied to ceria.[36] As shown in ref. 21, GGA+$U$ based on the xc functional after Perdew, Burke, and Ernzerhof[37] (PBE) overestimates the equilibrium lattice constant and underestimates the reduction energy of $CeO_2$. A reasonable value of $U$ acting on the Ce 4f orbitals (*i.e.* $U_{\text{Ce-4f}}$) is 4.5 eV and was calculated by Fabris and co-workers by virtue of linear response theory,[38] but other viable values ranging between 4 and 6 eV were explored by Hermansson and co-workers.[26] In contrast, hybrid functionals like HSE named after Heyd, Scuseria, and Ernzerhof,[39] predict values in excellent agreement with observation.[23,40] However, similar to the DFT+$U$ approach, whose results will depend on the value of $U$, hybrid functional results will, *e.g.*, depend on the amount of admixed FX. The abovementioned work by Sanz and coworkers showed that good agreement with experimental band gaps and reaction energies of cerium oxides is obtained with 8–16% FX admixed in PBE0 calculations.[36]

A large body of theoretical work on the interaction of gold adatoms with the clean, fully oxidized $CeO_2(111)$ surface has been published.[16,17,41–44] Zhang, Michaelides, and Jenkins recently reviewed results relying on GGA+$U$ calculations.[45] They conclude that adsorption of Au at the O–O bridge site is the most stable configuration, while Au atop oxygen is about 200 meV less stable. Branda *et al.* examined the effect of the utilized density functional, the stability of Au on $CeO_2(111)$ depending on its oxidation state, and the effect of strain by varying the unit cell parameter.[43] According to their results, the accurate prediction of the oxidation state of Au on $CeO_2(111)$ appears to be difficult, since solutions for the minimum energy structure involving $Au^0$ or $Au^+$ atop a surface oxygen atom are *de facto* degenerate in energy using GGA+$U$. Furthermore, LDA+$U$ predicts $Au^+/CeO_2(111)$ to be lower in energy by 51 meV compared with $Au^0$ on the surface, but the HSE hybrid predicts $Au^0/CeO_2(111)$ to be more stable by 150 meV. The latter finding is in agreement with recent STM results concluding on close-to-neutral charge states for Au atoms adsorbed on defect-poor ceria surfaces.[46]

The degree of complexity in the Au/ceria system increases significantly upon introduction of oxygen point defects. This is because the Au atom is not only exposed to $Ce^{4+}$ and $O^{2-}$, but also to $Ce^{3+}$ ions and the (electro-positively charged) vacancy. Concerning the position of the vacancy in the $O^{2-}$ lattice of $CeO_2(111)$, two possibilities are most relevant due to the stable O–Ce–O trilayer structure of the surface. The vacancy can either sit in the topmost layer (a surface vacancy) or in the next oxygen layer underneath the cerium layer (a subsurface vacancy). GGA+$U$ results on the interaction of gold atoms with the surface vacancy are reported in ref. 47 and 17 as well as reviewed in ref. 45. Upon adsorption at the vacant site, a 4f electron of a $Ce^{3+}$ ion is transferred into the Au 6s orbital thereby creating a $Ce^{4+}$ and a $Au^-$. This is a very exothermic process, because the negatively charged Au at the vacant site is electrostatically stabilized. Thus, it mimics an $O^{2-}$ ion.[23]

In contrast, a direct interaction between Au atoms and a subsurface O vacancy is not possible. Instead, the defect-induced $Ce^{3+}$ ions become potential adsorption sites. The interaction between Au atoms and $Ce^{3+}$ ions associated with the subsurface O vacancy has been studied by STM and DFT recently.[48] The formation of subsurface O defects was controlled by the pressure of oxygen in the final annealing step. By virtue of low-temperature STM (*ca.* 10 K) characteristic Au pairs with Au–Au distances commensurate to the lattice of the $CeO_2(111)$ surface were observed upon physical vapor deposition of Au. Importantly, the smallest pair distance found ($\sim$4.8 Å) is much larger than a typical Au–Au bond distance ($\sim$2.5 Å in the free molecule[49]). These Au pairs were found to be metastable species and could be rearranged to upright standing $Au_2$ dimers by applying a 3.0 V tip pulse. In several successful attempts, the subsurface vacancy in close vicinity to the Au pair could be identified experimentally.

These experiments have been combined with results obtained using the HSE hybrid functional. It was found that the 4f electron of a $Ce^{3+}$ is transferred to Au, thus forming $Au^-$. The oxidation of $Ce^{3+}$ induces structural relaxation, substantially lowering strain in the surface, which in turn reinforces the binding of Au on $Ce^{3+}$.

The present work examines the abovementioned $Au/CeO_{2-x}(111)$ system more extensively using PBE+$U$ as well as computationally more expensive, but supposedly more accurate, hybrid functionals like HSE and studies dependences on the $U$ parameter and the amount of admixed FX. We emphasize that this work does not intend to offer the optimal set of parameters for employed methods reproducing observation. Instead, we intend to shed light on the physical principles underlying thermodynamic stabilities. Moreover, note that these parameters (*i.e.*, $U$ as well as amount of FX) are motivated by quantum mechanics (see, *e.g.*, ref. 40 and references therein). For instance, we discuss the relation between relative orbital energies (of electron donating and accepting orbitals) and thermodynamic stabilities of individual adsorption sites. Compared with HSE, PBE+$U$ predicts that the relevant occupied Ce 4f electron donor level is substantially lower in energy than the half-filled Au 6s acceptor level. This renders the electron transfer from $Ce^{3+}$ to the concomitantly reduced $Au^0$ unfavourable. In addition, the O-defect concentration affects 4f orbital energies, in turn impacting stabilities of adsorption sites. This demonstrates that the order by energy of electron donor and acceptor levels affects computed adsorption energies. Similar results for reduced $TiO_2$

were reported by Dupuis and coworkers.[50] In this work, we focus on thermodynamic stabilities of various electron distributions over adsorption sites, but the herein reported results are also relevant for kinetic electron transfer phenomena in reduced oxide surfaces.[51–54]

## 2. Computational details

### A. Electronic and ionic structure optimizations

Calculations were performed using the projector augmented wave method (PAW)[55,56] to describe the interaction between ionic cores and valence electrons as implemented in the Vienna *ab initio* simulation package (VASP).[57,58] The PAW data sets released with VASP.5.2 were employed. Specifically, the "Au_pv_GW", "Ce_GW", and "O_GW" pseudopotentials, which include scalar relativistic corrections, were used. For Au, also the $5p^6$ electrons have been treated as valence electrons. Thus, Au uses 17 ($5p^6\ 5d^{10}\ 6s^1$), Ce uses 12 ($5s^2\ 5p^6\ 4f^1\ 5d^1\ 6s^2$), and O uses 6 ($2s^2\ 2p^4$) valence electrons in total. Spin-polarized calculations use a plane-wave cutoff of 600 eV and a Gaussian smearing of 0.02 eV width.

With regard to DFT+$U$ calculations, we use both the LDA as well as the gradient-corrected PBE[32] xc functionals. Unless stated otherwise, LDA and PBE calculations use an effective $U_{\text{Ce-4f}}$ parameter of 5.3 and 4.5 eV (see ref. 38), respectively. The specific implementation of DFT+$U$ used in this work follows Dudarev *et al.*[59,60] Forces in DFT+$U$ structure optimizations were converged to better than 0.02 eV $\text{Å}^{-1}$ employing a break criterion for the electronic optimization of $10^{-6}$ eV.

With regard to hybrid functional calculations, results reported in this work use the HSE (HSE06),[61] PBE0,[62,63] B3LYP,[31,86,87] and TPSSh[64] functionals. TPSSh mixes 10% FX and 90% of the meta-GGA TPSS exchange[65] as implemented in VASP.[66] The hybrid version of TPSS is based on a local modification of VASP. Test calculations on atomization energies of small molecules to check for correctness of the implementation are given in the ESI.† Since this work studies charge or electron localization in context of self-interaction errors in semilocal xc functionals, additional calculations with 50% of FX were accomplished based on HSE, PBE0, and B3LYP. With this amount of FX, B3LYP is equivalent to the so-called "Half-and-Half" functional after Becke, *i.e.* BHLYP.[67] The screening parameter in HSE for the range-separation was not varied (*i.e.*, HSE06 with 0.207 $\text{Å}^{-1}$ as introduced in ref. 61). All hybrid calculations, except those using TPSSh, employ surface unit cells with consistent lattice parameters (see ESI†). TPSSh calculations are single-points on top of HSE structures. Note that TPSSh and HSE lattice parameters as well as bulk moduli are similar. Regarding ionic relaxations using hybrids, the plane wave cutoff determining the Fourier grid for the FX related routines was equal to the plane wave cutoff applied to expand the orbitals (PRECFOCK = normal). Atomic forces have been converged to better than 0.04 eV $\text{Å}^{-1}$ using an SCF break criterion of $10^{-5}$ eV.

The effect of van der Waals-type dispersion interactions was estimated for selected structures using the approach after Grimme.[68] Adsorption energies employing the correction for dispersion effects are more exothermic by 0.10 to 0.28 eV (see Table S6 in the ESI†). However, relative stabilities of structures are not affected. Thus, we report uncorrected results in the present work.

We checked by normal mode analysis whether structures obtained with PBE+$U$ correspond to true (local) minima. Calculations used central differences to compute the gradient of forces for the Hessian or force constant matrix. The applied step size in the atomic Cartesian coordinates is 0.02 Å. In structures employing a $p(2 \times 2)$ $CeO_2(111)$ surface unit cell (see Section 2C), all atoms (including Au) of the first $CeO_2$ trilayer are free to move when calculating force constants, while calculations using a $p(4 \times 4)$ cell include a sufficient number of atoms centred around the Au adsorbate (typically three to five atoms).

### B. Orbitally projected densities of states

Projected densities of states (PDOS) and local magnetic moments of Ce and Au atoms are obtained by projection of crystal orbitals into spherical harmonics of f or s symmetry located in atom-centred PAW spheres with respective radii of 1.323 and 1.376 Å. A typical value for the local magnetic moment of $Ce^{3+}(4f^1)$ is $\pm 0.96\ \mu_B$ for up and down spins, respectively. For $Au^0(6s^1)$ atoms, the total moment is $\sim 0.4\ \mu_B$. Note that it involves 6s as well as 5d contributions. Magnetic moments of Ce and Au atoms for the various functionals are given in the ESI.† As expected, hybrid functionals using 50% FX show a more pronounced tendency to localize electrons compared with results obtained using 25%. Therefore, corresponding values of local magnetic moments are slightly larger than those obtained with hybrids employing less FX. TPSSh single-point calculations at HSE structures lead to a partial delocalization of the O-defect related electrons. To test whether these electrons localize upon ionic relaxation, we optimized the Au atop $Ce^{3+}$ structure in $p(2 \times 2)$ $CeO_{2-x}(111)$. Upon reaching convergence, the so-called excess electrons delocalized completely over three Ce ions leading to a local magnetic moment of $\sim 0.3\ \mu_B$ per ion. Similarly, delocalization occurred upon optimizing atomic positions in the Au atop $O_{surf}$ structure (see below). To double-check this behavior, we repeated the calculations using HSE with 10% FX starting from properly converged HSE (25% FX) orbitals having the excess electrons correctly localized. HSE (10% FX) also predicts delocalized defect-related electrons resulting in a distribution of magnetic moments over Ce ions like in TPSSh results. Hence, TPSSh does not properly describe O-defect related electrons in $CeO_{2-x}(111)$ surfaces. Single-point calculations employing TPSSh with 20% FX restore the proper localization of electrons and spins.

### C. Surface models

The surface models were built by cutting the bulk cell using optimized lattice parameters corresponding to respective functionals along the [111] plane. Lattice constants and bulk moduli of $CeO_2$ for the various DFT approaches were obtained by fitting single point total energies for different cell volumes to Murnaghan's equation of state[69] (seven points within ±3% centred around the equilibrium lattice constant). These results are presented in the ESI.† Slab models use nine atomic layers

 

(*i.e.* three trilayers), resulting in a composition of $Ce_{12}O_{24}$ and $Ce_{48}O_{96}$ for $p(2 \times 2)$ and $p(4 \times 4)$ cells, respectively. We use asymmetric slab models, *i.e.* atomic positions in the lowest $CeO_2$ trilayer were fixed. The Brillouin zone was sampled with a $\Gamma$-centered $2 \times 2 \times 1$ Monkhorst–Pack[70] mesh for the $p(2 \times 2)$ cell, while the $\Gamma$ point was used to sample the Brillouin zone of the $p(4 \times 4)$ cell. Test calculations showed that the applied vacuum layer of 10 Å suffices to avoid interactions between replicated images. Dipole and quadrupole interactions between consecutive surfaces are negligibly small as tested by applying the method after Makov and Payne.[71] Note that the electron transfer reactions studied in the present work refer to "local" electron transfer between different sites in the slab models used. Thus, slabs used in the present work maintain electro-neutrality.

## 3. Results and discussion

### A. Comparison of LDA+*U*, PBE+*U*, and HSE for $p(2 \times 2)$ cells

Prior to Au adsorption, the most stable structure for $CeO_{2-x}(111)$ with a subsurface O defect using the $p(2 \times 2)$ cell is characterized by one $Ce^{3+}$ located in the surface cation layer, whereas the second one is located in the subsurface cation layer.[72] Au adsorption energies and relative stabilities obtained using LDA+*U*, PBE+*U*, and HSE for adsorption atop $Ce^{3+}$ (Fig. 1a), $O_{sub}$ (Fig. 1b) and $O_{surf}$ (Fig. 1c), as well as at the oxygen–oxygen bridge site (Fig. 1d), are compiled in Table 1. Additionally, adsorption of a Au atom at (i) the hollow site on top of the subsurface vacancy (referred to as atop $V_{sub}$ throughout the present work) and (ii) the $Ce^{4+}$ ion was also studied. Importantly, the difference between $Ce^{3+}$ atop and $Ce^{4+}$ atop structures is in the origin of the transferred electron, which stems from the subsurface and surface cation layer, respectively. The more stable $Ce^{3+}$ atop structure was mentioned in a note added in proof of ref. 48. Furthermore, the $O_{surf}$ atop structure discussed in the present work involves a slightly larger tilting of the Au–O bond with respect to the surface normal (*ca.* 20.2°; see Fig. 1e).

LDA+*U*, PBE+*U* and HSE predict the $O_{sub}$ atop position to be the most stable adsorption site, while relative stabilities for the remaining adsorption sites depend on the employed density functional approximation (DFA). In terms of stability, $O_{sub}$ atop is followed by Au in atop position of $V_{sub}$ using LDA+*U*, while PBE+*U* and HSE predict $V_{sub}$ atop to be least stable. Relative energies for Au atop $Ce^{3+}$, $Ce^{4+}$, and $O_{surf}$ are almost identical using LDA+*U*. No minimum could be found for Au at the O–O bridge site using the LDA+*U* approach. Several attempts to locate the corresponding minimum energy structure led on to an Au atom adsorbed atop $V_{sub}$ at the end of the optimization.

PBE+*U* predicts that Au atop $O_{surf}$ is more stable by 0.14 eV compared to Au atop $Ce^{3+}$ (see Table 1). In contrast, HSE predicts that Au atop $Ce^{3+}$ is more stable by 0.09 eV compared to Au atop $O_{surf}$. As discussed above, adsorption of Au atop $Ce^{3+}$ and atop $Ce^{4+}$ involves electron transfer from the subsurface and surface cation layer, respectively. Oxidation of the subsurface

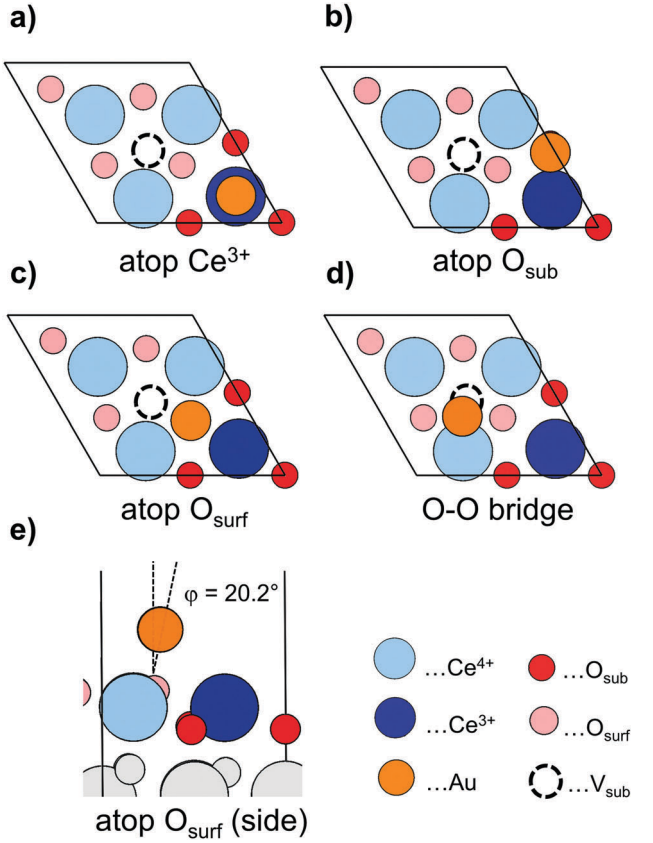


Fig. 1 Adsorption sites of a single Au atom on reduced $CeO_2(111)$ containing a subsurface O vacancy [$p(2 \times 2)$ unit cell; atop a $Ce^{3+}$ (a); atop a subsurface O, see ref. 73 (b); atop a surface O (c); O–O bridge site (d)]. (e) Shows the tilting of the Au–O bond in structure (c).

Table 1 Adsorption energy (eV) of a single Au atom on reduced $CeO_2(111)$ containing a subsurface O vacancy [$p(2 \times 2)$ unit cell]. Relative energies are given in parentheses

| Adsorption site | LDA+*U* | | PBE+*U* | | HSE | |
|---|---|---|---|---|---|---|
| $O_{sub}$ atop | −1.85 | (0) | −0.95 | (0) | −0.95 | (0) |
| $Ce^{3+}$ atop | −1.30 | (+0.55) | −0.64 | (+0.30) | −0.64 | (+0.31) |
| $Ce^{4+}$ atop | −1.29 | (+0.56) | −0.61 | (+0.34) | −0.58 | (+0.38) |
| $O_{surf}$ atop | −1.28 | (+0.57) | −0.78 | (+0.16) | −0.55 | (+0.40) |
| O–O bridge | [a] | (—[a]) | −0.69 | (+0.25) | −0.24 | (+0.71) |
| $V_{sub}$ atop | −1.63 | (+0.22) | −0.55 | (+0.40) | +0.09 | (+1.05) |

[a] Not stable; Au converges into the $V_{sub}$ atop position (see text).

$Ce^{3+}$ ion to $Ce^{4+}$ (and concomitant reduction of $Au^0$ to $Au^-$) is energetically more favourable by 0.03 eV (0.06 eV) compared to oxidation of the surface $Ce^{3+}$ ion using PBE+*U* (HSE). In other words, $Au^-$ adsorbed in atop position of $Ce^{3+}$ is more stable than atop $Ce^{4+}$ using a $p(2 \times 2)$ cell corresponding to an O-defect concentration of a $\frac{1}{4}$ ML ($\equiv 1.984\ nm^{-2}$). Using PBE+*U*, a third solution involving partial electron transfer, *i.e.* $Au^{\delta-}$ associated with two partially reduced Ce ions, is 0.01 eV less stable than $Au^-$ atop $Ce^{3+}$.

To check for the driving force on the oxidation of $Ce^{3+}$ in surface and subsurface positions excluding relaxation effects induced by the formation of an oxygen vacancy, we put a

Na adatom in a larger $p(4 \times 4)$ pristine $CeO_2(111)$ unit cell. After optimization, a $Na^+$ ion and a $Ce^{3+}$ ion are formed. We succeeded in creating a structure with a $Na^+$–$Ce^{3+}$ distance of more than 6 Å. Thus, we believe the $Ce^{3+}$ site to be unaffected from the Na dopant. The $Ce^{3+}$ ion in the second cation layer (*i.e.* $Ce^{3+}$ in subsurface position) is less stable than the $Ce^{3+}$ in the surface layer (see Section S6 in the ESI†). These calculations use LDA+*U*, PBE+*U*, and HSE and consistently confirm this trend. The energy difference is, depending on the approach, 0.10 to 0.38 eV. Analysing the corresponding PDOS, this is consistent with a $4f^1$ orbital energy corresponding to the subsurface $Ce^{3+}$ that is 0.40 (0.10) eV higher than the $4f^1$ energy of the surface $Ce^{3+}$ measured relative to the O 2p valence band edge using HSE (PBE+*U*).

Table 2 presents relevant bond distances and tilting angles of the aforementioned adsorption structures. LDA+*U* predicts bond distances to be approximately 0.1 Å shorter compared to PBE+*U* and HSE results. For Au adsorbed on top of oxygen, a tilting of the Au atom towards the $V_{sub}$ atop site was found. In contrast, Au is tilted towards the surface $Ce^{3+}$ cation using PBE+*U* and HSE. Hence, this structure may also be considered as a Au atom adsorbed at the O–Ce bridge site. Bond distances obtained with HSE compare well with PBE+*U* results, except for the O–O bridge adsorption structure featuring a Au–O distance which is 0.6 Å longer than the corresponding PBE+*U* result. This is plausible, because the hybrid functional does not predict charge or electron transfer from Au to the surface (see Table 3), whereas PBE+*U* favours formation of $Au^+$, which attractively interacts with the two oxygen anions reinforcing the bond.

Table 3 summarizes oxidation states of the Au adatom depending on the adsorption site for various DFA approximations. Au in atop position of $Ce^{3+}$ always adopts oxidation state (OS) −1. Thus, an electron was transferred from the surface to the Au adatom independent of the DFA. We reiterate that the electron transfer may follow two routes. Either the 4f electron of the $Ce^{3+}$ directly underneath the Au adatom or alternatively the electron of the $Ce^{3+}$ in subsurface position may be transferred into the Au 6s orbital. In contrast, Au remains electro-neutral or adopts oxidation state +1 at the various O sites. We emphasize that PBE+*U* and HSE disagree on the OS for Au at the O–O bridge site.

Table 2 Bond distances (Å) of a single Au atom on reduced $CeO_2(111)$ containing a subsurface O vacancy [$p(2 \times 2)$ unit cell]. Au–O tilting angles w.r.t. the surface normal are given in parentheses. For bidentate (O–O bridge) and tridentate ($O_{sub}$ atop, $V_{sub}$ atop) Au, average values are reported (see text)

| Adsorption site | LDA+*U* | PBE+*U* | HSE |
|---|---|---|---|
| $O_{sub}$ atop | 2.997 (O) | 3.144 (O) | 3.140 (O) |
| | 3.111 (Ce) | 3.249 (Ce) | 3.244 (Ce) |
| $Ce^{3+}$ atop | 2.793 | 2.882 | 2.894 |
| $Ce^{4+}$ atop | 2.717 | 2.809 | 2.805 |
| $O_{surf}$ atop | 2.118 (10.5) | 2.209 (23.2) | 2.212 (20.2) |
| O–O bridge | —[a] | 2.196 (O) | 2.790 (O) |
| | | 2.874 (Ce) | 3.193 (Ce) |
| $V_{sub}$ atop | 2.222 (O) | 2.301 (O) | 2.322 (O) |
| | 2.938 (Ce) | 3.089 (Ce) | 3.103 (Ce) |

[a] Not stable; Au converges into the $V_{sub}$ atop position (see text).

Table 3 Oxidation state (OS) of Au and the $Ce^{3+}$ configuration within the cell for various adsorption structures in the $p(2 \times 2)$ cell of $CeO_2(111)$ containing a subsurface O vacancy

| | LDA+*U* | | PBE+*U* | | HSE | |
|---|---|---|---|---|---|---|
| Adsorption site | OS(Au) | $Ce^{3+}$ | OS(Au) | $Ce^{3+}$ | OS(Au) | $Ce^{3+}$ |
| $O_{sub}$ atop | −1 | $2_1$[a] | −1 | $2_1$ | −1 | $2_1$ |
| $Ce^{3+}$ atop | −1 | $2_1$ | −1 | $2_1$ | −1 | $2_1$ |
| $Ce^{4+}$ atop | −1 | $2_2$ | −1 | $2_2$ | −1 | $2_2$ |
| $O_{surf}$ atop | 0 | $2_1$–$2_2$ | 0 | $2_1$–$2_2$ | 0 | $2_1$–$2_2$ |
| O–O bridge | [b] | [b] | +1 | $1_1$–$2_1$–$2_2$ | 0 | $2_1$–$2_2$ |
| $V_{sub}$ atop | +1 | $1_1$–$2_1$–$2_2$ | +1 | $1_1$–$2_2$–$2_2$ | +1 | $1_1$–$2_1$–$2_2$ |

[a] The notation $n_m$ refers to the $n$th coordination shell of Ce ions around the vacancy and the $m$th Ce-ion layer in the slab and applies to each $Ce^{3+}$ in the cell.[74] [b] Not stable; Au converges into the $V_{sub}$ atop position (see text).

### B. Electronic structure details of $p(2 \times 2)$ cells

Fig. 2 compares the orbitally projected densities of states (PDOS) calculated using LDA+*U*, PBE+*U*, and HSE for Au adsorbed in atop position of $O_{surf}$ and $Ce^{3+}$ sites. These two sites were chosen because their relative stabilities depend on the DFA employed.

HSE (see Fig. 2c) predicts a larger gap between occupied O 2p and unoccupied Ce 4f states. Regarding the adsorption at $O_{surf}$, the occupied Au 6s state is *ca.* 1 eV lower in energy than the highest occupied 4f orbital being a $Ce^{3+}$-related defect state. Projecting layer-by-layer, one realizes that the highest occupied 4f orbital corresponds to the subsurface $Ce^{3+}$ ion (see also Section 3A). The second $Ce^{3+}$-related 4f state is close in energy compared with Au 6s and splits into two peaks most likely due to a crystal-field effect induced by the Au atom. LDA+*U* and PBE+*U* predict subsurface Ce 4f and Au 6s to be *de facto* energetically degenerate. The energy gap between surface and subsurface $Ce^{3+}$ $4f^1$ states is larger compared to the $p(4 \times 4)$ cell with a Na adatom (see Section 3A). LDA+*U*, PBE+*U*, as well as HSE predict the $4f^1$ orbital in subsurface position to be 0.5–0.6 eV higher in energy than the $4f^1$ stemming from a surface $Ce^{3+}$.

The PDOS for Au atop $Ce^{3+}$ indicates the formation of a $Au^-$ anion with a symmetric up and down spin component of the Au 6s orbital. The integrals of the spin-resolved peaks are equal, indicating occupation of one electron per spin channel, *i.e.* formation of $Au^-$ with a doubly occupied $6s^2$ orbital. Using HSE, the PDOS of Au 6s (spin down) is hidden by the PDOS of the 4f orbital corresponding to the surface $Ce^{3+}$, which may indicate that the two atoms interact. This appears plausible, because the atoms are spatially close to each other enabling overlap between the 6s and 4f orbitals, and these orbitals are also close in energy. The Au 5d orbitals are substantially higher in energy than the O 2p band. This contrasts with the PDOS of Au atop $O_{surf}$ featuring Au 5d states within the O 2p valence band.

The characteristics of the PDOS (lhs and rhs of Fig. 2c) are qualitatively reflected in relative stabilities shown in Table 1. Considering Au atop $O_{surf}$, essentially two effects may contribute when the Au adatom is transferred to $Ce^{3+}$: (i) energy gain upon transfer of the highest occupied $4f^1$ electron (subsurface $Ce^{3+}$) into Au 6s and (ii) destabilizing upshift of Au $5d^{10}$, $6s^2$, and Ce $4f^1$ orbitals w.r.t. the valence band edge. Effect (i) solely

 

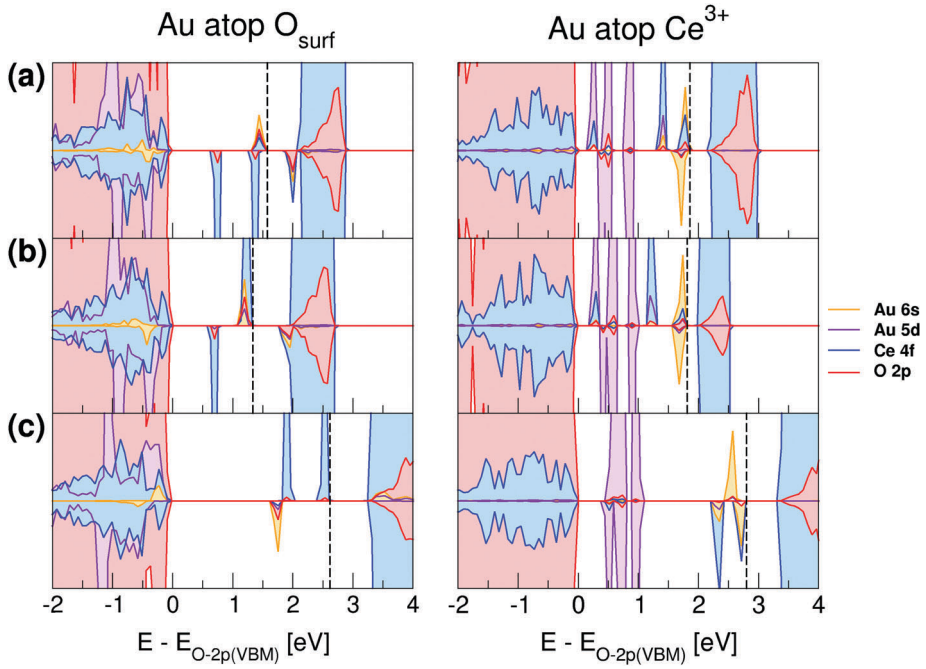


Fig. 2 Orbitally projected densities of states (PDOS) for Au adsorbed atop $O_{surf}$ (left) and atop $Ce^{3+}$ (right) using LDA+$U$ (a), PBE+$U$ (b) and HSE (c). Upper and lower half of each panel shows the up- and down-spin PDOS, respectively, aligned to the O 2p valence band maximum (VBM). The dashed line indicates the highest occupied energy level.

based on orbital energy differences suggests an energy gain of *ca.* 0.8 eV. This amount of energy certainly overestimates the energy difference between Au atop $Ce^{3+}$ and Au atop $O_{surf}$ structures. As shown in Table 1, HSE predicts 0.09 eV, a value almost one order of magnitude smaller. A large contribution to this decrease in relative stability is due to effect (ii). Fig. 2b (lhs) shows that Au $6s^1$ and Ce $4f^1$ orbital energies coincide using PBE+$U$, implying negligible stabilization by (i). Therefore, effect (ii) dominates and consequently Au atop $Ce^{3+}$ is less stable than Au atop $O_{surf}$. In contrast, these two adsorption sites are *de facto* degenerate in energy using LDA+$U$ although a very similar PDOS is obtained (see Fig. 2a). This points out the limits of interpreting DFT orbital energies as so-called quasi-particle energies representing particle excitations.[75]

### C. Effects upon varying $U_{eff}$

Upon increasing $U_{Ce\text{-}4f}$ in PBE+$U$ calculations, the occupied 4f states are, as expected, shifted towards lower energies (see Fig. 3). For Au adsorbed in atop position of $O_{surf}$, the effect is readily seen. The energy offset of the 4f orbital related to subsurface $Ce^{3+}$ relative to the Au 6s state is strongly influenced. This 4f level is higher in energy for $U_{Ce\text{-}4f}$ = 4 eV, is energetically degenerate for $U_{Ce\text{-}4f}$ = 4.5 eV, and is lower in energy than the Au 6s orbital for $U_{Ce\text{-}4f}$ = 5 eV.

To analyse the influence of the $U_{Ce\text{-}4f}$ parameter on adsorption energies, we varied $U_{Ce\text{-}4f}$ within a range of 3.5 and 5 eV in steps of 0.5 eV. The relative stability of the $O_{surf}$ site compared to the $Ce^{3+}$ site behaves proportional to the $U_{Ce\text{-}4f}$ parameter. The $Ce^{3+}$ site is more stable by 0.09 eV than Au atop $O_{surf}$ using $U_{Ce\text{-}4f}$ = 3.5 eV, while it is 0.21 eV higher in energy for $U_{Ce\text{-}4f}$ = 5 eV.

The interaction between Au and Ce was also studied by applying respective $U$ parameters to Au 6s ($U_{Au\text{-}6s}$) and 5d ($U_{Au\text{-}5d}$) states. We varied $U_{Au\text{-}6s}$ between 0.5 and 3 eV in steps of 0.5 eV, while keeping $U_{Ce\text{-}4f}$ constant at 4.5 eV. Increasing $U_{Au\text{-}6s}$ results in rather uniformly increasing total energies for both adsorption sites. Therefore, relative stabilities remained invariant with $U_{Au\text{-}6s}$ (see Fig. 4). Additional calculations with a $U_{Au\text{-}6s}$ of 4, 5 and 6 eV confirmed that this holds true for even larger values of $U_{Au\text{-}6s}$.

The oxidation state of Au in atop position of $Ce^{3+}$ depends on $U_{Au\text{-}6s}$. Complete charge transfer, creating a $Au^-$ anion, is energetically favoured for $U_{Au\text{-}6s}$ values up to 1.5 eV, partial charge transfer from the surface leading to $Au^{\delta-}$ is more favourable for $U_{Au\text{-}6s} \geq 2.0$ eV. The energy difference between these two charge states may be as large as 0.27 eV (partially charged Au more stable). The Au–Ce bond distance is *ca.* 0.1 to 0.2 Å larger in case of partial charge transfer compared with $Au^-$ atop $Ce^{3+}$.

For Au atop $O_{surf}$, the Au adatom remains electro-neutral in the ground state. However, for some of the applied $U_{Au\text{-}6s}$ values an additional solution involving partially oxidized $Au^{\delta+}$ was also found. Independent of $U_{Au\text{-}6s}$, the partially positively charged Au adsorbed at the surface is $\sim$0.13 eV less stable compared with $Au^0$. Regarding $Au^0$ atop O, the Au–O bond is tilted by *ca.* 20° relative to the surface normal, while $Au^{\delta+}$ sits in perfect atop position (*i.e.*, no tilting).

The $U_{Au\text{-}5d}$ value was varied between 1 and 7 eV in steps of 1 eV, keeping $U_{Ce\text{-}4f}$ constant at 4.5 eV. Increasing $U_{Au\text{-}5d}$ leads to a nonlinear increase of the total energy. However, the energy increase behaves in a site-specific manner, *i.e.* the energy of

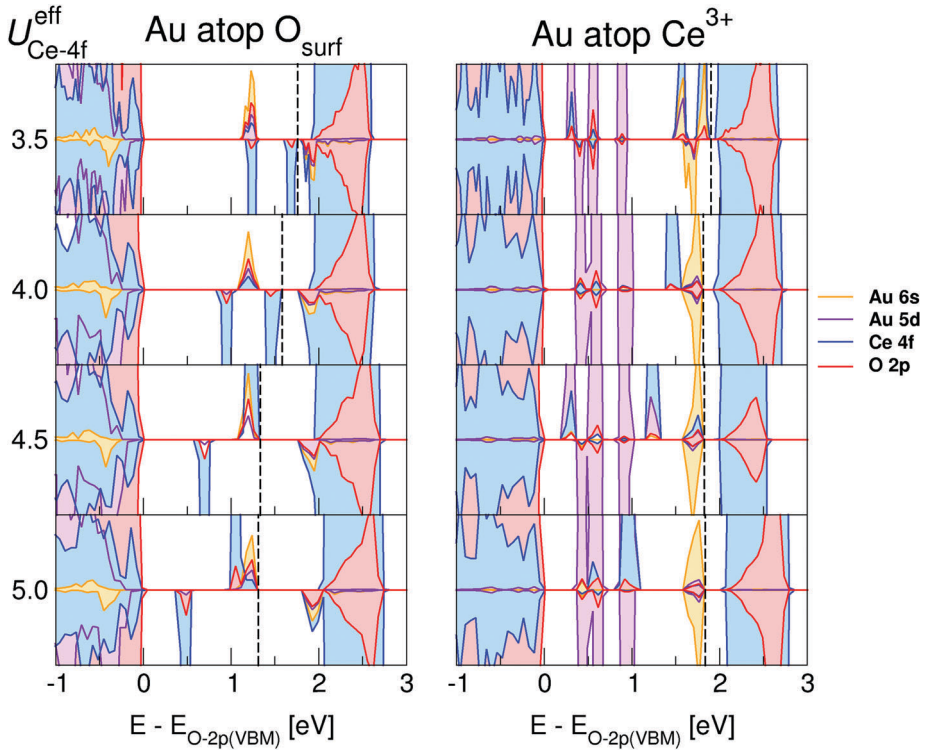


Fig. 3 PDOS of Au adsorbed atop $O_{surf}$ (left) and atop $Ce^{3+}$ (right) on the reduced $CeO_2$(111) surface using PBE+$U$ with $U_{Ce\text{-}4f}$ = 3.5, 4.0, 4.5, and 5.0 eV, aligned to the O 2p valence band maximum (VBM). The dashed line indicates the highest occupied energy level.

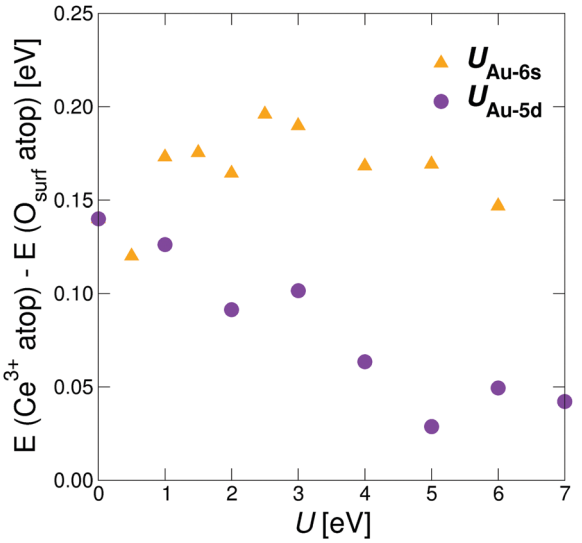


Fig. 4 Energy difference between Au atop $Ce^{3+}$ and Au atop $O_{surf}$ in the $p(2 \times 2)$ cell of $CeO_2$(111) with one subsurface O vacancy as a function of $U_{Au\text{-}6s}$ (gold) and $U_{Au\text{-}5d}$ (violet).

Au atop $O_{surf}$ approaches the energy of Au atop $Ce^{3+}$ upon increasing the $U_{Au\text{-}5d}$ (see Fig. 4). Thus, at large $U_{Au\text{-}5d}$ values, both adsorption sites are *de facto* equally favourable, with a difference in relative energies of only 0.03 eV using a $U_{Au\text{-}5d}$ = 5 eV.

The oxidation state of Au in atop position of $Ce^{3+}$ depends on the $U_{Au\text{-}5d}$ value. Conventional PBE+$U_{Ce\text{-}4f}$(4.5) or utilization of an additional (small) $U_{Au\text{-}5d}$ value of 1 eV results in a complete electron transfer creating a $Au^-$ anion, while electron delocalization or partial charge transfer involving a $Au^{\delta-}$ is energetically preferred for $U_{Au\text{-}5d} \geq 2$ eV. Upon increasing $U_{Au\text{-}5d}$, the energy difference between complete and partial charge transfer increases up to a maximum value of 0.2 eV for $U_{Au\text{-}5d}$ = 6 eV. For $U_{Au\text{-}5d}$ = 7 eV, only partial charge transfer was found. For Au atop O, both $Au^0$ and $Au^{\delta+}$ solutions exist, but similar to the scenario described for $U_{Au\text{-}6s}$, the electro-neutral $Au^0$ is more stable for all of the $U_{Au\text{-}5d}$ values tested in the present work.

Based on the above mentioned findings, an interaction between Au 6s and 5d orbitals is obvious. This is due to relativistic effects and has been amply discussed by Pyykkö.[49] Moreover, from a methodological point of view, a consistent treatment of Au 6s and 5d orbitals appears mandatory. This requirement is naturally met by hybrid functionals, but appears to be difficult to fulfil within the DFT+$U$ approach.

### D. Performance of other hybrid functionals for $p(2 \times 2)$ cells

HSE, PBE0, and B3LYP predict the same qualitative picture in terms of electronic structure (PDOS). The PDOS obtained using HSE (see Fig. 5) is representative for corresponding results obtained with PBE0 or B3LYP (see ESI†). Increasing the amount of FX in HSE to 50% shifts the occupied Ce $4f^1$ orbitals (of both, surface and subsurface $Ce^{3+}$) substantially below the Au 6s state. Analogous results are obtained for PBE0 (50% FX) and BHLYP.

In terms of electron localization, TPSSh results differ from those obtained using HSE, PBE0, or B3LYP. For Au adsorbed on $Ce^{3+}$, TPSSh predicts partial delocalization of the 4f electron into subsurface Ce 4f orbitals. Consequently, the former surface

 

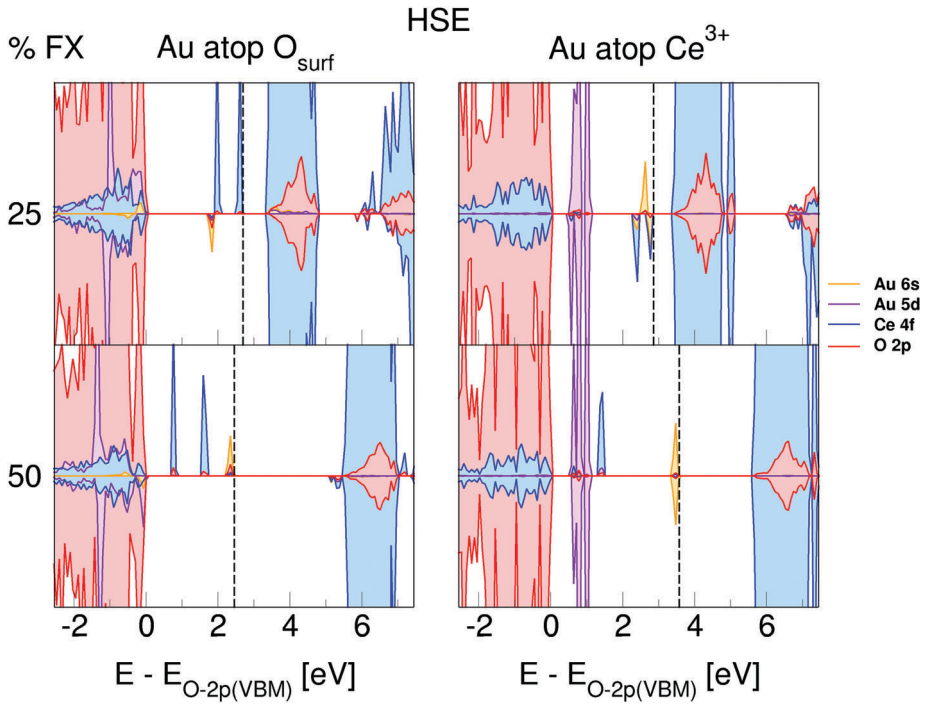


Fig. 5 PDOS of Au adsorbed atop $O_{surf}$ (left) and atop $Ce^{3+}$ (right) on the reduced $CeO_2$(111) surface, using HSE with 25% (top) and 50% (bottom) FX, aligned to the O 2p valence band maximum (VBM). The dashed line indicates the highest occupied energy level.

$Ce^{3+}$ ion carries a smaller local magnetic moment of 0.76 $\mu_B$ compared to 0.96 $\mu_B$ (see Section 2B). Similar delocalization of 4f electrons occurs in $O_{surf}$ and $O_{sub}$ atop structures. It appears that 10% of FX admixed in TPSSh is not sufficient to localize Ce 4f electrons. A test using HSE with 10% FX also leads to delocalization of these 4f electrons.

Relative energies and adsorption energies (see Tables 4 and 5) critically depend on the functional. HSE, PBE0, and TPSSh using the "as defined" amount of FX predict the $O_{sub}$ atop position to be the most stable adsorption site for a single Au atom. However, B3LYP slightly favours the atop position of $Ce^{3+}$. Depending on the employed functional, the $O_{surf}$ atop site is less stable than the $Ce^{3+}$ atop site by 0.08 to 0.38 eV.

Increasing the amount of FX to 50% using HSE, PBE0 and B3LYP (= BHLYP) changes the relative stability in favour of the $O_{surf}$ site. It is more stable by 0.42 to 0.59 eV relative to the $Ce^{3+}$ atop site (see Tables 4 and 5). Thus, in analogy to PBE+$U$ results discussed in Section 3C, we infer a correlation between relative stabilities of electron donor (Ce 4f) and acceptor (Au 6s) levels

Table 4 Relative energies in eV for various adsorption sites in the $p(2 \times 2)$ cell of $CeO_2$(111) with one subsurface O vacancy

| DFA | $a_{FX}$ | $O_{surf}$ atop | $Ce^{3+}$ atop | $O_{sub}$ atop |
|---|---|---|---|---|
| HSE | 0.25 | +0.40 | +0.31 | **0.00** |
| | 0.50 | **0.00** | +0.42 | +0.13 |
| B3LYP | 0.20 | +0.08 | **0.00** | +0.07 |
| BHLYP | 0.50 | **0.00** | +0.59 | +0.62 |
| PBE0 | 0.25 | +0.38 | +0.29 | **0.00** |
| | 0.50 | **0.00** | +0.45 | +0.19 |
| TPSSh | 0.10 | +0.74 | +0.36 | **0.00** |

Table 5 Adsorption energies in eV for various adsorption sites in the $p(2 \times 2)$ cell of $CeO_2$(111) with one subsurface O vacancy

| DFA | $a_{FX}$ | $O_{surf}$ atop | $Ce^{3+}$ atop | $O_{sub}$ atop |
|---|---|---|---|---|
| HSE | 0.25 | −0.55 | −0.64 | **−0.95** |
| | 0.50 | **−0.42** | +0.01 | −0.29 |
| B3LYP | 0.20 | −0.44 | **−0.52** | −0.45 |
| BHLYP | 0.50 | **−0.22** | +0.37 | +0.41 |
| PBE0 | 0.25 | −0.52 | −0.62 | **−0.91** |
| | 0.50 | **−0.32** | +0.13 | −0.13 |
| TPSSh | 0.10 | −0.57 | −0.95 | **−1.31** |

and the atop $Ce^{3+}$ and atop $O_{surf}$ sites. While adsorbing Au atop $Ce^{3+}$ involves electron transfer or equivalently reduction of Au, adsorption in atop position of $O_{surf}$ does not. In the latter case, the 4f orbitals remain partially occupied and hence contribute to the relative stability. Conversely, the energy difference between Au atop $Ce^{3+}$ and Au atop $O_{sub}$ is largely unaffected by the amount of FX because in both structures a $Au^-$ anion is formed leading to a consistent cancellation of energy contributions.

Validity of the alignment of Ce 4f and Au 6s orbitals relative to the O 2p valence band maximum was tested using non-selfconsistent as well as partially selfconsistent GW calculations (see Fig. S3 in the ESI†). These rather computationally expensive calculations have been accomplished for Au in atop position of $Ce^{3+}$ using the $p(2 \times 2)$ unit cell. According to results discussed in ref. 76, HSE orbitals and orbital energies have been used as an input. While HSE predicts virtually degenerate Ce $4f^1$ and Au $6s^2$ orbitals, GW results indicate a pronounced stabilization of the Au $6s^2$ orbitals. Also, the Au $5d^{10}$ orbitals, which are rather high in energy referenced to the O 2p valence

band edge, move back into the valence band employing non-selfconsistent and selfconsistent GW and are thus stabilized. The GW results, as the supposedly more accurate reference, suggest that electron transfer from $Ce^{3+}$ ($4f^1$) to $Au^0$ ($6s^1$) is even more favourable than predicted by HSE. In consequence, the Au atop $Ce^{3+}$ structure is expected to be further stabilized relative to Au atop $O_{surf}$ utilizing more accurate methods.

### E. Significance of the defect concentration

Table 6 shows PBE+$U$ and HSE adsorption energies of a single Au atom and the vertical $Au_2$ dimer on the pristine $CeO_2$(111) surface using both $p(2 \times 2)$ and $p(4 \times 4)$ unit cells. Independent of cell size, the $Au_2$ dimer is the most stable adsorption structure regardless of the DFA. Employing PBE+$U$, the O–O bridge site is the most stable adsorption site involving a single Au atom in oxidation state (OS) +1, which agrees with results reported in ref. 45. When Au adsorbs in atop position of a surface oxygen atom, it accommodates the oxidation state +1 and the structure is 0.13 eV less stable compared with the O–O bridge site. Note that relative stabilities do not change significantly using the $p(4 \times 4)$ cell, however, the adsorption proceeds substantially more exothermically, which is due to the lower $Ce^{3+}$ concentration (less strain). Although technical convergence for the structure optimization was reached, the other adsorption structures, *i.e.* $O_{sub}$ atop, O–Ce bridge, and $Ce^{4+}$ atop, were identified as saddle points on the PBE+$U$ potential energy surface using the $p(2 \times 2)$ cell. The O–Ce bridge site using a $p(4 \times 4)$ cell, however, is a local minimum as confirmed by normal mode analysis.

For the structures found using PBE+$U$, analogous HSE calculations have been accomplished. Using the $p(2 \times 2)$ cell, $Au^0$ at the O–Ce bridge site is the most stable adsorption structure. It is 0.05 eV more stable than $Au^0$ atop $O_{surf}$. These two adsorption sites are structurally similar. The main difference is a larger tilting angle of the Au–O bond for Au in O–Ce bridge position, while Au–O bond distances hardly deviate. A $Au^+$ in atop position of $O_{surf}$ was not considered in the present work, but as reported in ref. 43, it is about 0.15 eV higher in energy. For the adsorption of Au at the O–O bridge site, we found both solutions involving $Au^0$ and $Au^+$, the latter being 0.11 eV more stable. $Au^+$ in O–O bridge position is 0.10 eV less stable than $Au^0$ in O–Ce bridge position. These relative stabilities agree with the results reported by Branda *et al.* using GGA+$U$ with $U_{Ce\text{-}4f}$ = 3 eV and a lattice constant of 5.40 Å (*i.e.*, close to the experimental value).[43] In the $p(4 \times 4)$ cell, $Au^0$ at the O–Ce bridge site, $Au^0$ atop $O_{surf}$ and $Au^+$ in O–O bridge position are *de facto* degenerate in energy.

In contrast to HSE, PBE+$U$ adsorption energies are more exothermic and the PBE+$U$ method favours $Au^+$ over $Au^0$. This can be readily explained by the position of Ce 4f orbitals in the gap, which is affected by $U_{Ce\text{-}4f}$ (see Section 3C).[77,78] The lower the energy of the Ce 4f orbitals, the more favourable their occupation. In addition, $Ce^{3+}$ formation – as occurring upon oxidation of $Au^0$ to $Au^+$ – induces strain in the surface due to the larger ionic radius of $Ce^{3+}$ compared with $Ce^{4+}$. This elastic contribution to the total energy depends on two factors: (i) the description by the DFA approximation of elastic properties such as the bulk modulus of the material and (ii) the size of the surface unit cell. The smaller the cell, the higher the $Ce^{3+}$ concentration, which in turn relates to more pronounced and hence more stabilizing relaxation effects upon oxidizing $Ce^{3+}$.

Fig. 6 shows the $p(4 \times 4)$ unit cell of $CeO_2$(111) with one subsurface oxygen vacancy prior to Au adsorption. The subsurface O defect $V_{sub}$ is displayed by a dashed circle and the $Ce^{3+}$ ions are shown in dark blue. Both $Ce^{3+}$ are also marked with **1** and **2**. This, relative to the vacant site, symmetric $Ce^{3+}$ configuration having both $Ce^{3+}$ ions in the second cationic coordination shell with respect to $V_{sub}$, is the most stable $Ce^{3+}$ configuration.[48] Adsorption sites marked by **a** (site near $Ce^{3+}$ and $V_{sub}$), **b** (near $V_{sub}$), and **c** (far from $Ce^{3+}$ and $V_{sub}$) indicate surface oxygen atoms, while **d** indicates the position of a subsurface O ($O_{sub}$) atom near $V_{sub}$. The **d** site corresponds to the very stable $O_{sub}$ atop site in the $p(2 \times 2)$ unit cell.

Adsorption energies and oxidation states for the $p(2 \times 2)$ and $p(4 \times 4)$ cells obtained with PBE+$U$ and HSE are summarized in Table 7. We reproduced the finding reported in ref. 45,

Table 6 Adsorption energies (eV per atom) for one Au atom and the vertical $Au_2$ dimer on the pristine $CeO_2$(111) surface

| DFA | Site | OS(Au) | $p(2 \times 2)$ | OS(Au) | $p(4 \times 4)$ |
|---|---|---|---|---|---|
| PBE+$U$ | O–O bridge | +1 | −1.20 | +1 | −1.35 |
| | $O_{surf}$ atop | +1 | −1.07 | +1 | −1.24 |
| | $O_{sub}$ atop | +1 | −1.05[a] | +1 | −1.11[a] |
| | | 0 | −0.61[b] | — | — |
| | O–Ce bridge[c] | 0 | −0.79[a] | +1 | −1.01 |
| | $Ce^{4+}$ atop | 0 | −0.40[b] | 0 | −0.58[b] |
| | $Au_2$ atop $O_{surf}$ | 0 | −1.83 | 0 | −1.85 |
| HSE | $O_{surf}$ atop | 0 | −0.48 | 0 | −0.52 |
| | O–Ce bridge[c] | 0 | −0.52 | 0 | −0.53 |
| | O–O bridge | +1 | −0.43 | +1 | −0.53 |
| | | 0 | −0.31 | 0 | −0.30 |
| | $Au_2$ atop $O_{surf}$ | 0 | −1.58 | 0 | −1.63 |

[a] One imaginary frequency. [b] Two imaginary frequencies. [c] Tilting angle of the Au–O bond w.r.t. surface normal ~27°.

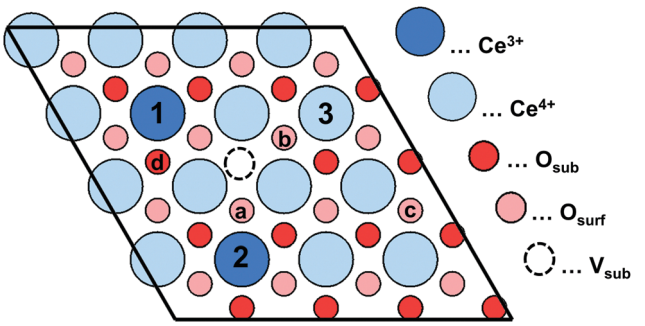


Fig. 6 Adsorption sites of a single Au atom on reduced $CeO_2$(111) containing one subsurface O vacancy in the $p(4 \times 4)$ surface unit cell. The two $Ce^{3+}$ ions in the structure prior to Au adsorption (*i.e.* the ground state, see ref. 48) are marked by **1** and **2**. The site marked by **3** indicates the electron accepting $Ce^{4+}$, when Au adsorbs at the site bridging $O_{surf}$ a and b (PBE+$U$, see text). $O_{surf}$ close to $V_{sub}$ and a $Ce^{3+}$ ion is marked by **a**, $O_{surf}$ close to $V_{sub}$ is marked by **b**, $O_{surf}$ far from $V_{sub}$ (and $Ce^{3+}$) is marked by **c**. The $O_{sub}$ site close to $Ce^{3+}$, as discussed in ref. 73, is marked by **d**.

Table 7 Adsorption energies (eV per atom) for one Au atom and the vertical $Au_2$ dimer on the reduced $CeO_{2-x}$(111) surface

| DFA | Site | OS(Au) | $p(2 \times 2)$ | Site | OS(Au) | $p(4 \times 4)$ |
|---|---|---|---|---|---|---|
| PBE+*U* | O–O bridge | +1 | −0.69 | O–O bridge | +1 | −1.15 |
| | $O_{surf}$ atop | 0 | −0.78[a,b] | $O_{surf}$ atop **a** | 0 | −0.86 |
| | | | | $O_{surf}$ atop **c** | +1 | −0.95 |
| | $O_{sub}$ atop | −1 | −0.95 | $O_{sub}$ atop **d** | 0 | −0.76 |
| | $Ce^{3+}$ atop | −1 | −0.64 | $Ce^{3+}$ atop **1** | $\delta-$ | −0.57[c,d] |
| | $Ce^{4+}$ atop | −1 | −0.61 | | | |
| | $V_{surf}$ atop | −1 | −2.44 | $V_{surf}$ atop | −1 | −2.10 |
| | $Au_2$ atop $V_{surf}$ | −1[e] | −1.70 | $Au_2$ atop $V_{surf}$ | −1[e] | −1.56[f] |
| HSE | $O_{surf}$ atop | 0 | −0.55[a,b] | $O_{surf}$ atop **a** | 0 | −0.56 |
| | | | | $O_{surf}$ atop **b** | 0 | −0.60 |
| | | | | $O_{surf}$ atop **c** | 0 | −0.50 |
| | $O_{sub}$ atop | −1 | −0.95 | $O_{sub}$ atop **d** | — | —[g] |
| | $Ce^{3+}$ atop | −1 | −0.64 | $Ce^{3+}$ atop **1** | — | —[c,d] |
| | $V_{surf}$ atop | −1 | −2.47 | $V_{surf}$ atop | −1 | −2.16 |
| | $Au_2$ atop $V_{surf}$ | −1[e] | −1.64 | | | |

[a] One imaginary frequency. [b] Tilting angle of the Au–O bond w.r.t. surface normal *ca.* 20° (see Table 2). [c] Upon complete electron transfer [OS(Au) = −1], reconstruction to $Au^-$ atop a surface oxygen vacancy occurs. [d] Site **1** is symmetry equivalent to site **2**. [e] Oxidation state of the entire $Au_2$ dimer ($Au_2^-$). [f] Without electron transfer, $O_{sub}$ fills $V_{surf}$ and $Au_2$ binds at the newly formed $O_{surf}$. This structure is 0.72 eV lower in energy than $Au_2^-$ atop $V_{surf}$. [g] No convergence reached upon several restarts.

hence $V_{surf}$ acts as an effective trap for Au atoms on the reduced $CeO_2$(111) surface. In atop position of $V_{surf}$, Au is always negatively charged, *i.e.* one electron from a $Ce^{3+}$ ion is transferred into the Au 6s orbital. For the $p(2 \times 2)$ cell, HSE predicts slightly more exothermic binding compared to PBE+*U*. Adsorption at surface oxygen vacancies on the $p(4 \times 4)$ cell is less exothermic, which is explained by (i) the smaller relaxation contribution due to the lower $Ce^{3+}$ concentration (less strain), and (ii) because the electron is transferred from a surface $Ce^{3+}$ ion instead of a subsurface $Ce^{3+}$ ion (see Section 3C). Note that the $2_1$–$2_2$ configuration in the $p(2 \times 2)$ cell for the surface defect was not considered in ref. 72. Independent of the approach, it is 0.07 eV more stable than $1_1$–$2_1$, and it has been taken as a reference for Au adsorption in the present work.

Adding a second Au atom, thus building an upright $Au_2$ dimer at the surface vacancy, is thermodynamically less favourable than the corresponding process on pristine $CeO_2$(111). This is explained by the occupation of an antibonding orbital of the Au–Au bond upon electron transfer from $Ce^{3+}$. On the $p(4 \times 4)$ cell, electron transfer is less favourable, and PBE+*U* predicts a reconstruction of this structure to (electro-neutral) $Au_2$ atop $O_{surf}$, *i.e.* an O atom in subsurface position fills $V_{surf}$ (thereby creating $V_{sub}$).

Results critically depend on the cell size upon adsorbing Au in atop position of $O_{sub}$ (**d** in Fig. 6). For the $p(2 \times 2)$ cell, PBE+*U* predicts an adsorption energy of −0.95 eV involving electron transfer from $Ce^{3+}$ to $Au^0$, while using the $p(4 \times 4)$ cell yields a significantly lower adsorption energy (−0.74 eV) involving no electron transfer. For the small cell, PBE+*U* agrees with HSE, but for the $p(4 \times 4)$ cell the HSE structure for Au atop d turned out to be unstable. Multiple attempts to converge the HSE energy as well as the atomic forces failed. This suggests that the $O_{sub}$ atop site is only relevant at high defect concentrations.

Adsorption of Au atop a $Ce^{3+}$ ion (**1** or **2** in Fig. 6) in the $p(4 \times 4)$ cell using PBE+*U* leads to two different solutions depending on the extent of charge transfer. Upon complete transfer of the Ce 4f electron to the Au, *i.e.* upon creation of $Au^-$, reconstruction of the surface occurs. One of the nearest neighbour surface O atoms relaxes into the $V_{sub}$ position, thereby creating $V_{surf}$, which is filled by $Au^-$. The driving force for this reconstruction is the very exothermic adsorption energy (−2.10 eV). Upon partial electron transfer, however, Au stays on top of the Ce ion. Using HSE, partial electron transfer could not be stabilized and hence only the solution involving reconstruction from $Au^-$ atop $Ce^{3+}$ to $Au^-$ atop $V_{surf}$ was found.

Based on HSE results for the $p(4 \times 4)$ unit cell, Au adsorption at the $O_{surf}$ **c** site is 0.10 eV less stable compared with the $O_{surf}$ **b** site, suggesting that adsorption near the vacancy is thermodynamically more favourable. In contrast, PBE+*U* adsorption energies are more exothermic for $O_{surf}$ sites far from the vacancy. A similar trend is found comparing adsorption energies for clean and oxygen-defective ceria. Disregarding Au atop $V_{surf}$, PBE+*U* adsorption energies are in general more exothermic for the clean $CeO_2$(111) surface than for the reduced one. In contrast, HSE results for the $p(4 \times 4)$ cell suggest a slightly more exothermic adsorption of Au atoms on the reduced surface.

### F. Comparison with other oxides

Adsorption energies of single Au atoms on defect-free metal oxide surfaces and at surface oxygen vacancies are reported in Table 8.

Table 8 Au adsorption energies, $\Delta E_{ads}$, in eV and oxidation state of Au, OS(Au), for various supports

| | | Defect-free surface | | | Surface O vacancy | |
|---|---|---|---|---|---|---|
| Support | Approach | Site | OS(Au) | $\Delta E_{ads}$ | $\Delta E_{ads}$ | Ref. |
| $CeO_2$(111) | PBE+*U*(4.5) | O–O bridge | +1 | −1.20 | −2.44 | This work |
| | HSE | O–Ce bridge | 0 | −0.52 | −2.49 | |
| Rutile $TiO_2$(110) | PW91 | O–Ti bridge | $\delta+$ | −0.68 | −2.33 | 84 |
| | PBE+*U*(4.2) | O–Ti bridge | $\delta+$ | −0.58 | −1.54 | 85 |
| Anatase $TiO_2$(101) | PBE+*U*(3.0) | Ti atop[a] | 0 | −0.61 | −3.07 | 79 |
| $ZrO_2$(101) | PBE+*U*(4.0) | O–Zr bridge | 0 | −1.20 | −4.22 | 79 |
| $V_2O_3$(0001) | PW91+*U*(2.5) | O–O bridge | $\delta+$ | −1.81 | −2.04 | 86 |
| $SiO_2$ bilayer | PW91 | Hollow[b] | 0 | −0.03 | −1.18[c] | 81 and 87 |
| $SiO_2$/Mo(112) | PW91 | Hollow[b] | 0 | −0.09 | −1.80[d] | 81 and 87 |
| α-$Al_2O_3$(0001) | PW91 | O atop | 0 | −0.81 | | 88 |

[a] Fig. 5 in ref. 79 indicates a slight tilting of the Au–Ti bond towards an O atom. [b] Au adsorbs above the centre of the hexagonal rings. [c] Au atom remains electro-neutral. [d] Instead of adsorption at the surface O vacancy, Au may also adsorb at the $SiO_2$–Mo interface (−2.87 eV).

As discussed in the previous section, adsorption energies depend on the approach and on the model (*e.g.*, cell size), nonetheless the strong binding of Au to surface oxygen vacancies is obvious. Adsorption at surface O vacancies is accompanied by electron transfer from the support to the adatom except for the $SiO_2$ bilayer. Similarly, adsorption near subsurface vacancies on anatase $TiO_2(101)$ (−1.61 eV) and $ZrO_2(101)$ (−2.43 eV) is more exothermic compared to respective defect-free surfaces.[79] Most stable structures are $Au^-$ atop $Ti^{4+}$ and $Zr^{4+}$, respectively. Other electron-rich defects such as Li[80] or Ti[81] dopants in $SiO_2$/Mo(112) films or additional Ti atoms in rutile $TiO_2(110)$ surfaces[82] also lead to a more exothermic Au adsorption compared to defect-free surfaces.

This work focuses on O vacancies as a source for electrons in the surface, and we refer the interested reader to the large body of work examining metal supported oxide films, where changes in the work function due to the nature of the metal oxide adlayer are crucial for the electron transfer (see ref. 83 and references therein).

# 4. Conclusions

PBE+*U* using $U = 4.5$ eV applied to Ce 4f predicts Au atoms on the pristine $CeO_2(111)$ surface to preferentially accommodate oxidation state +1, while HSE predicts the oxidation states 0 and +1 to be close in energy. The clear preference of PBE+*U* conflicts with recent experiments, whereas HSE results are reconcilable with observation.[46] Overall, HSE adsorption energies for the pristine surface are significantly less exothermic than corresponding PBE+*U* values.

Regardless of the method employed, surface oxygen vacancies serve as deep traps for single Au atoms. Moreover, we find that the dimerization reaction proceeds less exothermically than the adsorption of a single Au atom at the surface oxygen vacancy.

For the $p(2 \times 2)$ surface unit cell of reduced $CeO_2(111)$, we confirm that Au adsorbed atop of subsurface oxygen in nearest-neighbour position to the surface $Ce^{3+}$ ion represents the most stable adsorption structure.[73] A qualitatively different picture is obtained for the $p(4 \times 4)$ surface unit cell corresponding to a lower and (with regard to experiment) more realistic defect concentration. In this case, the aforementioned structure is not stable. Instead, PBE+*U* predicts the O–O bridge position to be the most favourable site for Au adsorption, while HSE favours Au atop surface O ions close to the vacancy. Both method as well as O-defect concentration (*i.e.* size of unit cell) impact stability of donor and acceptor orbitals, in turn affecting relative stabilities of adsorption sites. The DFT+*U* approach is a computationally efficient and useful method; however, for systems involving electron transfer careful checking of results is strongly advised. Although (conventional) hybrid functionals do not properly account for important electron correlation effects like van der Waals dispersion interactions, electron transfer related phenomena upon adsorption of Au atoms on $CeO_{2-x}(111)$ surfaces appear to be accurately described employing ∼25% of Fock exchange.

# Acknowledgements

It is our pleasure to thank Professor Joachim Sauer and Professor Hans-Joachim Freund for their continuous support and many insightful discussions. We also thank Dr M. Verónica Ganduglia-Pirovano for some discussions on the topic. This work has been supported by the ''Fonds der Chemischen Industrie'' (FCI) as well as by grants for computing time at the high-performance computer centers HLRN (North-German Supercomputing Alliance in Berlin and Hannover) and JUROPA (Forschungszentrum Jülich). Furthermore, we acknowledge COST action CM1104 entitled ''reducible oxide chemistry, structure, and functions'' and the ''Stiftung Industrieforschung der Humboldt-Universität zu Berlin'' for support.

# References

1 M. Haruta and M. Date, *Appl. Catal., A*, 2001, **222**, 427–437.
2 M. Haruta, *CATTECH*, 2002, **6**, 102–115.
3 M. Haruta, *Chem. Rec.*, 2003, **3**, 75–87.
4 M. Haruta, *Gold Bull.*, 2004, **37**, 27–36.
5 A. Trovarelli, *Catalysis by Ceria and Related Materials*, Imperial College Press, London, 2002.
6 Q. Fu, H. Saltsburg and M. Flytzani-Stephanopoulos, *Science*, 2003, **301**, 935–938.
7 Q. Fu, W. L. Deng, H. Saltsburg and M. Flytzani-Stephanopoulos, *Appl. Catal., B*, 2005, **56**, 57–68.
8 G. L. Haller and D. E. Resasco, *Adv. Catal.*, 1989, **36**, 173–235.
9 S. J. Tauster, *Acc. Chem. Res.*, 1987, **20**, 389–394.
10 C. T. Campbell, *Nat. Chem.*, 2012, **4**, 597–598.
11 J. A. Farmer and C. T. Campbell, *Science*, 2010, **329**, 933–936.
12 M. Skoda, M. Cabala, I. Matolinova, K. C. Prince, T. Skala, F. Sutara, K. Veltruska and V. Matolin, *J. Chem. Phys.*, 2009, **130**, 034703.
13 G. N. Vayssilov, Y. Lykhach, A. Migani, T. Staudt, G. P. Petrova, N. Tsud, T. Skala, A. Bruix, F. Illas, K. C. Prince, V. Matolin, K. M. Neyman and J. Libuda, *Nat. Mater.*, 2011, **10**, 310–315.
14 J. L. Lu, H. J. Gao, S. Shaikhutdinov and H. J. Freund, *Surf. Sci.*, 2006, **600**, 5004–5010.
15 J. L. Lu, H. J. Gao, S. Shaikhutdinov and H. J. Freund, *Catal. Lett.*, 2007, **114**, 8–16.
16 C. Zhang, A. Michaelides, D. A. King and S. J. Jenkins, *J. Chem. Phys.*, 2008, **129**, 194708.
17 N. C. Hernandez, R. Grau-Crespo, N. H. de Leeuw and J. F. Sanz, *Phys. Chem. Chem. Phys.*, 2009, **11**, 5246–5252.
18 M. F. Camellone and S. Fabris, *J. Am. Chem. Soc.*, 2009, **131**, 10473–10483.
19 N. V. Skorodumova, R. Ahuja, S. I. Simak, I. A. Abrikosov, B. Johansson and B. I. Lundqvist, *Phys. Rev. B: Condens. Matter Mater. Phys.*, 2001, **64**, 115108.
20 G. Kresse, P. Blaha, J. L. F. Da Silva and M. V. Ganduglia-Pirovano, *Phys. Rev. B: Condens. Matter Mater. Phys.*, 2005, **72**, 237101.
21 J. L. F. Da Silva, M. V. Ganduglia-Pirovano, J. Sauer, V. Bayer and G. Kresse, *Phys. Rev. B: Condens. Matter Mater. Phys.*, 2007, **75**, 045121.

 

22 V. Ganduglia-Pirovano, A. Hofmann and J. Sauer, *Surf. Sci. Rep.*, 2007, **62**, 219–270.
23 J. Paier, C. Penschke and J. Sauer, *Chem. Rev.*, 2013, **113**, 3949–3985.
24 V. I. Anisimov, J. Zaanen and O. K. Andersen, *Phys. Rev. B: Condens. Matter Mater. Phys.*, 1991, **44**, 943–954.
25 A. I. Liechtenstein, V. I. Anisimov and J. Zaanen, *Phys. Rev. B: Condens. Matter Mater. Phys.*, 1995, **52**, R5467–R5470.
26 C. W. M. Castleton, J. Kullgren and K. Hermansson, *J. Chem. Phys.*, 2007, **127**, 244704.
27 S. Lutfalla, V. Shapovalov and A. T. Bell, *J. Chem. Theory Comput.*, 2011, **7**, 2218–2223.
28 Z. Hu, B. Li, X. Sun and H. Metiu, *J. Phys. Chem. C*, 2011, **115**, 3065–3074.
29 M. Cococcioni and S. de Gironcoli, *Phys. Rev. B: Condens. Matter Mater. Phys.*, 2005, **71**, 035105.
30 F. Aryasetiawan, K. Karlsson, O. Jepsen and U. Schönberger, *Phys. Rev. B: Condens. Matter Mater. Phys.*, 2006, **74**, 125106.
31 A. D. Becke, *J. Chem. Phys.*, 1993, **98**, 5648–5652.
32 J. P. Perdew, M. Ernzerhof and K. Burke, *J. Chem. Phys.*, 1996, **105**, 9982–9985.
33 S. Chawla and G. A. Voth, *J. Chem. Phys.*, 1998, **108**, 4697–4700.
34 J. Paier, R. Hirschl, M. Marsman and G. Kresse, *J. Chem. Phys.*, 2005, **122**, 234102.
35 M. Betzinger, C. Friedrich and S. Bluegel, *Phys. Rev. B: Condens. Matter Mater. Phys.*, 2010, **81**, 195117.
36 J. Graciani, A. M. Marquez, J. J. Plata, Y. Ortega, N. C. Hernandez, A. Meyer, C. M. Zicovich-Wilson and J. F. Sanz, *J. Chem. Theory Comput.*, 2011, **7**, 56–65.
37 J. P. Perdew, K. Burke and M. Ernzerhof, *Phys. Rev. Lett.*, 1996, **77**, 3865–3868.
38 S. Fabris, S. de Gironcoli, S. Baroni, G. Vicario and G. Balducci, *Phys. Rev. B: Condens. Matter Mater. Phys.*, 2005, **72**, 237102.
39 J. Heyd, G. E. Scuseria and M. Ernzerhof, *J. Chem. Phys.*, 2003, **118**, 8207–8215.
40 J. Paier, *Catal. Lett.*, 2016, **146**, 861–885.
41 Z. P. Liu, S. J. Jenkins and D. A. King, *Phys. Rev. Lett.*, 2005, **94**, 196102.
42 N. J. Castellani, M. A. Branda, K. M. Neyman and F. Illas, *J. Phys. Chem. C*, 2009, **113**, 4948–4954.
43 M. M. Branda, N. J. Castellani, R. Grau-Crespo, N. H. de Leeuw, N. C. Hernandez, J. F. Sanz, K. M. Neyman and F. Illas, *J. Chem. Phys.*, 2009, **131**, 094702.
44 M. M. Branda, N. C. Hernandez, J. F. Sanz and F. Illas, *J. Phys. Chem. C*, 2010, **114**, 1934–1941.
45 C. J. Zhang, A. Michaelides and S. J. Jenkins, *Phys. Chem. Chem. Phys.*, 2011, **13**, 22–33.
46 Y. Pan, Y. Cui, C. Stiehler, N. Nilius and H. J. Freund, *J. Phys. Chem. C*, 2013, **117**, 21879–21885.
47 Y. Chen, P. Hu, M. H. Lee and H. F. Wang, *Surf. Sci.*, 2008, **602**, 1736–1741.
48 Y. Pan, N. Nilius, H.-J. Freund, J. Paier, C. Penschke and J. Sauer, *Phys. Rev. Lett.*, 2013, **111**, 206101, Erratum: *Phys. Rev. Lett.*, 2015, **115**, 269901.
49 P. Pyykkö, *Angew. Chem., Int. Ed.*, 2004, **43**, 4412–4456.
50 N. A. Deskins, R. Rousseau and M. Dupuis, *J. Phys. Chem. C*, 2010, **114**, 5891–5897.
51 N. A. Deskins and M. Dupuis, *Phys. Rev. B: Condens. Matter Mater. Phys.*, 2007, **75**, 195212.
52 J. J. Plata, A. M. Marquez and J. F. Sanz, *J. Phys. Chem. C*, 2013, **117**, 25497–25503.
53 J. J. Plata, A. M. Marquez and J. F. Sanz, *J. Phys. Chem. C*, 2013, **117**, 14502–14509.
54 P. G. Lustemberg, Y. Pan, B. J. Shaw, D. Grinter, C. Pang, G. Thornton, R. Perez, M. V. Ganduglia-Pirovano and N. Nilius, *Phys. Rev. Lett.*, 2016, **116**, 236101.
55 P. E. Blöchl, *Phys. Rev. B: Condens. Matter Mater. Phys.*, 1994, **50**, 17953–17979.
56 G. Kresse and D. Joubert, *Phys. Rev. B: Condens. Matter Mater. Phys.*, 1999, **59**, 1758–1775.
57 G. Kresse and J. Furthmüller, *Phys. Rev. B: Condens. Matter Mater. Phys.*, 1996, **54**, 11169–11186.
58 G. Kresse and J. Furthmüller, *Comput. Mater. Sci.*, 1996, **6**, 15–50.
59 S. L. Dudarev, G. A. Botton, S. Y. Savrasov, C. J. Humphreys and A. P. Sutton, *Phys. Rev. B: Condens. Matter Mater. Phys.*, 1998, **57**, 1505–1509.
60 O. Bengone, M. Alouani, P. Blöchl and J. Hugel, *Phys. Rev. B: Condens. Matter Mater. Phys.*, 2000, **62**, 16392–16401.
61 A. V. Krukau, O. A. Vydrov, A. F. Izmaylov and G. E. Scuseria, *J. Chem. Phys.*, 2006, **125**, 224106.
62 M. Ernzerhof and G. E. Scuseria, *J. Chem. Phys.*, 1999, **110**, 5029–5036.
63 C. Adamo and V. Barone, *J. Chem. Phys.*, 1999, **110**, 6158–6170.
64 V. N. Staroverov, G. E. Scuseria, J. M. Tao and J. P. Perdew, *J. Chem. Phys.*, 2003, **119**, 12129–12137.
65 J. M. Tao, J. P. Perdew, V. N. Staroverov and G. E. Scuseria, *Phys. Rev. Lett.*, 2003, **91**, 146401.
66 J. Sun, M. Marsman, G. I. Csonka, A. Ruzsinszky, P. Hao, Y.-S. Kim, G. Kresse and J. P. Perdew, *Phys. Rev. B: Condens. Matter Mater. Phys.*, 2011, **84**, 035117.
67 A. D. Becke, *J. Chem. Phys.*, 1993, **98**, 1372–1377.
68 S. Grimme, *J. Comput. Chem.*, 2006, **27**, 1787–1799.
69 F. D. Murnaghan, *Proc. Natl. Acad. Sci. U. S. A.*, 1944, **30**, 244–247.
70 H. J. Monkhorst and J. D. Pack, *Phys. Rev. B: Solid State*, 1976, **13**, 5188–5192.
71 G. Makov and M. C. Payne, *Phys. Rev. B: Condens. Matter Mater. Phys.*, 1995, **51**, 4014–4022.
72 M. V. Ganduglia-Pirovano, J. L. F. Da Silva and J. Sauer, *Phys. Rev. Lett.*, 2009, **102**, 02610101.
73 K. Kosmider, V. Brazdova, M. V. Ganduglia-Pirovano and R. Perez, *J. Phys. Chem. C*, 2016, **120**, 927–933.
74 J. F. Jerratsch, X. Shao, N. Nilius, H.-J. Freund, C. Popa, M. V. Ganduglia-Pirovano, A. M. Burow and J. Sauer, *Phys. Rev. Lett.*, 2011, **106**, 246801.
75 R. O. Jones and O. Gunnarsson, *Rev. Mod. Phys.*, 1989, **61**, 689–746.
76 F. Fuchs, J. Furthmüller, F. Bechstedt, M. Shishkin and G. Kresse, *Phys. Rev. B: Condens. Matter Mater. Phys.*, 2007, **76**, 115109.

77 M. Huang and S. Fabris, *J. Phys. Chem. C*, 2008, **112**, 8643–8648.
78 C. Loschen, J. Carrasco, K. M. Neyman and F. Illas, *Phys. Rev. B: Condens. Matter Mater. Phys.*, 2007, **75**, 035115.
79 P. Schlexer, A. R. Puigdollers and G. Pacchioni, *Phys. Chem. Chem. Phys.*, 2015, **17**, 22342–22360.
80 U. Martinez, L. Giordano and G. Pacchioni, *ChemPhysChem*, 2010, **11**, 412–418.
81 L. Giordano, A. Del Vitto and G. Pacchioni, *J. Chem. Phys.*, 2006, **124**, 034701.
82 U. Martinez and B. Hammer, *J. Chem. Phys.*, 2011, **134**, 194703.
83 G. Pacchioni and H.-J. Freund, *Chem. Rev.*, 2013, **113**, 4035–4072.
84 A. Vijay, G. Mills and H. Metiu, *J. Chem. Phys.*, 2003, **118**, 6536–6551.
85 M. F. Camellone, P. M. Kowalski and D. Marx, *Phys. Rev. B: Condens. Matter Mater. Phys.*, 2011, **84**, 035413.
86 N. Nilius, V. Brazdova, M. V. Ganduglia-Pirovano, V. Simic-Milosevic, J. Sauer and H. F. Freund, *New J. Phys.*, 2009, **11**, 093007.
87 U. Martinez, L. Giordano and G. Pacchioni, *J. Phys. Chem. B*, 2006, **110**, 17015–17023.
88 N. C. Hernandez, J. Graciani, A. Marquez and J. F. Sanz, *Surf. Sci.*, 2005, **575**, 189–196.

 

# P11

https://pubs.acs.org/doi/abs/10.1021/acs.inorgchem.6b00467

Inorganic Chemistry

Article

pubs.acs.org/IC

# Structural and Electronic Effects on the Properties of $Fe_2$(dobdc) upon Oxidation with $N_2O$

Joshua Borycz,[†,‡] Joachim Paier,*[,§] Pragya Verma,[†,‡] Lucy E. Darago,[‡,∥] Dianne J. Xiao,[‡,∥] Donald G. Truhlar,*[,†,‡] Jeffrey R. Long,*[,‡,∥,⊥,#] and Laura Gagliardi*[,†,‡]

[†]Department of Chemistry, Minnesota Supercomputing Institute, and Chemical Theory Center, University of Minnesota, 207 Pleasant Street SE, Minneapolis, Minnesota 55455-0431, United States

[‡]Nanoporous Materials Genome Center, University of Minnesota, 207 Pleasant Street SE, Minneapolis, Minnesota 55455-0431, United States

[§]Institut für Chemie, Humboldt-Universität zu Berlin, Unter den Linden 6, 10099 Berlin, Germany

[∥]Department of Chemistry, University of California, Berkeley, California 94720-1460, United States

[⊥]Department of Chemical and Biomolecular Engineering, University of California, Berkeley, California 94720-1462, United States

[#]Materials Sciences Division, Lawrence Berkeley National Laboratory, Berkeley, California 94720, United States

Supporting Information

**ABSTRACT:** We report electronic, vibrational, and magnetic properties, together with their structural dependences, for the metal−organic framework $Fe_2$(dobdc) (dobdc$^{4-}$ = 2,5-dioxido-1,4-benzenedicarboxylate) and its derivatives, $Fe_2(O)_2$(dobdc) and $Fe_2(OH)_2$(dobdc)—species arising in the previously proposed mechanism for the oxidation of ethane to ethanol using $N_2O$ as an oxidant. Magnetic susceptibility measurements reported for $Fe_2$(dobdc) in an earlier study and reported in the current study for $Fe^{II}_{0.26}[Fe^{III}(OH)]_{1.74}$(dobdc)$(DMF)_{0.15}(THF)_{0.22}$, which is more simply referred to as $Fe_2(OH)_2$(dobdc), were used to confirm the computational results. Theory was also compared to experiment for infrared spectra and powder X-ray diffraction structures. Structural and magnetic properties were computed by using Kohn−Sham density functional theory both with periodic boundary conditions and with cluster models. In addition, we studied the effects of different treatments of the exchange interactions on the magnetic coupling parameters by comparing several approaches to the exchange-correlation functional: generalized gradient approximation (GGA), GGA with empirical Coulomb and exchange integrals for 3*d* electrons (GGA+U), nonseparable gradient approximation (NGA) with empirical Coulomb and exchange integrals for 3*d* electrons (NGA+U), hybrid GGA, meta-GGA, and hybrid meta-GGA. We found the coupling between the metal centers along a chain to be ferromagnetic in the case of $Fe_2$(dobdc) and antiferromagnetic in the cases of $Fe_2(O)_2$(dobdc) and $Fe_2(OH)_2$(dobdc). The shift in magnetic coupling behavior correlates with the changing electronic structure of the framework, which derives from both structural and electronic changes that occur upon metal oxidation and addition of the charge-balancing oxo and hydroxo ligands.

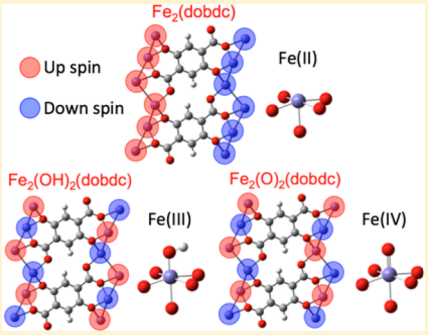


## 1. INTRODUCTION

The study of magnetic porous materials is interesting because of the many possible lightweight crystalline magnets and their potential applications.[1] Porous materials have been used as molecular magnetic sponges to absorb water[2] and to improve the sensitivity and efficiency of molecular sensors.[3,4] Established theories[5] and trends[6,7] regarding magnetism within metal-oxide complexes can be used to predict magnetic behaviors of newly discovered or even as-yet unsynthesized materials through the use of quantum mechanical calculations.

One class of porous materials that has garnered considerable attention in the field of magnetism is metal−organic frameworks (MOFs), which consist of metal-containing nodes connected by organic linkers. The tunability and structural diversity of MOFs make them attractive materials for a variety of potential applications. MOFs have been synthesized with magnetically isolated nodes,[8] magnetically coupled nodes,[3,9] flexible pores,[10] very large pore diameters,[11] and combinations of these features. The $M_2$(dobdc) series, where M = Mg, Mn, Fe, Co, Ni, Cu, Zn, or Cd, and dobdc$^{4-}$ = 2,5-dioxido-1,4-benzenedicarboxylate, has been studied extensively for its gas adsorption ability[12,13] and magnetic properties.[14] Recently, for example, it was shown that $Fe_2$(dobdc) can selectively adsorb olefins over paraffins.[15,16] Upon adsorption of olefins, the magnetic ordering of the Fe(II) centers changes from ferromagnetic coupling down the one-dimensional chains to antiferromagnetic exchange, which was attributed to enhanced superexchange upon olefin adsorption.[16,17] Furthermore, there is experimental and computational evidence that suggests that

**Received:** February 24, 2016
**Published:** May 2, 2016






DOI: 10.1021/acs.inorgchem.6b00467
*Inorg. Chem.* 2016, 55, 4924−4934

$Fe_2$(dobdc) exhibits metastable magnetic behavior that is sensitive to temperature, local coordination environment, and the type of guest molecules present in the pores of the MOF.[16,18]

Four derivatives of $Fe_2$(dobdc), namely $Fe_2(OH)_2$(dobdc), $Fe_2(O)_2$(dobdc), $Fe_{0.1}(OH)_{0.1}Mg_{1.9}$(dobdc), and $Fe_{0.1}(O)_{0.1}Mg_{1.9}$(dobdc), were shown to be involved (in the case of the first named derivative) or postulated to be involved (in the case of the other three) in studies of the catalytic conversion of ethane to ethanol.[19,20] The compound $Fe_2(OH)_2$(dobdc) is a product of the reaction of ethane, $N_2O$, and $Fe_2$(dobdc), which proceeds through $Fe_2(O)_2$(dobdc) as a theoretically calculated reactive intermediate.[19,20] In particular, the high-spin ($S = 2$) character of the Fe(IV)−oxo species contained within this intermediate was determined to be important for facilitating the ethane oxidation reaction. In order to provide insight into the tunability of the magnetic character of these MOFs, we study here the electronic structure effects resulting from differing metal oxidation states in synthesized $Fe_2$(dobdc) and $Fe_2(OH)_2$(dobdc) compounds, as well as the highly reactive—and, therefore, fleeting—intermediate $Fe_2(O)_2$(dobdc). The parent framework, $Fe_2$(dobdc), contains Fe(II) centers with a quintet ground state, while $Fe_2(OH)_2$(dobdc) contains Fe(III) centers with a sextet ground state, and $Fe_2(O)_2$(dobdc) contains Fe(IV) centers with a quintet ground state.[19,20]

The change in magnetic ordering upon adsorption of oxygen-containing species (e.g., $H_2O$) has been investigated previously for many MOFs,[1,21] and the magnetic properties of $Fe_2$(dobdc) with and without bound guests have previously been calculated using both cluster[18] and periodic[9,14,17] models. Kohn−Sham (KS) density functional calculations that employ local exchange-correlation functionals (local-spin-density approximations, generalized gradient approximations (GGAs), and meta-GGAs) have a tendency to overestimate the magnetic coupling constants between the magnetic centers within $Fe_2$(dobdc),[9,17,18] most likely due to overdelocalization of unpaired spins. To attempt to remediate this, one can use empirical Coulomb and exchange integrals for selected subshells (the 3*d* subshell of Fe in the present work), which is the DFT+U method,[22] or one can include a portion of Hartree−Fock exchange[18,23,24] by using hybrid exchange-correlation functionals. Guidance regarding the value of the *U* parameter of the DFT+U method or a suitable amount of Hartree−Fock exchange for the calculation of magnetic properties can be sought from previous studies on similar materials[14,25,26] or from general parametrization of exchange-correlation functionals.

Magnetic MOFs occupy an intermediate position between molecular magnets and bulk transition-metal oxide magnets. In MOFs, one can, in principle, tune the magnetic coupling constants by judicious choice of metal, linker, or both during synthesis and by post-synthetic guest molecule adsorption. Quantum mechanical computations can help to understand the underlying physics behind magnetically ordered MOFs and to predict properties that may currently be inaccessible by synthetic methods. The present work concerns magnetic exchange coupling, which is often quite small in MOFs (for example, 1−10 $cm^{-1}$), and the prediction of such small quantities is difficult. Understanding the capabilities and/or inadequacies of various methods is indispensable when assessing the accuracy of calculations, but the calculation of trends can yield insight even when absolute values show errors. When performing these calculations on MOFs, one can use either a periodic model or a cluster model. Calculations performed with cluster models can be performed with a wider array of methods, but cluster calculations can be inaccurate if the cluster is too small or must be constrained too tightly.

Here, we report structural and magnetic characteristics of $Fe_2$(dobdc), $Fe_2(O)_2$(dobdc), and $Fe_2(OH)_2$(dobdc) obtained using KS density functional methods with both periodic and cluster models, together with experimental magnetic susceptibility data for $Fe^{II}_{0.26}[Fe^{III}(OH)]_{1.74}$(dobdc)-$(DMF)_{0.15}(THF)_{0.22}$ (where DMF denotes dimethylformamide, and THF denotes tetrahydrofuran). Descriptions of the experimental and computational procedures can be found in section 2, while section 3 provides results and discussion, and section 4 summarizes our conclusions.

## 2. METHODS

**2.1. Preparation and Magnetic Susceptibility Measurements of Hydroxylated $Fe_2$(dobdc).** The material $Fe^{II}_{0.26}[Fe^{III}(OH)]_{1.74}$(dobdc)$(DMF)_{0.15}(THF)_{0.22}$ was prepared by exposure of $Fe_2$(dobdc) to excess $N_2O$(g) at 60 °C. Mössbauer spectroscopy of the resultant material indicated that 87% of the Fe(II) sites had been oxidized to Fe(III). Full oxidation to the exact formula $Fe_2(OH)_2$(dobdc) could not be achieved without a loss in crystallinity. Elemental analysis of this material indicated that residual amounts of DMF and THF were present in the material. Anal. Calcd for $C_{9.33}H_{6.55}Fe_2N_{0.15}O_{8.11}$: C, 30.94; H, 1.82; N, 0.58. Found: C, 30.90; H, 1.60; N, 0.58.

For the sake of convenience, the material $Fe^{II}_{0.26}[Fe^{III}(OH)]_{1.74}$(dobdc)$(DMF)_{0.15}(THF)_{0.22}$ will be referenced hereafter as $Fe_2(OH)_2$(dobdc). Direct current (DC) magnetic susceptibility measurements were performed on $Fe_2(OH)_2$(dobdc) under an applied magnetic field of 1000 Oe. Magnetic samples were prepared by adding powdered crystalline compounds to a 7-mm-diameter quartz tube with a raised quartz platform. Solid eicosane was added to cover the samples to prevent crystallite torqueing and provide good thermal contact between the sample and the cryogenic bath. The tubes were fitted with Teflon sealable adapters, evacuated on a Schlenk line or using a glovebox vacuum pump, and sealed under vacuum using an $H_2/O_2$ flame. Following flame sealing, the solid eicosane was melted in a water bath at 40 °C. Data for $Fe_2(OH)_2$(dobdc) were corrected for diamagnetic contributions from the core diamagnetism estimated using Pascal's constants[27] to give $\chi_D$ values of −0.00027434 emu/mol and −0.00024306 emu/mol (eicosane).

In earlier work on $Fe_2$(dobdc),[16] the temperature dependence of the magnetic susceptibility was interpreted using a two-parameter model, the Fisher model,[28,29] corresponding to a chain of Fe ions interacting with nearest neighbors in the same chain and with Fe ions in *z* other chains. The parameters are $J_{NN}$ and $zJ_{IC}$, where $J_{NN}$ is the magnetic coupling of nearest neighbors, and $J_{IC}$ is the magnetic coupling of Fe atoms in different chains. We also attempted to apply this to $Fe_2(OH)_2$(dobdc), and the results of this attempt are described in section 3.3.

**2.2. Electronic Structure Calculations.** *2.2.1. Exchange-Correlation Functionals.* We used several exchange-correlation functionals—in particular, PBE, PBE+U, HSE06, PBE-D2, PBE+U-D2, HSE06-D2, and GAM+U for periodic calculations and PBE, M06-L, PBE0, B3LYP, M06, and HSE06 for cluster calculations. The PBE[30] and GAM[31,32] exchange-correlation functionals are local gradient approximations, and M06-L[33,34] is a local meta approximation. Because local approximations have a tendency to underestimate band gaps[25,34−37] and overdelocalize charge distributions,[38−41] we also employed hybrid approximations that replace a percentage *X* of local exchange by nonlocal Hartree−Fock exchange. Inclusion of some Hartree−Fock exchange also affects the atomic spin distribution[42] and geometries.[42,43] B3LYP,[44−47] PBE0,[48,49] and M06[50] are global hybrids, which means that they use the same percentage *X* for all


DOI: 10.1021/acs.inorgchem.6b00467
Inorg. Chem. 2016, 55, 4924−4934

interelectronic separations. PBE0 and B3LYP are global-hybrid gradient approximations with $X$ = 25 and 20, respectively, and M06 is a global-hybrid meta approximation with $X$ = 27.

Periodic calculations were performed with plane-wave basis sets with the Vienna Ab initio Simulation Package (*VASP*).[51,52] Using global-hybrid functionals for plane-wave calculations can be very expensive. One way to cut the cost[53,54] is to decrease $X$ to zero at large interelectronic separations; in addition, this decrease is physically justified by the screening of nonlocal exchange by correlation effects at large interelectronic separations.[55,56] This strategy is used by the HSE06[53,57−59] range-separated-hybrid gradient approximation, which has $X$ = 25 at small interelectronic separation. This decreases the cost, but it is still expensive.

An alternative strategy, with a cost almost the same as local functionals, is to use rotationally invariant empirical modifications of Coulomb and exchange integrals for selected subshells;[22] calculations employing this modification with PBE are labeled PBE+U, and calculations employing this strategy with the GAM functional are called GAM+U. (The +U method of ref 22 that is used here is specified in *VASP* by using LDAUTYPE = 1.) For all the PBE+U and GAM+U calculations reported here, we empirically modified only the 3*d* subshells of the Fe centers, for which we used literature values[14,60] of 4 and 1 eV, respectively, for the Coulomb ($U$) and exchange ($J$) parameters.

In some calculations, a damped-dispersion molecular-mechanics term[61] was also added, and these are labeled as PBE-D2, PBE+U-D2, and HSE06-D2 calculations. The van der Waals $R_0$ and $C_6$ parameters determined by Grimme were used in the D2 terms; in particular, the global scaling parameter ($s_6$ = 0.75) fitted for PBE was used for PBE and PBE+U calculations, and the parameter ($s_6$ = 0.6) determined for the PBE0 functional was employed for the HSE06 calculations. Successful tests of these methods on extended crystalline systems are given in refs 62−64.

*2.2.2. Periodic Calculations.* For all periodic geometries, the nuclear positions, lattice parameters, and cell volumes of the structures were optimized in the ferromagnetic (FM) spin state, which corresponds to ferromagnetic coupling both along a chain of Fe centers and between the chains. These calculations employed a rhombohedral primitive cell (space group $R\bar{3}$, Figure 1) containing 54, 60, and 66 atoms for $Fe_2(dobdc)$, $Fe_2(O)_2(dobdc)$, and $Fe_2(OH)_2(dobdc)$, respectively.

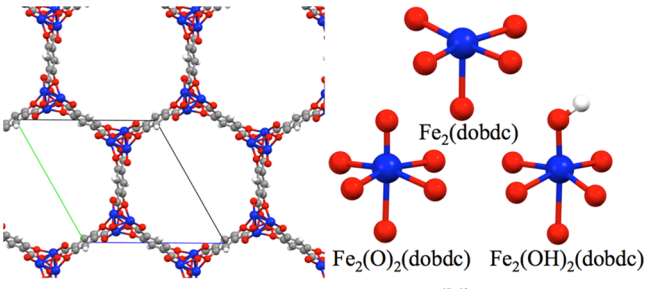


**Figure 1.** (Left) Primitive unit cell[67,68] of $Fe_2(dobdc)$; the figure also shows nearby atoms from other cells. (Right) First coordination sphere of the metal centers within the three MOFs studied. (Atom legend: blue = Fe, red = O, gray = C, and white = H.)

In these calculations, projector-augmented wave[65,66] (PAW) potentials were used to describe the interaction between explicitly treated electrons and the electrons treated as core electrons, namely, the inner 10 electrons of each Fe center. Two partial waves were used for each orbital: a cutoff radius of 2.0 bohrs ($a_0$) was used for the 3*p* and 4*s* states, and a cutoff radius of 2.2 $a_0$ was used for the 3*d* states.

Because of the relatively small band gap and weak long-range magnetic interactions reported for $Fe_2(dobdc)$,[14] it is especially important to converge the MOF structures and energies, with respect to the number of *k*-points used for quadratures over the Brillouin zone. Our convergence tests and final choices of grids are summarized in the Supporting Information (SI).

Density functional perturbation theory (DFPT),[69−72] also called linear response theory (LRT), was employed to compute the infrared spectra in the harmonic approximation. The PBE+U functional was used to compute all frequencies with an energy convergence threshold of $10^{-6}$ eV. Only the vibrations of Fe, carboxylate C, and O atoms were included in the DFPT calculation. The vibrational eigenmodes of each species were determined by the direct force constant approach.[71] The intensities of the infrared active modes were calculated in the dipole approximation by using Born Effective Charges (BECs).[69]

*2.2.3. Cluster Calculations.* All cluster calculations were performed using the *Gaussian 09*[73] software package on models similar to those used in previous research.[15,18] The models contain two or three Fe ions. For the model with two Fe ions, we can compute nearest-neighbor coupling, and for the models with three Fe ions both the nearest-neighbor and the next-nearest-neighbor couplings can be computed (Figure 2). The models with two Fe ions were cut from the

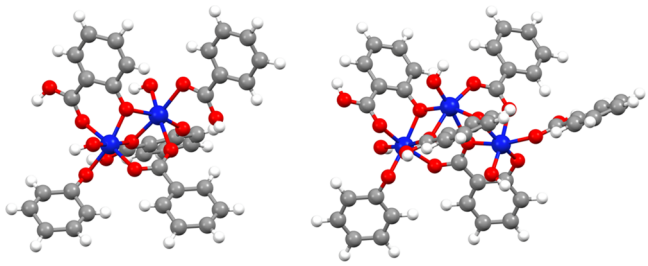

**Figure 2.** Cluster models with both (left) two Fe ions and (right) three Fe ions used for $Fe_2(OH)_2(dobdc)$. (Atom legend: blue = Fe, red = O, gray = C, and white = H.)

experimental structure of $Fe_2(dobdc)$, and the models with three Fe ions were cut from the periodically optimized PBE+U structures of each of the three MOFs. The cut bonds were then capped with H atoms. In the two-Fe model, the Fe···Fe distance and Fe−$O_c$−Fe angle (shown later in this work in Figure 5) were frozen to certain values, and the rest of the cluster was optimized using M06-L/def2-TZVP. This was followed by M06//M06-L single-point calculations with ferromagnetic and antiferromagnetic ordering to extract the nearest-neighbor magnetic coupling constant. In the models with three Fe ions, the hydrogen positions were optimized with M06-L[33] and the def2-SV(P)[74] basis set. Single-point calculations were then performed with ferromagnetic and antiferromagnetic ordering using the def2-TZVP[74] basis set and the PBE,[30] PBE0,[48,49] M06,[50] HSE06,[53,57−59] and B3LYP[44−47] exchange−correlation functionals.

*2.2.4. Magnetic Coupling Parameters.* Previous work has demonstrated that the Fe centers in each of the species have high-spin ground states; namely, $Fe_2(dobdc)$ contains quintet Fe(II) centers, $Fe_2(O)_2(dobdc)$ contains quintet Fe(IV) centers, and $Fe_2(OH)_2(dobdc)$ contains sextet Fe(III) centers.[9,14,16,19,20] Hence, only high-spin metal centers were considered in the magnetic coupling calculations. The periodic DFT calculations for $Fe_2(dobdc)$, $Fe_2(O)_2(dobdc)$, and $Fe_2(OH)_2(dobdc)$ were performed with the unit cells specified above[67,68] (Figure 1). The PBE, PBE+U, PBE+U-D2, HSE06, HSE06-D2, and GAM+U geometries were each fixed to those optimized for the FM spin state, and the plane-wave coefficients were optimized for each of the three spin configurations shown in Figure 3 with an energy convergence threshold of $10^{-6}$ eV.

The unit cell used in this study contains two vertices of one of the hexagonal channels of $Fe_2(dobdc)$ shown in Figure 1 with three Fe ions in each of the two vertices. The considered spin alignments of the six high-spin Fe ions are provided in Figure 3. The broken symmetry approximation[26] allowed us to use the energy differences between these three spin configurations to compute the nearest-neighbor ($J_{NN}$) and interchain ($J_{IC}$) coupling values with the Heisenberg−Dirac−Van Vleck (HDV) Hamiltonian:[75−77]



DOI: 10.1021/acs.inorgchem.6b00467
*Inorg. Chem.* 2016, 55, 4924−4934

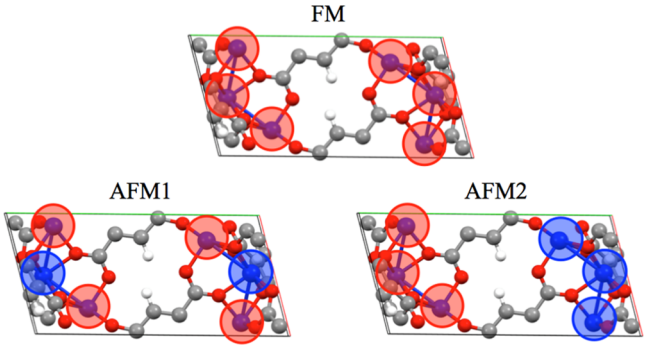


**Figure 3.** Side view of the primitive unit cell of $Fe_2$(dobdc) (atom legend: blue = Fe, red = O, gray = C, and white = H). Red and blue circles indicate the upward or downward spin of the high-spin Fe ions, respectively. The entirely ferromagnetic (FM), intrachain antiferromagnetic (AFM1), and interchain antiferromagnetic (AFM2) spin states were considered in this work. AFM1 is actually ferrimagnetic with this unit cell. Results with a doubled unit cell with strict intrachain AFM coupling are provided in the Supporting Information (SI).

$$H_{HDV} = -2\sum_{j>i}\sum_{i} J_{ij}\hat{S}_i\cdot\hat{S}_j \quad (1)$$

where the subscripts $i$ and $j$ represent the Fe sites of the unit cell shown in Figure 4, $J_{ij}$ is the isotropic magnetic coupling between

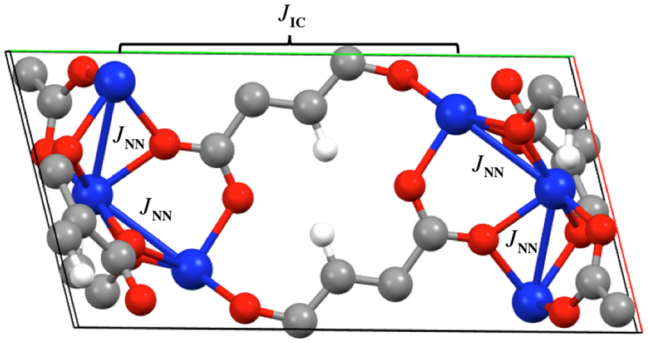


**Figure 4.** Schematic representation of the nearest-neighbor coupling constant ($J_{NN}$) and the interchain coupling constant ($J_{IC}$) of the primitive unit cell of $Fe_2$(dobdc). (Atom legend: blue = Fe, red = O, gray = C, and white = H.)

magnetic sites $i$ and $j$, and $\hat{S}_i$ is the spin vector on center $i$. A positive $J_{ij}$ in eq 1 denotes ferromagnetic (FM) coupling between centers $i$ and $j$, and a negative value indicates antiferromagnetic (AFM) coupling. Note that only matrix elements that contain high-spin Fe sites (i.e., diagonal matrix elements) are eigenfunctions of the HDV Hamiltonian. Also note that the diagonal matrix elements in the HDV Hamiltonian are equivalent to those of the Ising model, which is commonly used for magnetic systems.[9,78] We considered one FM state and two AFM states (AFM1 and AFM2) to be the ones that allow the most direct calculation of the magnetic couplings; note that AFM2 is the ground-state configuration of $Fe_2$(dobdc).

Since all Fe sites in $Fe_2$(dobdc) and its derivatives $Fe_2(O)_2$(dobdc) and $Fe_2(OH)_2$(dobdc) are equivalent, the four nearest-neighbor interactions represented by $J_{NN}$ in Figure 4 are all equivalent. For the atoms at the edge of the unit cell, additional nearest-neighbor interactions arise due to interaction with the periodic image of the unit cell. This accounts for two more $J_{NN}$ values, resulting in a total of six $J_{NN}$ for the primitive cell.

While the treatment described above for nearest-neighbor interactions is unambiguous, the treatment of interchain coupling requires more consideration. Each chain of Fe ions is surrounded by three other chains of Fe ions. Although the three neighboring chains are equally distant, the Fe ions are staggered, so that the smallest interchain Fe···Fe distance is not the same for all three neighboring chains of a given Fe ion; in particular, the distance to the nearest Fe ion in each of the three surrounding chains in $Fe_2$(dobdc) is 7.4, 8.1, and 9.0 Å. If the data were sufficient to accommodate a multiparameter analysis, one would recognize at least three different interchain couplings and also include next-nearest neighbors within a given chain. However, the interchain coupling was found to be small, and the theory might not be good enough to distinguish several different small couplings. Even more significantly, the experiment (as explained in section 2.1) was interpreted in terms of only two parameters, one intrachain parameter $J_{NN}$ and one interchain parameter $zJ_{IC}$. Therefore, we took the same approach computationally. However, we obtained slightly different results if we assumed that the interchain coupling was caused only by the nearest interchain interaction ($z = 1$) or was caused by equal interactions with the nearest neighbors in each of the three surrounding chains ($z = 3$). We will report the equations and the resulting magnetic coupling for the approach in which we computed the magnetic coupling values, assuming that each metal center would interact with only the closest metal center of the three neighboring chains, which was reasonable, because one of the interchain Fe···Fe distances was smaller than the other two. This limited interchain coupling model, corresponding to $z = 1$, leads to a total of six interactions per unit cell. The model with $z = 3$ would lead to 18. We note that the two treatments yield identical values of $zJ_{IC}$ but slightly different values of $J_{NN}$ (Table S5).

Using the energies calculated for the three spin states (FM, AFM1, and AFM2) shown in Figure 3, the $J_{NN}$ and $J_{IC}$ values can be extracted for $Fe_2$(dobdc) and $Fe_2(O)_2$(dobdc) (which have total spin magnitudes ($|M_S|$) of 2 on every Fe site) by solving the following three equations:

$$\langle 222, 222|H_{HDV}|222, 222\rangle = E_{222,222} = -2[6J_{NN}2\cdot2 + 6J_{IC}2\cdot2]$$
$$\langle 2\bar{2}2, 2\bar{2}2|H_{HDV}|2\bar{2}2, 2\bar{2}2\rangle = E_{2\bar{2}2,2\bar{2}2} = -2[-2J_{NN}2\cdot2 + 6J_{IC}2\cdot2]$$
$$\langle 222, \overline{222}|H_{HDV}|222, \overline{222}\rangle = E_{222,\overline{222}} = -2[6J_{NN}2\cdot2 - 6J_{IC}2\cdot2] \quad (2)$$

where $H_{HDV}$ is the HDV Hamiltonian of eq 2, $|222, 222\rangle$ and $E_{222,222}$ represent the Slater determinant and total energy of the FM case (Figure 3), $|2\bar{2}2, 2\bar{2}2\rangle$ and $E_{2\bar{2}2, 2\bar{2}2}$ represent the Slater determinant and total energy of the AFM1 case, and $|222, \overline{222}\rangle$ and $E_{222, \overline{222}}$ represent the Slater determinant and total energy of the AFM2 case. In the Slater determinants of eq 2, the $M_S$ values before the comma are the values for one chain containing three Fe centers and the ones after the comma are for the other chain. Solving the equations given by eq 2 results in the values of $J_{NN}$ and $J_{IC}$, which are represented by the following equations:

$$J_{IC} = \frac{1}{96}[E_{222,\overline{222}} - E_{222,222}]$$
$$J_{NN} = \frac{1}{64}[E_{2\bar{2}2,2\bar{2}2} - E_{222,222}] \quad (3)$$

For the unit cell of $Fe_2(OH)_2$(dobdc), where each Fe ion has a spin of 5/2, the $J_{NN}$ and $J_{IC}$ values can be extracted by solving the following three equations:


DOI: 10.1021/acs.inorgchem.6b00467
Inorg. Chem. 2016, 55, 4924−4934

$$\left\langle \frac{5}{2}\frac{5}{2}\frac{5}{2}, \frac{5}{2}\frac{5}{2}\frac{5}{2} | H_{HDV} | \frac{5}{2}\frac{5}{2}\frac{5}{2}, \frac{5}{2}\frac{5}{2}\frac{5}{2} \right\rangle = E_{\frac{5}{2}\frac{5}{2}\frac{5}{2},\frac{5}{2}\frac{5}{2}\frac{5}{2}} = -2\left[6J_{NN}\frac{5}{2}\cdot\frac{5}{2} + 6J_{IC}\frac{5}{2}\cdot\frac{5}{2}\right]$$

$$\left\langle \frac{5}{2}\frac{\bar{5}}{2}\frac{5}{2}, \frac{5}{2}\frac{\bar{5}}{2}\frac{5}{2} | H_{HDV} | \frac{5}{2}\frac{\bar{5}}{2}\frac{5}{2}, \frac{5}{2}\frac{\bar{5}}{2}\frac{5}{2} \right\rangle = E_{\frac{5}{2}\frac{\bar{5}}{2}\frac{5}{2},\frac{5}{2}\frac{\bar{5}}{2}\frac{5}{2}} = -2\left[-2J_{NN}\frac{5}{2}\cdot\frac{5}{2} + 6J_{IC}\frac{5}{2}\cdot\frac{5}{2}\right]$$

$$\left\langle \frac{5}{2}\frac{5}{2}\frac{5}{2}, \frac{\bar{5}}{2}\frac{\bar{5}}{2}\frac{\bar{5}}{2} | H_{HDV} | \frac{5}{2}\frac{5}{2}\frac{5}{2}, \frac{\bar{5}}{2}\frac{\bar{5}}{2}\frac{\bar{5}}{2} \right\rangle = E_{\frac{5}{2}\frac{5}{2}\frac{5}{2},\frac{\bar{5}}{2}\frac{\bar{5}}{2}\frac{\bar{5}}{2}} = -2\left[6J_{NN}\frac{5}{2}\cdot\frac{5}{2} - 6J_{IC}\frac{5}{2}\cdot\frac{5}{2}\right] \quad (4)$$

The only difference between the equations for the $Fe_2(dobdc)$ and $Fe_2(O)_2(dobdc)$ cases and the $Fe_2(OH)_2(dobdc)$ case is the spin ($M_S$) of the Fe ions. This change results in different prefactors for the $J_{NN}$ and $J_{IC}$ magnetic coupling values. Solving the relationships described in eq 4 gives the values of $J_{NN}$ and $J_{IC}$ for $Fe_2(OH)_2(dobdc)$, which are represented by eq 5:

$$J_{IC} = \frac{1}{150}\left[E_{\frac{5}{2}\frac{5}{2}\frac{5}{2},\frac{\bar{5}}{2}\frac{\bar{5}}{2}\frac{\bar{5}}{2}} - E_{\frac{5}{2}\frac{5}{2}\frac{5}{2},\frac{5}{2}\frac{5}{2}\frac{5}{2}}\right]$$

$$J_{NN} = \frac{1}{100}\left[E_{\frac{5}{2}\frac{\bar{5}}{2}\frac{5}{2},\frac{5}{2}\frac{\bar{5}}{2}\frac{5}{2}} - E_{\frac{5}{2}\frac{5}{2}\frac{5}{2},\frac{5}{2}\frac{5}{2}\frac{5}{2}}\right] \quad (5)$$

Additional considerations in the above two-parameter treatment are the neglect of next-nearest-neighbor interactions in a given chain and the fact that the periodically replicated AFM1 state is not strictly antiferromagnetic down each chain of metals. A more faithful representation of a fully antiferromagnetic chain can be obtained by doubling the size of the primitive cell along the *c*-axis (which runs parallel to the chains) from 54 atoms to 108 atoms for $Fe_2(dobdc)$ (Figure S15), from 60 atoms to 120 atoms for $Fe_2(O)_2(dobdc)$, and from 66 atoms to 132 atoms for $Fe_2(OH)_2(dobdc)$. Single-point calculations were performed on the doubled unit cells with PBE+U to test the validity of utilizing the smaller cells shown in Figures 3 and 4. We also computed the $J_{NN}$ and $J_{NNN}$ magnetic couplings with cluster models. For the cluster calculations, the Hamiltonian and equations used to compute the magnetic coupling values with the cluster models are described in the SI along with coordinates for each cluster model.

## 3. RESULTS AND DISCUSSION

**3.1. Equilibrium Structures and Infrared Spectra.** The SI compares equilibrium structures computed by PBE, PBE+U, PBE+U-D2, HSE06, HSE06-D2, and GAM+U. In the case of $Fe_2(dobdc)$, there is good agreement between the bond distances and angles computed with all the methods and the experiment, with the exception of PBE, which significantly underestimates the Fe···Fe distances and the Fe−$O_c$−Fe angle. Table S2 in the SI shows that, after oxidation to Fe(III), the experimental Fe···Fe distance increases by 0.15−0.16 Å. If we ignore PBE, because of its underestimation of the Fe···Fe distance in $Fe_2(dobdc)$, the density functional calculations predict that there is an increase in the Fe···Fe distance by 0.25−0.28 Å. Figure 5 shows the local environment of a metal center in $Fe_2(OH)_2(dobdc)$ and the organic linker.

The experimental infrared (IR) spectra of $Fe_2(dobdc)$ and $Fe_2(OH)_2(dobdc)$ in Figure 6 provide a good test of the PBE+U computations, which are depicted in Figure 7. The theoretical spectra were normalized to match the intensities of the experimental Fe−O stretches that occur at ∼820 $cm^{-1}$. The peaks occurring below 500 $cm^{-1}$ are likely due to Fe−O bending modes, while those between 600 and 1000 $cm^{-1}$ are due to Fe−O stretches. The PBE+U Fe(III)−OH stretching

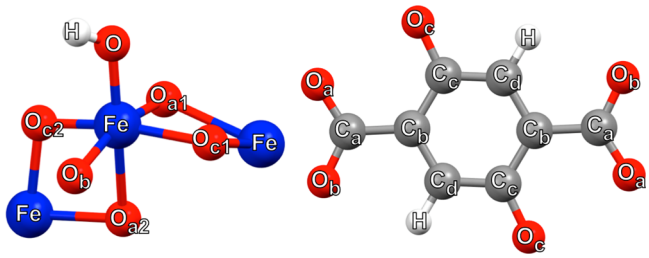


**Figure 5.** (left) The first coordination sphere of the metal center in $Fe_2(OH)_2(dobdc)$ and (right) the organic linker. The four unique oxygens, four unique carbons, and two unique hydrogens are shown. Note that the $O_{a1}$, $O_{a2}$, $O_{c1}$, and $O_{c2}$ labeling used here and in Table S2 distinguish the Fe−O bond positions, with respect to the central Fe. The Fe−$O_{a1}$−Fe and Fe−$O_{a2}$−Fe bond angles, as well as the Fe−$O_{c1}$−Fe and Fe−$O_{c2}$−Fe bond angles, are equivalent. (Atom legend: blue = Fe, red = O, gray = C, and white = H.)

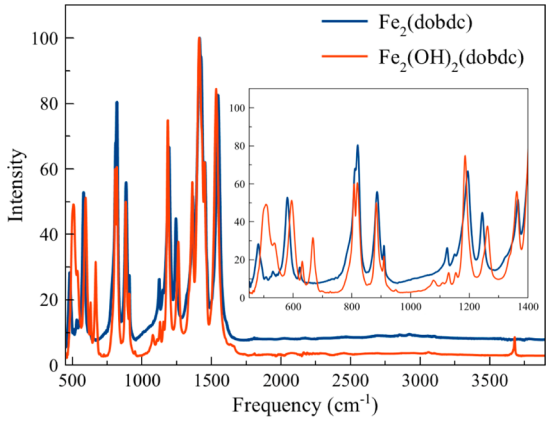


**Figure 6.** Experimental infrared spectra of $Fe_2(dobdc)$ and $Fe_2(OH)_2(dobdc)$ (see ref 19).

frequencies in $Fe_2(OH)_2(dobdc)$ occur between 619 and 630 $cm^{-1}$, which is ∼40 $cm^{-1}$ less than the experimental value of 667 $cm^{-1}$.[19]

The PBE+U O−H stretching frequency in $Fe_2(OH)_2(dobdc)$ is 3773 $cm^{-1}$, and the experimental value is 3683 $cm^{-1}$. The Fe(IV)−oxo stretch is known, in other cases, to occur between 776 $cm^{-1}$ and 843 $cm^{-1}$.[81] We find that the PBE+U Fe(IV)−oxo stretches occur here between 888 $cm^{-1}$ and 899 $cm^{-1}$. Thus, the theory underestimates the Fe(III)−OH stretching frequency and may overestimate the Fe(IV)−oxo stretching frequency. However, the experimental Fe(IV)−oxo-containing material is quite different than the theoretical model. Calculations with the actual experimental composition ($Fe_{0.1}(O)_{0.1}Mg_{1.9}(dobdc)$) may yield more accurate frequencies. Molecular DFT calculations are known to systematically overestimate experimental fundamental stretching frequencies, but usually by only 2%−5%.[82]

**3.2. Electronic Structure and Density of States.** To gain insight into the electronic structures, the orbital projected density of states (OP-DOS) is provided for each MOF in the SI. The OP-DOS plots were extracted using the default settings for atomic radii in *VASP*. The atomic radii could be considered tunable parameters that can be improved by computing and comparing to reasonable atomic charges,[83] but the default parameters yielded decent results, when compared to the experiment. Figures S3 and S4 show the OP-DOS obtained using PBE+U and HSE06, respectively, for each MOF in its


DOI: 10.1021/acs.inorgchem.6b00467
Inorg. Chem. 2016, 55, 4924−4934

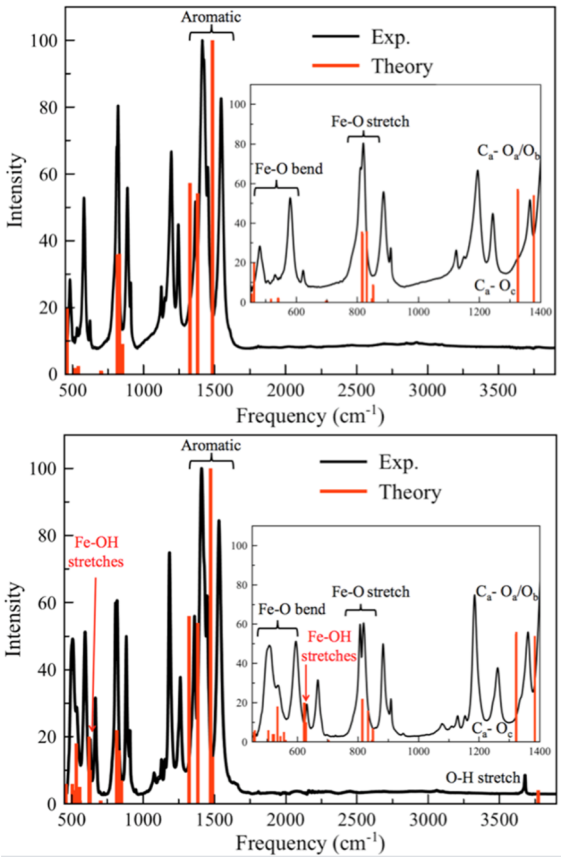


**Figure 7.** Experimental and theoretical (PBE+U) infrared spectra of (top) $Fe_2(dobdc)$ and (bottom) $Fe_2(OH)_2(dobdc)$. All spectra were normalized based on the highest peak. The experimental spectra for $Fe_2(dobdc)$ were taken from ref 19. The Fe−OH stretch theoretical peak intensities (those that are indicated by the red arrow in the range from 619 cm$^{-1}$ to 630 cm$^{-1}$) were multiplied by a factor of 10 for more visible comparison to the experiment.

lowest-energy spin state (Table 1). We consider only the projections of the DOS on the Fe 3*d* and O 2*p* orbitals, since the electrons occupying these orbitals are the ones mainly responsible for the magnetic properties. To identify the bands of the "additional" O atoms in $Fe_2(O)_2(dobdc)$ and $Fe_2(OH)_2(dobdc)$, the figures also show projections that include only the 2*p* orbitals of the added O atoms.

The main consideration in these plots is the band gap, i.e., the difference in energy between the highest occupied orbital and the lowest unoccupied one. PBE+U and HSE06 both predict a sizable band gap, in particular 1.3 and 2.1 eV, respectively, which are substantially larger than the gap of 0.3 eV reported by Zhang et al. ref 14). We investigated the reason for this discrepancy and found that the band gap decreased as the volume increased, but even with a 15% volume fluctuation, the band gap remained between 1.1 eV and 0.8 eV. Furthermore, a single-point calculation with the experimental structure gives the same band gap as that obtained from the equilibrium PBE+U structure determined in this work. The trend in the gap upon increasing the oxidation state of iron is different for PBE+U and HSE06. The PBE+U gaps for the Fe(IV) and Fe(III) MOFs are almost identical (0.8 eV), while HSE06 predicts a gap of 1.5 eV for $Fe_2(O)_2(dobdc)$, which contains Fe(IV), but predicts a larger gap of 1.8 eV for $Fe_2(OH)_2(dobdc)$, which contains Fe(III).

**3.3. Magnetic Susceptibility Measurements.** The magnetic susceptibility of $Fe(II)_{0.26}[Fe(III)(OH)]_{1.74}(dobdc)(DMF)_{0.15}(THF)_{0.22}$ ("$Fe_2(OH)_2(dobdc)$") was measured in the present work. DC magnetic susceptibility measurements were performed under an applied magnetic field of 1000 Oe across the temperature range of 2−300 K. The measurements of $Fe_2(OH)_2(dobdc)$ revealed a decreasing $\chi_M T$ product with decreasing temperature across the full temperature range measured (Figure 8). This trend supports the assignment of

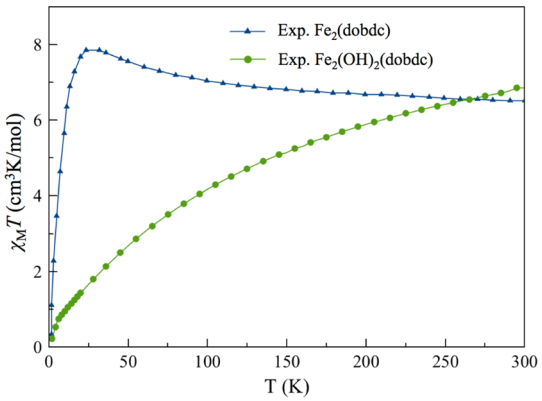


**Figure 8.** Experimental magnetic susceptibility times temperature curves of $Fe_2(dobdc)$[16] (blue) and $Fe_2(OH)_2(dobdc)$ (green). The applied magnetic field strength during the susceptibility measurement of each material was 1000 Oe.

both intrachain and interchain magnetic couplings as antiferromagnetic. The $\chi_M T$ value at 300 K and 1000 Oe is 6.85 emu K/mol, which is much lower than both the expected value for two isotropic $S = 5/2$ spins (8.75 emu K/mol) and the expected value assuming 0.26 mol (13% of iron sites) of $S = 2$ Fe(II) per formula unit (8.39 emu K/mol). The low magnetic moment is attributed to the presence of 13% Fe(II), which, in addition to simply having a lower magnetic moment than that of Fe(III), may also display enhanced antiferromagnetic coupling with its nearest-neighbor spins. The magnetic susceptibility of $Fe_2(dobdc)$ was measured in ref 16, where the fitting procedure used to compute the experimental coupling values for $Fe_2(dobdc)$ is also described. The fitting procedure is briefly summarized in section 2.1.

It was not feasible to extract the interchain and intrachain magnetic coupling parameters with the Fisher model, as was done for $Fe_2(dobdc)$.[16] The results in Figure 8 indicate that $Fe_2(dobdc)$ has ferromagnetic intrachain coupling and antiferromagnetic interchain coupling. The precise coupling parameters for $Fe_2(OH)_2(dobdc)$ could not be readily derived because of the fact that the synthesized MOF was only partially oxidized, with ∼13% of the Fe sites remaining in the Fe(II) state. However, a Curie−Weiss fit to the expression $1/\chi_M = (T - \theta)/C$ for the high-temperature regime (50−300 K) of the inverse magnetic susceptibility data for both $Fe_2(dobdc)$ and $Fe_2(OH)_2(dobdc)$ (Figure S18) permitted some assessment of the differences in magnetic coupling behaviors for the two frameworks. For $Fe_2(dobdc)$, the Curie−Weiss analysis resulted in a positive Weiss temperature of $\theta = 11$ K, which is consistent with ferromagnetic interactions being dominant, and a Curie constant of $C = 6.3$ emu K/mol. In contrast, the Curie−Weiss analysis for $Fe_2(OH)_2(dobdc)$ resulted in $\theta = -139$ K and $C = 10.0$ emu K/mol. The negative sign of the Weiss temperature ($\theta$) for $Fe_2(OH)_2(dobdc)$ indicates that antiferromagnetic


DOI: 10.1021/acs.inorgchem.6b00467
Inorg. Chem. 2016, 55, 4924−4934

Table 1. Periodic DFT Exchange and Coupling Energies of the Fe Centers[a]

| method | number of atoms | $E_{AFM1} - E_{FM}$ [b] ($cm^{-1}$) | $E_{AFM2} - E_{FM}$ ($cm^{-1}$) | $J_{NN}$ [c] ($cm^{-1}$) | $zJ_{IC}$ |
|---|---|---|---|---|---|
| | | **Fe(II) Case: $Fe_2$(dobdc)** | | | |
| PBE | 54 | 7287.7 | −160.0 | 113.9 | −5.0 |
| PBE+U[d] | 108 | 56.6 (92.9) | −121.1 | 0.5 (0.3) | −1.9 |
| PBE+U | 54 | 41.6 | −60.4 | 0.7 | −1.9 |
| PBE+U-D2 | 54 | 31.1 | −64.6 | 0.5 | −2.0 |
| HSE06 | 54 | 171.6 | −32.2 | 2.7 | −1.0 |
| HSE06-D2 | 54 | 163.2 | −47.5 | 2.6 | −1.5 |
| GAM+U | 54 | 145.4 | −52.8 | 2.3 | −1.7 |
| expt[e] | | | | 4.1 | −1.1 |
| | | **Fe(III) Case: $Fe_2(OH)_2$(dobdc)** | | | |
| PBE | 66 | −2308.1 | −2042.3 | −23.1 | −40.8 |
| PBE+U[d] | 132 | −3216.0 (−2259.0) | −630.7 | −10.2 (−1.1) | −6.3 |
| PBE+U | 66 | −1129.6 | −315.9 | −11.3 | −6.3 |
| PBE+U-D2 | 66 | −1133.9 | −311.7 | −11.3 | −6.2 |
| HSE06 | 66 | −562.0 | −169.8 | −5.6 | −3.4 |
| HSE06-D2 | 66 | −561.4 | −170.3 | −5.6 | −3.4 |
| GAM+U | 66 | −691.7 | −272.7 | −6.9 | −5.5 |
| | | **Fe(IV) Case: $Fe_2(O)_2$(dobdc)** | | | |
| PBE | 60 | −795.8 | −164.1 | −12.4 | −5.1 |
| PBE+U[d] | 120 | −205.6 (−270.2) | 81.1 | −1.2 (−0.9) | 1.3 |
| PBE+U | 60 | −133.8 | 40.9 | −2.1 | 1.3 |
| PBE+U-D2 | 60 | −157.6 | 36.1 | −2.5 | 1.1 |
| HSE06 | 60 | −31.8 | 17.9 | −0.5 | 0.6 |
| HSE06-D2 | 60 | −43.3 | 15.8 | −0.7 | 0.5 |
| GAM+U | 60 | 17.5 | −42.4 | 0.3 | −1.3 |

[a]All coupling values were extracted using geometries optimized with the FM spin state. $E_{FM}$ is the electronic energy of the ferromagnetic state, $E_{AFM1}$ is the electronic energy of antiferromagnetic state 1, and $E_{AFM2}$ is the electronic energy of antiferromagnetic state 2 (Figure 3). $E_{AFM3}$ is the electronic energy of antiferromagnetic state 3 of the supercell. $J_{NN}$, $J_{IC}$, and $J_{NNN}$ coupling parameters represent the nearest-neighbor, interchain, and next-nearest-neighbor magnetic couplings, respectively (Figure 4). [b]Values shown in parentheses represent the value of $E_{AFM3} - E_{FM}$ ($cm^{-1}$). [c]Values shown in parentheses represent the $J_{NNN}$ value ($cm^{-1}$). [d]The equations used to calculate the coupling parameters for the doubled cells are in the SI; the spin configurations for the doubled cells are shown in Figure S17 in the SI. [e]Data taken from ref 16.

interactions are prevalent. Concurrently, the large increase in the magnitude of $\theta$, which is dependent on the spin states present and the number and strength of the magnetic coupling pathways,[84] suggests that the magnetic interactions are stronger within $Fe_2(OH)_2$(dobdc), since the Fe spins involved only increase from quintet to sextet states, while the number of magnetic coupling pathways presumably remains unchanged. Thus, we can state qualitatively that adding a hydroxide anion and oxidizing the metal sites of $Fe_2$(dobdc) switches the nearest-neighbor magnetic coupling behavior from ferromagnetic to antiferromagnetic and increases the magnetic coupling strength.

**3.4. Magnetic Coupling Parameters.** The calculated magnetic coupling parameters for $Fe_2$(dobdc), $Fe_2(O)_2$(dobdc), and $Fe_2(OH)_2$(dobdc) are provided in Tables 1 and 2. As mentioned above, the PBE+U calculations were run with both primitive unit cells (54, 60, or 66 atoms) and doubled cells (108, 120, or 132 atoms), as indicated in the second column of Table 1. This table shows that there is no significant difference between the PBE+U calculations with 54 and 108 atoms in the unit cell, which indicates that the primitive cell is adequate for these computations. The same is true for couplings in $Fe_2(O)_2$(dobdc) and $Fe_2(OH)_2$(dobdc).

The PBE nearest-neighbor couplings in $Fe_2$(dobdc) are two orders of magnitude larger than both the experimental ones and those computed with the other methods tested in Table 1. The PBE values are calculated for the PBE geometry, which has short Fe···Fe distances. The overestimation of magnetic properties by GGA functionals is well-established.[85] A previous study[9] of magnetic interactions in $Fe_2$(dobdc) employed the PBE exchange-correlation functional with experimental geometries and obtained a $J_{NN}$ value of 28 $cm^{-1}$, which is smaller but still a significant overestimation. They concluded[9] that there is fairly strong ferromagnetic coupling in $Fe_2$(dobdc). It now appears that such large calculated $J_{NN}$ values are an artifact of the simple gradient approximation used in the PBE functional. This was shown in previous work,[18] where a calculation with a hybrid meta-GGA gave a value of 3.6 $cm^{-1}$, in good agreement with the experimental value of 4.1 $cm^{-1}$.

It was pointed out in section 2.2.4 that the magnetic coupling constants are slightly dependent on whether we perform the analysis with $z = 1$ or $z = 3$. The nearest-neighbor Fe···Fe distance is 3.0 Å, and the next-nearest neighbor Fe···Fe distance within a chain is 5.0 Å. Thus, the next-nearest-neighbor distance is significantly shorter than the shortest interchain Fe···Fe separation, which suggests that the next-nearest-neighbor intrachain coupling should be calculated. The next-nearest-neighbor coupling results are shown in Table 1, where we report the results with $z = 1$. (Note that the value computed for $J_{IC}$ is independent of whether or not $J_{NNN}$ is computed and is also independent of whether we use $z = 1$ or $z = 3$.) Excluding PBE, the nearest-neighbor couplings ($J_{NN}$) obtained with $z = 3$ are very similar for $Fe_2$(dobdc), $Fe_2(OH)_2$(dobdc), and $Fe_2(O)_2$(dobdc), whereas the results for $zJ_{IC}$ are unchanged. Table 1 shows that the PBE+U and HSE06 calculated values of $J_{NN}$ are smaller than the PBE value and are in more reasonable


DOI: 10.1021/acs.inorgchem.6b00467
Inorg. Chem. 2016, 55, 4924−4934

agreement with the experiment. For $Fe_2(dobdc)$, the coupling values obtained by HSE06 and HSE06-D2 are similar to each other and are larger than those predicted by PBE+U, whereas for the $Fe_2(O)_2(dobdc)$ and $Fe_2(OH)_2(dobdc)$ cases, HSE06 and HSE06-D2 yield magnetic couplings that are smaller than the values computed with PBE+U and PBE. PBE+U and HSE06 predict the same signs of the magnetic couplings.

Table 1 shows that the periodic calculations of $J_{NNN}$ using PBE+U yield values of 0.3, −1.1, and −0.9 $cm^{-1}$ for $Fe_2(dobdc)$, $Fe_2(OH)_2(dobdc)$, and $Fe_2(O)_2(dobdc)$, respectively. These $J_{NNN}$ values may be compared to the respective $J_{IC}$ coupling values of −0.6, −2.1, and 0.4 $cm^{-1}$. The magnitude of the PBE+U $J_{IC}$ coupling values for $Fe_2(dobdc)$ and $Fe_2(OH)_2(dobdc)$ are larger than the $J_{NNN}$ values, while the PBE+U $J_{IC}$ value of $Fe_2(O)_2(dobdc)$ is smaller than the $J_{NNN}$ value. Note that the $J_{IC}$ coupling values for $Fe_2(OH)_2(dobdc)$ are notably larger than the other two cases with all functionals. This may indicate that, separate from the oxidation of the metal centers, addition of the $(OH)^-$ groups enhances interchain magnetic coupling.

Table 2 provides the results of cluster model calculations that may be compared to the periodic calculations in Table 1.

**Table 2. Isotropic Magnetic Coupling Constants of the Fe Centers for Each Studied MOF, As Obtained by Cluster Calculations**[a]

| | $J_{NN}$[b] ($cm^{-1}$) | | |
|---|---|---|---|
| method | $Fe_2(dobdc)$ | $Fe_2(OH)_2(dobdc)$ | $Fe_2(O)_2(dobdc)$ |
| PBE//PBE | 64.6 | −18.2 | −9.9 |
| PBE//PBE+U | 14.3 | −18.7 | −9.0 |
| HSE06//PBE+U | 2.4 (0.4) | −3.2 (−0.1) | 0.3 (−0.2) |
| M06//PBE+U | 4.3 | −3.9 | −0.5 |
| PBE0//PBE+U | 2.5 | −3.1 | −0.1 |
| B3LYP//PBE+U | 2.7 | −4.1 | −0.5 |
| expt[c] | 4.1 | | |

[a] *X*//*Y* indicates a cluster calculation with method *X* employing a fragment of a MOF optimized by periodic calculations with method *Y*. Only nearest- and next-nearest-neighbor intrachain coupling values ($J_{NN}$ and $J_{NNN}$) were computed, and they may be compared with Table 1. [b] Values shown in parentheses represent the $J_{NNN}$ value (in $cm^{-1}$). [c] Data taken from ref 16.

Because they are very similar to the experimental geometries (Table S2), the PBE+U optimized periodic structures were used to make the clusters in all cases except one. The PBE//PBE $J_{NN}$ value is much larger than the PBE//PBE+U value, in part because the periodic PBE metal−metal bond distances are too small for $Fe_2(dobdc)$ (as noted above in the discussion of Table S2). The PBE//PBE cluster calculation predicts $J_{NN}$ values for $Fe_2(dobdc)$ that are significantly larger than experiment. However, the cluster $J_{NN}$ values obtained by HSE06, M06, PBE0, and B3LYP are all quite reasonable, when compared to both the periodic and experimental magnetic coupling parameters.

The results with PBE+U structures in Table 2 show that Hartree−Fock exchange in HSE06, PBE0, M06, and B3LYP decreases the predicted intrachain coupling values. If one assumes that one effect of the *U* parameter is to mimic Hartree−Fock exchange, this is consistent with the periodic results.

The cluster values of $J_{NNN}$ in Table 2 are considerably smaller than the periodic calculations of $J_{NNN}$ in Table 1. However, they do correctly predict the experimentally determined magnetic ordering of $Fe_2(dobdc)$ and $Fe_2(OH)_2(dobdc)$. In the case of $Fe_2(O)_2(dobdc)$, the magnetic coupling values are likely extremely weak, which is why GAM+U and HSE06//PBE+U in Table 2 predict different magnetic orderings than the other functionals. This demonstrates the difficulty of accurately calculating the small energies of these interactions.

It was suggested by Park et al.[17] that the changes in magnetism within $Fe_2(dobdc)$ upon guest adsorption are due to structural changes within the MOF. When the intrachain Fe···Fe distances were less than ∼3.12 Å, the magnetic interactions were interpreted as being dominated by direct exchange between the metal centers and were ferromagnetic; at longer Fe···Fe separations, the magnetic interactions were interpreted as dominated by superexchange through the bridging O atoms. In our work, $Fe_2(O)_2(dobdc)$ has intrachain Fe···Fe distances of ∼3.12 Å (Table S2) and the nearest-neighbor AFM coupling is calculated to be very weak (Tables 1 and 2). For comparison, $Fe_2(OH)_2(dobdc)$ has intrachain Fe···Fe distances of ∼3.22 Å and shows a larger AFM coupling. But the Fe···Fe separation is not the only geometrical parameter that changes. The Fe−$O_c$−Fe bond angles increase from $Fe_2(dobdc)$ to $Fe_2(O)_2(dobdc)$ to $Fe_2(OH)_2(dobdc)$ (see Table S2). Table 1 shows that these structural changes are associated with a switch from positive $J_{NN}$ values to negative $J_{NN}$ values—i.e., a switch from FM to AFM coupling of the nearest-neighbor metal centers. However, many factors besides geometry may contribute to the changes in magnetic coupling. These factors include electronic effects resulting from (1) the presence of the $(OH)^-$ and $O^{2-}$ ligands, (2) the change in oxidation state to Fe(III) for $(OH)^-$ and to Fe(IV) for $O^{2-}$, and (3) the change in spin state of the metal centers from quintet to sextet, resulting from the inclusion of the $(OH)^-$ ligands. The magnetic coupling equations for $Fe_2(OH)_2(dobdc)$ (eq 5) take into account the effect of the spin state change (3), but completely separating all three of these electronic contributions from the geometric contributions required a separate set of calculations, as discussed in the next two paragraphs.

To compute the aforementioned electronic contributions, two approaches were considered. In the first approach, the three-Fe cluster model of $Fe_2(OH)_2(dobdc)$ carved from the PBE+U periodic structure was used. The three $(OH)^-$ groups were removed from this cluster, which changed the Fe(III) centers to Fe(II) centers. While keeping the positions of all atoms in the cluster fixed, magnetic coupling constants were calculated using M06/def2-TZVP. This was done to separate the electronic and geometric contributions to the magnetic coupling. The coupling constant of this new cluster (−1.1 $cm^{-1}$) should be compared to the M06 magnetic coupling results for $Fe_2(dobdc)$ (4.3 $cm^{-1}$) and $Fe_2(OH)_2(dobdc)$ (−3.9 $cm^{-1}$) in Table 2. We can see that both electronic and geometric effects play important roles in the magnetic couplings studied here.

The second approach was to go in the reverse direction, meaning that we started with the $Fe_2(dobdc)$ cluster and then added $(OH)^-$ groups. Three $(OH)^-$ groups were added to the cluster model of $Fe_2(dobdc)$ carved from the PBE+U periodic structure, and only these added groups were optimized using M06/def2-TZVP, while the remainder of the cluster was kept fixed. The oxidation state and spin state of the metal centers were thus the same as for $Fe_2(OH)_2(dobdc)$, while the metal coordination geometry was the same as in $Fe_2(dobdc)$. The


DOI: 10.1021/acs.inorgchem.6b00467
Inorg. Chem. 2016, 55, 4924−4934

magnetic coupling of $Fe_2(dobdc)$ (4.3 $cm^{-1}$) (Table 2) changed to 0.2 $cm^{-1}$ when $(OH)^-$ was added, which is an effect of 4.1 $cm^{-1}$. The value of 0.2 $cm^{-1}$ can be compared to the M06 magnetic coupling result in Table 2 for $Fe_2(OH)_2(dobdc)$ of −3.9 $cm^{-1}$, which also has an effect of 4.1 $cm^{-1}$. This means that the metal oxidation and addition of $(OH)^-$ and the change in geometry had impacts of similar magnitude. These results show that the presence of the $(OH)^-$ groups (1), the change in oxidation state (2), and the change in spin state (3) all contribute considerably to the magnetic ordering of $Fe_2(OH)_2(dobdc)$. We also found that the geometry has an important effect on the magnetic coupling. To examine the overall effect of the geometry, we examined the OP-DOS results from the periodic calculations of each structure. However, we also wanted to understand how distinct geometrical parameters, such as Fe···Fe distance and Fe−O−Fe angle, contribute to the magnetic coupling. We thus designed cluster models to separate the contributions of these parameters.

The periodic calculations on $Fe_2(dobdc)$ (Table 1) are in general agreement with previous work.[9,14,16,18] The results for the hydroxylated case in Table 1 are consistent with the qualitative inference from the experiment in section 3.3 that oxidation of the metal sites of $Fe_2(dobdc)$ and concurrent addition of hydroxide anions to these sites switches the nearest-neighbor magnetic coupling behavior from ferromagnetic to antiferromagnetic and increases its strength. The interactions between the bridging O atoms and the Fe atoms can strongly influence the type and magnitude of the magnetic exchange within a material.[7] The OP-DOS calculations of the Fe 3*d* and the bridging O 2*p* orbitals show that overlap between these orbitals is larger for $Fe_2(O)_2(dobdc)$ and $Fe_2(OH)_2(dobdc)$ than for $Fe_2(dobdc)$. This may indicate that there is more interaction between the metal electrons through the bridging oxygens in $Fe_2(O)_2(dobdc)$ and $Fe_2(OH)_2(dobdc)$. The increasing Fe−O−Fe bond angle leads to an increase in the magnitude of the AFM coupling, because the electrons in the Fe 3*d* interact more strongly through the bridging oxygen electrons via superexchange (Figure 9). The superexchange interaction was developed into a set of semiempirical rules by Goodenough and Kanamori.[7] These rules predict an AFM interaction if the metal−ligand−metal angle is close to 180°, and a weak FM interaction if the angle is close to 90°. The computations performed in this work align reasonably well with these rules, although the actual situation is complicated by the fact that the Fe−O distances and Fe···Fe distances change, along with the change in bond angle. Similar interaction trends have been observed previously within $Fe_2(dobdc)$ when olefins were bound to the metal centers.[16,17]

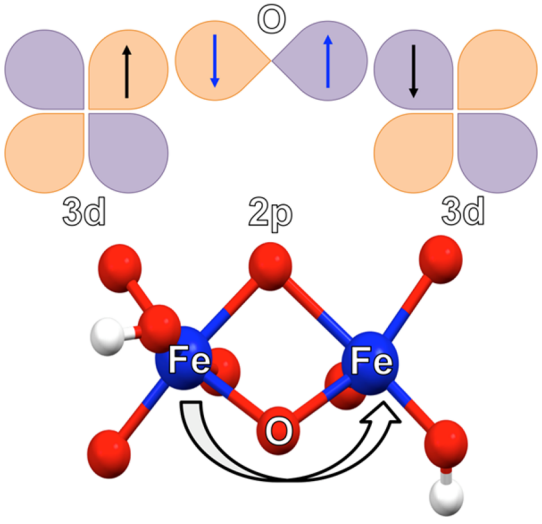


**Figure 9.** Schematic describing the superexchange interaction that occurs within $Fe_2(O)_2(dobdc)$ and $Fe_2(OH)_2(dobdc)$. (Atom legend: blue = Fe atoms, red = O atoms, and white = H atoms.)

In order to somewhat separate changes in intrachain Fe···Fe distances and Fe−O−Fe angles, we performed cluster calculations using the two-Fe model, where two degrees of freedom, Fe···Fe distance and Fe−$O_c$−Fe angle, were set to (2.9 Å, 85°), (2.9 Å, 105°), (3.1 Å, 95°), (3.3 Å, 85°), and (3.3 Å, 105°) to see how the change in either the Fe···Fe distance or the Fe−O−Fe angle affects the magnetic coupling. With these two internal coordinates frozen, all other coordinates were optimized. The $J_{NN}$ values were found to be 10, −6.3, 1.5, 5.0, and −1.2 $cm^{-1}$, respectively. This shows that if the Fe···Fe distance is kept fixed to 2.9 or 3.3 Å and the Fe−$O_c$−Fe angle is increased from 85° to 105°, $J_{NN}$ decreases and becomes negative. On the other hand, if the Fe−$O_c$−Fe angle is fixed to 85° or 105°, and the Fe···Fe distance is increased from 2.9 Å to 3.3 Å, the $J_{NN}$ value again decreases. Hence, changing either the Fe···Fe distance or the Fe−$O_c$−Fe angle has an effect on the magnetic coupling.

## 4. CONCLUSIONS

In contrast to $Fe_2(dobdc)$, $Fe_2(O)_2(dobdc)$ and $Fe_2(OH)_2(dobdc)$ feature antiferromagnetic (AFM) coupling down each metal chain (Figure 10). Previous work by Bloch et al.[16] and calculations performed by Park et al.[17] suggest that the shift from ferromagnetic (FM) to AFM coupling is the result of ligands changing the intrachain Fe···Fe distances and Fe−O−Fe angles. Here, we find that the effect can also be partially accounted for by the electronic effect of the ligands, the oxidation state of the metal centers, and/or the spin state of the metal centers, even in the absence of geometry changes. This indicates that structural and electronic changes upon framework oxidation likely act in concert to effect magnetic coupling.

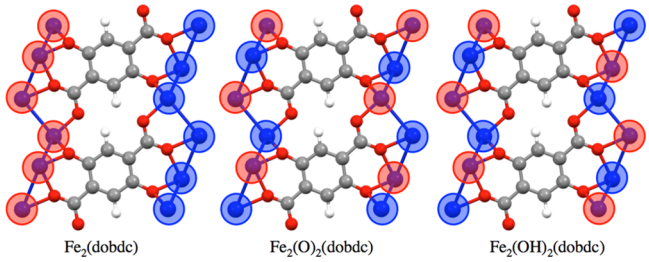


**Figure 10.** Representation of the spin configurations of the studied MOFs (atom legend: blue = Fe atoms, red = O atoms, gray = C atoms, and white = H atoms). Red circles indicate spin-up Fe spins and blue circles indicate spin-down Fe spins.

The computationally efficient PBE+U and GAM+U approaches predict structural properties that agree quite well with the values obtained using more expensive hybrid functionals. Inclusion of damped dispersion effects by molecular mechanics does alter equilibrium volumes; however, the effect is minor when compared to the inclusion of Hartree−Fock exchange. Thus, rescaling PBE+U or GAM+U unit cells


DOI: 10.1021/acs.inorgchem.6b00467
Inorg. Chem. 2016, 55, 4924−4934

and correcting for the electronic structure with single-point hybrid functional calculations appears to be an efficient approach to calculate magnetic properties of MOFs. Cluster models can be used to compute $J_{NN}$ coupling values quite accurately, and can be used conveniently with a wider array of computational methods at a lower cost. However, capturing both the $J_{NN}$ and $J_{IC}$ magnetic coupling dependency on the MOF structure does require periodic calculations. Overall, theory can correctly describe the magnetic and electronic properties and their structural dependences for these materials, provided one is aware of the strengths and limitations of both periodic and cluster-based modeling. Ongoing research is directed toward predicting these properties for as-yet-unsynthesized materials.

## ■ ASSOCIATED CONTENT

### Supporting Information

The Supporting Information is available free of charge on the ACS Publications website at DOI: 10.1021/acs.inorgchem.6b00467.

Equations that were used to extract the magnetic coupling parameters for the larger unit cell and the cluster model; the lattice parameters for all computed structures with all methods; the coordinates of the optimized structures using all methods; calculated bulk moduli for each MOF; computational and experimental infrared spectra; a *k*-points energy convergence test with $Fe_2$(dobdc); partial atomic charges; plots of the local density of states, including comparisons of all structures, computed with FM, AFM1, and AFM2 spin ordering (PDF)

## ■ AUTHOR INFORMATION


### Corresponding Authors

*E-mail: joachim.paier@chemie.hu-berlin.de (J. Paier).
*E-mail: truhlar@umn.edu (D. G. Truhlar).
*E-mail: gagliard@umn.edu (L. Gagliardi).
*E-mail: jrlong@berkeley.edu (J. R. Long).


### Notes

The authors declare no competing financial interest.

## ■ ACKNOWLEDGMENTS

We thank Professor Joachim Sauer for insightful discussions and comments on the manuscript. This work was supported by the U.S. DOE, Office of Basic Energy Sciences, Division of Chemical Sciences, Geosciences and Biosciences (Award No. DE-FG02-12ER16362). This work has been carried out using the Minnesota Supercomputing Institute computational resources and National Energy Research Scientific Computing center resources and using computing time granted by the high-performance computer centers HLRN (North-German Supercomputing Alliance in Berlin and Hannover) and JUROPA (Forschungszentrum Jülich). J.P. acknowledges financial support by the Fonds der Chemischen Industrie (FCI). P.V. and J.B. acknowledge financial support by the Doctoral Dissertation Fellowship. L.E.D. and D.J.X. thank the National Science Foundation (NSF) for providing graduate fellowship support.

## ■ REFERENCES


(1) Dechambenoit, P.; Long, J. R. *Chem. Soc. Rev.* **2011**, *40*, 3249–3265.
(2) Kahn, O.; Larionova, J.; Yakhmi, J. V. *Chem.—Eur. J.* **1999**, *5*, 3443–3449.
(3) Shen, L.; Yang, S.-W.; Xiang, S.; Liu, T.; Zhao, B.; Ng, M.-F.; Goeettlicher, J.; Yi, J.; Li, S.; Wang, L.; Ding, J.; Chen, B.; Wei, S.-H.; Feng, Y. P. *J. Am. Chem. Soc.* **2012**, *134*, 17286–17290.
(4) Mohapatra, S.; Rajeswaran, B.; Chakraborty, A.; Sundaresan, A.; Maji, T. K. *Chem. Mater.* **2013**, *25*, 1673–1679.
(5) Dzyaloshinsky, I. *J. Phys. Chem. Solids* **1958**, *4*, 241–255.
(6) Guha, B. C. *Nature* **1945**, *155*, 364–364.
(7) Goodenough, J. B. *Phys. Rev.* **1960**, *117*, 1442–1451.
(8) Odbadrakh, K.; Lewis, J. P.; Nicholson, D. M.; Petrova, T.; Michalkova, A.; Leszczynski, J. *J. Phys. Chem. C* **2010**, *114*, 3732–3736.
(9) Canepa, P.; Chabal, Y. J.; Thonhauser, T. *Phys. Rev. B: Condens. Matter Mater. Phys.* **2013**, *87*, 094407.
(10) Coudert, F.-X.; Ortiz, A. U.; Haigis, V.; Bousquet, D.; Fuchs, A. H.; Ballandras, A.; Weber, G.; Bezverkhyy, I.; Geoffroy, N.; Bellat, J.-P.; Ortiz, G.; Chaplais, G.; Patarin, J.; Boutin, A. *J. Phys. Chem. C* **2014**, *118*, 5397–5405.
(11) Deria, P.; Mondloch, J. E.; Tylianakis, E.; Ghosh, P.; Bury, W.; Snurr, R. Q.; Hupp, J. T.; Farha, O. K. *J. Am. Chem. Soc.* **2013**, *135*, 16801–16804.
(12) Yu, D.; Yazaydin, A. O.; Lane, J. R.; Dietzel, P. D. C.; Snurr, R. Q. *Chem. Sci.* **2013**, *4*, 3544–3556.
(13) Haldoupis, E.; Borycz, J.; Shi, H. L.; Vogiatzis, K. D.; Bai, P.; Queen, W. L.; Gagliardi, L.; Siepmann, J. I. *J. Phys. Chem. C* **2015**, *119*, 16058–16071.
(14) Zhang, Q.; Li, B.; Chen, L. *Inorg. Chem.* **2013**, *52*, 9356–9362.
(15) Verma, P.; Xu, X.; Truhlar, D. G. *J. Phys. Chem. C* **2013**, *117*, 12648–12660.
(16) Bloch, E. D.; Queen, W. L.; Krishna, R.; Zadrozny, J. M.; Brown, C. M.; Long, J. R. *Science* **2012**, *335*, 1606–1610.
(17) Park, J.; Kim, H.; Jung, Y. *J. Phys. Chem. Lett.* **2013**, *4*, 2530–2534.
(18) Maurice, R.; Verma, P.; Zadrozny, J. M.; Luo, S.; Borycz, J.; Long, J. R.; Truhlar, D. G.; Gagliardi, L. *Inorg. Chem.* **2013**, *52*, 9379–9389.
(19) Xiao, D. J.; Bloch, E. D.; Mason, J. A.; Queen, W. L.; Hudson, M. R.; Planas, N.; Borycz, J.; Dzubak, A. L.; Verma, P.; Lee, K.; Bonino, F.; Crocellà, V.; Yano, J.; Bordiga, S.; Truhlar, D. G.; Gagliardi, L.; Brown, C. M.; Long, J. R. *Nat. Chem.* **2014**, *6*, 590–595.
(20) Verma, P.; Vogiatzis, K. D.; Planas, N.; Borycz, J.; Xiao, D. J.; Long, J. R.; Gagliardi, L.; Truhlar, D. G. *J. Am. Chem. Soc.* **2015**, *137*, 5770–5781.
(21) Wriedt, M.; Yakovenko, A. A.; Halder, G. J.; Prosvirin, A. V.; Dunbar, K. R.; Zhou, H. C. *J. Am. Chem. Soc.* **2013**, *135*, 4040–4050.
(22) Liechtenstein, A. I.; Anisimov, V. I.; Zaanen, J. *Phys. Rev. B: Condens. Matter Mater. Phys.* **1995**, *52*, R5467–R5470.
(23) Iori, F.; Gatti, M.; Rubio, A. *Phys. Rev. B: Condens. Matter Mater. Phys.* **2012**, *85*, 115129.
(24) Grau-Crespo, R.; Wang, H.; Schwingenschloegl, U. *Phys. Rev. B: Condens. Matter Mater. Phys.* **2012**, *86*, 081101.
(25) Henderson, T. M.; Paier, J.; Scuseria, G. E. *Phys. Status Solidi B* **2011**, *248*, 767–774.
(26) Moreira, I. P. R.; Illas, F. *Phys. Chem. Chem. Phys.* **2006**, *8*, 1645–1659.
(27) Bain, G. A.; Berry, J. F. *J. Chem. Educ.* **2008**, *85*, 532–536.
(28) Kahn, O. *Molecular Magnetism*; Wiley–VCH: New York, 1993; pp 257–258.
(29) Georges, R.; Borras-Almenar, J. J.; Coronado, E.; Curély, J.; Drillon, M. *Magnetism: Molecules to Materials: Models and Experiments*; Wiley–VCH: Weinheim, Germany, 2002; Chapter 1, pp 1–47.
(30) Perdew, J. P.; Burke, K.; Ernzerhof, M. *Phys. Rev. Lett.* **1996**, *77*, 3865–3868.
(31) Yu, H. S.; Zhang, W.; Verma, P.; He, X.; Truhlar, D. G. *Phys. Chem. Chem. Phys.* **2015**, *17*, 12146–12160.
(32) Duanmu, K.; Luo, S.; Truhlar, D. G. *Minnesota—VASP Functional Module (MN-VFM – version 3.0)*; available via the Internet at: http://comp.chem.umn.edu/mn-vfm/.




DOI: 10.1021/acs.inorgchem.6b00467
*Inorg. Chem.* 2016, 55, 4924–4934

(33) Zhao, Y.; Truhlar, D. G. *J. Chem. Phys.* **2006**, *125*, 194101.
(34) Zhao, Y.; Truhlar, D. G. *J. Chem. Phys.* **2009**, *130*, 130.
(35) Booth, G. H.; Grüneis, A.; Kresse, G.; Alavi, A. *Nature* **2012**, *493*, 365−370.
(36) Paier, J.; Ren, X.; Rinke, P.; Scuseria, G. E.; Grüneis, A.; Kresse, G.; Scheffler, M. *New J. Phys.* **2012**, *14*, 043002.
(37) Cramer, C. J.; Truhlar, D. G. *Phys. Chem. Chem. Phys.* **2009**, *11*, 10757−10816.
(38) Asmis, K. R.; Santambrogio, G.; Brümmer, M.; Sauer, J. *Angew. Chem.* **2005**, *117*, 3182−3185.
(39) Chevrier, V. L.; Ong, S. P.; Armiento, R.; Chan, M. K. Y.; Ceder, G. *Phys. Rev. B: Condens. Matter Mater. Phys.* **2010**, *82*, 075122.
(40) Cohen, A. J.; Mori-Sanchez, P.; Yang, W. *J. Chem. Phys.* **2007**, *126*, 191109.
(41) Mori-Sanchez, P.; Cohen, A. J.; Yang, W. *Phys. Rev. Lett.* **2008**, *100*, 146401.
(42) Manz, T. A.; Sholl, D. S. *J. Chem. Theory Comput.* **2011**, *7*, 4146−4164.
(43) Krukau, A. V.; Vydrov, O. A.; Izmaylov, A. F.; Scuseria, G. E. *J. Chem. Phys.* **2006**, *125*, 224106.
(44) Becke, A. D. *J. Chem. Phys.* **1993**, *98*, 5648−5652.
(45) Lee, C. T.; Yang, W. T.; Parr, R. G. *Phys. Rev. B: Condens. Matter Mater. Phys.* **1988**, *37*, 785−789.
(46) Vosko, S. H.; Wilk, L.; Nusair, M. *Can. J. Phys.* **1980**, *58*, 1200−1211.
(47) Stephens, P. J.; Devlin, F. J.; Chabalowski, C. F.; Frisch, M. J. *J. Phys. Chem.* **1994**, *98*, 11623−11627.
(48) Ernzerhof, M.; Scuseria, G. E. *J. Chem. Phys.* **1999**, *110*, 5029−5036.
(49) Adamo, C.; Barone, V. *J. Chem. Phys.* **1999**, *110*, 6158−6170.
(50) Zhao, Y.; Truhlar, D. G. *Theor. Chem. Acc.* **2008**, *120*, 215−241.
(51) Kresse, G.; Furthmüller, J. *Phys. Rev. B: Condens. Matter Mater. Phys.* **1996**, *54*, 11169−11186.
(52) Kresse, G.; Furthmüller, J. *Comput. Mater. Sci.* **1996**, *6*, 15−50.
(53) Heyd, J.; Scuseria, G. E.; Ernzerhof, M. *J. Chem. Phys.* **2003**, *118*, 8207−8215.
(54) Paier, J.; Marsman, M.; Hummer, K.; Kresse, G.; Gerber, I. C.; Angyan, J. G. *J. Chem. Phys.* **2006**, *124*, 154709.
(55) Gygi, F.; Baldereschi, A. *Phys. Rev. B: Condens. Matter Mater. Phys.* **1986**, *34*, 4405−4408.
(56) Onida, G.; Reining, L.; Rubio, A. *Rev. Mod. Phys.* **2002**, *74*, 601−659.
(57) Heyd, J.; Scuseria, G. E. *J. Chem. Phys.* **2004**, *121*, 1187−1192.
(58) Heyd, J.; Scuseria, G. E.; Ernzerhof, M. *J. Chem. Phys.* **2006**, *124*, 219906.
(59) Rivero, P.; Moreira, I. d. P. R.; Illas, F.; Scuseria, G. E. *J. Chem. Phys.* **2008**, *129*, 184110.
(60) Zhou, J.; Sun, Q. *J. Am. Chem. Soc.* **2011**, *133*, 15113−15119.
(61) Grimme, S. *J. Comput. Chem.* **2006**, *27*, 1787−1799.
(62) Bucko, T.; Hafner, J.; Lebegue, S.; Angyan, J. G. *J. Phys. Chem. A* **2010**, *114*, 11814−11824.
(63) Kerber, T.; Sierka, M.; Sauer, J. *J. Comput. Chem.* **2008**, *29*, 2088−2097.
(64) Penschke, C.; Paier, J.; Sauer, J. *J. Phys. Chem. C* **2013**, *117*, 5274−5285.
(65) Blöchl, P. E. *Phys. Rev. B: Condens. Matter Mater. Phys.* **1994**, *50*, 17953−17979.
(66) Kresse, G.; Joubert, D. *Phys. Rev. B: Condens. Matter Mater. Phys.* **1999**, *59*, 1758−1775.
(67) Krivy, I.; Gruber, B. *Acta Crystallogr., Sect. A: Cryst. Phys., Diffr., Theor. Gen. Crystallogr.* **1976**, *32*, 297−298.
(68) Grosse-Kunstleve, R. W.; Sauter, N. K.; Adams, P. D. *Acta Crystallogr., Sect. A: Found. Crystallogr.* **2004**, *60*, 1−6.
(69) Gajdos, M.; Hummer, K.; Kresse, G.; Furthmüller, J.; Bechstedt, F. *Phys. Rev. B: Condens. Matter Mater. Phys.* **2006**, *73*, 045112.
(70) Baroni, S.; de Gironcoli, S.; Dal Corso, A.; Giannozzi, P. *Rev. Mod. Phys.* **2001**, *73*, 515−562.
(71) Born, M.; Huang, K. *Dynamical Theory of Crystal Lattices*; Oxford University Press: Oxford, U.K., 1954.
(72) Pick, R. M.; Cohen, M. H.; Martin, R. M. *Phys. Rev. B* **1970**, *1*, 910.
(73) Frisch, M. J.; Trucks, G. W.; Schlegel, H. B.; Scuseria, G. E.; Robb, M. A.; Cheeseman, J. R.; Scalmani, G.; Barone, V.; Mennucci, B.; Petersson, G. A.; Nakatsuji, H.; Caricato, M.; Li, X.; Hratchian, H. P.; Izmaylov, A. F.; Bloino, J.; Zheng, G.; Sonnenberg, J. L.; Hada, M.; Ehara, M.; Toyota, K.; Fukuda, R.; Hasegawa, J.; Ishida, M.; Nakajima, T.; Honda, Y.; Kitao, O.; Nakai, H.; Vreven, T.; Montgomery, J. A., Jr.; Peralta, J. E.; Ogliaro, F.; Bearpark, M. J.; Heyd, J.; Brothers, E. N.; Kudin, K. N.; Staroverov, V. N.; Kobayashi, R.; Normand, J.; Raghavachari, K.; Rendell, A. P.; Burant, J. C.; Iyengar, S. S.; Tomasi, J.; Cossi, M.; Rega, N.; Millam, N. J.; Klene, M.; Knox, J. E.; Cross, J. B.; Bakken, V.; Adamo, C.; Jaramillo, J.; Gomperts, R.; Stratmann, R. E.; Yazyev, O.; Austin, A. J.; Cammi, R.; Pomelli, C.; Ochterski, J. W.; Martin, R. L.; Morokuma, K.; Zakrzewski, V. G.; Voth, G. A.; Salvador, P.; Dannenberg, J. J.; Dapprich, S.; Daniels, A. D.; Farkas, Ö.; Foresman, J. B.; Ortiz, J. V.; Cioslowski, J.; Fox, D. J. *Gaussian 09*; Revision D.01; Gaussian, Inc.: Wallingford, CT, USA, 2013.
(74) Weigend, F.; Ahlrichs, R. *Phys. Chem. Chem. Phys.* **2005**, *7*, 3297−3305.
(75) Heisenberg, W. *Eur. Phys. J. A* **1928**, *49*, 619−636.
(76) Dirac, P. A. M. *Proc. R. Soc. London, Ser. A* **1929**, *123*, 714−733.
(77) Van Vleck, J. H. *Rev. Mod. Phys.* **1945**, *17*, 27−47.
(78) Hamida, Y.; Danilovic, D.; Yuen, T.; Li, K. H.; Li, J. *J. Appl. Phys.* **2012**, *111*, 07B332.
(79) Borycz, J.; Lin, L.-C.; Bloch, E. D.; Kim, J.; Dzubak, A. L.; Maurice, R.; Semrouni, D.; Lee, K.; Smit, B.; Gagliardi, L. *J. Phys. Chem. C* **2014**, *118*, 12230−12240.
(80) Bloch, E. D.; Murray, L. J.; Queen, W. L.; Chavan, S.; Maximoff, S. N.; Bigi, J. P.; Krishna, R.; Peterson, V. K.; Grandjean, F.; Long, G. J.; Smit, B.; Bordiga, S.; Brown, C. M.; Long, J. R. *J. Am. Chem. Soc.* **2011**, *133*, 14814−14822.
(81) Hohenberger, J.; Ray, K.; Meyer, K. *Nat. Commun.* **2012**, *3*, 720.
(82) Alecu, I. M.; Zheng, J.; Zhao, Y.; Truhlar, D. G. *J. Chem. Theory Comput.* **2010**, *6*, 2872−2887.
(83) Huang, S.; Wilson, B. E.; Wang, B.; Fang, Y.; Buffington, K.; Stein, A.; Truhlar, D. G. *J. Am. Chem. Soc.* **2015**, *137*, 10992−11003.
(84) Verdaguer, M.; Bleuzen, A.; Marvaud, V.; Vaissermann, J.; Seuleiman, M.; Desplanches, C.; Scuiller, A.; Train, C.; Garde, R.; Gelly, G.; Lomenech, C.; Rosenman, I.; Veillet, P.; Cartier, C.; Villain, F. *Coord. Chem. Rev.* **1999**, *190*−*192*, 1023−1047.
(85) Martin, R. L.; Illas, F. *Phys. Rev. Lett.* **1997**, *79*, 1539−1542.


DOI: 10.1021/acs.inorgchem.6b00467
*Inorg. Chem.* 2016, 55, 4924−4934

# P12

https://pubs.acs.org/doi/abs/10.1021/acs.jpcc.5b10560

THE JOURNAL OF PHYSICAL CHEMISTRY C

Article

pubs.acs.org/JPCC

# Adsorption of Water on the $Fe_3O_4(111)$ Surface: Structures, Stabilities, and Vibrational Properties Studied by Density Functional Theory

Xiaoke Li and Joachim Paier*

Institut für Chemie, Humboldt-Universität zu Berlin, Unter Linden 6, 10099 Berlin, Germany

Supporting Information

**ABSTRACT:** The majority of the theoretical work that attempted to provide atomic level details on the adsorption of water at the $Fe_3O_4(111)$ surface is based on conventional density functionals, which suffer from shortcomings such as, for example, self-interaction errors. In an effort to overcome these uncertainties in theoretical results, we use density functional theory (DFT) employing the Perdew, Burke, and Ernzerhof generalized-gradient corrected exchange-correlation functional augmented by a Hubbard-type $U$ parameter. We test for robustness of these results by application of the Heyd, Scuseria, Ernzerhof hybrid functional. For the two relevant metal terminations ($Fe_{oct2}$ and $Fe_{tet1}$) having ambient conditions in mind, we determined the minimum energy adsorption structures up to relatively high water coverage, that is, one, two, and three $H_2O$ molecules on the $p(1 \times 1)$ surface unit cells, respectively. Water adsorbs dissociatively and strongly exothermic on the $Fe_{oct2}$, whereas molecular adsorption occurs on the $Fe_{tet1}$ termination. Using $D_2O$, two IR signals at 2720 and 2695 $cm^{-1}$ (typical of OD stretching modes) can be observed for a wide range of temperatures and at moderate water vapor pressures. Our calculations reveal that these IR bands originate from a very stable water dimer-like species. However, at lower temperatures the creation of larger aggregations, such as trimers, appears to be thermodynamically favorable.

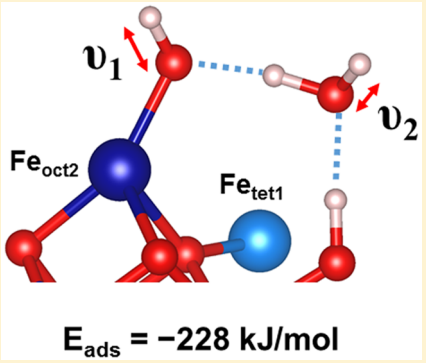


## 1. INTRODUCTION

Atomic level understanding of the interaction of water with iron oxides, one of the most abundant metal oxides in the earth's crust, is of great importance in many different fields, as, for example, in the catalysis research,[1,2] the electrochemistry,[3,4] and the geochemistry.[5,6] Although under most relevant conditions hematite ($Fe_2O_3$) represents the thermodynamically most stable iron oxide phase, under rather reducing conditions, that is, at higher temperatures and lower oxygen partial pressures, magnetite ($Fe_3O_4$) is the prevailing phase.[7,8] Also for other technologically relevant metal oxides, like $TiO_2$,[6,9−12] and ZnO,[13,14] much effort has been spent to elucidate atomic-level details in the hydration process of the oxide surfaces.

At temperatures above the so-called Verwey insulator to metal transition at about 122 K,[15] magnetite crystallizes in the cubic inverse spinel structure of space group $Fd\bar{3}m$ with an equilibrium lattice constant of 8.396 Å.[16,17] The iron cations ($Fe^{2+}$and $Fe^{3+}$) are located in the interstitial sites of a close-packed face-centered cubic (fcc) sublattice, which is formed by the oxygen anions ($O^{2-}$). With respect to coordination numbers, two different cation sites exist in the crystal; the first one (A site) is tetrahedrally coordinated by oxygen and occupied only by $Fe^{3+}$ ions, and the second one (B) is octahedrally coordinated and occupied by an equal number of randomly distributed $Fe^{2+}$ and $Fe^{3+}$ ions. Thus, $Fe_A^{3+}[Fe^{2+}Fe^{3+}]_BO_4$ is one way to indicate the multivalent character of iron in magnetite. Its bulk phase is a ferrimagnetic material, where local magnetic moments at $Fe_A$ and $Fe_B$ ions are antiparallel oriented.

The natural growth facet of magnetite is a surface in [111] orientation.[18−20] According to Tasker's rules,[21] six polar bulk terminations exist (cf. Figure 1), however, relaxation of the ions will minimize surface dipoles and therefore stabilize the surface.[22−24] Along the [111] direction and caused by the (layered) crystal structure, terminating the surface by $Fe_A$ and

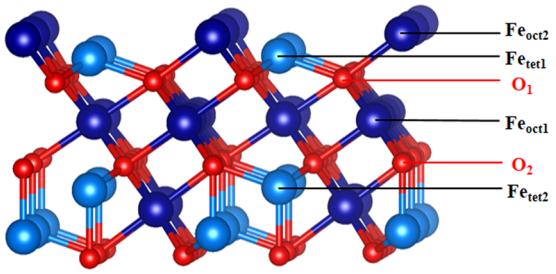


**Figure 1.** Sequence of atomic layers in a $Fe_3O_4(111)$ surface slab ($Fe_{oct2}$ terminated) in ideal bulk structure. Color code used throughout this work: $Fe_{oct1}$ and $Fe_{oct2}$, dark blue balls; $Fe_{tet1}$ and $Fe_{tet2}$, light blue balls; oxygen, small red balls. All figures were created using VESTA.[25]

**Received:** October 28, 2015
**Revised:** December 17, 2015
**Published:** December 21, 2015






DOI: 10.1021/acs.jpcc.5b10560
J. Phys. Chem. C 2016, 120, 1056−1065

$Fe_B$ sites is possible in two different ways for each termination, that is, $Fe_{tet1}$, $Fe_{tet2}$ and $Fe_{oct1}$, $Fe_{oct2}$. We prefer the latter notation, as it is unambiguous and is therefore used throughout this work.

On the basis of the low energy electron diffraction (LEED) and scanning tunneling microscopy (STM) studies by Weiss and co-workers, who focused on thin films of $Fe_3O_4(111)$ supported on Pt(111), the surface is terminated by a one-fourth monolayer (ML) of the $Fe_{tet1}$ ion over a hexagonal close-packed oxygen layer.[26−29] This agrees with earlier LEED studies by Somorjai and co-workers.[30,31] However, results from a study employing high-resolution electron energy loss spectroscopy (HREELS), infrared reflection absorption spectroscopy (IRAS), and temperature-programmed desorption (TPD) using CO as a probe molecule were reconcilable with a termination of two iron atoms, consisting of a topmost one-fourth ML of $Fe_{oct2}$ and a one-fourth ML of $Fe_{tet1}$ directly underneath.[32]

With regard to theoretical work, this section does not intend to be exhaustive about previous density functional theory (DFT) studies on the $Fe_3O_4(111)$ surface. Instead, we only mention four, which are in our opinion representative works, using LDA+$U$(4.0,4.5 eV),[33] PBE+$U$(3.8,4.0 eV),[34,35] as well as PW91+$U$(3.61 eV)[36] to calculate surface energies and stabilities of various terminations under varying chemical potentials of oxygen. Although different DFT-based approaches have been used, these studies agree on the fact that the $Fe_{tet1}$ and $Fe_{oct2}$ terminations are (i) comparably stable in terms of surface energy, and (ii) the most stable ones for a wide range of chemical potentials of oxygen.

A few studies on the adsorption of water on the $Fe_3O_4(100)$ surface exist;[37−39] however, despite the large body of work by Ranke and co-workers[7,29,40,41] focusing on the (111) facet, there are still some open questions. Al-Shamery and co-workers investigated the adsorption structure of small water aggregations based on TPD as well as IR spectroscopy.[41] Relying on the work by Joseph et al.,[40] they conjectured that upon dissociative $H_2O$ adsorption, the $OH^-$ coordinates to a surface Fe ion, and the $H^+$ binds to a neighboring surface O ion creating another hydroxyl group. This hypothesis naturally suggests the assignment of the two observed IR bands (2712 and 2691 $cm^{-1}$)[41] to respective vibrational modes of the aforementioned "water induced" OH groups. However, firm evidence has not been provided yet.

In another recent work, Batista and co-workers studied the adsorption of water on an iron-terminated $Fe_3O_4(111)$ surface by virtue of STM and DFT.[42] For temperatures below 235 K, they interpret their STM images as a signature of intact water molecules as well as hydroxyl groups bound to the surface, whereas for temperatures between 235 and 245 K, results are interpreted in favor of complete dissociation of adwater. Consequently, for this temperature range the authors claim that all water is converted into hydroxyl groups bound on top of the terminating $Fe^{3+}$ cations.[42]

Relatively few theoretical studies on the adsorption of water on the $Fe_3O_4(111)$ surface exist.[19,42−44] Importantly, as shown by Jiao and co-workers,[34] 12 atomic layers for the periodic slab model appear to be mandatory, because the ninth layer for the $Fe_{tet1}$ and the seventh layer for the $Fe_{oct2}$ termination play an important role in electron localization, which is coupled to ionic relaxation. However, the criterion of a large enough model, that is, employing a slab with a sufficient number of layers, is only met in ref 44. Unfortunately, due to technical issues described in this aforementioned work, no Hubbard-type $U$ parameter to correct for some of the correlation effects in the Fe 3d states was employed. A systematic theoretical study on water adsorption treating both important metal terminations has not been accomplished so far.

The present work addresses these issues and discusses novel results on the interaction between $H_2O$ molecules and the $Fe_{tet1}$- and $Fe_{oct2}$-terminated $Fe_3O_4(111)$ surfaces using periodic DFT and superposition error free plane waves as a basis set. We present a detailed, comparative report on minimum energy structures, adsorption thermodynamics, as well as IR frequencies including isotope effects with increasing water coverage, that is, one, two, and three $H_2O$ per primitive surface unit cell. This corresponds to water coverages of 3.2, 6.4, and $9.6 \times 10^{14}$ $cm^{-2}$, respectively.

## 2. COMPUTATIONAL DETAILS

**2.1. Methods.** *PBE+U Electronic and Ionic Structure Calculations.* Calculations were performed using the projector-augmented-wave (PAW) method[45,46] as implemented in the Vienna ab initio simulation package (VASP)[47,48] using plane waves up to a kinetic energy of 800 eV. We take care of corrections for the onsite Coulomb correlation of Fe 3d orbitals via the (spin-polarized) DFT+$U$[49,50] approach based on the Perdew−Burke−Ernzerhof (PBE)[51] exchange-correlation functional, that is, PBE+$U$. The specific implementation of DFT+$U$ used in this work follows Dudarev et al.[52,53] An effective Hubbard-type $U$ parameter of 3.8 eV was employed following previous LSDA[54,55] as well as PBE-GGA[34,56] studies on $Fe_3O_4$ surfaces. This appears to be an optimal choice, because local magnetic moments of the octahedrally and tetrahedrally coordinated Fe ions in the bulk amount to 3.9 and −4.1 $\mu_B$, respectively, which is in very good agreement with experiment (4.05 $\mu_B$)[57] and results reported in the literature.[34,36,56] In addition, the lattice parameter obtained using an effective $U$ of 3.8 eV and the PBE functional amounts to 8.508 Å (fit to Murnaghan's equation of state; cf. Supporting Information)[58] agrees reasonably well with experiment (8.396 Å).[16,17] The calculated bulk modulus amounts to 172 GPa, which underestimates the observed value (181−186 GPa)[17,59] by 5%. The overestimation of the lattice constant together with the aforementioned underestimation of the bulk modulus is typical of GGA functionals applied to crystalline solids.[60] The overestimation of lattice constants by a GGA approximation becomes usually even more pronounced within the DFT+$U$ approach, as for example, discussed by Bayer et al.[61]

We use the PAW potentials as released with VASP 5.2. The potential used to describe the electron−ion interaction in Fe comprises 14 valence electrons (Fe: [Mg] $3p^6$ $3d^7$ $4s^1$ as the atomic reference configuration). For oxygen, six ([He] $2s^2$ $2p^4$) valence electrons have been used.

For the $Fe_3O_4$ bulk calculations, a Γ-centered Monkhorst−Pack[62] $k$-mesh of a grid density of 8 × 8 × 8 was employed. Surface calculations (cf. Section 2.2) employ a 5 × 5 × 1 $k$-mesh.

Electronic optimization was performed using an energy break criterion of $10^{-5}$ eV. Structural optimizations were performed until all forces acting on the relaxed atoms were better than 0.02 eV/Å. Vibrational frequencies use central differences for the force derivative to calculate the (partial) Hessian matrix (cf. Section 2.2) employing atomic displacements of ±0.015 Å.

*Hybrid Functional Calculations.* In addition to PBE+$U$(3.8), adsorption energies required for thermodynamic


DOI: 10.1021/acs.jpcc.5b10560
J. Phys. Chem. C 2016, 120, 1056−1065

stabilities (cf. Section 3.4) were computed using the Heyd, Scuseria, and Ernzerhof (HSE) hybrid functional.[63] This functional uses 25% Fock and 75% PBE exchange energy as the mixing ratio similar to the PBE0 hybrid functional[64] and a screening parameter of 0.207 Å$^{-1}$. Energy and force calculations employ a Fourier grid for the Fock exchange related routines determined by 9/4 times the cutoff used to expand the orbitals (PRECFOCK = normal). This protocol was extensively tested and has been shown to result in accurate energies and forces.[65−67] To optimize the bulk lattice constant, a Γ-centered 4 × 4 × 4 Monkhorst−Pack *k*-mesh was used, and the surface slab calculations employ a *k*-mesh of 2 × 2 × 1 grid density. This ensured *k*-point convergence in the hybrid functional results.

To test for the influence of van der Waals dispersion-type of interactions on adsorption energies, we estimated this energy contribution by adding the semiempirical $C_6/R^6$ term following Grimme (DFT+D2) to energies and forces.[68,69] Standard van der Waals $C_6$ and $R_0$ parameters as provided by Grimme were employed for Fe, O, and H atoms (cf. Table 1). Functional

**Table 1. $C_6$ Parameters (J nm$^6$ mol$^{-1}$) and van der Waals Radii, $R_0$ (pm), Used in This Work (As Provided by Grimme[68])**

| | $C_6$ | $R_0$ |
|---|---|---|
| Fe | 10.80 | 156.2 |
| O | 0.70 | 134.2 |
| H | 0.14 | 100.1 |

specific global scaling factors for the dispersion contribution of 0.75 and 0.60 were employed in PBE+*U*(3.8) and HSE calculations, respectively. For more extensive assessments and discussions on the global scaling factors, we refer to refs 66 and 70.

**2.2. Models.** The conventional unit cell for the bulk crystal used comprises 56 atoms ($Fe_{24}O_{32}$). The surface unit cells cut in [111] orientation are primitive (1 × 1) cells with respect to the oxygen plane with a cell vector of $a_0/\sqrt{2}$ length (PBE +*U*(3.8), 601.6 pm; HSE, 594.8 pm) with $a_0$ being the equilibrium bulk lattice constant. Slab models use 12 atomic layers corresponding to a composition of $Fe_{12}O_{16}$ (cf. Figure 2). Periodically repeated images are separated by a vacuum layer of 10 Å. Spurious dipole−dipole interactions between periodic images are compensated by the approach suggested by Makov and Payne[71] as implemented in the VASP code.

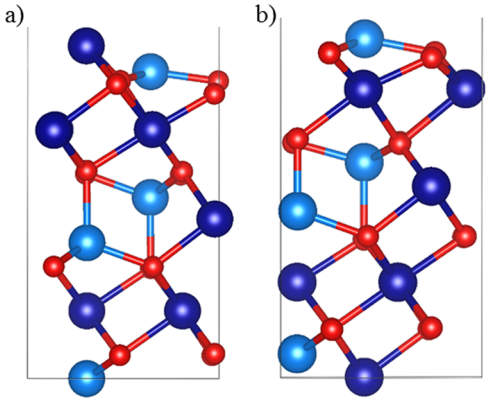


**Figure 2.** Slab models for the clean and optimized (a) $Fe_{oct2}$ and (b) $Fe_{tet1}$ terminated $Fe_3O_4(111)$ surfaces. See Figure 1 for the color code.

For the optimization of ionic positions, four atomic layers at the bottom of the slab are kept frozen in bulk positions (= asymmetric slab). Normal mode analysis uses the optimized slab involving adwater as well as four topmost surface layers, needed in the calculation of the partial Hessian. This means that the contribution from the remaining eight layers below the surface layers are not included in the calculation of harmonic frequencies. However, this contribution is supposed to largely cancel out in the calculation of adsorption energies.

**2.3. Thermodynamics.** The adsorption of water on the $Fe_{oct2}$ and $Fe_{tet1}$ terminated $Fe_3O_4(111)$ surfaces is described by the following equation

$$Fe_3O_4(111)_{oct2/tet1} + nH_2O \rightleftarrows [Fe_3O_4(111), nH_2O]_{oct2/tet1} \quad (1)$$

with $n$ = 1, 2, and 3.

The corresponding adsorption free energy, $\Delta G_{ads}$, is defined as

$$\Delta G_{ads} = \Delta G_{ads}(T, p, nH_2O) = G^{(s)}_{cmpl} - (G^{(s)}_{surf} + n\cdot\mu^{(g)}_{H2O}) \quad (2)$$

with $G^{(s)}_{cmpl}$, $G^{(s)}_{surf}$, $\mu^{(g)}_{H2O}$ as the free energies of the adsorption complex, the clean surface, and the chemical potential of water in the gas phase.

The enthalpy for solids is approximated as the sum of the DFT electronic energy and the zero-point vibrational energy (ZPVE) using harmonic frequencies. As commonly applied,[72] the volume work (pV) in solids is neglected

$$H^{(s)} = E_{el} + E_{ZPV} \quad (3)$$

Temperature dependence of the enthalpy and vibrational entropy of surfaces are calculated according to the procedure described in ref 73.

The chemical potential of water in the gas phase is defined as

$$\mu^{(g)}_{H2O}(T, p) = \mu^{(g)}_{H2O}(T, p^0) + RT\cdot\ln\left(\frac{p}{p^0}\right) \quad (4)$$

with $R$ as the universal gas constant and $p^0$ as the standard pressure (1 bar).

The chemical potential at $p^0$ reads

$$\mu^{(g)}_{H2O}(T, p^0) = \mu^{(g)}_{H2O}(0\ K) + [H(T, p^0) - H(0\ K, p^0)] - TS(T, p^0) \quad (5)$$

The chemical potential of water at 0 K, $\mu^{(g)}_{H2O}(0K)$, is defined as

$$\mu^{(g)}_{H2O}(0\ K) = E^{H2O}_{el} + E^{H2O}_{ZPV} \quad (6)$$

## 3. RESULTS

**3.1. Clean Surfaces.** Table 2 shows surface energy $\gamma$ and relative layer relaxation $\Delta z$ of the $Fe_{oct2}$ and $Fe_{tet1}$ terminated surfaces, respectively. The surface energy $\gamma$ is calculated according to

$$\gamma = \frac{1}{2A}(E_{surf} - E_{bulk}) \quad (7)$$

The layer relaxation $\Delta z$ is defined as the change in the *z*-coordinate of the atom with respect to the ideal (unrelaxed)


DOI: 10.1021/acs.jpcc.5b10560
J. Phys. Chem. C 2016, 120, 1056−1065

**Table 2. Surface Energy $\gamma$ (J/m$^2$) for the $Fe_{oct2}$ and $Fe_{tet1}$ Terminated $Fe_3O_4(111)$ Surfaces**[a]

| | | $\Delta z$ (%) | | | |
|---|---|---|---|---|---|
| | $\gamma$ (J/m$^2$) | 1L | 2L | 3L | 4L |
| $Fe_{oct2}$ | 1.176 | −1.70 | −2.84 | +1.70 | +0.38 |
| $Fe_{tet1}$ | 1.112 | −4.95 | −2.02 | +1.32 | −1.53 |

[a]Relative atomic layer relaxations $\Delta z$ with respect to the unrelaxed $z$-coordinate of the four topmost layers (1L−4L).

structure. For the $Fe_{oct2}$ termination, the first and second Fe layers relax inward by 1.70 and 2.84%, respectively. However, relaxation of the terminating $Fe_{tet1}$ atom is far more pronounced (−4.95%).

The relaxation, which will minimize the surface energy, is obvious in both surfaces due to their polarity.[22] After relaxation, numerical results for $\gamma$ of the $Fe_{oct2}$ (1.18 J/m$^2$) and $Fe_{tet1}$ (1.11 J/m$^2$) terminations are very close.

**3.2. Water Adsorption on the $Fe_{oct2}$ Termination.** *Monomer.* Depositing a single water molecule on the primitive surface unit cell leads to spontaneous dissociation. The PBE+$U$(3.8) adsorption energy of −140.0 kJ/mol is given in Table 3 and calculated following eq 1.

**Table 3. Adsorption Energies (kJ/mol) Obtained Using PBE+$U$(3.8) and Estimate for the Dispersion Contribution in PBE+$U$+D//PBE+$U$**[a]

| | 1 × $H_2O$ | 2 × $H_2O$ | 3 × $H_2O$ |
|---|---|---|---|
| $Fe_{oct2}$ | −140.0 (−26.9) | −228.1 (−42.1) | −270.6 (−61.8) |
| $Fe_{tet1}$ | −61.0 (−13.3) | −147.5 (−26.8) | −198.8 (−50.1) |

[a]Dispersion contribution of PBE+U+D//PBE+U is given in parentheses.

This result corresponds to a strongly exothermic adsorption process due to the dissociative reaction pathway. The related adsorption structure (**1O**) is shown in Figure 3a. The dissociation leads to two hydroxyl groups on the surface. One of it coordinates to the terminating iron atom with a Fe−O bond distance of 190.7 pm. The second OH group results from proton transfer to a surface oxygen. Its associated OH distance amounts to 99.2 pm.

*Dimer.* According to Figure 2b (**2O**), the additional, second water molecule does not dissociate. It adsorbs in a way such that two hydrogen bonds are created. The adsorption energy of the dimer at the $Fe_{oct2}$ terminated surface amounts to −228.1 kJ/mol.

*Trimer.* The third water molecule coordinates with its oxygen atom to the $Fe_{tet1}$ atom in the surface, such that only one additional hydrogen bond is formed. The adsorption energy amounts to −270.6 kJ/mol. Note that the gain in energy upon adding the third molecule is almost 50% smaller compared with the energy gain for creating **2O**. The proton acceptor in the aforementioned H bond is the oxygen atom in the OH group formed upon dissociation of the first $H_2O$, which is located at the $Fe_{oct2}$ atom (cf. Figure 3c, **3O**).

**3.3. Water Adsorption on the $Fe_{tet1}$ Termination.** *Monomer.* In contrast to the $Fe_{oct2}$ terminated surface, water adsorbs molecularly at the $Fe_{tet1}$ termination of $Fe_3O_4(111)$ associated with a much higher (that is, more positive) adsorption energy of −61.0 kJ/mol (cf. Table 3). Note that no surface hydroxyl groups are created. The oxygen atom of $H_2O$ binds on top of the terminating iron atom with a rather long bond distance of 217.6 pm. The two terminal OH groups in the molecule are oriented parallel to the surface (**1T**, cf. Figure 4a).

*Dimer.* The adsorption configuration involving a second water molecule (**2T**, cf. Figure 4b) is akin to the one in **2O**. However, no proton transfer is involved, that is, the molecules stay intact. The adsorption energy for **2T** amounts to −147.5 kJ/mol. The gain in energy relative to **1T** amounts to 86.5 kJ/mol and is similarly large as in case of the formation of **2O**.

*Trimer.* The adsorption structure of three water molecules on the $Fe_{tet1}$ terminated surface (**3T**, cf. Figure 4c) is similar to **2T**. The only difference is the additional $H_2O$ molecule, which occupies empty space behind the plane defined by the two water molecules in **2T**. Intramolecular bond distances of the third water molecule do not change significantly upon adsorption compared with the structure in the gas phase. The adsorption energy of **3T** amounts to −198.8 kJ/mol and, similarly to **3O**, the gain in energy relative to **2T**, is only 51.3 kJ/mol. van der Waals-type dispersion contributions have been estimated using PBE+U(3.8) structures and, as expected, provide further stabilization of the adwater by ca. 13 to 20 kJ/mol per water molecule.

**3.4. Thermodynamic Stability.** Table 4 lists enthalpy as well as entropy contributions to the Gibbs adsorption free energies at 100 and 300 K for water adsorption on the $Fe_{oct2}$ and $Fe_{tet1}$ terminated $Fe_3O_4(111)$ surfaces, respectively. Note that for the calculation of free energies according to eq 2, the

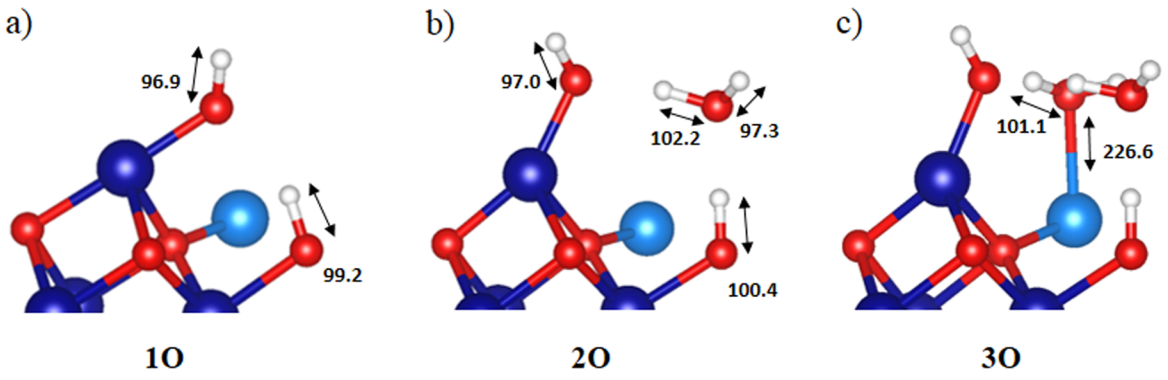


**Figure 3.** Structures optimized (bond distances in pm) using PBE+$U$(3.8) for one (a), two (b), and three (c) $H_2O$ molecules adsorbed at the $Fe_{oct2}$ terminated $Fe_3O_4(111)$ surface. Color code throughout this work: $Fe_{oct}$, large dark blue balls; $Fe_{tet}$, large light blue balls; oxygen, small red balls; hydrogen, small white balls.



DOI: 10.1021/acs.jpcc.5b10560
J. Phys. Chem. C 2016, 120, 1056−1065

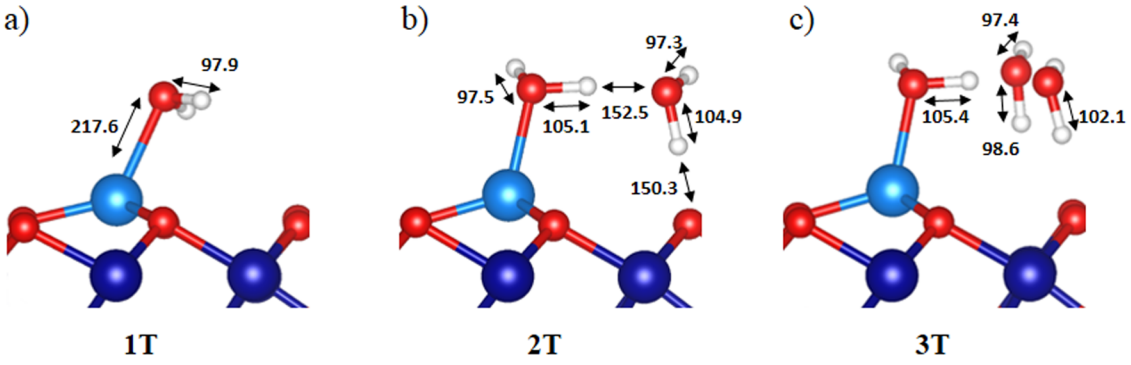


**Figure 4.** Structures optimized (bond distances in pm) using PBE+$U$(3.8) for one (a), two (b), and three (c) $H_2O$ molecules adsorbed at the $Fe_{tet1}$ terminated $Fe_3O_4(111)$ surface.

**Table 4. Adsorption Enthalpy, Entropy Contribution, as Well as Gibbs Free Energy in kJ/mol Obtained Using PBE +$U$(3.8)[a]**

| | $\Delta H$ | | $-T\Delta S$ | | $\Delta G$ | |
|---|---|---|---|---|---|---|
| structure | 100 K | 300 K | 100 K | 300 K | 100 K | 300 K |
| **1O** | −136.3 | −143.0 | 14.4 | 45.4 | −121.9 | −97.6 |
| **2O** | −217.2 | −230.5 | 28.4 | 91.0 | −188.8 | −139.5 |
| **3O** | −251.9 | −271.9 | 42.6 | 135.4 | −209.3 | −136.5 |
| **1T** | −52.7 | −59.4 | 13.8 | 34.8 | −38.9 | −24.6 |
| **2T** | −133.1 | −146.5 | 29.0 | 87.0 | −104.1 | −59.5 |
| **3T** | −176.7 | −196.7 | 42.5 | 128.8 | −134.2 | −67.9 |

[a]The reference (cf. Figure 5) refers to the clean $Fe_{oct2}$ terminated surface ($p^\circ \equiv 1$ bar).

$Fe_{oct2}$ terminated surface is used as the standard or reference. This approximation is considered to be reasonable, because of the very similar surface energies of these two surfaces (cf. Table 2).

Water adsorption occurs spontaneously regardless of the specific termination. Note that at low temperatures, water adsorption is "enthalpy driven". Specifically, **3O** is the most stable species according to $\Delta G$. At 300 K, both, enthalpy as well as entropy effects matter. Importantly, due to the lower loss of entropy upon adsorption, small water aggregations are favored over larger ones.

Figure 5 shows the corresponding stability diagrams, that is, the Gibbs free reaction energies (cf. eq 1) for water adsorption on both surfaces obtained using PBE+$U$(3.8) and HSE+D, respectively. Qualitatively both DFT-based approaches suggest a similar picture. Adsorption of water on the $Fe_{oct2}$ terminated $Fe_3O_4(111)$ surface is always thermodynamically preferred over adsorption on the $Fe_{tet1}$ terminated surface. Additionally, according to both methods, the adsorption equilibrium sets in with **1O** and upon increasing the pressure, the equilibrium

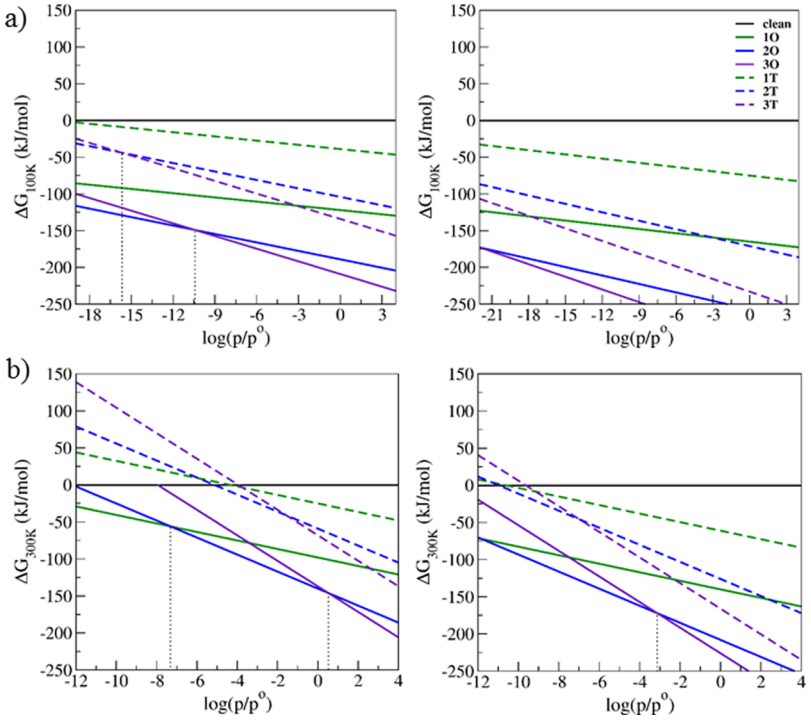


**Figure 5.** Stability diagrams at (a) 100 K and (b) 300 K obtained using PBE+$U$(3.8) (left) and HSE+D (right) as a function of the water vapor pressure. The reference of $\Delta G$ = 0 kJ/mol refers to the clean $Fe_{oct2}$ terminated surface ($p^\circ \equiv 1$ bar).



DOI: 10.1021/acs.jpcc.5b10560
J. Phys. Chem. C 2016, 120, 1056−1065

on the surface is pushed toward larger water clusters (**2O** and **3O**). Because of the more exothermic adsorption predicted by HSE+D (cf. Supporting Information), the transition pressure of, for example, **2O** → **3O**, is 3−4 orders of magnitude lower than the corresponding PBE+$U$(3.8) result.

**3.5. Coverage Effects.** A $p(2 \times 2)$ supercell was created for test purposes to check coverage effects. Two water molecules were adsorbed on that supercell. As shown in Table 5, the properties of the clean $Fe_{oct2}$ and $Fe_{tet1}$ terminated surfaces do not change upon creation of the supercell, as it should be. For instance, both supercells have virtually identical surface energies and magnetic moments per $Fe_3O_4$ formula unit.

**Table 5. Comparison of Properties of the $p(1 \times 1)$ and $p(2 \times 2)$ Surface Unit Cells (PBE+$U$(3.8))**

| cell size | termination | total energy (eV) | surface energy ($J/m^2$) | mag. moment ($\mu_B$) |
|---|---|---|---|---|
| $p(1 \times 1)$ | $Fe_{oct2}$ | −187.776 | 1.176 | 18 |
| $p(2 \times 2)$ | $Fe_{oct2}$ | −751.114 | 1.175 | 72 = 4 × 18 |
| $p(1 \times 1)$ | $Fe_{tet1}$ | −188.027 | 1.112 | 20.5 |
| $p(2 \times 2)$ | $Fe_{tet1}$ | −752.119 | 1.111 | 82 = 4 × 20.5 |

For the adsorption of two water molecules on the supercell, two configurations are considered (cf. Figure 6), that is, (a) two individual and well separated molecules and (b) the water dimer. The corresponding adsorption energies ($E_{ads}$) are shown in Table 6.

Compared with **1O**, the adsorption energy of $\mathbf{O_a}$ amounts to slightly more than twice the value of **1O**. The difference is −33.1 kJ/mol (≅ 12% of 2 × $E_{ads}$(**1O**)), which is very likely due to coverage effects (adsorbate−adsorbate interactions). With regard to the formation of a dimer on the supercell ($\mathbf{O_b}$), the difference amounts to even less (−18.6 kJ/mol ≅ 8% of $E_{ads}$(**2O**)).

On the $Fe_{tet1}$ surface, the adsorption energy of two separate water molecules ($\mathbf{T_a}$) is only 10 kJ/mol more positive compared with twice the value of **1T** (−122.0 kJ/mol). Similarly, the difference between $\mathbf{T_b}$ and **2T** amounts to −33.8 kJ/mol. On the basis of that, the coverage effect is estimated to be ca. 10−20 kJ/mol per water molecule and is thus considered to be small.

**3.6. Vibrational Frequencies.** Figures 7 and 8 show calculated wavenumbers obtained using PBE+$U$(3.8) for **1O**−**3O** and **1T**−**3T**, respectively. Panel a in each figure gives the observed wavenumbers upon dosing $D_2O$ at the surface, that is, 2720 and 2695 $cm^{-1}$.[74]

**Table 6. PBE+U(3.8) Adsorption Energies**

| | $E_{ads}$ (kJ/mol) | | $E_{ads}$ (kJ/mol) |
|---|---|---|---|
| $\mathbf{O_a}$ | −313.1 | $\mathbf{T_a}$ | −111.5 |
| $\mathbf{O_b}$ | −246.7 | $\mathbf{T_b}$ | −181.3 |
| **1O** | −140.0 | **1T** | −61.0 |
| **2O** | −228.1 | **2T** | −147.5 |

Note that each adsorbed water molecule contributes two stretching modes. For water on the $Fe_{oct2}$ termination, corresponding modes can be divided into two groups: the modes of (i) terminal OH groups (OH1−OH3) and (ii) hydrogen bonds (HB1−HB3). This labeling is chosen in accordance with the problem discussed in ref 74. Naturally, in **1O** there are no hydrogen bonds created but in addition to the terminal OH a surface hydroxyl group (H−$O_s$) is formed. We emphasize that vibrations of the hydrogen bond network at the $Fe_{oct2}$ surface are rather localized, that is, individual modes can be assigned to certain atom pairs. The vibrations of the HB network on the $Fe_{tet1}$ terminated surface are qualitatively different. This has to do with a rather strong coupling of modes due to pronounced interactions between adsorbed water molecules. Therefore, we prefer to categorize these water related modes as "symmetric" and "asymmetric" modes, similarly to the molecule in gas phase.

**3.7. Effect on Vibrations upon Isotopic Labeling.** To facilitate assignment of vibrational modes, effects induced by isotopic labeling with $^{18}O$ are presented in Table 7.

## 4. DISCUSSION

Replacing $^{16}O$ by $^{18}O$ in the slab model employed, that is, the surface, leads to an isotopic shift in the surface hydroxyl group of **1O**, while by obvious reasons the terminal OH is not affected. This does not agree with observation.[74] Experimentally, the two bands are only shifted upon $^{18}O$ labeling of $D_2O$ (cf. Table 7). Whenever a mode involves a surface oxygen atom, the $^{18}O$ labeling of the surface will naturally lead to a shift. So, as a consequence, the interpretation of Al-Shamery and co-workers,[41] which involves a Brønsted basic surface oxygen atom, has to be questioned.

The wetting behavior of the $Fe_{tet1}$ terminated surface is completely different due to the molecular adsorption process.

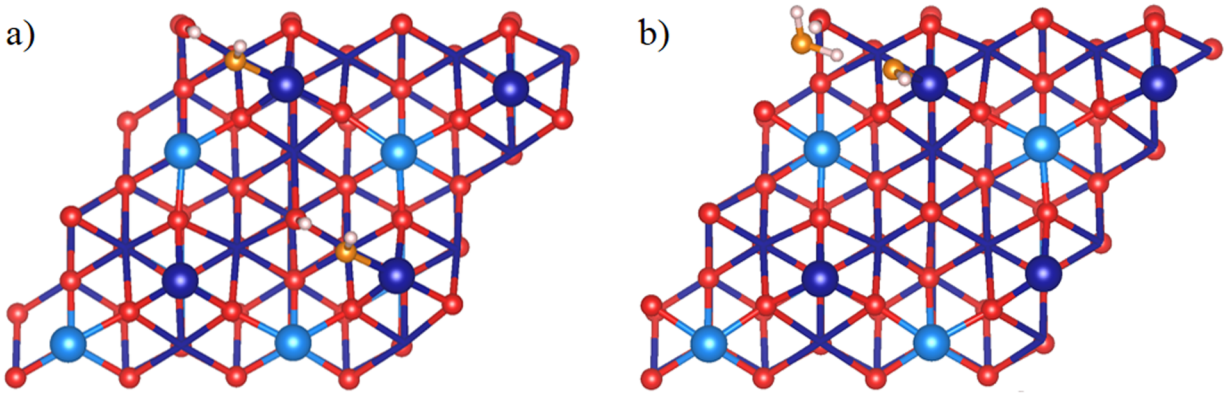


**Figure 6.** Adsorption of two water molecules on the $p(2 \times 2)$ $Fe_{oct2}$ terminated supercell. Panel a shows two individual molecules ($\mathbf{O_a}$) in diagonal configuration; panel b shows the water dimer ($\mathbf{O_b}$) on the supercell. The topmost layer (large dark blue spheres) consists of $Fe_{oct2}$ cations; large light blue spheres refer to the surface $Fe_{tet1}$ cations underneath; oxygen of water is orange.



DOI: 10.1021/acs.jpcc.5b10560
J. Phys. Chem. C 2016, 120, 1056−1065

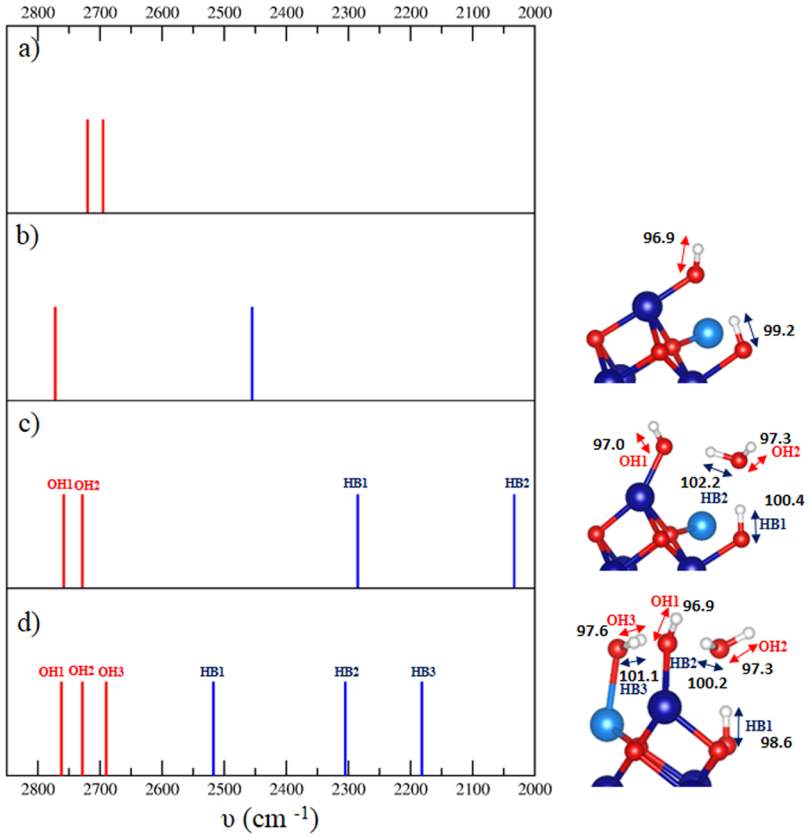


**Figure 7.** (a) Observed IR signals using $D_2O$ dosed on a $Fe_{oct2}$ terminated $Fe_3O_4(111)$ surface;[74] panels b–d represent respective stick spectra (term. OH in red; H-bonds in **2O** and **3O** in blue) for one, two, and three adsorbed $D_2O$ molecules. Corresponding structures (PBE+$U$(3.8)) show selected bond distances (pm). Blue and red arrows in **2O** and **3O** indicate vibrational modes related to H-bonds and terminal OH, respectively.

As a consequence, the water molecule remains intact and is adsorbed at a larger distance to the surface (cf. Figure 4). Therefore, the surface oxygen will be hardly involved. All the modes observed in the hydrated $Fe_{tet1}$ terminated surface can only be affected upon isotope exchange in the water.

GGA-type functionals slightly overestimate vibrational frequencies on average as, for example, shown in ref 75. Specifically, PBE frequencies are expected to be overestimated by approximately 1% according to scaling factors devised from quantum chemical calculations.[75] The small error in PBE frequencies is largely related to error compensation between the blue shift incurred by the harmonic approximation and the red shift due to the error incurred by the functional. Taking this into consideration, the wave numbers corresponding to the terminal OD stretching modes for **2O** (2758, 2728 $cm^{-1}$) **2T** (2725, 2710 $cm^{-1}$), and **3T** (2732, 2702 $cm^{-1}$) compare well with observed results (2720, 2695 $cm^{-1}$, cf. ref 74).

The thermodynamic stability of individual adsorption structures strongly supports water adsorption on the $Fe_{oct2}$ termination (cf. Figure 5). It is important to mention that the two IR signals were observed over a wide temperature range starting from 120 up to 300 K at moderate water vapor pressures.[74] However, according to Figure 5, **2T** and **3T** are not very stable species under these conditions. In a recent collaboration between experimentalists and theoreticians in the groups of Flytzani-Stephanopolous and Batista, the adsorption of water on the $Fe_3O_4(111)$ surface was studied by STM and DFT.[42] They accumulated evidence that molecularly adsorbed water on the $Fe_{tet1}$ terminated surface desorbs at temperatures higher than 245 K. Alternative to desorption, dissociation may set in. Therefore, additionally to the molecular water adsorption on the $Fe_{tet1}$ terminated $Fe_3O_4(111)$ surface, also dissociated adsorption complexes were studied in the present work. Dissociation on the $Fe_{tet1}$ termination has been previously discussed by Grillo et al.[43] Therefore, we created the dissociated water complexes, that is, monomer and dimer structures (cf. Figure 9). The dissociated water monomer is only 13.7 $kJ{\cdot}mol^{-1}$ more stable than the molecularly adsorbed water. The dissociated water dimer is 14.2 $kJ{\cdot}mol^{-1}$ more stable than the corresponding molecular adsorption complex featuring two intact water molecules. Note that most IR experiments focused on temperatures lower than or equal to 245 K.[74] Because of the observed isotopic shifts in both of the two reported IR signals in ref 74, it is obvious that the properties of the dissociated monomer (cf. Figure 9a) are inconsistent with observation. Concerning the dissociated dimer (cf. Figure 9b), IR properties of the molecular and dissociated complexes are very similar (cf. Figure 4b). However, the dimer on the $Fe_{oct2}$ termination (**2O**) is by 70 $kJ{\cdot}mol^{-1}$ more stable than the dissociated dimer on the $Fe_{tet1}$ termination.

Therefore, **2O** appears to be the most appropriate model to explain the two aforementioned signals, even though other adsorption structures such as **2T**, **3O**, and **3T** could potentially contribute upon increase of the coverage (cf. Figure 5). The energetically low lying modes of the hydrogen bonds (HB1, HB2; cf. Figure 7c) are difficult to detect experimentally, because of their very broad and indefinite absorption signature.



DOI: 10.1021/acs.jpcc.5b10560
J. Phys. Chem. C 2016, 120, 1056–1065

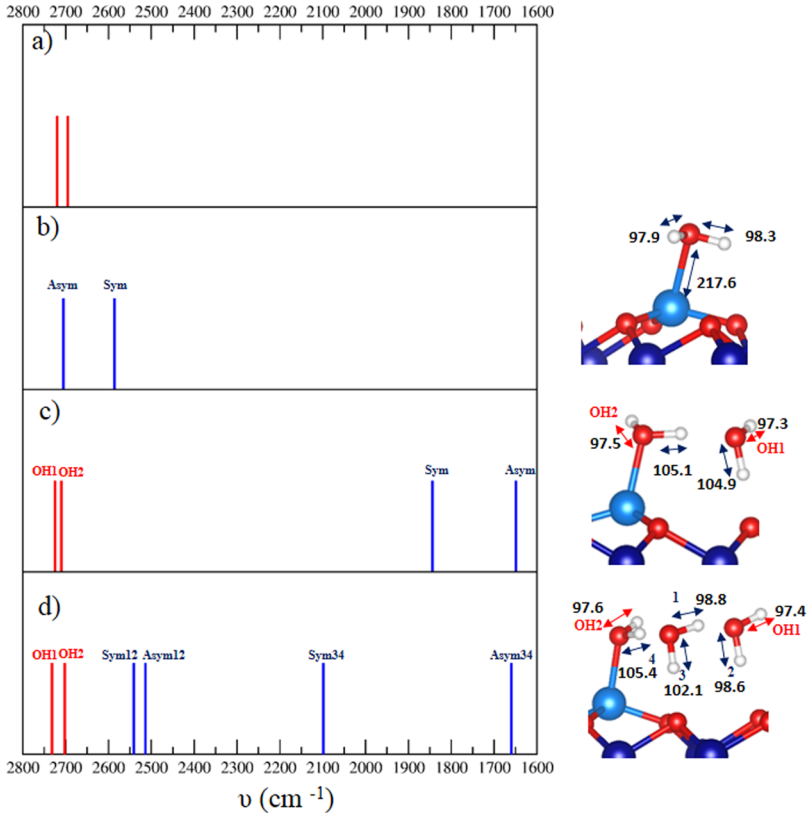


**Figure 8.** (a) Observed IR signals using $D_2O$ dosed on a $Fe_{tet1}$ terminated $Fe_3O_4(111)$ surface;[74] panels b–d represent stick spectra for **1T**, **2T**, and **3T**, respectively.

**Table 7. Isotopic Shifts $\Delta\upsilon$ (cm $^{-1}$)[a]**

| | | $r_{OH}$ | $\Delta\upsilon$ ($D_2{}^{18}O$) | $\Delta\upsilon$ ($Fe_3{}^{18}O_4$) |
|---|---|---|---|---|
| obsd.[b] | | | −18 | 0 |
| | | | −17 | 0 |
| **1O** | term. OH | 96.9 | −17 | 0 |
| | H–$O_s$ | 99.2 | 0 | −16 |
| **2O** | term. OH1 | 97.0 | −17 | 0 |
| | term. OH2 | 97.3 | −18 | 0 |
| | HB1 | | 0 | −15 |
| | HB2 | | −14 | 0 |
| **2T** | term. OH1 | 97.3 | −17 | 0 |
| | term. OH2 | 97.5 | −17 | 0 |
| | sym. | | −14 | 0 |
| | asym. | | −13 | 0 |

[a]Bond distances $r_{OH}$ (pm) of terminal OH groups in the **1O**, **2O**, and **2T** adsorption complexes are also presented. [b]Ref 74.

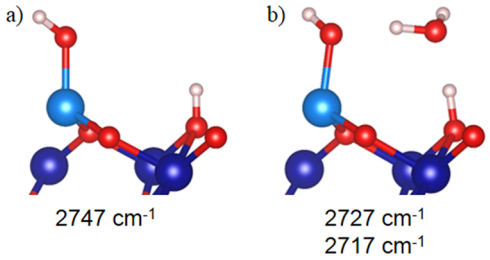


**Figure 9.** Dissociative adsorption of the water monomer (a) and dimer (b) on the $Fe_{tet1}$ terminated surface. The simulated IR wavenumbers of terminal OH stretching modes are shown below.

## 5. CONCLUSIONS

Using the PBE+$U$(3.8) approach, the adsorption of water on the $Fe_{oct2}$ terminated $Fe_3O_4(111)$ surface follows a dissociative pathway, while on the $Fe_{tet1}$ terminated surface, water adsorbs molecularly. This finding is robust upon inclusion of corrections to the adsorption energy obtained using the hybrid functional HSE. Upon $^{18}O$-labeling, observed IR signals can be unambiguously attributed to terminal OH groups of adwater rather than the newly formed surface OH group. Dimeric water clusters agree best with observation, however, results on the adsorption of water on $Fe_3O_4(111)$ favor the $Fe_{oct2}$ over the $Fe_{tet1}$ terminations.

## ■ ASSOCIATED CONTENT

### Supporting Information

The Supporting Information is available free of charge on the ACS Publications website at DOI: 10.1021/acs.jpcc.5b10560.

Murnaghan equation of state for $Fe_3O_4$; HSE+D adsorption energies; PBE+$U$(3.8), HSE+D total energies, as well as zero-point energies obtained using PBE +$U$(3.8). (PDF)

## ■ AUTHOR INFORMATION

### Corresponding Author

*E-mail joachim.paier@chemie.hu-berlin.de. Phone +(49)-30-2093-7139.

### Notes

The authors declare no competing financial interest.



DOI: 10.1021/acs.jpcc.5b10560
J. Phys. Chem. C 2016, 120, 1056–1065

## ■ ACKNOWLEDGMENTS

We wish to thank Professor Joachim Sauer and Professor Hajo Freund for their support and insightful discussions. This work has been supported by Deutsche Forschungsgemeinschaft within the Sonderforschungsbereich SFB 1109 and by grants for computing time at the high-performance computer center HLRN (North-German Supercomputing Alliance in Berlin and Hannover). We are grateful for financial support by the "Fonds der Chemischen Industrie (FCI)" as well as by the Stiftung Industrieforschung, Humboldt-Universität zu Berlin (Project number: S0234/10138/2014). Thomas Kropp and Christopher Penschke are gratefully acknowledged for many helpful discussions.

## ■ REFERENCES

(1) de Smit, E.; Weckhuysen, B. M. The renaissance of iron-based Fischer–Tropsch synthesis: on the multifaceted catalyst deactivation behaviour. *Chem. Soc. Rev.* **2008**, *37*, 2758–2781.
(2) Schüle, A.; Nieken, U.; Shekhah, O.; Ranke, W.; Schlögl, R.; Kolios, G. Styrene synthesis over iron oxide catalysts: from single crystal model system to real catalysts. *Phys. Chem. Chem. Phys.* **2007**, *9*, 3619–3634.
(3) Wang, J.-Z.; Zhong, C.; Wexler, D.; Idris, N. H.; Wang, Z.-X.; Chen, L.-Q.; Liu, H.-K. Graphene-encapsulated $Fe_3O_4$ nanoparticles with 3D laminated structure as superior anode in lithium ion batteries. *Chem. - Eur. J.* **2011**, *17*, 661–667.
(4) Thiel, P. A.; Madey, T. E. The interaction of water with solid-surfaces - fundamental-aspects. *Surf. Sci. Rep.* **1987**, *7*, 211–385.
(5) White, A. F.; Peterson, M. L.; Hochella, M. F. Electrochemistry and dissolution kinetics of magnetite and ilmenite. *Geochim. Cosmochim. Acta* **1994**, *58*, 1859–1875.
(6) Henderson, M. A. The interaction of water with solid surfaces: fundamental aspects revisited. *Surf. Sci. Rep.* **2002**, *46*, 1–308.
(7) Ketteler, G.; Weiss, W.; Ranke, W.; Schlögl, R. Bulk and surface phases of iron oxides in an oxygen and water atmosphere at low pressure. *Phys. Chem. Chem. Phys.* **2001**, *3*, 1114–1122.
(8) Muan, A. Phase equlibria at high temperatures in oxide systems involving changes in oxidation states. *Am. J. Sci.* **1958**, *256*, 171–207.
(9) Diebold, U. The surface science of titanium dioxide. *Surf. Sci. Rep.* **2003**, *48*, 53–229.
(10) Brookes, I. M.; Muryn, C. A.; Thornton, G. Imaging water dissociation on $TiO_2$(110). *Phys. Rev. Lett.* **2001**, *87*, 266103.
(11) Di Valentin, C.; Tilocca, A.; Selloni, A.; Beck, T. J.; Klust, A.; Batzill, M.; Losovyj, Y.; Diebold, U. Adsorption of water on reconstructed rutile $TiO_2$(011)-(2 × 1): Ti = O double bonds and surface reactivity. *J. Am. Chem. Soc.* **2005**, *127*, 9895–9903.
(12) Kimmel, G. A.; Baer, M.; Petrik, N. G.; VandeVondele, J.; Rousseau, R.; Mundy, C. J. Polarization- and azimuth-resolved infrared spectroscopy of water on $TiO_2$(110): Anisotropy and the hydrogen-bonding network. *J. Phys. Chem. Lett.* **2012**, *3*, 778–784.
(13) Meyer, B.; Marx, D.; Dulub, O.; Diebold, U.; Kunat, M.; Langenberg, D.; Wöll, C. Partial dissociation of water leads to stable superstructures on the surface of zinc oxide. *Angew. Chem., Int. Ed.* **2004**, *43*, 6642–6645; *Angew. Chem.* **2004**, *116*, 6809–6814.
(14) Noei, H.; Qiu, H.; Wang, Y.; Löffler, E.; Wöll, C.; Muhler, M. The identification of hydroxyl groups on ZnO nanoparticles by infrared spectroscopy. *Phys. Chem. Chem. Phys.* **2008**, *10*, 7092–7097.
(15) Verwey, E. J. W. Electronic conduction of magnetite ($Fe_3O_4$) and its transition point at low temperatures. *Nature* **1939**, *144*, 327–328.
(16) Finger, L. W.; Hazen, R. M.; Hofmeister, A. M. High-pressure crystal-chemistry of spinel ($MgAl_2O_4$) and magnetite ($Fe_3O_4$) - comparisons with silicate spinels. *Phys. Chem. Miner.* **1986**, *13*, 215–220.
(17) Okudera, H.; Kihara, K.; Matsumoto, T. Temperature dependence of structure parameters in natural magnetite: Single crystal x-ray studies from 126 to 773 K. *Acta Crystallogr., Sect. B: Struct. Sci.* **1996**, *52*, 450–457.
(18) Lennie, A. R.; Condon, N. G.; Leibsle, F. M.; Murray, P. W.; Thornton, G.; Vaughan, D. J. Structures of $Fe_3O_4$ (111) surfaces observed by scanning tunneling microscopy. *Phys. Rev. B: Condens. Matter Mater. Phys.* **1996**, *53*, 10244–10253.
(19) Yang, T.; Wen, X.-D.; Huo, C.-F.; Li, Y.-W.; Wang, J.; Jiao, H. Structure and energetics of hydrogen adsorption on $Fe_3O_4$(111). *J. Mol. Catal. A: Chem.* **2009**, *302*, 129–136.
(20) Ahdjoudj, J.; Martinsky, C.; Minot, C.; Van Hove, M. A.; Somorjai, G. A. Theoretical study of the termination of the $Fe_3O_4$ (111) surface. *Surf. Sci.* **1999**, *443*, 133–153.
(21) Tasker, P. W. Stability of ionic-crystal surfaces. *J. Phys. C: Solid State Phys.* **1979**, *12*, 4977–4984.
(22) Noguera, C. Polar oxide surfaces. *J. Phys.: Condens. Matter* **2000**, *12*, R367–R410.
(23) Goniakowski, J.; Finocchi, F.; Noguera, C. Polarity of oxide surfaces and nanostructures. *Rep. Prog. Phys.* **2008**, *71*, 016501.
(24) Santos-Carballal, D.; Roldan, A.; Grau-Crespo, R.; de Leeuw, N. H. A DFT study of the structures, stabilities and redox behaviour of the major surfaces of magnetite $Fe_3O_4$. *Phys. Chem. Chem. Phys.* **2014**, *16*, 21082–21097.
(25) Momma, K.; Izumi, F. VESTA 3 for three-dimensional visualization of crystal, volumetric and morphology data. *J. Appl. Crystallogr.* **2011**, *44*, 1272–1276.
(26) Shaikhutdinov, S. K.; Joseph, Y.; Kuhrs, C.; Ranke, W.; Weiss, W. Structure and reactivity of iron oxide surfaces. *Faraday Discuss.* **1999**, *114*, 363–380.
(27) Shaikhutdinov, S. K.; Ritter, M.; Wang, X. G.; Over, H.; Weiss, W. Defect structures on epitaxial $Fe_3O_4$(111) films. *Phys. Rev. B: Condens. Matter Mater. Phys.* **1999**, *60*, 11062–11069.
(28) Ritter, M.; Weiss, W. $Fe_3O_4$(111) surface structure determined by LEED crystallography. *Surf. Sci.* **1999**, *432*, 81–94.
(29) Weiss, W.; Ranke, W. Surface chemistry and catalysis on well-defined epitaxial iron-oxide layers. *Prog. Surf. Sci.* **2002**, *70*, 1–151.
(30) Weiss, W.; Barbieri, A.; Vanhove, M. A.; Somorjai, G. A. Surface-structure determination of an oxide film grown on a foreign substrate - $Fe_3O_4$ multilayer on Pt(111) identified by low-energy-electron diffraction. *Phys. Rev. Lett.* **1993**, *71*, 1848–1851.
(31) Barbieri, A.; Weiss, W.; Vanhove, M. A.; Somorjai, G. A. Magnetite $Fe_3O_4$(111) - surface-structure by LEED crystallography and energetics. *Surf. Sci.* **1994**, *302*, 259–279.
(32) Lemire, C.; Meyer, R.; Henrich, V. E.; Shaikhutdinov, S.; Freund, H. J. The surface structure of $Fe_3O_4$(111) films as studied by CO adsorption. *Surf. Sci.* **2004**, *572*, 103–114.
(33) Zhu, L.; Yao, K. L.; Liu, Z. L. First-principles study of the polar (111) surface of $Fe_3O_4$. *Phys. Rev. B: Condens. Matter Mater. Phys.* **2006**, *74*, 035409.
(34) Yu, X.; Huo, C.-F.; Li, Y.-W.; Wang, J.; Jiao, H. $Fe_3O_4$ surface electronic structures and stability from GGA+U. *Surf. Sci.* **2012**, *606*, 872–879.
(35) Noh, J.; Osman, O. I.; Aziz, S. G.; Winget, P.; Brédas, J.-L. Magnetite $Fe_3O_4$ (111) surfaces: Impact of defects on structure, stability, and electronic properties. *Chem. Mater.* **2015**, *27*, 5856–5867.
(36) Kiejna, A.; Ossowski, T.; Pabisiak, T. Surface properties of the clean and Au/Pd covered $Fe_3O_4$(111): DFT and DFT+U study. *Phys. Rev. B: Condens. Matter Mater. Phys.* **2012**, *85*, 125414.
(37) Kendelewicz, T.; Liu, P.; Doyle, C. S.; Brown, G. E.; Nelson, E. J.; Chambers, S. A. Reaction of water with the (100) and (111) surfaces of $Fe_3O_4$. *Surf. Sci.* **2000**, *453*, 32–46.
(38) Parkinson, G. S.; Novotny, Z.; Jacobson, P.; Schmid, M.; Diebold, U. Room temperature water splitting at the surface of magnetite. *J. Am. Chem. Soc.* **2011**, *133*, 12650–12655.
(39) Kendelewicz, T.; Kaya, S.; Newberg, J. T.; Bluhm, H.; Mulakaluri, N.; Moritz, W.; Scheffler, M.; Nilsson, A.; Pentcheva, R.; Brown, G. E., Jr. X-ray Photoemission and Density Functional Theory Study of the Interaction of Water Vapor with the $Fe_3O_4$(001) Surface at Near-Ambient Conditions. *J. Phys. Chem. C* **2013**, *117*, 2719–2733.


DOI: 10.1021/acs.jpcc.5b10560
J. Phys. Chem. C 2016, 120, 1056–1065

(40) Joseph, Y.; Ranke, W.; Weiss, W. Water on FeO(111) and $Fe_3O_4$(111): Adsorption behavior on different surface terminations. *J. Phys. Chem. B* **2000**, *104*, 3224−3236.
(41) Leist, U.; Ranke, W.; Al-Shamery, K. Water adsorption and growth of ice on epitaxial $Fe_3O_4$(111), FeO(111) and $Fe_2O_3$(biphase). *Phys. Chem. Chem. Phys.* **2003**, *5*, 2435−2441.
(42) Rim, K. T.; Eom, D.; Chan, S.-W.; Flytzani-Stephanopoulos, M.; Flynn, G. W.; Wen, X.-D.; Batista, E. R. Scanning tunneling microscopy and theoretical study of water adsorption on $Fe_3O_4$: Implications for catalysis. *J. Am. Chem. Soc.* **2012**, *134*, 18979−18985.
(43) Grillo, M. E.; Finnis, M. W.; Ranke, W. Surface structure and water adsorption on $Fe_3O_4$(111): Spin-density functional theory and on-site Coulomb interactions. *Phys. Rev. B: Condens. Matter Mater. Phys.* **2008**, *77*, 075407.
(44) Zhou, C.; Zhang, Q.; Chen, L.; Han, B.; Ni, G.; Wu, J.; Garg, D.; Cheng, H. Density functional theory study of water dissociative chemisorption on the $Fe_3O_4$(111) surface. *J. Phys. Chem. C* **2010**, *114*, 21405−21410.
(45) Blöchl, P. E. Projector augmented-wave method. *Phys. Rev. B: Condens. Matter Mater. Phys.* **1994**, *50*, 17953−17979.
(46) Kresse, G.; Joubert, D. From ultrasoft pseudopotentials to the projector augmented-wave method. *Phys. Rev. B: Condens. Matter Mater. Phys.* **1999**, *59*, 1758−1775.
(47) Kresse, G.; Furthmüller, J. Efficient iterative schemes for ab initio total-energy calculations using a plane-wave basis set. *Phys. Rev. B: Condens. Matter Mater. Phys.* **1996**, *54*, 11169−11186.
(48) Kresse, G.; Furthmüller, J. Efficiency of ab-initio total energy calculations for metals and semiconductors using a plane-wave basis set. *Comput. Mater. Sci.* **1996**, *6*, 15−50.
(49) Anisimov, V. I.; Zaanen, J.; Andersen, O. K. Band theory and Mott insulators - Hubbard-U instead of Stoner-I. *Phys. Rev. B: Condens. Matter Mater. Phys.* **1991**, *44*, 943−954.
(50) Liechtenstein, A. I.; Anisimov, V. I.; Zaanen, J. Density-functional theory and strong-interactions - orbital ordering in Mott-Hubbard insulators. *Phys. Rev. B: Condens. Matter Mater. Phys.* **1995**, *52*, R5467−R5470.
(51) (a) Perdew, J. P.; Burke, K.; Ernzerhof, M. Generalized gradient approximation made simple. *Phys. Rev. Lett.* **1996**, *77*, 3865−3868; (b) Perdew, J. P.; Burke, K.; Ernzerhof, M. Generalized gradient approximation made simple. *Phys. Rev. Lett.* **1997**, *78*, 1396−1396.
(52) Dudarev, S. L.; Botton, G. A.; Savrasov, S. Y.; Humphreys, C. J.; Sutton, A. P. Electron-energy-loss spectra and the structural stability of nickel oxide: An LSDA+U study. *Phys. Rev. B: Condens. Matter Mater. Phys.* **1998**, *57*, 1505−1509.
(53) Bengone, O.; Alouani, M.; Blöchl, P.; Hugel, J. Implementation of the projector augmented-wave LDA+U method: Application to the electronic structure of NiO. *Phys. Rev. B: Condens. Matter Mater. Phys.* **2000**, *62*, 16392−16401.
(54) Leonov, I.; Yaresko, A. N.; Antonov, V. N.; Korotin, M. A.; Anisimov, V. I. Charge and orbital order in $Fe_3O_4$. *Phys. Rev. Lett.* **2004**, *93*, 146404.
(55) Jeng, H. T.; Guo, G. Y.; Huang, D. J. Charge-orbital ordering and Verwey transition in magnetite. *Phys. Rev. Lett.* **2004**, *93*, 156403.
(56) Yu, X.; Li, Y.; Li, Y.-W.; Wang, J.; Jiao, H. DFT+U study of molecular and dissociative water adsorptions on the $Fe_3O_4$(110) surface. *J. Phys. Chem. C* **2013**, *117*, 7648−7655.
(57) Aragon, R. Magnetization and exchange in nonstoichiometric magnetite. *Phys. Rev. B: Condens. Matter Mater. Phys.* **1992**, *46*, 5328−5333.
(58) Murnaghan, F. D. The compressibility of media under extreme pressures. *Proc. Natl. Acad. Sci. U. S. A.* **1944**, *30*, 244−247.
(59) Roldan, A.; Santos-Carballal, D.; de Leeuw, N. H. A comparative DFT study of the mechanical and electronic properties of greigite $Fe_3S_4$ and magnetite $Fe_3O_4$. *J. Chem. Phys.* **2013**, *138*, 204712.
(60) Csonka, G. I.; Perdew, J. P.; Ruzsinszky, A.; Philipsen, P. H. T.; Lebegue, S.; Paier, J.; Vydrov, O. A.; Ángyán, J. G. Assessing the performance of recent density functionals for bulk solids. *Phys. Rev. B: Condens. Matter Mater. Phys.* **2009**, *79*, 155107.
(61) Da Silva, J. L. F.; Ganduglia-Pirovano, M. V.; Sauer, J.; Bayer, V.; Kresse, G. Hybrid functionals applied to rare-earth oxides: The example of ceria. *Phys. Rev. B: Condens. Matter Mater. Phys.* **2007**, *75*, 045121.
(62) Monkhorst, H. J.; Pack, J. D. Special points for Brillouin-zone integrations. *Phys. Rev. B* **1976**, *13*, 5188−5192.
(63) Heyd, J.; Scuseria, G. E.; Ernzerhof, M. Hybrid functionals based on a screened Coulomb potential. *J. Chem. Phys.* **2003**, *118*, 8207−8215.
(64) Adamo, C.; Barone, V. Toward reliable density functional methods without adjustable parameters: The PBE0 model. *J. Chem. Phys.* **1999**, *110*, 6158−6170.
(65) Pan, Y.; Nilius, N.; Freund, H.-J.; Paier, J.; Penschke, C.; Sauer, J. Titration of $Ce^{3+}$ ions in the $CeO_2$(111) surface by Au adatoms. *Phys. Rev. Lett.* **2013**, *111*, 206101.
(66) Kropp, T.; Paier, J. Reactions of methanol with pristine and defective ceria (111) surfaces: A comparison of density functionals. *J. Phys. Chem. C* **2014**, *118*, 23690−23700.
(67) Kropp, T.; Paier, J.; Sauer, J. Support effect in oxide catalysis: Methanol oxidation on vanadia/ceria. *J. Am. Chem. Soc.* **2014**, *136*, 14616−14625.
(68) Grimme, S. Semiempirical GGA-type density functional constructed with a long-range dispersion correction. *J. Comput. Chem.* **2006**, *27*, 1787−1799.
(69) Kerber, T.; Sierka, M.; Sauer, J. Application of semiempirical long-range dispersion corrections to periodic systems in density functional theory. *J. Comput. Chem.* **2008**, *29*, 2088−2097.
(70) Burns, L. A.; Vazquez-Mayagoitia, A.; Sumpter, B. G.; Sherrill, C. D. Density-functional approaches to noncovalent interactions: A comparison of dispersion corrections (DFT-D), exchange-hole dipole moment (XDM) theory, and specialized functionals. *J. Chem. Phys.* **2011**, *134*, 084107.
(71) Makov, G.; Payne, M. C. Periodic boundary-conditions in ab-initio calculations. *Phys. Rev. B: Condens. Matter Mater. Phys.* **1995**, *51*, 4014−4022.
(72) Reuter, K.; Scheffler, M. Composition, structure, and stability of $RuO_2$(110) as a function of oxygen pressure. *Phys. Rev. B: Condens. Matter Mater. Phys.* **2001**, *65*, 035406.
(73) Piccini, G.; Sauer, J. Quantum chemical free energies: Structure optimization and vibrational frequencies in normal modes. *J. Chem. Theory Comput.* **2013**, *9*, 5038−5045.
(74) Dementyev, P.; Dostert, K.-H.; Ivars-Barceló, F.; O'Brien, C. P.; Mirabella, F.; Schauermann, S.; Li, X.; Paier, J.; Sauer, J.; Freund, H.-J. Water interaction with iron oxides. *Angew. Chem.* **2015**, *127*, 14148−14152.
(75) Alecu, I. M.; Zheng, J. J.; Zhao, Y.; Truhlar, D. G. Computational thermochemistry: Scale factor databases and scale factors for vibrational frequencies obtained from electronic model chemistries. *J. Chem. Theory Comput.* **2010**, *6*, 2872−2887.


DOI: 10.1021/acs.jpcc.5b10560
*J. Phys. Chem. C* 2016, 120, 1056−1065

# P13

https://pubs.acs.org/doi/abs/10.1021/acs.jpcb.7b04228

THE JOURNAL OF PHYSICAL CHEMISTRY B

Article

pubs.acs.org/JPCB

# Surface Termination of $Fe_3O_4(111)$ Films Studied by CO Adsorption Revisited

X. Li,[†] J. Paier,*[,†] J. Sauer,[†] F. Mirabella,[‡] E. Zaki,[‡] F. Ivars-Barceló,[‡] S. Shaikhutdinov,*[,‡] and H.-J. Freund[‡]

[†]Institut für Chemie, Humboldt-Universität zu Berlin, 10099 Berlin, Germany

[‡]Fritz-Haber-Institute, Max Planck Society, Faradayweg 4-6, 14195 Berlin, Germany

Supporting Information

**ABSTRACT:** Although the (111) surface of $Fe_3O_4$ (magnetite) has been investigated for more than 20 years, substantial controversy remains in the literature regarding the surface termination proposed based on structural and adsorption studies. The present article provides density functional theory results that allow to rationalize experimental results of infrared reflection−absorption spectroscopy and temperature-programmed desorption studies on CO adsorption, thus leading to a unified picture in which the $Fe_3O_4(111)$ surface is terminated by a $^1/_4$ monolayer of tetrahedrally coordinated $Fe^{3+}$ ions on top of a close-packed oxygen layer as previously determined by low energy electron diffraction. However, surface defects play a crucial role in adsorption properties and may dominate chemical reactions on $Fe_3O_4(111)$ when exposed to the ambient.

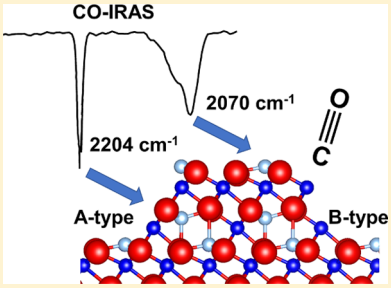


## INTRODUCTION

Due to their enormous importance in geology, physics, and chemistry, iron oxides in various compositions and structures and their surfaces, especially in contact with the environment, have been intensively studied.[1] Characterization of $Fe_3O_4$ (magnetite) surfaces, addressed in the present work, has come a long way. An excellent comprehensive review about the surface structures of iron oxides, following a much earlier one,[2] has recently been published.[3] This review considers the surface structure of the clean $Fe_3O_4(001)$ surface as solved. The situation is less clear for the $Fe_3O_4(111)$ surface. Low energy electron diffraction (LEED) studies, performed on $Fe_3O_4(111)$ thin films grown on Pt(111) and combined with scanning tunneling microscopy (STM) results, suggested a termination with a $^1/_4$ monolayer of (in the bulk) tetrahedrally coordinated $Fe^{3+}$ ions over a close−packed oxygen layer ($Fe_{tet1}$; for nomenclature see Figure 1).[4,5] This surface structure may be obtained by cutting along the $Fe_{tet1}$ layer in the magnetite (inverse spinel) structure with surface Fe ions strongly relaxed inward. A recent LEED I/V study[6] reinforced this conclusion by providing a very reasonable reliability (Pendry R-) factor of ~0.1, and must be taken as strong evidence of a proper and hence solved surface structure. Also, the surface stability diagram based on density functional theory (DFT) calculations suggests the $Fe_{tet1}$-terminated surface to be most stable at experimentally relevant pressures and temperatures.[7−11] On the contrary, an adsorption study[12] using CO as a probe molecule as well as a very recent study on water interaction with $Fe_3O_4(111)$[13] were both rationalized in terms of a surface terminated by octahedrally coordinated iron ions ($Fe_{oct2}$; see Figure 1) in the outermost layer.

Apparently, there is disagreement between surface structures derived from LEED and DFT studies on one hand and adsorption studies on the other. In the present work, we critically analyze the origin of this controversy and report DFT

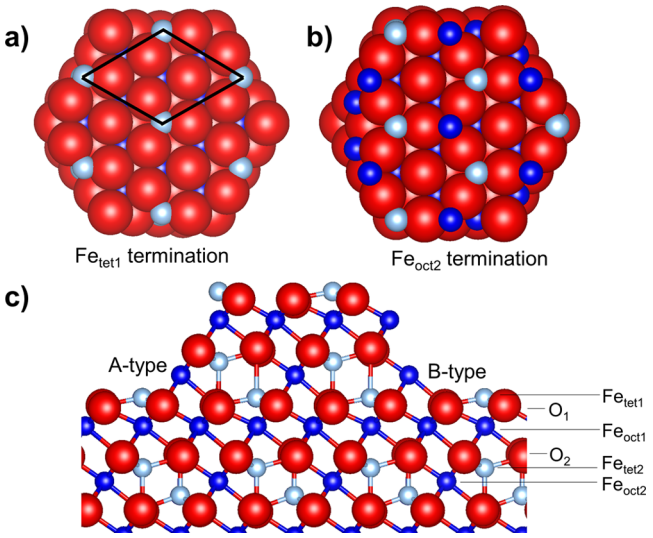


**Figure 1.** Top views on the $Fe_{tet1}$ (a) and $Fe_{oct2}$ (b) terminated $Fe_3O_4(111)$ surface. Cross-view on a stepped $Fe_3O_4(111)$ surface (c) showing the two step types A and B. Regular stacking sequence along [111] of atomic layers are shown on the right-hand side. Tetrahedrally coordinated $Fe^{3+}$ ions are light blue, octahedrally coordinated $Fe^{2+}$ ions are dark blue, and oxygen is red.

**Special Issue:** Miquel B. Salmeron Festschrift

**Received:** May 4, 2017
**Revised:** June 14, 2017
**Published:** June 16, 2017





DOI: 10.1021/acs.jpcb.7b04228
J. Phys. Chem. B 2018, 122, 527−533

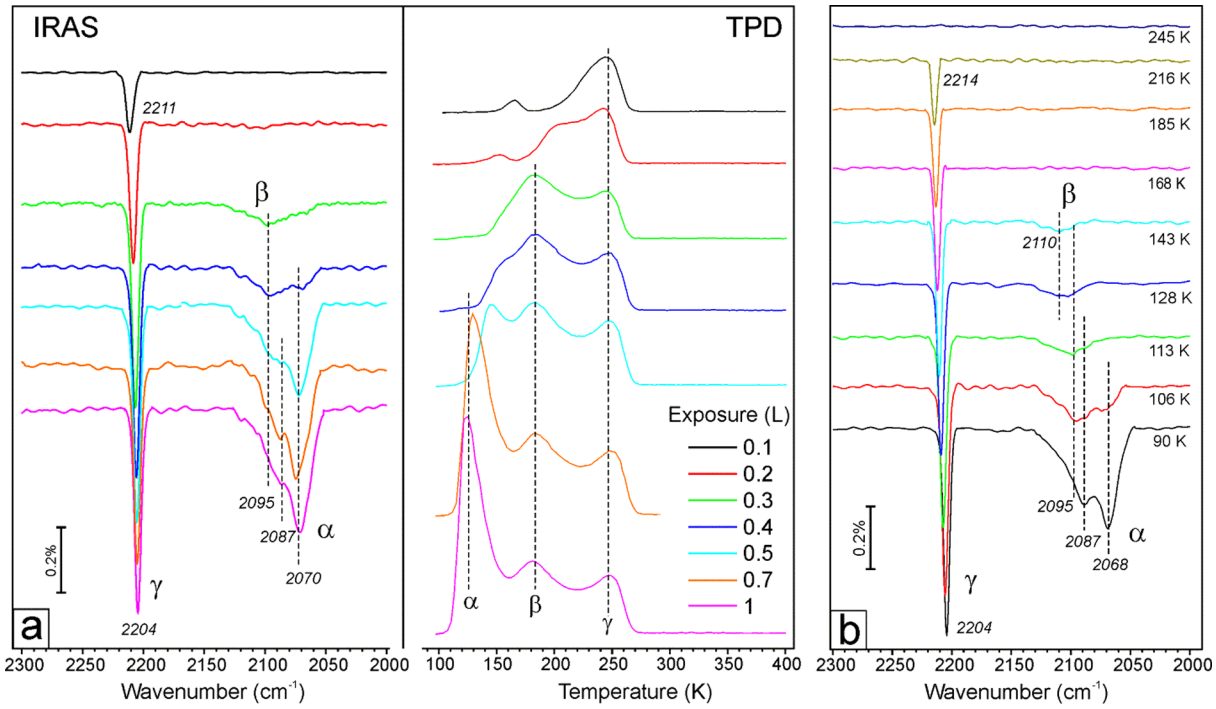


**Figure 2.** (a) Consecutive IRAS and TPD spectra (cut at 400 K) measured upon stepwise increasing CO dosage at 90 K on $Fe_3O_4(111)$ films (see text). (b) IRAS spectra of 1 L CO at 90 K and after thermal flash to the temperatures as indicated. The film was prepared by oxidation at 1000 K and flashed to 800 K in UHV prior to CO adsorption. The spectra are offset for clarity.

results, which allow us to provide a unified picture of the surface termination of $Fe_3O_4(111)$, in which the surface exposes a 1/4 monolayer of tetrahedrally coordinated $Fe^{3+}$ ions over a close-packed oxygen layer as previously determined by LEED.

## METHODS AND MATERIALS

**Experimental Details.** The experiments were carried out in several ultrahigh vacuum (UHV) chambers with a background pressure below $5 \times 10^{-10}$ mbar. All setups were equipped with standard facilities necessary to grow well-ordered thin magnetite films on clean Pt substrates. The quality of the films was checked by LEED which revealed sharp diffraction spots with low background intensity, and no other elements except Fe and O were observed in the Auger electron spectra (AES, both from Specs). The adsorption studies were performed via temperature-programmed desorption (TPD) using a differentially pumped quadrupole mass spectrometer (QMS, from Hiden) having a gold-plated cone shield to minimize signals from the heating stage. Vibrational spectra were measured by infrared reflection absorption spectroscopy (IRAS, Bruker 66 ivs). In one chamber, CO was dosed via calibrated molecular beam. In other setups, CO was dosed by backfilling the chamber. CO exposures are given in Langmuir (1 L = $10^{-6}$ Torr × sec). STM studies were performed in another UHV chamber equipped with LEED, AES, and a scanning tunneling microscope (from Omicron) operated at room temperature.

The $Fe_3O_4(111)$ films, with a thickness of about 5 nm, were grown on Pt(111) following a well-documented recipe[4−6,12] and will be discussed in detail in the text. Although the precise preparation parameters (Fe flux, oxidation temperature, time, and oxygen pressure) used in each setup may slightly differ, all oxide films exhibited a high degree of order as judged by LEED. In addition, the samples prepared in different chambers showed similar TPD spectra of CO allowing for cross-correlation of the results obtained by different techniques.

Preparation of the $Fe_3O_4(001)$ films on Pt(001) is described elsewhere.[14] The films show sharp LEED patterns of the $Fe_3O_4(001)$-$(\sqrt{2} \times \sqrt{2})R45°$ reconstructed surface and exhibit the same surface morphology as reported for a single crystal.[3]

TPD spectra were measured with a heating rate of 3 K/sec. IRA spectra were measured at grazing angle 8° with the resolution of 4 $cm^{-1}$. Note that the cooling time to reach the base temperature of 90 K is at least 5 min. STM images were recorded with commercial Pt−Ir tips (L.O.T. Oriel).

**Computational Details.** The details of DFT calculations are amply discussed in ref 11. In this section, we only report the most important points to be self-contained. DFT results were obtained using periodic slab models preserving the $Fe_3O_4$ composition. Primitive (1 × 1) surface unit cells were cut along the (111) crystallographic plane in the bulk. The equilibrium bulk lattice constant is determined by virtue of fitting a series of single points to the equation of state after Murnaghan.[15] It is 850.8 pm for the bulk and conveys to a surface unit cell vector length of 601.6 pm. Since this work compares two distinct surface terminations, we emphasize that respective slab models use identical compositions ($Fe_{12}O_{16}$), i.e., 12 atomic layers with the single metal ($Fe_{tet1}$; see Figure 1) termination as the topmost layer and the double metal ($Fe_{oct2}$; see Figure 1) termination as the bottommost layer (and *vice versa*). We use so-called asymmetric models constraining the atomic coordinates of the four bottommost layers to the bulk values during structure optimizations. Electronic structure calculations employ the so-called DFT+U[16] approach using an effective U value applied to the Fe 3d orbitals of 3.8 eV[9,17] together with the Perdew, Burke, and Ernzerhof (PBE)[18] exchange-correlation functional. We use the VASP[19,20] code


DOI: 10.1021/acs.jpcb.7b04228
J. Phys. Chem. B 2018, 122, 527−533

benefiting from the efficient projector-augmented wave method[21,22] to describe the electron−ion interaction on a full-potential level. The cutoff for the plane-wave basis set is 800 eV and Brillouin zones of surface unit cells are sampled for integration by a (5 × 5 × 1) Γ-centered Monkhorst−Pack[23] *k*-point mesh. To calculate vibrational frequencies of adsorbed CO molecules, we employ normal-mode analysis calculating the mass-weighted (partial) Hessian as the first derivative of atomic gradients with respect to their Cartesian components using central differences and a step size of 1.5 pm. Errors in wavenumbers incurred by the harmonic as well as the density functional approximation have been taken care of by scaling the wavenumber of $\nu$(CO) in the free molecule (calc. 2123 $cm^{-1}$) with respect to the experimental value (2143 $cm^{-1}$).[24]

## RESULTS AND DISCUSSION

**Experimental Results.** Results of CO adsorption on $Fe_3O_4$(111), obtained by TPD and IRAS, are shown in Figure 2. CO was first dosed at 90 K to a certain coverage monitored by IRAS, and the TPD spectrum was then recorded upon heating to 600 K. This was repeated several times while stepwise increasing the coverage up to the saturation limit. Clearly CO molecules chemisorb in, at least, three distinct states, referred to as $\alpha$, $\beta$, and $\gamma$ (see ref 12). (Due to additional adsorption from residual gas during the time it takes to place the sample in front of the QMS, TPD spectra may correspond to a slightly higher CO coverage than measured in IRAS experiments.) To further correlate the desorption peaks and the IRA bands, the IRA spectra were recorded at 90 K after thermal flash to the specified temperature (Figure 2b). Both sets of experiments clearly show that the $\gamma$ desorption state at ∼240 K is associated with CO molecules showing a sharp band at 2204 $cm^{-1}$. Accordingly, the $\beta$ state at ∼180 K correlates with a broad band in the 2110−2095 $cm^{-1}$ region, which remains after desorption of the weakest bonded CO in the $\alpha$ state. The band position at the highest coverage and hence corresponding to the $\alpha$ desorption state is very sensitive to the adsorption temperature and shifts from ∼2090 $cm^{-1}$ observed at 105 K to ∼2070 $cm^{-1}$ when adsorbed at 90 K. Note that this assignment of the $\alpha$ state differs from the previously reported one,[12] where it has been associated with a very weak band at 2141 $cm^{-1}$, i.e., very close to CO in the gas phase (2143 $cm^{-1}$). Note also that the intensity of the $\beta$ signal relative to $\gamma$ is considerably smaller than previously reported.[12] In fact, the intensities of both $\beta$ and $\gamma$ signals vary from sample to sample (see also Figures 2 and 6 in ref 12), although all films showed sharp LEED patterns.

To quantify the CO coverage in our films, we made use of CO TPD spectra obtained for the clean Pt(111) surface measured prior to film growth. The spectra (see Figure 3) suggest about 0.25 monolayer (ML) for the CO coverage in total for the $\beta$ and $\gamma$ states. (1 ML is defined as 3.2 × $10^{14}$ atoms $cm^{-2}$, i.e., one atom per $Fe_3O_4$(111) unit cell). Obviously, this coverage cannot account for the regular surface and, therefore, must be assigned to defect sites. In addition, the $\beta$ and $\gamma$ states are often missing in the spectra for "as prepared" films and only appear if the sample is flashed to high temperatures prior to CO adsorption. Tentatively, this effect is attributed to adsorption of water, which is always present in the UHV background, that prevents CO adsorption in the $\gamma$ state, as illustrated in Figure S1 (ESI).

For comparison, Figure 4 depicts a CO TPD spectrum obtained with the same setup on the clean ($\sqrt{2} \times \sqrt{2}$)R45°-reconstructed surface of a $Fe_3O_4$(001) film grown on Pt(001).

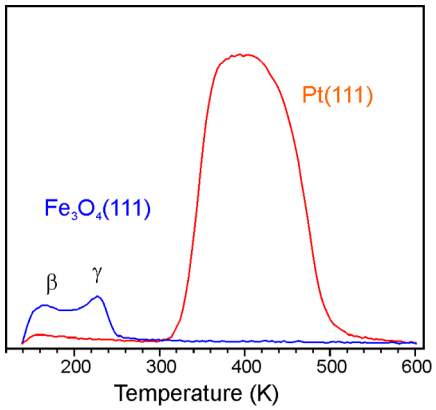


**Figure 3.** Comparison of TPD spectra of 1 L CO adsorbed on $Fe_3O_4$(111) film and clean Pt(111) at 140 K measured with the same setup. CO adsorption on Pt(111) results in the c(4 × 2)-CO structure at CO density of 7.4 × $10^{14}$ $cm^{-2}$. Using this value for calibration, the integral area of $\beta$ and $\gamma$ signals corresponds to 8 × $10^{13}$ $cm^{-2}$, thus resulting in ∼0.25 ML CO coverage (1 ML= 3.2 × $10^{14}$ $cm^{-2}$).

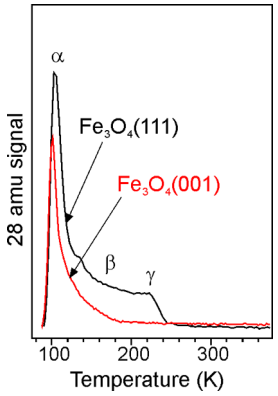


**Figure 4.** TPD spectra of 1 L CO adsorbed on $Fe_3O_4$(111) and $Fe_3O_4$(001) films at 90 K. The (111) film was prepared by oxidation at 940 K.

This surface does not show any signature of strongly adsorbed CO. Apparently, the $\alpha$ state at around 100 K on both (111) and (001) surfaces is associated with the "tail" of CO desorption having a maximum at a considerably lower temperature, as was, indeed, observed in TPD experiments on a $Fe_3O_4$(001) single crystal.

Importantly, LEED and STM studies of the $Fe_3O_4$(001)-($\sqrt{2} \times \sqrt{2}$)R45° surface both as thin films and single crystals revealed a uniform and atomically flat surface with a low amount of defects.[3,14] Taking into account the relatively low intensities of the $\beta$ and $\gamma$ desorption states only present on the (111) surface, which, in turn, depend on film preparation (see also ref 25) and vacuum conditions, it seems most likely that those are associated with surface imperfections, which are hard to control and quantify by conventional LEED usually employed to judge on the quality of the prepared films or single crystals.

Therefore, it is important to know the surface morphology of the prepared films (e.g., by STM) to link the CO adsorption results and the surface termination. Before we address STM results, it is instructive to look at the $Fe_3O_4$(111) film preparation in more detail. The first step includes the formation of an FeO(111) monolayer film on the clean Pt(111) surface.[2] This step is easy to control by LEED and CO titration of Pt,


DOI: 10.1021/acs.jpcb.7b04228
J. Phys. Chem. B 2018, 122, 527−533

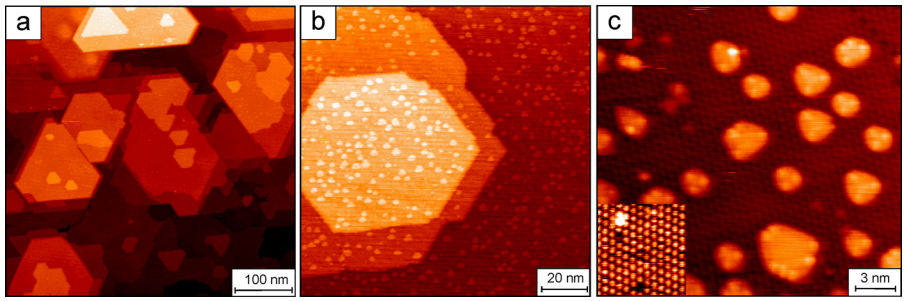


**Figure 5.** (a) STM image showing typical large-scale morphology of the $Fe_3O_4(111)$ films. When prepared by oxidation at ~1000 K, the films exhibit additional islands about 2.5 Å in height randomly distributed across the surface as shown in (b,c). The sample imaged in (c) was flashed to 800 K in UHV prior to imaging. The lattice of protrusions with a 6 Å periodicity is observed on the clean surface (see inset), which may additionally show adsorbate species (as bright protrusions) and vacancies (as missing protrusions). Tunneling conditions are sample bias +1.4 V, tunneling current 0.7 nA.

which is also used for calibration of the Fe deposition flux. The next step involves several (3−5) cycles of Fe deposition in amounts equivalent to 5−10 monolayers of FeO(111) onto a substrate kept at room temperature or below (down to 100 K), followed by oxidation in $5 \times 10^{-7}$ - $2 \times 10^{-6}$ mbar of $O_2$ at 870−950 K for 5−10 min. In the final step, the films are oxidized at a slightly higher temperature, e.g., 930−1020 K, for ca. 5 min. The final parameter to mention is the temperature, at which oxygen is pumped out, which is usually about 500 K, but may also be close to the oxidation temperature. Thus, there is a certain diversity in the film preparation which may, however, affect the adsorption results. In principle, this holds true for single crystal surfaces as well, see refs 26 and 27.

STM studies show that all well-ordered films exhibit wide hexagonally- or trigonally shaped terraces separated by monatomic steps or step bunches (see Figure 5a,b). STM images also revealed that oxidation at relatively high temperatures (~1000 K) and oxygen pumping out at 500 K, results in additional formation of small atomically flat islands (see Figure 5b,c). Once formed, these islands could not be removed by reoxidation at lower temperatures. Their formation is suppressed, however, if oxygen is pumped out simultaneously with sample cooling after high temperature oxidation at ~1000 K, or if the final oxidation is performed at relatively low temperatures (below 950 K). These islands, primarily of a trigonal shape, are all ~2.5 Å in height, that is about half of the distance between the equivalent layers in $Fe_3O_4(111)$ (= 4.6 Å), and must therefore expose a surface termination other than that of the surrounding terrace. The top facets showed no atomic corrugation, thus favoring its assignment to a surface which is terminated by the close-packed oxygen layer (i.e, $O_2$ layer; see Figure 1c). Origin and driving force for the island formation are not well understood, and it seems hardly possible to judge on their presence or absence without STM inspection.

STM images of the adsorbate-free $Fe_3O_4(111)$ surface, which can only be obtained after thermal flash to 800 K (as for TPD/IRAS studies), showed a lattice of protrusions with 6 Å periodicity, i.e., one protrusion per unit cell, independent of bias polarity. Based on previous DFT calculations and image simulations,[5,9] this picture corresponds to the single metal terminated surface, with the $Fe_{tet1}$ ions being imaged as protrusions. For the double metal terminated surface, i.e., exposing the $Fe_{oct2}$−$Fe_{tet1}$ layers, empty state STM images show one protrusion per unit cell, whereas filled state STM images show a honeycomb-like structure with two protrusions per unit cell, as observed on the $Fe_3O_4(111)$ single crystal surfaces after certain preparation treatments.[26,28] Such images were never observed in our films at any tunneling conditions, thus suggesting that our films are $Fe_{tet1}$-terminated.

**Computational Results.** According to DFT results published on thermodynamic stabilities of the various bulk terminations of $Fe_3O_4(111)$,[7,8] there is broad consensus (see ref 8 and references therein) that under reducing conditions the $Fe_{tet1}$ and $Fe_{oct2}$ terminations (see Figure 1c) are most stable, the first one distinctly more stable than the second one. The optimized structures **1** and **2** obtained for adsorption of CO on both surface terminations are displayed in Figure 6. Structure **2** refers to CO adsorbed on the $Fe_{oct2}^{2+}$ ion, which is by 76.5 kJ/mol more stable than CO adsorbed on the $Fe_{tet1}^{3+}$ ion of the $Fe_{oct2}$ terminated surface. This is in qualitative agreement with

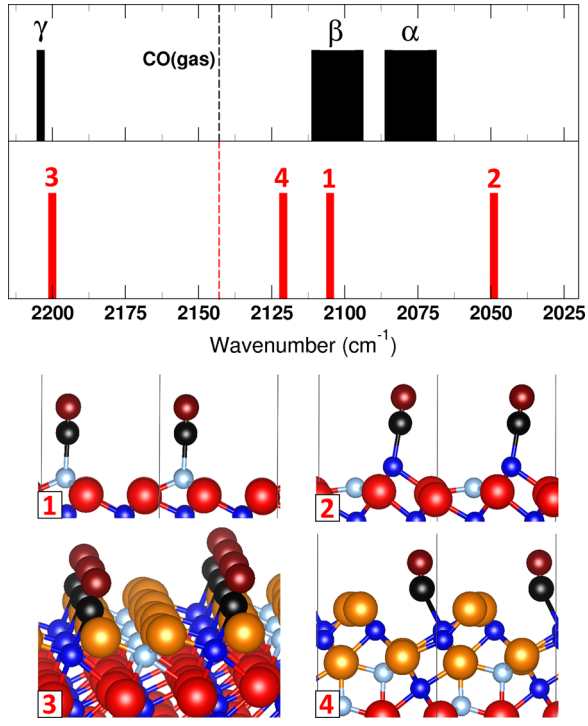


**Figure 6.** Comparison of experimentally observed and calculated $\nu$(CO) bands for corresponding structures (**1**−**4**) shown below the spectrum. The $Fe_{oct2}$ ions and $Fe_{tet1}$ ions are shown in dark and light blue, respectively. Lattice oxygen is red; oxygen in O-adlayers (structures **3** and **4**) is orange; carbon is black; oxygen in CO is dark red.



DOI: 10.1021/acs.jpcb.7b04228
J. Phys. Chem. B 2018, 122, 527−533

Table 1. Unscaled and Scaled CO Stretching Frequencies (in $cm^{-1}$) and Adsorption Energies (in kJ/mol)

| | | | $\nu$(CO) $cm^{-1}$ | | | |
|---|---|---|---|---|---|---|
| structure | termination | ads. site[a] | unscaled | scaled[b] | $E_{ads}$ kJ/mol | experiment |
| free CO | | | 2123 | 2143 | | |
| **1** | Tet1 | $Fe_{tet}^{3+}(4)$ | 2085 | 2105 | −44.0 | $\alpha$ |
| **2** | Oct2 | $Fe_{oct}^{2+}(4)$ | 2030 | 2049 | −102.6 | |
| **3** | Oct2 | $Fe_{oct}^{2+}(6)$ | 2180 | 2200 | −40.4 | $\gamma$ |
| **4** | Oct1 | $Fe_{oct}^{2+}(5)$ | 2101 | 2121 | −65.4 | $\beta$ |

[a]Coordination number including CO is given in parentheses. [b]Scaling factor 1.0094 is obtained for free CO to fit the experimental value, i.e. 2143 $cm^{-1}$.[24]

results reported in ref 29. Because one of the two iron ions binds CO so much stronger than the other, we only discuss structure **2** in the present work, i.e., CO adsorbed on the $Fe_{oct2}^{2+}$ ion. Table 1 presents corresponding vibrational frequencies of the CO stretching mode together with adsorption energies obtained for 1 ML CO coverage, i.e., one CO molecule per (1 × 1) unit cell. Structures **3** and **4** represent crude models of step edges (defect sites) of type A and B, respectively, as shown in Figure 1c.[12,30] Model **3** features an oxygen layer on top of the $Fe_{oct2}$ terminated surface and model **4** relates to the $Fe_{oct1}$ terminated $Fe_3O_4(111)$ surface. Both models are built starting from the 12-atomic layer slab described in the Computational Details Section. Note that additional O-layers in **3** and **4** are displayed in orange (see Figure 6).

The calculated and experimentally observed CO stretching frequencies are schematically shown for comparison in the top panel in Figure 6. The comparison allows us to draw several conclusions:

- First, the $\nu$(CO) frequency obtained for the double metal termination ($Fe_{oct2}^{2+}$, 2049 $cm^{-1}$, structure **2**) is considerably lower than any of the observed frequencies. The pronounced red shift with respect to free CO may be explained by substantial d-$\pi^*$ back-donation on the oxide surface.[31,32] In addition, adsorption on top of $Fe_{oct}^{2+}$ results in a strongly exothermic adsorption energy of −102.6 kJ/mol, in qualitative agreement with previous results reported in ref 29. In principle, such a strong CO binding would be consistent with the lower stability of the octahedrally terminated surface and the higher bond strength of CO to the $Fe_{oct2}$ termination as predicted by DFT, if one considers a bond-order conservation picture.[7] However, the calculated adsorption energy (which is the highest among the structures considered) results in a CO desorption temperature of around 400 K (using classical Redhead analysis with a prefactor of $10^{13}$ $s^{-1}$), which is, far outside the range of temperatures observed within the TPD spectra (see Figures 2 and S1). Therefore, the comparison provides strong evidence that the surface is not octahedrally but tetrahedrally terminated.
- The calculated frequency for structure **3** (2200 $cm^{-1}$) matches the $\gamma$ peak (2204 $cm^{-1}$) well. The observed blue shift with respect to the gas phase CO is explained by the repulsive interaction between the electron lone pair of the C atom and the surface $O^{2-}$ ions, also known as the "wall effect".[33] The geometric structure of step edges exposing such sites has previously been discussed using the criteria of charge neutrality and coordinative unsaturation.[30] DFT calculations, presented here, are consistent with this assignment. Moreover, the results clearly indicate that the blue-shifted $\nu$(CO) bands cannot be explained in terms of CO adsorbed on the "naked" protruding Fe ions either in +2 or +3 oxidation states as shown in Table 1. Instead, such bands are anticipated for Fe ions "embedded" into the O layer providing the appropriate environment for Pauli repulsion.
- The spectral region between 2110 and 2070 $cm^{-1}$ exhibits more complex features. In principle, the frequencies calculated for the $Fe_{tet1}$-terminated surface (2105 $cm^{-1}$, model **1**) and Fe-exposing step edge (2120 $cm^{-1}$, model **4**) both fall into the experimentally observed region. However, based on relative peak positions, we assign the $\beta$ state to CO adsorption on "Fe-rich" step edges (B-type, see Figure 1c). It is the $\alpha$ state that dominates the spectra at low temperatures (see Figure 2), which corresponds to the regular, $Fe_{tet1}$-terminated surface. The related band position is very sensitive to the adsorption temperature and may shift from 2090 $cm^{-1}$ observed at 100 K to 2070 $cm^{-1}$, when adsorbed at 90 K. This is an indication of a coverage effect. In addition, the $\alpha$ state is only populated at temperatures below the Verwey transition (~125 K), where charge ordering[34] may affect the vibrational frequencies.

## CONCLUSIONS

CO as a probe molecule on oxide surfaces is a useful tool to elucidate the complex surface morphology, but assignment to specific adsorption sites is impossible without theoretical calculations. The CO stretching vibrations are sensitive to the adsorption site's local atomic as well as electronic structures. Our DFT results combined with experimental data provide firm evidence that the regular $Fe_3O_4(111)$ surface is terminated by a 1/4 monolayer of $Fe_{tet1}$ ions over close-packed oxygen layer, in full agreement with previous LEED I/V results and thermodynamic stability of this surface predicted by DFT.

It therefore appears that the previously reported scheme for water adsorption[13] must be revisited. Although the proposed mechanism leading to a half-dissociated water dimer can still be operative, the existence of a clean double metal terminated surface in our films seems unlikely. Therefore, the water adsorption on the regular $Fe_3O_4(111)$ surface must be rationalized in terms of the surface terminated by $Fe_{tet1}$, albeit the role of defects, such as step edges, must be considered for the initial stages of water interaction. Surface defects may play a crucial role in adsorption properties and may dominate chemical reactions on $Fe_3O_4(111)$ when exposed to the ambient.



DOI: 10.1021/acs.jpcb.7b04228
J. Phys. Chem. B 2018, 122, 527−533

Finally, it is worth mentioning that a recent study on thin films of $Co_3O_4(111)$ reached the conclusion that the surface is terminated by a 1/4 monolayer of tetrahedrally coordinated $Co^{2+}$ ions.[35] It therefore appears that both $Fe_3O_4$ and $Co_3O_4$ sharing the spinel structure show a preference to grow in (111) orientation with a surface terminated by a single metal cation. However, all observed CO bands[36] (i.e., 2155−2175 $cm^{-1}$) are blue-shifted with respect to the gas phase, which in the case of magnetite would be only possible for the "O-rich" surfaces. In this case CO may adsorb on the metal cation and would repulsively interact with the surrounding oxygen (leading to a blue shift), as demonstrated for structure **3** (see Figure 6). Corresponding DFT calculations, which are expected to be even more demanding than for iron oxide, would probably shed light on this issue. We point out that the DFT results of the present work do not examine all possible defect structures, but serve, in our opinion, as a good benchmark for further studies.

## ■ ASSOCIATED CONTENT

### Supporting Information

The Supporting Information is available free of charge on the ACS Publications website at DOI: 10.1021/acs.jpcb.7b04228.

Effects of residual water on CO adsorption (PDF)

## ■ AUTHOR INFORMATION


### Corresponding Authors

*Phone: +(49)-30-2093-7139; E-mail: joachim.paier@chemie.hu-berlin.de.

*Phone: +(49)-30-8413-4114; E-mail: shaikhutdinov@fhi-berlin.mpg.de.

### ORCID

J. Sauer: 0000-0001-6798-6212

S. Shaikhutdinov: 0000-0001-9612-9949

H.-J. Freund: 0000-0001-5188-852X


### Notes

The authors declare no competing financial interest.

## ■ ACKNOWLEDGMENTS

We thank Céline Lemire for helpful discussions and Gareth S. Parkinson for providing us CO TPD spectra for a $Fe_3O_4(001)$ single crystal prior to publication. This work has been supported by the Deutsche Forschungsgemeinschaft within Sonderforschungsbereich SFB 1109 ("Understanding of Metal Oxide/Water Systems at the Molecular Scale: Structural Evolution, Interfaces, and Dissolution"), the "Fonds der Chemischen Industrie" (FCI) as well as by generous grants for computing time at the high-performance computer center HLRN (North-German Supercomputing Alliance in Berlin and Hannover). J.P. gratefully acknowledges the Stiftung Industrieforschung, Humboldt-Universität zu Berlin for financial support.

## ■ REFERENCES


(1) Cornell, R. M.; Schwertmann, U. *The iron oxides*; Wiley-VCH Verlag GmbH & Co. KGaA, 2004.

(2) Weiss, W.; Ranke, W. Surface chemistry and catalysis on well-defined epitaxial iron-oxide layers. *Prog. Surf. Sci.* **2002**, *70*, 1−151.

(3) Parkinson, G. S. Iron oxide surfaces. *Surf. Sci. Rep.* **2016**, *71*, 272−365.

(4) Ritter, M.; Weiss, W. $Fe_3O_4(111)$ surface structure determined by LEED crystallography. *Surf. Sci.* **1999**, *432*, 81−94.

(5) Shaikhutdinov, S. K.; Ritter, M.; Wang, X. G.; Over, H.; Weiss, W. Defect structures on epitaxial $Fe_3O_4(111)$ films. *Phys. Rev. B: Condens. Matter Mater. Phys.* **1999**, *60*, 11062−11069.

(6) Sala, A.; Marchetto, H.; Qin, Z. H.; Shaikhutdinov, S.; Schmidt, T.; Freund, H. J. Defects and inhomogeneities in $Fe_3O_4(111)$ thin film growth on Pt(111). *Phys. Rev. B: Condens. Matter Mater. Phys.* **2012**, *86*, 155430.

(7) Kiejna, A.; Ossowski, T.; Pabisiak, T. Surface properties of the clean and Au/Pd covered $Fe_3O_4(111)$: DFT and DFT+U study. *Phys. Rev. B: Condens. Matter Mater. Phys.* **2012**, *85*, 125414.

(8) Noh, J.; Osman, O. I.; Aziz, S. G.; Winget, P.; Brédas, J.-L. Magnetite $Fe_3O_4$ (111) surfaces: Impact of defects on structure, stability, and electronic properties. *Chem. Mater.* **2015**, *27*, 5856−5867.

(9) Yu, X.; Huo, C.-F.; Li, Y.-W.; Wang, J.; Jiao, H. $Fe_3O_4$ surface electronic structures and stability from GGA+U. *Surf. Sci.* **2012**, *606*, 872−879.

(10) Santos-Carballal, D.; Roldan, A.; Grau-Crespo, R.; de Leeuw, N. H. A DFT study of the structures, stabilities and redox behaviour of the major surfaces of magnetite $Fe_3O_4$. *Phys. Chem. Chem. Phys.* **2014**, *16*, 21082−21097.

(11) Li, X.; Paier, J. Adsorption of water on the $Fe_3O_4(111)$ surface: Structures, stabilities, and vibrational properties studied by density functional theory. *J. Phys. Chem. C* **2016**, *120*, 1056−1065.

(12) Lemire, C.; Meyer, R.; Henrich, V. E.; Shaikhutdinov, S.; Freund, H. J. The surface structure of $Fe_3O_4(111)$ films as studied by CO adsorption. *Surf. Sci.* **2004**, *572*, 103−114.

(13) Dementyev, P.; Dostert, K.-H.; Ivars-Barceló, F.; O'Brien, C. P.; Mirabella, F.; Schauermann, S.; Li, X.; Paier, J.; Sauer, J.; Freund, H.-J. Water interaction with iron oxides. *Angew. Chem.* **2015**, *127*, 14148−14152.

(14) Davis, E. M.; Zhang, K.; Cui, Y.; Kuhlenbeck, H.; Shaikhutdinov, S.; Freund, H. J. Growth of $Fe_3O_4(001)$ thin films on Pt(100): Tuning surface termination with an Fe buffer layer. *Surf. Sci.* **2015**, *636*, 42−46.

(15) Murnaghan, F. D. The compressibility of media under extreme pressures. *Proc. Natl. Acad. Sci. U. S. A.* **1944**, *30*, 244−247.

(16) Dudarev, S. L.; Botton, G. A.; Savrasov, S. Y.; Humphreys, C. J.; Sutton, A. P. Electron-energy-loss spectra and the structural stability of nickel oxide: An LSDA+U study. *Phys. Rev. B: Condens. Matter Mater. Phys.* **1998**, *57*, 1505−1509.

(17) Yu, X.; Li, Y.; Li, Y.-W.; Wang, J.; Jiao, H. DFT+U study of molecular and dissociative water adsorptions on the $Fe_3O_4(110)$ surface. *J. Phys. Chem. C* **2013**, *117*, 7648−7655.

(18) Perdew, J. P.; Burke, K.; Ernzerhof, M. Generalized gradient approximation made simple. *Phys. Rev. Lett.* **1996**, *77*, 3865−3868; *Phys. Rev. Lett.* **1997**, *78*, 1396−1396.

(19) Kresse, G.; Furthmüller, J. Efficient iterative schemes for ab initio total-energy calculations using a plane-wave basis set. *Phys. Rev. B: Condens. Matter Mater. Phys.* **1996**, *54*, 11169−11186.

(20) Kresse, G.; Furthmüller, J. Efficiency of ab-initio total energy calculations for metals and semiconductors using a plane-wave basis set. *Comput. Mater. Sci.* **1996**, *6*, 15−50.

(21) Blöchl, P. E. Projector augmented-wave method. *Phys. Rev. B: Condens. Matter Mater. Phys.* **1994**, *50*, 17953−17979.

(22) Kresse, G.; Joubert, D. From ultrasoft pseudopotentials to the projector augmented-wave method. *Phys. Rev. B: Condens. Matter Mater. Phys.* **1999**, *59*, 1758−1775.

(23) Monkhorst, H. J.; Pack, J. D. Special points for Brillouin-zone integrations. *Phys. Rev. B* **1976**, *13*, 5188−5192.

(24) Mantz, A. W.; Watson, J. K. G.; Rao, K. N.; Albritton, D. L.; Schmeltekopf, A. L.; Zare, R. N. Rydberg-Klein-Rees potential for $X^1\Sigma^+$ state of CO molecule. *J. Mol. Spectrosc.* **1971**, *39*, 180.

(25) Savara, A. Vibrational spectra of CO adsorbed on oxide thin films: A tool to probe the surface defects and phase changes of oxide thin films. *J. Vac. Sci. Technol., A* **2014**, *32*, 021505.

(26) Lennie, A. R.; Condon, N. G.; Leibsle, F. M.; Murray, P. W.; Thornton, G.; Vaughan, D. J. Structures of $Fe_3O_4(111)$ surfaces observed by scanning tunneling microscopy. *Phys. Rev. B: Condens. Matter Mater. Phys.* **1996**, *53*, 10244−10253.




DOI: 10.1021/acs.jpcb.7b04228
*J. Phys. Chem. B* 2018, 122, 527−533

(27) Cutting, R. S.; Muryn, C. A.; Vaughan, D. J.; Thornton, G. Substrate-termination and $H_2O$-coverage dependent dissociation of $H_2O$ on $Fe_3O_4$(111). *Surf. Sci.* **2008**, *602*, 1155−1165.
(28) Shimizu, T. K.; Jung, J.; Kato, H. S.; Kim, Y.; Kawai, M. Termination and Verwey transition of the (111) surface of magnetite studied by scanning tunneling microscopy and first-principles calculations. *Phys. Rev. B: Condens. Matter Mater. Phys.* **2010**, *81*, 235429.
(29) Huang, D.-M.; Cao, D.-B.; Li, Y.-W.; Jiao, H. Density function theory study of CO adsorption on $Fe_3O_4$(111) surface. *J. Phys. Chem. B* **2006**, *110*, 13920−13925.
(30) Henrich, V. E.; Shaikhutdinov, S. K. Atomic geometry of steps on metal-oxide single crystals. *Surf. Sci.* **2005**, *574*, 306−316.
(31) Chatt, J.; Duncanson, L. A. Olefin co-ordination compounds 0.3. Infra-red spectra and structure - attempted preparation of acetylene complexes. *J. Chem. Soc.* **1953**, 2939−2947.
(32) Blyholder, G. Molecular orbital view of chemisorbed carbon monoxide. *J. Phys. Chem.* **1964**, *68*, 2772.
(33) Pacchioni, G.; Cogliandro, G.; Bagus, P. S. Characterization of oxide surfaces by infrared-spectroscopy of adsorbed carbon-monoxide - a theoretical investigation of the frequency-shift of CO on MgO and NiO. *Surf. Sci.* **1991**, *255*, 344−354.
(34) Jeng, H. T.; Guo, G. Y.; Huang, D. J. Charge-orbital ordering and Verwey transition in magnetite. *Phys. Rev. Lett.* **2004**, *93*, 156403.
(35) Heinz, K.; Hammer, L. Epitaxial cobalt oxide films on Ir(100)-the importance of crystallographic analyses. *J. Phys.: Condens. Matter* **2013**, *25*, 173001.
(36) Ferstl, P.; Mehl, S.; Arman, M. A.; Schuler, M.; Toghan, A.; Laszlo, B.; Lykhach, Y.; Brummel, O.; Lundgren, E.; Knudsen, J.; et al. Adsorption and activation of CO on $Co_3O_4$(111) thin films. *J. Phys. Chem. C* **2015**, *119*, 16688−16699.



DOI: 10.1021/acs.jpcb.7b04228
*J. Phys. Chem. B* 2018, 122, 527−533

# P14

https://onlinelibrary.wiley.com/doi/full/10.1002/anie.201711890

Ordered Water Layers

P14

International Edition: DOI: 10.1002/anie.201711890
German Edition: DOI: 10.1002/ange.201711890

# Cooperative Formation of Long-Range Ordering in Water Ad-layers on $Fe_3O_4(111)$ Surfaces

*Francesca Mirabella[+], Eman Zaki[+], Francisco Ivars-Barceló, Xiaoke Li[+], Joachim Paier,* Joachim Sauer, Shamil Shaikhutdinov,* and Hans-Joachim Freund*

***Abstract:*** *The initial stages of water adsorption on magnetite $Fe_3O_4(111)$ surface and the atomic structure of the water/oxide interface remain controversial. Herein, we provide experimental results obtained by infrared reflection–absorption spectroscopy (IRAS) and temperature-programmed desorption (TPD), corroborated by density functional theory (DFT) calculations showing that water readily dissociates on $Fe_{tet}$ sites to form two hydroxo species. These act as an anchor for water molecules to form a dimer complex which self-assembles into an ordered (2×2) structure. Water ad-layer ordering is rationalized in terms of a cooperative effect induced by a hydrogen-bonding network.*

Water interaction with oxide surfaces plays an important role in geology, electrochemistry, corrosion, water splitting, and catalysis.[1] Iron oxides, in particular magnetite ($Fe_3O_4$), are some of the most studied oxides using a "surface science" approach.[2] Herein we provide the first compelling experimental and theoretical evidence that on the $Fe_3O_4(111)$ surface water adsorption leads to cooperative adsorption of dissociated and molecular water species, which induces the formation of an ordered water monolayer, monitored via structural and spectroscopic studies in combination with density functional theory (DFT) calculations.

While recent experimental and theoretical work on the structure of $Fe_3O_4(001)$ single crystal surfaces suggest that it is well-understood,[2b] the (111) surface remains controversial. On the basis of structural studies also corroborated by DFT calculations, a single metal (namely, $Fe_{tet1}$) termination is considered as the most stable,[3] whereas a double metal ($Fe_{oct2}$-$Fe_{tet1;}$ "tet1" and "oct2" being commonly used nomenclature for this particular oxide structure) termination was favored on the basis of CO and water adsorption studies using infrared reflection absorption spectroscopy (IRAS).[4] Our recent study[5] seems to have eliminated such a discrepancy by employing DFT calculations for CO adsorption. The combined experimental and theoretical results could only be rationalized in terms of the $Fe_{tet1}$-terminated $Fe_3O_4(111)$ surface, although octahedrally coordinated iron ions as a minority species may be present at surface defects. Note that, in contrast to CO that adsorbs intact under ultrahigh vacuum (UHV)-based conditions and has, therefore, been used as a probe molecule for surface termination, water readily dissociates on the $Fe_3O_4(111)$ surface,[2a,6] thus rendering determination of the surface termination by water adsorption difficult. Indeed, it was generally accepted that a water molecule dissociates on $Fe_{tet1}$-terminated $Fe_3O_4(111)$ ultimately forming two surface hydroxo species, that is, Fe-$O_wH$ and $O_sH$ (where $O_w$ and $O_s$ indicate oxygen atoms in water and on the oxide surface, respectively).[6,7] However, this scenario was questioned by results presented in Ref. [4b] suggesting spontaneous formation of a complex composed of dissociated and non-dissociated water molecules (a so-called "half-dissociated" water dimer) based on the assumption, however, that the surface is $Fe_{oct2}$-terminated.

To provide a unified picture for the structure and adsorption properties of the $Fe_3O_4(111)$ surface, herein we re-examined water adsorption models. Using well-characterized $Fe_3O_4(111)$ thin film surfaces and taking careful precautions with respect to the film preparation and surface termination, we show that all experimental results agree well with the "classical" dissociation mechanism resulting in a terminal (Fe-$O_wD$) hydroxy and surface hydroxy ($O_sD$) species at the initial stage. Analysis of the previous studies on $Fe_3O_4(111)$, both for single crystals and thin films, suggests that a certain controversy that exists in the literature may have resulted from the experimental difficulties of preparing well-defined, clean and uniform surfaces. In particular, single-crystal studies may suffer from having several surface structures coexisting. Although thin films grown on a metal substrate appear to be uniform, defect structures are still difficult to control and characterize. In addition, surface preparation and even vacuum conditions may play an important role as a result of adventitious adsorption of residual gases in the background. Finally, from a theoretical point of view, adsorption on the iron oxide systems needs careful consideration as far as electronic and magnetic properties are concerned (see Ref. [4c] and references therein).

In this work, we used well-ordered $Fe_3O_4(111)$ thin films grown on Pt(111) (see Experimental Section in the Supporting Information). Prior to water adsorption, the films were

[*] F. Mirabella,[+] E. Zaki,[+] Dr. F. Ivars-Barceló, S. Shaikhutdinov, H.-J. Freund
Fritz-Haber-Institute
Max Planck Society
Faradayweg 4–6, 14195 Berlin (Germany)
E-mail: shaikhutdinov@fhi-berlin.mpg.de
X. Li,[+] J. Paier, J. Sauer
Institut für Chemie
Humboldt Universität zu Berlin
10099 Berlin (Germany)
E-mail: joachim.paier@chemie.hu-berlin.de
[+] These authors contributed equally to this work.

Supporting information (Experimental Section) and the ORCID identification number(s) for the author(s) of this article can be found under:
https://doi.org/10.1002/anie.201711890.

characterized by CO adsorption in the same manner as described in Ref. [5] to ensure that the $Fe_{tet1}$-termination dominates the surface. We first address temperature-programmed desorption (TPD) results. Figure 1 a shows a series of TPD spectra as a function of water coverage obtained after $D_2O$ dosing at 140 K and heating to 700 K in each run. Beyond the desorption peak at approximately 160 K assigned to the onset of the amorphous solid water (ASW) film formation, several desorption peaks are clearly resolved at 201, 223, and 255 K which are sequentially populated at increasing exposure. The peak positions are independent of water coverage, indicating a first order desorption kinetics. In contrast, a broad signal above 270 K shows typical behavior for second order kinetics expected for recombinative desorption of dissociated water.[6c] Finally, a small signal at around 375 K, can safely be assigned to water adsorption on defect sites.

The desorption spectra can be transformed into coverage-dependent desorption energy plots using inversion analysis of the Polanyi–Wigner equation.[8] For first order desorption kinetics this procedure yields the desorption energies ($E$) as a function of water coverage ($\theta$) [Eq. (1)]

$$E(\theta) = -RT\ln\left(-\frac{d\theta/dT}{\beta \cdot \nu \cdot \theta}\right) \quad (1)$$

where $\beta$ is a heating rate, and $\nu$ is a pre-factor. Figure 1 b shows the results for $\nu = 10^{13}\,s^{-1}$ commonly used. Although the absolute values depend on the pre-factor (increasing the pre-factor to $10^{15}\,s^{-1}$ leads to a shift of all energies towards higher (i.e. more exothermic) values by about 15 kJ mol$^{-1}$), the results clearly show that the desorption energy considerably decreases with increasing coverage, most markedly in the low coverage regime ($\theta/\theta_{max} < 0.15$), in nice agreement with microcalorimetry results.[4b]

To quantify water coverage, we made use of TPD spectra on the clean Pt(111) surface showing a characteristic desorption feature upon formation a well-ordered ice film.[9] Since the measurements were performed with the same setup and on the same Pt crystal as used for the iron oxide film, all apparatus effects are self-cancelled. The results showed that the total amount of water adsorbed on $Fe_3O_4(111)$ before the ASW film starts to grow, corresponds to $2.3 \pm 0.2$ ML (ML = monolayer; 1 ML is defined as $3.2 \times 10^{14}\,cm^{-2}$, that is, one water molecule per $Fe_3O_4(111)$ unit cell). This value agrees fairly well with the model of a half-dissociated water dimer (i.e. two $H_2O$ per unit cell) forming at increasing water coverage, previously put forward by Joseph et al.[6a] However, their TPD spectra (see also Refs. [6c, 7b]) showed, in essence, featureless desorption traces in the 200–300 K region. Such a picture is often attributed to surface heterogeneity and/or reorganization of ad-species during the TPD run, thus broadening and smearing desorption features. In contrast, the presence of well-resolved peaks in our spectra favor the model where each desorption peak showing first order kinetics is associated with individual desorption of water molecules having discrete binding energies. In principle, this could be the case when several adsorption sites coexist on the surface, from which water desorbs independently. Such an explanation was essentially provided in Refs. [7c, 10] reporting TPD peaks of water on the $Fe_3O_4(111)$ selvedge surface of a hematite $Fe_2O_3(0001)$ natural crystal, since different surface

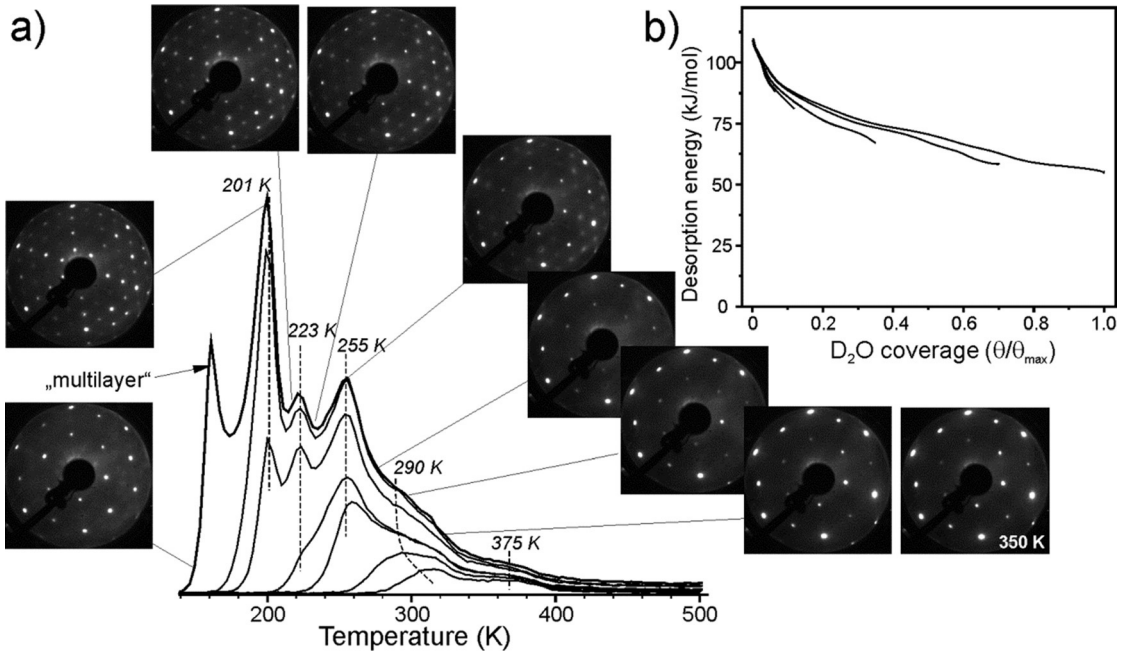


***Figure 1.*** a) TPD spectra of $D_2O$ adsorbed at 140 K at increasing exposures. The spectra are cut at 500 K, for clarity. At the highest exposure, the formation of "multilayer" (ASW) film sets in. The heating rate is 3 K s$^{-1}$. Snapshots from the LEED ($E = 64$ eV) movie recorded while heating the sample covered by the ASW film at 140 K synchronized with a TPD spectrum. b) Desorption energy as a function of water coverage, normalized to the total coverage ($\theta_{max}$) measured before ASW formation, obtained by inversion analysis of the Polanyi–Wigner equation applied to each spectrum shown in (a), see text.

  

phases are inevitably formed during surface preparation. This is clearly not the case for our films exposing a single termination.

Under the assumption that the TPD signal at high temperatures above 270 K is associated with dissociated water, the observation of three distinct desorption peaks at 200–255 K is difficult to rationalize within a simple dimer model having only one non-dissociated water molecule per unit cell. Therefore, this finding suggests the formation of water oligomers larger than a dimer (e.g. trimer and tetramer). Alternatively, three-dimensional water clusters are formed, from which water molecules desorb in a one-by-one manner. Sharp desorption signals imply species desorbing almost simultaneously, suggesting, in turn, a certain degree of ordering at the surface.

To examine whether water forms ordered structures on $Fe_3O_4(111)$ we employed low energy electron diffraction (LEED). Certainly, careful precautions had to be taken to minimize electron beam damaging effects. Figure 1a displays snapshots from the LEED movie recorded upon heating of the ASW film (formed by 1.5 L; 1 L = $10^{-6}$ Torr × s) of $D_2O$ at 140 K) to synchronize with the thermal desorption. Additional spots clearly identified as of $Fe_3O_4(111)$-$(2\times2)$ appear upon desorption of the ASW film and attenuates above about 260 K. The formation of the $(2\times2)$ structure depends on the water coverage and not on the adsorption temperature (140 K vs. 250 K). This finding indicates that ordering is thermodynamically driven and not kinetically limited. Note also, that the $(2\times2)$ spots appear in LEED immediately upon electron beam exposure and showed no intensity attenuation in time, at least, on the scale of a minute. Rapidly changing the spot position for sampling also showed no effect on the LEED spots intensity. Therefore, we can safely rule out beam effects on water ordering.

There are only a few examples in the literature of water/oxide interfaces which exhibited an ordered water ad-layer.[11] Water adsorption on the MgO(001) surface is likely the most intensively studied system (Ref. [12] and references therein) that showed $c(4\times2)$ and $p(3\times2)$ structures in LEED.[13] Using a genetic algorithm, DFT calculations predicted two stable structures. At low temperature, a $c(4\times2)$ structure is stable that contains ten water molecules in the cell thus leading to a nominal coverage 1.25 $H_2O$ per MgO(001) unit cell. A $p(3\times2)$ structure containing six water molecules per cell (1 $H_2O$ per surface cell) is more stable at high temperature. Both structures feature surface hydroxy groups resulting from the dissociation of water molecules. However, the way these structures form on MgO(001) remains poorly understood. In the case of adsorption on $ZnO(10\bar{1}0)$,[11a] the dissociation only occurs when two molecules occupy adjacent adsorption sites thus resulting in a half-dissociated dimer forming a $(2\times1)$ superstructure.

To shed light on the atomic structure of the water ad-layer on $Fe_3O_4(111)$, we performed IRAS measurements. Full analysis will be presented elsewhere;[14] here we only highlight key observations. Figure 2a shows a series of spectra obtained at the saturating exposure at the sample temperature as indicated. A sharp OD band at 2680 $cm^{-1}$ appears at 350 K and almost doubles intensity upon water dosing at 320 and 300 K. At increasing coverage achieved by water exposure at 250 K, the band at 2723 $cm^{-1}$ signal gains considerable intensity, and the peak shifts to 2714 $cm^{-1}$. Concomitantly, a new band at 2688 $cm^{-1}$ grows, whereas the band at 2680 $cm^{-1}$ disappears. In addition, a weak band shows up at 2565 $cm^{-1}$ which falls in the range of hydrogen -bonded OD vibrations. At 200 K, two bands, at 2710 and 2693 $cm^{-1}$, start to dominate the spectrum in this region, while very broad signals develop in the 2650–2450 $cm^{-1}$ region indicating the formation of a hydrogen-bonding network, culminating in the formation of the ASW film at 120 K. The ASW film shows a well-established band at 2726 $cm^{-1}$ assigned to a "dangling" OD vibration at the water surface and a broad band centered at 2580 $cm^{-1}$ of hydrogen-bonded OD species in the bulk.

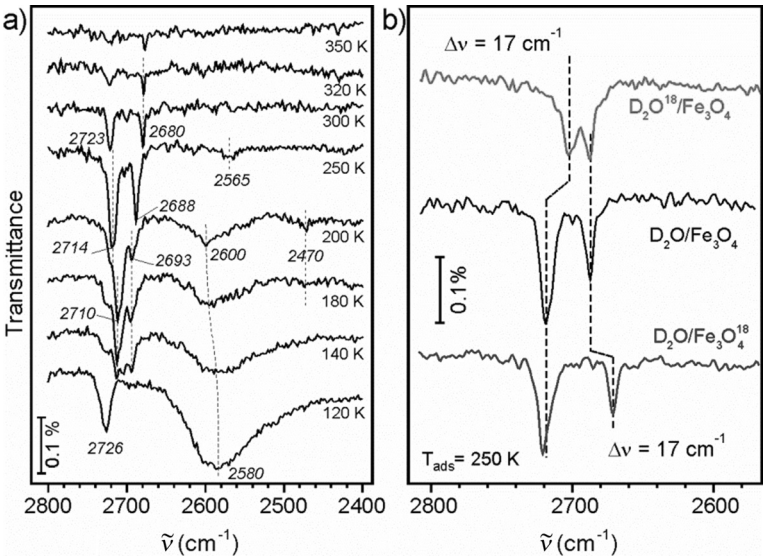


***Figure 2.*** a) IRA spectra obtained at the saturating exposure at the sample temperature as indicated (see text). b) IRA spectra obtained at 250 K for $^{18}O$-labelled water (top) and oxide film (bottom) for comparison with results on $D_2O/Fe_3O_4$-(111) (middle) shown in panel (a).

The band around 2720 $cm^{-1}$ falls in the range calculated by DFT[4b,c] for stretching vibrations of terminal $O_wD$ hydroxy formed by dissociation of a single water molecule on both surface terminations, that is, 2754 $cm^{-1}$ on $Fe_{oct2}$- and 2729 $cm^{-1}$ on $Fe_{tet1}$-terminated surfaces, when scaled using observed fundamentals of the water molecule (see Ref. [4b]). However, computed frequencies for surface hydroxy groups ($O_sD$) considerably differ and are expected to show up at approximately 2440 $cm^{-1}$ and 2705 $cm^{-1}$, for the $Fe_{oct2}$- and $Fe_{tet1}$- termination, respectively. To further identify the nature of the observed sharp bands in the 2720–2680 $cm^{-1}$ region with the help of isotopic labelling, we performed adsorption experiments with $D_2{}^{18}O$ water on the same film. In addition, "normal" $D_2O$ water was exposed to the oxide film prepared

  

with $^{18}O$. The results of adsorption at 250 K are summarized in Figure 3b for direct comparison with $D_2O/Fe_3O_4(111)$. Clearly, only the band at 2714 $cm^{-1}$ red-shifts upon $D_2{}^{18}O$ adsorption, whereas the 2688 $cm^{-1}$ band only shifts upon $^{18}O$ labeling in the oxide, both shifts being about 17 $cm^{-1}$.

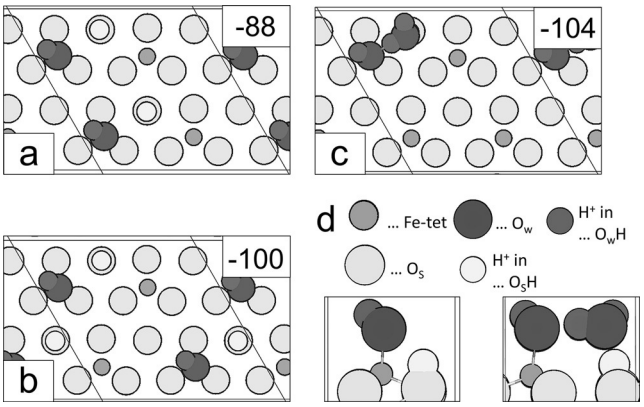


***Figure 3.*** a)–c) Top views of several computed structures containing two water molecules in the (2×2) cell. The calculated $\Delta E$ energies in kJ $mol^{-1}$ are shown in the top right corner. Side views of a "monomer" and a "dimer" are shown in (d).

Therefore, the high frequency bands above 2710 $cm^{-1}$ must be associated with terminal Fe-$O_w$D, and the bands below 2695 $cm^{-1}$ with the surface hydroxy groups $O_s$D, in agreement with the "classical" adsorption model involving dissociation of a single water molecule on a cation–anion pair resulting in two hydroxy groups as observed. However, these results are at variance with those reported in Ref. [4b] showing that the bands (at 2720 and 2695 $cm^{-1}$ in that case) are originating from water and do not involve surface oxygen. To validate our current bands assignment, we performed additional IRAS experiments in another UHV setup on several identically prepared samples which fully reproduced the isotopic shifts as in Figure 2b. To investigate such a discrepancy, we analyzed experimental details in both studies which revealed a critical role of the surface preparation and vacuum conditions on water adsorption results especially at low coverages (only presented in Ref. [4b]). It is found that UHV annealing at high temperatures (above 750 K) is important for the formation of a uniform $Fe_{tet1}$-terminated surface as highlighted in the LEED *I/V* study[3c] and also in our most recent IRAS/DFT study of CO adsorption.[5] Unfortunately, this condition was not carefully controlled in the previous water adsorption study.[4b]

The evolution of the spectra shown in Figure 2a is rather complex and suggests a rearrangement of water species upon increasing coverage up to the critical point where long-range ordering takes place as judged by LEED. In principle, two scenarios could be envisioned. In the first one, water molecules dissociate and give rise to hydroxo species which form a (2×2) array as a template which is maintained upon adding further water molecules. It is more plausible, however, that the formation of a (2×2) structure only occurs upon molecular-water adsorption. Indeed, water ordering is not observed by LEED at 300 K, that is, in relative abundance of dissociated water species. On the other hand, it cannot be ruled out that the high coverage, only reached at low temperatures, is needed for detection by conventional LEED which requires ordered structures in areas larger than 5–10 nm.

The formation of the (2×2) ordered structure was further analyzed on the basis of DFT calculations henceforth using a $Fe_3O_4(111)$-(2×2) supercell. Equation (2) describes the chemical reaction of sequential water adsorption:

$$Fe_3O_4(111)\cdot n\,H_2O + H_2O \rightleftharpoons Fe_3O_4(111)\cdot (n+1)\,H_2O,$$
$$\Delta E(n) = E_{n+1} - (E_n + E_{H_2O}) \qquad (2)$$

As previously observed for the (1×1) slabs, the first water molecule strongly adsorbs and readily dissociates ($\Delta E = -123$ kJ $mol^{-1}$). The second water molecule in the cell (i.e. 0.5 ML coverage) may either dissociate on available empty Fe-O sites or anchor to the preformed hydroxy groups to form a dimer (Figure 3). Although, according to calculated energies, both processes are equally possible (−100 vs. −104 kJ $mol^{-1}$ per water molecule), the energy gain is considerably smaller than for monomer formation on the clean surface (−123 kJ $mol^{-1}$).

Therefore, at coverages close to 1 ML (i.e. four $H_2O$ molecules in the cell), the oxide surface is predicted to be covered primarily by hydroxy groups, although dimers can also be found. To model structures at higher coverages, we performed calculations by adding water molecules one-by-one to a surface fully covered by monomers (=1 ML). Clearly, the first additional water molecule anchors to one of the monomers to form a dimer (not shown). The optimized structures and reaction energies $\Delta E$ for the case of 6, 7, and 8 molecules per (2×2) cell are shown in Figure 4. Note that zero point vibrational energy corrections per $H_2O$ molecule only cause a constant shift upon calculation of reaction energies for each of the (2×2) structures considered (see Table 1 in Supporting Information). Therefore, only PBE + U total energies are used for discussion. For six $H_2O$ molecules per cell (1.5 ML), the structure consisting of a trimer (the "clustered" structure, $\mathbf{6^{cl}}$) is more stable than of that of a hydrogen-bonded dimer and a monomer ($\mathbf{6^{n}}$). However,

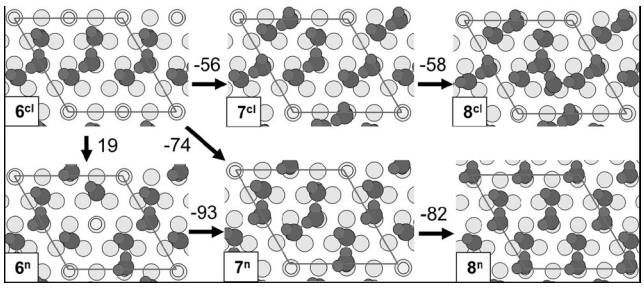


***Figure 4.*** Top and side views of several computed structures containing 6, 7 and 8 water molecules in a $Fe_3O_4(111)$-(2×2) cell. The top panel depicts the formation of cluster-like water oligomers ($\mathbf{6^{cl}}$, $\mathbf{7^{cl}}$, $\mathbf{8^{cl}}$), and the bottom panel shows development of the hydrogen bonding 2D-network (see text). Reaction energies upon adding one $H_2O$ are given in kJ $mol^{-1}$. Shading as in Figure 3.

  

adding one $H_2O$ to the structure $\mathbf{6^{cl}}$ yields $\Delta E = -56\ kJ\ mol^{-1}$, whereas a more exothermic reaction ($\Delta E = -74\ kJ\ mol^{-1}$) is obtained by the formation of the "network" structure $\mathbf{7^{n}}$, where dimers start to build a 2D network by maximizing hydrogen bonds. This reaction pathway further dominates for the case of 8 $H_2O$ molecules per cell, basically following the Bernal-Fowler rules.[15] Thus, the formation of the 2D water network is thermodynamically favored. Moreover, the structure $\mathbf{8^{n}}$ features a $(1\times1)$ symmetry that is in good agreement with LEED data (Figure 1) showing a sharp $(1\times1)$ pattern at 140 K before the $(2\times2)$ structure develops. Although there is no direct proof (e.g. by scanning tunneling microscopy) for the atomic structure of the unit cell in the network, the proposed scenario is consistent with the experimental findings.

In summary, the presented results of water adsorption on $Fe_3O_4(111)$ at the initial stages, that is, before the formation of amorphous solid water (or "ice") sets in, show that water readily dissociates on the surface $Fe_{tet}$-O cation–anion pair to form two hydroxy species. These act as anchors for molecular-water adsorption resulting in dimer complexes which self-assemble into a $(2\times2)$ ordered structure. The formation of a long-range ordered water ad-layer is thermodynamically driven and includes cooperative formation of a hydrogen bonding network. The results further manifest a delicate balance that exists between water–surface and water–water interaction that determines stability of water species on oxide surfaces as recently demonstrated for the $Cu_2O(111)$ surface solely on theoretical grounds.[16]

## Acknowledgements

This work has been supported by the Deutsche Forschungsgemeinschaft through SFB 1109, by the Fonds der Chemischen Industrie as well as by generous grants for computing time at the North-German Supercomputing Alliance in Berlin and Hannover. J.P. gratefully acknowledges the Stiftung Industrieforschung, Humboldt-Universität zu Berlin for financial support. F.M. thanks the International Max-Planck Research School "Functional Interfaces in Physics and Chemistry" for a fellowship.

## Conflict of interest

The authors declare no conflict of interest.

**Keywords:** density functional theory · iron oxides · magnetite · surface structures · water adsorption

**How to cite:** *Angew. Chem. Int. Ed.* **2018**, *57*, 1409–1413
*Angew. Chem.* **2018**, *130*, 1423–1428

[1] a) M. A. Henderson, *Surf. Sci. Rep.* **2002**, *46*, 1–308; b) P. A. Thiel, T. E. Madey, *Surf. Sci. Rep.* **1987**, *7*, 211–385.
[2] a) W. Weiss, W. Ranke, *Prog. Surf. Sci.* **2002**, *70*, 1–151; b) G. S. Parkinson, *Surf. Sci. Rep.* **2016**, *71*, 272–365; c) H. Kuhlenbeck, S. Shaikhutdinov, H.-J. Freund, *Chem. Rev.* **2013**, *113*, 3986–4034.
[3] a) M. Ritter, W. Weiss, *Surf. Sci.* **1999**, *432*, 81–94; b) S. K. Shaikhutdinov, M. Ritter, X. G. Wang, H. Over, W. Weiss, *Phys. Rev. B* **1999**, *60*, 11062–11069; c) A. Sala, H. Marchetto, Z. H. Qin, S. Shaikhutdinov, T. Schmidt, H. J. Freund, *Phys. Rev. B* **2012**, *86*, 155430; d) A. Kiejna, T. Ossowski, T. Pabisiak, *Phys. Rev. B* **2012**, *85*, 125414; e) J. Noh, O. I. Osman, S. G. Aziz, P. Winget, J.-L. Brédas, *Chem. Mater.* **2015**, *27*, 5856–5867; f) X. Yu, C.-F. Huo, Y.-W. Li, J. Wang, H. Jiao, *Surf. Sci.* **2012**, *606*, 872–879; g) D. Santos-Carballal, A. Roldan, R. Grau-Crespo, N. H. de Leeuw, *Phys. Chem. Chem. Phys.* **2014**, *16*, 21082–21097.
[4] a) C. Lemire, R. Meyer, V. E. Henrich, S. Shaikhutdinov, H. J. Freund, *Surf. Sci.* **2004**, *572*, 103–114; b) P. Dementyev, K.-H. Dostert, F. Ivars-Barceló, C. P. O'Brien, F. Mirabella, S. Schauermann, X. Li, J. Paier, J. Sauer, H.-J. Freund, *Angew. Chem. Int. Ed.* **2015**, *54*, 13942–13946; *Angew. Chem.* **2015**, *127*, 14148–14152; c) X. Li, J. Paier, *J. Phys. Chem. C* **2016**, *120*, 1056–1065.
[5] X. Li, J. Paier, J. Sauer, F. Mirabella, E. Zaki, F. Ivars-Barceló, S. Shaikhutdinov, H. J. Freund, *J. Phys. Chem. B* **2017**. https://doi.org/10.1021/acs.jpcb.7b04228.
[6] a) Y. Joseph, W. Ranke, W. Weiss, *J. Phys. Chem. B* **2000**, *104*, 3224–3236; b) T. Kendelewicz, P. Liu, C. S. Doyle, G. E. Brown, Jr, E. J. Nelson, S. A. Chambers, *Surf. Sci.* **2000**, *453*, 32–46; c) Y. Joseph, C. Kuhrs, W. Ranke, M. Ritter, W. Weiss, *Chem. Phys. Lett.* **1999**, *314*, 195–202.
[7] a) R. S. Cutting, C. A. Muryn, D. J. Vaughan, G. Thornton, *Surf. Sci.* **2008**, *602*, 1155–1165; b) U. Leist, W. Ranke, K. Al-Shamery, *Phys. Chem. Chem. Phys.* **2003**, *5*, 2435–2441; c) K. Adib, G. G. Totir, J. P. Fitts, K. T. Rim, T. Mueller, G. W. Flynn, S. A. Joyce, R. M. Osgood, Jr., *Surf. Sci.* **2003**, *537*, 191–204.
[8] S. L. Tait, Z. Dohnálek, C. T. Campbell, B. D. Kay, *J. Chem. Phys.* **2005**, *122*, 164707.
[9] S. Haq, J. Harnett, A. Hodgson, *Surf. Sci.* **2002**, *505*, 171–182.
[10] K. T. Rim, D. Eom, S.-W. Chan, M. Flytzani-Stephanopoulos, G. W. Flynn, X.-D. Wen, E. R. Batista, *J. Am. Chem. Soc.* **2012**, *134*, 18979–18985.
[11] a) B. Meyer, D. Marx, O. Dulub, U. Diebold, M. Kunat, D. Langenberg, C. Wöll, *Angew. Chem. Int. Ed.* **2004**, *43*, 6641–6645; *Angew. Chem.* **2004**, *116*, 6809–6814; b) Y. He, A. Tilocca, O. Dulub, A. Selloni, U. Diebold, *Nat. Mater.* **2009**, *8*, 585–589; c) S. Kaya, J. Weissenrieder, D. Stacchiola, S. Shaikhutdinov, H. J. Freund, *J. Phys. Chem. C* **2007**, *111*, 759–764.
[12] R. Włodarczyk, M. Sierka, K. Kwapień, J. Sauer, E. Carrasco, A. Aumer, J. F. Gomes, M. Sterrer, H.-J. Freund, *J. Phys. Chem. C* **2011**, *115*, 6764–6774.
[13] a) C. Xu, D. W. Goodman, *Chem. Phys. Lett.* **1997**, *265*, 341–346; b) J. Heidberg, B. Redlich, D. Wetter, *Ber. Bunsen-Ges.* **1995**, *99*, 1333–1337; c) D. Ferry, A. Glebov, V. Senz, J. Suzanne, J. P. Toennies, H. Weiss, *J. Phys. Chem.* **1996**, *105*, 1697–1701.
[14] E. Zaki, F. Mirabella, F. Ivars-Barceló, J. Seifert, X. Li, J. Paier, J. Sauer, S. Shaikhutdinov, H. J. Freund, unpublished results.
[15] J. D. Bernal, R. H. Fowler, *J. Phys. Chem.* **1933**, *1*, 515–548.
[16] C. Riplinger, E. A. Carter, *J. Phys. Chem. C* **2015**, *119*, 9311–9323.

Manuscript received: November 20, 2017
Accepted manuscript online: December 4, 2017
Version of record online: January 2, 2018

  

# P15

https://pubs.rsc.org/en/content/articlehtml/2018/cp/c8cp02333f

PCCP

P15

PAPER

View Article Online
View Journal | View Issue



Cite this: *Phys. Chem. Chem. Phys.*, 2018, **20**, 15764

# Water adsorption on the $Fe_3O_4(111)$ surface: dissociation and network formation†

Eman Zaki,‡[a] Francesca Mirabella,‡[a] Francisco Ivars-Barceló,[a] Jan Seifert,[a] Spencer Carey,[a] Shamil Shaikhutdinov,*[a] Hans-Joachim Freund,[a] Xiaoke Li,‡[b] Joachim Paier*[b] and Joachim Sauer[b]

Received 12th April 2018,
Accepted 30th May 2018

DOI: 10.1039/c8cp02333f

rsc.li/pccp

We monitored adsorption of water on a well-defined $Fe_3O_4(111)$ film surface at different temperatures as a function of coverage using infrared reflection–absorption spectroscopy, temperature programmed desorption, and single crystal adsorption calorimetry. Additionally, density functional theory was employed using a $Fe_3O_4(111)$-(2 × 2) slab model to generate 15 energy minimum structures for various coverages. Corresponding vibrational properties of the adsorbed water species were also computed. The results show that water molecules readily dissociate on regular surface $Fe_{tet1}$–O ion pairs to form "monomers", *i.e.*, terminal Fe–OH and surface OH groups. Further water molecules adsorb on the hydroxyl covered surface non-dissociatively and form "dimers" and larger oligomers, which ultimately assemble into an ordered (2 × 2) hydrogen-bonded network structure with increasing coverage prior to the formation of a solid water film.



## 1. Introduction

Water interaction with iron oxides plays an important role in geology, electrochemistry, corrosion, and catalysis, *etc.*[1,2] Among the various iron oxides, magnetite ($Fe_3O_4$) surfaces seem to be the most explored using a "surface science" approach.[3–5] While recent experimental and theoretical work on $Fe_3O_4(001)$ single crystal surfaces suggested that this surface is well-understood, a controversy remains for the (111) surface. Low energy electron diffraction (LEED) studies of $Fe_3O_4(111)$ thin films in combination with scanning tunneling microscopy (STM) characterization suggested a termination with a 1/4 monolayer of tetrahedrally coordinated $Fe^{3+}$ ions over the close-packed oxygen layer,[6–8] which can be obtained by cutting the magnetite structure along the $Fe_{tet1}$ layer. Also density functional theory (DFT) calculations predict the $Fe_{tet1}$-terminated surface as the most stable one under typical pressure and temperature conditions applied in UHV based experiments.[9–14] On the other hand, a double metal ($Fe_{oct2}$–$Fe_{tet1}$) termination was favored on the basis of infrared reflection–absorption spectroscopy (IRAS) studies of CO and water adsorption.[13,15,16] Our recent study[17] has eliminated such a discrepancy by providing DFT analysis of CO vibrational bands, which ruled out the presence of octahedrally coordinated iron ions ($Fe_{oct2}$) on the regular surface except for defect sites such as step edges.

It is instructive here to summarize the key findings of previous experimental studies on water adsorption on $Fe_3O_4(111)$ surfaces prepared either as thin films or single crystals. We only address water coverages below the formation of a "multilayer" amorphous solid water (ASW) film.

– Ultraviolet and X-ray photoelectron spectroscopy studies revealed electronic states, which were assigned to OH species[18–21] thus suggesting water dissociation. This was found both at room and low temperatures depending on the partial pressure of water.

– Temperature programmed desorption (TPD) studies revealed water desorption in a wide temperature range, between 200 and 400 K.[20,22,23] In particular, desorption signals above 300 K were attributed to the recombinative desorption of dissociated water.

– The heat of adsorption measured by single crystal adsorption calorimetry (SCAC),[16] falls in the range of 100 kJ mol$^{-1}$ at the limit of low water coverage and decreases down to 55 kJ mol$^{-1}$ with increasing coverage.

– The first appearing bands (at 2712 and 2691 cm$^{-1}$) in the IRA spectra[23] were originally assigned to stretching vibrations of two hydroxyls, Fe–$O_w$D and $O_s$D species, respectively, which were formed upon water dissociation. ($O_w$ and $O_s$ label oxygen atoms in water and in the oxide, respectively). This assignment was doubted in another IRAS study,[16] suggesting the formation of a half-dissociated dimer from the onset.

– STM studies of adsorbed water are scarce. STM images of the pristine $Fe_3O_4(111)$ films even showed a variety of adsorbate-like

[a] *Abteilung Chemische Physik, Fritz-Haber-Institut der Max-Planck-Gesellschaft, Faradayweg 4-6, 14195 Berlin, Germany. E-mail: shaikhutdinov@fhi-berlin.mpg.de*
[b] *Institut für Chemie, Humboldt-Universität zu Berlin, Unter den Linden 6, 10099 Berlin, Germany. E-mail: joachim.paier@chemie.hu-berlin.de*

† Electronic supplementary information (ESI) available: TPD spectra obtained in IRAS setup; selected IRA spectra for $D_2O$ adsorbed on an $O^{16}$ and $O^{18}$ labelled $Fe_3O_4$ films; top views on structures for higher coverage; table with computed frequencies for all structures; comparison of observed shifts and computed wavenumbers for other structures not shown in main text; total energies; structure coordinates. See DOI: 10.1039/c8cp02333f

‡ These authors contributed equally to the work.

species,[24] which were attributed to the reaction with traces of water in the UHV background. STM studies of water adsorption on a $Fe_3O_4(111)$ single crystal[19] suggested that water dissociation only occurs on the $Fe_{tet1}$-terminated surface. In essence, the same behavior was observed on the $Fe_3O_4(111)$ selvedge surface of a $Fe_2O_3(0001)$ single crystal.[25]

As for theoretical studies, DFT calculations were primarily applied to the $Fe_{tet1}$-terminated surface using a $(1 \times 1)$ slab model which implies, at least, one monolayer (ML) water coverage. For the case of dissociative water adsorption, Grillo *et al.*[14] found an adsorption energy of $-95$ kJ mol$^{-1}$. With respect to calculations using a $(2 \times 2)$ cell corresponding to the 1/4 ML water coverage, Rim *et al.*[25] reported an adsorption energy of $-126$ kJ mol$^{-1}$ for the dissociative pathway, which is by 47 kJ mol$^{-1}$ more stable than molecular adsorption. Also, these calculations found a small activation barrier for dissociation ($\sim$10 kJ mol$^{-1}$). Recently, a virtually identical result for dissociative adsorption ($-123$ kJ mol$^{-1}$) was obtained in our own study on the $(2 \times 2)$ cell.[26] Calculations for 1 ML coverage, using a single dissociated molecule in the $(1 \times 1)$ surface unit cell involving symmetry-related constraints, resulted in the reduced adsorption energy, *i.e.*, of $-75$ kJ mol$^{-1}$.[13] At increasing coverage up to two water molecules per unit cell, all theoretical studies converge to similar structures, *i.e.* a dimer composed of a dissociated and a non-dissociated water molecule (a "half-dissociated" water dimer). Regarding the role of surface termination, Yang *et al.*[27] reached the conclusion that the $Fe_{tet1}$-terminated surface is more favorable for water adsorption than the $Fe_{oct2}$-terminated one. However, Zhou *et al.*,[28] who addressed the dissociation mechanisms solely on the $Fe_{oct2}$-terminated surface, found it more active than the $Fe_{tet1}$-terminated surface. Although the latter calculations do not include a Hubbard-type $U$ parameter for correlation effects, these results suggested direct dissociation to be unfavorable. However, water dissociation can be facilitated by adjacent water molecules (*i.e.*, *via* dimer formation). The higher reactivity of the $Fe_{oct2}$-termination towards $H_2O$ and CO adsorption was confirmed by recent DFT+$U$ studies.[13,17]

Thus, the adsorption of water on the $Fe_3O_4(111)$ surface is controversially discussed in the literature. For all planar systems, surface preparation and even vacuum conditions play an important role. Also from a theoretical point of view, iron oxide systems need careful consideration as far as electronic and magnetic properties are concerned.[13]

In a recent communication,[26] we provided experimental results obtained by IRAS and TPD, corroborated by DFT calculations showing that water readily dissociates on $Fe_{tet1}$ sites to form two hydroxyl species. These act as an anchor for water molecules to form a dimer complex which self-assembles into an ordered $(2 \times 2)$ structure. The ordering in the water ad-layer is rationalized in terms of a cooperative effect induced by a hydrogen bonding network. In an attempt to provide a more detailed picture of the interaction of water with the $Fe_3O_4(111)$ surface that goes beyond the evidence from our previous study,[26] here we provide results obtained by different experimental techniques (IRAS, TPD, and SCAC), and DFT calculations.

# 2. Methods and materials

## 2.1. Experimental section

The experiments were performed in several UHV chambers with a background pressure below $2 \times 10^{-10}$ mbar. All setups were equipped with standard facilities necessary to grow well-ordered $F_3O_4(111)$ films on a Pt(111) substrate. The quality of the films was checked by LEED showing sharp diffraction spots with low background intensity, and no other elements beyond Fe and O were observed by Auger electron spectroscopy. TPD spectra were recorded using a quadrupole mass spectrometer (QMS) having a gold-plated cone shield in order to minimize signals from the heating stage. IRA spectra were measured with a spectrometer (Bruker 66 ivs) at grazing angle 8° with the resolution of 4 cm$^{-1}$. In the TPD/IRAS setup, water ($D_2O$, Sigma-Aldrich) was dosed with a calibrated molecular beam. In a second ("TPD") chamber, water was dosed using a directional doser.

Calorimetric results and sticking probabilities were measured with SCAC in a separate UHV chamber that is described in detail elsewhere.[29] Briefly, an effusive, doubly differentially pumped multi-channel array was used to produce a molecular beam of $D_2O$ water. A chopper cut this beam into pulses 266 ms in length. The heat of adsorption was measured with a heat detector consisting of a 9 μm-thick pyroelectric ribbon (β-polyvinylidene fluoride) coated with Au on both sides and calibrated with pulses of HeNe laser light ($\lambda$ = 632.8 nm, 5 mW). Simultaneously, the fraction of molecules that adsorb in a single pulse (*i.e.*, the sticking probability) was measured by the modified King–Wells method[30] with a non-line-of-sight QMS.

The $Fe_3O_4(111)$ films, with a thickness of about 5 nm, were grown on a Pt(111) substrate as described elsewhere.[6–8,15] The first step includes formation of the FeO(111) monolayer film on the clean Pt(111) surface.[3] This step is also used for calibration of the Fe deposition flux. The next step involves several (3–5) cycles of Fe deposition in amounts equivalent to 5–10 monolayers of FeO(111) onto a substrate (kept either at 100 or 300 K), followed by oxidation in $10^{-6}$ mbar of $O_2$ at $\sim$930 K for 5–10 minutes. Oxygen was pumped out at sample temperature around 500 K. In the final step, the films were oxidized at 930–940 K for *ca.* 5 min. The samples were always flashed in UHV to 900 K prior to the water adsorption measurements. Although the precise preparation parameters (Fe flux, oxidation temperature, time and oxygen pressure) may slightly deviate in the UHV setups used, all oxide films under study showed sharp LEED patterns with low background intensity.

## 2.2. Computational details

Electronic and ionic structure calculations were performed using the projector-augmented-wave (PAW) method[31,32] as implemented in the Vienna ab initio simulation package (VASP).[33,34] Plane waves up to a kinetic energy of 800 eV were employed as a basis set. Onsite Coulomb correlation effects of Fe 3d orbitals were taken care of *via* the spin-polarized DFT+$U$ approach[35,36] following Dudarev *et al.*[37,38] An effective $U$ parameter of 3.8 eV was employed following previous DFT studies on $Fe_3O_4$ surfaces.[11,39–41] Regarding the exchange–correlation

functional, we used the generalized-gradient approximation after Perdew, Burke, and Ernzerhof (PBE).[42]

We use PAW pseudopotentials to describe the electron–ion interaction as released with VASP 5.2. The potential for Fe uses 14 valence electrons (Fe_pv:[43] $3p^6\ 3d^7\ 4s^1$ as the atomic reference configuration) and the pseudopotential for O uses six valence electrons (O: [He] $2s^2\ 2p^4$). Electronic optimizations were performed using a break criterion of $10^{-5}$ eV and Gaussian-type of a smearing with a width of 0.1 eV. Structures have been optimized to better than 0.02 eV $Å^{-1}$, which is the modulus of the maximum force acting on the atoms as employed in ref. 13.

With respect to structural surface models, we employ asymmetric stoichiometric slabs comprising twelve atomic layers and a (2 × 2)-periodicity, *i.e.*, the clean $Fe_{tet1}$-terminated $Fe_3O_4(111)$ surface has a cell content equivalent to $Fe_{48}O_{64}$. To avoid image interactions in the direction normal to the surface unit cell, a vacuum distance of approximately 10 Å was employed. Extensive tests showed that this vacuum distance is sufficient to obtain converged results. Coordinates of the atoms in the bottommost four atomic layers were kept frozen, *i.e.*, during structure optimization their positions remain as in the bulk phase. For the Brillouin zone integration $\Gamma$-centered Monkhorst–Pack grids[44] with a (3 × 3 × 1) grid density were employed. Spurious dipole–dipole interactions between periodic images of slabs (in direction of the surface normal) were compensated by the approach after Makov and Payne[45] as implemented in the VASP code. Calculations of wavenumbers corresponding to the normal modes of adsorbed water uses all water related ad-atoms, as well as the coordinated Fe ions and protonated surface oxygen ions in the partial Hessian. Wavenumbers of deuterated ad-water were calculated by diagonalization of the mass-weighted partial Hessian using a mass of 2.014. Harmonic wavenumbers obtained using central finite differences (step size of 0.015 Å) based on the analytic Hellmann–Feynman gradient at atomic coordinates were scaled with a factor of 0.9935 (see ref. 16 and 26). This scaling was employed to effectively account for systematic errors in harmonic force constants and neglected anharmonicities. The water molecule was simulated in a box identical to the slab together with the identical plane wave cutoff used in surface calculations. Corrections for dispersive interactions[46,47] have been calculated at the PBE+*U* minimum energy structures, and a single water molecule contributes about −14 kJ $mol^{-1}$, on average (see below). Thus, results and conclusions of the present work are not affected qualitatively by adding an estimate for dispersion effects.

## 3. Results and discussion

### 3.1. Temperature programmed desorption (TPD)

Fig. 1a shows a series of TPD spectra obtained upon water exposure (in Langmuirs (L), 1 L = $10^{-6}$ Torr s) at 140 K to minimize the signal from an amorphous solid water (ASW) which is manifested by the peak at around 160 K. Desorption peaks at ~200, 225, and 255 K are sequentially populated with increasing exposure following first order desorption kinetics. In contrast, the broad signal above ~275 K shows characteristics of second order desorption due to the recombinative desorption of dissociated water. The small feature at ~375 K can be assigned to the adsorption on defects sites. These spectra differ substantially from those reported previously which revealed, in essence, featureless desorption traces in the 200–300 K region.[20,21,23]

Using the conventional Redhead analysis[48] and a typical pre-factor of $10^{13}$ $s^{-1}$, one obtains a range of desorption energies from 50 kJ $mol^{-1}$ for the peak at ~200 K up to 95 kJ $mol^{-1}$ for the peak at ~375 K. Changing the pre-factor by one order of magnitude up or down changes the desorption energies by approximately ±5 kJ $mol^{-1}$. We refer to ref. 50 for a general discussion. Another approach to determine water adsorption energies from TPD spectra is a "leading edge" analysis,[49,51] which, in principle, does not include an assumption about the

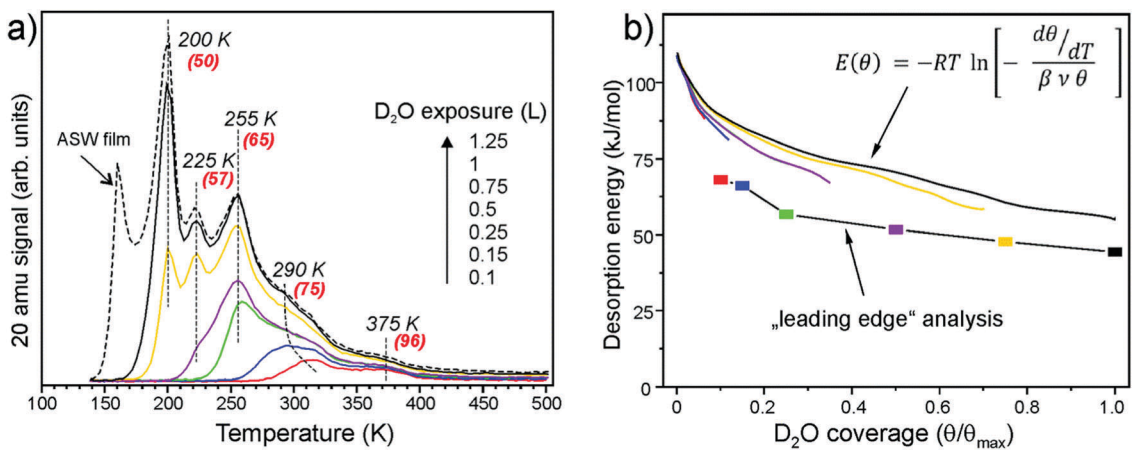


Fig. 1 (a) TPD spectra of $D_2O$ (20 amu) adsorbed at 140 K at increasing exposures as indicated. The heating rate was 3 K $s^{-1}$. At the highest exposure, the formation of an ASW film sets in. The numbers in parenthesis show desorption energies obtained by the Redhead formalism[48] using a pre-factor $\nu = 10^{13}$ $s^{-1}$. (b) Desorption energy as a function of water coverage obtained by a "leading edge" analysis[49] and by inversion analysis of the Polanyi–Wigner equation with a pre-factor $\nu = 10^{13}$ $s^{-1}$. Water coverage is normalized to the maximum obtained before the ASW related peak sets in.

 

pre-exponential factor. In this method, the desorption leading edge (the onset of desorption) is approximated by the Arrhenius-type behavior, and the changes in the initial coverage are neglected. When applied to the spectra shown in Fig. 1a, the analysis resulted in an energy of 68 kJ $mol^{-1}$ at low coverage that gradually decreases with the increasing coverage as shown in Fig. 1b. Basically, these results are very similar to those obtained by the Redhead analysis suggesting the pre-factor of $10^{13}$ $s^{-1}$ as a good approximation. Finally, we employed inversion analysis of the Polanyi–Wigner equation for the 1-st order desorption kinetics,[52] which results in a desorption energy ($E$):

$$E(\theta) = -RT \ln\left[-\frac{\frac{d\theta}{dT}}{\beta\nu\theta}\right]$$ where $\beta$ is a heating rate, $\nu$ is a pre-factor, and $\theta(T)$ is a temperature (or time) dependent coverage, which is determined by integration of the desorption curve. In this analysis, each spectrum can be transformed into a coverage dependent energy curve, all plotted in Fig. 1b, for $\nu = 10^{13}$ $s^{-1}$. Some deviation between the curves may be indicative of kinetic effects. These results show again, that the desorption energy decreases with increasing coverage, most markedly in the low coverage regime ($\theta/\theta_{max} < 0.1$). All applied methods give a similar picture.

Water coverage has been calibrated using $D_2O$ adsorption on the clean Pt(111) surface. It is well-documented in the literature that water forms a hexagonal ice film in one of two structures ($(\sqrt{3} \times \sqrt{3})R30^\circ$ or $(\sqrt{39} \times \sqrt{39})R16.1^\circ$) depending on exposure conditions.[53] The formation of ordered ice films manifests in TPD as desorption at a slightly higher temperature as compared to the ASW film. In our experiments, a $(\sqrt{3} \times \sqrt{3})R30^\circ$ ice film has been formed on Pt(111) as determined by LEED. Since the TPD measurements were performed with the same setup and on the same Pt crystal as used for the iron oxide film, all possible apparatus effects cancel. Therefore, the total amount of water adsorbed on $Fe_3O_4$(111) prior to the ASW film formation ($\theta_{max}$) corresponds to 2.3 ± 0.2 ML (where 1 ML is defined as one $H_2O$ molecule per $Fe_3O_4$(111) unit cell exposing one Fe ion, *i.e.* $3.2 \times 10^{14}$ $cm^{-2}$).

Well-resolved desorption peaks observed in our spectra (Fig. 1a) suggest desorption of species having discrete adsorption energies. In addition, sharp peaks imply that the corresponding water molecules desorb almost simultaneously in time, thus suggesting a certain degree of ordering at the surface, which was monitored by LEED.[26] LEED patterns of the ASW film, formed by 1.5 L of $D_2O$ exposure at 140 K and confirmed by TPD, only showed (1 × 1) diffraction spots of a $Fe_3O_4$(111) substrate. Also, in the low coverage regime, *i.e.* by adsorption at 300 K, LEED showed no new diffraction features. However, additional spots identified as $Fe_3O_4$(111)-(2 × 2) structure appeared if the sample is exposed to saturated amounts of water at temperatures between 200 and 255 K, that is in the range where thermal desorption peaks are observed. In addition, its formation was independent of the adsorption temperature, *i.e.* 140 K *vs.* 250 K. It only depends on the water coverage, suggesting that the ordering of water is thermodynamically driven.

### 3.2. Single-crystal adsorption calorimetry (SCAC)

Fig. 2a shows the average sticking probability measured as a function of water coverage at different surface temperatures between 120 and 300 K. Here we define the sticking probability as the probability that a gas water molecule strikes the surface, sticks, and remains on the surface until the next gas pulse starts (with the period of 5 s). Even if dissociation is occurring, the coverages reported here refer to the total amount of $D_2O$ that has adsorbed on the $Fe_3O_4$(111) surface, irrespective of the products formed. The initial sticking probabilities start off high, *i.e.* 0.71 to 0.93 (±0.05), at all temperatures. At 300, 240, and 180 K, the sticking probability approaches zero as $D_2O$ saturates the surface at an approximate coverage of 0.4, 1.0, and 2.2 ML, respectively, which are in nice agreement with coverages estimated by TPD (see above). At 120 K, the sticking probability remains high (~0.6) at high coverages, indicating growth of an ASW film.

The differential heats of adsorption of $D_2O$ on $Fe_3O_4$(111) at four different temperatures are shown in Fig. 2b. At 120 K, the

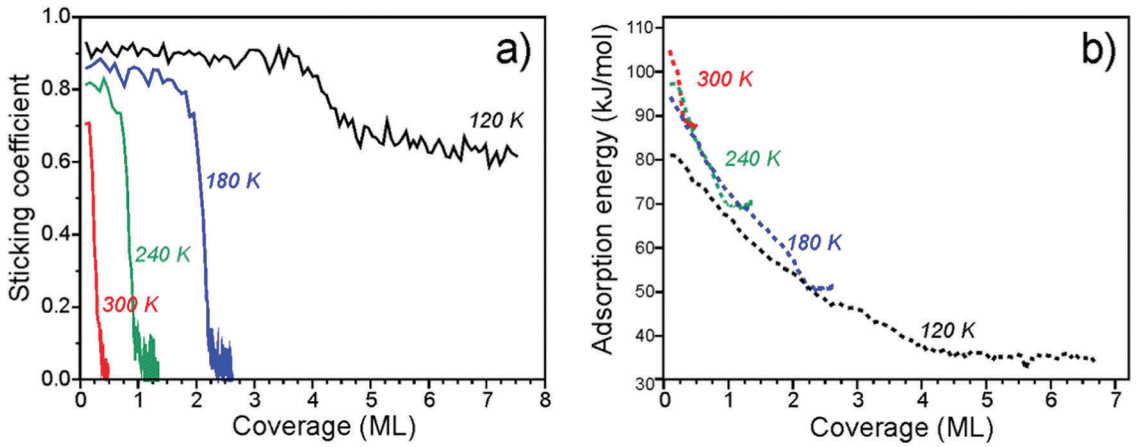


Fig. 2 Sticking coefficient (a) and differential heats of adsorption (b) of $D_2O$ on $Fe_3O_4$(111) as a function of coverage obtained at several different temperatures.

heat of adsorption is 82 kJ mol$^{-1}$ at the limit of low coverage and decreases with increasing coverage until multilayers of water are formed. The heats measured at 120 K are approximately 10 kJ mol$^{-1}$ lower than the heats measured at higher temperatures. This difference is likely related to kinetic effects of water dissociation, *i.e.* an activation barrier is required to overcome for dissociation. At higher temperatures (180–300 K), water initially adsorbs with a heat of 95–105 kJ mol$^{-1}$. All three of these heat of adsorption curves decrease with increasing coverage and largely overlap until each individual curve saturates.

The adsorption energies found here are consistent with what has been reported before for other oxide surfaces. For example, tetragonal zirconia ($ZrO_2$) values of 94 ± 19 and 70 ± 14 kJ mol$^{-1}$ have been obtained from adsorption experiments[54] and assigned to dissociative and molecular adsorption on the basis of DFT calculations performed for the (101) surface. The calculated average values were 123 and 95 kJ mol$^{-1}$ for water loadings of 0.5 and 1.0 molecules per $Zr^{4+}$ surface site.[55]

The measured adsorption energies and their coverage dependence are fully consistent with the TPD analysis above. Our calorimetric results give similar adsorption curves as determined by both inversion analysis of the Polanyi–Wigner equation and leading edge analysis. This suggests that the adsorption and dissociation of water is reversible under these conditions.

### 3.3. Infrared reflection–absorption spectroscopy (IRAS)

IRAS measurements were carried out in another UHV chamber on the films prepared using the same recipe and flashed to 900 K prior to the water exposure. TPD spectra revealed desorption profiles like those shown in Fig. 1, albeit with a lower resolution of the QMS available in the chamber (see Fig. S1 in the ESI†). This allows one to link the TPD and the IRAS results obtained in two different setups.

We first address water adsorption at room temperature. The four top spectra shown in Fig. 3 are recorded after sequential water pulses of 6 × 10$^{13}$ cm$^{-2}$ each. Two sharp bands at 2723 and 2680 cm$^{-1}$ appear immediately at almost saturated intensities. However, the spectra measured at 320 and 350 K depicted in the same panel suggest that these two bands behave independently. Indeed, the signal at 2680 cm$^{-1}$ shows up at temperatures as high as 350 K and slightly gains intensity upon dosing at 320 and 300 K. In contrast, the 2723 cm$^{-1}$ band only appears at 320 K and then doubles intensity at 300 K. Tentatively, the 2680 cm$^{-1}$ band can be assigned to adsorption on defects, whereas the 2723 cm$^{-1}$ band reflects the initial stages of adsorption on the regular sites.

Fig. 4a displays IRA spectra measured at 250 K. After the first pulse, the two bands (2722 and 2680 cm$^{-1}$) appear in the same manner as observed at 300 K (Fig. 3). At increasing dosage, both signals grow in intensity, but one shifts to a lower frequency (2718 cm$^{-1}$) while another to a higher (2688 cm$^{-1}$) frequency. In addition, a weak band at ~2565 cm$^{-1}$ is detected at high dosages. Spectral evolution, shown in more detail in Fig. 4b, indicates the presence of a new band at 2714 cm$^{-1}$ as a shoulder to the main band at 2722 cm$^{-1}$ which, in turn, gains

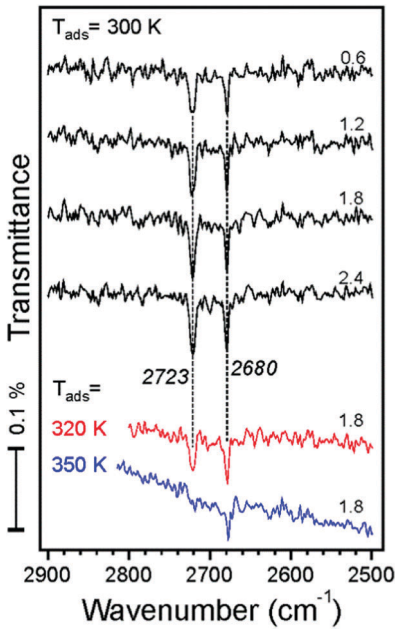


Fig. 3 IRA spectra recorded after dosing the $Fe_3O_4$(111) film to $D_2O$ molecular beam pulses (accumulative dosage (×10$^{14}$ cm$^{-2}$) is indicated). The spectra are offset for clarity.

intensity and shifts to 2120 cm$^{-1}$ at increasing coverage. This shift is quite small and is close to the spectral resolution (4 cm$^{-1}$). The changes in the low frequency band are more pronounced: the 2680 cm$^{-1}$ band attenuates, although may remain as a shoulder to the 2688 cm$^{-1}$ band, which definitely grows and starts to dominate in this region. The intensities of deconvoluted bands are plotted in Fig. 4c as a function of water dosage, although precise deconvolution may suffer from a relatively low signal-to-noise ratio. Apparently, both bands at 2720 and 2714 cm$^{-1}$ correlate with the one at 2688 cm$^{-1}$, and as such they all have likely the same origin. The band at 2680 cm$^{-1}$ practically vanishes at high exposures and inversely correlates with the one at ~2565 cm$^{-1}$. The latter falls in the range of hydrogen bonded species, and, therefore, may originate from further water interaction with OD on defect sites associated with the 2680 cm$^{-1}$ band.

To shed more light on the origin of spectral evolution we studied $H_2O$ adsorption onto the $D_2O$ pre-covered surface and *vice versa*. Fig. 5 compares IRA spectra obtained upon sequential pulses of $H_2O$ on the clean $Fe_3O_4$(111) surface and on the surface first exposed to one pulse of $D_2O$. The spectra for $H_2O$ adsorption on the clean surface exhibits essentially the same coverage-dependent behavior as for the case of $D_2O$ (see Fig. 4a). At increasing $H_2O$ dosage, the band at 3682 cm$^{-1}$ develops as a shoulder to the main band at 3690 cm$^{-1}$. In the low frequency region, the initial band at 3634 cm$^{-1}$ attenuates while the 3641 cm$^{-1}$ band gains in intensity. The first pulse of $D_2O$ onto the clean surface results in the same two bands (2722 and 2681 cm$^{-1}$) as discussed above (see Fig. 4a). When this surface is exposed to one pulse of $H_2O$, the 3682 and 3641 cm$^{-1}$ bands, which normally appear only at higher exposures, appear

 

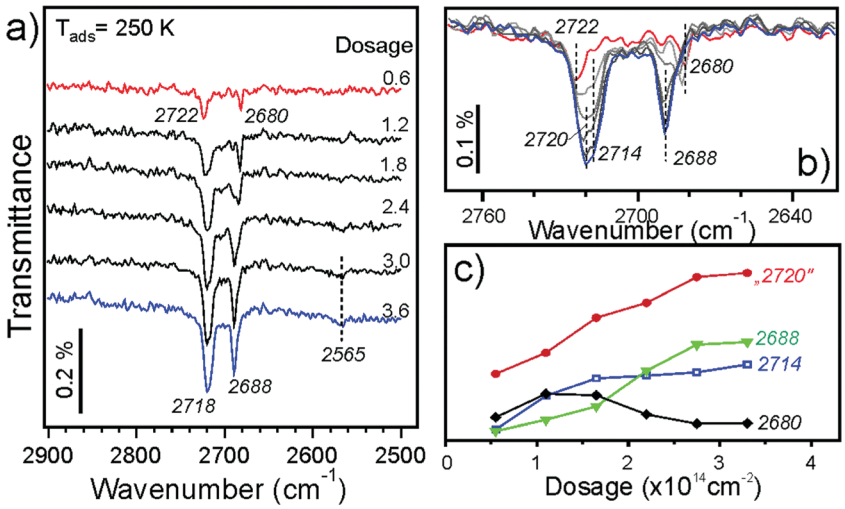


Fig. 4 (a) IRA spectra of $D_2O$ adsorption on $Fe_3O_4$(111) at 250 K at increasing dosage ($\times 10^{14}$ $cm^{-2}$). (b) The same spectra are superimposed to highlight spectral changes. The first and the last spectra are marked in red and in blue, respectively. (c) Integral intensity (in arb. units) of the deconvoluted bands as a function of $D_2O$ dosage.

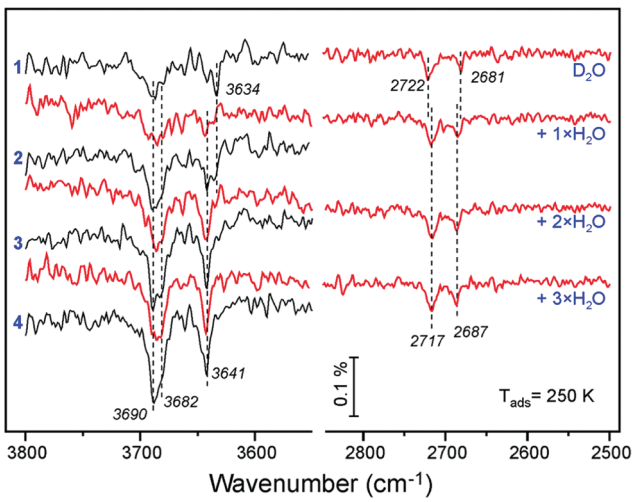


Fig. 5 $\nu$(OH) and $\nu$(OD) regions in the spectra obtained by $n$ pulses of $H_2O$ (as indicated) on the clean $Fe_3O_4$(111) surface (in black) and on the surface first exposed to one pulse of $D_2O$ (in red), all at 250 K. Each pulse contains $6 \times 10^{13}$ molecules $cm^{-2}$.

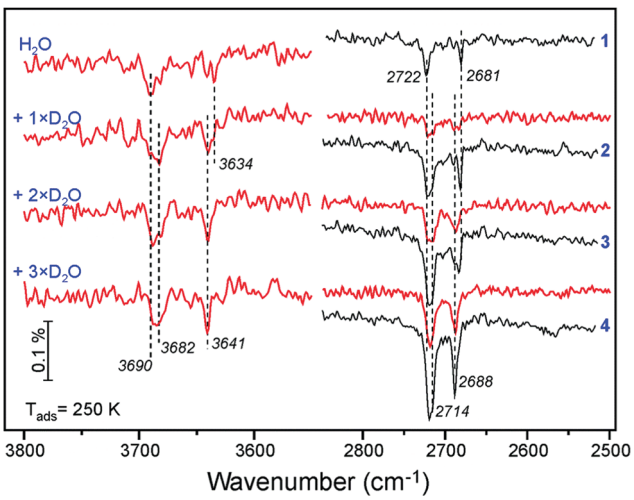


Fig. 6 $\nu$(OH) and $\nu$(OD) regions in the IRA spectra obtained by $n$ pulses of $D_2O$ (as indicated) on the clean $Fe_3O_4$(111) surface (in black) and on the surface first exposed to one pulse of $H_2O$ (in red), all at 250 K. Each pulse contains $6 \times 10^{13}$ molecules $cm^{-2}$.

immediately, since the species associated with the 3690 and 3634 $cm^{-1}$ bands were already formed from pre-exposed $D_2O$ as OD equivalent. It is interesting, however, that the $\nu$(OD) bands shift (to 2717 and 2687 $cm^{-1}$, respectively) in the same manner as observed for the case of pure $D_2O$ adsorption at increasing coverage (see Fig. 4b). Since the formation of new OD species upon $H_2O$ exposure is impossible, the observed shifts must be due to coverage-induced effects.

A similar picture evolves upon $D_2O$ adsorption onto the surface pre-covered with $H_2O$ (Fig. 6). Again, the first pulse of $D_2O$ causes the $\nu$(OH) bands shift, *i.e.* from 3690 to 3682 $cm^{-1}$, and from 3634 to 3641 $cm^{-1}$. Accordingly, the 2722 and 2681 $cm^{-1}$ bands in the $\nu$(OD) region are suppressed since the respective hydroxyl species are partially formed from pre-adsorbed $H_2O$. Therefore, the results of $H_2O$ and $D_2O$ co-adsorption experiments suggest that the spectral evolution in this low coverage regime is caused by progressive formation of hydroxyl species leading to coverage-induced frequency shifts. In principle, the shift may originate from interaction of neighboring oscillators or from the changes in electronic properties of the iron oxide surface as the coverage increases.

Now we address adsorption at higher coverages caused by adsorption at lower temperatures. Fig. 7a shows IRA spectra obtained at 200 K. The first pulse results in the 2722 $cm^{-1}$ band, as in the case for adsorption at 250 and 300 K. However, in the low frequency region a new band at 2669 $cm^{-1}$ appears, which was not previously observed. The band disappears after a few more pulses while the 2682 $cm^{-1}$ band increases in intensity, indicating that surface diffusion affects its formation.

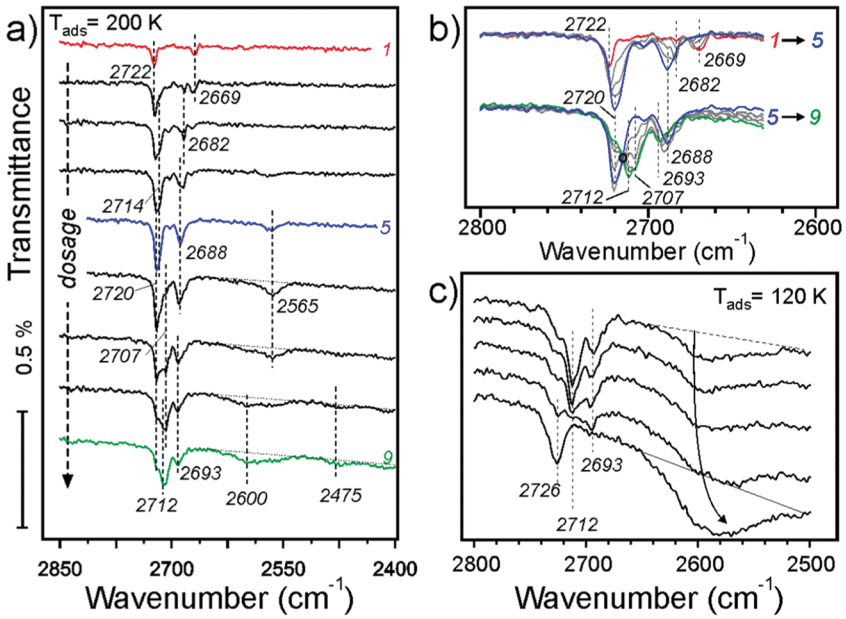


Fig. 7 (a) IRA spectra of $D_2O$ adsorption on $Fe_3O_4$(111) at 200 K at increasing dosage (from top to bottom). The spectra are offset for clarity. To highlight spectral changes, the same spectra are superimposed in two groups in panel (b) in the same color code as in panel (a). The isosbestic point is marked with a small circle. (c) Selected IRA spectra of $D_2O$ adsorption at 120 K, where the first spectrum corresponds to the coverage of the last (green) spectrum in panels (a) and (b). At high coverages, the ASW film starts to grow.

In principle, this finding is consistent with its tentative assignment of water reacting with defects.

At higher dosage the spectra follow the same evolution as for adsorption at 250 K (see Fig. 4b). The changes observed at further increasing coverage are highlighted in the second group of spectra (5–9) in Fig. 7b. The bands with an envelope peaked at 2720 $cm^{-1}$ attenuate while the bands at 2712 and 2707 $cm^{-1}$ grow up, resulting in an isosbestic point (marked with a circle). The picture is less obvious in the low frequency region. Apparently, the 2688 $cm^{-1}$ band shifts to 2693 $cm^{-1}$ and loses intensity. Finally, broad bands centered at 2600 and 2475 $cm^{-1}$ develop at highest exposures (see Fig. 7a), which are characteristic for systems with an extended network of hydrogen bonds.

Finally, water adsorption was examined at lower temperatures (120–180 K). As the spectral evolution at low coverages follows those studied at 200–300 K, Fig. 7c only displays the spectra obtained at high coverages, ultimately resulting in the ASW film. The latter shows an isolated band at 2726 $cm^{-1}$ and a broad band centered at $\sim$2580 $cm^{-1}$ which are assigned to stretching vibrations of dangling OH species at the surface and H-bonded OH species in water clusters, respectively. In this high coverage regime, the band at $\sim$2712 $cm^{-1}$ starts to attenuate before the band at 2693 $cm^{-1}$ does, both disappearing as the ASW film formation sets in.

To elucidate the adsorption mechanism, we employed isotopic labeling of oxygen in oxide and water with $^{18}O$. Our previously reported measurements at 250 K showed that the band at 2720 $cm^{-1}$ (see Fig. 4) involves oxygen in water ($O_w$) whereas the band at 2688 $cm^{-1}$ involves oxygen in the oxide ($O_s$). These results provided compelling evidence that water dissociates on anion–cation ($O^{2-}$–$Fe^{3+}$) pairs resulting in a terminal $O_wD$ hydroxyl on top of the $Fe_{tet1}$ ion with second D adsorbing on the surface O ion.

Further experiments with $D_2{}^{16}O$ adsorption on the $^{18}O$-labeled film showed isotopic shift also for the 2681 and 2669 $cm^{-1}$ bands (see Fig. S2 in ESI†) which are only observed at very low coverages and thus attributed to adsorption at defects. As the 2681 $cm^{-1}$ band may even appear before the terminal Fe–$O_w$D band sets in (see Fig. 3), it implies adsorption on such defects which may result in $O_wD$ species similar in nature to $O_sD$ species. This, for example, could be the case for water adsorption on oxygen vacancies resulting in $O_wD$ filling the vacancy and hence resembling $O_sD$ species.

Fig. 8 compares selected IRA spectra of $D_2{}^{16}O$ at moderate coverages obtained on the $Fe_3{}^{16}O_4$(111) and $Fe_3{}^{18}O_4$(111) films at 200 K. Again, the 2688 $cm^{-1}$ band experiences an isotopic shift ($\sim$16 $cm^{-1}$). Since the band at 2672 $cm^{-1}$ on the $^{18}O$-labelled film is now well-separated from the high-frequency region (compare to Fig. 7a), it becomes clear that the band slightly blue-shifts and considerably attenuates at increasing coverages at which isosbestic behavior for the high-frequency region is observed (Fig. 7b). This implies that $O_sD$ species are involved in further water coordination *via* H-bonding which usually causes a strong red-shift (about 250 $cm^{-1}$) and band broadening. Interestingly, the weak band at 2565 $cm^{-1}$ does not shift upon $^{18}O$ labeling, indicating that this vibrational band solely involves $O_wD$ species which experience hydrogen bonding, based on a strongly red-shifted frequency as compared to a terminal OD. Overall, the results of isotopic experiments showed that only the IRA bands in the 2690–2670 $cm^{-1}$ region include oxygen in the film, and as such their spectral changes are associated with coverage-dependent evolution of $O_sD$ hydroxyls that result from water dissociation.

 

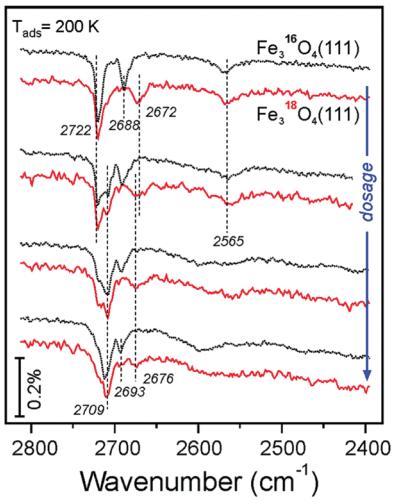


Fig. 8 Selected IRA spectra recorded upon $D_2{}^{16}O$ adsorption at 200 K onto $Fe_3{}^{16}O_4(111)$ (in black) and $Fe_3{}^{18}O_4(111)$ (in red) films. The spectra are offset and grouped in pairs for direct comparison.

### 3.4. Density functional theory (DFT) results

To rationalize the coverage-dependent IR spectra, we performed DFT calculations of harmonic wavenumbers for the water species in relevant energy minimum structures. For a direct comparison with observed fundamentals, we report scaled wavenumbers that effectively account for both systematic errors in the harmonic force constants and neglected anharmonicities. We use the scaling factor 0.9935 obtained from the ratio of observed and calculated wavenumbers for the symmetric and antisymmetric OH (OD) stretches of the gas phase water molecule as described in ref. 16 and 26.

Starting with a single water molecule per (2 × 2) unit cell, the computational results show that dissociative adsorption is thermodynamically most favorable. The energy minimum structure **1** shown in Fig. 9 involves two hydoxyl species $O_wD$ as well as $O_sD$ on the surface, which are schematically shown in Fig. 10. As outlined in ref. 13, dissociative adsorption of a single water molecule is more favorable (by ∼14 kJ mol$^{-1}$) than molecular (non-dissociative) adsorption. Note also that the previous theoretical calculations[25] revealed a low barrier, about

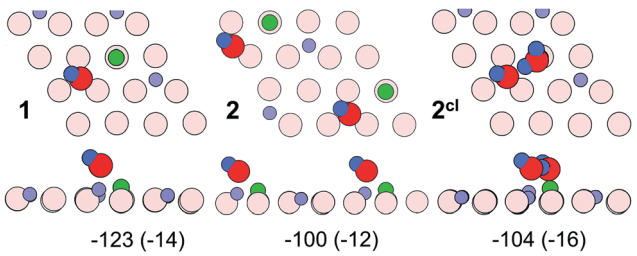


Fig. 9 Top and side views of a single dissociated water molecule (structure **1**), two dissociated molecules (**2**), and a "half-dissociated" dimer complex (**2$^{cl}$**) on the $Fe_3O_4(111)$-(2 × 2) cell obtained using PBE+*U*. Adsorption energies per molecule (in kJ mol$^{-1}$) are given below individual structures. The dispersion contribution per molecule is given in parenthesis. Surface $Fe_{tet1}$ ions are violet, surface $O_s$ ions are pink, oxygen in water ($O_w$) is red, proton atop $O_s$ is green, hydrogen in water or hydroxyl is blue.

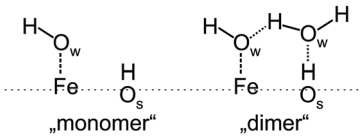


Fig. 10 Schemes for the dissociatively adsorbed water monomer (left) and water dimer (right).

0.1 eV, for the dissociative reaction pathway of a single water molecule. Therefore, thermodynamically driven water dissociation is expected not to be kinetically hindered.

The $O_wD$ and $O_sD$ groups are clearly discernable *via* their stretching wavenumbers of 2736 cm$^{-1}$ for $O_wD$ and 2699 cm$^{-1}$ for $O_sD$. These values, separated by $\Delta\nu$ = 37 cm$^{-1}$, compare well with the bands at 2720 and 2688 cm$^{-1}$ ($\Delta\nu$ = 32 cm$^{-1}$) observed in experiments at low coverage (see Fig. 4). This assignment assumes that the first appearing band at 2681 cm$^{-1}$ relates to adsorption on defects.

For two water molecules per (2 × 2) cell, one must consider the formation of a second dissociated "monomer" (structure **2**) as well as a half-dissociated "dimer" complex (structure **2$^{cl}$**, see Fig. 10, right panel). Henceforth, we use the superscript **cl** to highlight water clustering. The calculated adsorption energies per water molecule in the cell (−100 (−112) and −104 (−120) kJ mol$^{-1}$ for the structures **2** and **2$^{cl}$**, respectively) suggest that both structures are equally stable. The values given in parenthesis include the Grimme D2 dispersion correction (see Table S3 in the ESI†). The computed wavenumbers for $O_wD$ and $O_sD$ stretching vibrations of structure **2** (2729 and 2697 cm$^{-1}$) suggest a small red-shift for the $O_wD$ band when compared to a single monomer in the cell (structure **1**), *i.e.*, in agreement with the experimental finding at low coverage (Fig. 4). As far as the dimer structure **2$^{cl}$** is concerned, the computed wavenumbers for the stretching modes, 2735 cm$^{-1}$ for $O_wD$ coordinated to Fe, and 2732 cm$^{-1}$ for terminal OD in the non-dissociated water molecule, are close and the corresponding bands may overlap. Therefore, the spontaneous formation of a dimer from the onset will manifest itself in a single, presumably broad band at a frequency close to that of "monomeric" Fe–$O_wD$. However, the dimer lacks an $O_sD$-related band in this region, since all hydrogen-bonded OD species in this structure experience a strong red-shift of about 300–350 cm$^{-1}$.

Fig. 11 shows energy minimum structures for two, three, and four water molecules per (2 × 2) surface unit cell that correspond to the respective coverages of 0.5, 0.75 and 1 ML. Comparison of the adsorption energies per water molecule (displayed below each structure) suggests that the formation of dimers may have a stabilizing effect on a water ad-layer. For example, two dimers in the cell (**4$^{cl}$**) are more stable than four monomers (**4**).

Scaled harmonic wavenumbers obtained for these structures (see Table S1 in the ESI†) shows that high-frequency bands associated with Fe–$O_wD$ species in monomeric structures **2**, **3**, and **4** exhibit an envelope centered at a wavenumber close to the one observed for a single monomer (**1**). A similar effect is observed for the $O_sD$ region. These results agree with experimental spectra

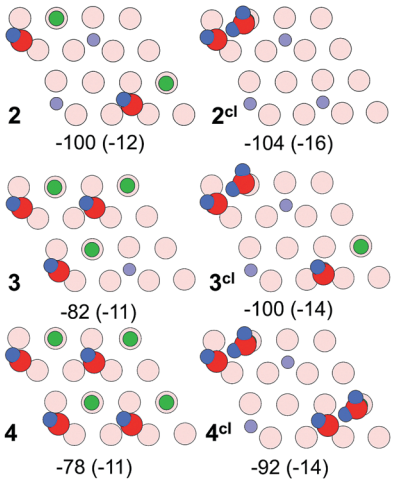


Fig. 11 Top views of energy minimum structures involving two, three and four water molecules per the $Fe_3O_4$(111)-(2 × 2) cell. The adsorption energies (in kJ mol$^{-1}$) are indicated below individual structures. The dispersion contribution per molecule is given in parenthesis. (Color code as in Fig. 9).

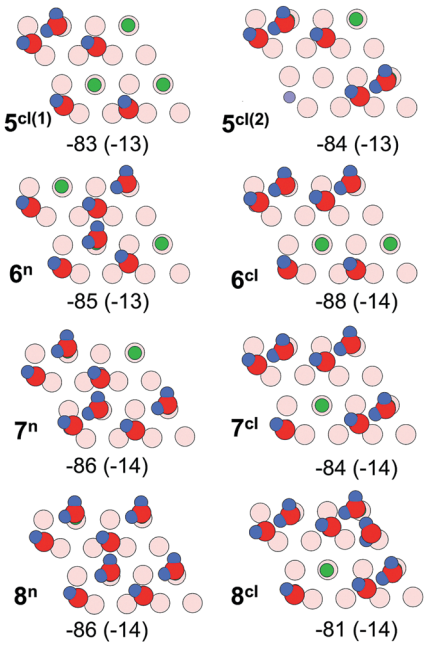


Fig. 12 Top views of energy minimum structures involving five to eight water molecules per $Fe_3O_4$(111)-(2 × 2) cell. The adsorption energies (in kJ mol$^{-1}$) are indicated below individual structures. The dispersion contribution per molecule is given in parenthesis. (Color code as in Fig. 9).

(Fig. 4) showing that both bands gain intensity at increasing dosage and only slightly shift, most likely due to crowding effects (see Fig. 5 and 6). For comparison, structure $\mathbf{4^{cl}}$ not only lacks the experimentally observed $O_sD$ band in this region, but also features the $O_wD$ band at ~2715 cm$^{-1}$, that is strongly (by *ca.* 15–20 cm$^{-1}$) red-shifted with respect to the monomeric Fe–$O_wD$ bands. Also, structure $\mathbf{3^{cl}}$ involving a coexisting dimer and a monomer reveals a considerably shifted $O_sD$ band (2710 cm$^{-1}$), *i.e.* not observed in experiment. This suggests that water first dissociates creating monomeric species, although adventitious dimer formation cannot be excluded at coverages approaching 1 ML.

Fig. 12 displays water adlayer structures obtained at higher coverage of five to eight water molecules per (2 × 2) cell, *i.e.* 1.25–2.0 ML. At these high coverages, all structures feature at least one dimer. In addition, we considered structures with dimers forming a hydrogen bonded network, henceforth labelled with the superscript **n**. Fig. 13 compares the calculated wavenumbers for selected structures. For other structures not shown here, we refer to Fig. S4 and Table S1 in the ESI.† Among the possible candidates, the calculated wavenumbers of $\mathbf{5^{cl(2)}}$ and $\mathbf{6^{n}}$ agree best with the experimental results obtained at 200 K (Fig. 7a) up to saturation corresponding to approximately 1.5 ML. The calculations revealed the red-shift of about 16 cm$^{-1}$ for $O_wD$ stretching mode (blue sticks in Fig. 13) and the blue-shift of about 5 cm$^{-1}$ for the $O_sD$ stretching (green sticks) taking the averaged wavenumbers for structures **1–4** as reference. Certainly, the formation of water aggregates occurs at the expense of monomeric species, ultimately resulting in the isosbestic point observed in IRAS (Fig. 7b). At further increasing coverage of 1.75 and 2 ML, all computed OD bands start to overlap and coalesce into one band, which (taking the systematic deviation into account) can be associated with a band at 2712 cm$^{-1}$ (Fig. 7c) dominating the spectra at 120 K prior to formation of the ASW film.

With respect to a comparison of TPD desorption energies discussed in Section 3.1. with calculated values, we refer to

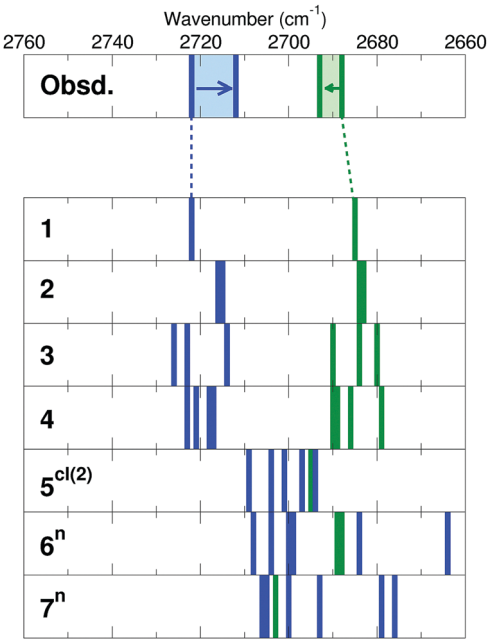


Fig. 13 Stick representation of $O_wD$ (blue) and $O_sD$ (green) stretching modes (cm$^{-1}$) calculated for structures shown in Fig. 9, 11 and 12 (see also Fig. S4 in the ESI†). Note that all calculated wavenumbers are red-shifted by 14 cm$^{-1}$ in order to facilitate the comparison with the experimental results shown on top panel. Original numbers are presented in Table S1 in the ESI.†

ref. 50 and 56. The experimental values are Arrhenius activation energies of desorption and differ from the enthalpy of desorption by *RT*. Table 1 summarizes (electronic or DFT) adsorption energies,

Table 1 Coverage, adsorption energies, zero-point-vibrational-energy correction (ZPVE), and heat of adsorption including $RT$ for $T$ = 200 K (kJ mol$^{-1}$). Results are given per $H_2O$ molecule

| | $\theta$ | $\Delta E^{ads}$ | ΔZPVE[a] | $\Delta H^{ads}$ | $\Delta H^{ads} + RT$ |
|---|---|---|---|---|---|
| **1** | 0.25 | −123.6 | 19.6 | −104.0 | −102.3 |
| **2** | 0.5 | −100.0 | 20.3 | −79.7 | −77.9 |
| **2$^{cl}$** | 0.5 | −103.7 | 15.0 | −88.7 | −87.1 |
| **3** | 0.75 | −82.1 | 19.4 | −62.7 | −61.1 |
| **3$^{cl}$** | 0.75 | −100.0 | 16.8 | −83.2 | −81.6 |
| **4** | 1 | −78.0 | 19.6 | −58.4 | −56.7 |
| **4$^{cl}$** | 1 | −92.2 | 15.7 | −76.5 | −74.9 |
| **5$^{cl(1)}$** | 1.25 | −83.5 | 18.0 | −65.5 | −63.8 |
| **5$^{cl(2)}$** | 1.25 | −83.9 | 16.5 | −67.4 | −65.8 |
| **6$^{n}$** | 1.5 | −85.1 | 17.3 | −67.8 | −66.2 |
| **6$^{cl}$** | 1.5 | −88.3 | 16.9 | −71.4 | −69.7 |
| **7$^{n}$** | 1.75 | −86.3 | 15.8 | −70.5 | −68.8 |
| **7$^{cl}$** | 1.75 | −83.7 | 16.3 | −67.4 | −65.8 |
| **8$^{n}$** | 2 | −85.8 | 15.9 | −69.9 | −68.3 |
| **8$^{cl}$** | 2 | −80.5 | 15.7 | −64.8 | −63.2 |

[a] The ZPVE for the $H_2O$ molecule is 54.8 kJ mol$^{-1}$.

$\Delta E^{ads}$, the zero-point-vibrational-energy correction (ZPVE), and the enthalpy in kJ mol$^{-1}$ per $H_2O$ molecule. The calculated value for $\Delta H^{ads}$ of −102 kJ mol$^{-1}$ for structure **1** agrees well with the differential heats of adsorption obtained by microcalorimetry (−95 to −105 kJ mol$^{-1}$, see Section 3.2) and the TPD desorption energies of ∼110 kJ mol$^{-1}$ at low coverage. This value is lowered by −14 kJ mol$^{-1}$ per water molecule upon inclusion of dispersion effects (see Table S3 in the ESI†). The calculated adsorption energies per water molecule revealed all structures shown in Fig. 12 to be thermodynamically stable, with network structures becoming more favorable at increasing coverage (see ref. 26 for a more detailed analysis).

# 4. Conclusions

A combined thermal desorption, microcalorimetry, and IR spectroscopy study was carried out for water adsorption on the well-defined $Fe_3O_4$(111) surfaces as a function of temperature and dosage. The results were corroborated by DFT (PBE+$U$) calculations using a $Fe_3O_4$(111)-(2 × 2) slab model to address energy minimum structures and vibrational properties of adsorbed water species in a wide range of coverages (0.25–2 ML).

Water adsorption on defects dominates at high temperatures, *e.g.* above ∼320 K. At increasing water coverage, dissociative adsorption takes place on the regular $Fe_{tet1}$-terminated surface thus resulting in a terminal Fe–$O_w$D hydroxyl showing an IRA band at 2720 cm$^{-1}$ and an $O_s$D hydroxyl band at 2688 cm$^{-1}$. Our DFT calculations are compatible with this observation. Specifically, the computed adsorption enthalpy of the monomer is −102 kJ mol$^{-1}$ and the aforementioned OD bands are 2736 and 2699 cm$^{-1}$, respectively. At increasing coverages up to 1 ML, both bands slightly shift as suggested by $D_2O$ and $H_2O$ co-adsorption experiments. At further increasing coverage, water molecules start to form dimer complexes with pre-existing hydroxyls which is reflected *via* an isosbestic point in the IRA spectra. At high coverages, dimers and oligomers ultimately assemble into an ordered (2 × 2) hydrogen-bonded network structure prior to the formation of a multilayer solid water film. Again, our DFT results are compatible with the observed shifts at higher coverage and adsorption energies predict thermodynamically favorable H-bonded 2D network structures. These results highlight a delicate balance that exists in water adlayers on oxide surfaces where hydrogen bonding may play an important role in stabilizing particular structures.

# Conflicts of interest

There are no conflicts to declare.

# Acknowledgements

This work has been supported by the Deutsche Forschungsgemeinschaft through SFB 1109, by the Fonds der Chemischen Industrie as well as by generous grants for computing time at the North-German Supercomputing Alliance in Berlin and Hannover. JP gratefully acknowledges the Stiftung Industrieforschung, Humboldt-Universität zu Berlin for financial support. FM thanks the International Max-Planck Research School "Functional Interfaces in Physics and Chemistry" for a fellowship. Open Access funding provided by the Max Planck Society.

# References

1 M. A. Henderson, *Surf. Sci. Rep.*, 2002, **46**, 1–308.
2 P. A. Thiel and T. E. Madey, *Surf. Sci. Rep.*, 1987, **7**, 211–385.
3 W. Weiss and W. Ranke, *Prog. Surf. Sci.*, 2002, **70**, 1–151.
4 G. S. Parkinson, *Surf. Sci. Rep.*, 2016, **71**, 272–365.
5 H. Kuhlenbeck, S. Shaikhutdinov and H.-J. Freund, *Chem. Rev.*, 2013, **113**, 3986–4034.
6 M. Ritter and W. Weiss, *Surf. Sci.*, 1999, **432**, 81–94.
7 S. K. Shaikhutdinov, M. Ritter, X. G. Wang, H. Over and W. Weiss, *Phys. Rev. B: Condens. Matter Mater. Phys.*, 1999, **60**, 11062–11069.
8 A. Sala, H. Marchetto, Z. H. Qin, S. Shaikhutdinov, T. Schmidt and H. J. Freund, *Phys. Rev. B: Condens. Matter Mater. Phys.*, 2012, **86**, 155430.
9 A. Kiejna, T. Ossowski and T. Pabisiak, *Phys. Rev. B: Condens. Matter Mater. Phys.*, 2012, **85**, 125414.
10 J. Noh, O. I. Osman, S. G. Aziz, P. Winget and J.-L. Brédas, *Chem. Mater.*, 2015, **27**, 5856–5867.
11 X. Yu, C.-F. Huo, Y.-W. Li, J. Wang and H. Jiao, *Surf. Sci.*, 2012, **606**, 872–879.
12 D. Santos-Carballal, A. Roldan, R. Grau-Crespo and N. H. de Leeuw, *Phys. Chem. Chem. Phys.*, 2014, **16**, 21082–21097.
13 X. Li and J. Paier, *J. Phys. Chem. C*, 2016, **120**, 1056–1065.
14 M. E. Grillo, M. W. Finnis and W. Ranke, *Phys. Rev. B: Condens. Matter Mater. Phys.*, 2008, **77**, 075407.
15 C. Lemire, R. Meyer, V. E. Henrich, S. Shaikhutdinov and H. J. Freund, *Surf. Sci.*, 2004, **572**, 103–114.
16 P. Dementyev, K.-H. Dostert, F. Ivars-Barceló, C. P. O'Brien, F. Mirabella, S. Schauermann, X. Li, J. Paier, J. Sauer and H.-J. Freund, *Angew. Chem., Int. Ed.*, 2015, **54**, 13942–13946.

17 X. Li, J. Paier, J. Sauer, F. Mirabella, E. Zaki, F. Ivars-Barceló, S. Shaikhutdinov and H. J. Freund, *J. Phys. Chem. B*, 2018, **122**, 527–533.
18 T. Kendelewicz, P. Liu, C. S. Doyle, G. E. Brown Jr, E. J. Nelson and S. A. Chambers, *Surf. Sci.*, 2000, **453**, 32–46.
19 R. S. Cutting, C. A. Muryn, D. J. Vaughan and G. Thornton, *Surf. Sci.*, 2008, **602**, 1155–1165.
20 Y. Joseph, C. Kuhrs, W. Ranke, M. Ritter and W. Weiss, *Chem. Phys. Lett.*, 1999, **314**, 195–202.
21 Y. Joseph, W. Ranke and W. Weiss, *J. Phys. Chem. B*, 2000, **104**, 3224–3236.
22 K. Adib, G. G. Totir, J. P. Fitts, K. T. Rim, T. Mueller, G. W. Flynn, S. A. Joyce and R. M. Osgood Jr, *Surf. Sci.*, 2003, **537**, 191–204.
23 U. Leist, W. Ranke and K. Al-Shamery, *Phys. Chem. Chem. Phys.*, 2003, **5**, 2435–2441.
24 S. Shaikhutdinov and W. Weiss, *J. Mol. Catal. A: Chem.*, 2000, **158**, 129–133.
25 K. T. Rim, D. Eom, S.-W. Chan, M. Flytzani-Stephanopoulos, G. W. Flynn, X.-D. Wen and E. R. Batista, *J. Am. Chem. Soc.*, 2012, **134**, 18979–18985.
26 F. Mirabella, E. Zaki, F. Ivars-Barcelo, X. Li, J. Paier, J. Sauer, S. Shaikhutdinov and H.-J. Freund, *Angew. Chem., Int. Ed.*, 2017, **57**, 1409–1413.
27 T. Yang, X.-d. Wen, D.-b. Cao, Y.-w. Li, J.-g. Wang and C.-f. Huo, *J. Fuel Chem. Technol.*, 2009, **37**, 506–512.
28 C. Zhou, Q. Zhang, L. Chen, B. Han, G. Ni, J. Wu, D. Garg and H. Cheng, *J. Phys. Chem. C*, 2010, **114**, 21405–21410.
29 J.-H. Fischer-Wolfarth, J. Hartmann, J. A. Farmer, J. M. Flores-Camacho, C. T. Campbell, S. Schauermann and H.-J. Freund, *Rev. Sci. Instrum.*, 2011, **82**, 024102.
30 D. A. King and M. G. Wells, *Surf. Sci.*, 1972, **29**, 454–482.
31 P. E. Blöchl, *Phys. Rev. B: Condens. Matter Mater. Phys.*, 1994, **50**, 17953–17979.
32 G. Kresse and D. Joubert, *Phys. Rev. B: Condens. Matter Mater. Phys.*, 1999, **59**, 1758–1775.
33 G. Kresse and J. Furthmüller, *Comput. Mater. Sci.*, 1996, **6**, 15–50.
34 G. Kresse and J. Furthmüller, *Phys. Rev. B: Condens. Matter Mater. Phys.*, 1996, **54**, 11169–11186.
35 V. I. Anisimov, J. Zaanen and O. K. Andersen, *Phys. Rev. B: Condens. Matter Mater. Phys.*, 1991, **44**, 943–954.
36 A. I. Liechtenstein, V. I. Anisimov and J. Zaanen, *Phys. Rev. B: Condens. Matter Mater. Phys.*, 1995, **52**, R5467–R5470.
37 S. L. Dudarev, G. A. Botton, S. Y. Savrasov, C. J. Humphreys and A. P. Sutton, *Phys. Rev. B: Condens. Matter Mater. Phys.*, 1998, **57**, 1505–1509.
38 O. Bengone, M. Alouani, P. Blöchl and J. Hugel, *Phys. Rev. B: Condens. Matter Mater. Phys.*, 2000, **62**, 16392–16401.
39 I. Leonov, A. N. Yaresko, V. N. Antonov, M. A. Korotin and V. I. Anisimov, *Phys. Rev. Lett.*, 2004, **93**, 146404.
40 H. T. Jeng, G. Y. Guo and D. J. Huang, *Phys. Rev. Lett.*, 2004, **93**, 156403.
41 X. Yu, Y. Li, Y.-W. Li, J. Wang and H. Jiao, *J. Phys. Chem. C*, 2013, **117**, 7648–7655.
42 J. P. Perdew, K. Burke and M. Ernzerhof, *Phys. Rev. Lett.*, 1996, **77**, 3865–3868.
43 A. Önsten, D. Stoltz, P. Palmgren, S. Yu, M. Göthelid and U. O. Karlsson, *J. Phys. Chem. C*, 2010, **114**, 11157–11161.
44 H. J. Monkhorst and J. D. Pack, *Phys. Rev. B: Condens. Matter Mater. Phys.*, 1976, **13**, 5188–5192.
45 G. Makov and M. C. Payne, *Phys. Rev. B: Condens. Matter Mater. Phys.*, 1995, **51**, 4014–4022.
46 S. Grimme, *J. Comput. Chem.*, 2006, **27**, 1787–1799.
47 T. Kerber, M. Sierka and J. Sauer, *J. Comput. Chem.*, 2008, **29**, 2088–2097.
48 P. A. Redhead, *Vacuum*, 1962, **12**, 203–211.
49 A. M. de Jong and J. W. Niemantsverdriet, *Surf. Sci.*, 1990, **233**, 355–365.
50 A. D. Boese and J. Sauer, *Phys. Chem. Chem. Phys.*, 2013, **15**, 16481–16493.
51 E. Habenschaden and J. Küppers, *Surf. Sci.*, 1984, **138**, L147–L150.
52 S. L. Tait, Z. Dohnálek, C. T. Campbell and B. D. Kay, *J. Chem. Phys.*, 2005, **122**, 164707.
53 S. Haq, J. Harnett and A. Hodgson, *Surf. Sci.*, 2002, **505**, 171–182.
54 S. Raz, K. Sasaki, J. Maier and I. Riess, *Solid State Ionics*, 2001, **143**, 181–204.
55 A. Hofmann and J. Sauer, *J. Phys. Chem. B*, 2004, **108**, 14652–14662.
56 S. Tosoni and J. Sauer, *Phys. Chem. Chem. Phys.*, 2010, **12**, 14330–14340.